ADA284984

Intermetallic Matrix Composites III

Symposium held April 4–6, 1994, San Francisco, California, U.S.A.

EDITORS:

J.A. Graves

GE Corporate Research & Development
Schenectady, New York, U.S.A.

R.R. Bowman

NASA Lewis Research Center
Cleveland, Ohio, U.S.A.

J.J. Lewandowski

Case Western Reserve University
Cleveland, Ohio, U.S.A.

94-30976

DTIC QUALITY INSPECTED 3

94 9 28 036

Single article reprints from this publication are available through
University Microfilms Inc., 300 North Zeeb Road, Ann Arbor, Michigan 48106

CODEN: MRSPDH

This book has been registered with Copyright Clearance Center, Inc. For further information, please contact the Copyright Clearance Center, Salem, Massachusetts.

Intermetallic Matrix Composites III

Accesion For		
NTIS CRA&I	☑	
DTIC TAB	☐	
Unannounced	☐	
Justification		
By		
Distribution /		
Availability Codes		
Dist	Avail and / or Special	
A-1		

Contents

PART I: INTERMETALLIC OVERVIEWS AND PROCESSING

PART II: FIBERS FOR IMC's

*Invited Paper

*Invited Paper

*Invited Paper

viii

Preface

These are the proceedings of the third MRS symposium dedicated to coverage of current research and development of intermetallic composites and multiphase materials based upon intermetallic constituents. The vigorous discussions and technical interchange, both during and after the symposium sessions, reflected the broad interest in this interdisciplinary field. This symposium focused on the basic science and engineering development of the materials, and approaches currently being pursued to achieve the requirements for advanced high temperature structural materials.

This symposium was built upon the strong foundation of the preceding two MRS symposia on this subject matter, held in 1990 and 1992. A strong emphasis on processing, chemical compatibility and first tier mechanical properties in the first MRS symposium on intermetallic composites (Intermetallic Matrix Composites, V. 194) was supplemented in the second symposium (Intermetallic Matrix Composites II, V. 273) by an expanded treatment of first and second tier mechanical properties, conventional and novel processing approaches, and testing techniques to quantify both interface and composite properties. With many of the larger, government-sponsored programs on intermetallic composites peaking over the last few years, and the broad down-turn in the aerospace industry, this third symposium served to summarize the major activities and development status in each class of intermetallic composite, and to illuminate future research directions. The symposium comprised twelve invited overview discussions, and over 40 contributed research papers on intermetallic composites. Following a critical review of intermetallic composite applications, overviews of advanced composite processing and characterization techniques, and critical review of each major class of intermetallic composites set the stage for detailed technical discussions and debate throughout the symposium.

This symposium was sponsored by the Office of Naval Research, NASA Lewis Research Center, Rockwell International Science Center, Concurrent Technologies Corporation and Saphikon, Inc. The support of these institutions is graciously acknowledged. We would also like to thank Ms. Phyllis Liu for her help in arranging the front and back matter for the proceedings. Finally, we would like to express our appreciation for the contribution of the session chairs and the individuals who served as reviewers for the manuscripts. Their efforts were vital to the successful conduct of the symposium and the rapid publication of these proceedings.

J.A. Graves
R.R. Bowman
J.J. Lewandowski

June 1994

MATERIALS RESEARCH SOCIETY SYMPOSIUM PROCEEDINGS

MATERIALS RESEARCH SOCIETY SYMPOSIUM PROCEEDINGS

PART I

**Intermetallic Overviews
and Processing**

ISSUES IN POTENTIAL IMC APPLICATION
FOR AEROSPACE STRUCTURES

CHARLES H. WARD* AND ANDREW S. CULBERTSON**
*Air Force Office of Scientific Research, AFOSR/NC, Bolling AFB, DC 20332-0001
**Naval Air Warfare Center, Aircraft Division, PO Box 7176, Trenton, NJ 08628-0176

ABSTRACT

Intermetallic-matrix composites (IMCs) are intended for applications involving higher temperatures and stresses than conventional metallic matrix composites. Consequently, environmental effects, thermo-mechanical fatigue, interfacial thermodynamic stability, creep resistance, processing and cost are only a few of the obstacles to introduction in real products. The primary goal of current IMC development efforts is to provide 'revolutionary' materials for components that are enabling technologies in advanced demonstrator gas turbine engines. As compared to production applications, the hurdles for entry into demonstrator engine programs are not as high due to the limited operating time and the small number of parts to be produced. This paper examines the barriers to the introduction of IMCs in the context of application to production aerospace structures.

INTRODUCTION

Under a very broad definition, all material systems comprised of more than one phase could be considered to be composited. For the purpose of this paper, therefore, we must define a much narrower scope for discussion. We have limited the definition of an intermetallic-matrix composite to a material system based on an intermetallic-matrix with either continuous or discontinuous ceramic reinforcement. We decided to make this distinction between ceramic reinforced composites and eutectic "in-situ composites" as, in our opinion, the eutectic alloys have much more in common with, and are in many ways indistinguishable from, "monolithic" intermetallics. This is not to say that underlying scientific concepts in processing, thermodynamics and mechanics can not apply to both intermetallics and IMCs. Obviously there are common issues to be resolved in both before application can be considered. However, there are unique barriers to be addressed in IMCs before use can be realized, and they will be the focus of this paper. Most IMCs of engineering interest fall into the continuously reinforced category since the largest improvement in mechanical properties can be realized with this architecture. Indeed, the only serious discontinuously reinforced IMC candidate for application is TiAl with a TiB_2 dispersion. This material, dispersion reinforced by the XD^{TM} process, is not being considered for application due to its composite-derived properties, but rather the TiB_2 is used as an inoculant during the casting operation to refine grain size.

Intermetallic-matrix composites have been pursued for application in aerospace systems. In particular, use of these materials in gas turbine engine applications would provide a substantial payoff. It is important to note that we will be discussing the potential for application in production systems. Therefore, the criticisms of particular IMC materials systems currently of interest in the scientific community must be considered in this light.

POTENTIAL APPLICATIONS

Discussion of applications for intermetallic-matrix composites will be limited to the aerospace industry as it is uniquely able to justify the expense of IMCs. IMCs have become an attractive candidate material for application due to their potential for providing the aerospace designer with a material possessing high specific strength and higher use temperature. This translates to lighter weight aerospace systems and increased operating temperatures. For a gas turbine engine this means greater engine performance, normally expressed as increased engine thrust-, or power-, to-weight ratio. A smaller, higher performance engine for a similarly sized airframe reduces fuel consumption and lowers life-cycle cost allowing the higher initial cost of an engine containing IMC parts to be justified. Typical values placed on life-cycle cost savings and performance premiums are $4000 per kilogram of weight saved in a military engine, and $600-1200 per kilogram of weight saved in a traditional commercial engine. The greatest payoff for IMC turbine engine application is in rotating components due to their ability to operate at higher stresses and decrease the momentum of rotating components. As an example, a common estimate is that one half a kilogram saved in a rotating blade cascades to a total of two to three kilograms saved in the system though a reduction in the required weight in the disk, shaft, bearings and support structure.

One-for-one substitution of parts made of IMCs for those made from conventional materials used in existing engines, and even those currently on the drawing board, is improbable. Aside from the technical reasons, the business reasons being that insufficient payoff will be realized through their use to justify their expense. IMCs would be most cost effective when the entire system design takes advantage of the cascading effects of their increased properties. The IMCs being substantially different in their mechanical behavior, a redesign of the component(s) would likely be required, significantly adding to the expense. Playing a large role in this business decision is the very substantial costs required to qualify a new material for use in an engine. The total expense involves not only capitalization of manufacturing facilities, but generation of a significant data base sufficient for full life design and in-service part life prediction and management, logistics and repair issues, as well as new designs and engine qualification testing -- an investment that can top one-hundred-million dollars.

There have been three major programs driving IMC development in the aerospace industry over the past several years. The Integrated High Performance Turbine Engine Technology (IHPTET) Initiative is a US Department of Defense/NASA sponsored program with the goal of doubling the performance of gas turbine engines by 2003.[1] A large proportion of this increase in performance is derived from the development and use of new materials. This program demonstrates the feasibility of advanced technology, but is not sufficient to promote the introduction of radically new materials such as IMCs into production systems. Another large program, the National Aerospace Plane (NASP), was a much quicker paced technology program with less realistic material application goals.[2] This program has now all but disappeared from the materials development community. The most recent entry to the large national initiatives is the High Speed Civil Transport (HSCT) program sponsored by NASA.[3] This program intends to supply industry with the technology to build a commercial supersonic airliner shortly after the turn of the century. In similar fashion to NASP, this program is very fast paced, requiring demonstrated material properties and processability in a short time. Recently the HSCT program has drastically reduced its effort in IMC development. Thus, only IHPTET remains of the national programs driving IMC development, and the only two IMC systems emphasized are based upon $Ti_2AlNb+B2$ matrices, generally referred to as orthorhombic alloys, and $TiAl+Ti_3Al$ matrices, also known as near-γ alloys. It is appropriate to again note that IHPTET is demonstrating advanced technology and not developing a production engine.

For most of the intermetallic-matrix composites, it is sufficient to talk in general terms of their applications. In all but one instance, no viable combination of matrix and reinforcing phase has been developed. This one system, $SiC/Ti_2AlNb+B2$, is unquestionably the only candidate

for relatively near-term application. Even for this system, application may be as much as fifteen to twenty years away.[4] A number of very good reviews on the mechanical properties of Ti_3Al- and $Ti_2AlNb+B2$-matrix composites exist in the literature.[5-8] We will not present properties in meticulous detail for the other IMCs as they have little bearing on application at this time, and are available elsewhere.[9-12]

In gas turbine engines the potential applications for IMCs are quite extensive. Applications can be divided into rotating and static parts, static parts typically sustaining less severe mechanical loads. As static parts are usually considered the less demanding application, they are also the preferable sites for initial material introduction into a production engine by designers. This has generally been the case for new materials, where cost was not as much an issue. Unfortunately, IMCs will be pushed to rotating component application faster due to their inherently high cost, undoubtedly placing designers in an uncomfortable position.

Continuously reinforced IMCs, like MMCs, are limited to applications where strong unidirectional loading is required. In all of the applications to be discussed both higher specific strength and higher temperature capability are being exploited. In almost all cases, IMCs are directly competing with nickel-based superalloys for substitution. It is important for the materials scientist to be aware of the truly unique capabilities of the superalloys. In order for the inertia of the status quo to be overcome, it is imperative that any new material not just better the properties of these alloys, but must offer a significant benefit over them. If this statement is true of any new material, then it is even more applicable to the IMCs for which substantially higher costs are anticipated. Typical properties for nickel-based superalloy blade and disk alloys are provided in Table 1 for the reader's benefit when examining the articles on IMCs presented in the remainder of this symposium's proceedings. The values in the top half of the table (above the double line) are from a single disk or blade alloy, the values in the bottom half of the table are more generic properties, as these can be harder to obtain in the literature for a particular alloy. A brief discussion of the potential components for insertion of IMCs follows.

Table 1 - Typical properties of current nickel-based superalloys

	Disk alloy		Blade alloy	
	20°C	700°C	20°C	1000°C
Yield (MPa)	1100	1000	870	630
UTS (MPa)	1600	1200	1100	770
Stress Rupture (1000hrs) (MPa)		550		195
LCF, 10^4 cycles, (MPa-Pseudo)	725 at 550°C		400 at 650°C	
HCF, 10^7 cycles (MPa-runout.)			60 at 980°C	
Impact Resistance			> 8.5 N-m at 870°C	
% Elongation	> 10 % at 20°C			
K_{Ic}	> 50MPa√m at 20°C			
Density (g/cm^3)	~8.3			
Melting Point (°C)	1370			

Static engine applications include exhaust nozzle parts such as flaps and seals, struts, acuators, shrouds and engine cases. These parts typically require high temperature strength and oxidation resistance to withstand the projected increases in gas path temperatures. Reduced weight in an engine is always a goal of designers, but removing weight from the nozzle section can be particularly beneficial in military aircraft, which must maintain their center of gravity, and in a commercial application such as the HSCT.[3] Use of IMCs in engine cases is driven by projected increases in operating temperature and requirements for improved stiffness. Improvements in case stiffness result in the prevention of out-of-round shape changes, which cause blade rubbing, and better matching of expansion characteristics between the rotors and

cases, which maintains tight blade clearance control for high aerodynamic efficiency. Application to engine rotating components include disks, impellers, integrally bladed rotors, blades, spacers and hub arms. Used in a rotating compressor drum design, the IMCs are considered to be an enabling technology - allowing designers to create a structure not producable with any other material. IMC airframe parts are limited to potential application on vehicles traveling at hypersonic speeds. These speeds result in much higher temperatures than seen by currently produced air vehicles. The primary component envisioned would be hat-channel stiffened panels.

ISSUES IN IMC APPLICATION

Only five intermetallic matrices have been considered seriously for application in IHPTET, NASP, and HSCT: $Ti_2AlNb+B2$, $Ti_3Al+\beta/B2$, $TiAl+Ti_3Al$, NiAl and $MoSi_2$. These matrices are listed in order of increasing technical risk, and decreasing probability of near-term production application. IMCs based on $Ti_2AlNb+B2$ and $Ti_3Al+\beta/B2$ have been the most widely studied IMC systems. The five matrices will only be discussed briefly as each has been reviewed in more detail, including in this proceedings.[8,10,12] The matrices can be roughly divided into temperature ranges in which they are expected to operate. The $Ti_2AlNb+B2$ and $Ti_3Al+\beta/B2$ systems are anticipated to operate above 500°C, but application will be limited by the environmental and creep resistances of the matrices. These materials will require prime-reliant environmentally resistant coatings at temperatures above 650°C, and maybe as low as 550°C. The best $Ti_3Al+\beta/B2$ alloys exhibit oxidation rates superior to those measured in the $Ti_2AlNb+B2$. However, environmental embrittlement of $Ti_3Al+\beta/B2$ severely debits composite properties upon limited exposure.[13] TiAl-based matrices offer increased environmental resistance, including resistance to ignition and combustion, and strength retention to higher temperatures than either of the two previously discussed matrices. Alloying and coating schemes may allow application of TiAl-matrix composites up to 900°C. Lack of a suitable ceramic reinforcement and difficulty in processing the matrix material have deterred development efforts.[9] The NiAl system has the potential to provide low density, attractive thermal conductivity and oxidation resistance to the 1200°C range. However, the absence of a promising reinforcing fiber, high anisotropy, moderate strength and low ductility plague this system.[11,12] A $MoSi_2$ matrix might be useful to 1400°C due to its attractive oxidation behavior, but the very high DBTT, very low toughness and difficulty in finding a fiber/matrix system with a matching CTE are major issues to be overcome.[10] A composited $MoSi_2$ is generally considered to be a competitor against ceramic-matrix composites for this temperature range.

As the matrices become less damage tolerant, the problem of devising a usable IMC system becomes increasing difficult. There are two reasons for this: The first is finding a matrix/interface/fiber system that can provide the seemingly paradoxical mechanical properties required. The interfacial bond between the fiber and the matrix must be sufficiently strong so as to provide load shedding from the matrix to the fiber at elevated temperatures for creep strength. However, the bond should be sufficiently weak that toughening by bridging can occur at lower temperatures. Second, the more brittle the matrix, the higher the intended operating temperature. This creates a tremendous problem of finding a suitable reinforcing phase with an appropriate coefficient of thermal expansion (CTE) that can provide elevated temperature strength while remaining somewhat chemically stable in the matrix, or with a interfacial coating scheme. In some regards, compositing a brittle intermetallic matrix, such as NiAl and $MoSi_2$, is a more challenging problem than compositing a ceramic matrix due to the CTE matching problem. A general discussion of some of the barriers to application of IMCs follows.

Cost: The application of any material in a production system will most importantly be driven by the cost of acquiring the material and fabricating a part. While IMCs may provide a benefit in life-cycle cost, the realities of the military procurement process dictate emphasis on

initial system cost. The issue of cost for acquiring IMC parts is deeply interwoven with the cost of the raw materials and processing, issues that will now be discussed.

Fiber: A crucial technological barrier to IMC application is adequate fiber properties and fiber availability. Without viable fiber reinforcements, there can be no practical IMC system. Aside from the embryonic commercial status of SiC-based monofilament fibers, such as SCS-6, currently used for titanium-based composites, there are very few reinforcement options which are compatible with the other possible intermetallic systems. SiC is suitable for conventional titanium and $Ti_2AlNb+B2$ composites, despite a mismatch in CTE between the fiber and matrix, due to the plastic tolerance of the matrix. For the more brittle TiAl, NiAl and $MoSi_2$ matrices the SiC fibers have too large a CTE mismatch. Single crystal Al_2O_3 fiber, available from Saphikon, is more thermodynamically stable in TiAl and NiAl and has a more closely matched CTE, but it is very sensitive to processing. The mechanical properties of Al_2O_3 degrade during processing due to fiber surface damage and by mechanical damage such as twinning and fiber breakage.[12,14] This characteristic of the alumina fiber and its low elevated temperature strength make it generally unacceptable for reinforcement of IMCs. Other fibers, such as Ti_5Si_3, TiC and TiB_2, have been proposed for use for reasons of good CTE match and anticipated thermodynamic stability. A $Y_3Al_5O_{12}$ (YAG) - Al_2O_3 eutectic composition has the potential for increased elevated temperature strengths compared to Al_2O_3. To date, these fibers have not been produced in sufficient quantity and quality for evaluation and are not considered to be viable reinforcements in the near term. $MoSi_2$ and alumina have a nearly perfect CTE match, but the creep resistance of single crystal alumina falls short well before reaching the intended use temperature of $MoSi_2$, nominally 1400°C+. SiC would be an attractive fiber for consideration in an $MoSi_2$ matrix, however, the CTE mismatch is prohibitive. Efforts to lower the CTE of $MoSi_2$ by adding low CTE dispersions in the matrix are only at an exploratory stage.[10] Other issues relating to fibers are their reproducibility of properties and cost. Currently available fibers cost from about $2000/kg for SiC to $45,000/kg for Al_2O_3. A problem in the development of these fibers is the lack of a definite market, which makes private investment very risky. The financial burden of development therefore rests primarily with the government, which has also found it difficult to support.

Processing: A number of processing approaches for making IMCs have been pursued, certainly more than the total number of viable IMC systems. In fact, manufacturing-oriented comparisons of processing techniques that have been made by systematic and objective evaluation still do not point to a single manufacturing process.[15] Perhaps the most widely recognized approach is the foil-fiber-foil technique, and its variations, which have been used to produce titanium-based MMCs and IMCs.[16,17] This technique's primary advantage is that very thin foils of titanium alloys can be produced rather easily and with minimal interstitial pick-up. However, foil techniques are labor intensive and limited to relatively ductile matrices. Common problems can include incomplete diffusion bonding of the intermetallic foils, fiber swimming, fiber breakage and cross weave/matrix alloy reaction. Powder techniques, such as powder tape casting, may be a tenuous processing route for interstitially sensitive materials such as the titanium aluminides. Excessive interstitial pick-up is unacceptable because it can result in embrittlement of the matrix. A significant effort in plasma spraying has been performed using titanium-matrix composites.[9] Problems have included thermal shock to the fibers and breakage, interstitial pick-up and loss of microstructural control. Despite these issues, both powder processes and plasma spraying techniques offer excellent control of fiber distribution and are amenable to scale-up and automation. Another method is physical vapor deposition (PVD), although the slow rate of deposition is a concern, this technique can offer good control of fiber spacing.[18] In terms of production rate, melt infiltration is an attractive approach. Unfortunately, there are serious problems in retaining fiber spacing and severe chemical reactivity between the matrix and the fiber at these very elevated temperatures. All of the processing methods exhibit some degree of difficulty in manipulating the matrix microstructure. This is primarily due to concerns of thermodynamic instability of the interface between the fiber

and the matrix which limits the range of processing conditions. A critical barrier to IMC application is the absence of commercial vendors who are able to support production part manufacturing. The first step to building the required vendor base for IMC manufacturing is the establishment of manufacturing capability for conventional titanium-based composites. Consequently, the success of IMCs may hinge on the success of lower temperature titanium-matrix composites.

Interfaces/fiber coatings: Another barrier to further development of IMCs, particularly for the more brittle matrices based on TiAl, NiAl and $MoSi_2$, is the understanding and development of fiber/matrix interfacial coatings. As previously discussed, the balance between high temperature interfacial strength for load shedding and low temperature debonding for toughening is an extremely complex problem. Extensive mechanical modeling has been done in an attempt to estimate the appropriate bond strength required at these interfaces. Still, little is know of the bonding between these matrix/coating/fiber interfaces and what provides an optimal bond for shear strength and normal strength.[19] The additional requirement of most systems for a diffusion barrier between the fiber and the matrix to limit interfacial reactions further complicates this task. One of the difficulties in determining these properties has been the inability to define a suitable method of measuring them. Unfortunately the methods used currently to determine interfacial strength cannot accurately measure the chemical bond strength due to geometrical limitations of the test, processing variables, and inconsistent methods. Furthermore, the techniques for application of coatings to fibers are not yet developed to a commercial scale. Methods which are capable of applying a thin, uniform coating are required. Any successful technique must avoid damage to the fiber which would degrade mechanical properties.

Component fabrication: A number of manufacturing issues must be overcome before application of IMCs can become reality. Among these, joining of IMCs to similar and conventional material parts by both mechanical or metallurgical means is critical. This problem may be very component specific and involve and number of design considerations. Typically, the use of mechanical joints in rotating engine hardware is to be avoided in favor of metallurgical bonds to eliminate the added weight of flanges and fasteners. However, there are valid logistics reasons for incorporating mechanical joints which ease the task of part removal and replacement. In the case of mechanical joints, there are potential problems in placement of fiber reinforcement and fiber exposure For metallurgical bonds, the potential problems can include detrimental phase formation, particularly the precipitation of brittle intermetallics and corrosion associated with heat affected zones. Machining of IMC parts will be required and will necessitate development of new techniques that may, despite the best of efforts, result in surface damage and fiber exposure. Designs for parts such as struts, vanes and blades, will require location specific placement of reinforcement and may involve complicated fiber architectures to achieve load transfer to a supporting structure providing vibration dampening.

Design: The IMCs present aerospace designers with a radically different set of mechanical properties and failure mechanisms than those to which they are accustomed. Before IMCs can be applied to production systems, designers must become familiar and comfortable with the different balance of mechanical properties. Such differences as reduced ductility are difficult to understand in that few if any engine parts are designed based on a requirement for ductility. However, plasticity is generally desirable for fatigue crack growth resistance and a certain amount is considered essential to survive the manufacturing process. The exact amount needed for any particular part is unknown. Consequently, designers will design parts using conservative or minimum properties which could negate the benefit of IMCs entirely.[20] This implies that new design philosophies will have to be adopted. Currently, mechanical models to describe the failure mechanisms necessary for predicting IMC part lives are in the early stages of development. Before IMCs can go into service, adequate predictive models will be necessary to accurately determine part life, and inspection and removal intervals.

8

Reliability and maintainability: These two concerns also encompass inspectability, repairability and supportability. Although techniques for inspecting MMCs and IMCs are being developed, the current methods are limited in their ability to assess fiber breakage and placement, and unbonded regions in multiple-ply composites. The need to inspect IMC parts with more complex geometries, possibly comprised of many tens of layers of fiber, will pose a difficult task. There is a strong push in the military and commercial aerospace industry to simplify the removal, repair and replacement of components in order to maximize operational capability. This is particularly important in the current environment where the total numbers of available engines and aircraft have declined due to economic factors. The most current engine designs strive for increased durability and part commonality to expedite maintenance. Most aerospace components made of current materials can be either easily repaired or replaced. To transition to production, IMCs should exhibit the potential for relatively inexpensive and simple component replacement and repair. These considerations enter into a material system life-cycle cost analysis, and are therefore important factors in determining a materials selection for use.

Properties: IMC properties have not been sufficiently established to permit serious consideration for production systems. The most advanced system, SiC/Ti$_2$AlNb+B2, is currently being evaluated to ascertain whether it has sufficient mechanical properties to satisfy IHPTET demonstrator engine goals. Application of these advanced materials in production systems will first require much better characterization and understanding of time dependent properties such as creep strength, fatigue and environmental resistance. Typically, the cold section parts of military gas turbine engines, including the turbine rotors, are designed to an 8000 hour life requirement, in commercial engine designs the comparable design part life requirements may exceed 20,000 hours. Other IMC systems have barely begun to scratch the surface of property generation necessary identify appropriate initial part applications. At this point, it is clear that MoSi$_2$ is not likely to be used in any fracture-critical applications such as a rotor or blade.

CONCLUSIONS

With very few new airframe/engine systems envisioned for either the military or civilian sector over the next ten to twenty years, (the Air Force's next generation F-22 fighter/F-119 engine designs are largely locked in place, and full scale development of the Navy's F-18-E/F fighter and F414 engine is well underway), design practices are unlikely to change rapidly to make aggressive use of new materials with radically different mechanical behavior. Those who anticipate that engine designers will be willing to accept toughnesses of 10-20MPa$\sqrt{m}$ probably are unlikely to see their hopes realized for 15-20 years.[20] Imminent applications require cost effective materials with damage tolerant properties that are similar to those currently in use. The SiC/Ti$_2$AlNb+B2 system is the best positioned IMC to be considered for potential application. Numerous issues must be resolved, however, before application of this system can become reality. It is difficult to envision potential production applications in the near-term (<~20 years) for the other candidate intermetallic matrices as no viable matrix/interface/fiber IMC systems have yet been developed.

The only system currently driving IMC application is IHPTET. This program requires IMCs to achieve its revolutionary engine performance goals and is an excellent vehicle for their demonstration. However, the purpose of IHPTET is to explore and demonstrate the feasibility of advanced technologies. The duration of these demonstrator engine tests is limited and so, unfortunately, is the opportunity to assess the long time structural and environmental behavior of the advanced materials and component under the appropriate stress and temperature conditions. Consequently, demonstration engine testing is only an initial step in the long arduous process of introducing an IMC part into true engine production.

REFERENCES

1. R. Sprague, Adv. Mats. & Proc., **133** (1), 67, (1988).

2. T.M.F. Ronald, Adv. Mats. & Proc., **135** (5), 29, (1989).

3. J. Doychak, JOM, **44** (6), 46, (1992).

4. J.C. Williams, International Symposium on Structural Intermetallics, Champion, PA, 1993.

5. J. M. Larsen, W.C. Revelos and M.L. Gambone, in Intermetallic Matrix Composites II, edited by D.B. Miracle, D.L. Anton and J.A. Graves, (Mater. Res. Soc. Proc. **273**, Pittsburgh, PA, 1992), pp. 3-16.

6. P.R. Smith, J.A. Graves and C.G. Rhodes, in Structural Intermetallics, Proc. 1st Intl. Conf. on Str. Intermetallics, edited by R. Darolia et al., (TMS, Warrendale, PA, 1993), pp. 765-771.

7. J.M. Larsen., S.M. Russ and J.W. Jones, in Characterization of Fibre Reinforced Titanium Metal Matrix Composites, Report AGARD-R-796, NATO Advisory Group for Aerospace Research and Development (AGARD), (Specialised Printing Services Ltd., Loughton, Essex, 1994), pp. 1.1-1.21.

8. D.B. Miracle and P.R. Smith, in Intermetallic Matrix Composites III, edited by J.A. Graves, R.R. Bowman and J.J. Lewandowski, (Mater. Res. Soc. Proc., Pittsburgh, PA, 1994).

9. G. DeBoer, J. Chesnutt, T. Grossman and M. Sensmeier, "Titanium Aluminide Composites," Final Technical Report, Contract F33657-86-C-2136, (Wright Laboratory, Wright-Patterson AFB, OH, 1993).

10. J.J. Petrovic and A.K. Vasudevan, in Intermetallic Matrix Composites II, edited by D.B. Miracle, D.L. Anton and J.A. Graves, (Mater. Res. Soc. Proc. **273**, Pittsburgh, PA, 1992), pp. 229-239.

11. R.R. Bowen, in Intermetallic Matrix Composites II, edited by D.B. Miracle, D.L. Anton and J.A. Graves, (Mater. Res. Soc. Proc. **273**, Pittsburgh, PA, 1992), pp. 145-155.

12. R.A. Amato, J-M. Yang and D.R. Pank, in Intermetallic Matrix Composites III, edited by J.A. Graves, R.R. Bowman and J.J. Lewandowski, (Mater. Res. Soc. Proc., Pittsburgh, PA, 1994).

13. W.C. Revelos and P.R. Smith, Metall. Trans. A, **23A**, 587, (1992).

14. F. Brisset and A. Vassel, in Structural Intermetallics, Proc. 1st Intl. Conf. on Str. Intermetallics, edited by R. Darolia et al., (TMS, Warrendale, PA, 1993), pp. 739-747.

15. J.A. Graves, A.H. Muir and C.G. Rhodes, "Manufacturing Science for Titanium Aluminide Composite Engine Structures," WL-TR-92-4100, (Wright Laboratory, Wright-Patterson AFB, OH, 1992).

16. M.L. Gambone, "Fatigue and Fracture of Titanium Aluminides, Vol. I," WRDC-TR-89-4145.I, (Wright Research and Development Center, Wright-Patterson AFB, OH, 1989).

17. M.L. Gambone, "Fatigue and Fracture of Titanium Aluminides, Vol. II," WRDC-TR-89-4145.II, (Wright Research and Development Center, Wright-Patterson AFB, OH, 1989).

18. J. Sorensen, in Structural Intermetallics, Proc. 1st Intl. Conf. on Str. Intermetallics, edited by R. Darolia *et al.*, (TMS, Warrendale, PA, 1993), pp. 717-726.

19. D. B. Miracle and M. Mendiratta; in Intermetallic Compounds: Principles and Practice, edited by J. H. Westbrook and R. L. Fleischer, (*John Wiley and Sons*, New York, NY 1994).

20. P.K. Wright, in Structural Intermetallics, Proc. 1st Intl. Conf. on Str. Intermetallics, edited by R. Darolia *et al.*, (TMS, Warrendale, PA, 1993), pp. 885-893.

Powder Metallurgy Processing of
Intermetallic Matrix Composites

Randall M. German and Ronald G. Iacocca
P/M Lab, 118 Research West, Engineering Science and Mechanics Department
The Pennsylvania State University, University Park, PA 16802-6809

ABSTRACT

Intermetallic compounds are similar to ceramics because they are stoichiometric, with limited compositional ranges and brittle behavior. The limited ductility forces a reliance on powder techniques for shaping and consolidation. The high temperature character of intermetallics is beneficial to high temperature service, but this same attribute contributes to difficulty in processing. This paper reviews the several powder approaches to forming intermetallic structures. Examples are given on powders, consolidation options, and properties. Densification maps are introduced for estimation of consolidation cycles. Unfortunately, many of the composites exhibit little strengthening benefit from incorporation of reinforcing phases.

INTRODUCTION

The net shaping capabilities of powder metallurgy (P/M) are attractive because of material utilization and elimination of machining or deformation steps. This is particularly useful for the brittle compounds. Additionally, many of the intermetallics have a high melt viscosity that inhibits casting. Moreover, even when cast, grain size control is difficult in intermetallics and segregation is a problem. Thus, P/M techniques are suited for the processing of intermetallic [1-3]. The microstructure of the consolidated material can be controlled via the powder characteristics and the processing cycle. This latitude offers considerable control over the microstructure, shape, composition, and processing expense.

Unfortunately, most of the intermetallics of interest for high temperature service lack the desired combination of oxidation resistance, ductility, strength, and toughness. Hence, considerable effort has been put into intermetallic matrix composites (IMCs) which are also processed by powder techniques. The titanium and nickel aluminide systems have received much attention along these lines, where both strength and toughness have been improved by incorporation of various reinforcing phases. There is major attention to microstructure, interface quality, and possible interfacial reactions between the matrix and reinforcement. The reinforcing phases are selected for stiffness, strength, or chemical compatibility from candidates that include continuous fibers (SiC, Nb, Al_2O_3, or W), chopped fibers (Al_2O_3 being typical), and particles (TiC, TiB_2, Al_2O_3, HfC, AlN, and Y_2O_3). Although the field is still under development, a few systems are reaching sufficient maturity to allow analysis and projection of future trends.

INTERMETALLIC POWDERS

Intermetallic powders can be synthesized by a wide variety of techniques. Elemental powders can be used to fabricate intermetallic compounds by reactive synthesis techniques, with some purification due to self-heating [4,5]. Alternatively, many of the traditional powder fabrication techniques have been applied to the intermetallics [6].

Direct chemical synthesis of intermetallics is not common as yet. Two reports are

13

available describing such routes for NiAl and Ni$_3$Al using chemical techniques [7,8]. Very small powders are available through chemical precipitation routes. However, high oxygen contents are a major problem. Milling techniques are generally useful for producing powders from brittle cast alloys. This is a slow technique that can be accelerated by hydriding the powder [9,10]. Mechanical alloying employs the attritioning motion between agitated balls to create an alloyed composite powder. Mechanical alloying suffers from contamination problems, but has been demonstrated for systems such as CuEr, CrNb$_2$ FeAl$_3$, FeTi, HfAl$_3$, Nb$_5$Si$_3$, NiAl, Ni$_3$Al, Ni$_3$Si, NiTi, Ni$_3$Ti, RuAl, RuSi, TaAl, TiAl, TiAl$_3$, and ZrAl$_3$ [11-13].

Atomization involves the formation of powder from molten metal using dispersed fine droplets which solidify during free flight. The flexibility of the approach, coupled to its applicability to several alloys, make it an attractive route to the production powders with melting temperatures below approximately 1700°C, such as Fe$_3$Al, NiAl, Ni$_3$Al, NiAl$_3$, and TiAl [14-27]. Generally the powder microstructures are similar to rapidly solidified ribbons of similar compositions. Kaysser *et al.* [28] reported success in forming a 1.5 μm powder size from NiAl by milling an inert gas atomized powder. Such a small powder gives excellent sintering without the application of external pressure. The melt explosion technique uses a hydrogen-saturated liquid and rapid desaturation in a vacuum to form a powder spray; atomization process has been applied to the fabrication of 50 μm Ni$_3$Al with a cellular microstructure [29,30].

Plasma rotating electrode process uses centrifugal forces to form powder from a consumable electrode made from the desired material. The plasma heated electrode rotates at velocities up to 50,000 RPM under an inert gas to produce spherical powder having an average particle size of 250 μm. Rotating electrode powders have a lower oxygen level (approximately 250 ppm) as compared to gas atomized powder, but a larger microstructural scale [27]. This approach has been applied to Fe$_3$Al, TiAl, and Ti$_3$Al [14,27,31-39]. A variant centrifugal atomizer pours molten metal onto a rapidly spinning disk. The resulting powder is quenched in helium at 10^5 °C/s [40]. In a similar manner, a composite powder of NiAl-HfC with a grain size below 50 nm has been generated by melt spinning. This extremely small grain size provided good microstructure control in subsequent densification [41].

Another atomization technique useful for producing high temperature intermetallic powders is plasma atomization [42,43]. An agglomerated powder is fed into a plasma torch where melting and rapid acceleration occur. A powder smaller than 30 μm can be generated via secondary impact against a substrate. The high velocity and high temperature of the plasma arc result in a high superheat. This approach is useful for higher temperature intermetallics [44].

CONSOLIDATION TECHNIQUES

Fundamental to powder processing is densification and the elimination of residual pores. The intermetallics generally are brittle and not responsive to cold compaction. Sintering is effective in densification of small powders via high temperature exposures. For example, 14 μm Ni$_3$Al has been sintered to 98% density at 1325°C for 1 h. The initial compact shape can be generated by die compaction, cold isostatic compaction, injection molding, slip casting, tape casting, powder rolling, and so on [45]. Formation of a liquid phase during sintering is useful since the liquid provides a higher diffusivity than encountered in the solid state [46]. Many studies have emphasized reactive synthesis (RS) as a process for forming intermetallics. The initial compact is composed of mixed elemental powders which are heated to a temperature where they react to form an intermetallic [46-49]. The reaction can be nearly spontaneous once the liquid forms. Reactive sintering is applied to Ni$_3$Al where there is a large body of knowledge [46,49-56]. Other systems include TiAl, NiAl, Ti$_2$CuAl$_5$, NbAl$_3$, Fe$_3$Al, Nb$_2$Al, TaAl$_3$ and their

14

composites [4,57-68]. However, for composites, sintering proves ineffective since the reinforcing phase provides more strengthening than can be overcome by the sintering force.

To aid in understanding the processes involved, densification maps are used to show the interactions between variables. The density can be predicted versus various processing factors, including green density, pressure, temperature, particle size, and time [69-72]. Vacuum hot pressing is a stress-enhanced densification process that is performed in a rigid die using uniaxial pressurization. For intermetallics the die is usually made from graphite to allow external induction heating. The approach is widely used in forming intermetallics and their composites. Flexible dies and hydrostatic pressurization are used in hot isostatic pressing (HIP). Temperatures higher than the minimum required for full densification often contribute to improved ductility [29]. Several intermetallics and IMCs have been successfully compacted *via* HIP and reactive HIP (RHIP). Because consolidation is by hydrostatic stress, there is little shear on the particle surfaces; hence, prior particle boundaries may be evident after HIP, requiring post-consolidation deformation such as extrusion. It has been used to fabricate structures based on Ti_5Si_3, Ni_3Al, $NbAl_3$, $NiAl$, $MoSi_2$, $TiAl$, $TiAl_2Mn$, Ti_3Al, $TaAl_3$, and Fe_3Al.

Alternative approaches use uniaxial pressures acting on a viscous medium containing a shaped component or a powder in a container. The medium (metal, graphite, or ceramic) transforms the uniaxial force into a pseudo-hydrostatic stress. Such processes are faster than HIP and can be performed directly on porous compacts because the granules will not penetrate the pores. Further, the consolidation is like forging since the stresses exceed the yield strength. The approach has been applied to $NbAl_3$, Ni_3Al, $TiAl$, and Ti_3Al [27,48,73,74]

The extrusion of an intermetallic powder at an elevated temperature is another approach to achieving full density [75]. One of the most common applications for hot extrusion is in consolidating mechanically alloyed powders [29,41,76-78]. The area reduction ratio usually exceeds 10 for adequate densification. Successful densification in the extrusion of prealloyed titanium aluminide powders ($TiAl$ and Ti_3Al) require temperatures of 1000°C [79]. As an alternative Dahms [80] employed cold extrusion of mixed aluminum and titanium powders with a 9:1 reduction ratio which were then reactively hot isostatically pressed to full density. Extruded IMCs have a strong process temperature affect on reinforcement distribution [76].

The high strain rates and instantaneous heating involved in explosive compaction have proven effective in consolidating intermetallics [25,59,81-85]. The final microstructure tends to be inhomogeneous and requires considerable further thermal processing. The dynamic techniques prove difficult to manage [84,86]. Compacts made *via* these methods often experience cracking or pores. HIP has been used to densify the compacts [59]. High energy consolidation techniques have been applied to titanium aluminides, nickel silicides, and nickel aluminides with densities generally reaching 95% of theoretical.

Spray forming uses an inert gas atomizer and substrate closely positioned below the atomization nozzle [87-89]. The rapid heat extraction results in microstructural homogeneity. In some instances the product is sufficiently dense for direct use while in other instances it is subjected to subsequent deformation. Because only a small volume of liquid is present at a given time, segregation is limited. One of the major drawbacks of this technique is that only simple shapes can be fabricated. IMCs are produced with this technique by co-spraying ceramic reinforcing phases into the semi-solid molten stream. Typical deposition rates are 0.5 to 2 kg/s. In a similar manner a plasma torch provides a means of depositing dense coatings [90,91]. Powder is fed into a plasma arc and rapidly heated and accelerated. The intermetallic powder melts and is projected onto an external substrate where it splats to form a layered structure. Reinforcing phases can be trapped in the splat layers to form composites. Deposit density usually is about 85% of theoretical when deposition takes place at atmospheric pressure. If the spraying

is performed in vacuum, then deposit densities of 95 to 99% of theoretical are possible. These are densified by post-spray HIP [92,93].

COMPOSITES BY P/M

The initial concern is with placement of the constituents and attaining the desired dispersion, homogeneity, and alignment using the fabrication approaches outlined earlier. Processing information with mechanical properties on some systems are presented in Tables I and II. The references must be consulted for the details, including alloying or doping additions, raw material condition, reinforcement shape, size, and quantity.

One technique that provides a net shape component and fiber alignment for discontinuous fibers is powder injection molding (PIM) [94]. Intermetallic matrix composites with alumina have been injection molded with matrix phases of Ni_3Al [95,96], NiAl and $MoSi_2$ [97,98], and $TaAl_3$ [99]. These composites require separate consolidation steps (HIP) to achieve densification.

Spray deposition techniques adapt gas atomization so that ceramic phases are injected into depositing intermetallic droplets to form an IMC. Plasma spraying uses a similar principle. It is possible to layup laminated IMCs with alternating layers of matrix and reinforcement. The reinforcement phase can also be fed directly into the plasma torch, thereby being codeposited with the rapidly solidified intermetallic matrix. Results by Tiwari *et al.* [100] show that TiB_2 particles codeposited with Ni_3Al in a plasma torch produce a higher ultimate tensile strength than Ni_3Al-TiB_2 composites formed by other methods.

One useful layup process uses a cloth of powder and binder as a basis for layering intermetallic phases, or encapsulation of fibers. The binder gives the newly formed component a higher initial handling strength, and prevents segregation of the powders [48,98,101]. Extrusion is a widely applied methods for the manufacture of IMCs. In addition to consolidating the material, the hot extrusion process will align fibrous reinforcements. Multiple layers have been densified by HIP to form Ni_3Al-Al_2O_3 or Ti_3Al-SiC compositions [102,103]. Another variant is to create pseudo-fibers, where the fibers are actually regions of two phase structure [60,104]. At low magnifications the two phase regions appear as fibers, but at high magnifications they are particulate reinforced portions of the structure.

PROPERTIES

The properties of intermetallics and composites formed from powders largely depend on the composition, microstructure, processing, and impurity level [94-130]. Much effort has been applied to the IMCs to correct problems with toughness, high temperature strength, or microstructure control. In many instances the matrix was not stoichiometric and was often alloyed for increased strength or environmental stability. The reinforcing phases were largely ceramic particles, although a few continuous fiber or whisker composites are known. Although some of the entries in this table are outstanding, many are not competitive with available commercial alternatives. Furthermore, there are no IMCs with maximum use temperatures better than existing nickel-base superalloys [105]. On a density basis there is a strength advantage to the titanium aluminides. For many of the IMCs, problems originate with the brittle character of the matrix phase. The low temperature brittleness causes failures during thermal cycling due to a mismatch between thermal expansion coefficients of the phases.

The Ni_3Al composition needs extensive alloying to generate competitive properties, but even when alloyed the high temperature properties are low; thus, the extensive interest in P/M composites based on this compound. The presence of aluminum in both the reinforcement and

16

Table I Example Properties Available from Various P/M Processing Routes (HIP = hot isostatic pressing, RHIP = reactive HIP, VHP = vacuum hot pressing, RS = reactive synthesis, MA = mechanically alloyed)

matrix	additive	form	vol %	fabrication	strength, MPa	behavior	ref
FeAl	Y_2O_3	particle	1	hot extrude 975°C	930	ductile	129
Fe₃Al	—	—	—	RHIP 1100°C/ 2 h/ 207 MPa	1100	ductile	68
Fe₃Al	Al_2O_3	particle	10	RHIP 1100°C/ 2 h/ 207 MPa	—	small grain	68
NbAl₃	—	—	0	RS 1200°C	—	95% dense	60
NbAl₃	Al_2O_3	particle	30	RHIP 1200°C/ 4 h/ 170 MPa	—	98% dense	60
NiAl	—	—	0	RS 700°C	890	98% dense	60
NiAl	Al_2O_3	fiber	15	HIP 1200°C/ 2 h/ 172 MPa	163, 800°C	brittle	97
NiAl	TiB_2	particle	15	RHIP 1200°C/ 1 h/ 170 MPa	1060	dense	60
NiAl	TiB_2	particle	10	VHP 1400°C/ 2 h/ 48 MPa	673	grain size	20
NiAl	TiB_2	particle	20	RHIP 1200°C/ 1 h/ 170 MPa	1350	dense	60
Ni₃Al	---	---	—	HIP 1150°C/ 1 h/ 172 MPa	1400	24% elong	—
Ni₃Al	—	---	—	HIP 1100°C/ 1 h/ 172 MPa	1440	16% elong	—
Ni₃Fe	---	---	—	HIP 1200°C/ 0.5 h/ 103 MPa	627	37% elong	130
Ni₃Fe	Y_2O_3	particle	5	HIP 1200°C/ 0.5 h/ 103 MPa	649	10%	130
TaAl₃	---	—	0	RHIP 1200°C	531	98% dense	60
TaAl₃	Al_2O_3	fiber	35	RS VHP 1000°C	174	brittle	62
TiAl	---	—	0	RHIP 1370°C/ 4 h/ 170 MPa	533	brittle	60
TiAl	—	—	0	HIP	480	brittle	103
TiAl	Al_2O_3	particle	30	RHIP 1370°C/ 3 h/ 186 MPa	—	brittle	60
TiAl	SiC	particle	10	VHP 900°C/ 0.25 h/ 4 MPa	95	porous	67
TiAl	TiB_2	particle	7	hot extrusion	875	brittle	76
Ti₃Al	Nb alloy	—	0	HIP 925°C/ 4 h/ 210 MPa	700	ductile	128
Ti₃Al	SiC	fibers	40	VHP powder-fiber laminate	700	reactions	114
Ti₃Al	SiC	fibers	35	VHP foil-fiber laminate	1480/270	anisotropic	103

17

Table II Tabulation of P/M Ni₃Al Composite Mechanical Properties

(YS = yield strength, UTS = ultimate tensile strength, ϵ_f = elongation, * = fracture occurred before yield, MA = mechanically alloyed)

alloy matrix	reinforce-ment	fabrication	mechanical properties					ref
			test temp	environ-ment	YS MPa	UTS MPa	ϵ_f %	
Ni₃Al	3% Al₂O₃	RHIP 800°C, 1 h, 170 MPa	room	air		548		55
Ni₃Al	20% Y₂O₃	RHIP 800°C, 1 h, 170 MPa	room	air		463		55
IC-15	20% Al₂O₃	VHP 1350°C, 1 h, 20.7 MPa	room	air	227	388	10	106
IC-15	20% Al₂O₃	VHP 1350°C, 1 h, 20.7 MPa	1000°C	vacuum		114	*	106
IC-15	20% Al₂O₃	VHP 1335°C, 1 h, 20.7 MPa	1000°C	vacuum	102	102	0.4	106
IC-218	20% Al₂O₃	VHP 1170°C, 1.5 h, 20.7 MPa	1000°C	vacuum		134	0.4	106
IC-218	20% Al₂O₃	VHP 1200°C, 1.5 h, 20.7 MPa	room	air	329	414	4	106
IC-218	20% Al₂O₃	VHP 1200°C, 1.5 h, 20.7 MPa	1000°C	vacuum	148	148	0.6	106
IC-218	20% Al₂O₃	VHP 1300°C, 1.5 h, 20.7 MPa	room	air	250	348	6	106
IC-218	20% Al₂O₃	VHP 1300°C, 1.5 h, 20.7 MPa	1000°C	vacuum	144	144	0.4	106
IC-50	10% Al₂O₃	extrude 1100°C	25°C	air	660	870	9	16
IC-50	10% Al₂O₃	extrude 1100°C	1000°C	air	86	125	13	16
IC-50	2 wt.% TiC		25°C	air	673	755	4	16
IC-50	2 wt.% TiC		1000°C	air	225	270	2	16
IC-50	7% Al₂O₃		25°C	air	552	803	9	102
IC-50	9% Al₂O₃		25°C	air	488	985	13	102
IC-50	10% Al₂O₃		25°C	air	485	1027	24	102
IC-50	14% Al₂O₃		25°C	air	523	763	11	102
IC-50	22% Al₂O₃		25°C	air	515	748	19	102
Ni₃Al + Hf,B	3% Al₂O₃	HIP 1300°C, 3 h, 103.4 MPa	room	air	—	924	---	12
Ni₃Al + Hf,B	4% Al₂O₃	HIP 1300°C, 3 h, 103 MPa	room	air	--	1241	—	12
Ni₃Al + Hf,B	3% Y₂O₃	HIP 1300°C, 3 h, 103 MPa	room	air	—	1172	---	12
Ni₃Al + Hf,B	3% ThO₂	HIP 1300°C, 3 h, 103 MPa	room	air	--	1172	—	12
Ni₃Al + B	3% Al₂O₃	RHIP 800°C, 1 h, 104 MPa	25°C	air	474	548	1	107
Ni₃Al + B	20% Y₂O₃	RHIP 800°C, 1 h, 104 MPa	25°C	air	391	464	2	107
IC-218	5% Al₂O₃	HIP 1150°C, 1 h, 172 MPa	20°C	air	500	855	6	---
IC-218	5% Al₂O₃	HIP 1150°C, 1 h, 172 MPa	600°C	air	815	870	1	..
IC-218	5% Al₂O₃	HIP 1150°C, 1 h, 172 MPa	600°C	vacuum	812	889	4	107
IC-218	5% TiB₂	HIP 1150°C, 1 h, 172 MPa	20	air	570	930	2	---
IC-218	5% TiB₂	HIP 1150°C, 1 h, 172 MPa	600	air	865	940	1	---
IC-218	5% Y₂O₃	HIP 1150°C, 1 h, 172 MPa	20	air	550	750	4	--
IC-218	5% Y₂O₃	HIP 1150°C, 1 h, 172 MPa	600	air	710	745	2	---
IC-221	5% Al₂O₃	HIP 1150°C, 1 h, 172 MPa	25°C	air	813	868	1	107

matrix phases aids the chemical stability in the $Ni_3Al-Al_2O_3$ system. Although the system does not qualify for high temperature applications, the ductility of Ni_3Al has sparked considerable interest. Various ceramic particles and fibers have been incorporated into the powder mixture, including Y_2O_3, Al_2O_3, TiB_2, and SiC. The composites include up to 30 vol.% ceramic phase.

The high melting temperature and high aluminum content of NiAl are favorable for high temperature use. However, the current estimate is a maximum use temperature below 1000°C [105]. High temperature strength is improved by incorporation of various ceramic phases (TiC, TiB_2, Al_2O_3, AlN, or HfC), with most attention to TiB_2 [20,98,108-110]. The strengthening is largely due to grain size reduction during processing; the strength for 0% TiB_2 is between 310 and 550 MPa while 20% addition gives a strength of 1350 MPa [111].

Titanium aluminides provide possible improvements over classic titanium alloys in terms of specific strength, melting temperature, and oxidation resistance. The titanium aluminide intermetallics have a low fracture toughness and require alloying with V, Nb, Mo, and Ta for ductility, and the composite phase is used to improve toughness and strength [103,113]. The light weight of this composite system coupled with the recognized oxidation resistance make TiAl-SiC a widely favored system. Several approaches have been explored for consolidation, generally with Al_2O_3, TiB_2, or SiC particles and Al_2O_3 or SiC fibers [58,105,110,114-117]. Early data on Ti_3Al-SiC shows good properties and reasonable interfacial stability. Subsequent evaluation determined poor environmental resistance and susceptibility to thermal fatigue [103]. Generally, the particle reinforced TiAl composites prove brittle [76,110] and the properties are unattractive, especially creep, fatigue, and fracture toughness. Titanium aluminide composites have extreme property degradation in oxidizing environments with cyclic loading or cyclic heating. Related intermetallics, such as Ti_3Al, prove to be brittle and result in unattractive properties. The TiAl-Ti_3Al composites have not improved on the inherent brittle behavior [25]. However, some progress has occurred using ternary compounds, such as Ti_2NbAl. This compound has a higher specific strength than the binary titanium aluminides.

In spite of high temperature oxidation resistance, $MoSi_2$ has several limitations, including room temperature brittleness and low strength at high temperatures. The addition of SiC increases the high temperature creep resistance [117]. Continuous SiC fibers induce a stress from a thermal expansion mismatch that causes matrix cracking. In comparison with other high temperature ceramic matrix composites, $MoSi_2$-SiC proves inferior and limits the near-term applications to electrical components such as heating elements. There is hope that the $MoSi_2$-WSi_2-SiC composite will have the desired high temperature strength [118].

Unfortunately, even with full density most of the IMCs show minimal property improvements, and more typically a decrement in properties due to impurities [122]. An example is given by Ni_3Al powder which was mixed with 15 vol.% TiC and consolidated to 100% density via HIP and extrusion [123]. The yield strength increased slightly from 700 to 780 MPa, but the ultimate strength decreased from 1050 MPa to 800 MPa and the elongation severely decreased from 10% to 0.5%. Similar trends persisted in tensile tests up to 1000°C. This degradation of properties is a disappointing characteristic of most IMCs.

PROBLEMS

Intermetallics are at a relatively early stage of development and P/M has been applied to several systems during this development stage. There are examples of improved high temperature properties for either the basic intermetallics or their composites fabricated by P/M. Even the systems that exhibit room temperature ductility become embrittled at intermediate temperatures due to oxygen penetration of grain boundaries [12,29,92]. This leads to a ductile-

brittle transformation that is dependent on prior history.

Oxygen contamination is a pervasive problem that requires attention through degassing treatments and inert handling. Auger analysis of Ni_3Al powders produces evidence of C and S contamination, with a 2 nm alumina film. The titanium aluminides represent a particularly sensitive system where 600 to 1000 ppm of oxygen is typical. Higher levels of oxygen are observed as the particle size decreases. Plastic deformation is one route to minimize the defects from surface films (for example by hot extrusion) which degrade properties [3,124].

P/M techniques for consolidation of intermetallic compounds suffer from processing difficulties. For plasma spray there is difficulty in maintaining stoichiometry. Hot pressing and hot isostatic compaction give poor compact degassing and low precision final components. The mechanical properties are not necessarily optimal even when 100% density is achieved and generally higher temperatures are required for good particle bonding [125]. Forging techniques involving granular pressure transmission media give surface contamination of the intermetallics. Explosive compaction often cracks the compact during consolidation. There is a clear need to control the grain size and impurities. A smaller powder gives a finer grain size with improved ductility and strength, but may limit creep behavior and introduce more impurities [126].

Intermetallic matrix composites fabricated by P/M suffer these same fundamental problems and have further complications involving stability between phases, fabrication, and long-term integrity. In many cases, the IMCs have inferior properties when compared to the monolithic intermetallics [57,113]. Although many potential reinforcing phases are discussed, in reality there is a relatively small number in use. Further, the discontinuous particle or whisker phases have been emphasized because of low cost, but with poor composite properties [127]. Consequently, only a few IMC systems fabricated by P/M are under serious consideration, and these have recognized limitations. Toughness is often inferior and in cases where microstructural toughening has been successful, other problems become fatal. Fatigue is a complex problem in these systems that involves consideration of orientation, temperature and stress cycles, frequency, environment, and damage. Thermal fatigue is a problem because of the differing thermal expansion between matrix and fiber. For example, in the Ti_3Al-SiC system the fibers prove very effective in promoting toughness. With 500 cycles from 150 to 815°C in air, the room temperature tensile strength of the composite decreased from 1260 MPa to 120 MPa [103].

Another fundamental problem is the low production volumes currently anticipated. There is no clear leading P/M system, although many are under active evaluation. Accordingly, the USA consumption is quite small with no dedicated production operations, leading to poor economies of scale and long lead times.

CONCLUSIONS

Intermetallic compounds represent a novel hybrid of stoichiometric (ceramic-like) materials and metals. They have recognized uses as reinforcing phases in many metallurgical systems, especially superalloys. Some of the intermetallic compounds are stable to high temperatures and offer possible uses because of inherent high temperature corrosion and oxidation resistance. Accordingly, developments in this field focus on the intermetallic compounds as well as possible composites. These materials are new and will require extensive effort to bring to maturity. However, as knowledge on composition, processing, structure, properties, and behavior emerge there are several near term applications using P/M. One of the first is use of Ni_3Al as a replacement for cobalt in bonding carbides and diamonds for abrasive and cutting tools. Other applications that appear to be maturing include furnace hardware, mining tools, diesel engine components, abradable seals, chemical filters, cutting tools, and

structural alloys for low temperature applications.

Probably the near-term applications will be in the 600 to 1000°C temperature range [103]. Special intermetallics such as the nickel and iron aluminides may find applications in wear components, oxidation barriers, and uses involving certain corrosion fluids. Here the high temperature strength is not important, but a composite might be useful for tailored properties. Many intermediate temperature applications should emerge and a diversity of industrial composites are very realistic. The P/M based processes generally offer a major advantage in their shaping capabilities. Accordingly, many of the IMCs will be developed using powder consolidation techniques. Not only are complex shapes possible, but the productivity, material utilization, energy expenditure, precision, and microstructural uniformity are attractions. The generic, widespread interest in net shape forming has focused considerable research and development interest on powder approaches.

ACKNOWLEDGMENTS

REFERENCES

1. E. M. Schulson, 1987. Inter. J. Powder Met. 23:25-32.
2. N. S. Stoloff, 1985. High-Temperature Ordered Intermetallic Alloys, ed. C. C. Koch, C. T. Liu, and N. S. Stoloff, 39(1):3-27. Pittsburgh: MRS.
3. K. Vedula, and J. R. Stephens. 1987. Prog. Powder Met. 43:561-573.
4. R. R. Oddone, and R. M. German. 1989. Advances in Powder Met. 3:475-489.
5. N. A. Martirosyan, S. K. Dolukhanyan, G. M. Mkrtchyan, I. P. Borovinskaya, and A. G. Merzhanov. 1976. Soviet Powder Met. Metal Ceramic 15:522-525.
6. R. M. German, 1994. Powder Metallurgy Science. second ed., Princeton: MPIF.
7. J. C. Withers, H- C. Shiao, R. O. Loutfy, and P. Wang. 1991. J. Metals 43 (Aug):36-39.
8. O. Abe, and A. Tsuge. 1991. J. Mater. Res. 6: 928-934.
9. C. Suryanarayana, R. Sundaresan, and F. H. Froes. 1990. Solid State Powder Processing, ed. A. Clauer and J. J. DeBarbadillo, pp. 55-64. Warrendale: TMS.
10. K. Majima, N. Niimi, S. Katsuyama, J. Tomizawa, and H. Nagai. 1992. J. Japan Soc. Powder Powder Met. 39:197-202.
11. K. Vedula, G. M. Michal, and A. M. Figueredo. 1988. Modern Developments in Powder Met. 20:491-502. Princeton: MPIF.
12. J. S. C. Wang, et al.. 1988. Inter. J. Powder Met. 24:315-325.
13. R. C. Benn, P. K. Mirchandani, and A. S. Watwe. 1988. Modern Developments in Powder Met. 21:479-493. Princeton: MPIF.
14. C. G. McKamey, et al.. 1991. J. Mater. Res. 6(8):1779-1805.
15. V. K. Sikka, R. H. Baldwin, and C. R. Howell. 1991. Adv. Powder Met. 6:147-158.
16. V. K. Sikka, E. K. Ohriner, and L. F. Allard. 1991. P/M in Aerospace and Defense Technologies Symposium Proceedings, pp.137-145. Princeton: MPIF.
17. R. Maurer, et al.. 1989. High-Temperature Ordered Intermetallic Alloys III 133:421-426. Pittsburgh: MRS.
18. R. M. German, A. Bose and G. Camus. 1994. Inter. J. Powder Met., 30:in press.
19. R. Laag, et al.. 1989. Science Sintering, ed. D. P. Uskokovic, pp. 295-309. New York:

Plenum Press.

20. J. D. Rigney, *et al.*. 1988. High-Temperature Ordered Intermetallic Alloys III 133:603-608. Pittsburgh: MRS.

21. J. C. Murray, *et al.*. 1990. Adv. Powder Met. 2:233-242.

22. S. C. Huang, and A. M. Ritter. 1989. J. Mater. Res. 4:288-293.

23. G. E. Fuchs, and W. H. Kao. 1988. Modern Developments Powder Met., 20:531-557. Princeton: MPIF.

24. S. Shiga, *et al.*. 1991. J. Japan Soc. Powder Powder Met. 38:971-975.

25. C. Persad, *et al.*. 1988. High-Temperature Ordered Intermetallic Alloys III 133:717-722. Pittsburgh: MRS.

26. D. S. Shih, G. K. Scarr, and J. C. Chesnutt. 1988. High-Temperature Ordered Intermetallic Alloys III 133:167-172. Pittsburgh: MRS.

27. W. J. Porter, *et al.*. 1990. Adv. Powder Met. 2:243-257.

28. W. A. Kaysser, *et al.*. 1991. Inter. J. Powder Met. 27(1):43-49.

29. R. N. Wright, R. L. Williamson, and J. R. Knibloe. 1990. Powder Met. 33:253-259.

30. R. N. Wright, B. H. Rabin, and J. R. Knibloe. 1989. Mater. Manuf. Proc. 4(1):25-37.

31. I . S. Apgar, and D. Eylon. 1991. ISIJ Inter. 31(8): 915-921.

32. M. Tokizane, K. Ameyama, and H. Sugimoto. 1990. Solid State Powder Processing, ed. A. Clauer and J. J. DeBarbadillo, pp. 67-75. Warrendale: TMS.

33. M. Tokizane, K. Isonishi, and S. Kido. 1990. PM90, World Conference on Powder Met. 2:93-96. London: The Institute Metals.

34. C. F. Yolton, *et al.*. 1986. Prog. Powder Met. 42:479-487.

35. J. A. Graves, *et al.*. 1987. Scripta Met. 21:567-572.

36. R. J. Schaefer, 1992. Inter. J. Powder Met. 28:161-173.

37. N. R. Osborne, W. J. Porter and D. Eylon. 1991. SAMPE Quarterly 22(4):21-28.

38. H. Kohmoto, and H. L. Fraser. 1989. Adv. Powder Met. 3:203-211.

39. L. M. Hsiung, T. A. Kuntz, and H. N. G. Wadley. 1991. Low Density, High Temperature Powder Met. Alloys, ed. W. E. Frazier, et al., pp. 21-34. Warrendale: TMS.

40. I. Baker *et al.* 1984. Metallography 17: 299-314.

41. R. Ray, 1990. Met. Powder Rpt. 45(1):56-59.

42. R. F. Cheney, and E. R. Seydel. 1990. Met. Powder Rpt. 45(1):43-46.

43. K. G. Shaw, W. Z. Misiolek, and R. M. German. 1991. Adv. Powder Met. 6:159-166.

44. K. G. Shaw, and R. M. German. 1991. Adv. Powder Met. 5:263-275.

45. W. Diehl, and D. Stover. 1990. Met. Powder Rpt. 45(5):333-338.

46. R. M. German, 1985. Liquid Phase Sintering. New York: Plenum Press.

47. Z. A. Munir, 1992. Metall. Trans. 23A:7-13.

48. R. M. German *et al.*. 1990. PM '90 Inter. Conference on Powder Met. 1:310-323. London: The Institute Metals.

49. R. M. German, 1990. Adv. Powder Met. 2:115-132.

50. D. M. Sims, A. Bose, and R. M. German. 1987. Prog. Powder Met. 43:575-596.

51. A. Bose, *et al.*. 1988. J. Metals 40(9): 14-17.

52. B. H. Rabin, A. Bose, and R. M. German. 1988. Modern Developments Powder Met. 21:511-529. Princeton: MPIF.

53. A. Bose, B. H. Rabin, and R. M. German. 1988. Powder Met. Inter. 20(3) 25-30.

54. R. M. German, and A. Bose. 1989. Mater. Sci. Eng., A107:107-116.

55. R. M. German, 1987. Science Sintering, pp. 439-451. New York: Plenum Press.

56. J. P. Lebrat, A. Varma, and A. E. Miller. 1992. Metall. Trans. 23A:69-76.

57. W. R. Wrzesinski, and J. C. Rawers. 1990. J. Mater. Science Let. 9(4):432-435.

58. A. J. Maeland, and D. Narasimhan. 1989. MRS Symp. Proc. 133:723-727.

59. O. Arkens et al.. 1989. MRS Symp. Proc. 133: 493-498.

60. W. Z. Misiolek, and R. M. German. 1991. Adv. Powder Met. 6:167-175.

61. W. Z. Misiolek, and R. M. German. 1991. Mater. Sci. Eng. A144:1-10.

62. D. L. Anton. 1988. High Temperature/High Performance Composites 120, pp. 57-64. Pittsburgh: MRS.

63. A. K. Bhattacharya. 1992. J. Amer. Ceramic Soc. 75: 1678-1681.

64. K. S. Hwang, and Y. C. Lu. 1990. Adv. Powder Met. 2:133-144.

65. A. Bose, et al.. 1991. Adv. Powder Met. 6: 131-145.

66. J. C. Murray, and R. M. German. 1992. Metall. Trans. 23A:2357-2364.

67. B. R. Krueger, A. H. Mutz, and T. Vreeland. 1992. Metall. Trans. 23A:55-58.

68. R. N. Wright, and B. H. Rabin. 1992. Adv. Powder Met. 9:283-294.

69. E. Arzt, M. F. Ashby, and K. E. Easterling. 1983. Metall. Trans. 14A: 211-221.

70. R. L. Coble. 1978. Powder Met. Inter. 10:128-130.

71. M. R. Notis, R. H. Smoak, and V. Krishnamachari. 1975. Sintering and Catalysis, ed. G.C. Kuczynski, pp. 493-507. New York: Plenum Press.

72. R. J. Schaefer, and M. Linzer, eds. 1991. Hot Isostatic Pressing: Theory and Applications, Mater. Park: ASM Inter..

72. V. K. Sikka, 1988. Modern Developments Powder Met. 20:543-557. Princeton: MPIF.

74. C. G. Levi, et al.. 1988. J. Mater. Shaping Tech. 6:125-132.

75. P. R. Roberts, and B. L. Ferguson. 1991. Inter. Mater. Reviews 36(2):62-79.

76. M. L. Adams, et al.. 1989. Adv. Powder Met. 3: 439-448.

77. R. N. Wright, and J. R. Knibloe. 1990. Acta Met. Mater. 38:1993-2001.

78. R. R. Bowman, et al.. 1992. Metall. Trans. 23A: 1493-1508.

79. J. H. Moll, C. F. Yolton, and B. J. McTiernan. 1990. Inter. J. Powder Met. 26(2):149-155.

80. M. Dahms, 1990. Solid State Powder Processing, ed. A. Clauer and J. J. DeBarbadillo, pp. 77-82. Warrendale: TMS.

81. M. A., Myers, B. B. Gupta, and L. E. Murr. 1981. J. Metals 33(10):21-26.

82. R. Prummer, 1983. Explosive Welding, Forming and Compaction, ed. Blazynski, T.Z., pp. 369-395. New York: Applied Science.

83. R. N. Wright, G. E. Korth, and J. E. Flinn. 1987. Adv. Mater. Proc. 137(4):56-59.

84. A. Ferreira, et al.. 1991. Metall. Trans. 22A:685-695.

85. S. A. Balankin, V. S. Sokolov, and A. O. Troitzikiy. 1990. Proceedings PM 90: Inter. Conference on Powder Met. 3, pp. 37-39. London: The Institute Metals.

86. N. N. Thadhani, et al.. 1990. Solid State Powder Processing, ed. A. Clauer and J. J. DeBarbadillo, pp. 97-109. Warrendale: TMS.

87. S. Annavarapu, D. Apelian, and A. Lawley. 1990. Metall. Trans. 21A: 3237-3256.

88. A. R. E. Singer, 1985. Inter. J. Powder Met. Powder Tech. 21(3):219-234.

88. E. Gutierrex-Miravete, et al.. 1989. Metall. Trans. 20A:71-85.

90. D. Apelian et al. 1983. Inter. Metals Review 28: 271-294.

91. H. Herman. 1988. MRS Bull. 13(Dec):60-67.

92. A. I. Taub, S. C. Huang, and K. M. Chang. 1984. High-Temperature Ordered Intermetallic Alloys 39:221-228. Pittsburgh: MRS.

93. K. M. Chang, A. J. Taub, and S. C. Huang. 1984. High-Temperature Ordered Intermetallic Alloys 39:335-42. Pittsburgh: MRS.

94. A. Bose, and R. M. German. 1988. Modern Developments Powder Met. 18:299-314. Princeton: MPIF.

95. B. Moore, et al.. 1988. High Temperature/High Performance Composites 120:51-56.

Pittsburgh: MRS.

96. A. Bose, and R. M. German. 1988. Adv. Mater. Manuf. Proc. 3: 37-56.

97. D. E. Alman, and N. S. Stoloff. 1991. Low Density, High Temperature Powder Met. Alloys (ed. W. E. Frazier, M. J. Koczak, and P. W. Lee), pp. 109-125. Warrendale: TMS. **98.** D. E. Alman, and N. S. Stoloff. 1991. Inter. J. Powder Met. 27: 29-41.

99. D. E. Alman et al. 1989. Processing Ceramic and Metal Matrix Composites, 217-227. New York: Pergamon Press.

100. R. Tiwari. 1990. unpublished.

101. A. Bose, and R. M. German. 1988. Indust. Heat. 55(5): 38-41.

102. J. H. Schneibel, et al. 1991. J. Mater. Res. 6(8):1673-1679.

103. J. M., Larsen, et al. 1990. High Temperature Aluminides and Intermetallics pp. 521-556. Warrendale: TMS.

104. V. C. Nardone, and J. R. Strife. 1991. Metall. Trans. 22A:183-189.

105. J. Doychak, 1992. J. Metals 44(Jun)46-51.

106. C. G. McKamey, et al. 1988. High-Temperature Ordered Intermetallic Alloys III 133:609-614. Pittsburgh: Mater. Res. Soc..

107. R. M. German, A. Bose, and N. S. Stoloff 1988. High-Temperature Ordered Intermetallic Alloys III 133:403-414. Pittsburgh: Mater. Res. Soc..

108. W. Z. Misiolek, and R. M. German. 1990. Adv. Powder Met. 2:161-172.

109. L. Wang, and R. J. Arsenault. 1991. Metall. Trans. 22A:3013-3018.

110. J. D. Whittenberger, et al. 1989. J. Mater. Res. 4(5):1164-1171.

111. N. S. Stoloff, and D. E. Alman. 1990. MRS Bull. 15(12):47-53.

112. K. S. Kumar, S. K. Mannan, and R. K. Viswandham. 1992. Acta Met. Mater. 40:1201-1222.

113. K. S. Kumar, et al. 1991. NASA Technical Memorandum #NASA TM-103724, Lewis Res. Center, Cleveland.

114. P. K. Brindley. 1986. High-Temperature Ordered Alloys II 81:419-424. Pittsburgh: MRS.

115. L. Christodoulou, P. A. Parrish, and C. R. Crowe. 1988. High Temperature/High Performance Composites 120:29-34. Pittsburgh: MRS.

116. H. Kimura, and S. Kobayashi. 1992. J. Japan Soc. Powder Powder Met. 39:287-290.

117. J. M. Yang, and S. M. Jeng. 1992. J. Metals 44(Jun):52-57.

118. L. M. Sheppard, 1990. Ceramic Bull. 69:666-673.

119. D. J. Larkin, L. V. Interrante, and A. Bose. 1990. J. Mater. Res. 5(11):2706-2717.

120. T. C. Chou, and T. G. Nieh. 1990. J. Mater. Res. 5(9):1985-1994.

121. J. M. Yang, W. H. Kao, and C. T. Liu. 1988. High-Temperature Ordered Intermetallic Alloys III 133:453-458. Pittsburgh: MRS.

122. Y. W. Kim, and F. H. Froes. 1989. Adv. Powder Met. 3:251-267.

123. G. E. Fuchs, 1989. High-Temperature Ordered Intermetallic Alloys III 133:615-620. Pittsburgh: MRS.

124. K. Vedula, and J. R. Stephens. 1987. Met. Powder Rpt. 42(Feb):84-89.

125. J. C. Beddoes, W. Wallace and M. C. de Malherbe. 1992. Inter. J. Powder Met. 28: 313-325.

126. E. A. Feest, and J. H. Tweed. 1992. Mater. Sci. Tech. 8:308-316.

127. D. L. Erich, 1987. Inter. J. Powder Met. 23(1):45-54.

128. V. S. Moxson, and G. I. Friedman. 1986. Prog. Powder Met. 42:489-500.

129. S. Strothers, and K. Vedula. 1987. Prog. Powder Met. 43:597-610.

130. A. Bose, et al. 1993. J. Mater. Res. 8:430-437.

MICROSTRUCTURE AND PROPERTIES OF INTERMETALLIC MATRIX COMPOSITES PRODUCED BY REACTION SYNTHESIS

D.E. Alman, J.A. Hawk, C.P. Dogan, M. Ziomek-Moroz* and A.V. Petty, Jr.
U.S Bureau of Mines, Albany Research Center, Albany, Oregon 97321
Department of Materials Science and Engineering, Oregon Graduate Institute of Science and Technology, Beaverton, Oregon 97006

ABSTRACT

In this US Bureau of Mines study, a variety of TiAl based composites were produced *in situ* by reaction synthesis. Mixtures of elemental Ti, Al and B and Ti, Al, and Si powders were reactive hot-pressed to form TiAl reinforced with 10, 20, 25 or 60 vol. pct. TiB_2 or Ti_5Si_3. Microstructural evaluation of the resultant composites confirmed that the reaction products were primarily TiAl and TiB_2 or Ti_5Si_3, with a small amount of Ti_3Al. The hot-press temperature and pressure had a significant effect on the density of the composites. In general, higher temperatures and initiating the reaction under pressure promoted dense composites. Room temperature biaxial flexure strength tests indicated that the addition of the reinforcing phases can improve the strength of TiAl. Potentiodynamic experiments revealed that TiAl, $TiAl+TiB_2$, and $TiAl+Ti_5Si_3$ composites display active-passive corrosion behavior in both acidic and alkaline solutions.

INTRODUCTION

Intermetallic compounds and intermetallic base composites possess an attractive combination of properties (i.e., high melting points, low densities, and oxidation and corrosion resistance) that make them good candidates for use as structural materials at elevated temperatures in aggressive environments. Recently, it has been recognized that these compounds and composites may have applications in industries, such as the automotive industry, where cost is frequently a major factor in materials selection [1,2]. However, for intermetallic compounds and composites to be used in a these types of industries, low cost fabrication methods will be a requirement. One potentially economical and environmentally benign fabrication technique is reaction synthesis (also termed combustion synthesis or self-propagating, high-temperature synthesis (SHS)). This technique involves forming compounds *in situ* from reactions between elemental constituents. Monolithic intermetallics, ceramics, and dual phase composites have been produced by this method [3-8]. There is an economic advantage to this approach, as elemental components are readily available in a wide variety of forms and purities, and at relatively low cost when compared to prealloyed powders. The driving force for the reactions is the negative heat of mixing during compound formation. This results in the release of energy (heat), which sustains the reaction through the body of the reactants. For aluminides, the reaction is accompanied by the formation of a transient liquid phase, which through capillary forces, enhances densification. Thus the required processing parameters, such as time, temperature and pressure, needed to produce dense products by reactive synthesis techniques can be quite different from those of more conventional powder metallurgical approaches. This paper discusses the microstructure and preliminary properties of $TiAl+TiB_2$ and $TiAl+Ti_5Si_3$ composites formed *in situ* from mixtures of Ti, Al and B, or Si powders.

25

Mat. Res. Soc. Symp. Proc. Vol. 350. °1994 Materials Research Society

EXPERIMENTAL PROCEDURE

Commercially available, -325 mesh Ti, Al, B, and Si powders were mixed to the stoichiometric proportions of TiAl + 10, 20, 25, or 60 vol. pct. TiB$_2$ or Ti$_5$Si$_3$. Monolithic TiAl, TiB$_2$, and Ti$_5$Si$_3$ were also produced from mixtures of elemental powders. The mixed powders were placed in graphite dies (31.75 mm in diameter) which were placed between the platens of an induction heated hot-press. The chamber of the hot-press was backfilled with Ar and the powders were consolidated using the various parameters shown in Table I. These experiments were designed to determine the effect of hot-press temperature (800, 1000 or 1200°C), time (5, 15 or 60 min) and pressure (10 or 20 MPa) on the structure of the resultant composites. Two different hot-pressing schedules were run: cycle a, where the reaction was initiated under no applied pressure; and cycle b, where pressure was applied prior to the initiation of the reaction. The reactions were initiated at about 660°C, the melting point of Al. At this temperature the platen of the hot-press (if pressurized) rapidly fell, indicating that the powders in the graphite molds had reacted, forming a transient liquid phase.
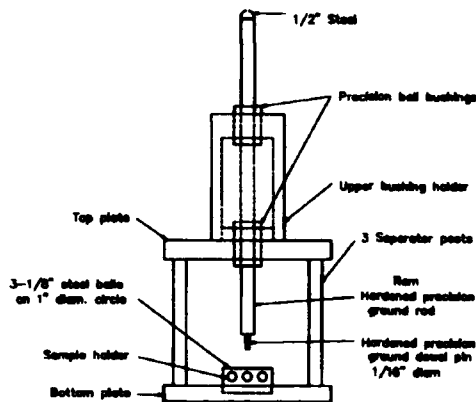
Figure 1. Schematic of the biaxial flexure testing apparatus

The apparent densities of the composites were determined from the weight divided by the volume calculated from the dimensions of each specimen. The microstructures of the composites were evaluated by Scanning Electron Microscopy (SEM) in both secondary and backscattered electron (bse) imaging modes. Phase determination was through a combination of X-ray diffraction and Transmission Electron Microscopy (TEM) analyses.

Biaxial flexure tests were performed on some of the composites (hot-pressed at 1200°C-20MPa-1hr) to evaluate room temperature strength, using testing procedures described in ASTM standard F-394-78 (Reapproved 1991). A schematic of the biaxial flexural experimental configuration is shown in Fig. 1. An advantage of the biaxial flexure test is that the specimens are relatively easy to produce (a disk, roughly 31.75mm in diameter by 2 mm thick). The tests were run on a screw driven testing machine at a constant cross head speed of 0.5mm/min. Either 4 or 5 duplicate tests were run for each composite condition. Prior to testing, the specimens were mechanically polished to a 0.25 μm diamond paste finish. The biaxial flexure strength (σ) is given by:

$$\sigma = 0.2387 P(X-Y)/d^2$$

where P is the load at fracture and d is the specimens thickness. X and Y are constants related to the Poisson's ratio of the specimen (assumed to be 0.25 for these materials) and the geometry

26

Table 1
Processing Effects on Composite Density

TEMP (°C)	CYC*	PRES (MPa)	TIME (min)	v% TiB_2	DENSITY (% T.D)[1]
800	a	10	60	10	65
				25	53
				60	47
800	b	10	60	10	83
				25	77
				60	58
1200	a	10	60	10	75
				25	75
				60	73
1200	b	10	60	10	93
				25	92
				60	84
1000	b	10	5	10	81
				25	77
				60	72
1000	b	10	15	10	85
				25	81
				60	72
1000	b	10	60	10	85
				25	82
				60	72
1000	b	20	60	0	95
				10	90
				25	87
				60	74
				100	66
1200	b	20	60	0	96
				10	90
				20	94

TEMP (°C)	CYC*	PRES (MPa)	TIME (min)	v% Ti_5Si_3	DENSITY (% T.D)[1]
1000	b	20	60	0	95
				10	97
				25	95
				60	97
				100	55
1200	b	20	60	0	96
				10	98
				20	99

1) Percent Theoretical Density
*) hot press cycle (a) pressurized after initiation of reaction;
(b) pressurized before initiation of reaction

of the experimental apparatus. The formulation of the constants can be found in the ASTM standard.

The corrosion behavior of the composites was evaluated in both acidic (0.5M H_2SO_4) and alkaline (0.5M NaOH) solutions. An electrical contact was made by attaching a stainless steel wire (teflon shielded to protect from corrosion) to the back of the specimen. The specimens and contact wires were mounted in epoxy and the front surfaces of the specimens were mechanically polished with 600 grit SiC paper prior to testing. Poteniodynamic experiments were performed at 25°C, at a scan rate of 1.6 mV/sec from 50mV more negative than the open circut potential. The solutions were deaerated with Argon gas. Platinum was used as a counter electrode.

RESULTS AND DISCUSSION

The apparent densities of the composites as a percentage of the theoretical density are listed in Table I. It is emphasized that the theoretical density used for comparison was the volumetric rule of mixtures density, assuming all the powders reacted to form TiAl (ρ=3.8 g/cm³) and either TiB_2 (ρ=4.25 g/cm³) or Ti_5Si_3 (ρ=4.32 g/cm³). Inspection of these values reveals several important trends: First, application of pressure prior to initiating the reaction promotes denser composites. Thus, composites fabricated using hot-press cycle b are more dense than similar composites fabricated using cycle a. Second, the time at processing temperature has little or no effect on density. Composites that are hot-pressed at 1000°C for 60 minutes are no more dense than composites hot-pressed for 5 or 15 minutes. Third, increasing the applied pressure improves the density of only the lowest volume fraction TiB_2 composites. Finally, increasing the hot-pressing temperature increases the density of all the composites. These trends are not surprising; since for any diffusion related process, such as hot-pressing,
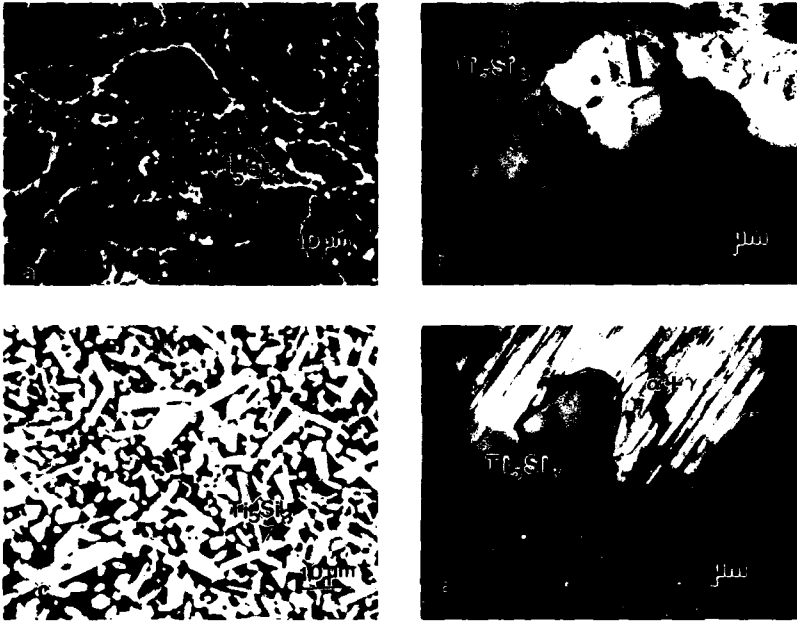
27

Figure 2 Microstructures of TiAl/Ti₅Si₃ composites. (a) 25v°o Ti₅Si₃, bse image. (b) 25v°o Ti₅Si₃, TEM image. (c) 60v°o Ti₅Si₃, bse image. (d) 60v°o Ti₅Si₃, TEM image
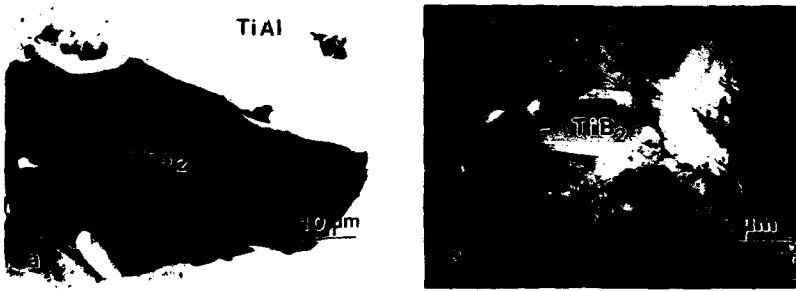

Figure 3 Typical microstructures of TiAl/TiB₂ composites (a) bse image. (b) TEM image

temperature is a more significant factor, than either pressure or time. However, as discussed below, all these parameters do affect the homogeneity of the composites.

Another interesting feature is the effect of B and Si additions on the density of the composites. Note from Table I, that the densities of the TiAl/TiB$_2$ composites decrease with increasing TiB$_2$ content. The densities of these composites follow a linear trend between the as processed densities of the reactively synthesized monolithic TiAl and TiB$_2$. By contrast, the TiAl/Ti$_5$Si$_3$ composites are dense, even at large Ti$_5$Si$_3$ volume fractions, even though, the reactive hot-pressed Ti$_5$Si$_3$ is quite porous. Thus, there is some synergistic effect when simultaneously forming TiAl and Ti$_5$Si$_3$ that leads to dense composites.

X-ray diffraction reveals that each of the composites contains primarily TiAl and TiB$_2$ or Ti$_5$Si$_3$, regardless of the processing conditions. No elemental Ti, Al, B or Si is detected. All of the composites contain a trace amount (<10%) of Ti$_3$Al. Figure 2, shows typical microstructures for the TiAl/Ti$_5$Si$_3$ composites. The Ti$_5$Si$_3$ phase precipitates both intra- and inter-granularly at the low Ti$_5$Si$_3$ volume fractions (10 and 25 vol. pct), Figs. 2a-b. At higher concentrations of Ti$_5$Si$_3$, the microstructure changes dramatically, and Ti$_5$Si$_3$ becomes the primary phase. However, TiAl still acts as the matrix or binder phase (Fig 2c-d). Typical microstructures of the TiAl/TiB$_2$ composites are shown in Fig, 3. Notice the large TiB$_2$ particles within the TiAl matrix. The microstructure does not change significantly with higher volume fraction of TiB$_2$, unlike the Ti$_5$Si$_3$ composites. Close, examination of the matrix indicates that it is actually composed of two phases. In the more Ti rich regions of the matrix, a lamellar α_2+γ (Ti$_3$Al+TiAl) structure has developed.

The processing conditions do little to alter the structure of the TiB$_2$ reinforcement of the in situ composites. However, by varying the processing parameters (time, temperature and pressure), the microstructure of the TiAl matrix is significantly altered. Generally, with increasing processing time, pressure and temperature, the matrix becomes more homogenous as the concentration of Ti$_3$Al in the matrix, decreases due to diffusion. Also, the TiAl matrix of the composites produced from hot-pressing cycle a (pressure applied after the reaction was initiated) is more homogenous than thar produced from cycle b (pressure applied before initiation of the reaction). This is due to the effect of pressure on the transient liquid phase that forms during the early stages of the reaction synthesis process [4]. The applied pressure forces the transient liquid phase into interstitial voids between the Ti powder. The liquid is presumably Al rich, and when it solidifies results in the microstructural inhomogeneity (i e., presence of Ti$_3$Al) observed in the TiAl matrix.

Figure 4. Biaxial Flexure strengths for TiAl matrix composites.

Figure 4 shows the results of the bi-axial flexural tests. There is a decrease strength with increasing Ti$_5$Si$_3$ content, probably due to the Ti$_5$Si$_3$ particles acting as a path for fast fracture. The strength of the TiB$_2$ composites increases with increasing TiB$_2$ content, even though the porosity increases with increasing reinforcement content. Monolithic TiAl fractures in a mixed mode; transgranular through areas of large TiAl grains, intergranular in regions of small TiAl grains, and "interlamellar" in areas of the lamellar α_2+γ duplex structure. The TiAl+Ti$_5$Si$_3$ (10 and 20 vol. pct.) composite also fractures in mixed mode, with fracture primarily transgranular

through the TiAl grains and intergranular around the Ti.Si, particles (Fig 5) Fracture of the TiAl TiB (10 and 20vol pct) composites again is primarily transgranular, but with some intergranular fracture in the fine-grained regions It appears that the TiB particles debond from the TiAl matrix as the crack swept through, resulting in pull out of the particles

Monolithic TiAl and the TiAl composites display active-passive corrosion behavior in the alkaline (0 5M NaOH) solution (Fig 6) From these curves it is evident that the Ti.Si, composite behaves in a similar manner to that of the monolithic TiAl Monolithic TiAl possesses the lowest corrosion potential (E_{corr}), followed by the TiAl/Ti.Si, composite, with the TiAl/10v% TiB composite
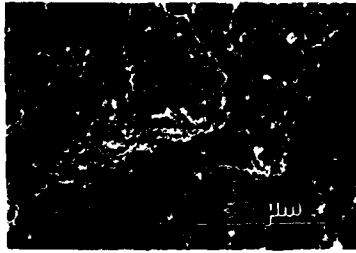
Figure 5 Fracture surface of the TiAl/20v% Ti.Si, composite in biaxial flexure

having the highest corrosion potential Of the three materials of interest, TiAl has the lowest passive current density, followed by the Ti.Si, composite, with the TiB composite possessing the highest value It is interesting that a reactive hot-pressed TiAl/TiC composite possesses a lower critical corrosion density than the monolithic TiAl composite Likewise, all the materials display active-passive behavior when exposed to the 0 5M H.SO, acidic solution The same trends in corrosion behavior are observed, with both the TiAl and the TiAl/Ti.Si, composite possessing a similar critical passive corrosion density, while the TiAl/TiB composite possesses a much higher critical passive current density Thus it appears the addition of TiB alters the corrosion behavior of TiAl, while the addition of Ti.Si, does not significantly change the behavior of TiAl
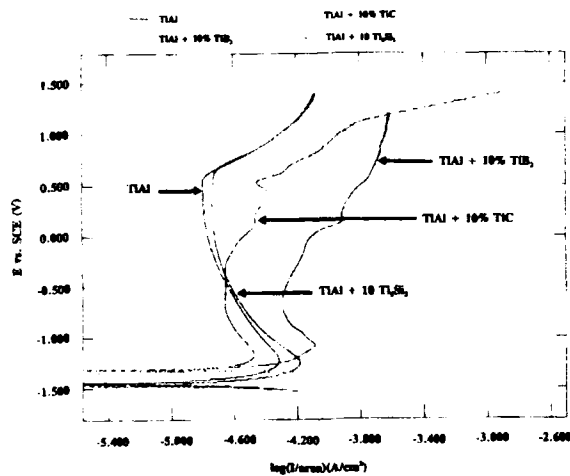
Figure 6   Polarization curves for TiAl matrix composites in 0 5 M NaOH solution

30

SUMMARY

The feasibility of forming *in situ* composites by reaction synthesis of mixtures of elemental powders is demonstrated. In general, dense composites are produced by applying pressure prior to initiating the reaction between the powders. Preliminary results of biaxial flexure tests indicate that the composites can be stronger than monolithic TiAl. Corrosion studies in acidic and alkaline solutions indicate that the addition of Ti_5Si_3 particles does not significantly alter the corrosion behavior of TiAl, whereas the addition of TiB_2 particles does alter the behavior of TiAl. Besides, making the composites reported herein; this technique has been used to produce TiAl/TiC [5,9] and $MoSi_2$/SiC [6,9] composites.

REFERENCES

1   Y. Nishiyama, T. Miyatshita, S. Isobe and T. Noda, in High Temperature Aluminides and Intermetallics, eds. S.H. Whang et. al, (TMS: Warrendale, Pa, 1990) p.557.
2.   M.C. Flemings, *Adv. Matls. and Processes,* 145 (1), 22 (1994).
3.   A.Bose, B. Moore, R.M. German and N.S. Stoloff, J. Metals, 40 (9), 14 (1988).
4.   D.E. Alman and N.S. Stoloff, *Intl. J. of Powder Met.,* 27 (1), 29 (1991).
5.   J.C. Rawers and W.R. Wrzesinski, *J. Mater. Sci.,* 27, 2877 (1992).
6.   D.E. Alman and N.S. Stoloff, *Scripta Met. et Mater.,* 28, 1525 (1993).
7   D.E. Alman, J.A. Hawk, A.V. Petty, Jr., and J.C. Rawers, *JOM,* 46 (3), 31 (1994).
8.   Z.A. Munir, *Bull. Am. Ceram. Soc.,*67 (2), 34 (1988).
9.   D.E. Alman, J.A. Hawk, C.P. Dogan and A.V. Petty, Jr., Presented at the 18th Annual Conference on Composite Materials (Restricted Sessions), Cocoa Beach, Florida Jan. 12-14, 1994. in press.

COMBUSTION SYNTHESIS OF NIOBIUM ALUMINIDE MATRIX COMPOSITES

C. R. KACHELMYER AND A. VARMA
University of Notre Dame, Department of Chemical Engineering, Notre Dame, IN 46556

ABSTRACT

Combustion synthesis of $NbAl_3$-matrix composites with Al_2O_3 and B additions was studied using the thermal explosion mode. The addition of B to the reaction mixture resulted in the formation of NbB_2, small amounts of NbB and unreacted Al. The Al_2O_3 addition did not affect the $NbAl_3$-matrix reaction completion but the final product density increased with increasing Al_2O_3 loading. In both $NbAl_3$-matrix composites, the reaction was initiated above the melting point of Al.

INTRODUCTION

Intermetallic aluminide compounds are considered to be promising candidates for structural applications owing to their attractive properties at elevated temperatures. These ordered intermetallics have high-temperature strength and exhibit resistance to oxidation and corrosion, high melting points and relatively low density [1]. Despite their potential, one drawback of these materials is embrittlement. However, ductility can be improved by alloying or by adding reinforcements, resulting in enhanced mechanical and metallurgical properties [2].

Aluminides are usually prepared by powder processing, plasma spray and arc melting and casting, which can be followed by either high-temperature extrusion or alternate cold rolling and recrystallization treatments [3]. Although these techniques are successful in the synthesis of intermetallics, they require several processing steps and complex equipment.

An alternative method of producing intermetallics is by combustion synthesis. In this method, the exothermic reaction between powder reactants is initiated by an external energy source (e.g. heated coil, laser beam) and becomes self-sustaining to yield the final product progressively without requiring additional heat. This process has advantages over conventional methods due to its simplicity and relatively low energy requirements. Combustion synthesis can be conducted in two modes: the self-propagating high-temperature synthesis (SHS) mode and the thermal explosion mode. In the SHS mode, the reaction is initiated at one end of the sample, and a combustion wave self-propagates through the mixture of reactants. In the thermal explosion mode, the sample is heated uniformly in a controlled manner until reaction takes place essentially simultaneously throughout the sample volume. Combustion synthesis has attracted considerable interest in recent years, and details of this process and its prospects have been discussed in several review articles [4-7].

In order to control the process and prepare materials with tailored properties, basic steps of the synthesis need to be identified. By varying processing conditions such as green density and heating rate in the thermal explosion mode, the extent of reaction can be altered and some mechanistic information can be retrieved. This approach has been successfully utilized in combustion synthesis of materials such as aluminides of nickel, iron, copper, and titanium. Particularly, details of the synthesis of nickel aluminides [8, 9] and niobium aluminides [10] in the SHS mode, and nickel aluminides in the thermal explosion mode [11, 12] have been identified. Similarly, the Fe-Al [13] and Cu-Al [14] systems have been investigated by the thermal explosion mode, leading to mechanistic descriptions of product formation. The effects of processing variables were studied for the synthesis of Ti-Al compounds, including Ti_3Al [15] and TiAl [16].

Table I. Reactant Powders

Powder	Vendor	Size	Purity (%)
Nb	Atlantic Equipment Engineers	1-5 μm	99.8
Al	Johnson Matthey Electronics	-325 mesh	99.5
B	Aesar	-325 mesh	92
Al₂O₃	Johnson Matthey Electronics	22 μm	99.5
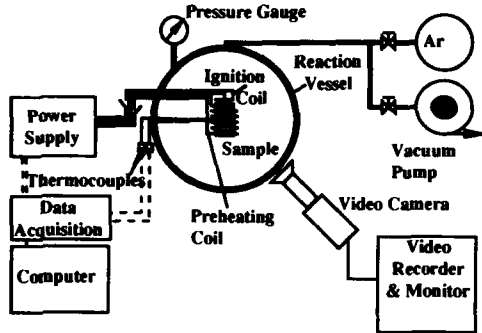
Figure 1. Schematic of the experimental set-up.
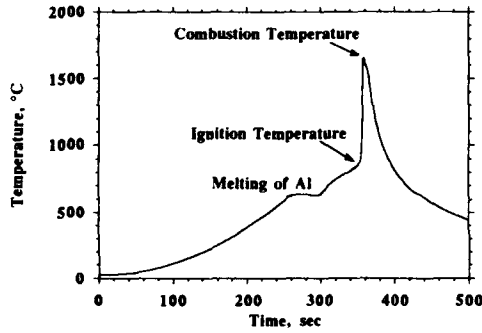
Figure 2. Temperature during NbAl$_3$-matrix composite synthesis with 1 wt% B.

The synthesis of reinforced nickel [9, 17], iron [18] and niobium [19, 20] aluminide matrix composites has also been investigated.

In previous work [21], we have synthesized various niobium aluminides by the thermal explosion mode. In the present work, we have directed our efforts toward the study NbAl$_3$-matrix composites produced by combustion synthesis. The addition of Al$_2$O$_3$ [12] and B [19, 20] reinforcements have been reported by other investigators to improve the mechanical properties of niobium aluminides. The optimal processing conditions identified earlier [21] for synthesis of NbAl$_3$ without reinforcement additions, were utilized for the synthesis of composites as well.

EXPERIMENTAL PROCEDURE

The reactant powders used in the experiments are described in Table I. The Nb and Al in a stoichiometric ratio of 1/3 were combined with the required amount of Al_2O_3 and B in hexane and the resulting slurry was mixed by an ultrasonic homogenizer. The dried mixture was pressed uniaxially at 140 MPa into 10 mm diameter, 10 to 15 mm long pellets. The density was evaluated from weight and geometric measurements, and kept fixed at 90% of the theoretical density of ρ_{NbAl_3} (4.54 g/cm^3).

The experimental set-up used is shown in Figure 1 and has been described in detail previously [22, 17]. It consists of a reaction vessel, a computerized data acquisition system and a video system. The pellet with thermocouples (W-Re, 10 mil) embedded at the center-line was placed in the reaction vessel which was evacuated to 10^{-3} torr. The vessel was then filled with argon gas at 1 atm. Samples are ignited in the SHS mode by a tungsten coil placed above the top end of the pellet, that is heated by a current pulse (50 A at 0-22 V) using a DC power supply. In the thermal explosion mode, the mode of synthesis used in the present study, a tungsten was coil wrapped around the pellet to heat the sample. The heating rate was controlled by varying the current (0-50 A at 0-22 V) passing through the wire. The temperature outside the sample was monitored continuously and the current was adjusted accordingly via a PID controller. This enabled us to achieve precise heating rates. The power to the coil was shut off immediately after the pellet experienced a sharp temperature rise.

Upon cooling to room temperature, the pellets were analyzed for phase composition by X-ray diffraction (XRD). Features of the microstructure were revealed by optical micrographs and analyzed for local phase composition by scanning electron microscopy (SEM) used in conjunction with energy dispersive X-ray spectrometry (EDXS).

RESULTS

The addition of B and Al_2O_3 to form $NbAl_3$-matrix composites was investigated. The samples were processed with a heating rate of 200°C/min. A typical temperature profile during combustion is shown in Figure 2 for the $NbAl_3$-matrix composite with B added. As the sample is heated, the temperature follows the programmed set-point until the aluminum melting point is reached (660°C). The melting takes ~40 seconds and is indicated by the plateau in the temperature profile. During this time of melting, the heating is continued. After the completion of melting, the sample continues to heat to the ignition temperature of 890°C where the temperature increases sharply to the combustion temperature, T_c.
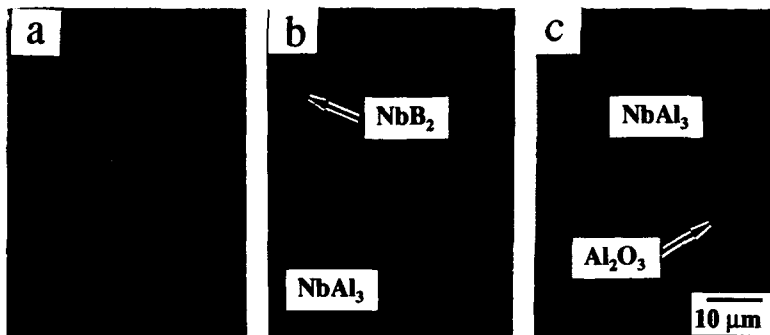
Figure 3. Optical micrographs of etched microstructures:
(a) $NbAl_3$ product and $NbAl_3$-matrix composites with (b) 2 wt% B and (c) 2 wt% Al_2O_3.

35
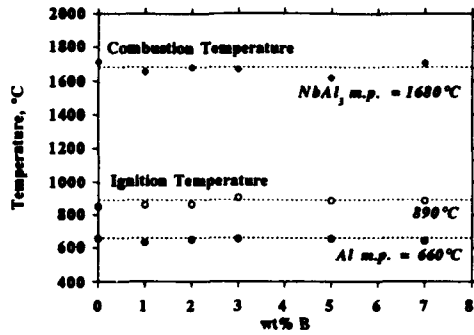
Figure 4. Effect of B loading on temperature.
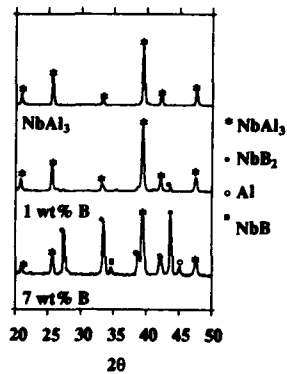
Figure 5. XRD patterns of (a) NbAl$_3$ product and
NbAl$_3$-matrix composites with (b) 1 wt% B and (c) 7 wt% B.

Optical micrographs of etched microstructures are shown in Figure 3 for the NbAl$_3$ product without any addition, and reacted samples with 2 wt% B and Al$_2$O$_3$ added to the reactant mixture. In each microstructure, there is the presence of NbAl$_3$ grains. The rounded equilibrium shape of the grains is characteristic of grain growth from a melt. When 2 wt% B is added, interaction between Nb and B results in the formation of NbB$_2$ phase that appears between the grains of NbAl$_3$ (Figure 3b). The presence of NbB and unreacted Al was also detected by XRD analysis, whereas the formation of boron aluminides was not detected. In the sample with Al$_2$O$_3$ added (Figure 3c), the Al$_2$O$_3$ did not interact with Nb or Al and is located in between the NbAl$_3$ product grains.

The effect of B addition on the characteristic temperatures during synthesis is shown in Figure 4. After melting of Al, the sample heating is continued to ~890°C, where the reaction is initiated and the temperature increases sharply to the NbAl$_3$ m.p. (1680°C). These temperatures are essentially independent of B loading for the range studied. XRD analysis showed that as the B content is increased, there is a greater formation of NbB$_2$ and a greater amount of unreacted Al, as shown in Figure 5.

36
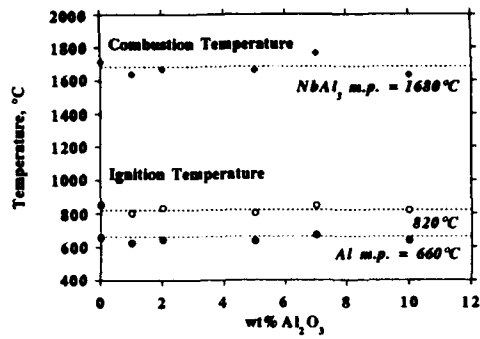
Figure 6. Effect of Al_2O_3 loading on temperature.
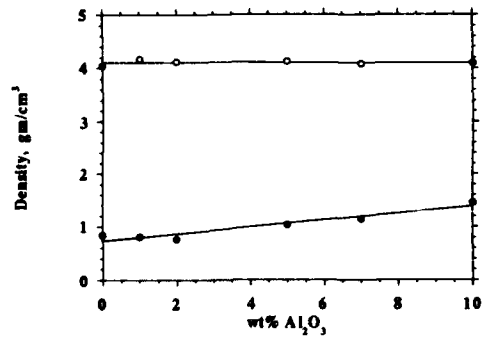
Figure 7. Effect of Al_2O_3 loading on product density.
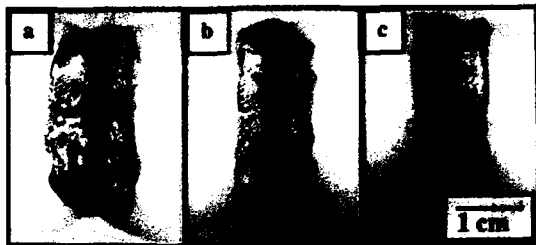
Figure 8. Reacted $NbAl_3$-matrix composites with
(a) 2 wt%, (b) 5 wt% and (c) 10 wt% Al_2O_3.

37

The effect of Al_2O_3 loading on temperature is shown in Figure 6. As in the other studies, melting of Al is followed by ignition (820°C) and the temperature increases sharply to the combustion temperature of 1680°C. The characteristic temperatures during synthesis are also independent of the Al_2O_3 addition (Figure 6). XRD analysis indicated that the $NbAl_3$ matrix formation is independent of Al_2O_3 loading and is essentially complete. However, measurements of the density after reaction revealed that the product density increased with Al_2O_3 loading (Figure 7). Photographs of the reacted samples with 2, 5 and 10 wt% Al_2O_3 illustrate the increase in product density (Figure 8).

DISCUSSION

As in the synthesis of $NbAl_3$, ignition of $NbAl_3$-matrix composites occurs at a temperature above the melting point of Al. In previous work, insight into why the T_{ig} is greater than the Al melting point was obtained with a particle-foil experiment where the interaction of molten Al with solid Nb was isolated [21]. This experiment revealed that after melting, Al initially forms a spherical drop and does not wet the Nb foil surface. As the temperature increases, the contact angle is reduced and there is formation of niobium aluminides where molten Al can spread. This observation with the particle-foil experiment provides a possible explanation for the results in pellets, where the initial non-wetting characteristic of Al over Nb may be responsible for ignition above the Al melting point.

The ignition and combustion temperatures during synthesis are independent of B addition (Figure 4). However, the formation of NbB_2 and the amount of unreacted Al, both increase with increasing B content (Figure 5). At the reaction temperature (1680°C), Nb and B both exist as solids where one would expect limited interaction. However, this temperature exceeds the eutectic temperature of 1600°C, present in the Nb-B system. Thus, the formation of the eutectic provides additional liquid, enhancing contact between Nb and B. In addition, since the NbB_2 heat of formation (-60 kcal/mol) is greater than that for $NbAl_3$ (-28.1 kcal/mol), the formation of the niobium boride is thermodynamically favored over the aluminide.

The characteristic temperatures and reaction completion are independent of Al_2O_3 loading (Figure 6). Since the sample is heated uniformly during synthesis in the thermal explosion mode, the presence of an inert phase does not affect the synthesis. This observation is in contrast to the case of Ni_3Al samples with Al_2O_3 added and ignited in the SHS mode, where heat losses to Al_2O_3 resulted in a slower combustion wave velocity, lower temperature and subsequently incomplete reaction as the amount of Al_2O_3 was increased [17]. The density of $NbAl_3$-matrix composite product increases with increasing Al_2O_3 content. At lower Al_2O_3 loadings, large pores can be observed in the samples. A sample was heated in vacuum and resulted in a higher density product, as compared to samples reacted under an argon atmosphere. This has also been observed previously in the reactive sintering of $NbAl_3$ where samples reacted under vacuum yield a higher density product than samples synthesized in argon [12]. It appears that the entrapped gases in the pellet expand during heating and this expansion is obstructed by the presence of Al_2O_3 particles, resulting in a higher product density.

CONCLUDING REMARKS

In this study, the effects of Al_2O_3 and B additions on the synthesis of $NbAl_3$-matrix composites by the thermal explosion mode were investigated. With the addition of B to the (Nb + 3Al) reaction mixture, B competes with the Al to react with Nb. This results in the formation of NbB_2, along with NbB, as the B content is increased. Thus, an excess of Nb added to the reaction

mixture may be beneficial in order to form a fully reacted $NbAl_3$ matrix. The Al_2O_3 reinforcement is inert in the presence of Nb and Al, in the amounts added (1-10 wt%), and does not influence reaction completion since the sample is heated uniformly in the thermal explosion mode. Higher density $NbAl_3$-matrix composites result with larger amounts of Al_2O_3 due to the disruption of expanding gases during synthesis. This may allow control of the product density. The final product density may be increased further by degassing the unreacted sample with some heating. The reactions are initiated above, rather than at, the melting point of Al. The initial non-wetting characteristic of Al over a Nb surface, as determined in the synthesis of $NbAl_3$ [21], may be responsible for this behavior.

ACKNOWLEDGEMENTS

REFERENCES

1. C. T. Liu and J. O. Stiegler, in Metals Handbook, edited by S.R. Lampman et al., (ASM International, Materials Park, OH, 1990) Vol. 2, pp. 913-942.
2. I. Baker and P. R. Munroe, J. Met., **40**, 28 (1988).
3. N. S. Stoloff and C. T. Sims, in Superalloys II, edited by C. T. Sims, N. S. Stoloff and W. C. Hagel, (John Wiley & Sons, Inc., New York, 1987), pp. 519-527.
4. Z. A. Munir and U. Anselmi-Tamburini, Mater. Sci. Rep. **3**, 277 (1989).
5. A. G. Merzhanov, in Combustion and Plasma Synthesis of High-Temperature Materials, edited by Z. A. Munir and J. B. Holt, (VCH Publishers, New York, 1990) pp.1-53.
6. J. B. Holt and S. D. Dunmead, Annu. Rev. Mater. Sci. **21**, 305 (1991).
7. A. Varma and J.-P. Lebrat, Chem. Eng. Sci. **47**, 2179 (1992).
8. J.-P. Lebrat and A. Varma, Comb. Sci. Tech. **88**, 211 (1992).
9. J.-P. Lebrat, A. Varma, and P. J. McGinn, J. Mater. Res. (in press).
10. V. M. Maslov, I. P. Borovinskaya, and M. Kh. Ziatdinov, Combust. Explos. Shock Waves **15**, 41 (1979).
11. K. A. Philpot, Z. A.Munir, and J. B. Holt, J. Mater. Sci. **22**, 159 (1987).
12. W. Misiolek and R. M. German, Mater. Sci. Eng. **A144**, 1 (1991).
13. B. H. Rabin and R. N. Wright, Metall. Trans. A **22A**, 277 (1991).
14. L. L. Wang, Z. A. Munir, and J. B. Holt, Metall. Trans. B **21B**, 567 (1990).
15. C. R. Kachelmyer, J.-P. Lebrat, A. Varma, and P.J. McGinn, in Heat Transfer in Fire and Combustion Systems, edited by P. Farouk, M. P. Pinar Menguc, R. Viskanta, C. Presser, and S. Chellaiah, (ASME, New York, 1993) pp. 271-276.
16. H. C. Yi, A. Petric, and J. J. Moore, Solid State Phenomena **25 & 26**, 225 (1992).
17. J.-P. Lebrat, A. Varma, and A. E. Miller, Metall. Trans. A **23A**, 69 (1992).
18. B. H. Rabin and R. N. Wright, Metall. Trans. A **22A**, 277 (1991).
19. C. T. Ho, M. G. Lakshmikantha, and J. A. Sekhar, in Processing and Fabrication of Advanced Materials for High Temperature Applications, edited by V.A. Ravi and T.S. Srivastan, (Warrendale, Pennsylvania, 1992) pp. 23-43.
20. A. K. Bhattacharya, J. Am. Ceram. Soc. **75**, 1678 (1992).
21. C. R. Kachelmyer and A. Varma, J. Mater. Res. (in review).
22. J.-P. Lebrat and A. Varma, Physica C **184**, 220 (1991).

AMBIENT TEMPERATURE SYNTHESIS OF BULK INTERMETALLICS

M. RATZKER[1], D.S. LASHMORE[2] and M.P. DARIEL[3]

[1] American Dental Association Health Foundation, Paffenbarger Research Center
[2] Materials Science and Engineering Laboratory, Metallurgy Division
National Institute of Standards and Technology, Gaithersburg MD, 20899
[3] Department of Materials Engineering, Ben-Gurion University of the Negev, Beer-Sheva, Israel

ABSTRACT

Room-temperature intermetallic compound formation occurs when one of the component metals has a very low melting point or when two metals in close contact interdiffuse very rapidly. Compound formation at room temperature at the interface of superposed thin films has been observed in several instances, often in systems relating to electronic materials. The overall amount of compound produced in such configurations, however, is limited, due to the intrinsic limitations involved in the thin layer geometry. Bulk quantities of intermetallic can be produced at ambient temperature in solids by increasing the interface area between the components that interdiffuse rapidly. This condition can be achieved by having small size powder particles of one component coated with a layer of the second component. The very large interface area leads to rapid formation of bulk quantities of compounds even at ambient temperature. By appropriate control of the initial constituents and the coating parameters, it is possible to custom-prepare various intermetallic compounds present in binary systems such as silver-tin, gold-tin and silver-indium in which fast interdiffusion takes place.

INTRODUCTION

The high melting points, the low ductility and low fracture toughness of intermetallic compounds make it difficult and often impossible to use conventional metal shaping and forming operations. Powder metallurgy techniques can be employed, although the mostly brittle pre-alloyed intermetallic compounds do not compact well, and therefore, the green strength and density of intermetallic compound compacts are low. In order to overcome this problem, the elemental ductile constituents of the intermetallic compounds are blended and compacted. Compound formation and sintering in the compacted mixtures result from mutual interdiffusion of the constituents and take place during the high temperature treatment of the compacts.

In some instances, high temperature has to be avoided, although intermetallic compound formation and shaping are still required. Ambient temperature synthesis and shaping of intermetallic compounds take place when one of the constituents is a liquid metal at or close to room temperature. The reaction between the liquid metal and the other constituents in a powdered form takes place in appropriate molds, and custom-shaped intermetallic products can be formed. A well-known example of this procedure is the formation of dental restorations consisting of the reaction product between liquid mercury or gallium and various silver-tin-copper alloy powders.

Room-temperature compound formation also takes place at the interface of two metals in close contact when one of these metals is either copper or a noble metal (palladium, silver or gold) and the other is a polyvalent metal such as indium, tin or lead, located in columns III-A or IV-A of the periodic table. Room-temperature compound formation in these systems is related to the well established fast diffusion behavior of the noble or near-noble component in the matrices of the group III-A or IV-A metals [1]. The quasi-totality of the room-temperature intermetallic compound formation studies in these systems have made use of a thin film configuration [2]. This configuration yields samples with a high interface-to-total volume ratio permitting effective study of compound formation at the interface. The thin film configuration, due to its intrinsic geometrical limitations, does not lend itself to the production of bulk quantities of intermetallic compounds.

A significant volume of intermetallic compound can be produced by solid state interdiffusion if the contact area between the two reacting constituents is sufficiently large. Preliminary experiments

have shown that compound formation in very homogeneous mechanical mixtures of the two components of such systems does indeed take place, but the relative amount of compound formed at ambient temperature is very small. Even though small size powder particles display a large surface area-to-volume ratio, the contact area between adjacent particles of two different randomly mixed constituents is limited. The problem to be solved is, therefore, how to transform the external surface of the powder particles into an interface of the two different constituents across which efficient compound formation can take place.

Our approach to increase the contact interface area was to have one of the constituent metals applied as a coated layer to the external surface of the powder particles of the second constituent metal. Examination of the binary systems in which room temperature compound formation takes place by solid state interdiffusion shows that they consist of copper or a noble metal and of a more reactive metal, lying lower in the electromotive series of elements. This suggests the possibility of using displacement or immersion coating techniques [3,4]. In the present communication, we show that immersion coating of silver or gold on tin or indium powder yields a material with an extremely high interface area across which rapid compound formation takes place.

RESULTS AND DISCUSSION

The more reactive metal, indium or tin powder (In < 60 μm particle size, Sn < 10 μm particle size) was immersion coated in a solution of silver fluoroborate, $AgBF_4$, or gold chloride, AuCl. The initial amount of tin or indium, the concentration of $AgBF_4$ or AuCl in the solution, its pH and the immersion time were the parameters which determined the final reactive metal (indium or tin)-to-(silver or gold) ratio in the intermetallic. The powder was stirred in the solution for a predetermined duration; it was then allowed to settle and the excess solution was decanted. Some of the reactive metal dissolves in the solution or is oxidized, thereby permitting the reduction of the silver or gold ions and the subsequent precipitation of metallic silver or gold. The latter deposits on the free surface of the reactive metal and produces a large interface area of the two metals. The slurry-like deposit can be placed in appropriate molds and compressed to a desired shape; alternatively, it can be left to dry as a powder.

X-ray diffraction spectra of the product either in powder form or as a compressed solid are shown in Figs.1 to 4. The results indicate that a large fraction of the product material transforms into intermetallic compounds within the length of time that elapses from the settling and deflocculation of the deposit to the x-ray examination. The actual composition and structure of the product material depend on the free parameters of the immersion coating procedure, on the phases present in the binary diagram of the system and on some kinetic features of the nucleation and growth characteristics of the various phases.

The silver-tin phase diagram includes, in addition to terminal solid solutions, two intermetallic compounds, Ag_4Sn and Ag_3Sn. The structures of the two compounds are related, Ag_3Sn being an ordered orthorhombic variant of hexagonal Ag_4Sn, and have very similar diffraction patterns, Fig.1. Careful examination indicates that Ag_4Sn is formed preferentially as an outcome of the immersion coating process. Equilibration of the Ag-Sn product takes place even at room temperature, although at a slower pace than in the Ag-In system to be discussed next.

Four compounds are present in the silver-indium system at room temperature and two more at higher temperatures. The interdiffusion processes taking place in the coated powder are more complex than those in the silver-tin system. In the silver-indium system, the compound with the highest indium content is $AgIn_2$; the other compounds fall in the range of 20 to 34 at. pct. indium. By adjusting the initial amount of indium powder placed in the solution, its particle size, the total amount of dissolved silver in the form of $AgBF_4$ and the duration of the immersion

42

Fig.1. XRD-pattern of tin powder immersion coated with silver, 16 h after consolidation. The diffraction pattern consists mainly of the Ag_xSn lines that can be attributed to either Ag_4Sn or Ag_3Sn and of the Ag(Sn) lines that are due to the silver-rich solid solution with tin. The broadening and shifting of the latter is due to (i) the very small grain size of the silver deposit; (ii) the presence of a solid solution with variable tin content and consequently with a variable lattice parameter. The addition of tin causes an expansion of the silver lattice.
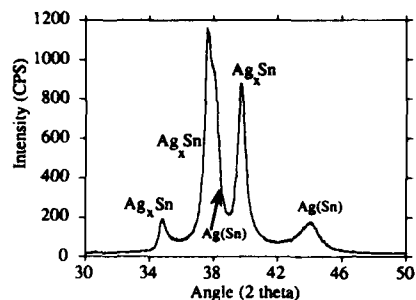
process, it was possible to predetermine the final silver to indium ratio and, thereby, the nature and amount of the compounds present in the product material, as illustrated in Figs. 2 and 3. In Fig. 2, the silver-to-indium ratio was adjusted to yield an indium-rich composition corresponding to the $AgIn_2$, denoted as the Φ phase. Immediately after consolidation of the mixture, the sample consisted of a mixture of 3 intermetallic compounds, free indium and silver (Fig. 2a). After 142 d at room temperature, the sample consisted essentially of the Φ phase with roughly 10 pct. of γ, or Ag_9In_4, as shown in Fig. 2b. Fig. 3 shows the diffraction patterns of the sample with a higher silver content. Immediately following the deposition of silver and consolidation of the slurry, the sample consisted of several compounds that are present in the system, in addition to indium metal and the terminal solid solutions Ag(In), Fig. 3a. Noteworthy is the significant fraction of the ζ phase, which has an extended solubility range above 300 °C and only a very narrow range at room temperature [5]. The diffraction pattern after 20 h at room-temperature shows the gradual decrease of the ζ phase (Fig. 3b) until its disappearance along

Fig. 2. XRD-patterns of indium powder immersion coated with silver. Pattern (a) was obtained immediately following the consolidation of the slurry-like mixture consisting of indium and silver deposit. Pattern (b) is of a sample maintained for 142 d at room temperature. The indium-to- silver ratio in this sample was adjusted to yield a sample consisting essentially of the $AgIn_2$ compound.
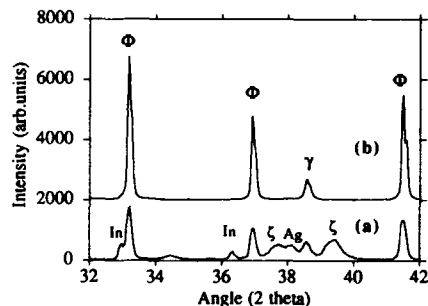
with that of free indium and silver and their replacement by a mixture of γ and α' phases (Fig.3c). In these particular systems, the atomic mobility is sufficient to permit significant diffusion processes even at room temperature . Diffusion processes act to promote equilibration of the compound, both in the sense of reducing composition gradients and in allowing the nucleation and growth of equilibrium crystal structures.

43

Fig.3. XRD patterns of indium powders immersion coated with silver. The indium-to-silver ratio is higher in this sample than in the one shown in Fig.2. After consolidation (a), the sample consists of the initial metal components, silver and indium, and of a mixture of several intermetallic compounds, namely $AgIn_2$ (Φ), some Ag_9In_4 (γ) and the ζ phase, which at equilibrium exists in only a very narrow composition range at room temperature. After 20 h at room temperature, (b), the concentration gradients are reduced and the system shifts towards the room-temperature equilibrium structure, which is shown in (c) and where the sample consists of a mixture of Ag_3In (α') and the γ phase.
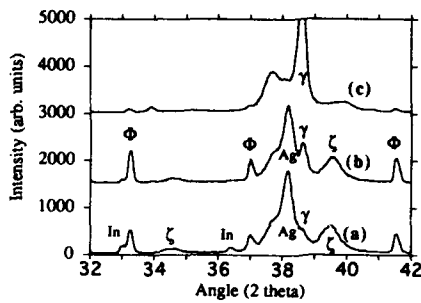
The gold-tin system is also relatively complex, with four intermetallic compounds at room-temperature in addition to the terminal solid solutions [6]. Two more intermetallic phases are present in gold-rich alloys at elevated temperatures. The deposit of tin powder particles immersion coated with gold yields after consolidation a nearly single phase structure of the δ phase, AuSn, with some unalloyed gold and a small amount of ϵ phase, $AuSn_2$, as shown in Fig. 4. In this system, the congruently melting AuSn appears to nucleate and grow preferentially and is the first compound that appears.

Fig.4. XRD pattern of tin powder immersion coated with gold. The pattern was obtained immediately following the consolidation of the slurry-like mixture consisting of tin and gold deposit. At this point, the sample consists essentially of the δ (AuSn) compound with some excess gold and approximately 5 pct. of the ϵ ($AuSn_2$) compound.
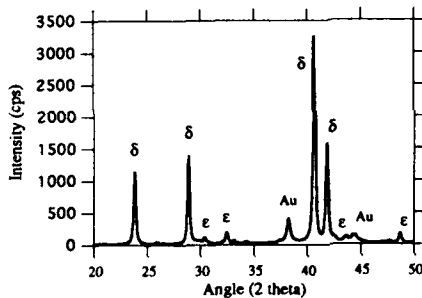
By consolidating the slurry-like mixture after the immersion deposition process in appropriate molds, it was possible to manufacture near-net shape samples that could be used for mechanical testing. The green strength of these samples, compressed at pressures as low as 200 MPa, was sufficient to allow handling. Compressive strength and rupture strength were measured, both as a function of the compression pressure and of various chemical surface treatments to which the powder was exposed prior to its consolidation. Rupture strength values deduced from three-point-bending test measurements, according to a modified ASTM B-312 method, are shown in Fig. 5. Samples a to c are various cast and annealed constituents of the Ag-Sn binary system and are shown for reference purposes. Samples d to e were prepared by variants of the methods

44

described in this communication. Noteworthy is the result for sample d (the diffraction pattern of which is similar to that shown in Fig.1), indicating that even though this sample had not been exposed to any high temperature treatment, it still displayed favorable rupture test values.

Fig.5. Rupture strength, as measured in three-point-bending tests, of various samples in the Ag-Sn system. Each measurement represents the average of 6 specimens: (a) is cast and annealed silver; (b) is cast and annealed Ag_3Sn; (c) is cast and annealed Ag_4Sn; (d) is tin powder immersion coated with silver and compressed at 360 MPa with no further treatment. The XRD pattern of this sample is shown in Fig.1; (e) is atomized Ag60pct.Sn 40 pct. alloy immersion coated with

silver and compressed at 350 MPa; (f) is the same as (e) with thermal anneal of 48 h at 200 °C, 48 h at 460 °C further anneal of 48 h at 640 °C. The XRD pattern of this sample after the thermal anneal showed that it consisted of Ag_4Sn.
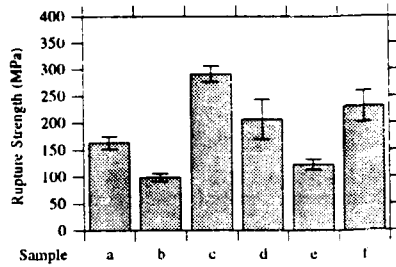
CONCLUSIONS

We have developed a powder-metallurgical process for producing bulk quantities of intermetallic compounds in custom-tailored shapes at room temperature. The method is applicable to intermetallic compounds occurring in binary metallic systems in which fast diffusion promotes compound formation at ambient temperatures. The method relies on the formation of a large interface area, across which compound formation takes place, by having one of the constituent metals to deposit from an appropriate solution on the external surface of the powder particles of the second constituent. The slurry like mixture of the initial powder with immersion-deposited silver or gold can be compressed under low pressure to near-net shape samples that display relatively high green rupture strength values.

ACKNOWLEDGMENT

REFERENCES

1.   W.K. Warburton and D. Turnbull, in Diffusion in Solids, Recent Developments   edited by   A.S.Nowick and J.J. Burton (Academic Press, New York, 1975), p.172.

2. K.N. Tu and R. Rosenberg, Jap. J. Appl. Phys. Suppl. **2**, Pt.1, 633 (1974); K.N. Tu, Ann. Rev. Mater. Sci. **15**, 147 (1985).

3. F.A. Lowenheim, Electroplating, (McGraw-Hill Inc., New-York, 1978), chap. 18.

4. E.A. Parker, in Gold Plating Technology, edited by F.H. Reid and W. Goldie (Electrochemical Publications Limited, Glasgow, 1974), chap. 10.

5. M.R. Baren, in Binary Phase Diagrams, 2nd edition, edited by T.B. Massalski (ASM International, Materials Park, 1990), p.47.

6. H Okamoto and T.B. Massalski, in Binary Alloy Phase Diagrams, edited by T.B. Massalski (ASM International, Materials Park, 1986), p.315.

WEAR BEHAVIOR OF SHS INTERMETALLIC MATRIX COMPOSITES

J.A. HAWK and D.E. ALMAN
U.S. Bureau of Mines, Albany Research Center, Albany, OR 97321

ABSTRACT

A number of discontinuously reinforced, intermetallic matrix composites (i.e., TiAl/TiC, TiAl/TiB$_2$, TiAl/Ti$_5$Si$_3$) were formed *in situ* through self-propagating, high-temperature synthesis (SHS) between elemental powders. *This Bureau of Mines study characterizes the abrasive wear* behavior of these composites. Wear behavior is discussed with respect to process history, and type and volume fraction of reinforcement. Generally, higher process temperatures lead to dense composites, resulting in better wear resistance. The wear behavior of the SHS intermetallic composites is compared to other intermetallics, produced by conventional techniques.

INTRODUCTION

The high strengths and high elastic moduli of intermetallics can be combined with the ductile properties of selected metals to produce composite materials which possess unique mechanical properties. *Self-propagating high-temperature synthesis (SHS) uses the heat of* formation of the resulting compound to form intermetallics from elemental powders [1]. SHS has also been used to form two phase composites [2-6]. Researchers at the Bureau of Mines have subsequently used a vacuum hot press to form near fully dense intermetallics and intermetallic matrix composites from elemental starting powders [3-5]. These materials are being investigated for their abrasive wear resistance because of the possibility of forming *in situ* hard, wear resistant second phase constituents.

In SHS processing the initial powder reactants are ignited, initiating a self-sustaining, heat-generating chemical reaction that results in their transformation into compounds or intermetallic phases [7,8]. When a compacted mixture of elemental Ti and Al powder is heated at one end, the Ti and Al react, producing titanium aluminide (TiAl). Because of the exothermic heat liberated during the formation of TiAl, powder immediately adjacent to the reaction also reacts. These reactions continue, increasing in magnitude, until they form a self-sustaining front. This reaction front then propagates through the entire powder compact, converting it to TiAl. Once initiated, the reaction requires no additional external heat source. SHS processing has been successfully used to form metal-aluminides, -borides, -carbides, -nitrides, and -silicides. In this research, SHS is used to create a number of dual phase composites, i.e., a TiAl matrix with TiB$_2$, TiC, and Ti$_5$Si$_3$ reinforcing phases and their abrasive wear properties have been evaluated.

MATERIALS AND PROCESSING PROCEDURE

The materials selected for study were based on metals that would react with Al to form a metal-aluminide. The powder material system studied was Ti-Al with intermetallic-ceramic particulate composites formed, utilizing TiAl as the matrix. Ternary additions of C, B, and Si

47

were added to stoichiometric TiAl to make composites with TiC, TiB_2 and Ti_5Si_3 reinforcements, with volume fractions of up to 60% [11].

Composite formation was accomplished in a vacuum hot-press, with the following processing: (1) the material was placed in a graphite die and transferred to the hot-press; (2) pressure was applied to the sample as the temperature was ramped to the SHS ignition temperature; (3) at the point where the SHS reaction began, the applied pressure was increased, and the sample was either held at the reaction temperature, or given a post-reaction heat-treatment at an elevated temperature; and finally, (4) the sample was cooled to room temperature under pressure. The application of pressure to the composite during the SHS reaction, and during post-SHS heat treatment, reduced composite porosity and improved composite density. Previous studies [2-4] have shown that maximum density and optimum strength are obtained by hot-pressing elemental powders for long times at high temperatures. Therefore, the post SHS heat treatments were performed at temperatures between 1000°C and 1200°C and pressures between 10-20 MPa for times up to one hour.

Abrasive wear tests were performed on the Bureau of Mines pin abrasion wear tester. A description of the pin abrasion test and the general operating procedures are given in References 12 and 13. For the wear tests performed in this study, cylindrical pins of the SHS processed intermetallics and intermetallic composites were abraded on 150 grit garnet, a naturally occurring mineral. The garnet had a Vickers hardness (VHN) of 1336 kg/mm^2, and the averag$_3$ abrasive particle size fell in the range of 80 to 100 μm. The wear rates (W_c) for the monolithic and composite materials were corrected for their density, thus providing an intrinsic comparison of the wear behavior of the materials.

RESULTS AND DISCUSSION

SHS Intermetallic/Ceramic Composites: Effect of Processing on Wear

The primary goal of this research is to determine the feasibility of creating intermetallic-ceramic composites with differing reinforcement type and volume fractions. A second goal is to determine which reinforcement (i.e., Ti_5Si_3, TiC, and TiB_2) is most effective in improving the abrasive wear resistance of the TiAl matrix. Table I provides information on the quality of the SHS produced TiAl-TiB_2 composites as measured by the percent theoretical density and process history. For the other compositions, the TiAl-Ti_5Si_3 composites are more fully dense than the TiAl-TiB_2 composites, for equivalent SHS process conditions. Alternatively, the TiAl-TiC composites possess the same general morphology as the TiAl-TiB_2 composites, i.e., at high TiC volume fractions, the composite becomes more porous. Information on microstructure and mechanical properties for these materials can be found in Reference 14. Also included in Table I are the measured wear rates for each TiAl-TiB_2 composite. Please note the following from these results: (i) the higher the post SHS heat treatment temperature, the more dense the final composite; (ii) for equivalent temperature and post heat treatment time at temperature, increased pressure during the SHS cycle leads to a more fully dense composite; and (iii) for the TiAl-TiB_2 composite, the higher the volume fraction (i.e., > 20 %) of TiB_2, the less dense the final composite. Lower abrasive wear rates are associated with the more dense TiAl-TiB_2 composites.

For the TiAl-TiB_2 composites, lower wear rates are obtained with increased volume fraction of TiB_2, when the theoretical densities are nearly equal. Only the TiAl composite with 10% TiB_2 exhibits consistent wear behavior for all process conditions. The measured wear rate in this case is 0.965 ± 0.064 mm^3/m. For the other compositions and process histories, the density of the final composite greatly affects the wear behavior.

48

Table I. Processing Conditions and Wear Rates for TiAl-TiB$_2$ Composites

Temperature (°C)	Pressure (MPa)	Time (min)	Density as Processed		Wear Rate (mm^3/m)
			Vol% TiB$_2$	% T.D.	
1200	10	60	10	93	0.81 ± 0.06
			25	92	0.34 ± 0.03
			60	84	3.95 ± 0.73
1000	10	5	10	81	1.04 ± 0.10
			25	77	0.64 ± 0.14
			60	72	0.42 ± 0.19
1000	10	15	10	85	0.91 ± 0.07
			25	81	1.15 ± 0.07
			60	72	1.30 ± 0.59
1000	10	60	10	85	1.00 ± 0.06
			25	82	0.88 ± 0.05
			60	72	1.61 ± 0.33
1000	20	60	10	90	0.91 ± 0.03
			25	87	0.77 ± 0.05
			60	74	0.99 ± 0.20

SHS Intermetallic/Ceramic Composites: Microstructure

The microstructures developed in these composites depend upon their compositions. The 10 vol% materials consist of a TiAl matrix with the Ti-based phases dispersed throughout the matrix. As the volume fraction increases, the reinforcement becomes interconnected and continuous. This is illustrated in Figure 1, in photomicrographs of the 10 and 60 vol% TiAl-TiB$_2$ composites. In the 10 vol% material (1a), the TiB$_2$ particles are typically small (approximately 10 μm or less in diameter), although some larger particles (e.g., 25 μm) can also be found. In the 60 vol% composite (1b), on the other hand, many large particles (i.e., in excess of 50 μm) are found. This same general trend is followed for the TiAl composites reinforced with TiC and Ti$_5$Si$_3$.

SHS Intermetallic/Ceramic Composites: Wear Behavior

Table II tabulates the wear rates of the TiAl-TiB$_2$ composites as a function of TiB$_2$ volume fraction. These composites were all processed at 1200°C, resulting in relatively dense materials. It is clear from Table II that for dense composites, the wear rate decreases as the volume fraction of TiB$_2$ increases. When the composite is porous, however, the wear rate will increase as the volume fraction increases (Table III).

Table III shows that TiB$_2$ is generally the more effective wear resistance phase. In general for abrasive wear tests, the harder the reinforcing phase, and the more fully dense the composite, the more wear resistant is the material. However, having a more fully dense composite in which the reinforcement is well bonded with the matrix is more important for improving wear resistance than simply having a hard reinforcement. If the composite cannot
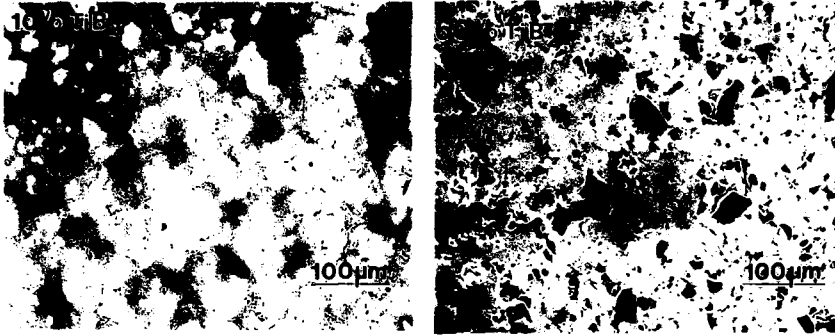
Figure 1   Backscattered electron micrographs of the TiAl-TiB$_2$ composites: (a) 10 vol%
TiB$_2$ and (b) 60 vol% TiB$_2$.

Table II.   Density (mg/mm^3) and Abrasive Wear Rate (mm^3/m) as a Function of TiB$_2$
Volume Fraction (Value in parentheses is percent theoretical density.)

Volume Percent TiB$_2$ Reinforcement		
10%	20%	35%
Density	3.46 (87%)	3.73 (93%)	3.96 (96%)
Wear Rate	0.70 ± 0.01	0.28 ± 0.03	0.09 ± 0.02

SHS process conditions: 1200°C, 20 MPa, 1 hour

Table III.   Comparison of Abrasive Wear Rates (mm^3/m) for More Porous TiAl Composites

Reinforcing Phase	Vol% Reinforcing Phase		
	10	25	60
TiC	1.21 ± 0.02	1.29 ± 0.04	---
Ti$_5$Si$_3$	1.17 ± 0.03	1.15 ± 0.02	0.80 ± 0.01
TiB$_2$	0.90 ± 0.03	0.75 ± 0.05	0.79 ± 0.14

SHS process conditions: 1000°C, 20 MPa, 1 hour

Table IV.   Comparison of Abrasive Wear Rates (mm³/m) for 10 vol% TiAl Composites at
            1000°C and 1200°C (20 MPa; 1 hour)

Alloy/Composite	1000°C	1200°C
TiAl + TiC	1.21 ± 0.02	---
TiAl + Ti₅Si₃	1.17 ± 0.03	0.85 ± 0.02
TiAl + TiB₂	0.90 ± 0.03	0.70 ± 0.01

remain intact under the compressive loading during abrasion, fracture will occur and the hard
second phase reinforcement will drop out, accelerating the material removal rate.

Table IV highlights the differences in wear rates with SHS processing temperature. Note
that for both the TiAl-TiB₂ and the TiAl-TiC composites, a more fully dense composite is
obtained at 1200°C [14]. Thus, in both instances the wear rate has decreased significantly. The
results in Tables III and IV also highlight the superior wear resistance of the TiAl-TiB₂
composite. It is clear that this composite is more wear resistant than the one with Ti₅Si₃, which
in turn is more wear resistant than the composite with TiC.

SHS Intermetallics: Wear Behavior

Table V shows the wear rates of various intermetallic alloys produced by the SHS
technique. The SHS materials were processed at 1100°C (20 MPa pressure, 1 hour). Also
provided in the table, for comparative purposes, is the wear behavior of more conventionally
processed intermetallic alloys. Notice that in each case, the wear rate of the SHS processed
intermetallics is equivalent to, or lower than, the wear rates of the conventionally produced (i.e.,
melted and cast) intermetallics. Also note that the Ti rich intermetallic alloys (i.e., TiAl and
Ti₃Al) possess lower wear rates than the Al rich intermetallic, i.e., TiAl₃.

Table V.   Abrasive Wear Rates For Selected SHS and Cast Intermetallic Alloys

Alloy Composition	Density (mg/mm³)	Wear Rate (mm³/m)
Fe₃Al (cast)	6.7	1.08
Fe₃Al (SHS)	6.7	1.11
TiAl (cast)	3.9	1.19
TiAl (SHS)	3.9	1.09
Ti₃Al (SHS)	4.2	1.08
TiAl₃ (SHS)	3.4	1.21

51

SUMMARY OF POWDER COMPOSITE RESEARCH

SHS process technology can be used to form wear resistant intermetallic composites. In particular, abrasive wear resistance is enhanced for near fully dense intermetallic composites containing a hard second phase, e.g., low volume fractions (up to 35%) TiB_2 in TiAl.

SHS process conditions are important parameters; that is, (1) high processing temperatures leads to dense composites; (2) powders reacted under pressure lead to dense composites; and (3) high volume fractions of B, C result in porous composites.

Abrasive wear resistance depends primarily on composite density and matrix-reinforcement integrity:

$$dense\ composite \rightarrow superior\ wear\ resistance$$

and on the hardness and volume fraction of the reinforcement:

$$high\ hardness,\ high\ volume\ fraction \rightarrow superior\ wear\ resistance$$

The following trend in wear resistance with reinforcing phase type emerges from the wear testing of TiAl-X composites:

$$wear\ resistance\ of\ TiAl\text{-}TiC\ <\ TiAl\text{-}Ti_5Si_3\ <\ TiAl\text{-}TiB_2$$

for dense composites.

REFERENCES

1. K. A. Philpot, Z. A. Munir, and J. B. Holt, *J. Mater. Sci.*, **22(1)** (1987) 159.
2. J. C. Rawers, H. E. Maupin and W.R. Wrzesinski, in <u>Advances in High Temperature Structural Materials and Protective Coatings</u>, edited by A.K. Koul, V.R. Parameswaran, J-P. Immarigeon, and W. Wallace (National Research Council of Canada, Ottawa, Canada, 1994), p. 348.
3. W. R. Wrzesinski and J. C. Rawers, *J. Mater. Sci. Letts.*, **9(3)** (1990) 432.
4. W. R. Wrzesinski and J. C. Rawers, *Scripta Metal.*, **24(10)** (1990) 1985.
5. Z. Munir, *Ceramic Bulletin*, **67(2)** (1988) 342.
6. J. H. Westbrook, in "Mechanical Properties of Intermetallic Compounds," John Wiley & Sons, New York, NY, 1960.
7. Z. A. Munir, Ceram. Bull. <u>67</u>, 342 (1988).
8. J. Subrahmanyam and M. Vijayakumar, J. Mater. Sci. <u>27</u>, 6249 (1992).
9. J. C. Rawers, W. R. Wrzesinski, E. K. Roub and R. R. Brown, Mater. Sci. Technol. <u>6</u>, 187 (1990).
10. J. C. Rawers and W. R. Wrzesinski, J. Mater. Sci. <u>24</u>, 2877 (1992).
11. H. E. Maupin, J. C. Rawers and J. A. Hawk, in <u>The Advanced Synthesis of Engineered Structural Materials</u>, edited by J. J. Moore, E. J. Lavernia and F. H. Froes (ASM, Materials Park, OH, 1993), p. 9.
12. R. Blickensderfer and G. Laird II, J. Test. Eval. **16**, 516 (1988).
13. R. Blickensderfer, J.H. Tylczak and B.W. Madsen, Bureau of Mines Information Circular (IC 9001), 1985.
14. D.E. Alman, J.A. Hawk, C.P. Dogan, M. Ziomek-Moroz and A.V. Petty, Jr., Proceedings MRS Symposium on *Intermetallic Matrix Composites III* (this volume).

FRACTURE CHARACTERISTICS OF METAL-INTERMETALLIC LAMINATES PRODUCED BY SHS REACTIONS

D.E. ALMAN AND J.C. RAWERS
U.S. Bureau of Mines, Albany Research Center, Albany, Oregon 97321

ABSTRACT

The tensile behavior of metal-intermetallic layered composites produced by reacting dissimilar elemental foils was studied by U.S. Bureau of Mines researchers. The layered composites were produced by initiating an SHS reaction between Ni and Al foils or Ti and Al foils. The reaction consumed the aluminum foil, resulting in well bonded metal (Ni or Ti) metal-aluminide layered composites. Tensile tests revealed that the tensile behavior of the composites was dependent upon the thickness of the intermetallic layer (which in the present case corresponds directly to volume fraction). Composites, in which the intermetallic layers had cracked extensively, behaved in a ductile or tough manner. Not surprisingly, these composites consisted of a relatively thick metal layer compared to the intermetallic layer. It was found that the cracking of the intermetallic layers occurred prior to the deformation of the metal layer. Those composites that had relatively thick intermetallic layers, compared to the metal layer, behaved in a brittle manner. These composites had few cracks in the intermetallic region.

INTRODUCTION

Metal-intermetallic laminar composites offer an attractive combination of properties from both constituent phases (e.g., combining the low density, high strength and oxidation resistance of the intermetallic with the high fracture toughness of the metallic phase). Methods such as diffusion bonding of intermetallic powders with metallic foils, plasma spraying and sputtering or vapor deposition of sequential layers have been used to fabricate laminar composites consisting of at least one brittle phase [1-4]. These fabrication techniques are time/temperature/pressure intensive, require sophisticated equipment, or are limited in the shape of component that can be produced. Recently, researchers at the U.S. Bureau of Mines have developed a technique to produce laminar composites that overcomes these limitations [5-8]. This method consists of initiating a self-propagating, high-temperature synthesis (SHS) reaction at the interface between thin dissimilar metal foils. The reaction consumes one of the metal foils; thus synthesizing the intermetallic phase. The resultant structures comprise of a well bonded metal-intermetallic layered composite.

SHS reactions between elemental metals are initiated at low temperatures, and in some instances (for aluminides) the reactions are followed by the formation of a transient liquid phase. Both of these factors result in lower processing temperatures and pressures to produce a well bonded structure than is normally required for conventional bonding techniques. Because this technique uses metallic foils which are ductile, the foils can be readily shaped prior to synthesizing the brittle intermetallic, producing a near-net-shape composite. Metallic foils are readily available in a wide variety of chemistries and thicknesses. This allows for tailoring of the composite microstructure by altering the chemistry and thickness of the starting foils to produce a composite that is strong, tough, lightweight and resistant to the environment. All of which make the foil-SHS technique an attractive method for the production of inexpensive, high-performance, advanced layered composites. This paper discusses the failure characteristics of

different metal (Ni or Ti)-metal aluminide composites produced by this foil-SHS technique.

EXPERIMENTAL PROCEDURE

The following is a brief description of the fabrication procedures used to make composites for this study. Complete details can be found elsewhere [5-8]. Dissimilar metallic foils were stacked in an alternating sequence of metal (Ni or Ti) and Al foils. The SHS reaction was initiated at the foil interfaces by heating the stack in an induction-heated hot-press to just below 660°C, the melting point of Al. After 60 minutes at this temperature, the composites were thermally aged at 800°C and 27 MPa for 1 hour. Table I summarizes the microstructural features for all the composites produced for this study. Figure 1 shows typical microstructures for the Ti-Al composites produced.

Tensile tests were performed at room temperature to assess the failure characteristics of these composites. Flat dog-bone shaped specimens (Fig. 2) were electro-discharge-machined (EDM) from the composite sheets. Tensile tests were performed on a screw driven testing machine at a constant crosshead-speed of 0.5 mm/min. Fracture surfaces were viewed by scanning electron microscopy (SEM).
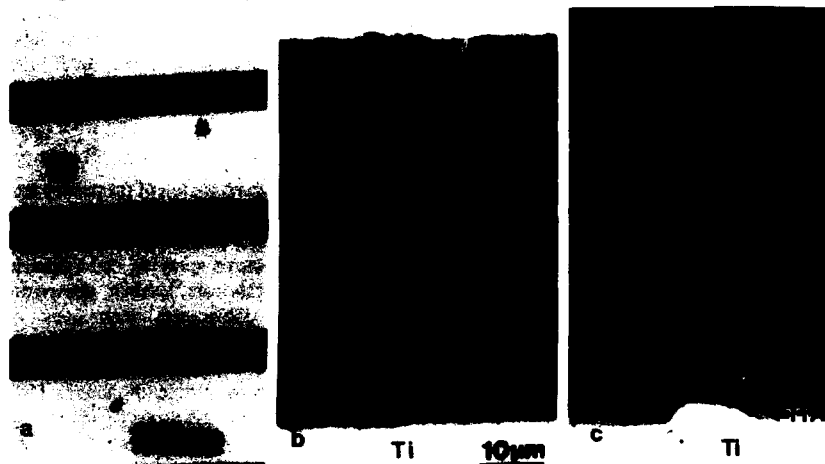
Figure 1.   Microstructures of the Ti-Al composites: (a) typical low magnification of the titanium-titanium aluminide layered composite; (b) the interface of composite produced from 0.25mm Ti and 0.15mm Al foils; (c) the of interface of composite produced from 0.15mm Ti and 0.15mm Al foils, note the solidification crack in the center of the aluminide layer.

RESULTS AND DISCUSSIONS

The results of the room-temperature tensile tests are summarized in Table I and Fig. 3. These results indicate that for the Ni-Al composites the tensile behavior is insensitive to the resultant layer thicknesses (for the composites produced). All of the Ni-Al composites behaved in a ductile manner, with appreciable accumulation of strain prior to failure (Table I). By
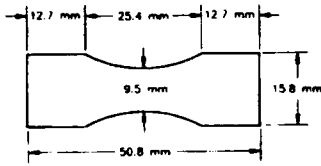
Figure 2.   Schematic of the tensile
             specimen.

contrast the behavior of the Ti-Al composites appears very sensitive to the layer thicknesses (Table I and Fig. 3). Notice that the Ti-Al composite produced from the thick Ti foils behaved in a manner similar to that of the Ni-Al composites, whereas the Ti-Al composite produced from the thin Ti foils behaved in a brittle manner.

Fractography revealed that the Ni layer in the Ni-Al composites necked to a knife edge and multiple cracks formed in the intermetallic layer prior to composite failure (Fig. 4). This behavior is typical of ductile phase toughened composites. The ductile phase bridges many cracks in the brittle phase prior to plastically deforming. Final composite failure occurred through the connection of multiple cracks as opposed to the propagation of a single crack through the system. The Ti-Al composite produced from the thick Ti foils fractured (Fig. 5) in a manner similar to that of the Ni-Al composites. In these composites there are two types of cracks in the intermetallic layers; (1) cracks that run perpendicular to the load direction and the layers, and (2) longitudinal cracks that run parallel to the layers. Also, notice that the perpendicular cracks branch as they approached the metal. This phenomena has been attributed to elastic mismatches (Poisson's ratio and coefficient of thermal expansion mismatch) between the constituent phases of the composite [9,10].

TABLE I.
SUMMARY OF MICROSTRUCTURES AND TENSILE PROPERTIES OF LAYERED
METAL-INTERMETALLIC LAMINATE COMPOSITES

Composite	Starting foil thickness (mm)		Approximate composite layer thickness (mm)		V_f*	Aluminide phases present	σ_{ys} (MPa)	σ_{UTS} (MPa)	Displacement at fracture (mm)**
	Metal	Al	Metal	Aluminide					
Ni-Al	0.250	0.250	0.185	0.105	36	Ni$_2$Al$_3$[1],NiAl,	80	240	4.30
	0.250	0.150	0.180	0.145	45	Ni$_5$Al$_3$	80	219	4.40
	0.250	0.050	0.195	0.070	26		67	250	4.80
	0.150	0.150	0.115	0.110	49		110	200	2.70
	0.150	0.100	0.116	0.090	43		81	220	3.90
Ti-Al	0.15	0.15	0.044	0.111	72	TiAl$_3$[1], TiAl	101	166	0.83
	0.25	0.15	0.140	0.060	30		73	460	5.50

[1] Major aluminide phase. * volume percent aluminide layer (calculated from thicknesses)
** tensile specimen gauge length = 25.4mm

The Ti-Al composite produced from thin Ti foils failed in a brittle manner (Fig. 6), although multiple perpendicular cracks had formed in the intermetallic. Final failure occurs through the propagation of a single crack in the composite. Even though a pre-existing solidification crack was present in the aluminide layer running parallel to the metal layer (Fig.

55

1c) the layers remained well bonded to each other during testing. (The pre-existing crack occurred during solidification of the transient liquid phase [7,8]). Absent were the longitudinal cracks that were prevalent in the other composites.

The longitudinal cracks were found to form prior to significant deformation of the metallic layer. A few tensile tests were performed on a Ti-Al composite produced from 0.25mm thick Ti and 0.15mm thick Al foils and stopped at the point where the change in the slope of the load displacement curve occurred (Fig. 3), and the specimens were examined (Fig. 7). Longitudinal and

Figure 3.   Tensile behavior of the Ti-Al composites. Curves represent 0.25 mm and 0.15mm Ti foil used in original layup.

perpendicular cracks are clearly visible in the intermetallic layer, yet the Ti layer has not significantly deformed. These cracks relax the constraint of the brittle layer which resists the deformation of the metallic layer. In essence these cracks debond the metal layer from the intermetallic layer.

During the initial loading of the composites, a tri-axial stress state exists in the metallic layer due to the strong chemical bond existing between the intermetallic and metal. This state of stress arises from differences in elastic properties of the constituent phases. This constraint increases the stress required to produce metal yield beyond that normally required in a uniaxial tensile test performed on the constituent metal alone. If the increase in stress is sufficiently large, the metal stress-to-yield may be greater than the fracture strength of the metallic layer. This results in the brittle behavior for a normally ductile

Figure 4.   Typical fracture behavior of the Ni-Al composites.

material. This behavior was observed for the composite produced from the thin Ti foil.

The formation of multiple perpendicular cracks in the intermetallic was not sufficient to relax the constraint on the metal. The reason for this is as follows: for the metal layer to elongate it must contract laterally (conservation of volume); however, the intermetallic layer (beneath any cracks) resists this contraction (Fig. 8). The contraction of adjacent metal layers results in a transverse tensile stress acting on the intermetallic layer. If this stress is insufficient to fracture the intermetallic (through the formation of the longitudinal cracks), then the matrix constraint is not relaxed and the metal will fail in a brittle manner. The magnitude of this stress is related to the volume fraction of the metal in the composite, and directly related to the thickness of the metal. Thus, composites with the thicker metal layers behaved in a tough manner.

CONCLUSIONS

Tough metal-intermetallic layered composites can be produced using the foils-SHS technique described in this paper. The behavior of the composites is a function of the thicknesses of the resultant intermetallic and metal layers. Tough behavior requires a metal thickness sufficient to form cracks in the intermetallic layer both longitudinal and perpendicular to the applied load. Insufficient metal thickness result in a high stress constraint raising the metal yield stress above the tensile stress, resulting in brittle fracture of the metal. Both forms of cracks (perpendicular and longitudinal) in the intermetallic layer occur prior to the deformation of the metallic layer.
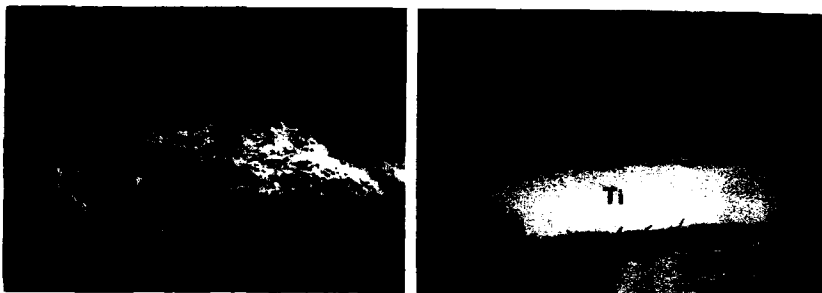
Figure 5.   Fracture behavior of the Ti-Al composite produced from the thick (0.25mm) Ti foils. Notice the deformation of the Ti layer and the longitudinal and perpendicular cracks in the intermetallic layer.
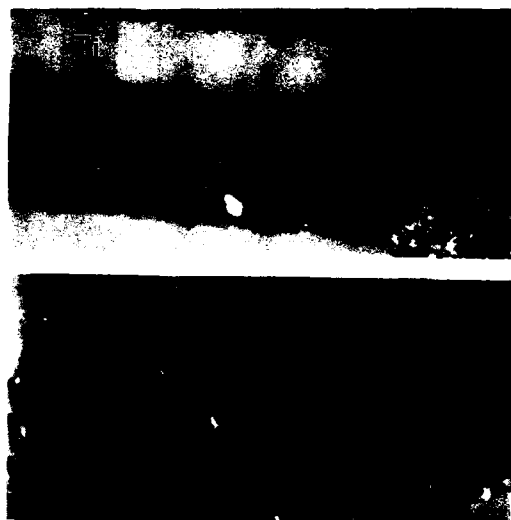
Figure. 6
Fracture behavior of the Ti-Al composite produced from the thin (0.15mm) Ti foils. Note the brittle behavior of the Ti layer and only perpendicular cracks in the intermetallic layer.

Figure 7.
The surface of a Ti-Al composite
tested until the slope of the load
displacement curve changed.
Note the extensive cracking of
the intermetallic layer.

Figure 8.
The stress state acting on
the intermetallic layer from
the lateral contraction of the
metal layer, after fracture of
the intermetallic.
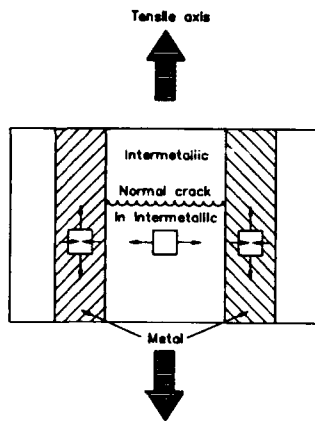
REFERENCES

1. N.S. Stoloff and D.E. Alman, in Intermetallic Matrix Composites, edited by D.L. Anton, P.L. Martin,
   D.B. Miracle and R. McMeeking (Mater. Res. Soc. Proc. 194, Pittsburgh, PA, 1990) pp. 31-43.
2. D.A. Hardwick and R.C. Cordi, in Intermetallic Matrix Composites, edited by D.L. Anton, P.L. Martin,
   D.B. Miracle and R. McMeeking (Mater. Res. Soc. Proc. 194, Pittsburgh, PA, 1990) pp. 65-70.
3. R.G. Rowe and D.W. Skelly, in Intermetallic Matrix Composites, edited by D.B. Miracle, D.L. Anton
   and J.A. Graves (Mater. Res. Soc. Proc. 273, Pittsburgh, PA, 1992) pp. 411-416.
4. D.E. Alman, K.G. Shaw, N.S. Stoloff and K. Rajan, Mater. Sci. Engr., A155, 85 (1992).
5. J.C. Rawers, D.E. Alman and J.A. Hawk, Intl. J. Self-Prop. High-Temp. Synthesis, 2 (1), 12 (1993).
6. D.E. Alman, J.A. Hawk, A.V. Petty and J.C. Rawers, JOM, 46 (3), 31 (1994).
7. D.E. Alman, J.C. Rawers and J.A. Hawk, submitted to Met. Trans., 1994.
8. J.C. Rawers, J.S. Hansen, D.E. Alman and J.A. Hawk, submitted to J. Mater. Sci. Letters, 1993.
9. D.E. Alman and N.S. Stoloff, submitted to Met. Trans., (1994).
10. D.E. Alman, Ph.D. Thesis, Rensselaer Polytechnic Institute, Troy, NY 1992.

VAPOR PHASE SYNTHESIS OF Ti ALUMINIDES AND THE INTERFACIAL BONDING EFFECT ON THE MECHANICAL PROPERTY OF MICRO-COMPOSITES REINFORCED BY PYROLIZED SIC FIBERS

T. SUZUKI*, H. UMEHARA*, AND R. HAYASHI*
*National Institute of Materials and Chemical Research (NIMC),
Agency of Industrial Science and Technolog,, M.I.T.I.,
1-1 Higashi, Tsukuba, Ibaraki 305, Japan

ABSTRACT

Vapor phase processings for manufacturing near-net-shaped composites, continuous fiber reinforced composites or lamellar composite will be hopeful methods. The method for synthesis of TiAl by a magnetron sputtering using a multiple target has been successfully established, and the tensile property of the microcomposite with SiC fibers has been studied. The TiAl produced by a vapor phase processing was evaluated by Auger electron spectroscopy and the x-ray analysis. The tensile strength properties of the SiC/TiAl microcomposites of which the interface bonding was controlled with the powers of sputtering were estimated. The properties of SiC/TiAl microcomposites are decreasing with increasing the sputtering power. The irradiation-cured SiC fiber has better compatibility with TiAl than the oxidation-cured SiC fiber. The strength of the microcomposite has been improved with using a thin C-coated irradiation-cured SiC fiber.

INTRODUCTION

Many innovative techniques have been developed to produce intermetallic matrix composites. The majority of processes involve use of powders, although increasing attention is being directed towards vapor phase techniques [1]. Studies of the synthesis of Ti aluminides by vapor deposition processings are very few [2][3]. Hardwick and Cordi have been reported that TiAl deposited by sputtering from targets of composition Ti-53Al-3Nb and TiB$_2$ never contained less than 6 at.% oxygen.

We have been able to establish the synthesis of purer TiAl than others by using a rf magnetron sputtering with multiple target made of Al and Ti, and have clarified the relationship between the sputtering powers and the strength of SiC/TiAl microcomposites. We have also studied the TiAl by chemical vapor deposition using metal-organic compounds [4], however, the results of the magnetron sputtering are the focus of this paper.

EXPERIMENTAL

Apparatus for rf magnetron sputtering

The apparatus for sputtering was a conventional one. The two-way process in which a substrate was replaced during the operation was effective to produce uniform deposit on a fibrous substrate. The radial target made of Ti and Al was used to search an

optimum condition for the TiAl deposition. A 99.9 wt.% purity Ti plate and a 99.999 wt.% purity Al plate of 0.1 m in diameter and 0.005 m in thickness were used as a multiple target. The deposits' compositions with the variable target were assigned by an x-ray microanalysis.

Preparation of TiAl and SiC/TiAl composites

TiAl was deposited on quartz plate or SiC fibers with the various sputtering powers (100W-400W) by using multiple target [5]. The atmospheric pressure of Ar was 0.80 Pa. The sputtering periods were selected at the range of 600s-2400s. The films' thicknesses were kept constant with various sputtering pow.rs by controlling the sputtering period. The properties of SiC fibers used in this study are shown in Table I

Table I Properties of the SiC fibers used in this study

	Oxidation-cured	Electron beam Irradiation-cured	C-coated irradi. cured
Mean diameter (10^{-6} m)	14.0	14.0	14.0
Density (10^{-1}kg/m^3)	2550	2740	2750
Tensile strength (GPa)	3.0	2.8	2.8
Young's modulus (GPa)	220	270	276
Oxygen content (wt.%)	12.0	0.5	0.5
Carbon layer (nm)	non	non	45

Tensile strength properties of SiC fibers and of SiC/TiAl microcomposites

The tensile strength properties of the fibers and of TiAl coated-SiC fibers which are defined as SiC/TiAl microcomposites were measured by using a tensile machine. Each specimen is mounted to a paper holder with an epoxy adhesive and set up to the machine. Tensile strength properties of the specimens were estimated from the breaking loads and the diameters. The tensile speed was 5×10^{-4} m/min. More than 20 specimens were applied for each series, and all the data were statistically treated with Weibull analysis [6]. The microcomposites were immersed into a 0.5% HF aqueous solution at room temperature for 30 s and up for the TiAl completely removed.

RESULTS AND DISCUSSION

Area percentage of Ti on multiple target versus composition in deposit

Figure 1 shows the relationship of the area percentage of Ti on the target and Ti composition in the deposit. The x-ray microanalysis determined that the target of 63% Ti was able to synthesize TiAl, while the target of 80% Ti was able to synthesize Ti$_3$Al.

Morphology and the structure of synthesized TiAl

Figure 2 shows the AES depth profile of the deposit. An AES depth profile of 99.94 wt.% purity TiAl bulky plate that contains Ti 63.31 wt.36.63 wt.%, and O 0.045 wt.% is shown as a dotted line in Fig.2. A uniform deposit was formed. The ratio of Ti toAl was approximately 1:1, which will be assigned as TiAl. The result of an x-ray diffraction showed that TiAl as deposited was an amorphous phase. While with elevated temperature of more than 973 K, several peaks have been observed, which can be assigned as TiAl. This means the deposit has been crystallized at the elevated temperature.
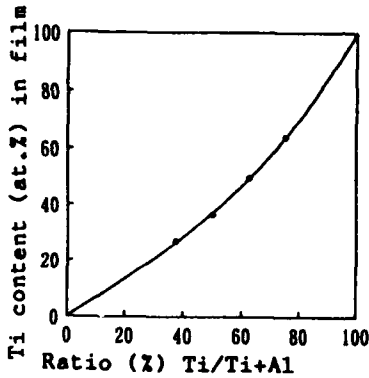
FIG.1 The relationship of Ti area % &
Ti content in the deposited films

SPUTTERING TIME(min.)
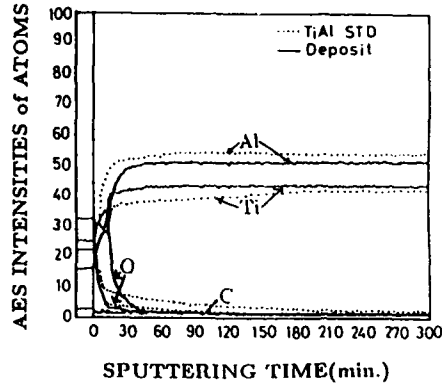
FIG.2 AES depth profile of a deposited TiAl film on a Si wafer

Tensile strength properties of SiC fibers and the SiC/TiAlmicrocomposites with various powers of sputtering

The results based on Weibull analysis are shown in Tables II-IV. The mean diameter of SiC/TiAl microcomposites was assumed to be approximately 18×10^{-6}m. The strength of the SiC/TiAl has been reduced broadly compared with SiC fibers. These decreases of the strength are supposed to be caused by the addition of brittle TiAl layers on SiC fibers. The tensile strength of the SiC/TiAl can be calculated from a rule of mixtures (ROM) to a fiber with a thin coating [7]. It was clarified that the strength properties of SiC/TiAl microcomposites were decreasing with increasing the sputtering power. Since a bonding strength of the interface is enhanced as the power of sputtering is increased, the interface properties will contributed to such a change in strength. On the other hand The strength of C-coated SiC /TiAl composite was only decreasing slightly with increasing the sputtering power.

The difference of this behavior will be explained with strengthening mechanism for the control of crack propagation in an all-brittle system by Cook and Gordon [8]. It is schematically shown in Fig. 3(a)-3(d). The initial crack has been created in TiAl with tension stresses shown in Figure 10(a) and will propagate as follows: If the interface of TiAl and SiC fiber is very weak, it will rupture some distance ahead of the main crack and a secondary crack will be created, as shown in Fig. 3(b). The stronger the interface becomes, the closer to the main crack will rupturing occur. The strongest interface that will fail under the effect of the stress parallel to the length of the crack (σ_x) will break about one tip radius ahead of the main crack where σ_x reaches a maximum. As the primary crack continues to propagate, it runs into the ruptured interface and the T-shape situation occurs, as shown in Figure 3(c). If the interface does not failunder the circumstances described above, then the primary crack willcross the interface and may, of course, proceed in the normal mannerof a crack in a homogeneous brittle material, as shown in Fig. 3(d). This mechanism suggests that a weak interface condition is favorable to achieve the higher performance of TiAl composites.

61

Table II Tensile strength properties of the oxidation-cured
SiC fiber and its composites

Fiber	Matrix	Sputtering power	Tensile strength	Coefficient of variation	Maintaining strength versus ROM[b]
SiC (Oxidation -cured)	---		2980 MPa	0.31	
	TiAl Removal	100W	825 MPa 2950*MPa	0.42 0.22	43%
	TiAl Removal	200W	924 MPa 3000*MPa	0.40 0.43	49%
	TiAl Removal	400W	464 MPa 1820*MPa	0.44 0.35	24%

Table III Tensile strength of the irradiation cured SiC fiber and its composites

Fiber	Matrix	Sputtering power	Tensile strength	Coefficient of variation	Maintaining strength versus ROM[b]
SiC (low oxygen) (Irradiation- cured)	--- Removal		3310 MPa 3249*MPa	0.20	
	TiAl Removal	100W	1890 MPa 2930*MPa	0.25 0.18	91%
	TiAl Removal	200W	730 MPa 3010*MPa	0.44 0.24	35%
	TiAl Removal	400W	500 MPa 2930*MPa	0.49 0.31	24%

*: The strength after being immersed in a 0.5% HF aqueous solution for 30 s or more.
The strength is calculated on the assumption that the fiber is 14.0 x 10^{-6} m
in diameter.
[b]ROM: rule of mixtures

Table IV Tensile strength of C-coated irradiation cured SiC fiber
and its composites

Fiber	Matrix	Sputtering power	Tensile strength	Maintaining strength versus ROM[b]
C-coated SiC (45nm) (irr.-cured)	---		2897MPa	
	TiAl	100W	1831MPa	100%
	TiAl	200W	1623MPa	89%
	TiAl	400W	1662MPa	91%

Strength of the fibers after chemical removal of TiAl

The tensile strength of SiC fibers removed from TiAl has almost recovered the
original strength. However, the result of the oxidation-cured SiC fiber sputtered at 400W
shows a possibility of the deterioration. On the other hand irradiation-cured SiC fiber does
not show this kind of deterioration behavior by the sputtering process; therefore, it seemed
to have better compatibility with TiAl than oxidation-cured SiC fiber which has the higher
oxygen content than that of irradiation-cured SiC.
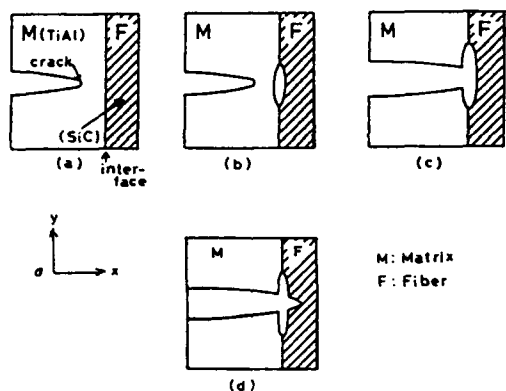
FIG. 3 The interaction between an advancing crack and a plane of weakness under various conditions. (a) The initial deflection of the crack. (b) A secondary crack creation at the weak interface (c) The primary crack propagation into the ruptured interface. (d) A penetration of the primary crack through the interface which may or may notbreak afterwards.

Tensile strength properties of SiC/TiAl microcomposites heated up to 1073 K

Table V shows that the strength of the SiC/TiAl which is heated at 1073K under 10^{-4} Pa for 7.2 ks has been obviously decreasing. This behavior seems to be explained by a reaction at the interface of TiAl and SiC [9][10]. The deterioration tends to be increased with increasing sputtering power. Since there is degradation of fibers by interface reactions with TiAl, those fibers will not recover the original strength, even after the chemical removal of TiAl. From these facts, indeed some kind of diffusion barriers will be proposed for strong and tough SiC fiber-reinforced titanium aluminide composites [11][12].

Table V Tensile strength properties of the SiC/TiAl composites after heating at 1073K under 10^{-4} Pa

Fiber	Matrix	Sputtering power	Tensile strength
SiC(irrad.-cured)	---		2858 MPa
	TiAl Removal	100W	118 MPa 1020*MPa
	TiAl Removal	300W	67 MPa 767*MPa
	TiAl	400W	34 MPa
C coated SiC (irrrad.-cured)	---		2605 MPa
	TiAl	200W	338 MPa
	TiAl	300W	142 MPa
	TiAl	400W	60 MPa

*: The strength after being immersed in a 0.5% HF aqueous solution for 30 s or more.

63

SURMARY

By using the rf magnetron sputtering process the uniform and fine TiAl intermetallic compound films are successfully synthesized on SiC fibers. The power of sputtering is able to control the bonding strength at the interface of the deposit and the fibers, which affects the mechanical properties of SiC/TiAl composites. The strength properties of SiC/TiAl microcomposites decrease with increasing power of the sputtering. A weak interface condition is favorable to achieve the higher performance of TiAl composites. The effectiveness of a stress release or a blunting coating for more improved properties of fiber-reinforced TiAl is suggested from the result of a thin C-coated SiC/TiAl microcomposite system. The irradiation-cured SiC fiber has better compatibility with TiAl than the oxidation-cured SiC fiber.

REFERENCES

1. N.S. Stoloff and D.E. Alman, in Intermetallic Matrix Composites, edited by D.L. Anton, P.L. Martin, D.B. Miracle, and R. McMeeking (Mater. Res. Soc. Symp. Proc. 194, Pittsburgh, PA, 1990), p.30;MRS Bull. 15 (12), 47 (1990).
2. A. Hardwick and R.C. Cordi, in Intermetallic Matrix Composites, edited by D.L. Anton, P.L. Martin, D.B. Miracle, and R. McMeeking (Mater. Res. Soc. Symp. Proc. 194, Pittsburgh, PA, 1990), p.65.
3. T. Suzuki, H. Umehara, and R. Hayashi, J. Mater. Res. 9, No.4 (in press)
4. T. Suzuki, H. Umehara, and R. Hayashi, in Proc. 2nd Meeting of the High Performance Materials for Severe Environments (R & D Institute of Metals and Composites for Future Industries, Tokyo, Japan, 1991), pp. 63-70
5. T. Suzuki, H. Umehara, and R. Hayashi, in Proc. 4th Meeting of High Performance Materials for Severe Environments(RIMCOF, Tokyo, Japan, 1993),pp.317-324
6. W. Weibull, J. Appl. Mech.,18, 293 (1951)
7. T. Suzuki, H. Umehara, R. Hayashi, and S. Watanabe, J. Mater. Res. 8, 2492 (1993)
8. J. Cook and J.E. Gordon, Proc. R. Soc. London A228, 508 (1964)
9. A.M. Ritter, E.L. Hall, and N. Lewis, in Intermetallic Matrix Composites, edited by D.L. Anton, P.L. Martin, D.B. Miracle and R. McMeeking (Mater. Res. Soc. Symp. Proc. 194, Pittsburgh, PA, 1990), p.413.
10. C.G. Rhodes, in Intermetallic Matrix Composites II, edited by D.B. Miracle, D.L. Anton, and J.A. Graves (Mater. Res. Soc. Symp. Proc. 273, Pittsburgh, PA, 1992), p.17.
11. S.M. Jeng, J-M. Yang, and J.A. Graves, J. Mater. Res., 8, 905 (1993).
12. H-P. Chiu, S.M. Jeng, and J-M. Yang, J. Mater. Res. 8, 2040 (1993)

NUMERICAL SIMULATIONS OF CREEP IN DUCTILE-PHASE TOUGHENED INTERMETALLIC MATRIX COMPOSITES

GREGORY A. HENSHALL AND MICHAEL J. STRUM
Lawrence Livermore National Laboratory, Livermore, CA 94551 (USA)

ABSTRACT

Analytical and finite element method (FEM) simulations of creep in idealized ductile-phase toughened intermetallic composites are described. For these strong-matrix materials, the two types of analyses predict similar time-independent composite creep rates if each phase individually exhibits only steady-state creep. The composite creep rate increases above that of the monolithic intermetallic with increases in the stress exponent of the intermetallic, the volume fraction of the ductile phase, and the creep rate of the ductile phase. FEM analysis shows that the shape of the ductile phase does not affect the creep rate but may affect the internal stress and strain distributions, and thus damage accumulation rates. If primary creep occurs in one or both of the individual phases, the composite also exhibits primary creep. In this case, there can be significant deviations in the creep curves computed by the analytical and FEM models. The model predictions are compared with data for the Nb_5Si_3/Nb system.

INTRODUCTION

The use of a ductile phase to toughen brittle intermetallics has been examined widely in the past several years (e.g. [1,2]) as a means of developing advanced materials for high temperature structural use. The focus of the research to date on these ductile-phase toughened (DPT) materials has been on improving low temperature toughness. The high temperature deformation behavior of these intermetallic matrix composites (IMCs) has received only limited attention, e.g. [3-5]. There are two features of deformation in these DPT IMCs that separate them from the well-studied case of metal matrix composites (MMCs): (1) both phases undergo time-dependent deformation, and (2) the matrix (i.e. the continuous phase) is likely to be the stronger, or more creep resistant, phase. The purpose of the work presented here was to begin exploring time-dependent deformation of discontinuously reinforced IMCs using numerical techniques. These efforts supplement earlier numerical studies in which either one phase [6,7] or both phases [4,8-11] deform by creep.

The numerical models used in this study, both analytical and finite element method (FEM), rely upon a continuum description of deformation in each phase. As discussed by Dragone and co-workers [6,7] for creep of metal matrix composites (MMCs) with elastic reinforcements, this simplification provides accurate predictions of deformation for some systems but not for others. The situation for composites in which both phases undergo creep is less clear. In any case, solution of the continuum problem is a useful first step in understanding creep of these ductile two-phase materials.

The majority of simulations performed in this study were for discontinuous fiber composites, though limited results for spherical reinforcement geometries are presented. Efforts were focused on idealized DPT composites, for which the "strong" matrix has the lower intrinsic creep rate. These results are compared with those for conventional MMCs, in which the "weak" matrix creeps at a faster rate than the discontinuous reinforcement. One major goal was to determine quantitatively how severely the creep resistance of strong intermetallic materials is degraded by forming a composite with a ductile, creep-weak phase. In addition, this research addresses the usefulness of relatively complex FEM analyses compared with a simple analytical approach. Finally, the predictions of these continuum models are compared with preliminary data for the steady-state creep of Nb_5Si_3/Nb composites [5], for which Nb_5Si_3 is the continous phase.

NUMERICAL METHODS

Following many previous numerical investigations [6,8,12,13], simulations were performed for uniaxially loaded, idealized composites consisting of a regular array of discontinuous cylindrical fibers or spheres embedded in a continuous matrix. Due to the regularity of this geometry, only a "unit cell" of material was considered. This unit cell consists of one fiber or sphere that, in two dimensions, is embedded within a cylinder of the surrounding matrix in proportions to match the volume fractions actually present in the idealized composite. Perfect bonding between the two phases was assumed. Thus, the important effects of cavity formation or interphase sliding [4,7,8] were not simulated. More complete descriptions of the unit cell approximation are available elsewhere [6,8,12,13].

As discussed in detail elsewhere [14], the idealized composite geometry and uniaxial tensile loading allowed for a two-dimensional axisymmetric FEM model. The reinforcement volume fractions were varied from 21.6 to 51.2%. For the short fibers, length-to-diameter ratios of 5.0 were used in all of the simulations for both the fiber and the unit cell (actual dimensions of arbitrary scale). The well-established "unit cell" boundary conditions were employed to ensure continuity during deformation between unit cells in a repeating array [6,8,12,13]. The FEM calculations were performed using the implicit, two-dimensional, non-linear, solid mechanics code NIKE2D [15]. A constant applied stress was simulated by continuously decreasing the applied force during the simulation to account for the reduction in the radius of the deformed mesh. In addition to elastic deformation, both of the phases in the composite were assumed to creep according to the equation [16]:

$$\varepsilon_{cr} = A \, (\sigma_{eff})^n \, t^m , \tag{1}$$

where ε_{cr} is the von Mises effective creep strain, σ_{eff} is the von Mises effective stress, t is time, n is the stress exponent, and A and m are constants. Transient creep is simulated by a time exponent, m, other than unity. For the case of $m = 1$, or steady-state creep, the strain rate reduces to the familiar Norton power law.

For comparison with the complex FEM analysis, a simple analytical model of composite creep based on the work of Bullock et al. [9] and Tanaka et al. [11] was developed. For simplicity, this model assumes strain compatibility between the phases and uniform stress and strain states within each phase (the FEM approach does not require these assumptions). For each phase, i, the total strain, ε_i^{tot}, is:

$$\varepsilon_i^{tot} = (\sigma_i / E_i) + A_i \, \sigma_i^{n_i} \, t^{m_i} , \tag{2}$$

where σ is the stress and E is Young's modulus. From strain compatibility,

$$\dot{\varepsilon}_w - \dot{\varepsilon}_s = 0, \tag{3}$$

where the subscripts w and s refer to the weak and strong phases. Differentiating (2) with respect to time for each phase and substituting into (3) yields a nonlinear expression for the two unknowns: the stresses in the strong and weak phases, σ_s and σ_w. At each time step in the simulation, these stresses can be computed using Newton's method [17], with the rule-of-mixtures constraint:

$$V_s \, \sigma_s + (1-V_s)\sigma_w = \sigma_{app} , \tag{4}$$

where V_s is the volume fraction of the strong phase and σ_{app} is the applied stress. Once σ_s and σ_w are determined for the current time step, the increment in total strain for each phase (and thus the composite) can be computed by substitution into the incremental form of eq. (2). Integrating

these incremental results over all time steps in the simulation gives the stress in each phase and the total composite strain as a function of time.

NUMERICAL RESULTS AND DISCUSSION

To assess some of the trends in creep behavior, computations were performed first for model composites (which approximately represent V/V_3Si composites being studied in the authors' laboratory). To simplify the calculations, the two phases were given identical stress exponents of 4.9. The creep rate in each phase was varied by varying the constant A. The volume fractions of the two phases also were varied, as was the position of the strong phase: strong matrix, $i.e.$ DPT IMCs, or weak matrix, $i.e.$ MMCs. The focus was on steady-state creep but preliminary calculations also were performed for primary creep, $n < 1$.

For the constant applied stress conditions simulated, both models predict linear composite creep strain vs time curves when $m = 1$ in both phases. The presence of two phases with different individual steady-state creep rates (due to differences in A) did not cause non-linearity of the strain–time curves. This finding differs from that for a steady-state creeping matrix with discontinuous elastic reinforcements, where non-linearity in the strain–time curve initially occurs due to the redistribution of internal stresses [6,10]. In the present study, both models show that the (non-uniform) stress state developed immediately after loading and remained essentially unchanged with increasing time and strain. The result of this constant stress state is a linear strain–time curve.

For an applied stress of 6.23 MPa and $A_w/A_s = 1000$, Fig. 1 presents predictions of the steady-state ($m = 1$) composite creep rate relative to that of the monolithic strong phase ($\dot{\varepsilon}_c/\dot{\varepsilon}_s$) as a function of the volume fraction of the weak phase, V_w. Results for both strong- and weak-phase matrices are presented. Similar behavior was observed for other applied stresses and A_w/A_s ratios. Except where noted, Fig. 1 gives FEM results for the short fiber composites. Clearly, the simple analytical model accurately reproduces the FEM results for the fiber geometry. Thus, within the approximations of continuum behavior, perfect interfacial bonding, and steady-state creep in both phases, the analytical strain-compatibility model, including its inherent assumptions, appears to be valid for this reinforcement geometry.

For the short fiber composites, Fig. 1 also shows that the predicted composite creep rate depends only on the relative amounts of the two phases, not on which is the matrix and which is the discontinuous reinforcement. Examination of the FEM results for V_w near 50% ($V_f = 51.2\%$) shows that interchaning the properties of the two phases does not significantly affect the composite strain rate. This finding is not unexpected based on the success of the analytical model in reproducing the FEM results for short fibers; for a reinforcement volume fraction of 50%, the analytical model must predict the same creep rate when the properties of the two phases are interchanged.

The behavior predicted by the FEM model for spherical reinforcements is more complex than that of the short fiber composites. For composites in which the strong phase is the matrix (open circles and open diamonds in Fig. 1), the creep rates are nearly the same as those predicted analytically and by FEM for short fiber composites. The similarity in creep rate for strong-matrix composites with varying reinforcement geometries also was predicted by Biner [4]. In contrast to the strong-matrix composites, Fig. 1 shows that the reinforcement shape significantly affects the deformation behavior of weak-matrix composites (open squares and solid diamonds), just as for elastically reinforced MMCs [6,7,12,13]. For example, the creep rate for the spherical reinforcement geometry with $V_w = 78.4\%$ is almost four times greater than that of the corresponding short fiber geometry. Also note the large deviation between the analytical and FEM results for the spherical geometry. In fact, for $V_w = 78.4\%$ the creep rate predicted by FEM approaches that computed using a simple iso-stress rule-of-mixtures model. FEM calculations show that the high creep rate for the spherical geometry is due to a less effective transfer of stress from the weak matrix to the strong reinforcement compared with the fiber geometry [14].

As stated in the introduction, one goal of this study was to determine the effect of a creep-weak phase on the creep rate of a strong matrix material. Focusing on the short fiber geometry, Fig. 2 presents FEM predictions of the relative composite creep rate as a function of
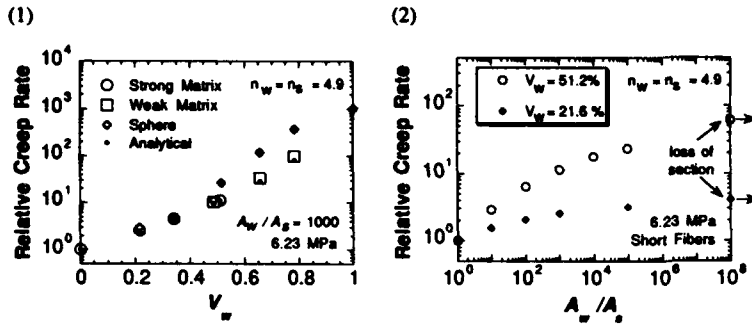
67

(1)

(2)

Figure 1. FEM and analytical predictions of the relative composite creep rate as a function of the volume fraction of weak phase, V_w, for $A_w/A_s = 1000$.

Figure 2. The effect of A_w/A_s ratio on the relative composite strain rate predicted by FEM for short fiber composites with a strong matrix and $n_w = n_s = 4.9$.

the disparity in monolithic creep rates, *i.e.* A_w/A_s, for two weak fiber volume fractions. In addition, an upper bound on the composite creep rate was computed by replacing the fiber with a void, thereby reducing the net section of material available to carry load. The FEM results of this "loss-of-section" model are indicated in Fig. 2 for the two fiber fractions. Figure 2 shows that the composite creep rate increases as A_w/A_s increases, apparently reaching the loss-of-section bound asymptotically. In general, for the case of $n_w=n_s=n$, the creep resistance of the strong phase tends to be less severely degraded by the weak phase if V_w, A_w/A_s, and n are small.

For example, for $n = 4.9$, Fig. 2 shows that the relative composite creep rate, $(\dot{\varepsilon}_c/\dot{\varepsilon}_s)$, is less than 10 if $V_w = 21.6\%$ or if $V_w = 51.2\%$ and $A_w/A_s < 500$. Relative creep rates above 10 are predicted for $V_w = 51.2\%$ and $A_w/A_s > 500$. Similar calculations using $V_w = 51.2\%$, but setting $n = 1$, predict that the relative composite creep rate saturates at a value of only about 2 for $A_w/A_s \geq 1000$. For $n = 10$, however, the same calculations show a relative composite creep rate of about 75 when $A_w/A_s = 10^5$, compared with a value of only 23 for $n = 4.9$ (Fig. 2).

The iso-strain analytical model successfully predicts the steady-state composite creep rate in most cases, particularly when the matrix is the strong phase (Fig. 1). However, it cannot provide details of the non-uniform internal stresses, *e.g.* the hydrostatic component, nor the localization of creep strain. Such information is valuable since it provides insights into damage accumulation during creep [6,12,13]. This provides justification for the use of FEM models, which provide the detailed field quantities, in studying these steady-state problems. As discussed elsewhere [14], the reinforcement shape significantly affects the detailed internal stress and strain states, even in cases where it has little influence on the steady-state composite creep rate. For the case of strong fibers in a weak matrix, large creep strains and hydrostatic stresses accumulate near the fiber ends, which has been associated with damage accumulation in the matrix at these locations [6,12,13]. For strong matrix, *i.e.* DPT, composites, the gradients in stress and strain appear to be somewhat less than in corresponding weak-matrix composites.

While the analytical model appears to be accurate for steady-state creep in most cases, preliminary calculations for the model composites show that it may be less accurate for transient creep. Figure 3 shows the results of calculations for a strong-matrix fiber composite in which $m_m = 0.25$. First, both models require time step sizes much smaller than those used in the steady-state calculations in order to reach a solution that is essentially independent of time step size. The difficulty in converging on an accurate solution appears to be due to the continuous redistribution of stresses within the composite during transient creep. Second, there is a clear deviation in the creep curves predicted by the two models. For a time of 2000 s, there is a 14.4% difference in the predicted creep strains. Preliminary analysis suggests that this
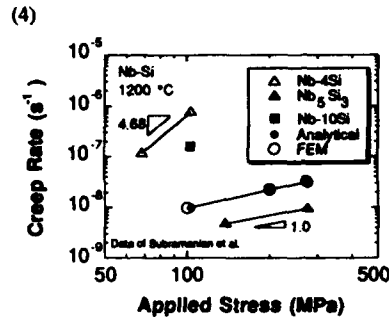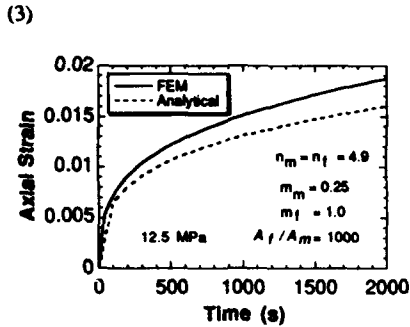
(3)

(4)

Figure 3. Analytical and FEM predictions of the creep curve for a model composite in which the matrix material exhibits primary creep.

Figure 4. Predictions of the steady-state creep rate as a function of the applied stress are compared with data for Nb-Si alloys. Data of Subramanian *et al.* [5].

discrepancy results from the better representation of the internal stresses and their redistribution using FEM compared with the simple analytical model.

It is desirable to compare the predictions of the models described here with data for real DPT IMCs. To do so, creep data are required for the composite and its component phases. Unfortunately, such data sets are scarce. However, comparison of the model predictions can be made using the preliminary data of Subramanian *et al.* [5] for a Nb$_5$Si$_3$/Nb in-situ composite. This composite was produced by casting a Nb-10%Si alloy, extruding to a 10:1 ratio at 1482 °C, and annealing at 1500 °C for 100 h. The resulting microstructure consisted of large (~50 μm) elongated proeutectic Nb-Si solid solution, (Nb), "fibers" in a eutectic matrix composed of small (~5 μm) (Nb) particles dispersed within the continuous Nb$_5$Si$_3$ phase. The total (Nb) content was approximately 73%. Based on the predicted insensitivity of the composite creep rate to phase morphology when the strong phase (*e.g.* Nb$_5$Si$_3$) is the continuous matrix (Fig. 1), it was assumed that this material could be modeled as a regular array of ductile (Nb) fibers in a matrix of Nb$_5$Si$_3$. This assumption has yet to be verified for complex microstructures.

Figure 4 presents the salient data gathered by Subramanian *et al.* at 1200 °C. The steady-state creep properties of the intermetallic were computed from the data in Fig. 4, giving: $n_m = 1.0$, $A_m = 3.63 \times 10^{-11}$ (MPa·s)$^{-1}$. For the ductile solid solution, the creep properties were estimated from those of the Nb-4%Si alloy data shown in the figure, giving: $n_f = 4.68$, $A_f = 2.98 \times 10^{-16}$ (MPa$^{4.68}$·s)$^{-1}$. Using these values, the circles in Fig. 4 show the predicted steady-state creep rate of the composite. Both models predict the same results, as expected for this strong matrix composite (see Fig. 1). The predicted composite stress exponent is approximately 1.0, as expected from the results of model system calculations showing that the composite stress exponent essentially equals that of the slower creeping phase, in this case Nb$_5$Si$_3$. Unfortunately, the preliminary data do not allow for confirmation of this prediction. However, comparison of the absolute creep rate for the Nb-10% Si composite with the predicted rate is possible for an applied stress of 100 MPa. At this stress, the predicted creep rate is more than an order of magnitude less than the experimental value. A similar creep rate was predicted using pure Nb as the ductile phase, which creeps much faster than Nb-4%Si. Based on the earlier discussion of Fig. 2 and the fact that $n = 1$ for the intermetallic, the insensitivity of the predicted composite creep rate to the ductile phase properties is not unexpected. One possible reason for the discrepancy between the experimental and predicted creep rates is that microcracks and voids were observed following creep testing of the composite. These damage processes are not included in the models, contributing to a predicted creep lower than the experimentally observed

value. The complexity of the composite microstructure may also contribute to deviations between the experimental and predicted creep rates.

CONCLUSIONS

Based on analytical and finite element method continuum analyses of deformation in composites for which both phases exhibit creep, the following conclusions have been drawn.
1. For strong matrix IMCs, the simple analytical model based on strain compatibility between phases predicts composite creep rates consistent with those computed by the finite element method. However, significant deviations in the strain vs. time curves predicted by the two models occur for transient creep.
2. The steady-state composite creep rate is predicted to be nearly independent of the reinforcement geometry for ductile-phase toughened composites, for which the matrix is the strong phase.
3. For ductile-phase toughened IMCs, the addition of the weak ductile phase is predicted to degrade the creep resistance of the intermetallic more severely with increases in the stress exponent of the intermetallic and the volume fraction and creep rate of the ductile phase.
4. Unlike simple analytical models, the finite element method provides detailed internal stress and strain distributions that can provide insights into possible damage accumulation during creep.
5. Predictions of the steady-state creep rate for a Nb_5Si_3/Nb in-situ composite deviate from the data by more than an order of magnitude. This discrepancy may be due in part to damage evolution and microstructural complexities present in the composite that were not simulated in the models.

ACKNOWLEDGMENTS

REFERENCES

1) L. S. Sigl, P. A. Mataga, B. J. Dalgleish, R. M. McMeeking and A. G. Evans, *Acta Metall.* **39** (1988), 945-953.
2) M. G. Mendiratta, J. J. Lewandowski and D. M. Dimiduk, *Metall. Trans.* **22A**, 1573 (1991).
3) M. Thirukkonda, B. Cockeram, M. Saqib, L. E. Matson, R. Srinivasan and I. Weiss, *Scripta Metall. Mater.* **27**, 711 (1992).
4) S. B. Biner, in *Processing and Fabrication of Advanced Materials*, TMS Publications, Warrendale, PA, to appear.
5) P. R. Subramanian, M. G. Mendiratta, and D. M. Dimiduk, presented at the MRS Fall Meeting, Boston, MA, 1992 (unpublished).
6) T. L. Dragone and W. D. Nix, *Acta Metall.* **38**, 1941 (1990).
7) T. L. Dragone, J. J. Schlautmann and W. D. Nix, *Metall. Trans.* **22A**, 1029 (1991).
8) Y. Ii. Park, J. W. Holmes, *J. Mater. Sci.* **27**, 6341 (1992).
9) E. Bullock, M. McLean, and D. E. Miles, *Acta Metall.* **25**, 333 (1977).
10) M. McLean, in *Mat. Res. Soc. Proc. Vol. 120*, F. D. Lemkey *et al.*, eds., Materials Research Society, Pittsburgh, PA, p. 67 (1988).
11) M. Tanaka, T. Sakaki, and H. Iizuka, *Acta Metall. Mater.* **39**, 1549 (1991).
12) T. Christman, A. Needleman, S. Suresh, *Acta Metall.* **37**, 3029 (1989).
13) V. Tvergaard, *Acta Metall. Mater.* **38**, 185 (1990).
14) G. A. Henshall and M. J. Strum, *Scr. Metall. Mater.* **30**, 845 (1994).
15) B. E. Engelmann, "NIKE2D User Manual," University of California - Lawrence Livermore National Laboratory, UCRL-MA-105413, 1991.
16) R. G. Whirley and G. A. Henshall, *Int. J. Numer. Methods Engng.* **35**, 1427 (1992).
17) G. E. Forsythe, M. A. Malcom, and C. B. Moler, *Computer Methods for Mathematical Computations*. (Prentice-Hall, Englewood Cliffs, NJ, 1977), p.170.

PART II

Fibers for IMC's

FIBERS AND FIBER COATINGS FOR IMCs

Ajay K. Misra
NYMA, Inc
NASA Lewis Research Center Group
Cleveland, OH 44135

ABSTRACT

This paper presents a review of the current status of fibers and fiber coatings for intermetallic matrix composites (IMCs). The properties of commercial and developmental fibers are reviewed and their potential as reinforcements for various intermetallics discussed. The potential fibers for near-term IMC applications are SiC (both monofilament and tow), single crystal Al_2O_3 and YAG/Al_2O_3 eutectic monofilaments, and sol-gel derived Al_2O_3-mullite nanocomposite tow fiber. The chemical compatibility of these fibers with various intermetallic matrices is reviewed. The issues related to the coefficient of thermal expansion (CTE) mismatch between the fiber and the matrix, attaining optimum interfacial bond strength, and fiber damage during composite processing are addressed. The effectiveness and limitations of fiber coatings in accommodating various fiber-matrix incompabilities, both chemical and mechanical, are discussed.

INTRODUCTION

High melting points and low densities make many intermetallic compounds attractive as high temperature structural materials for future aerospace engine applications. The intermetallic compounds of current interest are Ti_3Al, TiAl, NiAl, Ni_3Al, FeAl and $MoSi_2$. Although these intermetallic compounds have many attractive properties, reinforcing them with continuous fibers can provide unique properties that are not possible with monolithic materials.

Many factors need to be considered in selecting a fiber for a given matrix. Ideally, a fiber should have high strength at high temperature, be chemically compatible with the matrix, and have matching coefficient of thermal expansion (CTE) with the matrix. For incompatible fiber-matrix combinations, the fiber-matrix interface needs to be modified by application of fiber coatings to accommodate the fiber-matrix incompatibilities. For example, an interfacial reaction barrier is needed for a chemically reacting fiber-matrix combination. An interface coating also might offer the potential of decreasing the residual stresses caused by the fiber-matrix CTE mismatch. Another function of the interface coating is to optimize the interfacial bond strength.

This paper reviews the current status of fibers and fiber coatings for various intermetallic matrix composites. The intermetallic matrices include Ti_3Al+Nb (α_2 and orthorhombic), γ TiAl, NiAl, Ni_3Al, FeAl and $MoSi_2$. The properties of various fibers are reviewed first, followed by a discussion of the problems associated with various fiber-matrix combinations, which include interfacial reaction, and coefficient of thermal expansion (CTE) mismatch between the fiber and the matrix, fiber damage during composite processing, and obtaining optimum interfacial bond strength. The potential of fiber coatings in solving some of these problems is discussed.

PROPERTIES OF COMMERCIAL AND DEVELOPMENTAL FIBERS

Currently available commercial and developmental fibers are either SiC-based or oxide-based. The fibers can be grouped into four categories: (1) polymer derived SiC tow fibers (10-25 μm diameter), (2) chemical vapor deposited (CVD) SiC monofilaments (120-150 μm dia) (3) sol-gel derived Al_2O_3-based tow fibers (10-20 μm dia), and (4) single crystal oxide monofilament (120-150 μm dia).

The polymer derived SiC tow fibers include Nicalon and HiNicalon, both from Nippon Carbon, Inc., Japan. The Nicalon fiber contains significant amounts of oxygen in addition to Si and C, and is thermally unstable at temperatures above 1473 K [1]. The oxygen content of HiNicalon is less than 1 wt. % [2] and has outstanding thermal stability compared to other polymer-derived SiC fibers. The HiNicalon fiber, however, contains significant amount of excess carbon (C/Si ratio of ¯1.6), which may have adverse effects on the chemical compatibility of this fiber with various intermetallic matrices. Recently, Dow Corning has developed a stoichiometric SiC tow fiber [3] with strengths comparable to that of HiNicalon. Efforts are also continuing at Carborundum to develop stoichiometric SiC fiber by conventional ceramic approach [4].

The CVD SiC monofilaments include the SCS-6 fiber and the small diameter (¯50 μm dia) fiber from Textron Specialty Materials, Inc. The sol-gel derived oxide fibers include Nextel610 (α-Al_2O_3) and the Al_2O_3-mullite nanocomposite fiber from 3M, FP fiber (α-Al_2O_3) and PRD-166 (Al_2O_3-ZrO_2) from DuPont. Among single crystal oxide fibers, c-axis Al_2O_3 and YAG/Al_2O_3 eutectic fibers, commercially available from Saphikon, are of interest to IMCs.

The fiber properties that affect the composite properties are tensile strength, creep, stress rupture, and coefficient of thermal expansion (CTE). Among sol-gel oxide fibers, only the properties Nextel 610 and Al_2O_3-mullite nanocomposite fibers are reported here, to maintain clarity in presenting the data. The mechanical properties of other sol-gel derived oxide fibers are either similar to or inferior than these two fibers.

Tensile strength: The strengths of various fibers [2, 5-9] as a function of temperature are shown in Fig. 1. The high temperature strengths of oxide fibers (both tow and monofilament), in general, are lower than that of SiC fibers. For example, at 1373 K the highest strength for an oxide fiber (YAG/Al_2O_3 eutectic) is 1.38 GPa, compared to 1.6 GPa for the weakest SiC fiber (Nicalon fiber). Among SiC fibers, the CVD SiC monofilaments have the highest strength.

Creep of fibers: Figure 2 shows the creep rate [10-13] for different fibers as a function of temperature. The creep rates reported in Fig. 2 include data taken from tensile creep measurements as well as from bend stress relaxation (BSR) tests.

The sol-gel derived Al_2O_3 tow fiber (Nextel 610) has the highest creep rate among all the fibers shown in Fig. 2. The creep resistance of sol-gel derived Al_2O_3 is increased by three orders of magnitude by adding 15 w/o SiO_2 to Al_2O_3 [10]. The resulting fiber is a Al_2O_3-mullite nanocomposite, with the mullite component of the fiber being responsible for the increased creep resistance. The creep resistance of Al_2O_3-mullite nanocomposite fiber, although higher than that of other sol-gel derived oxide fibers, is still lower than that of many SiC and single crystal oxide fibers.

Among SiC fibers, the creep resistance of fibers increases in the following order: Nicalon, HiNicalon and SCS-6, small diameter CVD SiC, Carborundum stoichiometric SiC
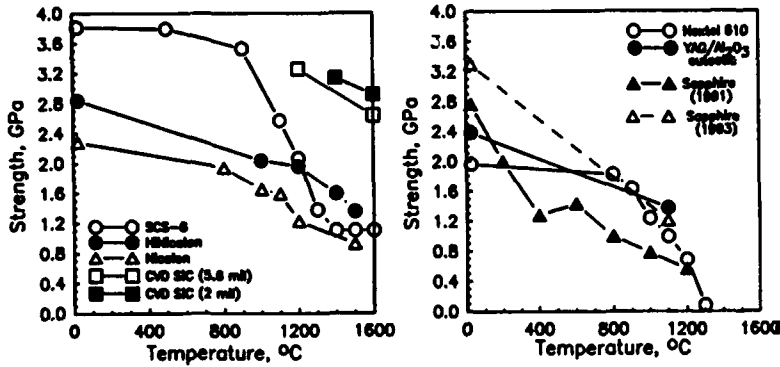
Fig.1: Tensile strength of various fibers as a function of temperature
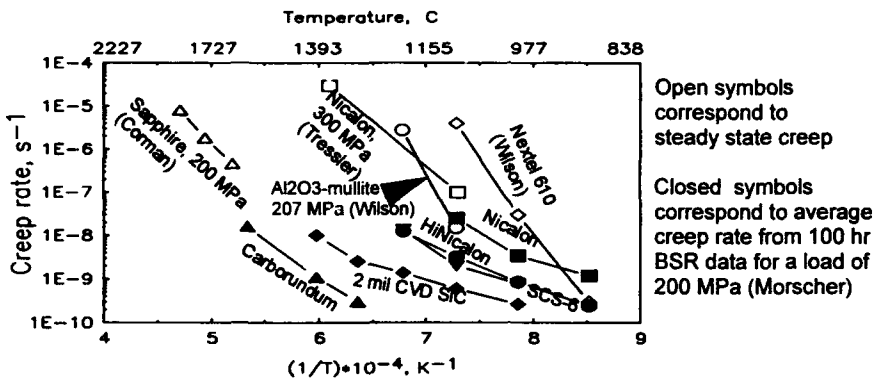
Fig. 2: Creep rate as a function of temperature for different fibers

fiber. Single crystal (c-axis) Al_2O_3 fiber is highly creep resistant at temperatures lower than 1673 K. Depending on the strain rate, the creep resistance of YAG/Al_2O_3 eutectic is equal to or better than that of single crystal Al_2O_3 [14].

Stress rupture strength: Yun and DiCarlo [15] have measured the stress rupture strength of different fibers and extrapolated the data, using the Larson-Miller parameter, to predict 1000-hr stress rupture strength as a function of temperature. The predicted stress rupture strengths for different fibers are shown in Fig. 3.

The 1000-hr stress rupture strengths for all oxide tow fibers are relatively low, compared to that of SiC and single crystal oxide fibers. Among the sol-gel derived oxide tow fibers, the Al_2O_3-mullite nanocomposite fiber has the best stress rupture strength. Although single crystal Al_2O_3 fiber is highly creep resistant, it has poor stress rupture properties, which

is due to slow crack growth [18]. The stress rupture strength of YAG/Al$_2$O$_3$ eutectic fiber at 1373 K ($\tilde{}$ 1100 MPa) is much higher than that of single crystal Al$_2$O$_3$ fiber ($\tilde{}$600 MPa).

The stress rupture strength of all SiC fibers is greater than that of single crystal Al$_2$O$_3$ fibers at temperatures lower than 1373 K. However, above 1473 K the stress rupture
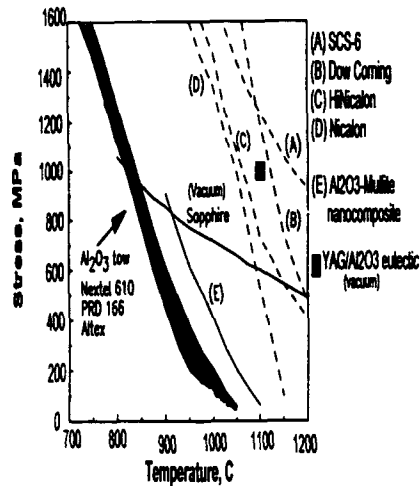

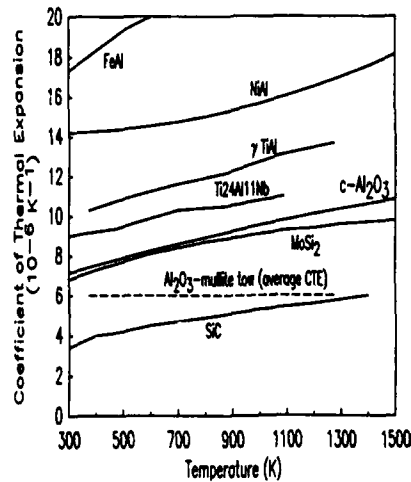Fig. 3: 1000-hr stress rupture strength of fibers as a function of temperature (Yun and DiCarlo)

Fig. 4: CTEs of fibers and intermetallic matrices

strength of single crystal alumina fiber is greater than that of tow SiC fibers. The stress rupture strength of CVD SiC fiber (SCS-6) is greater than that of single crystal alumina and tow SiC fibers at all temperatures. Based on limited stress rupture data for the YAG/Al$_2$O$_3$ eutectic fiber, it appears that the stress rupture properties of this fiber is similar to that of SiC fibers.

Coefficient of thermal expansion: Fig. 4 compares the CTEs of SiC [16], Al$_2$O$_3$ [16], and Al$_2$O$_3$-mullite nanocomposite [19] with that of various intermetallic matrices [16,17]. There are no published data on the CTE of YAG/Al$_2$O$_3$ eutectic fibers. However, the CTE of YAG [18] is close to that of Al$_2$O$_3$; thus, the CTE of YAG/Al$_2$O$_3$ eutectic is expected to be similar to that of Al$_2$O$_3$.

Except for the Al$_2$O$_3$/MoSi$_2$ composite systems, all other composites reinforced with currently available fiber have CTE mismatch between the fiber and the matrix. The CTE mismatch in Al$_2$O$_3$ (and YAG/Al$_2$O$_3$ eutectic) fiber reinforced titanium aluminides is relatively small compared to other composites.

Summary of fiber properties: From a strength standpoint, the SiC fibers are far superior than the oxide fibers. The single crystal oxide fibers, such as Al$_2$O$_3$ and YAG/Al$_2$O$_3$ eutectic, are the most creep resistant of all fibers at temperatures of interest to IMCs. However, single crystal Al$_2$O$_3$ fiber has poor stress rupture strength at temperatures of interest for

most IMCs. Silicon carbide fibers, as well as the YAG/Al_2O_3 eutectic fiber, have stress rupture strengths much greater than that of single crystal Al_2O_3. In summary, based on fiber properties alone, SiC fibers would be desirable for many IMCs, but othe: factors such as chemical compatibility and CTE mismatch might limit the use of SiC fibers in IMCs. Among oxide fibers investigated to date, single crystal Al_2O_3/YAG eutectic fiber has the best properties at temperatures of interest to IMCs. If a tow oxide fiber is required for an application, the Al_2O_3-mullite nanocomposite fiber would be the fiber of choice.

CHEMICAL COMPATIBILITY OF FIBERS WITH INTERMETALLIC MATRICES

The chemical compatibility of currently available commercial and developmental fibers, which include SiC, Al_2O_3, YAG/Al_2O_3 eutectic, and Al_2O_3-SiO_2 compositions, with various intermetallic matrices will be reviewed. The potential for interfacial reaction barrier coatings will be discussed.
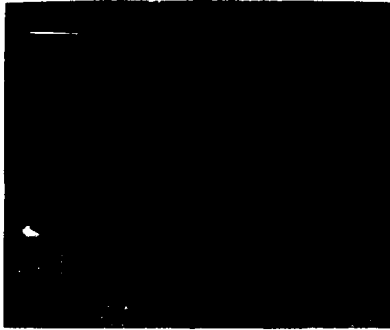
Fig. 5: Interfacial reaction in as-processed SCS-6/Ti-24Al-11Nb composite

β phase
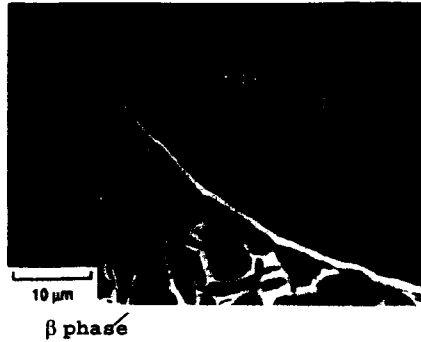
Fig. 6: Interfacial reaction in SCS-6/Ti-24Al-11Nb composite with a thin interlayer of Nb

SiC/Titanium aluminide composites: All titanium aluminide compositions, α_2, orthorhombic, and γ, react with SiC fibers [20,21], resulting in the formation of complex carbides and silicides. Fig. 5, shows the fiber-matrix reaction in an as-processed SCS-6/α_2(Ti-24Al-11Nb)* composite. The fiber-matrix reaction results in the formation of a reaction zone next to the fiber surface, identified as complex carbides and silicides [20], and a ß-depleted zone in the matrix near the fiber-matrix interface. The thickness of the reaction zone and the ß-depleted zone increases parabolically with time [20].

The ß-depleted zone near the interface for a SiC/Ti-24Al-11Nb composite can be eliminated by applying an interfacial coating of a ß-stabilizer such as Nb [22,23], as shown in Fig. 6. Reaction of Nb with the matrix increases the amount of ß phase in the matrix, thus preventing depletion of the ß phase near the interface. Other ß-stabilizer coatings such as Ta and Mo are also expected to have similar effects. For example, a dual layer Ag/Ta coating [24] was effective in preventing depletion of the ß phase near the interface for a

---

* Unless otherwise stated, all alloy compositions are in atom percent.

SiC(SCS-6)/Ti-24Al-11Nb composite.

The extent of reaction between SiC fiber (SCS-6) and an orthorhombic (Ti-22Al-23Nb) alloy is much lower than that in a SiC/α_2 composite [25]. More important, there is no ß-depleted zone in SiC/orthorhombic composite, which is due to the increased concentration of Nb in the alloy.

Although the beneficial effect of ß-stabilizer coatings, such as Nb and Ta, has been demonstrated during composite processing, the long-term chemical stability of the interfacial region is yet to be demonstrated. Of particular concern is reaction of Nb(or Ta) with the fiber and diffusion of Nb(or Ta) into the matrix. For long-term interfacial stability, a higher Nb-containing alloy (e.g., the Ti-22Al-23Nb orthorhombic alloy) might be preferable.

Interfacial coatings other than ß-stabilizers can also be used to prevent fiber-matrix reaction. One candidate coating composition is Y_2O_3, which is thermodynamically compatible with SiC, C, and titanium aluminides. Other possibilities include the use of reaction products (Ti_xAl_yC and Ti_xAl_ySi) as interfacial coatings.
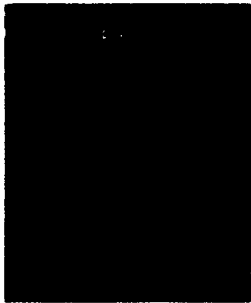
Fig. 7: Reaction of NiAl with SiC (SCS-0) fiber without any carbon coating after hot pressing at 1573 K for 2 hr
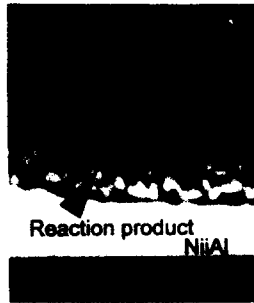
Fig. 8: Reaction of NiAl with SCS-6 fiber after hot pressing at 1573 K for 2 hr and then annealing at 1373 K for 100 hr
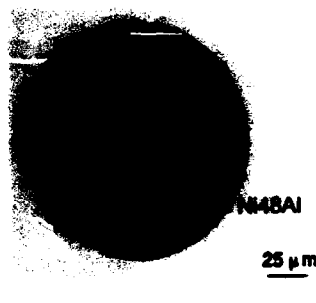
Fig. 9: Reaction of Ni48Al with SCS-6 fiber after 2 hr of hot pressing at 1573 K

SiC/NiAl composites: Stoichiometric NiAl reacts with SiC, as shown in Fig. 7. An outer carbon coating on SiC fiber, as is the case with the SCS-6 fiber, prevents reaction between SiC and NiAl, as shown in Fig. 8. There is some reaction product inside the outermost carbon layer of the two-layer carbon coating; however, the inner carbon coating and the fiber are intact. An interfacial TiB_2 coating on the SCS-6 fiber completely eliminates the reaction between NiAl and SCS-6 fiber [26].

Reaction of NiAl with SiC fibers is a strong function of the Al concentration in the alloy [26]. A small decrease in Al concentration from the stoichiometric composition causes extensive reaction between NiAl and the SCS-6 fiber, as shown in Fig. 9. A TiB_2 interfacial coating is not effective in preventing reaction between Ni48Al and SCS-6 fiber [26].

Silicon carbide fibers can be potential reinforcements for NiAl, provided the alloy composition is maintained at the stoichiometric composition. For a SiC fiber reinforced stoichiometric NiAl composite, long-term interfacial stability can be maintained by a suitable interface coating. However, this may not be the case for composites with Al-deficient NiAl

compositions.

SiC/FeAl: Extensive reaction occurs between FeAl and SiC during hot pressing, resulting in the formation of a Fe-Al-Si compound and free carbon [27]. Whether a reaction barrier can be effective in preventing reaction between FeAl and SiC has not been demonstrated.

SiC/MoSi$_2$: Silicon carbide is thermodynamically compatible with MoSi$_2$. However, MoSi$_2$ powders frequently contain oxygen impurities, primarily as surface SiO$_2$ layer on MoSi$_2$ particle. The surface SiO$_2$ can react with SiC fiber during hot pressing to form SiO and CO(g),

$$2SiO_2 + SiC = 3SiO + CO(g) \qquad (1)$$

which can degrade the fiber.

The carbon coating on SiC fibers is not thermodynamically compatible with MoSi$_2$. The Si component in MoSi$_2$ can react with C to form SiC,

$$Si(in\ MoSi_2) + C = SiC \qquad (2)$$

which can deplete MoSi$_2$ of Si and result in the formation of Mo$_5$Si$_3$.
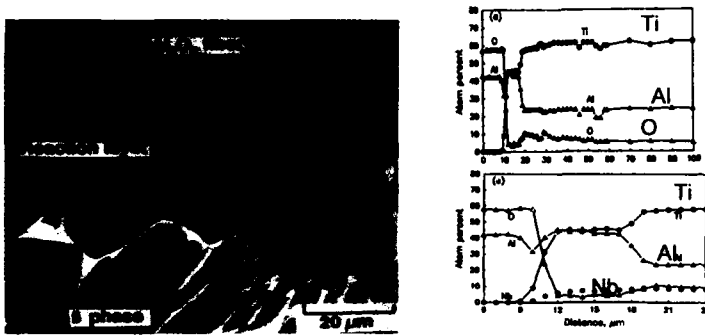
Fig. 10: Reaction of Ti-24Al-11Nb with single crystal alumina fiber after hot pressing for 2 hr at 1363 K

Al$_2$O$_3$/titanium aluminide: From thermodynamic considerations [28], binary titanium aluminides with Al concentrations less than that corresponding to the γ-TiAl phase (⁻50 a/o Al) are not chemically compatible with Al$_2$O$_3$, and diffusion couple studies have confirmed this [28]. The reaction mechanism is determined to be dissolution of Al and atomic oxygen from Al$_2$O$_3$ into Ti-Al alloys. Fig. 10 shows the cross section and the microprobe analysis across the fiber-matrix interface for a hot pressed Al$_2$O$_3$/Ti-24Al-11Nb composite. Both Al and atomic oxygen have diffused from the fiber into the alloy. Diffusion of Al into the alloy has resulted in the formation of an Al-rich region next to the fiber, which is γ TiAl containing a small amount of Nb. The dissolution of atomic oxygen in the alloy has resulted in a ß-depleted zone near the interface. The reaction of Al$_2$O$_3$ with orthorhombic alloys [29] is similar to that with the Ti-24Al-11Nb (α$_2$ + ß) alloy.

Although a binary γ TiAl alloy is chemically compatible with Al$_2$O$_3$, a two-phase γ TiAl (such as Ti-48Al-2Cr-2Nb) which has some α$_2$ phase in addition to the γ phase, would react with Al$_2$O$_3$. The reaction would occur between Al$_2$O$_3$ and the α$_2$ phase in such alloys.

79

Indeed, enrichment of Al near the fiber-matrix interface has been observed in hot-pressed Al_2O_3/γ TiAl (two phase) composites [30]. The extent of reaction in Al_2O_3/γ TiAl (two phase) composites is much lower than that in an Al_2O_3/Ti-24Al-11Nb composite. However, the small extent of reaction might be sufficient to degrade the fiber strength.

It is clear that interfacial reaction barriers would be needed for Al_2O_3 fiber reinforced titanium aluminide composites. Some potential reaction barrier coatings include Nb/Y_2O_3 and $C/Y_2O_3/TiN$ multilayer coatings [31].

$Al_2O_3/NiAl$ and $Al_2O_3/FeAl$: Both NiAl and FeAl are thermodynamically compatible with Al_2O_3. However, impurities in the alloy can cause fiber-matrix reaction $Al_2O_3/NiAl$ and $Al_2O_3/FeAl$ composites. One common impurity in many intermetallic powders is oxygen. During hot pressing, the oxygen impurity in the alloy powder can lead to the formation of Al_2O_3 along the alloy grain boundaries, which can then sinter with the fiber.

$Al_2O_3/MoSi_2$: Al_2O_3 is thermodynamically compatible with $MoSi_2$. However, there could be interfacial reaction due to the oxygen impurities in $MoSi_2$. The oxygen in $MoSi_2$ powder is present as SiO_2, which can react with Al_2O_3 fiber to form mullite or other aluminosilicates.

Reaction of Al_2O_3/YAG eutectic fiber with various intermetallics: Because Al_2O_3 is one of the major constituents in the Al_2O_3/YAG eutectic fiber, the reaction of various intermetallics with this eutectic fiber is expected to be similar to that with Al_2O_3. For example, the reaction of Al_2O_3/YAG eutectic fiber with γTiAl matrices is due to reaction of the Al_2O_3 component of the fiber with the matrix [32].

Reaction of Al_2O_3-mullite nanocomposite fiber with various intermetallics: The mullite component of the fiber is thermodynamically compatible with $MoSi_2$, but not with the aluminides. The reaction of mullite with NiAl results in the formation of Al_2O_3 at the interface, as shown in Fig. 11. Similar results can be expected for reaction between mullite and FeAl. Reaction between α_2-based titanium aluminides and mullite would result in the formation of TiO_2 at the interface. Reaction of γTiAl with mullite is likely to result in the formation of Al_2O_3 at the interface.

Mullite

Reaction product
Al2O3

Alloy
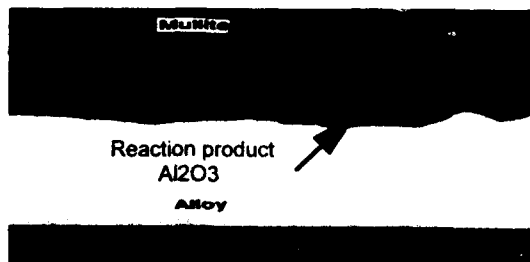
Fig. 11: Reaction of sol-gel mullite with NiAl after hot pressing at 1573 K for 2 hr

FIBER-MATRIX CTE MISMATCH

The fiber-matrix CTE mismatch causes the development of residual stresses in the composite after cooling from the processing temperature to room temperature and during thermal cycling. After cooling from the processing temperature to room temperature, the

residual stresses in the fiber are compressive in all three directions, i.e., axial, radial, and circumferential (or hoop). The residual stresses in the matrix at room temperature are tensile in axial and hoop direction, and compressive in the radial direction. The tensile stresses in the matrix can cause matrix cracking [38,39], as shown in Fig. 12.

SiC(SCS-6)/Ti-24Al-11Nb   Al2O3/NiAl

500 thermal cycles from R T to 1300 K

As-processed   1000 thermal cycles   1.5 mm
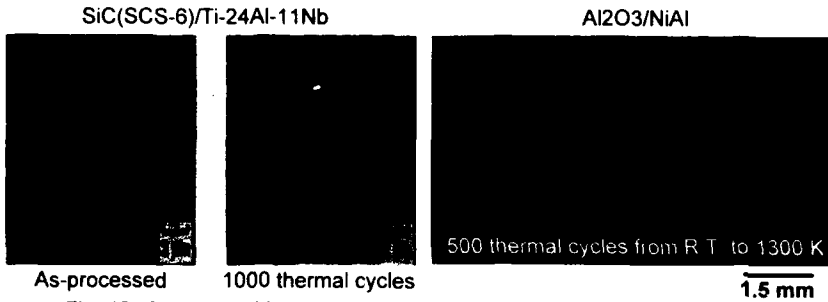
Fig. 12 : Matrix cracking due to CTE mismatch induced residual stresses

Role of matrix ductility: The extent of matrix cracking due to the residual stresses in the matrix is a function of the ductility in the matrix. For a ductile matrix, residual stresses can be relieved by plastic deformation of the matrix. However, interfacial reaction can result in the creation of a brittle zone near the interface, and cracks can form in this brittle interfacial zone. Indeed, such is the case for SiC/Ti-24Al-11Nb composite in which the interfacial reaction causes depletion of the ductile ß phase near the interface, and radial cracks are always observed in the ß-depleted zone [33]. Application of a thin interfacial layer of Nb eliminates the ß-depleted zone [22,23] and thereby eliminates the radial cracks in the matrix, as shown in Fig. 13. The key to eliminating residual stress induced matrix cracking in ductile matrix composites is to preserve the matrix ductility during composite processing.

No Nb coating   Nb coating

(Radial cracking in β-depleted zone)   (No β-depleted zone)
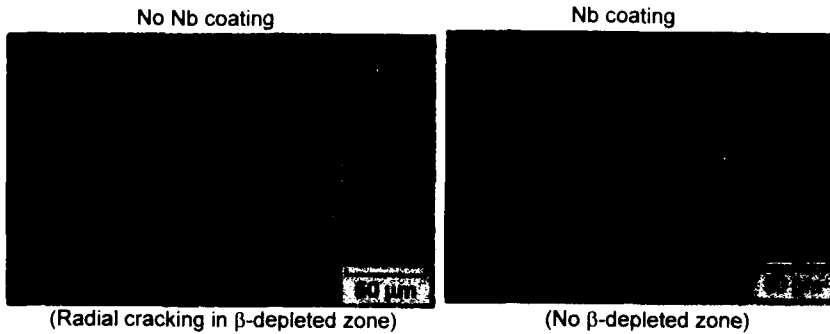
Fig. 13: Elimination of radial matrix cracks in a SiC(SCS-6)/Ti-24Al-11Nb composite due to a thin interfacial layer of Nb

81

The concept of "compensating" interfacial layer in reducing matrix stresses: The potential of interfacial coating in reducing CTE mismatch induced residual stresses in IMCs has been examined by Arnold et al.[34]. It has been shown from analytical models [34] that the residual hoop and radial stresses in the matrix can be reduced, if not eliminated, with an interfacial "compensating layer" . The prime requirement for such a compensating layer is that it must have a CTE higher than that of the matrix. The interfacial layer must have other secondary characteristics such as low elastic modulus and lower yield stress compared to that of the matrix; however, the most important characteristics of the interfacial layer is its CTE in comparison to the matrix.

There are some practical limitations to the use of a compensating layer coating for reducing residual stresses in IMCs. First, the already high CTE of many aluminide intermetallics, such as NiAl and FeAl, makes it difficult, in some cases almost impossible, to find a material with a CTE higher than that of the matrix. Secondly, a multilayer coating may be required to prevent chemical reaction between the compensating layer and the fiber and/or the matrix.

The compensating layer, although not practical for high CTE matrices, such as FeAl and NiAl, might find some use for composites with relatively low CTE matrices such as titanium aluminides (α_2, orthorhombic, and γ) and MoSi$_2$. Some potential composite systems where a compensating interfacial layer might be beneficial are Al$_2$O$_3$/γ TiAl, YAG-Al$_2$O$_3$ eutectic/γ TiAl, and SiC/MoSi$_2$.

Compliant interfacial layer: For composites containing matrices that are brittle at room temperature, such as Al$_2$O$_3$/NiAl composite, CTE mismatch induced residual stresses can cause matrix cracking at room temperature. One concept to prevent the matrix cracks from propagating through the composite is to apply an interfacial ductile layer, called a "compliant layer", that can blunt the matrix cracks by plastic deformation of the coating. This concept is similar to that in which ductile reinforcements are used to increase the toughness of brittle ceramics and intermetallics [35,36]. Molybdenum has been proposed [37] as a compliant interfacial coating for Al$_2$O$_3$/NiAl composite because of its chemical compatibility with both NiAl and Al$_2$O$_3$. It is likely that coating thicknesses on the order of 5 to 10 μm (or higher) would be required for the coating to be effective in blunting the cracks.

Elimination of matrix cracking by use of small diameter fibers: From fracture mechanics considerations, it has been demonstrated [38] that residual stress induced matrix cracking can be eliminated by using small diameter fibers. It has been established [39] that a critical reinforcement size exists below which residual stress induced matrix cracking is suppressed. The critical reinforcement size is a function of misfit strain, elastic modulus, and matrix toughness, and needs to be established for each composite system. Recent work by Lu et al. [39] on SiC/MoSi$_2$ composites has shown that radial cracking of the matrix can be suppressed by using small diameter fibers.

The fact that residual stress induced matrix cracking can be eliminated by using small diameter fibers offers the potential of using tow fibers as reinforcements for aluminide matrices. Recently developed Al$_2$O$_3$-mullite nanocomposite tow fiber and stoichiometric SiC tow fibers (HiNicalon and Dow Corning) can be potential reinforcements for NiAl and other aluminides if suitable interfacial reaction barriers can be identified. Particularly, the high strength and creep resistance of newly developed stochiometric SiC tow fibers make them attractive candidates as reinforcements for NiAl and other brittle aluminides if the problem of interfacial reaction can be solved. The fact that a carbon coating can prevent reaction

82

between SiC fiber and stoichiometric NiAl [26] offers some promise for SiC tow fiber reinforced NiAl composites.

Potential for high-CTE fibers: Because of the fiber-matrix CTE mismatch in many IMCs of current interest, there have been ongoing efforts to develop high-CTE fibers. To date, several high-CTE fibers, such as Nb_2Be_{17} [40], CrB_2 [41], cubic ZrO_2 [42], Ti_xSi_yC [43], and Ti_xAl_yC [43,44], have been produced in the laboratory. So far, these fibers have not demonstrated room temperature strengths comparable to that of SiC and Al_2O_3. Much more developmental efforts would be needed before these fibers become commercially viable. It appears that the choice of fibers for IMCS will be limited to SiC, Al_2O_3, and possibly Al_2O_3/YAG eutectic, and Al_2O_3-mullite nanocomposite for near-term applications.

FIBER-MATRIX INTERFACIAL BOND STRENGTH

It is generally agreed that some degree of weakness at the fiber-matrix interface is desirable [45] for attaining high strength in the fiber direction and high fracture toughness [51]. On the other hand, a strong interfacial bond is required for a variety of reasons, which include: (1) obtaining high transverse strength, (2) withstanding radial tensile stresses at the interface during the heating cycle [46], and (3) preventing oxidation along the fiber-matrix interface [47]. An optimum interfacial bond strength that can satisfy the various conflicting bonding requirements is desirable.

The interfacial bond strength can be modified by the application of fiber coatings. For example, a weak interface is created in Al_2O_3/γ TiAl composites [48] by applying a thin carbon coating onto the fibers. A strong interface can be created in Al_2O_3/FeAl composite [49] by applying an interfacial Ti coating. It is more than likely that the creation of a strong interface would require limited chemical reaction or interdiffusion at the interface, which might have adverse effects on the fiber strength. The key challenge is to optimize the interfacial bond strength without causing fiber strength loss.

FIBER DAMAGE DURING COMPOSITE PROCESSING

Fiber damage during composite processing, resulting in the loss of fiber strength and fiber breakage, is of concern for composites reinforced with single crystal Al_2O_3 fibers. Fig. 14 compares the room temperature tensile strengths of fibers etched from different composites [50-52] with that of the as-received fibers. For a SiC/Ti-24Al-11Nb composite, the fibers etched out of the composite have nearly the same strengths as that of the as-received fibers, suggesting no loss of fiber strength during composite processing. In contrast, single crystal Al_2O_3 fibers loose nearly half of their original strength after composite processing. In addition to fiber strength loss, fiber fragmentation in as-processed composites has also been observed in an Al_2O_3/NiAl composite [53].

The mechanisms for the loss of fiber strength in single crystal Al_2O_3 fiber reinforced composites are not yet clear. One possible mechanism would be the creation of surface flaws due to chemical reaction. For thermodynamically compatible fiber-matrix combinations, such as Al_2O_3/NiAl and Al_2O_3/FeAl composites, impurities present either in the alloy or introduced during composite processing can cause interfacial reaction. Even in the absence of any chemical reaction, surface tension effects can cause the formation of grain boundary ridges (the impression of metal grain boundaries) on the fiber surface, which
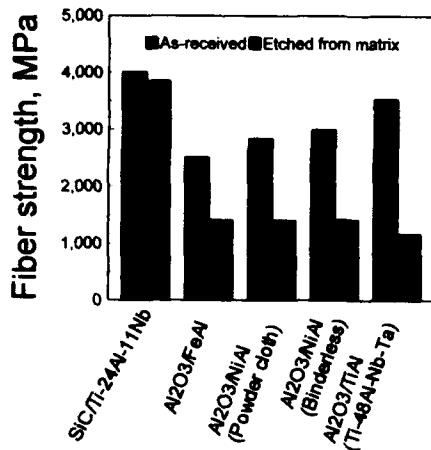
83

Fig. 14: A comparison of fiber strengths after etching from the matrix (shown in ighter shade) with that of as-received fibers (shown in dark shade)

can be potential sites for fracture initiation [52].

Another possible mechanism for sapphire fiber damage during composite processing is that the fiber is subjected to a compressive axial stress during cooling of the composite, due to the fiber-matrix CTE mismatch. Single crystal Al_2O_3 is susceptible to twinning during compression [54], and the twins can be the sites for crack initiation during subsequent tensile testing.

If the fiber damage in sapphire fiber reinforced composites is due to the creation of surface flaws resulting from chemical reaction at processing temperature, an interfacial reaction barrier can prevent the fiber damage. However, if the fiber damage is due to the development of compressive stresses in the fiber during cooling, an interfacial coating may not be the solution.

Fiber damage during composite processing is one of the major technical barriers to the use of single crystal Al_2O_3 fibers as reinforcements for intermetallic matrix composites. Clearly, more work needs to be done to understand the mechanisms of fiber damage. Whether fiber damage during composite processing occurs for other oxide fibers is not known.

SUMMARY AND CONCLUDING REMARKS

Currently, the practical choice of fibers (monofilaments and tows) for IMCs (and other composites as well) is limited to SiC, Al_2O_3, YAG/Al_2O_3 eutectic, and Al_2O_3-mullite nanocomposite, all of which have low CTEs compared to that of many intermetallics. Among all fibers, monofilament CVD SiC fibers have the best mechanical properties at temperatures of interest for IMC application. Thus, the potential of monofilament SiC fibers for various intermetallic matrices needs to be fully explored.

With the currently available fibers, it becomes apparent that the problem of CTE mismatch is going to be there for most IMCs, except for Al_2O_3 or YAG/Al_2O_3 fiber reinforced $MoSi_2$ and titanium aluminide composites. The effect of CTE mismatch can be

manageable for composites with ductile matrices. The main challenge here is to preserve the matrix ductility during composite processing. For composites with brittle matrices, alternative solutions must be devised to accommodate the effect of CTE mismatch. One potential solution is the use of small diameter tow fibers to eliminate matrix cracking resulting from CTE mismatch induced residual stresses. The recent development of Al_2O_3-mullite nanocomposite and stoichiometric SiC (HiNicalon and Dow Corning) tow fibers with improved high temperature properties offers some new opportunities. Clearly, the potential of using small diameter fibers in IMCs needs to be explored further. Interfacial reaction barrier coatings will be needed for many composites using Al_2O_3-mullite nanocomposite and SiC tow fibers.

Single crystal Al_2O_3 and YAG/Al_2O_3 eutectic fibers can be potential reinforcements for titanium aluminides, if suitable interfacial reaction barriers can be found, and for $MoSi_2$. However, they will not find use in high-CTE and brittle matrices like NiAl. Based on stress rupture properties, YAG/Al_2O_3 eutectic is the preferred fiber; however, the lack of availability of this fiber in large quantities may preclude its use for near-term applications. The successful use of single crystal Al_2O_3 fibers in composites requires that the problem of fiber damage during composite processing be solved. Whether similar fiber damage occurs in Al_2O_3/YAG eutectic fiber reinforced composites needs to be determined.

Fiber coatings will be needed to accommodate various fiber-matrix incompatibilities. Because of the problem of fiber-matrix reaction in many IMCs, one major function of a fiber coating would be to act as an interfacial reaction barrier. Several examples were given, demonstrating the effectiveness of interfacial reaction barriers in various composites. Although the interfacial reaction barrier coatings have been proved to be effective in preventing fiber-matrix reaction during composite processing, their effectiveness over long time periods is yet to be demonstrated.

Another clear function of a fiber coating is to optimize the interfacial bond strength. With regards to reduce the CTE mismatch induced residual stresses, fiber coatings may not offer practical solutions. Thus, the primary role of fiber coatings in IMCs is to prevent fiber-matrix reaction and to optimize the interfacial bond strength.

The morphology and microstructure of the coating are important variables in determining the long-term effectiveness of coatings as reaction barrier and need to be optimized for any composite. Furthermore, failure mechanisms within the coating itself need to be examined. For example, fracture may originate within the coating, which could adversely affect composite properties.

REFERENCES

1. M. H. Jaskowiak and J. A. DiCarlo, J. Amer. Ceram. Soc., 2, 192 (1989).

2. M. Takeda, Y. Imai, H. Ichikawa, T. Ishikawa, N. Kasai, T. Seguchi, and K. Okamura, Ceramic Engg. and Science Proceedings, 13, 209 (1992).

3. J. Lipowitz, J. A. Rabe, L. D. Orr, and R. R. Androl, presented at the 1994 MRS Spring Meeting, San Francisco, CA, 1994 (published in this Proceedings).

4. G. V. Srinivasan and V. Venkateswaran, Ceramic Engg. and Science Proceedings, 14, 563 (1993).

5. A. Sayir and L. E. Matson, in Proceedings of the 4th Annual HITEMP Review, October 29-30, 1991, NASA Conference Publication 10082, 83-1 (1991).

6. A. Sayir, NASA Lewis Research Center, unpublished data

7. R. T. Bhatt and M. D. Kraitchman, NASA TM 86981 (1985).

8. Textron Specialty Material, private communication.

9. M. M. Vogel and D. M. Wilson in Proceedings of the 16th Conference on Metal Matrix, Carbon, and Ceramic Matrix Composites, NASA Conf. Publication 3175, 519 (1992).

10. D. M. Wilson, D. C. Lueneburg, and S. L. Lieder, Ceramic Engg. and Science Proceedings, 14, 609 (1993).

11. L. A. Giannuzzi and R. E. Tressler in Proceedings of the 6th Annual HITEMP Review, October 25-27, 1993, NASA Conference Publication 19117, 87-1 (1993).

12. G. N. Morscher and J. A. DiCarlo in Proceedings of the 6th Annual HITEMP Review, October 25-27, 1993, NASA Conference Publication 19117, 88-1 (1993).

13. G. S. Corman, Ceramic Engg. and Science Proceedings, 12, 1745 (1991).

14. T. Mah, T. A. Parthasarathy, and M. D. Petry, Ceramic Engg. and Science Proceedings, 14, 622 (1993).

15. H. M. Yun and J. DiCarlo, NASA Lewis Research Center, unpublished data (1994).

16. Y. S. Touloukian, R. K. Kirby, R. E. Taylor, and P. D. Desai, Thermophysical Properties of Matter (IFI/Plenum, New York, 1975, Vol. 12 and 1976, Vol. 13).

17. P. K. Brindley, NASA Lewis Research Center, unpublished data on Ti aluminide CTE.

18. A. Sayir and L. E. Matson in Proceedings of the 4th Annual HITEMP Review, October 29-30, 1991, NASA Conference Publication 10082, 83-1 (1991).

19. D. M. Wilson, S. L. Leider, and D. C. Lueneburg, presented at the 1994 MRS Spring Meeting, San Francisco, CA, 1994 (to be publishhed in this Proceedings).

20. S. F. Baumann, P. K. Brindley, and S. D. Smith, Metall. Trans., 21A, 1559 (1990).

21. S. Krishnamurthy in Interfaces in Metal-Ceramic Composites, edited by R. Y. Lin, R. J. Arsenault, G. P. Martins, and S. G. Fishman (TMS publication, Warrendale, PA, 1990), p. 59.

22. A. K. Misra, Composites Science and Technology, 50, 37 (1994).

23. P. A. Siemers and A. M. Ritter, U. S. Patent No. 5017438 (1991).

24. S. M. Jeng, J. M. Yang, and J. A. Graves, J. Mater. Res., 8, 905 (1993).

25. P. R. Smith, J. A. Graves, C. G. Rhodes, M. R. James, and J. R. Porter, unpublished results.

26. A. K. Misra, submitted for publication in J. Mater. Res.

27. S. Draper, D. J. Gaydosh, A. K. Misra, and M. V. Nathal, J. Mater. Res., 5, 1976 (1990).

28. A. K. Misra, Metall. Trans., 22A, 715 (1990).

29. J. A. Nesbitt and A. K. Misra, Proceedings of the 5th Annual HITEMP Review, October 27-28, 1992, NASA Conference Publication 10104, 40-1 (1992).

30. D. S. Shih and R. A. Amato, Scripta Metallurgica et Materialia, 24, 2053 (1990).

31. C. McCullough and R. R. Kieschke, presented at the 1995 MRS Spring Meeting, San Francisco, CA, 1994 (to be published in this Proceedings).

32. T. Mah, P. R. Subramanian, and L. E. Matson, Scripta Met. et Mater. 28, 961 (1993).

33. P. K. Brindley, P. A. Bartolotta, and S. J. Klima, NASA TM 100956 (1988).

34. S. M. Arnold, V. K. Arya, and M. E. Melis, J. of Composite Materials, 26, 1287 (1992).

35. B. D. Flinn, M. Ruhle, and A. G. Evans, Acta Metall. Mater.., 37, 3001 (1989).

36. H. E. Deve and M. J. Maloney, Acta Metall. Mater., 39, 2275 (1991).

37. A. K. Misra, R. Bowman, I. Locci, and M. Matthiesen, Proceedings of the 6th Annual HITEMP Review, October 25-27, 1993, NASA Conf. Publication 19117, 58-1 (1993).

38. G. A. Cooper and J. M. Sillwood, J. Mater. Sci., 7, 325 (1972).

39. T. C. Lu, J. Yang, Z. Suo, A. G. Evans, R. Hecht, and R. Mehrabian, Acta Metall. Mater., 39, 1883 (1991).

40. R. C. Krutenat in Proceedings of the 4th Annual HITEMP Review, October 29-30, 1991, NASA Conference Publication 10082, p. 16-1 (1991).

41. M. L. Emiliani, Proceedings of the 3rd Annual HITEMP Review, October 30-31, 1990, NASA Confernce Publication 10051, 12-1 (1990).

42. K. J. McClellan, H. Sayir, A. H. Heuer, A. Sayir, J. S. Haggerty, and J. Sigalovsky, Ceramic Engg. and Science Proceedings, 14, 651 (1993).

43. MSNW, Inc., San Marcos, CA, unpublished data.

44. J. D. Casey, E. Honig, R. Krutenat, R. Suplinskas, and F. Wawner, Proceedings of the 14th conference on Metal Matrix, Carbon, and Ceramic Matrix Composites, NASA Conference Publication 3097, 89 (1990).

45. D. B. Marshall, M. C. Shaw, and W. L. Morris, Acta Metall. Mater.,40, 443 (1992).

46. A. K. Misra, Scripta Metall Mater., 28, 1189 (1993).

47. J. Doychak, J. A. Nesbitt, R. D. Noebe, and R. R. Bowman, Oxid. Met., 38, 45 (1992).

48. C. H. Weber, J. Y. Yang, J. P. A. Lofvander, C. G. Levi, and A. G. Evans, Acta Metall. Mater, 41, 2681 (1993).

49. D. J. Gaydosh, S. L. draper, J. I. Eldridge, and P. Tsui, Proceedings of the 3rd Annual HITEMP Review, October 30-31, 1990, NASA Conf. Publication 10051, 39-1 (1990).

50. S. L. Draper, P. K. Brindley, M. V. Nathal, and J. I. Eldridge, Proceedings of the 4th Annual HITEMP Review, October 29-30, 1991, NASA CP 10082, 44-1 (1991).

51. J. R. Porter and M. C. Shaw in Proceedings of the 15th Conference on Metal matrix, Carbon, and Ceramic Matrix Composites, NASA Conf. Publication 3133, 181 (1991).

52. S. L. Draper and I. E. Locci, Accepted for publication in J. Mater. Res. (1994).

53. R. R. Bowman, I. E. Locci, S. L. Draper, and A. K. Misra, presented at the 1994 MRS Spring Meeting, San Francisco, CA, 1994 (to be published in this Proceedings).

54. W. D. Scott and K. K. Orr, J. Amer. Ceram. Soc., 66, 27 (1983).

MICROSTRUCTURE AND HIGH TEMPERATURE
PROPERTIES OF 85% Al$_2$O$_3$-15% SiO$_2$ FIBERS

D. M. WILSON, S. L. LIEDER AND D. C. LUENEBURG
Metal Matrix Composite Department
3M Co., St. Paul, MN 55144-1000

ABSTRACT

A new sol/gel fiber which exhibits exceptional high temperature properties was recently developed at 3M. This fiber has the composition 85% Al$_2$O$_3$-15% SiO$_2$ (85A-15S). High temperature tensile strength and creep properties were measured in the temperature range 1000°C - 1300°C. The creep rate for the 85A-15S fibers was three orders of magnitude less than single phase polycrystalline alumina fibers such as Nextel 610, and 90% of room tensile strength was retained at 1250°C. These exceptional high temperature properties were attributed to a unique, two-phase microstructure consisting of globular and elongated grains of α-Al$_2$O$_3$ and mullite (3Al$_2$O$_3$-2SiO$_2$). The room temperature single filament strength of the 85% Al$_2$O$_3$-15% SiO$_2$ fibers was 2130 MPa, and the elastic modulus was 260 GPa.

INTRODUCTION

The commercialization of high temperature ceramic and intermetallic matrix composites will require low cost, oxidation-resistant fibers which retain strength and creep resistance above 1000°C. Polycrystalline alumina fibers such as Nextel 610 have many properties which are desirable for the reinforcement for iron- and nickel-based superalloy composites and ceramic matrix composites. These include oxidation resistance, high strength, high elastic modulus, high thermal expansion and excellent thermochemical stability in superalloy matrices. However, currently available commercial polycrystalline alumina and other oxide fibers have limited utility in structural composites at high temperatures, since the fine-grained polycrystalline microstructure of these fibers leads to high creep rates and reduced strength above 900°C.

The creep resistance of polycrystalline ceramics can be increased by the addition of hard second phase particles[1]. Mullite (3Al$_2$O$_3$-2SiO$_2$) is a prime candidate for hardening alumina due to its excellent creep-resistance and low density. Creep test results on crystalline mullite fibers produced at 3M (Nextel 480) found that the creep rate was 50X less than Nextel 610[2]. Both fibers had a grain size of approximately 0.1 μm. Sol-gel alumina-silica fibers have been commercially available for a number of years[3], but most of these fibers consist of a mixture of alumina spinel and amorphous silica. The presence of amorphous silica provides poor creep resistance compared with mullite, and also makes them unstable with respect to crystallization at temperature above 1200°C. A unique sol/gel processing route to the production of fully crystallized, high strength α-Al$_2$O$_3$-mullite fibers has been developed. In this paper, the microstructure, room and elevated temperature properties of 85% Al$_2$O$_3$-15% SiO$_2$ were evaluated.

The temperature - stress dependence of the steady state creep rate of alumina can be described by the following equation[3]:

$$d\varepsilon/dt = A \, (\exp(-E_a/RT)) \, (1/d)^p \, (\sigma/G)^n \qquad (1)$$

where $d\varepsilon/dt$ is the steady-state creep rate, A is a constant, G is the shear modulus, E_a is the activation energy, σ is the applied stress, d is the grain size, p is the grain size exponent, and n is the stress exponent. The deformation of polycrystalline alumina with a grain size greater than a few micrometers is controlled by either lattice or grain boundary diffusion of aluminum, depending on grain size[4]. In fine-grained fibers, however, specific grain boundary effects become very important due to the short diffusion distances and large grain boundary areas. Interface-reaction rate controlled creep occurs in alumina with grain sizes of ≤ 1 μm[5], where bulk or grain boundary diffusion is so rapid that the creation and annihilation of point defects at grain boundaries is rate-limiting. Other mechanisms for interface-controlled creep include defect creation or annihilation at grain boundaries, grain boundary sliding, grain switching, grain rotation and/or the interaction of gliding or climbing dislocations with grain boundaries or impurities[6,7,8]. For these mechanisms, the stress exponent n is usually 2-3 and the grain size exponent is 1.

FIBER PROCESSING

85% Al_2O_3-15% SiO_2 (85A-15S) fibers were produced using the sol/gel process. Fibers were fired at temperatures above 1350°C to crystallize the fiber to mullite and α-Al_2O_3. The 85% alumina composition produced a fiber with approximately 59 vol% mullite and 41 vol% α-Al_2O_3. The temperature for mullite formation was above 1250°C, as is commonly reported for mullite produced via the sol/gel process[9,10,11]. Continuous tows were produced in two forms: 20 μm diameter fibers were produced as 112 end tows and 12 μm diameter tows were produced as 420 end tows. The 20 μm diameter form may be useful for the preparation of unidirectional or cross-plied MMCs and IMCs. 12 μm diameter fibers would be suitable for weaving into fabrics for CMC applications. Figure 1 shows a SEM micrograph of the 12 μm fibers. The fibers were round and had an apparent grain size of 0.1 μm. The fiber microstructure, appearance, and high temperature properties for both the large and small diameter fibers were very similar.

FIBER TENSILE STRENGTH

Single filament strength testing was performed at 25 mm gauge length using rubber-faced clamp grips with 25 x 25 mm grip faces. Alignment of fibers was critical to obtaining accurate load values. Fiber diameter was measured using a Measure-Rite image analysis system (Model M25-6002 Dolan-Jenner Industries, Lawrence, MA), attached to a light microscope at 1000X magnification. In this system, fiber ends were measured relative to a round template. This method was determined to be accurate within 0.1 μm relative to SEM measurements. Figure 2 shows the Weibull plot of single filament strength for the 12 μm and 20 μm diameter 85A-15S fiber. Fracture probability was determined using the estimator i-0.5/n, which is the most accurate method for small sample numbers[12,13]. The least-squares fit agreed well with the strength data, which indicated a single population of critical flaws. The average strength of the 12 μm diameter fiber was 2130 MPa, but the average strength was only 1490 MPa for the 20 μm fiber. In sol/gel processing, drying and pyrolysis of large diameter fibers is difficult due to the larger diffusion distances required to remove water and fugitive organic materials. This can cause critical defects such as welds, blisters and voids during processing of large diameter fibers. Also, Weibull statistics predict a decrease in fiber strength with increased fiber diameter with increased tested volume, so the lower

90

Figure 1.   Scanning Electron Micrograph of 85% Al$_2$O$_3$ - 15% SiO$_2$ Fiber Tow (600X, 1 cm on print = 16.7 μm)
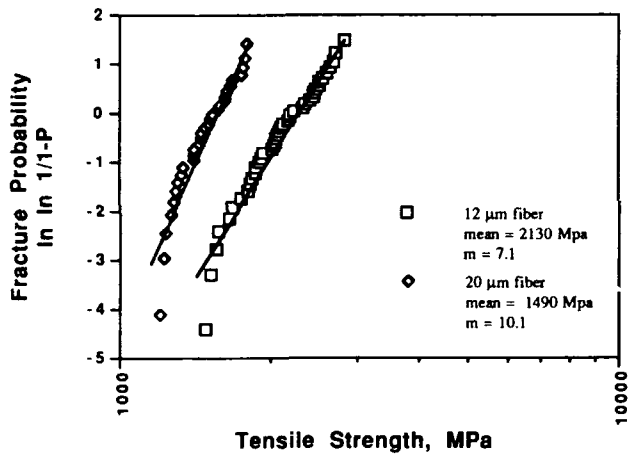
Figure 2.   Weibull Plot of Single Filament Strength of 12 μm and 20 μm Diameter 85% Al$_2$O$_3$ - 15% SiO$_2$ Fiber

strengths of the large diameter fibers was not surprising. The Weibull modulus was 7.1 and 10.1 for the 12 μm and 20 μm diameter fibers, respectively.

A summary of the physical properties of the 85A-15S fiber is shown in Table 1. Elastic modulus was determined by measuring fiber compliance as a function of gauge length[14]. The coefficient of thermal expansion (CTE) was determined by measuring total fiber strain during heating of a fiber in the creep furnace. Since the fiber was gripped outside of the heated zone, a correction for the temperature-gradient zones at the ends of the furnace was applied to this data. Saphikon fiber (CTE = 8.8/°C) was used to confirm the system accuracy to within 2%. Density was measured using the Archimedes method.

Table 1.   Physical Properties of 85% Al_2O_3 - 15% SiO_2 Fibers

Filament Diameter:	12 μm, 20 μm
Composition	85% Al_2O_3 - 15% SiO_2
Crystal Form:	α-Al_2O_3 plus mullite
Tensile Strength (25 mm gauge):	2130 MPa (12 μm dia.)
	1490 MPa (20 μm dia.)
Elastic Modulus:	260 GPa
Density:	3.4 g/cm^3
CTE (25-1000°C):	6.0/°C

FIBER MICROSTRUCTURE

The microstructure of 85% Al_2O_3 - 15% SiO_2 (85A-15S) fibers was very complex. Transmission electron microscopy showed that two phases, α-Al_2O_3 and mullite ($3Al_2O_3$-$2SiO_2$), were present in two different morphologies. Most of the microstructure was made up of small grains of α-Al_2O_3 and mullite less than 100 nm in size (Figure 3a). The grains were globular or rounded rather than faceted. Many of these grains were elongated, with aspect ratios up to 4:1. Large, globular mosaic crystals of both mullite and α-Al_2O_3 up to 0.5 μm in size were also present (Figure 3b). A mosaic crystal is made up of multiple grains, where the grains all have almost identical crystal orientation and are separated by low angle grain boundaries[15]. Mosaic crystals are common in sol/gel-derived α-Al_2O_3 due to the re-nucleation of additional alumina grains from existing alumina grains[16]. In many cases, the mosaic crystals contained occluded second phase grains. These were probably trapped due to the rapid growth of the mosaic crystals during crystallization. There was no evidence of any liquid or amorphous phases in these fibers. Very little porosity was observed.

HIGH TEMPERATURE SINGLE FILAMENT TESTING

For high temperature testing, a slot furnace with a hot zone 25 mm long was used. Testing was carried out by pulling the preheated furnace around the fibers, equilibrating for <15 seconds, and testing to failure at a strain rate of 0.02/min. For the Nextel 610, a cold grip technique (215 mm gauge length) was used. For the 85A-15S fiber, a "hot grip" technique was developed. For hot grip testing, the ends of a single filament were glued to two alumina tows with dilute alumina sol. A 25 mm length of the single filament remained between the two tow sections. The tow

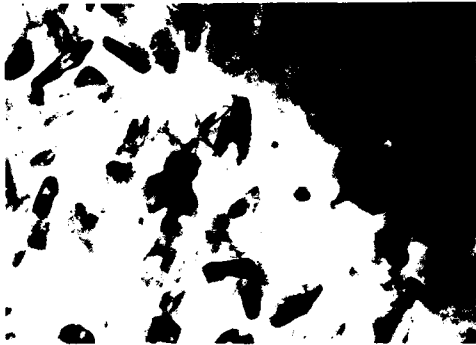Figure 3a.   Transmission Electron Micrograph of 85% Al2O3 - 15% SiO2 Fiber Tow
              (100,000X; 1 cm on print = 100 nm)

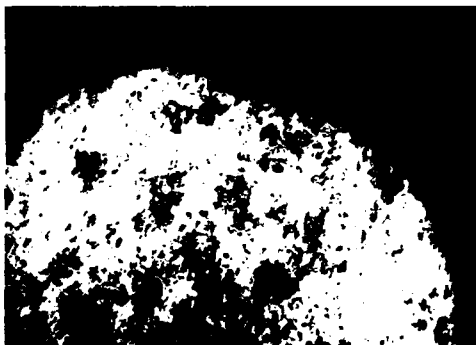Figure 3b.   Transmission Electron Micrograph of 85% Al2O3 - 15% SiO2 Fiber Tow
              (20,000X; 1 cm on print = 500 nm)

93

sections were gripped outside the hot zone so that the single filament section was located in the hot zone of the furnace.

Figure 4 shows a comparison of the high temperature single filament strength for 85A-15S fiber and Nextel 610. The RT strength of the 85A-15S fiber was 1700 MPa, somewhat lower than the strength using the clamp grips described above. Thus, high temperature strength values for the 85A-15S fiber are conservative. Note that the strength of Nextel 610 was higher than the strength of any other commercial oxide fiber at 1200°C[17]. However, the 85A-15S fiber maintained 85% of RT tensile strength (1500 MPa) at 1200°C, an increase in temperature capacity of 150°C compared with than Nextel 610. 50% of the RT strength of the 85A-15S fiber was retained at 1300°C.
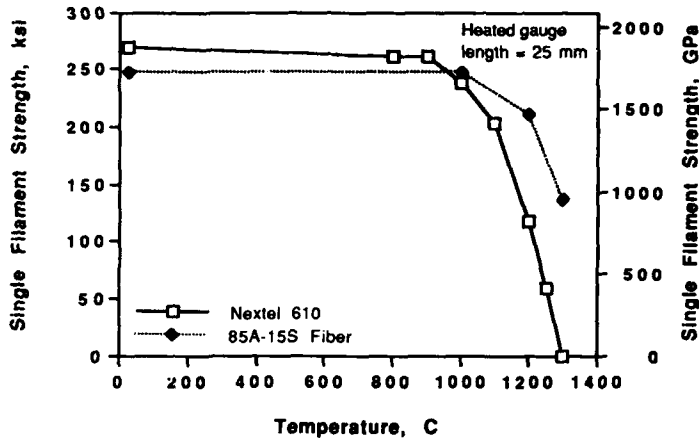
Figure 4.   High Temperature Tensile Strength of Nextel 610 and 85% Al_2O_3 - 15% SiO_2 Fiber

CREEP TESTING

A single filament, dead load testing system was used to provide an accurate and consistent load. Sample elongation was measured with a Zygo® laser extensometer (Model 1101, Zygo Corp, Middlefield, CT) with a repeatability of 0.7 μm. The creep system used a resistance-heated, three zone alumina tube furnace with platinum heating elements. Hot zone temperature was accurate to within 7°C of the setpoint over the entire 106 mm gauge length. The creep rate was assumed to be uniform over this gauge length. Details of this creep system have been described previously[2].

For 85A-15S fibers, transient creep behavior occurred during the early stages of most tests. However, in most cases, steady state creep was observed after the initial transient period. For fibers which broke during testing, no tertiary region of increasing deformation rate was observed prior to rupture.

Figure 5 compares the steady state creep rate of the 85A-15S fiber to some selected commercially available polycrystalline oxide fibers (10 ksi = 69 Mpa). The commercial fibers all had creep rates within approximately one order of magnitude of each other. The creep rate increased in the following order: Altex $\cong$ Fiber FP < Nextel 610 $\cong$ Nextel 550 < Almax. Fiber FP, Nextel 610 and Almax fibers are polycrystalline α-Al_2O_3 fibers, and Nextel 550 and Altex consist of transition alumina and amorphous silica.

The strain rate for the 85A-15S fiber was approximately three orders of magnitude less than any of the commercially available polycrystalline alumina fibers. The load at which total strain will exceed 1% in 1000 hours (2.7×10^{-9}/sec) for the 85A-15S fibers was 276 MPa at 1100°C and 690 MPa at 1000°C. Nextel 610 will exceed this creep limit at 276 GPa at 950°C. This represents an increase of at least 150°C in projected use temperature over the commercially available fibers.
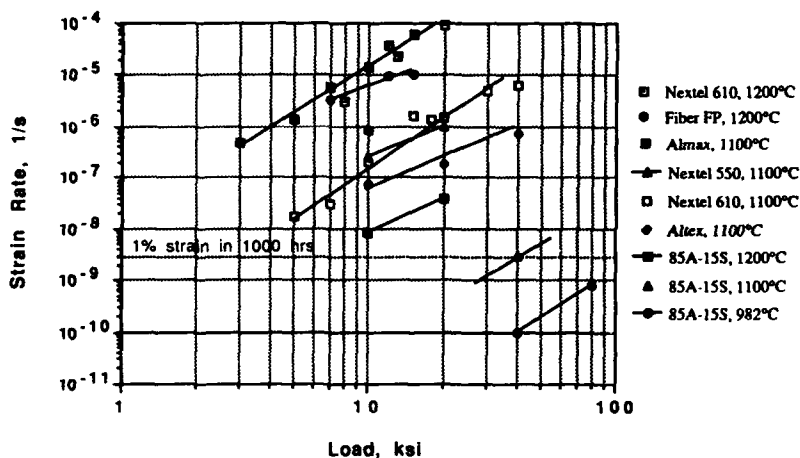
Figure 5. Plot of Strain Rate vs. Applied Load for 85% Al_2O_3 - 15% SiO_2 Fiber and Other Commercially Available Polycrystalline Oxide Fibers

In addition to the low steady-state creep rates, creep tests at 1093°C determined that the fibers exhibited negative creep below 138 MPa stress. Figure 6 shows the elongation - time curve for 85A-15S fibers tested at 1093°C at 69 MPa, 138 MPa and 276 MPa. 100 µm elongation is equivalent to ~0.1% strain. Shrinkage continued at a decreasing rate for the entire duration of the tests at 69 MPa and 138 MPa tests (257 hr and 130 hr, respectively). Total shrinkage was 0.12% at 69 MPa. Fibers tested at 276 MPa showed a positive creep response, which appeared to reach steady state. Previous creep tests results at 3M on fibers which crystallized during testing (e.g., Nicalon) have shown shrinkage at low loads and creep at high loads. Creep tests at 1200°C and 10 ksi showed a period of shrinkage followed by steady state creep.

95

The shrinkage of 85A-15S fibers during creep testing probably resulted from the crystallization of α-Al$_2$O$_3$ from mullite supersaturated with alumina. X-ray diffraction analysis of fibers thermally aged at 1400°C showed that the α-Al$_2$O$_3$ x-ray peak height increased by 30% over as-prepared fibers. However, the mullite peak did not increase after further thermal aging. Mullite (nominally 3Al$_2$O$_3$-2SiO$_2$ or 72 wt% Al$_2$O$_3$) is not a line compound. The composition of the fiber is much higher in Al$_2$O$_3$ than mullite. Since the alumina and silica precursors in these fibers are intimately mixed and firing times were very short (seconds), the formation of alumina-rich mullite would not be surprising. Alumina-rich mullite with up to 78% Al$_2$O$_3$ (2Al$_2$O$_3$-SiO$_2$ or "2:1" mullite) has been reported via both melt and sol/gel processing[19]. However, further experiments will be required to confirm the presence of super-saturated mullite in 85A-15S fibers.
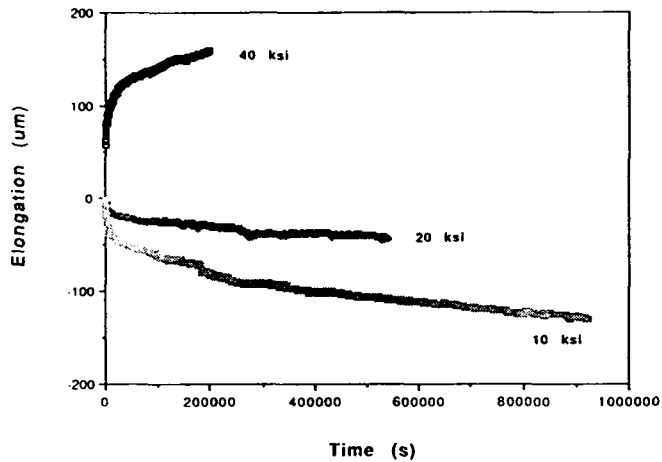
Figure 6.   Elongation of 85A-15S Fiber at 1093°C and 69 MPa, 138 MPa and 276 MPa (106 μm strain = 0.1%)

DISCUSSION OF CREEP MECHANISMS

As discussed in the introduction, grain boundary phenomena, such as grain boundary sliding, would be expected to control creep deformation in fine-grained polycrystalline ceramics such as fibers. In both Nextel 610 and 85A-15S fiber, the stress exponent n (see Equation 1) was 3. This confirmed that the deformation mechanism was interface-controlled[5,6]. However, identifying the exact deformation mechanism operating in 85A-15S fibers is difficult due to the complexity of the fiber microstructure. Certain effects are clear. Mullite is more creep-resistant than alumina. For example, the creep rate of Nextel 480 is 50X lower than Nextel 610[2]. Thus, a two-phase mixture of mullite and alumina would be expected to have a lower creep rate than single phase alumina. However, the creep rate of the 85A-15S fiber was an additional 20X less than Nextel 480. Thus, other factors must have additional hardening effect in 85A-15S fibers. In 85A-15S fibers, almost

all of the small grains were globular and/or elongated. The deformation rate of a continuum matrix reinforced by rigid inclusions has been described by Chen[1]. For 50 vol% equiaxed particles in a matrix with n=3, the deformation rate will be reduced by a factor of 10 over the unreinforced matrix. For rigid particles with an aspect ratio of 4:1 (similar to 85A-15S fibers), the creep rate would be 100X less. Thus, the elongated grains observed in the 85A-15S microstructure would be expected to strongly reduce deformation rates. In addition, the 0.5 μm mosaic crystals in the 85A-15S fibers were 5 times larger than the grains of polycrystalline alumina fibers such at Nextel 610. This would also reduce the deformation rate further by at least a factor of 5.

Grain boundary sliding will also be inhibited in 85A-15S fibers. Almost all of the small grains were globular and/or elongated, and the large, 0.5 μm mosaic crystals of α-Al_2O_3 and mullite had very rough, non-uniform shapes. Virtually no faceted grains or straight grain boundaries were present anywhere in the fiber microstructure. Grain boundary sliding has been found to be greatly reduced in polycrystalline alumina containing SiC whiskers[20,21]. In these materials, failure strains were low due to rapid cavitation near whiskers. This is consistent with low failure strains observed in 85A-15S fibers (~1%) compared with 20% for Nextel 610[2].

Thus, several mechanisms contribute to the low creep rate of the 85A-15S fiber relative to polycrystalline alumina and other fibers. These include hardening by the addition of second phase mullite, reduced grain boundary sliding due to the absence of faceted grains with planar grain boundaries, the presence of elongated grains in the microstructure, and an increased grain size compared with other polycrystalline oxide fibers.

CONCLUSIONS

85A-15S fibers have been produced in tow form as 12 μm and 20 μm diameter fibers. The average single filament strength of the 12 μm diameter fibers was 2130 MPa at room temperature and 1450 MPa at 1200°C. At 1093°C, creep was negative below 138 MPa. At higher loads, creep was 1000X less than commercial fibers. TEM analysis showed that the microstructure of the 85A-15S fibers consisted of elongated grains of α-Al_2O_3 and mullite, plus large mosaic crystals of α-Al_2O_3 and mullite. The excellent creep performance of the fibers was attributed to improved creep resistance of mullite, plus the presence globular and elongated particles of both phases. The coefficient of thermal expansion of 85A-15S fibers was 6.0×10^{-6}/°C, and the elastic modulus was 260 GPa.

ACKNOWLEDGMENTS

REFERENCES

1. I-W. Chen and L. A. Xue, "Development of Superplastic Structural Ceramics", J. Am. Ceram. Soc., 73 (9) 2585-2609 (1990).
2. D. M. Wilson, D. C. Lueneburg and S. L. Lieder, "High Temperature Properties of Nextel 610 and Alumina-Based Nanocomposite Fibers:, Cer. Eng. Sci. Proc. 14 (7-8) 609-621 (1993).
3. T. F. Cooke, "Inorganic Fibers-A Literature Review", J. Am. Ceram. Soc. 74 (12) 2959-78 (1991).
4. W. R. Cannon and T. R. Langdon, "Review: Creep of Ceramics Part 1: Mechanical Properties", J. Mat. Sci., 18 (1983) 1-50.
5. R. M. Cannon, W. H. Rhodes, and A. H. Heuer, "Plastic Deformation of Fine-Grained Alumina (Al_2O_3): I, Interface-Controlled Diffusional Creep", J. Am. Ceram. Soc., 63 (1-2) 46-53 (1980).
6. O. D. Sherby and J. Wadsworth, "Observations on Historical and Contemporary Developments in Superplasticity", pp. 3-14 in Mat. Res. Soc. Symp. Proc. Vol. 196 ®1990 Materials Research Society.
7. E. Arzt, M. F. Ashby, and R. A. Verrall, "Interface Controlled Diffusional Creep", Acta Met., 31 (12) 1977-1989 (1983).
8. R. Raj and M. F. Ashby, "On Grain Boundary Sliding and Diffusional Creep", Met. Trans., 2 (1113-1127) 1971.
9. B. E. Yoldas, "Effect of Ultrastructure on Crystallization of Mullite", J. Mat. Sci., 27 (1992) 6667-6672.
10. I. M. Low and R. McPherson, "The Origins of Mullite Formation", J. Mat. Sci., 24 (1989) 926-936.
11. E. A. Richards, C. J. Goodbrake, and H. G. Sowman, "Reactions and Microstructure Development in Mullite Fibers", J. Am. Ceram. Soc. 74 (10) 2404-409 (1991).
12. S. Van der Zwang, "The Concept of Filament Strength and the Weibull Modulus", J. Test. Eval. 17 (5) 292-298 (1989).
13. B. Bergman, "On the Estimation of the Weibull Modulus", J. Mat. Sci., 3 (1984) 689-692.
14. C-T. Li and N. R. Langley, "Improvement in Fiber Testing of High-Modulus Single Filament Materials", J. Am. Ceram. Soc., 68 (8) C-202-C-204 (1985).
15. B. D. Cullity, Elements of X-Ray Diffraction, 2nd Ed., p 103. Publ. by Addison-Wesley, 1978.
16. J. L. McArdle and G. L. Messing "Transformation, Microstructure Development and Densification in α-Fe_2O_3-Seeded Boehmite-Derived Alumina", J. Am. Ceram. Soc., 76 (1) 214-222 (1993).
17. D. J. Pysher, K. C. Goretta, R. S. Hodder, Jr. and R. E. Tressler, " Strengths of Ceramic Fibers at Elevated Temperatures", J. Am. Ceram. Soc., 72 (2) 284-88 (1989).
18. R. F. Davis and J. A. Pask, "Mullite", pp. 37-76 in High Temperature Oxides, Part IV, A. M. Alper, ed., Academic Press, N.Y. (1971).
19. A. R. De Arellano-Lopez, A. Domingues-Rodrigues, K. C. Goretta, and J. L. Routbort, "Plastic Deformation Mechanisms in SiC-Whisker-Reinforced Alumina", J. Am. Ceram. Soc., 76 (6) 1425-32 (1993).
20. P. Wang, G. Grathwohl, and F. Thummler, "Creep Behaviour of SiC-Whisker-Reinforced Al_2O_3-ZrO_2 Composites", Powder Met. Int., 24 (6) 365-372 (1992).

POLYMER DERIVED, STOICHIOMETRIC SiC FIBERS

J. LIPOWITZ, J.A. RABE, L.D. ORR and R.R. ANDROL
Dow Corning Corporation, Midland, MI 48686

ABSTRACT

Polycrystalline, stoichiometric β- silicon carbide fiber tow suitable for ceramic or metallic matrix composite use has been prepared using a polymer precursor route to obtain textile grade, weavable fibers. Individual filaments have a diameter of 10 μm, an average tensile strength of up to 3.4 GPa (500 ksi), an elastic modulus up to 430 GPa (62 msi) and a density > 3.1 g/cm^3. Crystallites average about 60 nm by x-ray line broadening. The SiC fiber shows improved mechanical and thermal stability properties, especially in an inert atmosphere, as compared to commercial polymer-derived SiC ceramic fibers. Thermochemical and mechanical properties, as well as fractography and microstructure will be presented.

INTRODUCTION

Polycrystalline silicon carbide has a high modulus, thermal and oxidative stability, creep resistance and thermal conductivity. The density and coefficient of thermal expansion are lower than that of many metal oxides. This combination of properties make continuous SiC fiber a suitable candidate for reinforcement of ceramic or metallic matrix composites intended for high temperature use. Small diameter SiC fibers, which are best prepared by a polymer precursor route, are desired for ease of weaving and other preforming techniques such as knitting and braiding [1].

Commercial SiC-containing fibers are available in a suitable diameter range for preform preparation; NICALON™ Fiber (Nippon Carbon Co., Japan) [2] and TYRANNO fiber (Ube Industries, Ltd.) [3]. The preparation, properties, and structure of these fibers have been recently reviewed [4]. The NICALON and TYRANNO fibers are prepared from a polycarbosilane precursor which is melt-spun, crosslinked ("cured") by oxidation in air at ~200 °C, and pyrolyzed at ~1100- 1300 °C in argon or nitrogen to produce a ceramic fiber.[5,6] The dominant, continuous phase is not SiC but an amorphous silicon oxycarbide (Si-C-O) with turbostratic carbon also present. The presence of an oxycarbide phase and a carbon phase leads to carbothermal reduction reactions above ~1200 °C which result in CO and SiO evolution, producing a weak, porous, large-grained SiC residue.[7,8]

RESULTS AND DISCUSSION

We found that incorporation of boron into the polycarbosilane fiber leads to formation of a ceramic fiber which could be heated above the temperature of the carbothermic reduction reaction, and converted to a dense, polycrystalline SiC fiber [9,10].

We have recently learned to produce continuous, stoichiometric SiC fiber tow (Figure 1). Properties compare favorably with the NICALON and TYRANNO fibers as shown in Table I.
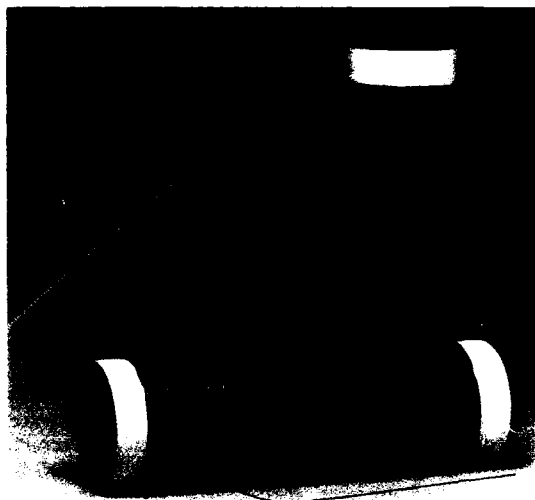
Figure 1:
Spools of Continuous
SiC fiber tow
(75mm diameter spool)

TABLE I: TYPICAL FIBER PROPERTIES COMPARISON

	CERAMIC GRADE NICALON	TYRANNO Lox M	HI-NICALON	DOW CORNING SiC
Tensile Strength GPa (ksi)	2.9 (420)	3.2 (460)	2.8 (400)	2.4 (350)
Elastic Modulus GPa (msi)	190 (28)	180 (26)	270 (39)	400 (58)
Elongation, %	1.5	1.75	1.0	0.7
Diameter, μm	15	12	14	10
Density, g/cm^3	2.6	2.4	2.7	>3.1

Figure 2:
Loop of SiC
filaments in
comparison with
a dime. Loop is
~2.5mm. in diameter.

Both ceramic grade NICALON and TYRANNO Lox M fiber contain ~13 wt% oxygen. The HI-NICALON fiber is a recently developed product containing less than 1 wt% oxygen [11]. It is prepared from polycarbosilane by an electron beam crosslinking process rather than an air cure process to maintain minimal oxygen in the product.

The Dow Corning SiC product is produced by intentionally introducing oxygen which is eliminated as CO in a carbothermal reduction step above 1600 C to give a stoichiometric β-SiC fiber. The boron present permits densification without growth of a porous, large grained structure. Average tensile strength of the SiC fibers produced range up to 3.5 GPa (500 ksi) with individual fiber strengths as high as 4.8 GPa (700 ksi). Elastic modulus ranges up to 425 GPa (62 Msi), similar to the value of pressureless sintered SiC monolithic materials. The density obtained varies up to > 97% of theoretical. The SiC fiber tow consists of ≥500 filaments, each ~10 μm in diameter. A typical β-SiC pattern is found by x-ray diffraction. An average crystallite size of ~60 nm is calculated from Scherrer line-broadening measurements of the (111) reflection.

The high flexibility of the fiber is demonstrated by a loop of filaments next to a dime (Figure 2). The smooth fiber surface appearance is shown in Figure 3. At higher magnification a slight surface texture is noticeable. Figure 4 shows a high strength fracture surface. The fiber is clearly crystalline, not glassy in appearance as are the other fibers in Table I. Some fine porosity (< 0.1 μm) is apparent at grain junctions in the fiber interior. The porosity is too fine to be a strength-limiting flaw, but probably causes a reduction in elastic modulus below the fully dense polycrystalline value of ~450 GPa (65 Msi). Scanning Auger depth profiles show a thin C-rich surface layer with a stoichiometric SiC composition in the interior. A typical strength limiting flaw in a primary tensile fracture surface is shown in Figure 5. Scanning electron microprobe analysis of such flaws often finds concentrations of metallic impurities which implicate stainless steel or brass particulates inadvertently introduced during processing. Additional flaw types found by fractography are sites of interfilament bonding introduced during high temperature densification.

Figure 3:
Smooth appearance
of SiC fiber surface
(10 μm bar).

Figure 4.
Primary fracture
surface of high
strength
(4.0 Gpa)
SiC fiber
(1 μm bar).
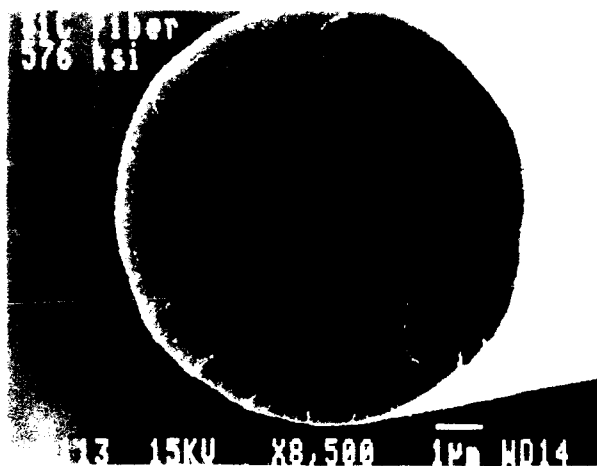
Figure 5:
Primary fracture
surface of a SiC
fiber, showing
a granular
critical flaw
at the surface
(1 μm bar); 2.1 GPa
tensile strength.
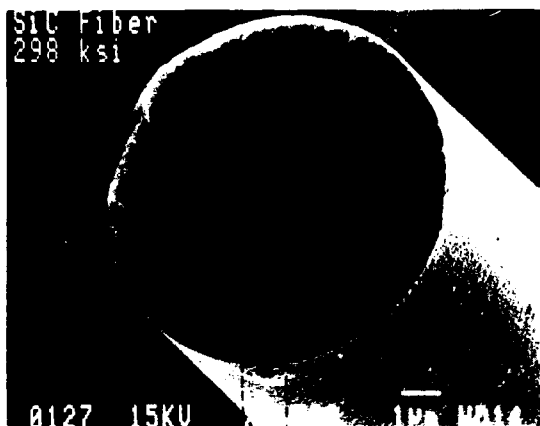
SiC fibers were compared to other non-oxide fibers after exposure to various aging environments (Table II). The SiC and HI-NICALON fibers are the most thermally stable. Dry air aging of the SiC fiber at 1200 °C, as individually suspended filaments, found no strength change in the first five hours and a decrease to 2.3 GPa (330 ksi) after 24 hours and to 1.72 GPa (250 ksi) after 100 hours. Oxide layer thicknesses found were consistent with parabolic oxidation kinetics.

TABLE II: Room Temperature Strength in GPa (ksi) after Various Aging Exposures.

FIBER	INITIAL STRENGTH	30min/1300° C/Ar	10hr/1550° C/Ar	12hr/1800° C/Ar
C.G NICALON	3.0 (435)	1.1 (157)	weak*	- -
TYRANNO Lox M	3.2 (463)	- -	weak*	- -
HI-NICALON	2.6 (371)	2.3 (335)	2.2 (321)	1.7 (240)
SiC	2.9 (420)	2.7 (387)	- -	2.1 (309)
SiC	2.9 (358)	- -	2.4 (343)	- -

*too weak to test

CONCLUSIONS

SiC fiber with desirable features has been obtained as summarized in Table III.

TABLE III: SiC FIBER FEATURES

- continuous, multifilament fiber tow
- grain size small and controllable
- Si/C ratio = 1
- high strength, to 3.4 GPa (500 ksi)
- high modulus, to 430 GPa (62 msi)
- weavable, 10μm fiber diameter
- high thermochemical stability
- coefficient of thermal expansion 4.5×10^{-6}/ °C (20-1300 °C)

Additional properties which are being measured at the NASA-Lewis Research Center include tensile strength at temperature, creep and stress fracture. Ceramic matrix composites are being fabricated and evaluated within the EPM/HSCT Program. We are presently scaling up the continuous tow capability to several pounds per month.

ACKNOWLEDGEMENTS

REFERENCES

1. J.DiCarlo, NASA Technical Memorandum 87085 (1985).
2. S. Yajima, Am. Ceram. Soc. Bull., 62, 893 (1983).
3. S. Yajima, T. Iwai, T. Yamamura, K. Okamura, and Y. Hasegawa, J. Mater. Sci. 16, 1349 (1981).
4. a. J. Lipowitz, J.A. Rabe and R.M. Salinger, in Handbook of Fiber Science and Technology: Vol III. High Technology Fibers, Part C, edited by M.Lewin and J. Preston (Marcel Dekker, Inc., New York, 1993), pp. 207-273.
   b. R. M. Laine and F. Babonneau, Chem. Mater., 5, 260-279 (1993).
5. Y. Hasegawa, M. Iimura, and S. Yajima, J. Mater, Sci., 15, 720-728 (1980).
6. Y.C. Song, Y. Hasegawa, S.J. Yang and M. Sato, J. Mater. Sci., 23, 1911-1920 (1988).
7. T. Mah, N.L. Hecht, D.E. McCullum, J.R. Hoenigman, H.M. Kim, A.P. Katz and H.A. Lipsitt, J.Mater. Sci, 19, 1191 (1984).
8. D.B. Fischbach, P.M. Lemoine and G.V. Yen, J. Mater. Sci., 23, 987-993 (1988).
9. J. Lipowitz, J.A. Rabe and G.A. Zank, Ceram. Eng. Sci. Proc., 12, 1819-1831 (1991).
10. D.C. DeLeeuw, J. Lipowitz and P.P. Lu, U.S. Patent 5 071 600 (10 December 1991).
11. M. Takeda, Y. Imai, H. Ichikawa, T. Ishikawa, T. Seguchi and K. Okamura, Ceram. Eng. Sci. Proc. 12 [7-8], 1007-1018 (1991).

STRENGTH OF SINGLE CRYSTAL Al$_2$O$_3$ FIBERS
IN Ni-BASED INTERMETALLIC AND SUPERALLOY COMPOSITES

RANDY R. BOWMAN[1], IVAN E. LOCCI[1,2], SUSAN L. DRAPER[1], and AJAY K. MISRA[3]
[1]NASA Lewis Research Center, 21000 Brookpark Road, Cleveland, Ohio 44135.
[2]Case Western Reserve University, Cleveland, Ohio 44106.
[3]NYMA Inc., NASA-Lewis Group, BrookPark, Ohio 44142.

ABSTRACT

Strength degradation of single crystal Al$_2$O$_3$ fibers due to the effect of fiber/matrix interaction and processing of NiAl and superalloy matrix composites, was investigated. Strength loss was quantified by tensile testing fibers that were exposed to the matrix alloy using two different methods. In one method, the fibers were incorporated into a composite by either the Powder Cloth (P-C) or binderless powder technique. The fibers were then extracted from the composite by chemical dissolution of the matrix and subsequently tensile tested and examined by scanning electron microscopy. In the other method, fibers were sputter-coated with a similar matrix composition and heat-treated to simulate conditions similar to those experienced during composite powder fabrication methods. In the sputter coating method, the contribution of fiber-matrix reaction on fiber strength loss was isolated from the effects of the various mechanical loads which are present during powder fabrication. For all matrices studied, significant strength loss was observed both in fibers extracted from composites and in fibers sputter-coated and annealed. Although surface ridges and pores were observed on the degraded fibers, it remains uncertain whether these features were responsible for the strength loss.

INTRODUCTION

Alumina fibers have long been recognized as potential reinforcements for high-temperature, Ni-base (intermetallic and superalloy) composites due to their high modulus and strength, low density, and chemical stability. In early studies, concerns about fiber reactions, coefficient of thermal expansion (CTE) mismatch, fiber-matrix bonding, and high cost resulted in pessimistic views about the prospects of ceramic whiskers or fibers as reinforcements in metal matrix composites [1]. Since composite strength is derived primarily from the fiber, especially at high temperatures, achieving adequate composite properties requires the retention of fiber strength after fabrication and after exposure to high temperatures.

Recent advances in fiber development, combined with a strong need for materials capability beyond that exhibited by monolithic superalloys, have resulted in new interest in composites. As such, single crystal Al$_2$O$_3$ is currently being evaluated for use as a potential reinforcing fiber in intermetallic and superalloy-based matrices. The goal is to develop composites with a balance of properties which are competitive with conventional high-temperature materials. In this paper, properties of Al$_2$O$_3$ fibers extracted from composites or sputter-coated with Ni- and Fe-based matrix materials are compared to as-received fibers.

EXPERIMENTAL PROCEDURES

All composites in this study were fabricated from 50- to 150 μm diameter vacuum-atomized, prealloyed powders of Ni-50Al and Ni-32.5Al-20Fe (at.%). The composites were reinforced with continuous, uncoated, 125-μm diameter, c-axis-oriented, single-crystal Al_2O_3 fibers supplied by Saphikon, Inc., Milford, CT.

The composites were fabricated using the Powder-Cloth (P-C) technique [2] or a binderless technique. In the P-C process, the matrix material is processed into flexible cloth-like sheets by combining matrix powders with poly(tetrafluoroethylene) (Teflon®). Likewise, fiber mats are produced by winding the fibers at a spacing of 40 fibers/cm on a drum and applying another organic binder, poly(methyl methacrylate) (PMMA). A composite panel is assembled by stacking alternate layers of matrix cloth and fiber mats. This assemblage is then hot-pressed, during which the fugitive binders are volatilized and the composite is consolidated to near full density. This is followed by hot isostatic pressing (HIP'ing) to ensure complete densification of the composite. As an alternative to the P-C technique, composite plates were fabricated without the use of fugitive binders by directly hot-pressing fibers in a die of matrix powders, followed by HIP'ing. After HIP'ing, the steel containment can and Mo cladding, required in the consolidation process, are removed by chemical etching in a bath of 45% nitric acid, 45% water, and 10% sulfuric acid. The resulting composite plates measured 15 cm long by 5 cm wide and 0.3 cm thick with 6 plys of fibers comprising a total of about 30 volume fraction (V_f) of the composite.

To isolate the effect of fiber-matrix interaction on fiber strength loss, unsized Al_2O_3 fibers were sputter-coated with 0.5 to 3 μm of NiAl, Ni-35Al-13Fe, or Haynes 214 (HA214). The coated fibers were annealed at 1533 K for 4 hours in flowing argon with 5% H_2 to minimize oxidation and to simulate the temperature profile used during the composite hot isostatic pressing (HIP'ing) cycle. To confirm that the temperature and the environment were not contributing to the fiber strength degradation, as-received (uncoated) Al_2O_3 fibers were heat treated under the same conditions. All fibers were tensile tested at room temperature with a crosshead speed of ~1 mm/min and a gage length of 12.7 mm.

Fiber extraction and sputter-coated matrix removal was performed by immersing the sample (composite or coated fibers) in a bath of 50% water, 33% nitric acid, and 17% hydrochloric acid at 345 K.

RESULTS AND DISCUSSION

Fiber Strength Degradation

The main driving force for using fiber reinforced composites is based on predictions that the fibers will provide significant strength and creep resistance to the system. In the systems studied, several unexpected issues have caused concern over whether or not rule-of-mixtures (ROM) strengths, based on as-received fiber strength, can be achieved. Fiber strength degradation after processing is perhaps the most critical issue that needs to be understood and resolved. Figure 1a shows the strength of as-received fibers and fibers extracted from an NiAl composite fabricated by the P-C technique. Room-temperature tensile strengths are reduced from 3000 to 1200 MPa (60% decrease compared to the as-received strength) after composite processing while 1200 K strengths drop from 900 to 400 MPa (55% decrease compared to the as-
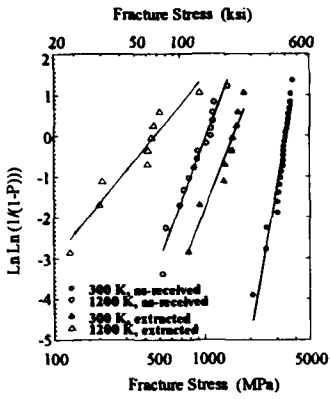
Figure 1a. Strength of as-received and extracted fibers from a NiAl composite fabricated by the Powder-Cloth technique.
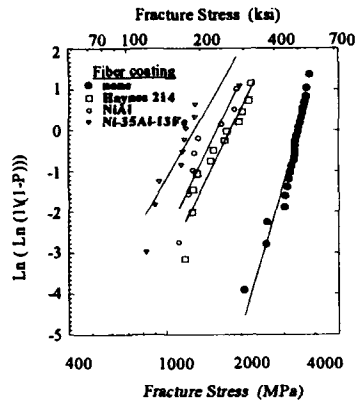
Figure 1b. Room temperature (300 K) strength of as-received and coated fibers exposed to 1533 K for 4 hours.

Figure 2. (a) and (b) Typical grain boundary imprints observed on the surface of Al_2O_3 fibers etched from binderless-processed Al_2O_3 /NiAl composites.

107

received strength). Figure 1b shows the room-temperature (300 K) strength of the coated and heat-treated fibers. Room-temperature tensile testing of sputter-coated and heat-treated fibers have also shown a decrease in strength similar to that for the fibers extracted from the NiAl composite. Specifically, exposure to NiAl reduced the fiber strength by 51%, while the other two compositions, Ni-35Al-13Fe and HA214 reduced the strength by 60% and 45%, respectively. These strength losses are consistent with observations of Al_2O_3 fiber strength degradation in other metals and intermetallic matrices [3]. Tensile strengths of the as-received fibers exposed to the 1533 K heat treatment or as-coated fibers were similar to the as-received fibers (~3013 MPa) [3] indicating that exposure to high temperatures is required before fiber degradation is observed.

Fiber Surface Observations

Scanning electron microscopic examination of the extracted fibers revealed the presence of ridges and pores on the surface of the fiber, corresponding to the NiAl matrix grain boundaries, on both P-C and binderless processed fibers. Figure 2 depicts typical imprints observed in extracted fibers from a NiAl composite fabricated by the binderless technique. Also, fibers extracted from P-C processed material, unlike the binderless material, often had C-rich areas on the fiber surface [3]. These C-rich areas are residue left from incomplete volatilization of the binder material. Although fiber strength degradation occurred, and ridges and pores also formed on the surface of the fibers extracted from Ni-32.5Al-20Fe composites, two particular observations are special to this composite system as compared to the NiAl system. Namely, most of the fibers extracted from the composite were full length (as-contrasted with fibers extracted from NiAl, see fiber fragmentation section) and no C residue was detected even though the P-C technique was also used to process this composite.

Figure 3a shows a cross section of the NiAl coating (2 to 2.5 µm thick) deposited onto the Al_2O_3 fiber. The coating consists of fine columnar grains and appears to be very open (Fig.3b). Energy dispersive spectroscopy (EDS) analysis of the coating detected a small oxygen peak which suggests the matrix had probably picked up oxygen during sputter deposition (Fig. 3c). To compare surface attack in the sputter-coated fibers with that observed in the extracted fibers, the sputter-coated fibers were immersed in the acid bath to remove the coating in order to reveal the fiber surface morphology. Unfortunately, the coating had oxidized during the anneal cycle and could not be completely removed. However, several areas where the coating had cracked or spalled off were available to characterize the surface of the fiber. Figure 4 shows a typical region of the fiber where ridges and some porosity can be observed. The ridges are again reflections of the grain boundaries of the NiAl matrix. Two other matrix compositions, Ni-35Al-13Fe (in at.%) and a Ni-based superalloy HA214, were sputter-coated to understand the effect of a more ductile matrix on the strength degradation of Al_2O_3 fibers. The results were very similar to NiAl. Both coatings had absorbed some oxygen, oxidized during the annealing cycle, and showed pores and imprints of the matrix grain boundaries on the surfaces of the Al_2O_3 fiber.

While the ridging phenomena may play a role, the mechanism for the fiber strength loss is still unclear. Simple stress intensity calculations [3] based on the height of the ridges suggest that the ridges in themselves can not account for the magnitude of the strength loss observed. The presence of pores, spaced 1 to 2 µm, may have a much more critical role on the fiber strength degradation observed in these systems. However, it has been concluded [3] that fiber-matrix reaction is the dominant mechanism for the strength loss. In this context, fiber-matrix reaction is used in a generic sense to describe the fiber-matrix interaction and does not imply the formation of observable second phases.

Counts
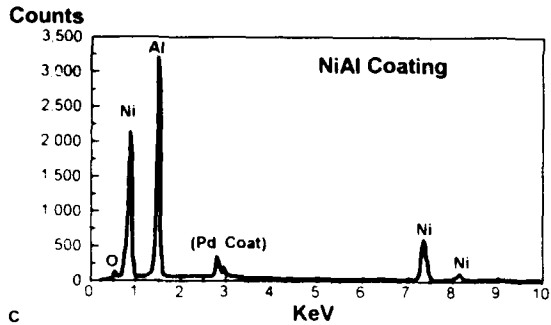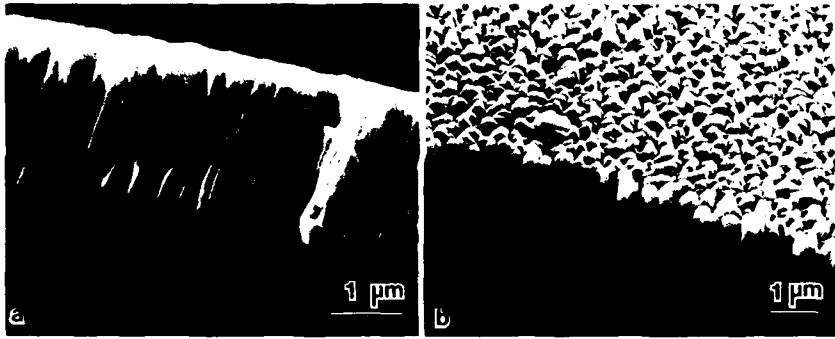
Figure 3 (a) Cross section of NiAl coating deposited by sputtering on Al₂O₃ fiber (b) Higher magnification of the NiAl coating showing open columnar grains (c) EDS analysis of the NiAl coating deposited on the Al₂O₃ fiber
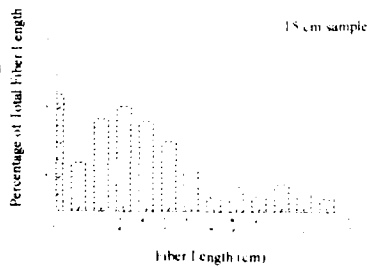

Figure 4 Grain boundary ridges and pores observed on the surface of NiAl coated and annealed Al₂O₃ fibers after removing NiAl coating

Figure 5 Fiber size distribution for an as-fabricated, 15-cm NiAl/ Al₂O₃ composite

109

Fiber Fragmentation

Fiber fragmentation is another critical issue that needs to be addressed. Figure 5 shows the fiber size distribution for a 15-cm NiAl composite. For both the P-C and binderless processed composites, the average extracted fiber length was substantially less than the original 15 cm. While fiber strength loss certainly plays a role in fiber fragmentation, low fiber strength does not necessarily result in fragmentation during processing. For instance, the Ni-32.5Al-20Fe matrix composite reinforced with 30 vol.% Al_2O_3 fibers resulted in both fiber ridging and strength loss, but no fiber fragmentation occurred during processing. While fiber strength loss undoubtedly plays a role, so does the mechanical properties and perhaps chemistry of the matrix. These results also show that the fiber extraction process itself is not responsible for the fiber fractures since full-length fibers were extracted from the alloyed matrix in every specimen examined.

In terms of achieving ROM strengths, fiber fragmentation in itself is of secondary importance compared to fiber strength loss. The fragmented fiber lengths were still significantly longer than the critical length [4] needed for full load transfer to the fibers. However, the presence of embedded fiber ends can have significant influence on the composite fracture behavior since the local stress concentrations at the fiber ends can reduce the fracture stress of a discontinuous composite by promoting matrix cracking.

SUMMARY AND CONCLUSIONS

Binary NiAl, Ni-35Al-20Fe and HA214 matrices were used to evaluate the effect of fiber/matrix interaction with single crystal Al_2O_3 fibers. In general, composite properties were observed to be well below expected ROM properties. The main reason for this is the loss of strength of the fiber, as evidenced by the tensile strength of the fibers extracted from composites. To isolate the effects of mechanical loads which are present during fabrication, fibers were sputter-coated with binary NiAl, Ni-35Al-13Fe and HA214 matrices and exposed to heat treatments that simulated the composite processing parameters. This exposure resulted in a similar fiber strength degradation to that seen in full composites. Multiple fiber fragmentation was observed in the Al_2O_3/NiAl system, but limited fragmentation was observed in the Al_2O_3/Ni-35Al-13Fe composite even though, their extracted fiber strengths were similar. In order for Al_2O_3 to become a viable reinforcement for NiAl matrix composites, a compatible and optimized coating is required. Otherwise, a new fiber, less sensitive to matrix/fiber interaction and with similar properties as Al_2O_3, is required to produce composite systems with attractive properties.

ACKNOWLEDGMENTS

REFERENCES

1.   C. Calow and A. Moore, J. Mat. Sci., 7, 543 (1972).

2.   J. W. Pickens, R. D. Noebe, G. K. Watson, P. K. Brindley, S. L. Draper: NASA Technical Memorandum 102060 (1989).

3.   S. L. Draper and I. E. Locci: J. Mater. Res., 9, No. 6, June 1994.

4.   R. R. Bowman, A. K. Misra, and S. M. Arnold, submitted to Metall. Trans., 1994.

THE EFFECT OF ELEVATED TEMPERATURE EXPOSURE OF COMPOSITES ON THE STRENGTH DISTRIBUTION OF THE REINFORCING FIBERS

M. L. GAMBONE* AND F. E. WAWNER**
* Wright Laboratory/MLLM, 2230 Tenth St. Ste. 1, WPAFB, OH 45433-7187
**University of Virginia, Department of Materials Science and Engineering, Thornton Hall, Charlottesville, VA 22903

ABSTRACT

Unidirectionally-reinforced Timetal® 21S composite specimens were subjected to elevated temperature heat treatments. The SiC fibers were then chemically extracted from the matrix, and their tensile strengths were measured at room temperature. A Weibull statistical analysis of fiber strength distribution was performed to compare the Weibull parameters of fibers from the as-consolidated and heat-treated composites. Fractographic analysis of the tested fibers was used to identify the flaws which caused failure in each condition. Surface flaws were found to initiate low strength failures in all conditions, and the number of surface initiated failures increased with an increase in severity of heat-treatment. A relationship between the fiber/matrix chemical reaction and surface flaw development is demonstrated. A fracture mechanics analysis that explains the relationship between surface flaw size, fiber fracture toughness, and the measured tensile strengths is suggested.

INTRODUCTION

Knowledge of constituent properties is essential for predicting composite behavior. The mean fiber strength or strength distribution of virgin fiber is often used in models of metal matrix composites (MMC). It is necessary, though, to know that these properties will be maintained when the fibers are incorporated into the composite. Research has been carried out which defines and quantifies the reaction between fiber and matrix in various titanium-alloy matrix composites [1], and studies have been performed to relate virgin fiber strength with composite tensile strength [2]. The goal of this work was to establish the effect of the composite environment on fiber chemistry and structure and fiber strength distribution. By extracting fibers from specimens of an SiC/Timetal® 21S composite, both in the as-consolidated condition (A-C) and after heat-treatment, alterations in fiber mechanical response were observed and related to morphology changes in the fiber and fiber/matrix interface. It is hoped that this effort will provide insight to the MMC community as to the critical effects of thermal exposure of composites on fiber strength.

<u>Material</u>

The composite system studied in this work is a 4-ply, unidirectionally-reinforced titanium-alloy matrix composite. Timetal® 21S, produced by Timet, Inc., was employed as the matrix. It is a high-temperature, metastable beta alloy containing 15% Mo, 2.7% Nb, 3% Al, and 0.2% Si by weight. [3]

The SiC fiber, SCS-6, was manufactured by chemical vapor deposition by Textron Specialty Materials Division (TSMD). It was designed for use in titanium matrix composites and is coated with two carbonaceous layers to protect it from handling damage and chemical reaction with titanium-based matrices. Several authors [4-6] have described the structure and chemistry of this fiber in detail.

The composite was manufactured at TSMD by hot isostatic pressing of alternating layers of matrix foil and fiber mat at a temperature and pressure sufficient to cause the matrix to flow around the fibers and create a fully dense structure. The volume fraction fibers was approximately 0.40.

Weibull Statistics

The distribution in strength of a population of ceramic fibers may be described using Weibull statistics [7]. This representation assumes that the probability of survival, P_S, of a specific length of fiber loaded to a stress, σ, is given by:

$$P_S = \exp\{-(\sigma/\sigma_o)^m\} \qquad (1)$$

where m and σ_o are Weibull parameters known as the modulus and the scale factor, respectively. There are several ways in which the Weibull parameters may be determined [8]. In this study, the tensile data of each fiber group was ranked in ascending order and assigned a value of P_S based on the estimator:

$$P_S = 1-(n-0.5)/N \qquad (2)$$

Here n is the rank of each data point and N is the total number of data points in each group. This estimator was found by Porter [9] to converge most rapidly and thus be most accurate for small data sets. Equation (1) may be manipulated to produce a linear relationship between P_S and tensile strength, σ:

$$\ln (\ln (1/P_S)) = m\ln(\sigma)-m\ln(\sigma_o) \qquad (3)$$

and a least squares fit used to determine the slope, m, and the scale factor, σ_o. In this way the statistical properties of each fiber group were compared.

PROCEDURE

Samples of 4-ply SCS-6/Timetal® 21S composite approximately 12 cm x 0.75 cm were sectioned from a panel fabricated by TSMD. One specimen was reserved in the A-C condition. Two of each of the others were heat-treated at 650°C and 800°C for 700 hours, one encapsulated in argon and the other exposed to stagnant air. A fifth specimen was heat-treated in an encapsulated inert environment at 900°C for 300 hours.

The fibers were extracted from each composite specimen by dissolving the matrix using an etchant of 10% bromine in methanol saturated with tartaric acid. This solution has no effect on bare fibers as no change in the tensile strength distribution of SCS-6 fibers was observed after soaking in this solution for 175 hours. The etchant dissolves titanium alloys but does not act on either titanium oxides or carbides; so, the product of the reaction between fiber and matrix remains on the fiber after the extraction is completed. The fibers in the specimen exposed at 800°C in air could not be extracted using the bromine etchant because the matrix had fully oxidized. These fibers were separated from the matrix by crumbling the matrix using ultrasonic vibration.

Following extraction from the composite tensile tests were performed at room temperature on at least 45 fibers from each composite specimen. Tests were conducted on two screw-driven load frames, one vertical and one horizontal. All specimens were tested at a gage length of 2.5 cm, and the strain rate in all tests was 1.32×10^{-2} sec^{-1}. The tensile strength was recorded for each test performed. Stress was derived from the measured load and the cross-sectional area calculated from the mean fiber diameter, assuming the fibers were cylindrical. The mean diameter was calculated from a minimum of 30 random optical measurements on each group of fiber extracted from a particular composite specimen.

Only failures which occurred in the gage length of the fiber were considered in the statistical analysis of strength distribution. When possible, one or both fracture surfaces of each failure were preserved for examination by scanning electron microscopy (SEM) to identify the failure initiation site. However, many of the fractures were obviously secondary failures resulting from the shattering of fibers after the primary fracture occurred; no initiation site was identified in these instances. Only 16% of the primary fractures of fibers extracted from the as-consolidated composite were distinguishable. However, 33% of those from the 650 heat-treated composite and at least 50% of those from the higher temperature heat-treatments were identified. The majority of the fractures examined were those resulting from low strength failures; these specimens were least likely to shatter.

112

RESULTS

The A-C fiber strength distribution is shown in Figure 1 with those of two different spools of virgin SCS-6. The values of m and σ_0 calculated for the extracted fiber were 6.2 and 3943 MPa, respectively. The majority of fractures indicated initiations from internal flaws on or near the core/SiC interface. The value of m calculated here is less than half that measured for both spools of as-received SCS-6 fiber, but the value of σ_0 lies between the two.
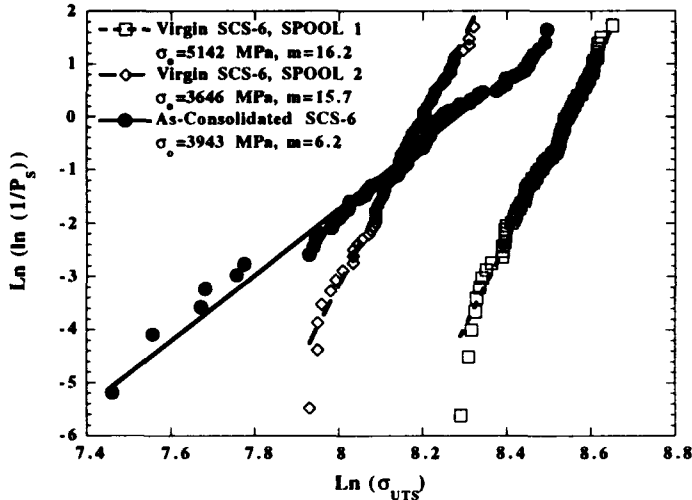

Figure 1:   Comparison of the Weibull strength distribution of virgin SCS-6 and SCS-6 extracted from a Timetal® 21S matrix.

A comparison of the strength distributions of SCS-6 fibers extracted from the heat-treated composite specimens is shown in Figure 2. Both the composite specimens exposed at 650°C for 700 hours and that exposed at 800°C for 700 hours in encapsulated argon developed a bimodal strength distribution. Only a small number (10% or fewer) of the fibers extracted from the 650°C heat-treated composite demonstrated significant deviation from the strength distribution of the A-C fibers. The tensile strengths of 20% of the fibers from the 800°C, inert atmosphere heat-treatment fell into a low strength distribution, and the higher strengths measured fell on the A-C distribution. As explained previously, the matrix of the specimen exposed at the same time and temperature in stagnant air was completely oxidized and the fiber coating and outer SiC was oxidized as well. The fiber extracted from this specimen had a mean diameter of 130 µm and a significantly reduced strength distribution with m=3.3 and σ_0=1455 MPa. The 900°C heat-treatment produced a strength distribution with a significantly lower σ_0 value, 2493 MPa, than measured for the other inert environment exposures or the A-C fibers, but this decrease in σ_0 was not an environmental effect. The value of m, 6.0, was similar to that calculated for the A-C SCS-6 fibers.

DISCUSSION

An underlying assumption of the Weibull analysis of fiber strength is that a single distribution of flaws controls failure [10]. Fractography of A-C specimens revealed that three of the six low strength failures were surface-initiated. In Figure 3, the strength distributions of
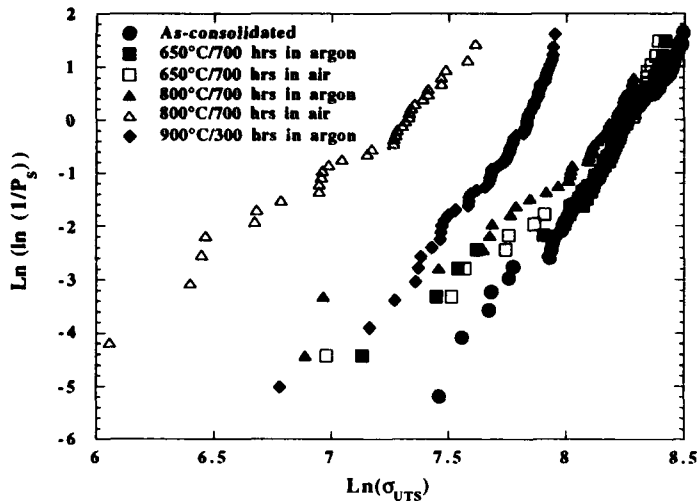
113

Figure 2: Comparison of the Weibull distributions of fiber strength for SCS-6 fiber extracted from as-consolidated and heat-treated SCS-6/Timetal® 21S composite.

the fibers from heat-treated composite are shown with initiating flaws marked. Surface flaws were observed primarily as initiation sites of low strength failures and internal flaws for higher strength failures. If it is assumed that all low strength tests in the vicinity of identified surface-initiated fractures were also surface-initiated, the surface and internally initiated failures may be separated and the strength distribution resulting from each flaw population analyzed using a statistical technique for dealing with 'censored' data [11,12]. This type of analysis has been performed previously on alumina fibers [13].

Such an analysis was performed on all surface initiated failures and, separately, on all internally initiated failures from the A-C composite, both 650°C heat-treatments, and the 800°C heat-treatment in argon. The results are shown in Figure 4 with the pertinent data points of each distribution for comparison. The analysis of internally-initiated tensile failures produces a distribution with an m of 9.5 and a σ_0 of 3945 MPa, and the surface-initiated failures demonstrate an m of 4.2 and a σ_0 of 2188 MPa. It was expected that the Weibull modulus of the internally-initiated failures would be similar to that for virgin SCS-6 fibers, but, while it is closer, it is still significantly lower. This appears to suggest some increase in severity of internal flaws due to the consolidation process, but the data in this study is not sufficient to make that conclusion. The difference might also be attributed to scatter in the Weibull modulus of virgin SCS-6.

The 900°C composite heat-treatment produced a distribution much closer to that for surface-initiated failures than that initiated by internal flaws. From Figure 3 it is evident that surface initiated failures occurred throughout the strength distribution for this heat-treatment.

The number and density of surface flaws appears to increase with the severity of heat-treatment that the composite receives even in an inert environment. The origin of these flaws must then be assumed to lie in the interaction between fiber and matrix. Figure 5 shows an example of a surface flaw that initiated failure. Most of the observed surface flaws had similar morphology; the reaction product is observed in contact with the SiC at the initiation with no carbon coating remaining at the flaw site. Gundel [1] demonstrated that the growth in reaction
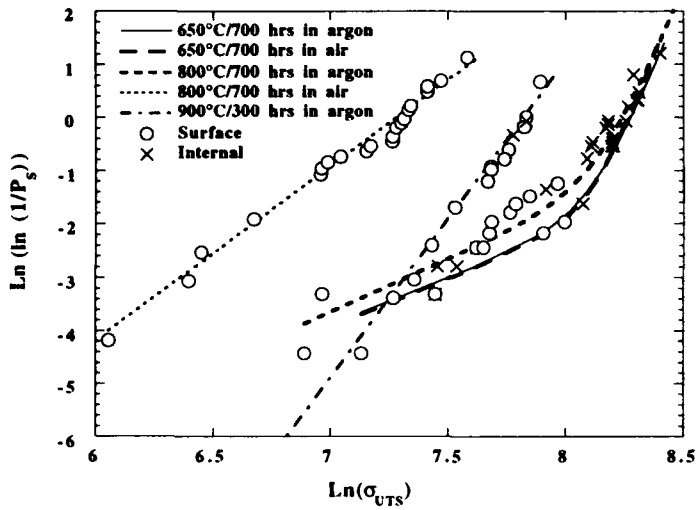
114

Figure 3: Weibull strength distributions of extracted SCS-6 fibers from heat-treated composite are plotted as lines; the symbols represent those specimens for which the primary fracture initiation site was identfied.
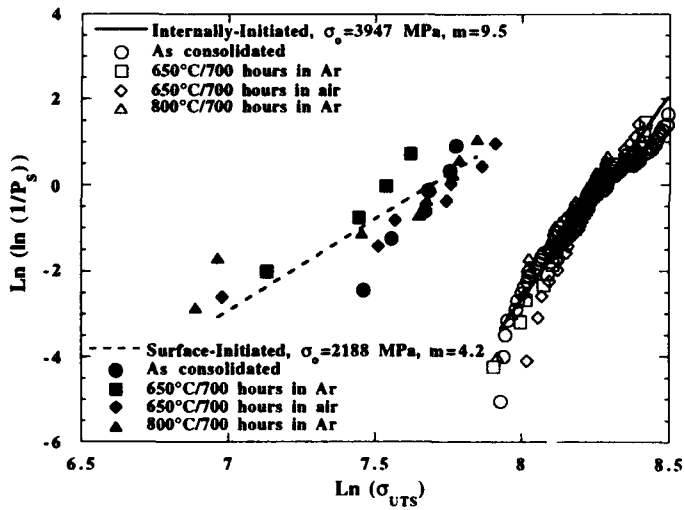

Figure 4: Weibull distributions of internally initiated and surface initiated tensile failures.

115

product between fiber and matrix has an Arrhenius-type dependence on time and temperature, increasing linearly with the square root of time and exponentially with the inverse of absolute temperature. As the reaction zone increases in thickness, the protective carbon coating on the SCS-6 fiber is consumed. Table I shows the average reaction zone thickness and remaining coating thickness observed for the various heat-treatments applied in this study. In previous work, [14] it was shown that potential surface flaws may exist on SCS-6 fibers from variations in coating thickness. Thus, as the reaction zone thickens and consumes more coating, more potential surface flaws will become active surface flaws and initiate low strength failures. After some degree of reaction, the surface flaws will begin to dominate the fiber strength distribution as occurred in the 900°C heat-treatment. When the fiber coating has been completely consumed and the SiC is chemically attacked on a global scale only surface failures will occur and the distribution will be similar to that of the 800°C exposure in air.

Table I: Thickness of Reaction Product and Remaining Coating for SCS-6/Timetal® 21S Composite Heat-treatments

Heat Treatment Cond.	Reaction Zone Thick. (μm)	Remaining Coating Thickness (μm)
As- Consolidated	0.90	3.00
650°C/700 hours	1.13	2.50
800°C/700 hours	2.50	2.25
900°C/300 hours	5.20	1.25

50 μm

5 μm
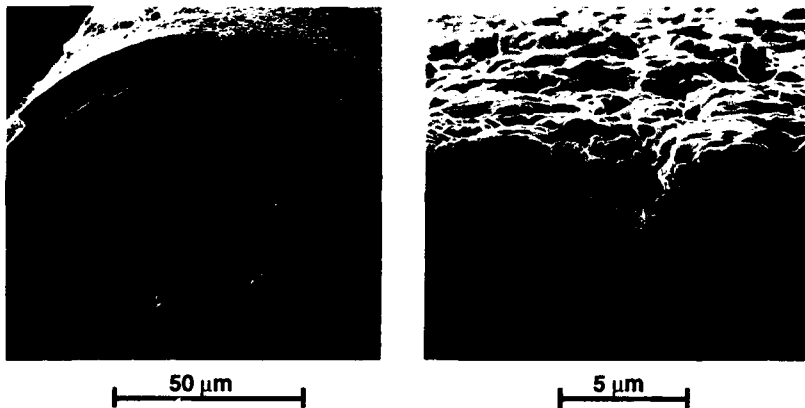
Figure 5:   An example of a surface initiated tensile fracture of SCS-6 fibers extracted from an SCS-6/Timetal® 21S composite heat-treated at 800°C for 700 hours in argon.

It may be possible to use fracture mechanics to understand fiber strength distribution. If the SCS-6 fiber is assumed to have a unique fracture toughness (K_{IC}) then the strength distribution which results from a series of tensile tests depends solely on the flaw size and distribution.

Other researchers [15] have related fiber tensile strength to measured flaw sizes using the relationship:

$$K_{IC} = Y\sigma\sqrt{r_f} \qquad (4)$$

where Y is a geometric term that incorporates flaw shape and placement, σ is the tensile strength, and r_f is the major flaw radius. The analysis here was performed only on the observed surface flaws and only on those for which a reasonably accurate measure of both depth and length could be made. Although analyses of semi-elliptical flaws on the surface of cylinders has been performed [16], the flaws in this study were much smaller compared to fiber diameter than the limits of that analysis. Therefore an expression for K_{IC} was used which assumed an elliptical flaw on the surface of a semi-infinite solid [17]:

$$K_{I(max)} = \frac{\sigma\sqrt{\pi a}}{\{3\pi/8 + \pi a^2/8c^2\}} \qquad (5)$$

Here a and c are the depth and half the breadth of the flaw, respectively. Table I lists the data with which these calculations were performed and the resulting values of K_{IC}. The average with this small amount of data is 2.1 MPa√m with a standard deviation of 0.73MPa√m. The fracture toughness of Nicalon, a SiC fiber manufactured by pyrolysis, is reported to be 2.3 MPa√m [16], and that for bulk SiC is in the range of 3 - 5 MPa√m; the mean value calculated here is comparable to these figures.

Table I: Calculation of $K_{I(max)}$ from Tensile Strength and Surface Flaw Dimensions

σ (MPa)	a (μm)	2c (μm)	a/c	a/D	$K_{I(max)}$ (MPa√m)
981	0.85	8.3	0.206	0.00607	1.34
1058	1.20	33	0.073	0.00857	1.74
1074	1.30	5.0	0.520	0.00929	1.69
1251	0.28	6.0	0.0196	0.00196	0.984
2355	0.80	6.0	0.267	0.00571	3.10
2380	0.45	6.3	0.143	0.00321	2.38
2410	0.85	4.0	0.425	0.00607	3.15
2881	0.25	1.6	0.312	0.00179	2.10
3923	0.15	—	—	0.00107	2.24

SUMMARY

It has been shown through this work that exposure of an SCS-6/Timetal® 21S composite at elevated temperature may cause a deterioration in the extracted fiber strength distribution. A small number of low strength failures developed after the heat-treatment of this composite at 650°C and produced a bimodal Weibull distribution. The percentage of fibers that fell into a low strength distribution increased with heat-treatment at a higher temperature, 800°C. Surface initiations were observed on the fractures of most of the fiber specimens which failed at low tensile stress. These initiation sites were produced by chemical reaction of the matrix with the SiC of the fiber at locations where the protective carbon coating on the fiber was absent or had

been consumed. Heat-treatment of the composite at 900°C in an inert environment reduced the average coating thickness between fiber and matrix to 1.25 μm and produced a strength distribution dominated by surface initiated failures. The strength distribution that results from surface flaws is related to the fracture toughness of SiC and the size distribution of surface flaws.

REFERENCES

1. F. E. Wawner and D. B. Gundel, NASA Tech. Report, Grant No. NAG-1-745 (1991), pp. 34-47.

2. S. L. Draper, P. K. Brindley, M. V. Nathal, Met. Trans. A, **23A**, 2541 (1992).

3. P. J. Bania and W. M. Parris, presented at the 1990 TDA International Conference, Orlando, FL, 1990 (unpublished).

4. F.E. Wawner, in Fibre Reinforcements for Composite Materials, edited by A. R. Bunsell (Elsevier Science Publishers, New York, 1988), pp. 371-425.

5. S. R. Nutt and F. E. Wawner, J. Mat. Sci. **20**, 1953 (1985).

6. X. J. Ning and P. Pirouz, J. Mater. Res. **6** (10), 2234 (1991).

7. W. Weibull, J. Appl. Mech. **18**, 293 (1951).

8. K. Trustrum and A. de S. Jayatilaka, J. Mat. Sci. **14**, 1080 (1979).

9. J.R. Porter, in Intermetallic Composites II, edited by D. B. Miracle, D. L. Anton, and J. A. Graves (Mater. Res. Soc. Proc. **273**, Pittsburgh, PA, 1992) pp. 315-324.

10. K. Goda and H. Fukunaga, J. Mat. Sci. **21**, 4475 (1986).

11. L. G. Johnson, The Statistical Treatment of Fatigue Experiments, (Elsevier Publishing Company, New York, 1964), p. 37.

12. K. Jakus, J. E. Ritter Jr., T. Service, D. Sonderman, Comm. of Am. Cer. Soc. 1981, C-174.

13. E. R. Trumbauer, J. R. Hellmann, D. L. Shelleman, D. A. Koss, to be published in J. Amer. Cer. Soc. (1994).

14. M. L. Gambone and F. E. Wawner, submitted to J. Mat. Sci. (1994).

15. W. H. Atwell, et. al. Final Report on Air Force Contract No. WRDC-TR-89-4050, Vol. 1, 1989, pp. 105-112.

16. I. S. Raju and J. C. Newman, in Fracture Mechanics: Seventeenth Volume, ASTM, STP 905, edited by J. H. Underwood, et. al. (ASTM, Philadelphia, PA, 1986) pp. 789-805.

17. D. Broek, Elementary Engineering Fracture Mechanics, 4th ed. (Martinus Nijhoff Publishers, Boston, MA, 1986), pp. 88-90.

FIBER COATING PERFORMANCE IN TiAl

C. McCULLOUGH AND R.R. KIESCHKE,
3M Company, Metal Matrix Composites Program, 3M Center, Bldg. 60-1N-01, St. Paul, MN
55144-1000.

ABSTRACT

The interfacial chemical behavior of two candidate coating systems for use on fine diameter ($\sim$10 μm) Al_2O_3 in TiAl is presented. The performance of the Nb/Y_2O_3 system appears to be related to the transport rate of Ti through the Y_2O_3 layer. Interfacial reaction is then observed at points where the Y_2O_3 thickness is less than about 1 μm. The main reaction product formed appears to be an oxygen saturated TiAl phase. An alternative system, $C/TiN/Y_2O_3$ is then presented as a solution to the Ti transport problem and may offer more desirable interfacial mechanical properties.

INTRODUCTION

The reinforcement of γ-TiAl with Al_2O_3 fibers may offer an increased material damage tolerance with closely matched thermal expansion coefficients. Although the Al_2O_3/TiAl system has been identified by many as thermochemically stable[1], some dissolution has been observed[2] and in two phase $\alpha_2+\gamma$ alloys some limited reaction may take place[3]. The result of this interaction/reaction is likely not only to reduce the in-situ filament strength but to give rise to high interfacial bonding. The aim of this work is to explore the performance of a Nb/Y_2O_3 fiber coating to avoid fiber/matrix interaction.

In addition to the criterion for fiber protection, the coating must provide a mechanism for fiber/matrix debonding and sliding. Interfacial sliding is necessary to achieve maximum (rule-of-mixtures) mechanical properties in the fiber direction due to the non-deterministic nature of the fiber strength and the need to reduce the stress concentrating effect of fiber breaks. These effects become more significant at higher fiber fractions such that the composite fracture behavior changes from a global load sharing (fiber break tolerant) to local load sharing (break intolerant) mechanism. The coating described here is a layer of metallic Nb directly in contact with the tow based ($\sim$10 μm diameter) polycrystalline alumina fiber, with a dense Y_2O_3 layer over this. The selection of these layers is based on maintaining the good thermal expansion match of all the components in the system. The Nb layer is necessary to chemically separate the Y_2O_3 layer from the Al_2O_3 fiber (avoiding reaction of these two phases). Y_2O_3 has been identified as thermochemically stable in high activity Ti alloys and in addition, the relatively low lattice mobility with suitable microstructure holds sufficient promise for its selection as a possible diffusion barrier material. The coatings used in this work were developed originally for use in high activity titanium alloys such as Ti-6Al-4V. It was felt that the coating performance in these alloys justified further examination in TiAl.

EXPERIMENTAL

A 3M-Nextel^{TM} 610, alumina fiber tow (>99% Al_2O_3) was used in this study, which is a polycrystalline fiber with $\sim$100nm grain size and 420 filaments ($\sim$10μm dia. each) per tow. Onto this layers of Nb and Y_2O_3 were applied by PVD and reactive PVD techniques respectively. Although various fiber handling and spreading techniques were applied to the fiber tow, the coatings are in general of non-uniform thickness. This is due to the self shadowing problems inherent when trying to coat a fiber tow with a line-of-sight deposition process. Typical layer thicknesses were 200 nm of Nb and 1 μm of Y_2O_3. (The coating system $C/TiN/Y_2O_3$ described later in the paper was applied by CVD techniques.)
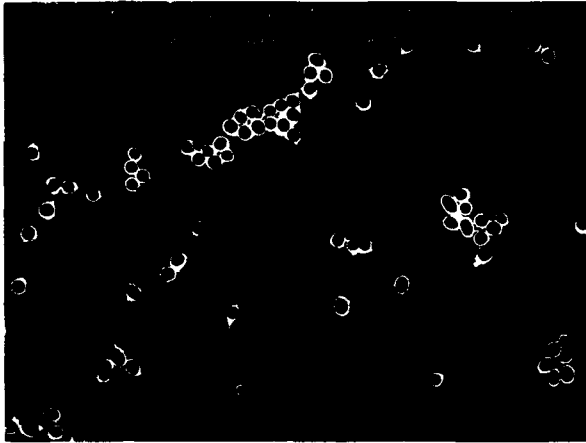
Figure 1a. Alumina fibers with Nb/Y_2O_3 coatings remain intact after consolidation of TiAl with no gross attack.

Figure 1b   Coatings of Nb/Y_2O_3 have variations in thickness. Some regions retain the original Nb (inner bright coating regions) and protect the fibers while other regions have Ti and Al in the Nb coating (darker regions).

Model composite systems were fabricated by consolidating coated fiber tows in Ti-33Al-3Mn-1V-0.1Cr (Ti-47at.%Al) powder using a hot isostatic press. Consolidation conditions were 1070°C for 4 hrs. at 180 MPa. Sections were then cut and polished transverse to the fiber direction. These sections were initially examined using a Cambridge Instruments S360 SEM with light element EDS, while more detailed chemical spatial information was gathered using a PHI 670 field emission scanning auger nanoprobe.

RESULTS

A low magnification SEM micrograph (Figure 1a) shows the distribution of fibers in the TiAl matrix. At this scale the Nb/Y_2O_3 coating combination serves to protect the fibers from any gross attack. The back-scattered imaging produces bright contrast from the coating layers around the fibers, indicating coating continuity and general integrity. Under higher magnification (Figure 1b), the gray background is the TiAl matrix and the black is the alumina fiber. The outer of the two coatings is clearly intact, continuous and homogeneous. EDS data acquired from this coating yielded only Y and O signals, consistent with an unreacted Y_2O_3 coating. However the inner coating exhibited two levels of contrast. The brighter contrast was associated with EDS spectra that yielded only Nb signals while the darker areas gave signals of Ti, Al and Nb. Quantification of such spectra gave a composition of Ti-47Al-5Nb (at.%): a composition that suggests the Nb layer has been converted to TiAl by intrusion of Ti from the matrix.

Scanning Auger microscopy gives some insight into the changes induced by the processing temperature excursion. Figure 2 shows two line scans taken across the fiber/coating/matrix interface. The first (Figure 2a) is across an unreacted Nb layer in which the Y_2O_3 layer is ~1μm thick. Note there is no intrusion of Al or Ti into the Nb. Within the Y_2O_3 layer adjacent to the matrix, the line scan shows a shoulder on the Ti line suggesting an ingress into Y_2O_3 over a distance of 0.5-0.75μm. This ingression may be a result of a transient diffusive flux due to the fine grain size of the PVD Y_2O_3 layer[4]. However the Al does not penetrate the Y_2O_3 at all. The second line scan is taken across a region in which in the Nb was reacted and the Y_2O_3 layer was thinner: only 0.75μm.. The signals from the Nb layer include both Ti and Al, consistent with the EDS data in the SEM. In the Y_2O_3 layer, a low level Ti signal is seen across the entire Y_2O_3 layer which has some increase towards the matrix side.

These results suggest the Y_2O_3 layer acts as a diffusion barrier to Al but that Ti is permitted to diffuse through the Y_2O_3. For the consolidation cycle employed here 1μm of Y_2O_3 is enough to prevent this Ti flux from reaching the Nb, but that 0.75μm is not. Once the Ti reaches the Nb it will go into solution since Ti and Nb are mutually soluble, and when the Ti activity is high enough the Ti attacks the Al_2O_3 fiber, releasing Al into the Nb layer. Ultimately there is enough Ti and Al to form a Nb containing γ-TiAl. Thus this coating scheme will protect the fiber if sufficient Y_2O_3 is present. However thick Y_2O_3 coatings are not desirable as they begin to represent some significant fraction of the composite, e.g. a 1μm coating around a 10μm fiber represents 30% of the total reinforcement volume.

From the above work, incorporation of a Ti barrier into the coating scheme is desirable. Moreover, Nb is likely to have too high a sliding stress to confer good damage tolerance and thus strength to the composite[5]. Thus a weak interface layer such as carbon would be preferred. In fact carbon is the only such layer that is currently deemed to possess the correct mechanical characteristics. Carbon is reported to be stable next to alumina[6]. However a thin layer of Y_2O_3 over the carbon would still permit Ti from the matrix to reach the carbon and then form TiC which would not have the required debonding and sliding characteristics. From work within the 3M MMC model factory program, TiN has been found to be a good Ti barrier as it has a low Ti sub-lattice mobility (by analogy to the lattice kinetics of isostructural TiC[7]). Thus a coating combination of C/TiN/Y_2O_3 is chosen. Noteworthy is that TiN alone will react with the matrix by Al reaction with TiN to form the equilibrium Ti_2AlN phase[8], thus a Y_2O_3 layer is still required.

A scanning Auger line scan across this coating scheme is presented in Figure 3. This shows the Y_2O_3 layer is only ~0.2μm thick and Ti is detected in this layer but Al is not. The remaining layers of TiN, C and Al_2O_3 all remain discrete and unpenetrated. Note that total protection is achieved with a total coating scheme thickness of under 0.6μm. Figure 4a shows an SEM micrograph of the fiber with the intact coating scheme and each layer can be clearly seen as
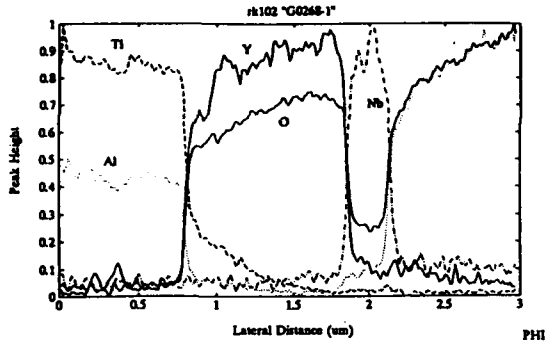
Figure 2a. Auger line scan through Nb/Y$_2$O$_3$ coated fiber with a thick 1μm Y$_2$O$_3$ layer showing discrete layers, and some partial diffusion of Ti into the edge of the Y$_2$O$_3$ layer. The Nb layer remains unaffected.
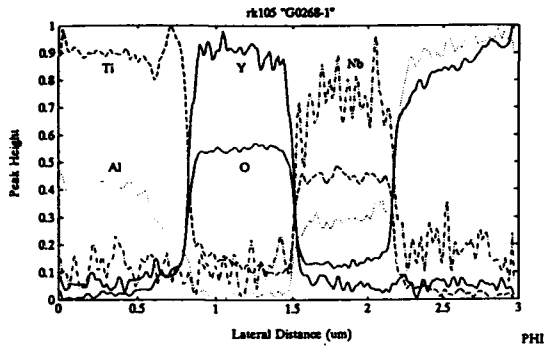
Figure 2b. Auger line scan through a coated fiber showing Ti has diffused through the thin Y$_2$O$_3$ layer (0.7μm) and combined with the Nb, producing a Nb-Ti layer. Subsequent reaction of Ti with Al$_2$O$_3$ then releases Al into the layer.
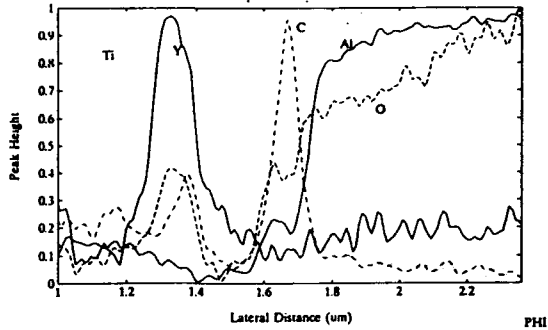
Figure 3. Auger line scan across a C/TiN/Y$_2$O$_3$ coated fiber showing discrete layers and no reactions. Note thin nature of barrier layers (0.6μm total).

122

Figure 4a. SEM of the fiber coatings showing protection and individual layers.

Figure 4b. Scanning auger Ti map showing thin, yet discrete and isolated C, TiN and Y_2O_3 layers.

discrete. The lack of interpenetration is nicely imaged in the scanning auger microscope, by taking a Ti map (Figure 4b). The dark area on the right is the fiber, the bright area on the left the matrix, the thin dark band is the Y_2O_3, the bright band the TiN, and then there is a carbon layer between this and the fiber which is e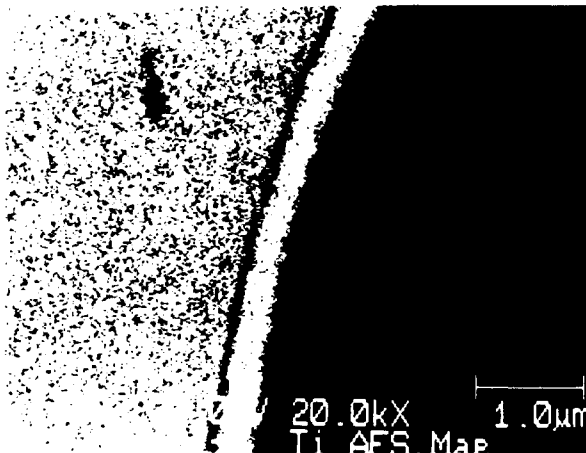asily picked out with a carbon map (not shown). Thus the $C/TiN/Y_2O_3$ combination seems not only to be an excellent protection scheme but may offer the required interfacial mechanical characteristics.

SUMMARY

A Nb/Y_2O_3 coating scheme will protect alumina fibers through a typical TiAl consolidation cycle if the Y_2O_3 thickness is greater than $1\mu m$. Below this level Ti diffuses far enough through the layer to reach the Nb and then to react with the alumina fiber. In order to ensure global load sharing operates in the composite, carbon interfaces are desirable which may be protected using only thin layers of TiN and Y_2O_3, with the TiN acting as a Ti barrier.

ACKNOWLEDGMENTS

REFERENCES

1. S.M.L. Sastry, P.J. Meschter & J.E O'Neal, Met. Trans. A, **15A**, 1451-1463 (1984).
2. H.E. Déve, A.G. Evans, G.R. Odette, R. Mehrabian, M.L. Emiliani & R.J. Hecht, Acta Metall. Mater. **39**(8), 1915-24 (1991).
3. Misra A.K., Met. Trans. A, **22A**, 715 (1991)
4. R.R. Kieschke, R.E. Somekh & T.W. Clyne, Acta Metall. Mater. **39**, 427-435 (1991).
5. J.B. Davis, J.P.A. Löfvander & A.G. Evans, J. Am. Ceram. Soc. **76**(5) 1249-57 (1993).
6. T.J. Makin, J. Yang, C.G. Levi and A.G. Evans, Mater. Sci. Engng A,.
7. S. Sarian, J.A.P. **39**, 5036, (1968).
8. J.J. Valencia, C. McCullough, J. Rösler, C.G. Levi and R. Mehrabian, in <u>Solidification of Metal Matrix Composites</u>, edited by P. Rohatgi (TMS, Warrendale PA, 1990), pp 133-150.

EFFECTS OF PROCESSING ON FIBER/MATRIX INTERFACES IN Ni₃Al/SAPPHIRE SINGLE CRYSTAL COMPOSITES

D. RINGER AND C.L. WHITE
Michigan Technological University, Department of Metallurgical and Materials Engineering, Houghton, MI 49931-1295, USA

ABSTRACT

Composites consisting of Ni_3Al modified with Zr, Fe, and B (IC-50) reinforced with continuous sapphire single crystal fibers have been prepared by vacuum hot pressing foil/fiber multilayers. Previous research detected formation of Zr-rich precipitates and sulfur segregation at fiber/matrix interfaces in these materials subsequent to fabrication. In this work, fiber bonding to the Ni_3Al matrix has been characterized using fiber push-out tests. Segregation and precipitation at fiber/matrix interfaces has been examined using scanning Auger electron spectroscopy and scanning electron microscopy. For comparison, composites have also been prepared from Ni, Ni-Al, and Ni-Al-Zr solid solution matrices, to evaluate the effects of matrix strength and reactivity on processing and fiber/matrix reactions.

INTRODUCTION

Information concerning the matrix, the fiber, and fiber/matrix interface properties are required to predict the basic mechanical behavior of a metal or intermetallic matrix composite (MMC or IMC). While matrix and fiber properties are reasonably well known, little is reported about the mechanical properties of the fiber/matrix interface in sapphire/Ni_3Al composites. The lack of adequate fiber/matrix bonding [1,2,3] as well as chemical reactions between matrix and fiber are believed to be a limiting factor in the performance of such composites [2].

While the matrix initially carries part of the applied load at elevated temperature, eventually the fibers carry the full load on a composite component [4]. So long as the matrix transfers adequate load to the fiber, the high temperature creep strength of continuous fiber reinforced composites will be determined by the strength of the fiber [4]. A high fiber/matrix shear strength insures effective load transfer to the fibers under these circumstances. A strong fiber/matrix bond also contributes to improved composite performance when it is loaded in the transverse direction.

The shear strength of the fiber/matrix interface is directly related to the shear strength of the matrix, and may be influenced by local work hardening of the matrix if the fiber/matrix is perfectly bonded. There are three major factors that influence the overall bond strength. First, there is chemical bonding, which is independent of any residual compressive stresses that may act normal to the interface. Second, there may be physical bonding due to friction and mechanical interlocking. Physical bonding is dependent on the normal stresses at the interface and on its topology. Stresses affecting physical bonding can be generated during cooling due to coefficient of thermal expansion (CTE) mismatch of fiber and matrix. The third factor that influences bonding is segregation of alloying and impurity elements at the fiber/matrix interface, which may affect both chemical bonding, and the tribological properties of the fiber/matrix interface.

In this paper, we discuss interactions between an Ni_3Al based intermetallic alloy designated IC-50, and continuous sapphire fiber reinforcements. Additional results on composites with Ni, Ni-Al, and Ni-Al-Zr matrices are also reported. Effects of composite processing on fiber damage are discussed, and effects of fiber/matrix interactions on fiber push-out strengths are reported.

EXPERIMENTAL

Matrix and fibers

Ni$_3$Al with the designation IC-50 (Ni-21.4at%Al-0.5at%Zr-0.2at%B-0.4at%Fe) was provided by the Oak Ridge National Laboratory (ORNL) as a roll-cast sheet. The Ni-Al (Ni-4.4at%Al), and Ni-Al-Zr (Ni-4.5at%Al-0.2at%Zr) alloys were produced by arc melting Ni 99.99%, Al 99.999%, and Zr >99.5%, and were homogenized for 100 h at 1200°C in vacuum. The pure Ni was electrolytically deposited sheet and was rolled as received. All materials were cold rolled in steps to a final foil thickness of 0.2 mm, with intermediate vacuum annealing at 1000°C. A final annealing of 1 hour was introduced to avoid extensive grain growth during hot pressing of the composites. The chemical analysis of IC-50 was provided from ORNL. Ni-Al, and Ni-Al-Zr were analyzed by energy dispersive X-ray spectroscopy (EDS). The sulfur concentration of the matrix materials is between 3 and 4 weight ppm as measured by LECO CS244. Unsized single crystal alpha-alumina (sapphire) fibers from Saphikon Inc. with 132 (±15) μm in diameter were used as reinforcements.

Production of IMC/MMC

Composite samples measuring 10 mm x 40 mm were produced by vacuum hot pressing (VHPing) foil/fiber multilayers. Five layers of fibers (25 fibers total) were positioned with small amounts of cellulose acetate tape between 200 μm thick foils. The multilayer specimen assembly was pressed between BN coated Mo plates in a graphite die at 1300°C under a load of 1300 N. This caused the matrix foils to deform around the fibers and diffusion bond to each other. Because the specimens did not conform to the die circumference, there was no constraint against transverse deformation, as is common in many die pressing operations. After VHPing, specimens were hot isostatic pressed (HIPed) at 1200°C for 2 h at 190 MPa to eliminate remaining cavities between fiber and matrix. Further details on VHPing and HIPing will be published elsewhere. Optical microscopy combined with a fluorescent dye epoxy and UV light was us. ' to monitor closure of the matrix around the fiber.

Measurements

Fiber push-out test specimens, ≅ 0.5 mm thick, were prepared by cutting composite specimens transverse to the fiber direction using a wire saw and abrasive slurry (earlier work has shown that cutting with a diamond wafering saw can cause significant fiber delamination [5]). Cut ends of the specimens were polished on both ends and inspected for fiber damage, which was detected by examining the fibers using transmitted light [5].

Fiber push-out tests were performed using a LECO V-100-C2 hardness tester, modified to control the indenter displacement with an Instron 4206 tension/compression testing machine. The test specimens were supported on a ground steel support having a 0.2 mm x 0.2 mm square hole, over which the fiber was positioned. The square hole was kept small to minimize plastic deformation of the matrix and to minimize tensile stresses in the fiber/matrix interface [6]. The indenter was then positioned, and its displacement rate was computer controlled at 1 μm/s using the software resident on the Instron machine's computer. The load was monitored using a 10 kN load cell and the load displacement curve for the fiber push-out was recorded. In specimens where fiber cracking occurred before or during fiber push-out, displacements were interrupted at load increments of 5 N to see if the fiber had cracked. A minimum of five push-out tests were conducted for each type of composite. Control tests, involving indentation of a 0.4 mm thick sapphire sheet, were performed in order to evaluate displacements associated with movement

and deflection of the loading apparatus. Because each specimen contained several fibers for testing, fibers were pushed back into the matrix after testing, in order to provide a planar specimen surface for the next test.

Auger electron spectroscopy (AES) was used to analyze alloying and impurity element segregation to fiber/matrix interfaces. The samples were fractured in-situ to observe the fiber surface as well as the mating matrix surface (which appeared as a trough in the matrix) without exposure to air [5]. Again, the samples were cut with a wire saw to avoid delamination and contamination of the fiber/matrix interface with oil or solvents. Samples measuring 1 mm x 2 mm x 10 mm were cut out of the composites, with the long dimension perpendicular to the fiber direction. The matrix adjoining the length of the fibers was then pre-notched to promote preferential fracture along the fiber/matrix interface. Auger spectra were obtained using a 10 keV electron beam with a beam current typically between 1 and 10 nA.

RESULTS AND DISCUSSION

Microstructure

EDS analysis of the Ni-Al matrix material (before fabrication to a composite) shows uniform distribution of Ni and Al. The Ni-Al-Zr alloy shows a few Zr rich precipitates with a diameter of less than 1 μm. The grain size of Ni, Ni-Al, and Ni-Al-Zr are in the order of 200 μm, whereas the grain size of IC-50 is approximately 25 μm. Backscattered electron imaging (BEI) and EDS mapping of IC-50 show areas of different elemental compositions, probably reflecting a two phase ($\gamma + \gamma'$) microstructure.

Figure 1 shows BEI's of polished cross sections of the composites after vacuum hot pressing and subsequent HIPing. The formation of precipitates along the fiber/matrix interface are clearly visible for Ni-Al-Zr and IC-50. Elemental analysis by wavelength dispersive X-ray spectroscopy (WDS) shows, that the precipitates in IC-50 and Ni-Al-Zr are Zr and O rich, which is consistent with previous findings for IC-50 [7]. The light regions in the matrix of IC-50 are deficient in Al and Zr and indicate the disordered γ phase.

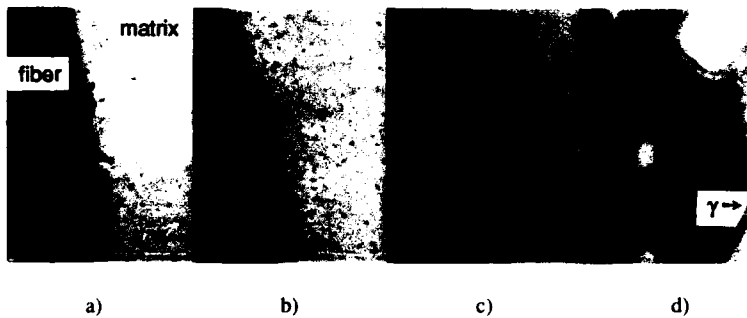a)   b)   c)   d)

Figure 1:   Backscattered electron images of composites after hot pressing at 1300°C for 1 h and subsequent HIPing at 1200°C for 2 h. a) Ni, b) Ni-Al(4.4at%), c) Ni-Al(4.5at%)-Zr(0.2at%), d) IC-50 (Ni-21.4at%Al-0.5at%Zr-0.2at%B-0.4at%Fe)

Fiber damage during vacuum hot pressing

Two kinds of fiber damage can be observed in the processed composite using transmission light microscopy. The fiber can either fracture transverse to the fiber axis, or split along the fiber axis. The transverse fiber fracture appears to result from matrix flow in the fiber direction during vacuum hot pressing. This flow appears to pull the fiber apart, indicating significant fiber/matrix interface shear strength at elevated temperature. Transverse fiber fracture can be minimized using low pressures, providing high friction between the outer matrix layers and the graphite punch, and by using a high fiber volume fraction. Each of these steps appears to reduce the plastic flow responsible for fiber fracture.

Longitudinal fiber splitting can result from loading the fiber in the transverse mode, or the shear mode. Stresses in the transverse direction can be created due to fiber bonding to the matrix and simultaneous poor foil-to-foil bonding. Poor foil-to-foil bonding can result in transverse tensile loads on the fiber upon release of pressure in the VHP, or upon the release of internal stresses when the composite is cut. Shear stresses can be generated due to asymmetric plastic flow of the matrix during pressing, or during cooling due to asymmetrical fiber distribution.

Fiber push-out

Figure 2 shows typical load displacement curves for fiber push-out tests where the fiber did not crack. This curve reflects the actual fiber displacement, after the elastic deflection of the testing apparatus ($\cong 1\mu m/N$) has been subtracted. The accuracy of machine displacement measurements in these tests was approximately $\pm 1\mu m$. Three types of push-out curves have been observed in Ni, and Ni-Al respectively. Type I shows an increase in load at a constant rate and sudden displacement. Type II and III show a change in slope before significant displacement. Type II shows constant or increasing load during displacement, whereas in type I and III the load drops significantly during displacement. The arrow indicates the onset of fiber push-out, and the load used to determine the push-out strength. The onset could be initiated due to fiber/ matrix crack propagation as suggested in [6], due to local plastic deformation, or a combination of the two. Fiber push-out strength is defined as the push-out load divided by the fiber/matrix area in the untested specimen. The average fiber diameter of 132 µm was used to calculate the surface area. Results of these calculations are given in Table I. The increasing load observed after push-out is due to contact of the spherical indenter with the matrix. Results for IC-50 and the Ni-Al-Zr alloy are lower limits, since fibers in these composites cracked before push-out. When cracks were observed in the fibers, they usually started on the end contacted by the indenter, in agreement with numerical modeling of the localized compressive stress in the fiber [6].
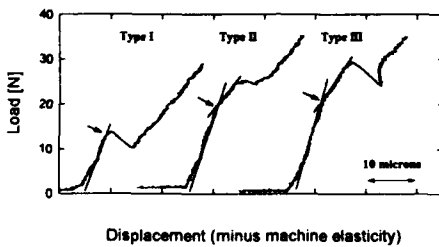
Table I: Push-out results

matrix material	push-out strength (95% conf.) [MPa]	Vicker's Hardness number of matrix [1 kg for 15 s]
Ni 99.99%	85 (±19)	66
Ni-Al	124 (±17)	96
Ni-Al-Zr	> 165 (±31)	101
IC-50	> 214 (±63)	235

Figure 2: Typical load-displacement curves during the fiber push-out tests. The arrows indicate the loads used for the push-out strength calculation. See text for details.

Fiber/matrix interface

In Ni, and Ni-Al the fiber and trough surfaces were free of precipitates, whereas in the Ni-Al-Zr and IC-50 composites the fiber surfaces contained many precipitates. WDS analyses show that the precipitates are Zr and O rich. On the fiber surface of all composites O, Al, and Ca peaks were found. On the matrix side Ni, S, and Al (exception for pure Ni) peaks were found. The observation of S, and precipitates is consistent with earlier findings for IC-50 [5]. Other research on surface segregation in sapphire indicate that Ca can segregate from the bulk of the sapphire [8]. Figure 3 shows the typical AES spectrum for the fiber surface and the matrix trough surface for the different composites. The spectra from the Ni and Ni-Al composites are very similar. The Ca peaks in IC-50 and Ni-Al-Zr are smaller than those in Ni and Ni-Al without Zr. The ZrO_2-CaO phase diagram indicates that Ca may form $CaZrO_3$ or go into solid solution in cubic ZrO_2 [9]. Ni has been found on all fiber surfaces, however it is not evenly distributed. The presence of Ni is either due to chemical bonding or due to mechanical deposition during impact bending in the AES system.

The S and Ca peaks vanished after sputtering for 30-60 seconds. This is consistent with earlier findings for S and indicates that these elements are enriched in a layer only about one atomic layer thick [5]. Comparing peak to peak ratios and using standard sensitivity factors for pure elements, the surface concentration of S and Ca are estimated to be 15-20%, and 4-10% [10].
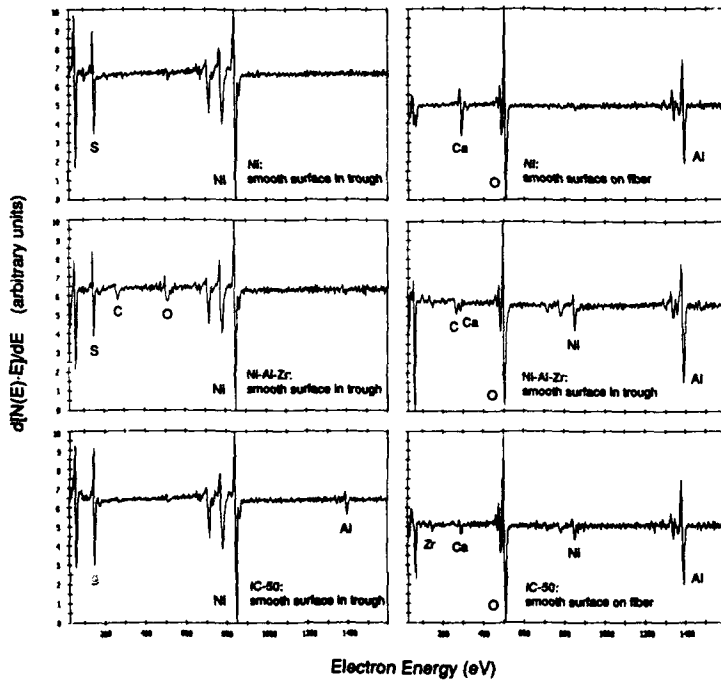

Figure 3:   A selection of AES spectra from the as fractured trough and fiber surfaces.

CONCLUSIONS

1) Two kinds of fiber damage have been observed. The fiber can either fracture transverse to the fiber axis, or split along the fiber axis.

2) Sulfur segregates to the fiber/matrix interface in all specimens and remains on the surface of the trough in the matrix subsequent to fracture. Zr seems not to influence the amount of S segregation. Calcium segregates to the fiber/matrix interface in all specimens, and adheres to the fiber surface during separation. Less Ca is found at the interface of the matrices containing Zr, however. Some Ca may have reacted with ZrO_2 and became incorporated into the precipitates. The thickness of the S and Ca layers are approximately one atomic layer.

3) Precipitates (in contrast to a continuous film) are formed at the fiber/matrix interface in Ni-Al-Zr, even if there are only a few grain boundaries intersecting the fiber due to large grain size. This suggests that the formation of precipitates is not controlled by preferred transportation of Zr along grain boundaries.

4) The push-out strength of the Ni-Al composite was higher than the Ni composite, although both composites were free of precipitates at the fiber/matrix interface and had similar fiber/matrix compositions. The Ni-Al matrix was harder than the Ni matrix, however, suggesting the possibility that its higher push-out strength may be associated with resistance to local plastic deformation along the fiber/matrix interface. One other possibility is that the higher strength matrix undergoes less stress relaxation during processing, leading to higher residual compressive stresses and greater mechanical bonding.

5) The push-out strength of Ni-Al-Zr composites increased significantly compared to Ni-Al, due to the formation of precipitates at the fiber/matrix interface. Ni-Al and Ni-Al-Zr have only a little change in hardness and should have therefore only a little difference in yield stress and residual compressive stresses. The high push-out strength of Ni-Al-Zr demonstrates the mechanical interlocking between fiber and matrix. However, it is not clear to what extend chemical bonding is present.

6) The fibers in IC-50 and Ni-Al-Zr fracture during the push-out test of 0.5 mm thick samples due to localized compressive load at the side of the indenter, indicating a very strong fiber/matrix interaction in the direction of the fiber.

REFERENCES

1. J.H. Schneibel, E.P. George, C.G. McKamey, E.K. Ohriner, M.L. Santella, and C.A. Carmichael, J. Mater. Res. **6** (8), 1673-79 (1991).

2. C.G. McKamey and E.H. Lee in *Intermetallic Matrix Composites*, edited by D.L. Anton, P.L. Martin, D.B. Miracle, and R. McMeeking (Mater. Res. Soc. Proc. **194**, Pittsburgh, PA, 1990) pp. 163-68.

3. R.D. Noebe, R.R. Bowman, and J.I. Eldridge in *Intermetallic Matrix Composites*, edited by D.L. Anton, P.L. Martin, D.B. Miracle, and R. McMeeking (Mater. Res. Soc. Proc. **194**, Pittsburgh, PA, 1990) pp. 323-331.

4. Malcolm McLean in *High Temperature/High Performance Composites*, edited by F.D. Lemkey, S.G. Fishman, A.G. Evans, and J.R. Strife (Mater. Res. Soc. Proc. **120**, Pittsburgh, PA, 1988) pp. 67-79.

5. D. Ringer and C.L. White, Intermetallics **1**, 127-137 (1993).

6. D.A. Koss, M.N. Kallas, and J.R. Hellmann in *Intermetallic Matrix Composites II*, edited by D.B. Miracle, D.L. Anton, J.A. Graves (Mater. Res. Soc. Proc. **273**, Pittsburgh, PA, 1992) pp. 303-313.

7. D. Ringer and C.L. White in *Processing and Fabrication of Advanced Materials for High Temperature Applications II*, edited by V.A. Ravi and T.S. Srivatsan (The Minerals, Metals & Materials Society, Warrendale PA, 1993) pp. 487-499.

8. S. Baik, and C.L. White, J. Am. Ceram. Soc. **70** (9), 682-88 (1987).

9. E.M. Levin and H.F. McMurdie, *Phase Diagrams for Ceramists 1975 Supplement (Figure 4313)* (The American Ceramic Society, Inc., 1975) p. 105.

10. Perkin Elmer 660 SAM System, Technical Manual Part No. 617678, Physical Electronics Division, Eden Prairie, MN.

Ti Aluminide and MoSi$_2$ Composites

A REVIEW OF THE STATUS AND DEVELOPMENTAL ISSUES FOR CONTINUOUSLY-REINFORCED TI-ALUMINIDE COMPOSITES FOR STRUCTURAL APPLICATIONS

D. B. MIRACLE*, P. R. SMITH*, AND J. A. GRAVES‡
*Air Force Wright Laboratory, Wright-Patterson AFB, OH
‡General Electric Corporate Research and Development Laboratory, Schenectady, NY

ABSTRACT

A significant materials-based activity to develop Ti-aluminide metal matrix composites for high temperature aerospace structural applications is now underway. A review of the approaches, progress, and status of the development of continuously-reinforced Ti-aluminide metal matrix composites with matrices which contain a significant volume fraction of the ordered orthorhombic Ti_2AlNb phase will be presented. The principal application considered is a gas turbine compressor rotor ring, and this influences the development approaches and properties goals. Specific development activity that will be presented includes modification and control of the matrix composition and microstructure, fiber coating treatments to control interdiffusion between the fiber and the matrix, and to improve the ability of the interface to support a mechanical load, and efforts to improve the properties of SiC monofilaments used as reinforcements. Critical issues that define the requirements for additional studies will be presented.

INTRODUCTION

A concerted effort to understand and characterize continuously-reinforced Ti-aluminide metal matrix composites (MMC's) for aerospace structural applications has been underway for nearly a decade. The activity on Ti-aluminide MMC's was first established in 1985 [1] in support of an Air Force initiative to improve the propulsion capability of gas turbine engines. Early activity focused on microstructural characterization, processing, life prediction, and determination of the mechanical response under a range of monotonic, cyclic, and time-dependent loading conditions. More recently, a strong materials-based activity has been established to develop new composites to overcome the deficiencies of earlier systems. This development activity includes not only microstructural characterization, but is also pursuing control of the matrix microstructure and composition modification of the fiber coating and the fiber/matrix interface, and improvements in reinforcing fiber technology. A wide range other activities which impact materials development are being coordinated with this effort, including processing, environmental resistance, and mechanical behavior and life prediction.

Several product forms have been produced, representing a wide range of possible applications. These include (a) flat plate and sheet product for skins, casings, flaps, and structural members (such as I-beams and hat stiffeners); (b) tube structures for shafts, rods, and struts; and (c) ring components (primarily for compressor rings). Rods and plates are likely to see earliest qualification due to less stringent mechanical properties requirements and the simplicity of fabrication. In contrast, composite rings for compressor rotors are more difficult to process and require a more demanding balance of properties. While these applications are likely to be further in the future, the revolutionary payoffs for this application are a particularly strong motivation. The application defines the operating environment (stress, temperature, mission cycle), therefore the development approaches specified to achieve the required physical and mechanical property goals follow from the definition of the intended application. The current discussion will focus on development activity in support of advanced turbine compressor rotor ring and compressor impeller applications.

Projected operating temperatures for Ti-based MMC's extend to as high as 800°C for limited times and low stresses. 'Conventional' (or disordered) Ti-alloy matrices are likely to be used below 600°C, since they possess adequate mechanical properties and are less costly due to ease of

manufacture. More aggressive applications occur in this 600-800°C temperature interval, and MMC's with disordered matrices provide inadequate properties, particularly strength and creep resistance. For these important applications, Ti-based matrices consisting (wholly or in part) of ordered Ti-aluminide phases are required to achieve the necessary properties at the operating temperatures. The ordered Ti-aluminide phases currently of most interest are those based on Ti_3Al (α_2), Ti_2AlNb (orthorhombic, or O), and an ordered body-centered cubic phase (B2). TiAl-based composite technology is significantly less mature than the activity based on the Ti-aluminide compounds listed above, since a fiber with a compatible coefficient of thermal expansion as well as adequate strength is not yet available. The feasibility of MMC's based on gamma TiAl is therefore still being established.

The present manuscript will report on the efforts to develop Ti-aluminide MMC's for high temperature compressor rotor applications in advanced gas turbine engines. The large collaborative activity initiated at the Air Force Materials Directorate to develop Ti-aluminide MMC's based on matrices containing the orthorhombic (Ti_2AlNb) phase will provide a relevant point of focus. Discussion of the materials-based approaches to improve the physical and mechanical properties of Ti-aluminide MMC's will be emphasized, rather than providing a detailed compilation of the mechanical properties that have been achieved with currently-available composite systems. Selected comparison of material characteristics will be provided, however, to illustrate progress toward improved mechanical properties at elevated temperatures. Development approaches will be presented by composite constituent (matrix, interface, and reinforcement). Composites using discontinuous reinforcements, disordered matrices, or matrices based on the γ-TiAl compound will not be discussed in this paper.

Ti-ALUMINIDE COMPOSITE BASELINE (Ti-24Al-11Nb/SiC)

The earliest significant activity to produce and characterize continuously-reinforced Ti-aluminide MMC's was conducted on Ti-24Al-11Nb/SiC composites (all matrix compositions are provided in atom percent, unless otherwise specified). Details of this composite system are well-reported in the literature [2,3 and references therein], and a brief summary is given below to provide a baseline against which advanced composites will be compared. The characteristics and deficiencies of this system will help to focus attention on critical issues, and may identify opportunities for improvements.

In the as-processed condition, the Ti-24Al-11Nb matrix alloy typically consists of 95% (all phase and reinforcement fractions are given by volume) of the ordered hexagonal (hP8, Ni_3Sn prototype) Ti_3Al, or α_2, phase, and 5% of a disordered β-Ti phase. The α_2 phase occurs as equiaxed grains 10-20 μm in diameter, with the β phase occurring at triple points and grain boundaries. The properties of the continuous α_2 phase dominate the matrix response. Particular characteristics of the Ti_3Al phase which limit the usefulness of the Ti-24Al-11Nb matrix include limited ductility, chemical incompatibility with the C-rich coating employed on the SiC monofilaments, low strength, inadequate transverse properties, poor creep resistance, and environmental embrittlement when exposed to oxygen at elevated temperatures. These will each be briefly discussed.

Both analytical studies and experimental observations have suggested that a minimum level of ductility is required to effectively utilize the full load-carrying capability of the reinforcing fiber [4]. This minimum level depends upon the residual stress in the composite and the strain to failure of the reinforcing fiber, and is typically of the order of 2-3% for Ti-based MMC's reinforced with the SCS-6 SiC monofilament. Ti-24Al-11Nb typically possesses about 1-2% ductility in the as-processed condition and in 'neat' panels, which typically contain >1000 parts per million by weight (wppm) oxygen [3,4]. The poor ductility of the α_2 phase results from interstitial embrittlement, and from an inadequate number of independent slip systems [5]. The longitudinal ductility of textured sheet can be as high as 12% [6], but the transverse ductility is still low.

The Ti-24Al-11Nb matrix is chemically incompatible with both the C-rich outer layers of the SCS-6 fiber and the SiC fiber itself. A layer of brittle reaction products consisting of Ti-carbides and Ti-silicides forms during processing [7], and the growth of this layer follows a parabolic law [8]. In addition, the diffusion of C into the $\alpha_2+\beta$ matrix stabilizes the α_2 phase, thereby forming a

brittle β-depleted zone around each fiber. High residual stresses are produced upon cooling from the processing temperature as a result of the mismatch in the coefficient of thermal expansion (CTE) between the fiber and the matrix [9]. The large residual tensile stress in the matrix results in matrix plasticity at relatively low applied loads, and may also nucleate cracks in the reaction zone and β-depleted region around the fiber.

Although the axial properties of Ti-aluminide intermetallic composites are clearly superior to existing materials [2], most applications will require at least some resistance to off-axis loading. A weak bond exists between the outer C layers in SCS-6 monofilaments [10] and also between the outer carbon layer and the reaction products [11], and this weakness leads to inadequate transverse tensile and creep properties [2]. In addition, the fine-grained equiaxed microstructure of Ti-24Al-11Nb in the as-processed condition is optimal for ease of foil production and consolidation of the matrix around the SiC fibers, but produces off-axis creep rates that are unacceptably high. Thus, transverse creep is a critical concern that needs to be addressed in the development of new Ti-aluminide MMC's.

Finally, the Ti-24Al-11Nb matrix is embrittled when exposed to air at elevated temperatures, leading to a significant reduction in tensile elongation [12]. Ti-24Al-11Nb/SCS-6 composites lose as much as 85% of their RT tensile strength after 500 cycles in air between 150°C and 815°C, due to a combination of environmental embrittlement of the matrix and thermally-induced stresses resulting from the CTE mismatch between the matrix and the fiber [8,13,14]. Similar thermal cycling in an inert environment does not result in significant loss of tensile properties [14], although a drop in properties is observed after 10,000 cycles in vacuum [15].

DEVELOPMENT ACTIVITY

It is important to emphasize that a focused and systematic development activity on Ti-aluminide MMC's has been in place for a relatively short period of time, and so detailed and extensive mechanical property comparisons and evaluations are not yet available. Further, a basic understanding which establishes the relationship between constituent properties (especially the properties of the fiber/matrix interface region) and composite properties does not yet exist [16]. Therefore, the potential for successful development and application is still difficult to accurately assess. Simple extrapolation of past data and experience cannot adequately predict the potential improvements in composite response that may be achieved by modifying the matrix composition and microstructure, the interface and interphase region between the fiber and the matrix, and fiber properties. It is clear, however, that a number of relatively unexplored approaches yet exist for the improvement of composite response, each of which have the potential to significantly improve the properties of continuously-reinforced Ti-aluminide MMC's.

A broad activity initiated at the Air Force Materials Directorate is underway to develop continuously-reinforced Ti-based MMC's for structural applications, especially gas turbine compressor rotors. This activity is comprehensive in scope, and is addressing issues associated with processing, life prediction, extensive mechanical characterization, and development of the composite constituents. The development activity is emphasizing ordered Ti-aluminide matrices which contain a significant volume fraction of the orthorhombic Ti_2AlNb (O) phase, and is also addressing development issues associated with the fiber/matrix interface region, and the development of improved reinforcing fibers. The critical composite properties which are guiding the development activity include monotonic tensile strength, creep response (especially transverse to the fiber axis), fatigue crack growth and thermo-mechanical fatigue. Environmental resistance is not a primary consideration, since the composite ring will likely be embedded in a thick sheath of monolithic material for both ring rotor and impeller components. The materials-based approaches to improve the properties of the composite constituents, and hence the composites, are described below. Selected properties will be compared with the properties of Ti-24Al-11Nb/SiC composites to highlight progress that has been made.

135

Matrix Alloys

Increasing the Nb content of α_2-based alloys has been found to introduce an orthorhombic Ti$_2$AlNb phase (oC16, NaHg prototype) [17], and a recent review of the phase equilibria, phase stability, transformation kinetics, and microstructure/property relationships of several Ti-Al-Nb alloys containing the orthorhombic, or O phase, has been published [18]. Results of initial studies on Ti-aluminide MMC's produced with a matrix alloy which contains the O phase have also been published [19-26]. The matrix compositions of interest range from Ti-(22 to 25)Al-(17 to 27)Nb, which typically lie within the two-phase O+ordered β, or B2 (cP2, CsCl prototype), phase field [18]. However, significant levels of oxygen ($\geq$~1000 wppm) stabilize the α_2 phase [24], and so commercially-produced O alloys in sheet and foil product forms typically possess a significant volume fraction of the α_2 phase. For simplicity, these alloys will be referred to as orthorhombic, or O, alloys throughout the remainder of the paper, although it is understood that these alloys also contain the B2 and/or α_2 phases.

Alloys containing the O phase have been shown to possess improved specific strength over α_2 alloys (even though O alloys are typically more dense), while maintaining ductility sufficient to achieve rule-of-mixtures properties [19,25]. The ductility of the O phase results from an increased multiplicity of independent slip systems compared to the α_2 phase [27], to which the O phase is related. Ti-aluminide MMC's produced with O matrices also have improved chemical compatibility with the SCS-6 SiC fiber [20], and have markedly improved strength retention after 500 thermal cycles in air [25]. Orthorhombic matrix alloys show reduced sensitivity to interstitial contamination, and can be rolled to 90 μm thick (0.0035 in) foil, even with as much as 1790 wppm of oxygen [19]. Matrix development activity beyond the initial feasibility studies just cited is now underway, and is proceeding broadly in the areas of microstructural control and modification of the matrix composition.

Orthorhombic alloys containing quaternary and higher-order additions have been produced, with the principal goal of maintaining adequate levels of strength and toughness, while improving the creep resistance and environmental stability. The effects of compositional modifications to O alloys are now being established [18, and references therein], and this information is being used to define alloying approaches. In addition, the selection of alloying elements and levels of addition are guided by traditional metallurgical concepts developed for conventional Ti-based alloys and alloys based on Ti$_3$Al. Additions of Ta, Si, and Mo have been made to Ti-22Al-23Nb and Ti-22Al-27Nb, the two Ti-Al-Nb base compositions under investigation. Si additions are often considered for improved creep resistance of Ti-based alloys, such as Ti-1100 and Ti-6242S. Further, Si additions (singly or with Mo) to an alloy based on Ti-22Al-27Nb have been found to improve the strain-to-failure after thermal exposure [22]. Mo additions to Ti-25Al-17Nb have been found to significantly increase the creep resistance of this alloy [28]. This improvement occurs with only a small change in the morphology of the phases present. However, the volume fraction of the orthorhombic phase increases and the amount of B2 phase decreases. While Banerjee *et al.* claim that Mo has only a marginal effect on creep response (presumably based on the magnitude of primary creep strain and the secondary creep strain rate), these same authors show a significant increase in the stress rupture life at 650°C [18], which is consistent with the data of Smith [28]. Additions of Ta have been found to enhance the oxidation resistance of a Ti$_3$Al-based alloy in previous studies [29]. In each of the above alloys, Mo and Ta have been added such that they replace Nb, so that a constant level of β-stabilizing elements exists in the alloy. This assumes that each stabilizes the β-phase with equal strength, although more recent results show that Mo stabilizes the O phase, while Ta stabilizes the α_2 phase [18].

A study to establish the effects of ternary (Ti-Al-Nb) composition on the properties of alloys in the O+B2 two phase field is being conducted concurrently with the above alloying efforts [30]. Eleven ternary alloys in the O+B2 two phase field have been produced in small (1-2 kg) ingots. The ingots have been produced by containerless casting, so that the level of interstitials (especially oxygen) have been controlled within the range of 600-800 wppm. Further, the objective is to control the thermomechanical processing of the alloys, so that comparable microstructures may be tested. Initial difficulties have been encountered in producing chemically and microstructurally homogeneous materials, and studies are still underway.

Studies of Ti-24Al-11Nb/SiC MMC's have not considered post-consolidation heat treatment as a method to vary the microstructure of the matrix. This was due, in large part, to minimize the thermal exposure of the material, thereby limiting degradation of composite properties induced by

fiber damage and the growth of deleterious reaction products at the fiber/matrix interface. The fine-grained, equiaxed microstructure which results from the foil rolling and composite consolidation cycle of Ti-24Al-11Nb/SiC MMC's is well-suited for foil production and easy consolidation, but produces unacceptable creep characteristics. With the development of the less reactive O alloys, additional flexibility may be available to modify the matrix microstructure to improve those composite properties which are sensitive to matrix properties. Such efforts are now underway to improve the creep response of O alloys, especially in the transverse direction.

A lath microstructure generally produces a more desirable creep response in α_2 alloys [18] and in TiAl-based alloys [31] than does a fine, equiaxed grain structure. Therefore, efforts to emphasize a lamellar or lath microstructure at the expense of the equiaxed morphology are underway in O matrix alloys. Both sub-transus and supra-transus heat treatments are being performed, followed by controlled cooling rates which are consistent with those which may be achieved in commercial HIP units. Initial results have been promising. The time to 0.4% creep strain of a Ti-22Al-23Nb 'neat' composite has been increased from 2.3 hr to 98 hr at 650°C/172 MPa. The O laths are refined by the heat treatment, and the volume fraction of the O phase increases to 50% (from 33% before heat treatment), while the fraction of the α_2 phase drops from 37% to 15% (Figure 1). In addition to modifying the phase morphology by post-consolidation heat treatment, efforts to vary the volume fractions of the various phase constituents are underway. For example, heat treatments which disrupt the continuity of the α_2 phase have produced improvements in ductility [32]. Single phase O alloys deform at a much lower creep rate than typical α_2 alloys, while the presence of the β phase decreases the creep resistance in both cases [18]. Therefore, efforts to break the continuity of the β-phase may be beneficial for creep response.

Additional studies are required to establish the long-term microstructural stability of O alloys of interest, to ensure that the properties do not vary during service life. Limited data concerning kinetics of transformations is available, and additional information is required to help define the processing of O alloys, including ingot breakdown, foil rolling, and consolidation. The effects of oxygen need to be established in O alloys. While decreasing the oxygen level has been shown to reduce the volume fraction of the α_2 phase [24], it is likely that the strength of the alloy will also decrease. Optimum levels of oxygen may be required for a balance of ductility and strength.

Interfaces

The primary characteristics of importance at the fiber/matrix interface region in Ti-aluminide MMC's include chemical compatibility and mechanical response. The mechanical response of the interface depends upon the intrinsic chemical bond, the magnitude of residual stresses, and microstructural features (such as surface roughness). There is currently an inadequate fundamental understanding of the chemical effects of bonding at bimaterial interfaces to guide the selection of candidate interface coatings for MMC's. A similar lack of data and understanding exists for the establishment of the quantitative effects of surface roughness and residual stresses on load transfer, crack deflection, and other important responses. Therefore, candidate fiber coatings have thus far been selected based upon the criteria of chemical compatibility, simply because thermodynamic data and calculation methodologies exist to provide an adequate basis for selection. The control of residual stresses is a criteria that is sometimes considered, once again because it can be calculated or measured with some certainty. However, an improbable balance of physical and mechanical properties is required of an interface coating to effectively reduce the residual stresses at the fiber/matrix interface region, and so this is generally not considered as a viable selection criteria [33]. In the absence of a fundamental understanding of the chemical and microstructural features which influence interface bonding, a clear need exists to establish simple, reproducible experimental techniques and analyses capable of quantifying the appropriate mechanical parameters of candidate interface treatments. Until both the chemical and mechanical response of interfaces can be accurately predicted, the semi-empirical approach of modifying interfaces and subsequently quantifying the mechanical response of the interface and the composite must be pursued, rather than attempting to 'tailor' interfaces to a specific and predetermined balance of properties.

The SiC monofilaments that have typically been employed in Ti-aluminide MMC's each have a carbon coating on the outer surface. The most commonly-used SiC monofilament to date has a

137

Table I   Properties of SiC Fibers

Fiber	Diameter (μm)	Core/ Coating	Density (g/cm³)	UTS (MPa)	Standard Deviation	Weibull Modulus	Modulus (GPa)
Amercom	127	W/none	3.3	3540	5.8%	18	427
Sigma	100	W/none	3.4	3750	6%		400
Textron (SCS-6)	142	C/C+Si	3.0	4130	13.9%*	9	395
Textron (Ultra-SCS)	142	C/C+Si	3.0	6430	~19.4%‡	~14‡	365
Textron (Ultra-SCS) Extracted	142	C/C+Si	3.0	5370	11.3%	11	371

* Coefficient of variance
‡ Preliminary values

Table II   Tensile Properties of Ti-22Al-23Nb/Ultra-SCS MMC's

TEMPERATURE (°C)	σ_y (MPa)	σ_{uts} (MPa)	ε_f (%)	MODULUS (GPa)
RT (4 pts)	1690±63	2213±35	1.48±0.02	201±8
649 (1 pt)		1820	1.35	173
760 (2 pts)		1248±133	1.22±0.04	135±8

(a)   (b)
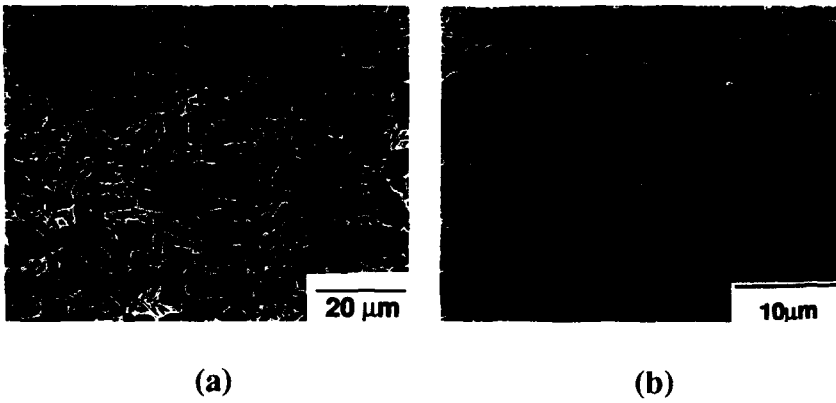
Figure 1   Microstructure of Ti-22Al-23Nb in (a) the as-consolidated condition, and (b) after heat treatment. The heat-treated material has a larger volume fraction of the orthorhombic phase, and a finer lath structure.

graded outer coating which consists of two layers with a varying concentration of carbon and silicon, and is called the SCS-6 coating (or fiber). In most Ti-based matrices, and in Ti-24Al-11Nb, this coating reacts rapidly with the matrix. However, this coating produces only minimal reaction with orthorhombic alloys. After processing, a reaction zone is formed which is about 0.3 μm thick [34,35], and this grows very little with exposure up to 1000 hr at 800°C[35]. Although specific details concerning the crystallography and chemical constitution of the phases in this reaction layer are available [34,35], it is not clear how this information may be used to predict the response of the interface to mechanical loads, since the physical and mechanical properties of the non-stoichiometric ternary compounds in the reaction layer, and the mechanical characteristics of the interfaces which form between the reaction products, the fiber coating, and the matrix are not known. In addition to forming reaction products, diffusion of carbon into the matrix has the potential to modify the phase constituency. A β-depleted zone is formed in Ti-24Al-11Nb/SiC MMC's, and preliminary observations in Ti-22Al-23Nb/SiC composites suggest that the diffusion of carbon into the matrix may stabilize the α_2 phase in the vicinity of the fiber after post-consolidation thermal treatments [28]. It is not yet known if this is detrimental to the mechanical response of the composite. However, fiber coatings that eliminate the reaction products and the β-depleted zone can provide significant improvements in the mechanical response of the MMC, even though no significant change in the strength of the interphase region is effected. For example, a Ag/Ta coating on SCS-6 SiC monofilaments in a Ti-25Al-10Nb-3V-1Mo matrix eliminated the reaction products and produced a β-enriched (rather than a β-depleted) zone around the reinforcement. These modifications doubled the transverse strength of the MMC [36].

The most significant feature of the SCS-6 interface is the weak mechanical bond which exists between the two carbon-rich outer layers. Failure is nearly always seen to initiate between these two layers, and so this fiber coating provides a weak mechanical link at the fiber/matrix interface region. While a weak interfacial bond is generally considered to be desirable for good damage tolerance via crack deflection and crack bridging, theoretical calculations have shown that shear and normal interface strengths much higher than those which currently exist may be tolerated before a debit in toughening properties is expected [37]. Current estimates suggest that shear and normal interface strengths 2-4 times the levels currently available may exist without decreasing the toughness response of MMC's, and these levels may be necessary to achieve the aggressive mechanical properties (principally tensile and creep strength) required for compressor rotor applications [38].

In view of the discussion above, several modified interface coatings have been chosen for characterization in orthorhombic MMC's [33,38,39]. These are generally described as dual layer coatings which consist of a refractory metal carbide adjacent to the SiC and a refractory metal next to the matrix. Selection of these coatings was based upon analytical and experimental determination of chemical compatibility [33]. Further, it was reasoned that the bond strength of the interphase region would be increased if some solubility existed between the materials in contact with one another (SiC/refractory metal carbide, refractory metal carbide/refractory metal, refractory metal/matrix), without the formation of new phases or compounds. It should be emphasized that this is a purely intuitive line of reasoning, but one with limited experimental corroboration [40]. These dual layer coatings have been deposited on uncoated SiC fibers, so that the weak bond associated with carbon coatings will be avoided. Measurement of the mechanical characteristics of these interfaces and the effect of these coatings on fiber strength is now underway.

Reinforcements

Although long-term activities are underway to develop new fibers (such as Ti5Si3) as reinforcements for Ti-based MMC's, SiC monofilaments are currently the only commercially-available fibers with a balance of physical and mechanical properties appropriate for reinforcements in Ti-aluminide MMC's. A brief summary of the most relevant fiber characteristics is provided in Table I below [16,41]. Each of the fibers have roughly equivalent values of the coefficient of thermal expansion, so that there is no important distinction between the fibers in this respect. Significant fiber development activity has occurred over the past several years. In addition to the Sigma uncoated SiC monofilament (the '1040' fiber), three coatings have been applied to this fiber; a pure carbon coating 2-3 μm thick (the '1140' fiber), a 2-3 μm carbon coating with 0.5 μm of TiB$_2$

(the '1240' fiber), and a 3-layer carbon coating 5-6 μm thick (the '1140+' fiber). Amercom SiC monofilaments include an uncoated fiber, a fiber with a 'hard' carbon coating 2 μm thick, and fiber with a 'triplex' coating, which consists of an inner and outer layer of 'hard' carbon surrounding a central layer of 'soft' carbon. Amercom has also deposited SiC on a carbon core, in an effort to replace the tungsten core typically employed by Amercom. While the available data suggests that there is not a significant effect of the various coatings just described on the mechanical properties of the as-coated fiber, the different coating systems do provide improved fiber strength in the composite after processing [42] by better protecting the fiber from damage during consolidation. Efforts at Textron Specialty Materials to produce a SiC monofilament with a reduced diameter (<100 μm) on a carbon monofilament core have been underway [43]. In addition, an experimental SiC monofilament with strength levels significantly higher than that of the SCS-6 fiber have been reported [43]. Preliminary data are shown in Table I for this Ultra-SCS fiber in both the as-received condition, and after extraction from a Ti-22Al-23Nb/Ultra-SCS composite panel [41]. While the value reported for the ultimate tensile strength is likely to be reasonably accurate, the values of the standard deviation and Weibull modulus of the as-received fiber are likely to require further refinement, as low-stress failures resulting from handling-induced damage are identified and removed from the data set.

The development of SiC fibers with strength levels significantly higher than currently available will provide significant benefits for the properties of Ti-aluminide MMC's, since improved axial properties will result. Alternatively, axial properties may be maintained at current levels with a lower volume fraction of reinforcing fibers, resulting in improved transverse properties. Since transverse properties are one aspect currently limiting the application of continuously-reinforced Ti-aluminide MMC's, the development of high-strength fibers may provide an important approach to the successful development of MMC's. Preliminary mechanical properties of an 8-ply Ti-22Al-23Nb/SiC composite with 30% Ultra-SCS fibers are shown in Table II [44]. The ultimate tensile strengths are significantly higher than values obtained in composites reinforced with the SCS-6 monofilament. For example, a Ti-22Al-23Nb/SCS-6 composite with 35% reinforcement typically has an ultimate tensile strength around 1800 MPa.

CONCLUDING REMARKS

Significant improvements have been achieved in the areas of matrix alloying, microstructural control through heat treatment, and the development of improved SiC fibers. Additional significant improvements may also result from modified fiber coatings. These improvements have been achieved singly, and so effort must proceed to integrate each of these advancements in a single composite system. The potential for achieving an acceptable balance of properties in Ti-aluminide MMC's based on matrix alloys which contain a significant volume fraction of the orthorhombic Ti₂AlNb phase currently appears to be promising. Activity addressing other required technology-related issues required for the successful implementation of orthorhombic MMC's, such as processability, life prediction, and design are being addressed concurrently.

ACKNOWLEDGMENTS

REFERENCES

1. M. L. Gambone, "Fatigue and Fracture of Titanium Aluminides", WRDC-TR-89-4145, Air Force Wright Laboratory, Wright-Patterson AFB, OH (1990)

2. J. M. Larsen, W. C. Revelos, and M. L. Gambone; in "Intermetallic Matrix Composites II", (eds. D. B. Miracle, D. L. Anton, and J. A. Graves), MRS Proceedings, 273, 3 (1992)

3. P. K. Brindley, S. L. Draper, J. I. Eldridge, M. V. Nathal, and S. M. Arnold; *Metall. Trans.*, 23A, 2527 (1992)

4. R. Amato and D. Pank; in "Titanium Matrix Composites", (eds. P. Smith and W. Revelos), WL-TR-92-4035, Air Force Wright Laboratory, Wright-Patterson AFB, OH 80 (1992)

5. S. A. Court, J. P. A. Lofvander, M. H. Loretto, and H. L. Fraser; *Phil. Mag. A*, 61, 109 (1990)

6. W. P. Hon, S. K. Wu, and C. H. Koo; *Mat. Sci. Eng.*, A131, 85 (1991)

7. C. G. Rhodes; in "Intermetallic Matrix Composites II", (eds. D. B. Miracle, D. L. Anton, and J. A. Graves), MRS Symp. Proc., Vol. 273, 17 (1992)

8. P. R. Smith, J. A. Graves, and C. G. Rhodes; in "Intermetallic Matrix Composites II", (eds. D. B. Miracle, D. L. Anton, and J. A. Graves), MRS Symp. Proc., Vol. 273, 43 (1992)

9. B. N. Cox, M. R. James, D. B. Marshall, and R. C. Addison, Jr.; *Metall. Trans.*, 21A, 2701 (1990)

10. M. L. Gambone and K. R. Bain; in "Proceedings of the 2nd International SAMPE Metals Conference", Volume 2, (eds. F. H. Froes and R. A. Cull), SAMPE, Covina CA 487 (1988)

11. D. B. Marshall, M. C. Shaw, and W. L. Morris; *Acta Metall. Mater.*, 40, 443 (1992)

12. S. J. Balsone; in "Oxidation of High Temperature Intermetallics", (eds. T. Grobstein and J. Doychak), TMS, Warrendale, PA 219 (1989)

13. S. M. Russ; *Metall. Trans.*, 21A, 1595 (1990)

14. W. C. Revelos and P. R. Smith; *Metall. Trans.*, 23A, 587 (1992)

15. P. K. Brindley, R. A. MacKay, and P. A. Bartolotta; in "Titanium Aluminide Composites", (eds. P. R. Smith, S. J. Balsone, and T. Nicholas), Air Force Wright Laboratory, WL-TR-91-4020, Wright-Patterson AFB, OH 484 (1991)

16. D. B. Miracle and M. Mendiratta; in "Intermetallic Compounds: Principles and Practice", (eds. J. H. Westbrook and R. L. Fleischer), John Wiley and Sons, New York, NY In Press

17. R. G. Rowe; *Advanced Materials and Processes*, 3, 33 (1992)

18. D. Banerjee, A. K. Gogia, T. K. Nandy, K. Muraleedharan, and R. S. Mishra; in "Structural Intermetallics", Proc. 1st Intl. Conf. on Structural Intermetallics, (eds. R. Darolia *et al..*), TMS, Warrendale, PA 19 (1993)

19. J. A. Graves, P. R. Smith, and C. G. Rhodes; in "Intermetallic Matrix Composites II", (eds. D. B. Miracle, D. L. Anton, and J. A. Graves), MRS Symp. Proc., Vol. 273, 31 (1992)

20. P. R. Smith, J. A. Graves, and C. G. Rhodes; in "Intermetallic Matrix Composites II", (eds. D. B. Miracle, D. L. Anton, and J. A. Graves), MRS Symp. Proc., Vol. 273, 43 (1992)

21. P. R. Smith, J. A. Graves, C. G. Rhodes, M. R. James, and J. R. Porter; in "Titanium Matrix Composites", (eds. P. R. Smith and W. C. Revelos), WL-TR-92-4035, Air Force Wright Laboratory, Wright-Patterson AFB, OH 115 (1992)

22. J. A. Graves, C. G. Rhodes, J. Hall, J. Chesnutt, and H. Lipsitt; in "Titanium Metal Matrix Composites II", (eds. P. R. Smith and W. C. Revelos), WL-TR-93-4105, Air Force Wright Laboratory, Wright-Patterson AFB, OH 6 (1993)

23. S. Krishnamurthy, P. R. Smith, and D. B. Miracle; in "Titanium Metal Matrix Composites II", (eds. P. R. Smith and W. C. Revelos), WL-TR-93-4105, Air Force Wright Laboratory, Wright-Patterson AFB, OH 59 (1993)

24. C. Rhodes, J. Graves, P. Smith, and M. James; in "Structural Intermetallics", Proc. 1st Intl. Conf. on Structural Intermetallics, (eds. R. Darolia et al..), TMS, Warrendale, PA 45 (1993)

25. P. R. Smith, J. A. Graves, and C. G. Rhodes; in "Structural Intermetallics", Proc. 1st Intl. Conf. on Structural Intermetallics, (eds. R. Darolia et al..), TMS, Warrendale, PA 765 (1993)

26. P. R. Smith, J. A. Graves, and C. G. Rhodes; Metall. Trans. A, in press

27. D. Banerjee, R. G. Rowe, and E. L. Hall; in "High Temperature Ordered Intermetallic Alloys IV", (eds. L. A. Johnson, D. P. Pope, and J. O. Stiegler), MRS Symp. Proc., Vol. 213, MRS, Pittsburgh, PA 285 (1991)

28. P. Smith; Unpublished Research, Air Force Wright Laboratory (1994)

29. P. Godavarti, M. Lipschutz, and M. Mendiratta; "Environmental Effects on Titanium Aluminides", WL-TR-92-4059, Air Force Wright Laboratory, Wright-Patterson AFB, OH (1992)

30. K. Williams; Unpublished Research, Air Force Wright Laboratory (1994)

31. Y.-W. Kim and D. Dimiduk; J. of Metals, 43, 40 (1991)

32. B. Majumdar; Unpublished Research, Air Force Wright Laboratory (1994)

33. C. G. Rhodes, J. A. Graves, D. B. Marshall, and Y. A. Chang; in "Titanium Metal Matrix Composites II", (eds. P. R. Smith and W. C. Revelos), WL-TR-93-4105, Air Force Wright Laboratory, Wright-Patterson AFB, OH 88 (1993)

34. C. G. Rhodes; in "Intermetallic Matrix Composites II", (eds. D. B. Miracle, D. L. Anton, and J. A. Graves), MRS Symp. Proc., Vol. 273, 17 (1992)

35. I. W. Hall; in "Thermal Stability of an SCS-6/Ti-22Al-23Nb Composite", Final Technical Report, University of Delaware, In Press

36. D. B. Marshall, W. L. Morris, B. N. Cox, J. Graves, J. R. Porter, D. Kouris, and R. Everett; in "Titanium Metal Matrix Composites II", (eds. P. R. Smith and W. C. Revelos), WL-TR-93-4105, Air Force Wright Laboratory, Wright-Patterson AFB, OH 291 (1993)

37. D. R. Schuyler, M. M. Sohi, R. L. Hollars, and J. D. Pugnale; in "Feasibility of Aluminide Meta Matrix Composites for 1400°F Application", Final Technical Report No. 21-7798, U.S. Navy, NADC (1991)

38. J. A. Graves, C. G. Rhodes, J. Chesnutt, and J. Hall; in "Advanced Ti-Based MMC Development", Interim Technical Report, WL-TR-93-4031, Air Force Wright Laboratory, Wright-Patterson AFB, OH (1993)

39. J. A. Graves, C. G. Rhodes, J. Chesnutt, and J. Hall; in "Advanced Ti-Based MMC Development", Interim Technical Report, WL-TR-93-4038, Air Force Wright Laboratory, Wright-Patterson AFB, OH (1993)

40. P.R. Subramanian, M. G. Mendiratta, and D. B. Miracle; Metall. Trans. A, In Press

41. M. L. Gambone; Unpublished Research, Air Force Wright Laboratory (1994)

42. V. Fry; Private Communication, Amercom (1994)

43. R. Lewis, S. Kraus, R. Loszewski, J. Henshaw, and T. Schoenberg; in "Titanium Metal Matrix Composites II", (eds. P. R. Smith and W. C. Revelos), WL-TR-93-4105, Air Force Wright Laboratory, Wright-Patterson AFB, OH 104 (1993)

44. R. Zordan (Allison Engine Company) and S. Kraus (Textron Specialty Materials), Unpublished Research (1994)

THE CONTRIBUTION OF MATRIX PLASTICITY TO THE "FRICTIONAL" SLIDING OF DEBONDED FIBERS IN SAPPHIRE-REINFORCED TiAl MATRIX COMPOSITES

J. M. GALBRAITH*, D. A. KOSS**, AND J. R. HELLMANN**
* Structures and Controls Division, Directorate of Space and Missiles Technology, Phillips Laboratory, Edwards AFB, CA 93524-7400
** Center for Advanced Materials, The Pennsylvania State University, University Park, PA 16802

ABSTRACT

Large-scale fiber displacement behavior, usually characterized by a "frictional" sliding stress (τ_{slide}), has been studied in two sapphire-reinforced TiAl systems. Experimental results from fiber pushout and reverse push-back tests indicate that the large-scale sliding behavior of debonded fibers leads to an average τ_{slide}-value which progressively decreases during fiber displacements. Previous studies of SCS-6 (SiC) fiber-reinforced glass and metal matrix composites have attributed decreases in τ_{slide} to the fracture and wear of fiber asperities. However, given a matrix in which fiber asperities do not easily wear (e.g., a TiAl alloy), SEM examination of the fiber/matrix interface indicates that matrix plasticity plays a dominant role in the decrease of τ_{slide} with fiber displacement. Experimental evidence suggests that the observed decrease in τ_{slide} can be attributed to (1) a decrease in fiber roughness perceived by the matrix due to matrix grooving and (2) a relaxation of radial clamping as a result of material removal from the interface.

INTRODUCTION

In an attempt to quantify the shear behavior of a fiber/matrix interface in brittle matrix composites, both mechanics and experimental approaches have separated the interfacial shear process into two distinct events: (1) interface debonding characterized by an average interfacial shear strength (τ_{AVG}) and (2) subsequent large-scale fiber displacement described by a "frictional" sliding stress (τ_{slide}) [1-3]. The term "frictional sliding stress" is commonly used to describe the interfacial shear stress that resists large-scale fiber displacement following complete fiber debond. For many metal and intermetallic matrix composites (MMCs and IMCs), however, the sliding stress may not be purely frictional, i.e., in order to accommodate asperities on the fiber surface, it must be of sufficient magnitude to plastically deform the matrix. Despite their tendency to be brittle in tension, many intermetallics may plastically deform on a localized level where stress states consist of large compressive and high equivalent stresses [4].

The "frictional" sliding of debonded fibers during monotonic and cyclic loading makes an important contribution to the toughening mechanisms of fiber pullout and crack-tip bridging in

ceramic and intermetallic matrix composites (CMCs and IMCs) [5-7]. Previous studies have addressed the importance of residual stress and fiber surface roughness to τ_{slide}, primarily in brittle matrix composites or MMCs with brittle layers at the fiber/matrix interface [5-14]. The purpose of this study is to examine the role that matrix plastic deformation can play in determining the magnitude of τ_{slide} during large-scale fiber displacement following complete fiber debond in a system where matrix plasticity is significant.

EXPERIMENTAL PROCEDURE

This study is based on low volume fraction fiber-reinforced matrices consisting of sapphire fibers (Saphikon) embedded in two different matrices based on the intermetallic TiAl: Ti-48Al-1V (hereafter referred to as Ti-48-1) and Ti-48Al-2Cr-2Nb (i.e., Ti-48-2-2) where compositions are given in atomic percent. Unidirectionally reinforced fiber composites were prepared via vacuum hot pressing pre-alloyed matrix powder and 160 μm (average) diameter fibers. The Ti-48-2-2 matrix material was consolidated by G. E. Aircraft Engines, Evendale, OH, and contained approximately 9 volume percent of uncoated sapphire fibers. A much lower volume fraction of sapphire reinforcement (0.1 volume percent) was produced for the Ti-48-1 material where both uncoated and tantalum-coated fibers were incorporated in the matrix. This material (i.e., Ti-48-1) was consolidated at Penn State as part of this study. The tantalum (Ta) coating (on fibers supplied by Pratt and Whitney, East Hartford, CT) was deposited via sputtering at Midwest Research Technologies, Milwaukee, WI with a coating thickness of ~0.2 μm.

Indentation fiber pushout and push-back tests were performed on thin-slice specimens ranging in thickness from 0.31 to 0.37 mm. Care was taken to align the fibers normal to the specimen surface. The specimen surface was ground flat and polished to a 1 μm diamond paste finish on nylon cloth. The tests were performed with an Instron universal test frame using a flat-bottomed tungsten carbide indenter (127 μm diameter for the 160 μm diameter fibers). Fibers were concentrically aligned over a 254 μm diameter support hole that was electro-discharge machined through a stainless steel support plate. Precise alignment of the fiber with the support hole was accomplished by observing fiber positioning in an inverted stage metallograph. Alignment of the indenter with the fiber end-face was achieved through the use of a precision x-y table and two 50x optical microscopes offset at ~90°. Load measurements were recorded every 0.1 seconds using a PC-based data acquisition system. Tests were done using a constant cross-head displacement rate of 50 μm/minute.

Two types of tests were performed using the indentation test apparatus. First, tests were performed in which the fiber was loaded, debonded, and displaced out of the matrix by as much as 120 μm. This was done in order to assess the general interfacial failure (e.g., maximum load, load-drop following fiber/matrix debond, etc.) and fiber sliding behavior. Other tests were performed in which an initially debonded and displaced fiber was subsequently pushed back beyond its original position (i.e., the "origin") to characterize fiber sliding and interfacial wear/degradation behavior.

144

RESULTS AND DISCUSSION

Figure 1 shows typical load versus cross-head displacement responses recorded during fiber pushout testing of a 0.35 mm thick Ta-coated sapphire/Ti-48-1 specimen and a 0.31 mm thick sapphire/Ti-48-2-2 specimen. Based on scanning electron microscope (SEM) examination and scanning laser microscope (SLM) fiber displacement measurements, a previous analysis [15] has divided the interfacial failure sequence into five regions as shown: (1) elastic loading of the specimen (Region 1); (2) initiation and growth of a mixed-mode I/II circumferential interface crack at the specimen's backface, opposite the indenter (Region 2); (3) small-scale (i.e., ≤ 2 μm) displacement of the entire fiber under increasing loads (Region 3); (4) large-scale fiber displacement accompanied by a load-drop (Region 4); and (5) "frictional" sliding of the debonded

(a)

(b)
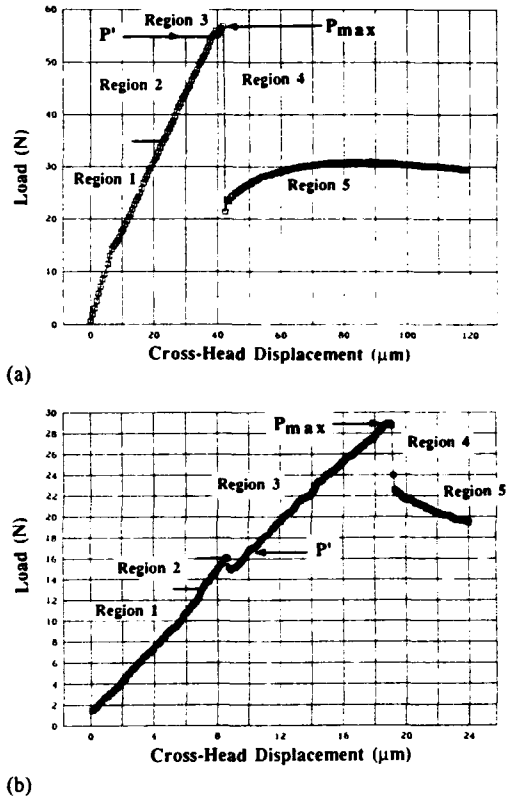
Figure 1. Typical load-displacement behavior of the (a) Ta-coated sapphire/Ti-48Al-1V and (b) sapphire/Ti-48Al-2Cr-2Nb systems during fiber pushout testing.

fiber (Region 5). The present research examines Region 5 "frictional" sliding of debonded fibers in Ta-coated sapphire/Ti-48-1 and sapphire/Ti-48-2-2 systems.

Even though the interfacial failure sequences that lead to complete fiber debond (usually accompanied by a load-drop and large-scale displacement of the fiber from the matrix) are markedly different in these two composite systems (as shown in Figure 1 and Table I), the large-scale "frictional" sliding behavior of debonded fibers during pushout (i.e., Region 5) and reverse push-back is similar. In both systems, the average fiber sliding stress (τ_{slide}) at the initiation of large-scale sliding was found to be ~160 MPa (from 6 tests) immediately following load-drop, i.e., note the similar indenter loads after the load-drops shown in Figure 1. Unlike previous studies examining the sliding behavior of carbon-coated sapphire fibers in a TiAl matrix [10, 13], no fiber surface roughness-induced sinusoidal modulations in the load-displacement plots were observed.

Typical fiber sliding behavior during pushout and reverse push-back tests is shown in Figure 2. As during initial pushout, fiber surface roughness-induced sinusoidal modulations in the reverse pushout curve [13] were not observed here. In order to account for the continuous change in interfacial area during large-scale fiber displacement, the interfacial shear stress (i.e., indenter load

Table I. Summary of the thin-slice fiber pushout test results for the Ta-coated sapphire/Ti-48Al-1V and sapphire/Ti-48Al-2Cr-2Nb systems. In all cases, ± one standard deviation is reported for 3 to 7 tests.

System	τ_{AVG} @ P_{max}	τ_{slide}
Ta-coated sapphire/Ti-48Al-1V	336±11 MPa	173±58 MPa
Sapphire/Ti-48Al-2Cr-2Nb	170±22 MPa	146±10 MPa
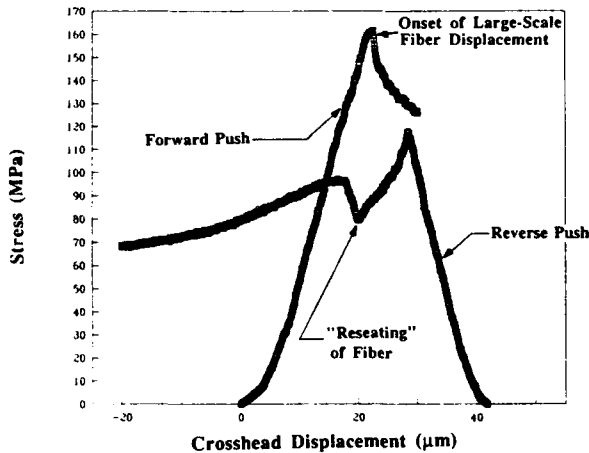
Figure 2. Typical fiber sliding behavior during pushout and reverse push-back tests of a sapphire/Ti-48Al-2Cr-2Nb specimen. In order to account for the continuous change in interfacial area during large-scale fiber displacement, interfacial shear stress is plotted as a function of cross-head displacement.

146

divided by the instantaneous interfacial area) is plotted as a function of cross-head displacement in Figure 2 for a sapphire/Ti-48-2-2 specimen. An examination of the sliding stress response during forward pushout reveals that, following complete fiber debond (which signals the onset of large-scale fiber displacement), τ_{slide} decreases rapidly with increasing fiber displacement. If the specimen is unloaded and then reloaded in the reverse direction, the stress increases until fiber displacement resumes, at which load τ_{slide} again decreases with increasing fiber displacement until the fiber reaches its original position prior to debonding, i.e., see Figure 2.

Liang and Hutchinson [3] analyzed fiber sliding using a generalized sliding law where they combined the cases of constant friction and Coulomb friction from results in an earlier paper by Hutchinson and Jensen [2]:

$$\tau_{slide} = \tau_0 - \mu\sigma_{rr}, \tag{1}$$

where τ_0 is a constant friction term, μ is the friction coefficient, and σ_{rr} is the radial clamping stress acting across the sliding fiber/matrix interface. Mackin et al. [10] suggested that the constant friction term, τ_0, is the sliding stress that would be experienced by the fiber if $\sigma_{rr} = 0$. For example, τ_0 may be governed by the surface roughness of the fiber, such as that addressed by Jero and Kerans [8, 9]. Furthermore, the sliding stress is not usually constant because of fiber asperity effects and wear processes, especially when a brittle matrix or brittle layer at the fiber/matrix interface is present [10, 12, 13]. Thus, previous results based on carbon-coated sapphire in TiAl could be interpreted primarily on the basis of elastic-based analyses [10, 12, 13].

By considering equation (1), a decrease in τ_{slide} may be explained in terms of a decrease in the constant friction term (τ_0) or the radial clamping stress (σ_{rr}) or both. In previous studies of fiber-reinforced metal and intermetallic matrix composites [7, 10-13], the observed decrease in τ_{slide} during continued fiber displacement was accounted for by a decrease in τ_0 and σ_{rr} due to the fracture and wear of the outer carbon coatings on either the SCS-6 or sapphire fibers. (One exception was proposed by Mackin et al. [10, 11], who suggested that matrix plasticity may account for a reduction in radial clamping during pushout testing of a SiC/β-Ti system. However, they gave no explanation of how this may occur.)

In the sapphire/TiAl system without a carbon fiber coating, where fiber roughness/asperities will not "wear" as readily and there are not brittle carbon layers to wear, it is suggested that matrix plasticity plays a dominant role in the observed decrease in τ_{slide}. For example, a decrease in the constant friction term (τ_0) may occur by wide-spread grooving of the matrix wall during continued fiber displacement, such as is shown in Figure 3, and not by fiber asperity wear. Thus, during continued fiber displacement, the fiber roughness perceived by the matrix decreases as the deformation-induced grooving increases. This effect should be most pronounced when the fiber is pushed-back in the reverse direction up to the initial position of the fiber prior to debonding. In this case, the asperities are accommodated in the grooves formed during the forward push. As a result, the stress required to resume fiber displacement in the reverse direction is smaller than the sliding stress measured when the forward pushout test was stopped (i.e., see Figure 2).

Matrix plastic deformation during large-scale fiber displacement may also give rise to the relaxation of radial clamping on the fiber; this would affect the second term in equation (1). In order to relieve fiber/matrix misfit strain and to decrease σ_{rr}, material must be removed from the interface [11]. By adapting the elasticity solution for internal pressure within a cylinder, Kantzos [16] used the following expression to calculate the thickness (t') of a concentric cylinder of

147
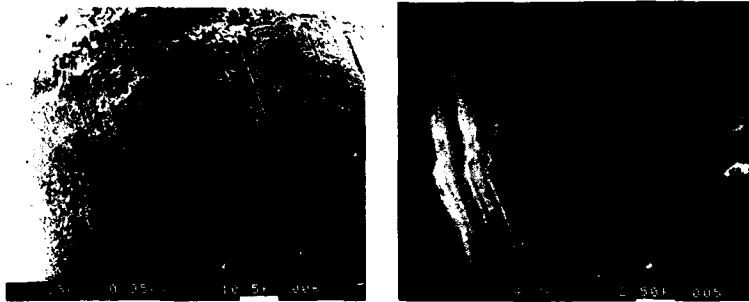
(a)   (b)

Figure 3   Evidence that large-scale fiber displacement requires localized matrix plasticity in the
form of grooves to accommodate asperities on the fiber surface   SEM micrographs of
the matrix wall in (a) a Ta-coated sapphire/Ti-48Al-1V specimen following fiber
pushout testing and (b) a sapphire Ti-48Al-2Cr-2Nb specimen following fiber pushout
and push-back testing

material that must be removed from around the fiber in order to fully relax the residual radial
clamping stress (σ_{rr})

$$ t' \approx \sigma \cdot \frac{R(1+v^m)}{E^m} \left[V_f \cdot \left(\frac{1-v^m}{1+v^m} \right) \atop V_f^{-1} - 1 \right] $$ (2)

where R is the fiber's radius. V_f is the fiber volume fraction. v^m is the Poisson's ratio of the
matrix. and E^m is the matrix's elastic modulus   By substituting the appropriate values for the
sapphire Ti-Al system into equation (2) and solving for t', this solution predicts that only a 0 10 to
0 12 μm thick concentric cylinder of matrix material must be removed from the interface in order
to fully relax radial clamping on the fiber

Evidence that matrix material is removed from the interface during reverse push-back testing is
clearly shown in Figure 3b   This figure reveals that, as the fiber is pushed back in the reverse
direction, matrix material is plowed-out in front of it, analogous to material plowed-out in front of
a cutting tool in a machining operation   Furthermore, close examination of Figure 3b shows that
the continuous ribbons of material plowed-out of the Ti-48-2-2 matrix are at least 0 1 μm thick
Thus, at least some of the measured decrease in τ_{slide} during reverse push-back testing can be
directly related to the resulting relaxation of radial clamping on the fiber   However, it is

148

questionable that such a contribution to a decrease in frictional sliding could occur along a continuous fiber bridging a fatigue crack, for example.

Another distinctive feature of the stress versus cross-head displacement response during the reverse push-back test shown in Figure 2 is the abrupt stress increase that occurs after "fiber reseating", i.e., as the fiber is pushed back beyond its original position (i.e., the "origin") [8]. In CMCs, fiber reseating is manifested by a distinct load (or stress) drop, which occurs as rough surfaces mate [8, 9]. This occurs when the fiber is pushed back to its original position, the fiber and matrix surface topographies mesh, and the additional sliding friction associated with their misfit disappears, resulting in a load drop in the load-displacement response [8].

In the present case, the matrix deforms elastically and plastically during fiber sliding. Specifically, the matrix deforms to create grooves to accommodate asperities on the fiber surface during large-scale fiber displacement. When the fiber is pushed back to its original position, the asperities on the fiber surface, which had been accommodated in the grooves formed during the forward push, must now form new grooves in the matrix in order for continued fiber displacement to occur. Thus, as shown in Figure 2, fiber reseating is manifested by a temporary pause in fiber displacement as the interfacial shear stress increases to the magnitude required to form new grooves in the matrix. By comparing the slope of the stress versus displacement plot at fiber reseating with that before large-scale fiber displacement resumes during the reverse push, it is evident that fiber displacement temporarily stops at the fiber's origin until sufficient stress is applied to re-initiate the grooving operation.

Finally, although not shown here, it was found that with increasing amounts of fiber displacement during forward pushout, the load increase at fiber reseating decreases. In fact, for fibers that undergo displacements >120 μm during the forward push, evidence of fiber reseating disappears. The same explanation given for the decrease in the constant friction term (τ_o) during continued fiber displacement may account for these observations. Thus, we speculate that fiber-induced grooving of the matrix becomes more wide-spread as fiber displacement increases. Thus, after large fiber displacements during the forward push, so much deformation-induced grooving of the matrix occurs that the fiber roughness perceived by the matrix becomes negligible. As a result, little or no additional stress is required for the fiber to be pushed back beyond its original position. Similar behavior during reverse push-back tests of a SiC-reinforced β-Ti composite has been reported by Mackin [18] for fibers displaced >60 μm during the forward push and Warren et al. [11] for specimens previously subjected to cyclic fatigue.

SUMMARY

Results from fiber pushout and reverse push-back tests were used to address the contribution of matrix plasticity to the "frictional" sliding resistance of debonded fibers and its role in interface wear/degradation. It was found that the large-scale displacement behavior of debonded fibers was similar in both composite systems and resulted in "frictional" sliding stress (i.e., τ_{slide}) values of ~160 MPa immediately following load-drop; these subsequently decreased to values ranging from 50 to 80 MPa following fiber displacements totaling ~180 μm. Previous studies have attributed the decrease in τ_{slide} after reverse sliding to the fracture and wear of fiber asperities [7, 10-12]. However, given the present sapphire/TiAl system in which fiber asperities do not easily wear, it is suggested that matrix plasticity plays a dominant role in the decrease of τ_{slide} with fiber

149

displacement. Experimental evidence suggests that the observed decrease in τ_{slide} can be attributed to (1) a decrease in fiber roughness perceived by the matrix due to wide-spread matrix grooving and (2) a relaxation of radial clamping as a result of material removal from the interface.

ACKNOWLEDGEMENTS

REFERENCES

1. A. G. Evans, F. W. Zok, and J. Davis, Composites Sci. and Tech. **42**, 3-24 (1991).

2. J. W. Hutchinson and H. M. Jensen, Mech. Mater. **9**, 139-163 (1990).

3. C. Liang and J. W. Hutchinson, Harvard University, 1992 (to be published).

4. D. A. Koss, M. N. Kallas, and J. R. Hellmann in Intermetallic Matrix Composites II, edited by D. B. Miracle, D. L. Anton, and J. A. Graves (Mater. Res. Soc. Proc. **273**, Pittsburgh, PA, 1992) pp. 303-313.

5. L. S. Sigl and A. G. Evans, Mech. Mater. **8**, 1-12 (1989).

6. A. G. Evans and R. M. McMeeking, Acta Metall. Mater. **34**, 2435-2441 (1986).

7. P. T. Kantzos, J. I. Eldridge, D. A. Koss, and L. J. Ghosn in Intermetallic Matrix Composites II, edited by D. B. Miracle, D. L. Anton, and J. A. Graves (Mater. Res. Soc. Proc. **273**, Pittsburgh, PA, 1992) pp. 135-142.

8. P. D. Jero and R. J. Kerans, Scripta Metall. Mater. **24** (12), 2315-2318 (1990).

9. P. D. Jero, R. J. Kerans, and T. A. Parthasarathy, J. Am. Ceram. Soc. **74** (11), 2793-2801 (1991).

10. T. J. Mackin, P. D. Warren, and A. G. Evans, Acta Metall. Mater. **40** (6), 1251-1257 (1992).

11. P. D. Warren, T. J. Mackin, and A. G. Evans, Acta Metall. Mater. **40** (6), 1243-1249 (1992).

12. T. J. Mackin, J. Y. Yang, and P. D. Warren, J. Am. Ceram. Soc. **75** (12), 3358-3362 (1992).

13. T. J. Mackin, J. Y. Yang, C. G. Levi, and A. G. Evans, Mat. Sci. and Eng. **A161**, 258-293 (1993).

14. J. I. Eldridge in <u>Intermetallic Matrix Composites II</u>, edited by D. B. Miracle, D. L. Anton, and J. A. Graves (Mater. Res. Soc. Proc. **273**, Pittsburgh, PA, 1992) pp. 325-330.

15. J. M. Galbraith, <u>Interfacial Shear Behavior and Its Influence on Fiber Damage in Sapphire-Reinforced Gamma Titanium Aluminide Composites</u>, Ph.D. Thesis, The Pennsylvania State University, 1993.

16. P. T. Kantzos, <u>Fatigue Crack Growth and Crack Bridging in Ti-Based Metal Matrix Composites</u>, M. S. Thesis, The Pennsylvania State University, 1991.

17. R. J. Kerans and T. A. Parthasarathy, J. Am. Ceram. Soc. **74** (7), 1585-1596 (1991).

18. T. J. Mackin, University of California, 1992 (private communication).

151

Fracture and Fatigue Resistance of Ag/Ta-coated
SCS-6/Ti₃Al Composites

Hsing-Pang Chiu and J.-M. Yang
Department of Materials Science and Engineering,
University of California, Los Angeles
Los Angeles, CA 90024

ABSTRACT

The effect of a Ag/Ta coating on the fracture resistance of a notched SCS-6 fiber-reinforced Ti₃Al matrix composite under both static and fatigue loading was investigated. The crack propagation patterns and damage mechanisms under various loading conditions were characterized and compared with the uncoated composite counterparts. The results show that the Ag/Ta-coated composites exhibit typical mode-I failure patterns under both static and fatigue loading, while mixed mode-I & II failure patterns were observed in the uncoated SCS-6/Ti-25-10 composite. Localized interfacial debonding, matrix cracking and fiber fracture in the crack wake were the responsible damage mechanisms for the Ag/Ta-coated SCS-6/Ti-25-10 composite. Extensive interfacial debonding, crack splitting and branching, however, were found to be the dominant mechanisms in the uncoated SCS-6/Ti-25-10 composite.

INTRODUCTION

SiC fiber-reinforced titanium aluminide matrix composites are the most promising engineering materials for high temperature aerospace structural applications. However, the high reactivity and large mismatch in the coefficients of thermal expansion (CTE) between the fiber and matrix will induce both brittle interfacial reaction zone as well as significant residual tensile stresses [1]. The combined effect will lead to premature interfacial and matrix microcracking. Fiber coatings have been shown to be the most effective approach to resolve these critical issues [2]. Recently, a Ag/Ta duplex fiber coating has been successfully used to improve the chemical and physical compatibility between SiC fibers and Ti₃Al matrices [3]. The Ag/Ta coating has shown to improve the tensile and flexural creep resistance under longitudinal and transverse loading, mostly due to its ability to eliminate the brittle reaction products as well as to create a ductile β-Ti rich layer adjacent to the fiber [4,5].

The purpose of this work is to study the fracture characteristics of both Ag/Ta-coated and uncoated SCS-6 fiber-reinforced titanium aluminide matrix composites under static and fatigue loading. Particular emphasis will be placed upon the effect of interfacial morphology on damage progression.

MATERIALS AND EXPERIMENTAL PROCEDURES

Ag/Ta-coated and uncoated SCS-6/Ti-25-10 (Ti-25at%Al-10at%Nb-3at%V-1at%Mo) composites were used in this study. The matrix is an alloy with $\alpha_2 + \beta$ structure which has limited ductility at ambient temperatures. The Ag/Ta layer was coated onto the fiber via PVD with initial thicknesses of 2 and 5 μm, respectively. 4-ply unidirectional composites containing

approximately 33% of either coated or uncoated fibers were fabricated by the foil/fiber/foil route and consolidated using the vacuum diffusion bonding technique.

Specimens for three-point bending were cut into 50 x 5 x 1 mm with fibers parallel to the longitudinal direction. A single-edge chevron notch was prepared with a/w ratios ranging from 1/5 to 2/5, where a is the notch length and w is the specimen width. A critical load P_c was identified by the first discontinuous point in the load-deflection curve. P_c has also been shown to correspond to the occurrence of the first fiber breakage [6]. The fracture toughness was calculated using a formula based on linear elastic fracture mechanics [7] :

$$K_c = (P_c S/tw^{1.5})*(2.9(a/w)^{0.5} - 4.6(a/w)^{1.5} + 21.8(a/w)^{2.5} - 37.6(a/w)^{3.5} + 38.7(a/w)^{4.5}) \qquad (1)$$

where S is the span length, and t is the thickness of the specimen.

Fatigue specimens with a single-edge notch, a/w = 1/5, were prepared with fibers parallel to the loading direction. Fatigue crack propagation tests were conducted in the tension-tension mode under load-control at a frequency of 20 Hz, and stress ratio R (= $\sigma_{min}/\sigma_{max}$) equal to 0.1. The gauge length was kept as 50 mm. The maximum applied stress intensity factor was calculated using [7] :

$$K_1 = Yw^{0.5}\sigma_{max} \qquad (2)$$

where

$$Y = 1.99(a/w)^{0.5} - 0.41(a/w)^{1.5} + 18.7(a/w)^{2.5} - 38.48(a/w)^{3.5} + 53.85(a/w)^{4.5}$$

The crack propagation patterns and growth length were measured using a 250X optical microscope. All tested specimens were metallographically examined using optical and scanning electron microscopes to elucidate the responsible damage mechanisms under each loading condition.

RESULTS AND DISCUSSIONS

Fracture Resistance Under Static Loading

Figs. 1(a) and 1(b) show the crack propagation patterns under three-point bending for Ag/Ta-coated and uncoated composites. For the Ag/Ta-coated composite, the crack path is nearly perpendicular to the fiber direction, exhibiting a typical mode-I failure pattern. Little or no interfacial debonding was found near the crack tip. Fiber breakage is also confined to the vicinity of the crack path. It indicates that the high interfacial bond strength (140 MPa [8]) prevented the fiber/matrix interface closest to the notch tip from debonding extensively. The stress builds up at the notch tip, leading to fiber fracture and subsequent matrix cracking. This results in a self-similar crack propagation pattern. For the uncoated composite, the crack propagation is more wavy, with the first fiber breakage occurred at approximately 45° to the notch tip. Meanwhile, the closest interface ahead of the notch tip was found to be heavily debonded. The crack was seen to deflect along the debonded interface (mode-II). At some distance away from the notch plane, the crack was again seen to propagate perpendicular to the fiber direction (mode-I). The above observation shows that the extensive interfacial debonding ahead of the notch tip was the first damage event, due to its lower interfacial bond strength (115 MPa [8]). Upon further loading, the crack deflected along the debonded interface until fiber fractured at some distance away from the notch plane. After the fiber breakage, the load will be immediately transferred to the neighboring matrix, resulting in subsequent matrix cracking. Due to the statistical nature of fiber strength, the subsequent fibers will fail randomly above and below the notch plane, forming a wavy crack path.

154

The fracture toughness, K_{IC}, was determined to be 45 and 65 MPa-m$^{1/2}$ for Ag/Ta-coated and uncoated SCS-6/Ti-25-10 composites, respectively. The higher K_{IC} value for the uncoated composite is related to the significant interfacial debonding which provides additional toughening mechanisms to resist the crack growth.

(a)   (b)
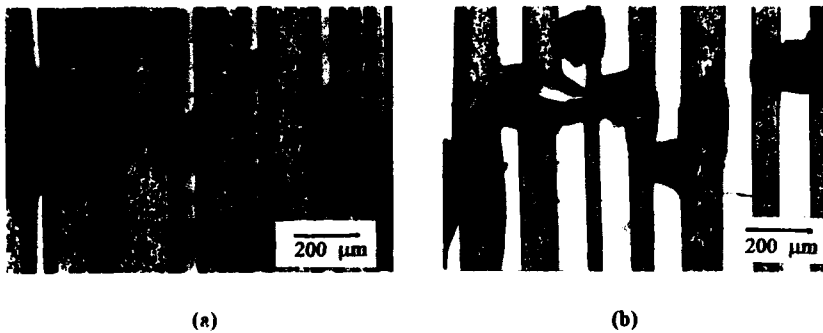
Fig.1 Crack Propagation pattern under three-point bending for
(a) Ag/Ta-coated, (b) uncoated SCS-6/Ti-25-10 composites.

Fatigue Crack Propagation Behavior

Typical crack propagation lengths vs. fatigue cycles for the Ag/Ta-coated and uncoated SCS-6/Ti-25-10 composite are plotted in Fig.2. Two tests were performed at each loading condition. The results of the second test were similar to the first one. It is found that the transition from "run-out" (fiber bridging) to "catastrophic failure" occurs within a very narrow range of stress intensity levels. It also shows that the uncoated composites exhibit better fatigue fracture resistance than the Ag/Ta-coated composites. *In-situ* observation of the Ag/Ta-coated composites indicates that only one primary crack initiated from the notch tip and propagated normal to the fiber direction, exhibiting a typical mode-I behavior. *Localized interfacial debonding was evident near the crack wake*. The debonding was found to be mostly along the Ag/outer carbon layer interface, but also occurred within the outer carbon and Ag layers. Also, only one through crack was formed within the interfacial β-Ti layer. As the crack entered the dual $\alpha_2 + \beta$ phase region, it bifurcated and propagated either along the α_2/β grain boundaries or through the α_2 grains, as shown in Fig.3. As this process continued, the crack was found to propagate exclusively in the matrix, leaving behind intact fibers bridging the crack path, and eventually the crack was arrested. However, if $K_1 = 39$ MPa-m$^{1/2}$ or above, the stress concentration is high enough to cause the fiber fracture and results in a "cut-through" failure. The fracture morphology, Fig.4, shows a flat surface with little or no fiber pull-out. Typical brittle transgranular matrix failure was also evident. Interfacial debonding, fiber breakage and matrix cracking was confined exclusively near the fracture plane. The transition from "fiber bridging" to "catastrophic failure" has been shown to be due to the first fiber breakage in the wake of the crack [9].
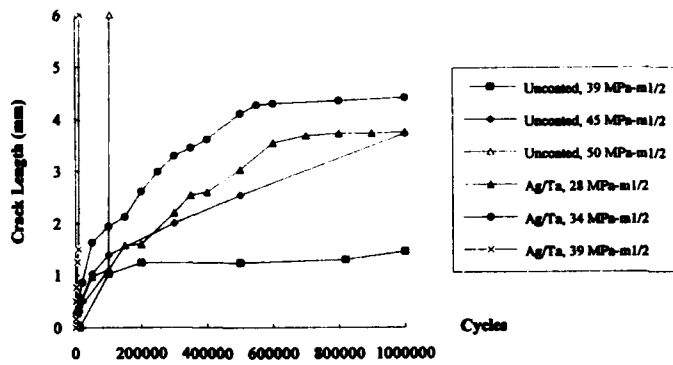
Fig.2 The crack lengths vs. fatigue cycles for Ag/Ta-coated and uncoated composites.

Fig.3 The crack propagation near the interface of Ag/Ta-coated SCS-6/Ti-25-10 composite.
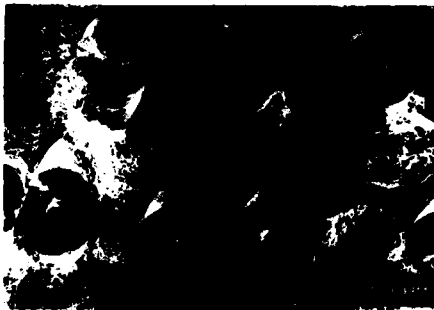
Fig.4 Fracture surface of Ag/Ta-coated SCS-6/Ti-25-10 composite.

156

For the uncoated SCS-6/Ti-25-10 composite, the crack propagation pattern is distinctly different. Originally one primary crack was formed from the notch tip. Extensive interfacial debonding was obvious, causing the crack to deflect along the debonded interface. Random fiber breakage is observed at some distance away from the notch plane. Multiple cracks were found to emanate from these locations, leading to both "crack splitting" and "crack branching", as shown in Fig.5. This failure phenomenon is a mixed pattern of mode-I and II failure. At higher K_i, the fracture surface, Fig.6, exhibits a multi-plane, step-like morphology with extensive fiber pull-out.
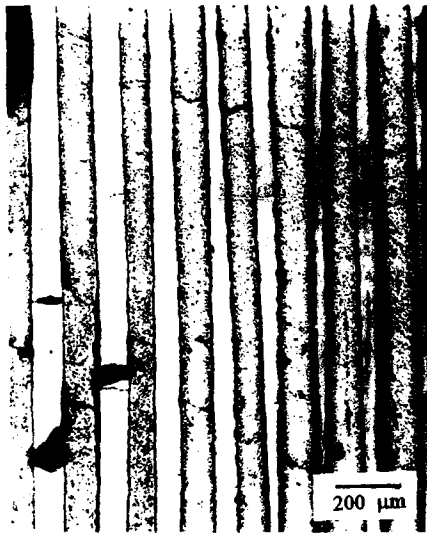
Fig. 5 Crack splitting and branching of uncoated SCS-6/Ti-25-10 composite.

Fig.6 Fracture surface of uncoated SCS-6/Ti-25-10 composite.

The preliminary observations indicate that the crack propagation pattern and damage mechanisms of the Ag/Ta-coated and uncoated SCS-6/Ti-25-10 composites are different. For the Ag/Ta-coated SCS-6/Ti-25-10 composite, the higher interfacial bond strength appears to prevent the extensive interfacial debonding along the longitudinal direction, and therefore confines the crack propagation along the notch plane. This leads to a pure mode-I crack propagation behavior. The uncoated SCS-6/Ti-25-10 composite, on the other hand, shows extensive interfacial debonding and phenomena such as crack splitting and branching, leading to a mixed mode-I&II behavior. However, with only two data points per each loading condition, more experiments will be needed to confirm the above argument.

SUMMARY AND CONCLUSIONS

The Ag/Ta coating improves the transverse tensile, flexural and creep resistance properties of the SCS-6/Ti-25-10 composite. However, on the other hand, it appears to change the fracture mode from mixed mode-I&II to pure mode-I under both static and fatigue loading, and consequently decreases the fracture resistance as compared with uncoated composite. More extensive studies are needed to further clarify the above observation. Factors other than interfacial bond strength and interfacial morphology should also be taken into consideration. Finally, with the example of Ag/Ta coating, it appears that a balanced interfacial property is needed to optimize the overall composite properties.

ACKNOWLEDGMENTS

REFERENCES

1. J.-M. Yang and S. M. Jeng, JOM, November, 56 (1989).
2. T. W. Clyne and M. C. Watson, Comp. Sci. & Tech., 42, 25 (1991).
3. Hsing-Pang Chiu, S. M. Jeng and J.-M. Yang, J. Mater. Res. 8(8), 2040 (1993).
4. Hsing-Pang Chiu, J.-M. Yang, and J. A. Graves, J. Mater. Res. 9(1), 198 (1994).
5. D. B. Marshall, W. L. Morris, B. N. Cox, J. A. Graves, J. R. Porter, D. Kouris and R. Everett, to be published in Acta. Metall. Mater. (1994)
6. Hsing-Pang Chiu, S. M. Jeng and J.-M. Yang, to be published in J. Mater. Res. (1994)
7. D. Broek, _Elementary Engineering Fracture Mechanics_, 4th revised ed., (Martinus Nijhoff Publishers, Dordrecht, 1986), p. 85.
8. S. M. Jeng, J.-M. Yang and J. A. Graves, J. Mater. Res. 8(4), 905 (1993).
9. S. M. Jeng, P. Alssoeur and J.-M. Yang, Mater. Sci. & Eng., A154, 11 (1992).

ADDITIVITY OF DIRECT AND INDIRECT STRENGTHENING IN
TiB2-REINFORCED NEAR-γ TITANIUM ALUMINIDES

S.L. Kampe*, P. Sadler**, L. Christodoulou***, and D.E. Larsen****
*   Virginia Polytechnic Institute and State University, Blacksburg, Virginia 24061-0237
**   Martin Marietta Laboratories, 1450 S. Rolling Road, Baltimore, MD 21227
*** BDM, International, 4001 N. Fairfax Dr., Arlington, Virginia 22203
**** Howmet Corporation, 1500 S. Warner St., Whitehall, MI 49461

ABSTRACT

An experimentally-based description of strengthening in a series of TiB2-reinforced near-γ titanium aluminides is presented. The analysis provides a means to examine the strengthening contributions which are individually attributable to compositional variants, to indirect sources which are present due to the influence of the particulate on the underlying microstructure, and to those directly evolving from the presence of the reinforcement and its interaction with dislocations. Once the indirect strengthening contributions are isolated and arithmetically removed from the magnitude of the experimentally determined composite strength, the resulting direct strengthening increments are found to obey a linear relationship with the inverse-square-root of the edge-to-edge interparticle spacing. The description of the dependence on spacing is found to be compatible with other studies where similar relationships have been reported.

INTRODUCTION

INTERMETALLIC MATRIX COMPOSITES reinforced with discontinuous particulate or fiber offer the important technological and economic advantage of being generally processable by conventional metallurgical means. For example, composites can be produced by conventional investment casting strategies [1, 2], or by traditional thermomechanical means such as isothermal forging or extrusion [3]. As applied conventionally to monolithic materials, these processes will generally lead to distinct microstructures which are, to some extent, characteristic of the specific process employed. However, when these processes are extended to include microstructures which contain a non-deforming, dispersed reinforcing phase (i.e., composites), dramatically-dissimilar microstructures will generally result; the origin of the dissimilarities is obviously related to the presence of the dispersed phase and its influence on the microstructure which evolves during processing.

It is likely that the microstructural features that are characteristic of a processed composite, relative to those of its monolithic counterpart to which it is often directly compared, will exert influence on its resulting mechanical properties and stability. Microstructural features that are not common to those observed in similarly processed unreinforced matrix compositions will hence create an additional component of strengthening, relative to that measured in the reference alloy, attributable to the microstructural changes which have occurred due to the presence of the particulate. Examples of these microstructurally-induced indirect strengthening contributions in composites would include those due to a general refinement of grain size and substructure stabilization; in addition, partial dissolution of the reinforcing phase can lead to an additional increment of solid solution strengthening, modifications to the deformability of the matrix, or phase constituency changes within the matrix.

This study examines the role of the underlying microstructure on the strength of a series of investment-cast near-γ titanium aluminide composites. Magnitudes of the indirect strengthening contributions arising from the microstructural influences of the particulate during processing are estimated. Once an assessment of the indirect strengthening contributions is made, strengthening directly attributable to the particulate is assessed.

EXPERIMENTAL PROCEDURE

Matrix compositions of Ti-47Al-2Mn-2V, Ti-47Al-2Mn-2Cr, and Ti-47Al-2Mn-2V-2Cr were reinforced with TiB_2 in the form of particulate at volume percentages (v%) of 0, 7, and 12 percent. The TiB_2 was introduced by way of XD® processing (Martin Marietta Laboratories, Baltimore, MD) into a vacuum arc remelt (VAR) ingot which was subsequently remelted and investment cast (Howmet Corporation, Whitehall, MI) into 16 mm diameter by 150 mm length cylindrical test bars. The bars were hot isostatically pressed (HIP'd; 1260°C/172 MPa/4 h) and subsequently vacuum-encapsulated in quartz tubing and heat treated using conditions of either 900°C/16h, 900°C/50 h, or 1100°C/16h. Cylindrical tensile specimens of diameter 5 mm and a gauge length of 25 mm were subsequently machined from the core of the as-cast bars. Tensile tests were performed at an initial strain rate of 1×10^{-4} s^{-1}. Quantitative optical microscopy was performed using standard techniques.

RESULTS AND DISCUSSION

Example microstructures for one of the three composite compositions examined given one of the three heat treatments utilized (in this instance, Ti-47Al-2Mn-2Cr heat treated at 900°C for 16 hours) is shown in Fig. 1. Given identical processing, the microstructure of the unreinforced reference alloy (Fig. 1a) is shown to be dramatically dissimilar relative to that which is characteristic of the composite variants (Figs. 1b and 1c), especially as discerned from the large difference in grain size and grain size-distribution. The TiB_2 present in the composites is distributed uniformly throughout the interiors of the two phase α_2-Ti_3Al+γ-TiAl matrix grains. Depending upon the matrix composition within which they reside, the average measured TiB_2 diameter varies from approximately 1.8 to 2.6 μm.

The 0.2% plastic offset stress for each matrix alloy, heat treatment, and volume percentage of TiB_2 is shown in Fig. 2. Though compositionally-similar, each unreinforced variant (0 v%) is characterized by a unique value of offset stress. As shown by data for the Ti-47Al-2Mn-2Cr and Ti-47Al-2Mn-2V-2Cr matrices, the strengths attained by the composite variants rely in part upon the strengths of the underlying matrices. This suggests that the strengthening imparted by the TiB_2 is additive to the inherent strength of the matrix within which it resides. Also notable from Fig. 2 is that the magnitude of the response to increasing TiB_2 percentage (i.e., the slopes) can vary with matrix composition, as evidenced by the data for Ti-47Al-2Mn-2V when compared to that for other matrix compositions.
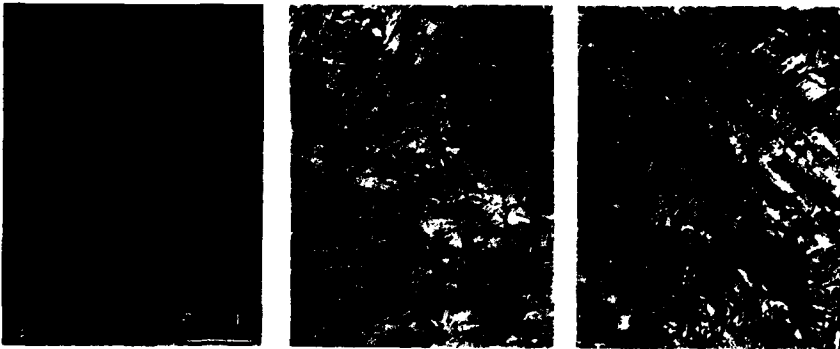
Figure 1. Example microstructures as exhibited by Ti-47Al-2Mn-2Cr heat treated at 900°C for 16 h: a) unreinforced (reference), b) with 7 v% TiB_2, and c) with 12 v% TiB_2.

Figure 3 illustrates the offset stress of Fig. 2, but normalized with respect to the magnitude of the offset stress of the appropriate reference alloy. The normalization provides a means to compare the relative strengthening capability of the TiB$_2$ among the range of matrix compositions and reference stresses inherent to each. As shown for each heat treatment, the normalized offset stress tends to fall along two distinct lines. Matrix compositions containing chromium are observed to fall along the lower lines, whereas the non-chromium containing composition yields the data comprising the upper curve.

Figure 4 shows, in this instance for the Ti-47Al-2Mn-2V matrix composition, that heat treatment has the overall effect of displacing the offset stress of the composite vertically, that is, to higher or lower values. The change in strength occurs with little or no change in the magnitude of the response (i.e., slope) to increasing TiB$_2$ percentages. Since the stability of TiB$_2$ in near-γ titanium aluminides has been established to be essentially kinetically-absolute [4, 5], the change in offset stress must therefore be the consequence of changes occurring in the matrix only, i.e., such as modifications in the proportions of α_2/γ, to differences in the amount of reinforcement-derived interstitial boron, to changes in the matrix grain size, or to modifications in the deformation behavior of the matrix due to any of the above. Each of the aforementioned effects can be sensitive to the nature of the heat treatment employed, and can be also indirectly related to the presence of TiB$_2$ in the titanium aluminide matrix.

The results of the above can be understood if the strengthening contributions in these composites are categorized according to the following additive strengthening relationship:

$$\sigma_c = \sigma_o + \Delta\sigma_i + \Delta\sigma_p \tag{1}$$

where σ_c = strength of the composite

σ_o = strength of the reference alloy, given identical processing to that of the composite

$\Delta\sigma_i$ = strength increment due to the indirect contributions arising from microstructural features present due to the presence of the dispersed phase during processing

and $\Delta\sigma_p$ = strength increment directly attributable to the particulate.

Comprising $\Delta\sigma_i$ will be any active contributions from the possibilities discussed above. The magnitudes of the individual contributions to $\Delta\sigma_i$ in some instances can be easily estimated, as for example the magnitude of the influence of grain size (i.e., Hall-Petch constants), while others are more quantitatively elusive. If the magnitude of each contribution could be isolated and the form of the additivity equation known (i.e., linear versus non-linear and their associated depen-
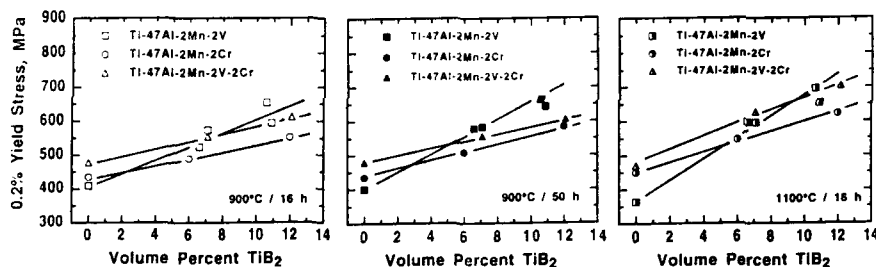
Figure 2. The 0.2% offset stress at room temperature as influenced by volume percentage TiB$_2$ and heat treatment: a) following heat treatment at 900°C/16 h, b) 900°C/50 h, and c) 1100°C/16 h.

dencies), then the magnitude of $\Delta\sigma_i$ could conceivably be predicted. However, in the absence of this level of known detail one can estimate the summed contributions which comprise $\Delta\sigma_i$ by quantifying the stress levels attained by the composite matrices containing the TiB_2 reinforcement, i.e., the vertical position of the curves shown in Fig. 4. Extrapolation of the curves shown in Fig. 4 to TiB_2 volume percentages of zero leads to an estimation of $\Delta\sigma_i$, or

$$\Delta\sigma_i \approx \lim_{v\% \to 0} \sigma_c \tag{2}$$

The magnitudes of $\Delta\sigma_i$ so determined are compatible with the actual or perceived effects on mechanical behavior as reported and discussed for grain size by Thompson and Chu [6] and by Vasudevan et al. [7], and for the influences of interstitial boron on phase constituency and/or mechanical properties as reported by Gigliotti and Huang [8], Guillard and Rack [9], Khowash et al. [10], and Wheeler et. al. [11].

Further support for the above assumption regarding $\Delta\sigma_i$ is obtained from an analysis of the remaining component of the composite strength in Eq. 1. Arithmetically removing the previously-estimated indirect contribution leads to a direct assessment of the strengthening capability provided by the particulate, that is,

$$\sigma_c - \Delta\sigma_i = \sigma_0 + \Delta\sigma_p \tag{3}$$

or, alternatively, employing the normalization as in Fig. 2,

$$(\sigma_c - \Delta\sigma_i)/\sigma_0 = (\sigma_0 + \Delta\sigma_p)/\sigma_0 \tag{4}$$

where the right hand side of Eq. 4 represents the resulting "strengthening factor" directly provided by the TiB_2 particulate in the composite. Figure 5 illustrates this strengthening factor, as calculated from Eq. 4, as influenced by the value of the edge-to-edge particulate spacing (λ-$2 \cdot r_p$) for all of the compositional and heat treatment variants presented. Specifically, Fig. 5 indicates that once the component of strength attributable to the indirect contributions is removed, the resulting component, i.e., that due to the strengthening effect of the particulate, is linear with respect to the inverse-square root of the interparticle spacing. It is noted that the interparticle spacing provides a means to combine the otherwise independent influences of volume fraction and particulate size into one microstructural variable. The particulate sizes and size-distributions, as well as the spacings and used in Fig. 5 for each composite have been reported and discussed elsewhere [1].

The dependency of strength on the inverse-square-root of particle spacing is consistent with reported studies where the size of the reinforcing entity is generally too large, i.e., of too great a
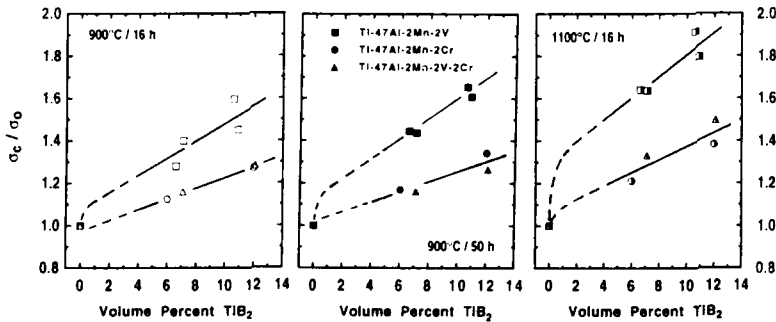
Figure 3. The 0.2% offset stress normalized with respect to that of the applicable base (reference) alloy.

162

spacing, to provide significant strengths via the Orowan dislocation looping mechanism [12, 13]. In such instances, strengthening is provided by the interaction of statistical dislocations with those created and stabilized by the incompatibility strains which exist between the matrix and the reinforcement. This mechanism is similar to that advanced for SiC-reinforced aluminum-based composites, where dislocations accommodating the strains associated with thermal expansion mismatch (ΔCTE) between the SiC reinforcement and the aluminum matrix act as obstacles and produce hardening within the aluminum matrix [14].

The magnitude of the slope obtained from a relationship such as that presented in Fig. 5 is representative of those factors which exist that affect the degree of strain-incompatibility between the reinforcement and the matrix, and the resistance to dislocation nucleation and mobility within the reinforcing phase. Qualitatively, these criteria will be influenced by the difference in moduli between the matrix and the reinforcement (i.e., ΔE and/or ΔG), and the details of the crystallography of slip within both components. As a illustration, Table I compares the values of the strengthening constant, k, in the present study to a variety of materials which similarly obey an inverse-square-root dependence of strength on "reinforcement" spacing. Included for illustration are constants (Hall-Petch) for planar-obstacle (i.e., grain boundary) strengthened metals. In general, particles (or boundaries) become more effective as strengthening entities as their moduli increase, or as the symmetry of their crystallography decreases (indicating increased resistance to slip or decreased accommodation of strain incompatibilities). Within the dislocation-generating matrices, high moduli and low crystallographic symmetry (large Burger's vectors) suggest the capability for effective dislocation-based strengthening.

SUMMARY

The strengthening response of a series of near-γ titanium aluminide compositions to the incorporation of TiB$_2$ particulate reinforcement at volume percentages of 7 and 12 percent has been analyzed. The analysis indicates that the strengthening can be quantitatively separated into three components: the inherent strength of the unreinforced reference alloy given identical processing as that of the composite, an increment of indirect strengthening due to the microstructural changes which have occurred due to the presence of the reinforcement during processing, and an increment whose magnitude is directly attributable to the presence of the reinforcement and its interactions with dislocations. The analysis is found to be qualitatively compatible with other mechanisms of strengthening which rely upon the interactions of dislocations with a plastically incompatible interface.
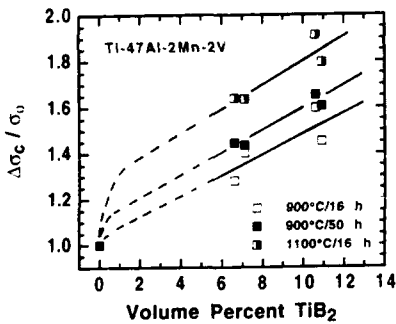
Figure 4. The normalized offset-stress of the Ti-47Al-2Mn-2V matrix composites as influenced by heat treatment.
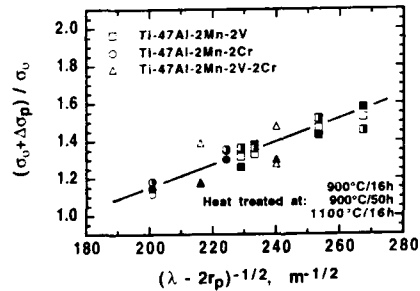
Figure 5. The offset-stress strengthening factor directly attributable to the presence of the particulate $(\sigma_o + \Delta\sigma_p/\sigma_o)$, as influenced by the edge-to-edge particle spacing (λ-2·r$_p$).

163

Table I.

Strengthening constants for materials exhibiting a flow stress which is proportional to the inverse-square-root of obstacle (e.g., reinforcement or grain boundaries) spacing.

Matrix (crystal, modulus)	Reinforcement (crystal, modulus)	k MN·m$^{1/2}$	Reference
MoSi$_2$ at 800°C: (C11$_b$, E = 340 GPa)	SiC: (B3; E=382)	2.8	13
MoSi$_2$ at 1000°C: (C11$_b$, E = 310 GPa)	SiC: (B3; E = 380 GPa)	2.4	13
TiAl/Ti$_3$Al at 25°C: (L1$_o$/DO$_{19}$ E = 162 GPa)	TiB$_2$: (C32; E = 550 GPa)	2.4	This study
TiAl/Ti$_3$Al at 815°C: (L1$_o$/DO$_{19}$ E = 76 GPa)	TiB$_2$:(C32; E = 483 GPa)	1.9	15
MoSi$_2$ at 1200°C (C11$_b$, E = 290 GPa)	SiC: (B3; E = 379 GPa)	1.4	13
MoSi$_2$ at 1400°C: (C11$_b$, E = 265 GPa)	SiC: (B3; E= 378 GPa)	0.5	13
Aluminum at 25°C: (fcc, E= 70 GPa)	TiB$_2$: (C32; E = 550 GPa)	0.25	16
Molybdenum at 25°C: (bcc, E= 310)	Grain boundary	1.768	17
Titanium at 25°C: (hcp, E=117 GPa)	Grain Boundary	0.403	17
TiAl/Ti$_3$Al at 25°C (L1$_o$/DO$_{19}$, E=62 GPa)	Grain Boundary	0.130 1.4	6 7
Copper at 25°C: (fcc, E=114 GPa)	Grain Boundary	0.112	17
Aluminum at 25°C: (fcc, E=70 GPa)	Grain Boundary	0.068	17

REFERENCES

1. S.L. Kampe, P. Sadler, L. Christodoulou, and D.E. Larsen, Metall. et Mater. Trans., (in press).
2. D.E. Larsen, L. Christodoulou, S.L. Kampe, and P. Sadler: Mater. Sci. Eng., A144, 1991, 45-49.
3. S.L. Kampe, J.A. Clarke, and L. Christodoulou, in Intermetallic Matrix Composites, edited by D.L. Anton, P.L. Martin, D.B. Miracle, and R. McMeeking ((Mater. Res. Soc. Proc. 194, Pittsburgh, PA, 1990), 225-232.
4. D.S. Shih and R.A. Amato, Scripta Metall., 24, 1990, 2053-2058.
5. S.L. Kampe, J.D. Bryant, and L. Christodoulou: Metall. Trans., 22A, 1991, 447-454.
6. A.W. Thompson and W-Y Chu in Microstructure/Property Relationships in Titanium Aluminides and Alloys, edited by Y-W Kim and R.R. Boyer, TMS, Warrendale, PA, 1991, 165-177.
7. V.K. Vasudevan, S.A. Court, P. Kurath, and H.L. Fraser, Scripta Metall., 23, 1989, 467-469.
8. S-C. Huang and M.F.X. Gigliotti, U.S. Patent No. 4,842,820; 1991.
9. S. Guillard and H.J. Rack, Mater. Sci. Eng., 1994 (in press).
10. P.K. Khowash, D.L. Price, and B.R. Cooper in High Temperature Ordered Intermetallics IV, (Mater. Res. Soc. Proc. 213, Pittsburgh, PA, 1991), 31-36.
11. D.J. Wheeler, D.E. Larsen, and B. London, 1992 TMS Fall Meeting, Chicago, 1992 (unpublished).
12. L. Anand and J. Gurland, Metall. Trans., 7A, 1976, 191-197.
13. R.M. Aikin, Jr., Mater. Sci. Eng., A155, 1992, 121-133.
14. R.J. Arsenault, L. Wang, and C.R. Feng, Acta Metall. et Mater., 39, 1991, 47-57.
15. S.L. Kampe, D.E. Larsen, and P. Sadler, (unpublished work).
16. R.M. Aikin and L. Christodoulou, Scripta Metall., 25, 1991, 9-14.
17. Compiled by T.H. Courtney in Mechanical Behavior of Materials (McGraw-Hill, New York, 1990), p. 171.

COMPOSITES BASED ON MOLYBDENUM DISILICIDE: PROGRESS AND PROSPECTS

D. A. HARDWICK
Rockwell Science Center, 1049 Camino Dos Rios, Thousand Oaks, CA 91360

Abstract

As the temperature demands increase in advanced aerospace systems, engineering materials that can withstand 1200° to 1600°C exposure in air must be developed. $MoSi_2$ is an intermetallic compound that has many, though not all, of the necessary physical and mechanical properties for use in this temperature regime. At ambient and moderate temperatures $MoSi_2$ is brittle, but once the ductile-to-brittle transition temperature (DBTT) is exceeded, it rapidly loses strength. Recent progress in, and current status of, the research efforts in $MoSi_2$ matrix composites will be reviewed, with an emphasis on the critical issues that currently impede progress to application.

Introduction

Well-known as a heating element material (1), $MoSi_2$ was first examined for structural use by NACA (predecessor to NASA) by Maxwell (2,3) and Long (4). This early work centered on the production of $MoSi_2$ powders, that were then densified by uniaxial hot pressing. In addition to hot tensile and stress rupture testing, turbine blade shapes were subjected to thermal shock tests. Maxwell and Long found that $MoSi_2$ was very brittle at temperatures below 1000°C with monotonically increasing ductility and decreasing strength at temperatures above 1000°C.

Over the years, a number of composite designs have been used to address the lack of low temperature toughness and high temperature creep resistance exhibited by $MoSi_2$. Attempts to improve the low temperature mechanical properties have relied extensively on two major approaches to composite toughening, namely brittle fiber pull-out and ductile fiber fracture. Approaches to increase the elevated temperature strength have included the addition of ceramic whiskers or particulates and solid solution alloying. Ductile phase toughening of $MoSi_2$ was first investigated by Fitzer, who incorporated refractory metal wires into a $MoSi_2$ matrix (5-7). The refractory metals are not in thermodynamic equilibrum with $MoSi_2$ at any temperature and Fitzer established the parabolic rate constants for interdiffusion and conversion to the R_5Si_3 compounds (R=refractory metal). Work on ductile fiber toughening has continued with emphasis on coatings to limit interdiffusion and examination of alternate ductile reinforcement morphologies including particles and layers. Research has also focussed on $MoSi_2$ composites

reinforced with ceramic whiskers or particulates. Many potential carbide, nitride, oxide and boride ceramic reinforcements are known to be thermodynamically stable in $MoSi_2$, including SiC, TiC, Si_3N_4, Al_2O_3, Y_2O_3, ZrO_2, TiB_2 and ZrB_2 (8, 9). In recent years, most of these reinforcements have been incorporated into $MoSi_2$ and most investigators report improvements in the toughness, strength and creep resistance over monolithic $MoSi_2$.

A critical assessment of such improvements necessarily rests on comparisons with the properties of monolithic material. Initial comparisons are usually made with a monolithic material processed in a similar fashion to the composite material. However, this may be the appropriate comparison. For example, it is well established that silica is detrimental to the properties of $MoSi_2$. If a particular composite processing route favors the incorporation of additional silica, then the resultant material may exhibit improved properties over a similarly processed monolithic material but have degraded properties compared with monolithic $MoSi_2$ processed such that it has a lower silica content. Thus, any discussion of $MoSi_2$ composites should begin with an overview of the properties of monolithic $MoSi_2$, with an emphasis on the effects of processing route on properties. This should enable us to select a set of property data that will facilitate comparisons between various composite strategies.

Monolithic Molybdenum Disilicide

Elevated Temperature Strength

Figure 1 is a plot of the yield strength as a function of temperature, obtained by either compression or bend testing, of monolithic polycrystalline $MoSi_2$. When compression testing was the method used, the initial strain rate is indicated. These materials were produced using a variety of techniques that fall into two groups. The first group involves a synthesis step from elemental powders and includes the reactive HIP of elemental powders (10), mechanical alloying of elemental powders followed by hot pressing (11,12) and hot pressing followed by HIP of reactively sintered elemental powders (13). Materials in the second group are produced by the densification of commercial $MoSi_2$ powder by either hot pressing (14, 15) or HIP'ing (16). The extreme variability in elevated temperature strength levels is a reflection of the efficacy of these various processing routes. Both the highest and the lowest strengths are exhibited by materials synthesized from elemental powders. Synthesis by mechanical alloying (MA) yields very low strength material, most likely due to the incorporation of oxygen during the milling process. MA materials have very high levels of oxygen, $>1wt\%$ (10). This translates into a very high volume fraction of SiO_2 particles with a resultant strength decrement. Reaction sintering or reaction HIP on the other hand, can lead to very low oxygen material, $\approx600wppm$ (17). These materials retain high strength to temperatures as high as 1400°C. Materials produced from commercial powders fall between these two extremes and again the variability can be related to processing parameters. Materials densified by hot pressing (filled symbols in Figure 1) are not as strong as those produced by HIP consolidation

(empty symbols in Figure 1); this difference is probably due to the lower density of the hot pressed materials. In fact, fully dense $MoSi_2$ produced by HIP processing of commercial powder (CERAC) exhibits strengths similar to synthesized + HIPed material despite its higher oxygen content (16). Slip casting, which produces a green body from a wet powder slurry, results in lower strengths (15) compared with dry handled powder (14) when both are hot pressed. Again, this difference is probably due to impurities introduced during the processing. Figure 1 also indicates that the strength of $MoSi_2$ is strain rate sensitive, i.e. the strength increases with increasing strain rate. Strength data for NASAIR 100 (18), a "first generation" single crystal superalloy, is also plotted on Figure 1 for comparison with the $MoSi_2$ data.
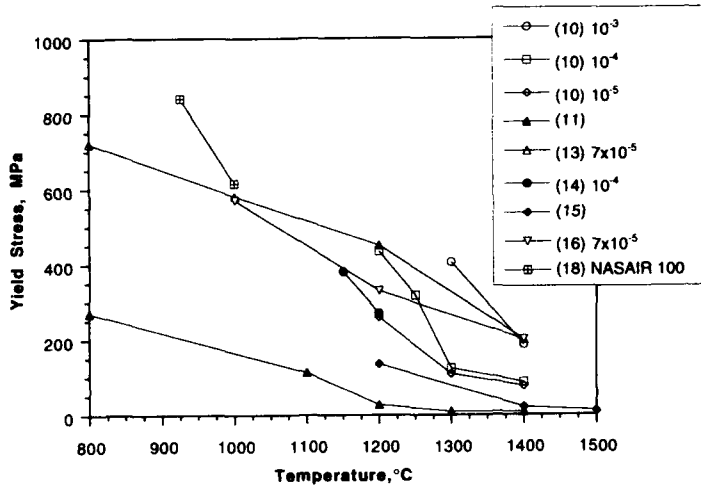
Figure 1: Yield strength of monolithic $MoSi_2$ as a function of temperature; filled symbols (●) = material consolidated by hot pressing; empty symbols (o) = material consolidated by HIP'ing.

Creep Behavior

Creep behavior is a better indicator of a material's usefulness at high temperatures than yield strength. Figure 2 shows creep data at 1200°C for monlithic $MoSi_2$ produced from commercial powder by either hot pressing or HIP'ing (19-23). Creep data at 1200°C has been plotted, as this temperature is just beyond the highest operating temperature for superalloys and therefore close to a lower operating temperature limit for advanced intermetallic-based materials. Again the material produced by HIP (empty symbols) has superior properties to that produced by hot pressing (filled symbols). Solid solution strengthening with W does not result in improved creep resistance. The superior properties exhibited by $MoSi_2$ on testing in air compared with testing in nitrogen indicate that the properties may be sensitive to testing environment (22).

167
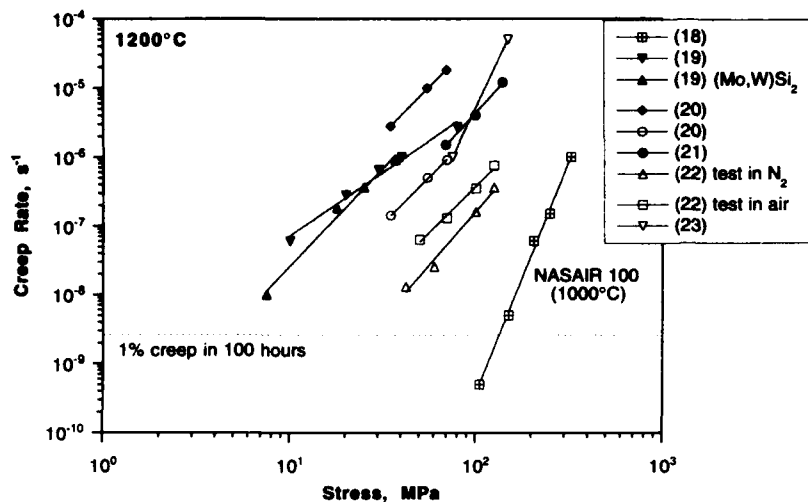
Figure 2: Compressive creep rate as a function of applied stress at 1200°C for monolithic MoSi$_2$; filled symbols (●) = hot pressed material; empty symbols (o) = HIP'ed material.

Recent work with single crystal MoSi$_2$ indicates that although it has a sufficient number of independent slip systems, the critical resolved shear stress necessary to activate the hardest orientations is extremely high at temperatures below ≈1300°C (24). A temperature of 1200°C is too low to activate the five slip systems required for the general shape change of a grain through dislocation glide. Both transgranular and intergranular microcracks have been observed in large grain (≈20-40μm) MoSi$_2$ following creep deformation at 1200°C (23). Such microcracking would be difficult to observe and, in fact, may not be present in high silica MoSi$_2$. With its very fine grain size, ≤5μm, and glassy grain boundary films, the predominant creep deformation mode in impure MoSi$_2$ is likely to be grain boundary sliding. Most researchers infer the creep deformation mechanism from the slope (n) of their creep rate versus applied stress plots coupled with a measurement of activation energy. Such indirect methods are irrelevant if the material is not deforming by mechanisms involving dislocation glide and climb processes.

The creep behavior at 1000°C of the "first generation" single crystal superalloy NASAIR 100 is also plotted on Figure 2. Typical static structures in gas turbine engines encounter stresses ≤14MPa, while rotating components such as turbine blades experience much higher stresses, ≥150MPa (20). If we ignore contributions from primary creep, we can plot a horizontal line corresponding to 1% creep in 100hrs which is a reasonable value for a structural component (25). This is the dotted line in Figure 2. The intersection of the creep curves with this line will give a value for the stress to cause 1% creep in 100 hours. Based on this data,

HIP'ed monolithic MoSi$_2$ could find application in static components at 1200°C as loads ≤16MPa will give rise to ≤1% creep in 100 hours. However, before it can be considered as a viable material for rotating components at 1200°C, MoSi$_2$ will need to be able to sustain a load of 150MPa with only ≈1% creep in 100 hours; i.e. it will need to exhibit creep properties at least comparable to those exhibited by NASAIR 100 at 1000°C.

Fracture Toughness

Unlike strength and creep resistance, fracture toughness does not appear to be highly dependent on processing variables. The ambient temperature fracture toughness of MoSi$_2$ falls in the range 3.2-5.7 MPa√m (26-31). The highest values were obtained on plasma sprayed material when the fracture toughness was measured parallel to the substrate (26, 27). These high values resulted from delamination of layers within the as-sprayed deposit (27). Diffusion bonding of the splat layers by a HIP cycle at 1200°C reduced the fracture toughness from 5.7 to 3.6 MPa√m. The ductile-to-brittle transition temperature (DBTT) of HIP'ed MoSi$_2$ is ≈1300°C (10, 16). The sharpness of the brittle-to-ductile transition in MoSi$_2$ is borne out by the very modest increase, from 3.4 to 5.2 MPa√m, in the toughness of (Mo,W)Si$_2$ as the temperature is raised to 1200°C (29).

Fatigue Crack Growth

Not suprisingly, MoSi$_2$ does not exhibit stable crack growth at room temperature (32). Ramamurty et al. (29) have shown that for the monolithic material (Mo$_{0.5}$,W$_{0.5}$)Si$_2$, subcritical fatigue crack growth occurs over a narrow ΔK range at 1200°C; threshold occurred at ΔK ≈ 3.7MPa√m and final fracture at ΔK ≈ 4.2MPa√m. Detailed microstructural examination led them to state that "...controlled grain boundary cavitation and microcracking and, to a lesser extent, enhanced dislocation activity provided the mechanism for subcritical crack growth". TEM examination revealed glassy ligaments bridging the crack faces and they concluded that "cavitation induced by the viscous flow of the amorphous glass phase appears to have a *decidedly more dominant effect on deformation than any dislocation plasticity...*" (29).

These crack growth experiments were conducted in air. Suzuki et al. found a significant increase in the volume fraction of glassy SiO$_2$ phase in samples crept in air compared with samples tested in dry nitrogen (22). Diffusion of oxygen into crack tips and the highly stressed regions ahead of them will promote the formation of glassy SiO$_2$ and this, in concert with pre-existing glass films developed during processing from powder, will impart an apparent "ductility".

Summary

This overview of the properties of monolithic MoSi$_2$ has emphasized that increases in the strength, toughness and creep resistance will be necessary before MoSi$_2$ becomes a viable

material for hot structures, particularly hot rotating components, where the payoff will be most beneficial. Our review of the data has shown that the properties, particularly the elevated temperature strength and creep behavior, are dependent on the processing route. There are indications that the elevated temperature response of $MoSi_2$ may be sensitive to test environment; SiO_2 formation during deformation may progressively degrade properties. Finally, with this overview we have established a basis for the comparison of the properties of composite materials based on $MoSi_2$.

Composites based on MoSi$_2$

$MoSi_2$ is a line compound and has been found to be quite intolerant of alloying additions (33, 34), with the notable exception of refractory metals such as W that form isomorphous compounds with $MoSi_2$ (35, 36) and can therefore be used as solid solution alloying additions. Our review has shown however, that such additions have only a minor influence on the properties of monolithic material. Therefore, to achieve the necessary improvements in low temperature toughness coupled with increased creep resistance, researchers have focussed on a variety of composite processing approaches. The design of both ductile and brittle matrix composite materials for optimized properties continues to receive considerable attention but the basic principles are well established. Manipulation of the size, aspect ratio, volume fraction and distribution of ceramic reinforcing elements in $MoSi_2$ should lead to at least rule of mixtures strengthening and fracture toughness improvements through crack bridging and whisker or fiber pull-out. Improvements in creep properties will certainly occur if ceramic fibers are used but will probably be only minor with ceramic particulates or whiskers, unless their aspect ratio is $\geq 10:1$. The incorporation of ductile fibers or layers will obviously have a greater influence for improving toughness than ductile particulates. On the other hand, ductile particulates will probably degrade the creep resistance of $MoSi_2$. The majority of refractory metal fibers will have a similar effect as their strengths and elastic moduli are lower than that of $MoSi_2$ with W being the only exception. The incorporation of very strong W-based alloy wires, such a W-Re-HfC, may be beneficial for both toughness and creep resistance.

From this discussion it is easy to develop the impression that improving the properties of $MoSi_2$ is as simple as choosing a reinforcement and selecting a suitable processing method. However, the process is rendered more difficult by the inherent physical and chemical properties of $MoSi_2$. The chemical instability of the refractory metals in $MoSi_2$ has already been mentioned (5-7). The refractory metal silicide phases that form are brittle, so that retention of any ductilizing effect is dependent on protection of the refractory metal from interdiffusion with Si. With respect to physical properties, the high coefficient of thermal expansion (CTE) of $MoSi_2$ is a stumbling block for the production of crack-free long-fiber composites. Ideally, the thermal expansion of a fiber and matrix should be closely matched to minimize the development of stresses during processing. As illustrated in Figure 3, most of the potential refractory metal and ceramic reinforcements exhibit CTE values quite different from

MoSi₂. Lu et al. have shown, both theoretically and experimentally, that reducing the diameter of reinforcement fibers can lead to the elimination of brittle matrix cracking (37). An alternative approach is the addition of fine particles of a low thermal expansion phase, e.g. SiC in $MoSi_2$ (25). As shown in Figure 3, this lowers the overall CTE of the composite matrix and reduces the CTE mismatch between $MoSi_2$ and other reinforcing phases.
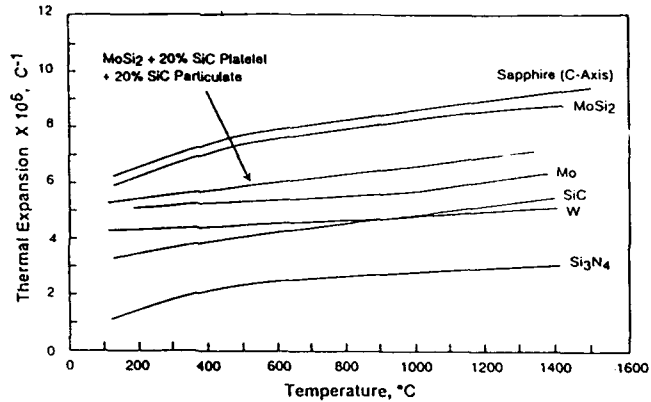
Figure 3: Mean coefficient of thermal expansion of $MoSi_2$, several potential reinforcement
phases and an $MoSi_2$-SiC composite (25).

Properties of MoSi₂ based Composites

Having reviewed the properties of monolithic $MoSi_2$ and touched on the difficulties associated with composite processing, we will now review the progress and property improvements that have been achieved in $MoSi_2$-based composites.

<u>Elevated Temperature Strength</u>

Figure 4 is a plot of the compressive or flexural yield strength as a function of temperature, of a number of $MoSi_2$-based composites containing a variety of ceramic reinforcements. When an investigation included several composite variations, the data plotted is the highest reported in that investigation. Four variants of the XD™ processed composites are included as these were, by far, the strongest composites reported. The dotted line on Figure 4 is the yield strength of monolithic $MoSi_2$ processed by HIP from reactively sintered elemental powder (13, 16). The strength of the hot pressed material containing 20 vol% SiC whiskers approaches that of the HIP'ed monolithic material. The only materials that exhibit greater strength than the unreinforced material are the XD™ processed composites (13). In these materials, the yield strength was proportional to the inverse square root of the interparticle spacing, indicating that

the composite strength was due to the particle-matrix interfaces acting as obstacles to dislocation motion. A unique feature of the XD™ process is that the ceramic particles are generated in situ; they are typically high purity single crystals with clean, unoxidized interfaces. The much lower strength exhibited by the in situ composite produced by the displacement reaction between Mo_2C and Si is most probably due to the influence of impurities, particularly silica, introduced during processing (14).
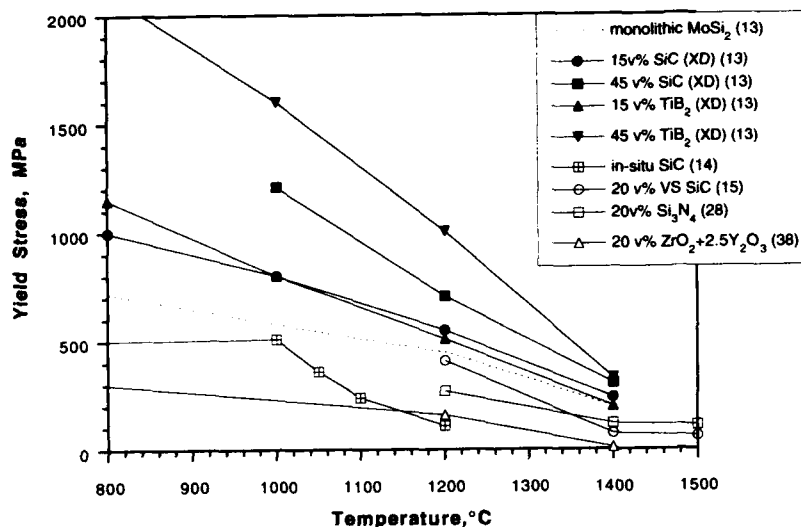
Figure 4: Yield strength of $MoSi_2$-based composites as a function of temperature; the dotted line is the yield strength of monolithic $MoSi_2$ produced by HIP of reacted elemental powders.

Creep

The steady state compressive creep rate at 1200°C of $MoSi_2$-based composites as a function of applied stress is plotted in Figure 5. The creep rate at 1200°C of HIP'ed monolithic $MoSi_2$ and the creep rate of NASAIR 100 at 1000°C are also plotted. As discussed previously, the creep rate of $MoSi_2$-based composites at 1200°C would need to approach the levels achieved by NASAIR 100 at 1000°C before it can be considered a serious contender for application in rotating aerospace components. Reinforcement with ceramic particulates can result in incremental improvements in creep strength. The true creep rate of the composite containing refractory metal particulates may be higher than the plotted values. Extensive internal oxidation of the Nb particles occurred during creep exposure and volume expansion associated with this oxidation probably neutralized a portion of the compressive creep strain leading to a lower apparent creep rate (20).

172
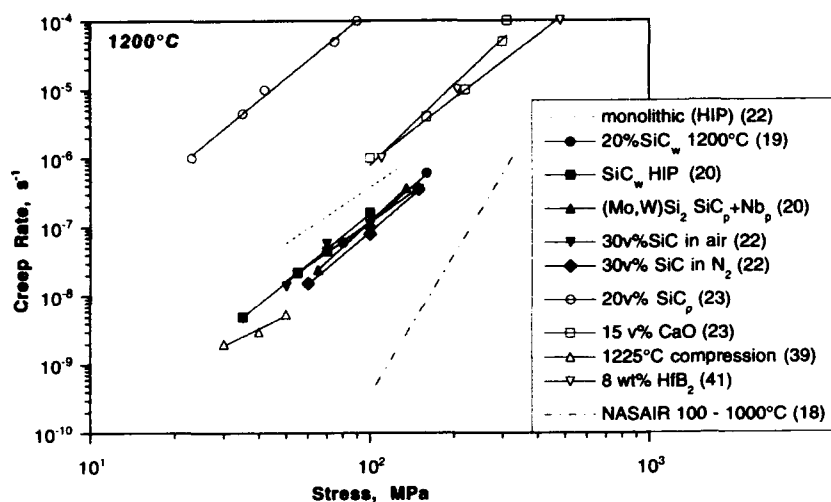
Figure 5: Compressive creep rate as a function of applied stress
at 1200°C for MoSi₂-based composites

In the studies reported to date (20, 39), creep rates in tension are faster than those observed under compression loading. The difference in creep behavior between tension and compression is usually attributed to volume expansion due to cavity formation which contributes to the rate of creep in tension but not in compression. In both of these investigations, cavities were observed in crept tensile samples. No mention was made of cavity formation in compression samples but they have been observed by other researchers (23). Possibly, the higher creep rates observed in tension are associated with in situ silica formation as surface connnected cracks develop during deformation.

Fracture Toughness

The ambient temperature fracture toughness of MoSi₂-based composites containing ceramic whiskers and particulates (14, 26, 29-31, 38, 42) varies from 5.0MPa√m for hot pressed MoSi₂ containing 20 vol% TiC particulate (31) to 8.2MPa√m for slip cast and hot pressed MoSi₂ incorporating 20 vol% SiC whiskers (30). These values represent marginal increases in the fracture toughness. Some benefits of ceramic whiskers were also seen at elevated temperatures; the measured fracture toughness of both (Mo,W)Si₂+30vol%SiC particulate (29) and MoSi₂+30vol%SiC particulate produced by in situ displacement reaction (14) increased from 5-6MPa√m to 11-14MPa√m as the test temperature was increased to 1200°C. The introduction of refractory metal particulates (27, 43) also produces only

173

incremental improvements in fracture toughness. However, the incorporation of refractory metal layers (44, 45) and filaments (5-7, 45) can give fracture toughness values as high as 15.2MPa$\sqrt{m}$ (20 vol% Nb layered and tested $\perp$ to the layers).

Fatigue Crack Growth

Similar to the monolithic material, (Mo,W)Si$_2$ containing SiC particulates did not exhibit stable crack growth at room temperature (29); catastrophic fracture occurred at $\Delta K \approx$ 4.2MPa$\sqrt{m}$, a value close to the ambient temperature fracture toughness. At 1200°C, the composite exhibited a higher fatigue fracture threshold and a more extended range of stable crack growth than the monolithic material. However, Ramamurthy et al. (29) concluded that the high temperature crack growth response of the silicide matrix composite is still dominated by the pre-existing and "in-situ-formed" glass phases at intergranular and interfacial boundaries. Similar effects have also been observed in alumina and SiC-reinforced alumina composites (29).

Dève et al. (46) have investigated the ambient temperature fatigue response of MoSi$_2$-40vol% SiC matrix reinforced with 30 vol% alumina-coated Mo fibers. Their experiments were carried out on fully pre-cracked tensile specimens so that the only resistance to crack opening was provided by the fiber tractions. The results indicated that if the applied stress was below a threshold value governed by the flow stress of the ductile fibers, then the crack opening remained constant over a large number of cycles. Final failure began with the propogation of fatigue microcracking across the Mo fibers while ultimate failure involved ductile rupture of the remaining fibers.

While the data indicates that ductile phase toughnening with refractory metal fibers is an effective mechanism at ambient temperatures, the question of its efficacy under elevated temperature oxidizing conditions has not yet been addressed. Refractory metals oxidize extremely rapidly at even moderately elevated temperatures. The refractory metal fibers would need to be coated with a ceramic layer to prevent interdiffusion of silicon but it is not clear whether this layer will provide any environmental protection to exposed fibers in a cracked region.

Progress and Prospects

Despite the large amount of effort devoted to MoSi$_2$-based composites in recent years, this review demonstrates that progress has been only incremental. Marginal improvements in damage tolerance and creep resistance have been obtained by the incorporation of stable ceramic particles and whiskers. More dramatic improvements would be expected if ceramic fibers such as Saphikon or SCS6-SiC could be used but CTE mismatch problems have so far proved insurmountable; successful fabrication of an MoSi$_2$-based composite based on these

fibers has not been reported. Problems associated with fabrication of long fiber composites with refractory metal fibers are equally intractable. Some of the problems have been overcome. $MoSi_2$ composites incorporating Mo wires have been successfully fabricated using substantial volume fractions of SiC particles to reduce the CTE of the matrix and alleviate cracking during cool-down from the processing temperature. The ultimate composite using this approach would probably use fine Si_3N_4 to reduce the matix CTE and high strength W-Re-HfC wire reinforcements to impart damage tolerance and creep resistance. Stategies such as slurry and sol-gel processing have been developed for the application of diffusion barrier coatings to refractory metal fibers. However, the assurrance of coating integrity through final processing will always be a question. The development of processing techniques for the in situ coating of pre-oxidized refractory metal fibers in an $MoSi_2$ matrix containing Al (47, 48) may provide a way around this dilemma. What has developed as a result of the recent flurry of activity in this area of brittle-matrix composites is a greater understanding of not only the mechanisms of toughening and strengthening in these materials but also an appreciation for the importance of processing methods for achieving improved properties.

Acknowledgements

References

1. V. Bizzarri, B. Linder and N. Lindskog, Ceramic Bulletin, **68** (1989) 1834.
2. W. A. Maxwell: NACA-RM-E9G01, Lewis Flight Propulsion Laboratory (1949).
3. W. A. Maxwell: NACA-RM-E52D09, Lewis Flight Propulsion Laboratory (1952).
4. R. A. Long: NACA-RM-E50F22, Lewis Flight Propulsion Laboratory (1950).
5. E. Fitzer and F. K. Schmnidt, High Temperatures-High Pressures, **3**, 445-460 (1971).
6. J. Schlichting, High Temperatures-High Pressures, **10**, 241 (1978).
7. E. Fitzer and W. Remmele, in Proc. Fifth International Conference on Composite Materials, ICCM-V, ed. W. C. Harrigan, Jr., J. Strife and A. K. Dhingra, 515-530 (1985).
8. P. J. Meschter and S. S. Schwartz, JOM, **41**, (1989) 52.
9. A. K. Vasudevan and J. J. Petrovic, Mater. Sci. Eng., **A155**, (1992) 1.
10. D. A. Hardwick, P. L. Martin, S. N. Patankar and J. J. Lewandowski, in Proc.International Symposium on Structural Intermetallics, (1993) pp 665-674.
11. R. B. Schwarz, S. R. Srinivasan, J. J. Petrovic and C. J. Maggiore, Mat. Sci. Eng. A, **A155** (1992) 75.
12. S. R. Srinivasen, R. B. Schwartz and J. D. Embury, Mat. Res. Soc. Proc. **288**, (1993) pp 1099-1104.
13. R. M. Aiken, Mat. Sci. Eng. A, **A155** (1992) 121.
14. C. H. Henager, Jr., J. L. Brimhall and J. P. Hirth, Mat. Sci. Eng. A, **A155** (1992) 109.
15. J. J. Petrovic and R. E. Honnell, Ceramic Engineering and Science Proceedings, **11** (7-8), 734 (1990).

16. R. M. Aikin, Jr, Scripta Metall. Mater. **26**, 1025 (1992).

17. D.A. Hardwick, P.L. Martin and R.J. Moores, Scripta Metall. Mater., **27**, 391 (1992).

18. M. V. Nathal and L. J. Ebert, Metall. Trans. A, **16A** (1985) 430.

19. K. Sadananda, C. R. Feng and H. Jones, Mat. Sci. Eng. A, **A155** (1992) 227.

20. S. Bose, Mat. Sci. Eng. A, **A155** (1992) 217.

21. D. M. Shah, D. Berczik, D. L. Anton and R. Hecht, Mat. Sci. Eng. A, **A155** (1992) 45.

22. M. Suzuki, S. R. Nutt and R. M. Aiken, Jr., Mat. Res. Soc. Proc. **273**, (1992) pp 267-274.

23. A. K. Ghosh, A. Basu and H. Kung, Mat. Res. Soc. Proc. **273**, (1992) pp 259-266.

24. S. A. Maloy, T. E. Mitchell, J. J. Petrovic, A. H. Heuer and J. J. Lewandowski to be published Proc. MRS Symposium Silicides and Refractory Metals, Fall 1993.

25. M. J. Maloney and R. J. Hecht, Mat. Sci. Eng. A, **A155** (1992) 19.

26. R. Tiwari, H. Herman and S. Sampath, Mat. Res. Soc. Proc. **213**, (1991) pp 807-813.

27. R. G. Castro, R. W. Smith, A. D. Rollett and P. W. Stanek, Scripta Met. et Mater. **26** (1992) 207.

28. J. J. Petrovic and R. E. Honnell, J. Mat. Sci. Letters, **9** (1990) 1083.

29. U. Ramamurty, A. S. Kim, S. Suresh and J. J. Petrovic, J. Am. Ceram. Soc., **76** (1993) 1953.

30. D. H. Carter, J. J. Petrovic, R. E. Honnell and W. S. Gibbs, Ceram. Eng. Sci. Proc., **10**, 1121 (1989).

31. J-M. Yang, W. Kai and S. M. Jeng, Scripta Met. et Mater. **23** (1989) 1953.

32. K. T. V. Rao, W. O. Soboyejo and R. O. Ritchie, Met. Trans. A., **23A** (1992) 2249.

33. W. J. Boettinger, J. H. Perepezko and P. S. Frankwicz, Mat. Sci. Eng. A, **A155** (1992) 33.

34. P. S. Frankwicz, J. H. Perepezko and D. L. Anton, Mat. Res. Soc. Proc. **288**, (1993) pp 159-164.

35. D. M. Shah, D. Berczik, D. L. Anton and R. Hecht, Mat. Sci. Eng. A, **A155** (1992) 45.

36. A. K. Vasudevan and J. J. Petrovic, Mat. Sci. Eng. A, **A155** (1992) 1.

37. T. C. Lu, J. Yang, Z. Suo, A. G. Evans, R. Hecht and R. Mehrabian, Acta Metall. Mater. **39** (1991) 1853.

38. J. J. Petrovic, A. K. Bhattacharya, T. E. Mitchell, R. K. Wade and K. J. McClellan, Mat. Sci. Eng. A, **A155** (1992) 259.

39. S. M. Wiederhorn, R. J. Gettings, D. E. Roberts, C. Ostertag and J. J. Petrovic, Mat. Sci. Eng. A, **A155** (1992) 209.

40. H. E. Dève, C. H. Weber and M. J. Maloney, Mat. Sci. Eng. A, **A153** (1992) 668.

41. R. Ray and J. D. Whittenberger, J. Mat. Sci. Letters, **12** (1993) 260.

42. S. Maloy, J. J. Lewandowski, A. H. Heuer and J. J. Petrovic, Mater. Sci. Eng., **A155**, (1992) 159.

43. R. G. Castro, R. W. Smith, A. D. Rollett and P. W. Stanek, Mater. Sci. Eng., **A155**, (1992) 101.

44. L.Xiao and R. Abbaschian, Mat. Sci. Eng. A, **A155** (1992) 135.

45. L. Xiao, Y. S. Kim, R. Abbaschian and R. J. Hecht, Mat. Sci. Eng.A, **A144** (1991) 277.

46. H. E. Dève, S. M. Spearing and M. J. Maloney, Mat. Sci. Eng. A, **A160** (1993) 209.

47. A. Costa e Silva and M. J. Kaufman, Scripta Metall. Mater. **29** (1993) 1141.

48. A. Costa e Silva and M. J. Kaufman, to be published in Processing and Fabrication of Advanced Materials III, ed. V. A. Ravi and T. S. Srivatsan, TMS, Warrendale, PA, 1994.

PEST RESISTANT AND LOW CTE MoSi$_2$-MATRIX FOR HIGH TEMPERATURE STRUCTURAL APPLICATIONS

M. G. Hebsur, NYMA Inc., NASA-LeRC Group, Brookpark. OH 44142

ABSTRACT

The objective of this investigation was to identify a pest resistant MoSi$_2$-base matrix composition having properties suitable for SiC reinforcement. A 30 vol.% addition of fine Si$_3$N$_4$ particulates to MoSi$_2$ significantly improved the low temperature accelerated oxidation resistance and thereby eliminated pest failure. Addition of Si$_3$N$_4$ also improved the high temperature oxidation resistance, strength and more importantly lowered the CTE of MoSi$_2$ such that cracking was eliminated in a hybrid composite consisting of 30 vol.% Si$_3$N$_4$ and 30 vol.% SCS-6 fibers.

INTRODUCTION

The intermetallic compound MoSi$_2$ is an attractive structural material due to its excellent oxidation resistance, high melting point (2303 K), relatively low density (6.2 gm/cm^3), high thermal conductivity and ease of machining. Unfortunately, its use has been hindered due to brittleness at low temperatures, inadequate creep resistance at high temperatures, accelerated oxidation (also known as 'pest' oxidation) at temperatures between approximately 673 and 773 K and its relatively high coefficient of thermal expansion (CTE) compared to potential reinforcing fibers such as SiC. The CTE mismatch between the fiber and the matrix results in severe matrix-cracking during thermal cycling.

Recently, extensive work has been carried out in efforts to improve the high temperature properties of MoSi$_2$ by solid solution alloying, dispersion strengthening, and fiber reinforcing [1-3]. However, it appears that the strength and damage tolerance of MoSi$_2$ required for structural applications may only be achieved by fiber reinforcement. Only a limited effort has been directed toward fiber reinforcement of MoSi$_2$ [3]. Matrix cracking was observed during consolidation of a SCS-6 fiber reinforced composite, even with the MoSi$_2$ matrix containing up to 40 vol. % SiC whiskers to modify thermal expansion. The SCS-6/MoSi$_2$-40SiC composite survived 5 thermal cycles from 1573 K to 300 K but disintegrated due to pesting within 100 hours of exposure in air at 773 K.

The pesting is most pronounced approximately at 773 K [4]. The pesting phenomenon in MoSi$_2$ has been attributed to the accelerated formation of voluminous MoO$_3$ in microcracks. The accelerated oxidation is a necessary, but not sufficient condition for pesting [5]. At 773 K both monolithic MoSi$_2$ and its composites suffered total disintegration within 100 hours, and the pesting of the MoSi$_2$ was little affected by the material density. The pested samples resulted in powdery products consisting of MoO$_3$ whiskers [6]. Thus, pesting and CTE mismatch with SiC reinforcement phase are two major issues that need to be resolved to achieve adequate mechanical properties for MoSi$_2$ composites. The objective of this investigation was to identify a new MoSi$_2$-base matrix composition which provides excellent pest resistance, lower CTE, and good mechanical properties for SiC fiber reinforcement.

EXPERIMENTAL

To achieve this objective, the addition of Si_3N_4 as a thermodynamically stable, low CTE phase was investigated. About 500 gm of a mixture containing commercial purity $MoSi_2$ powder and 30 volume % of fine Si_3N_4 powder was prepared by mechanical blending in an attritor. Both the $MoSi_2$-30Si_3N_4 and as-recieved $MoSi_2$ powders were consolidated into 55 mm long x 50 mm wide x 12 mm rectangular plates by vacuum hot pressing followed by hot isostatic pressing. Oxidation specimens typically 1.2 mm dia x 0.25 cm, were obtained from fully dense plates of $MoSi_2$-30Si_3N_4 and $MoSi_2$ by electric discharge machining. The oxidation coupons were final polished with 1 μm diamond finish, then ultrasonically cleaned and dried. The surface area and weights of the coupons were measured prior to oxidation. Cyclic oxidation tests were conducted between 773 and 300 K for 200 cycles. Each cycle consisted of 55 minutes of heating and 5 minutes of cooling. Isothermal oxidation tests were carried out in a quartz tube furnace between 1173 and 1773 K. The oxidation coupons were placed in high purity alumina boats and inserted into the center of a tube furnace. Weight gains were measured with a high resolution balance. The oxidized specimens were examined using x-ray diffraction (XRD) and scanning electron microscope (SEM) with energy dispersive spectroscopy (EDS). Similarly cylindrical specimens (4 mm dia x 8 mm long) and rectangular bars (25 mm long x 6 mm wide x 3 mm thick) were also machined for compression strength and dilatometry testing respectively. Compression tests were conducted on an universal test machine between 1073 and 1473 K in air using 0.0002 mm/s crosshead speed.

RESULTS AND DISCUSSION

An analysis of the $MoSi_2$-30Si_3N_4 mixture indicated the mean particle size was 1.25 ± 0.71 μm at 99% confidence limit. The consolidated samples were fully dense and exhibited a fine grained microstructure as shown in Figure 1. The Si_3N_4 particles are interconnected and well dispersed in the $MoSi_2$ matrix. However, some particle-free regions are also evident. The Si_3N_4 particles appear to be quite stable, with little or no reaction with the $MoSi_2$. In some isolated areas, the Mo_5Si_3 phase was detected. The presence of Mo_5Si_3 may be due to the composition of the commercially available $MoSi_2$ being slightly off-stoichiometry.
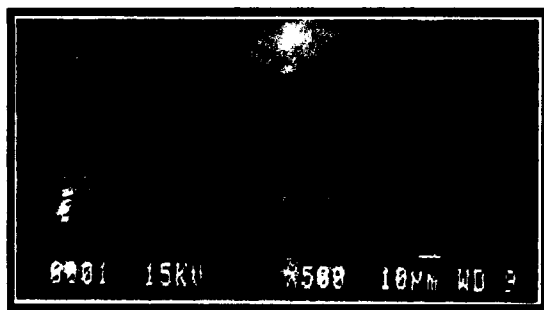
Figure 1: SEM-SE image of the consolidated $MoSi_2$-30Si_3N_4

The cyclic oxidation tests carried out at various temperatures for both $MoSi_2$ and $MoSi_2$-30Si_3N_4 alloys showed that the weight gain at 773 K was comparatively more than at 673 K and 873 K, confirming the previous observation [4] that 773 K is the temperature where accelerated oxidation is near the maximum for $MoSi_2$-base alloys.
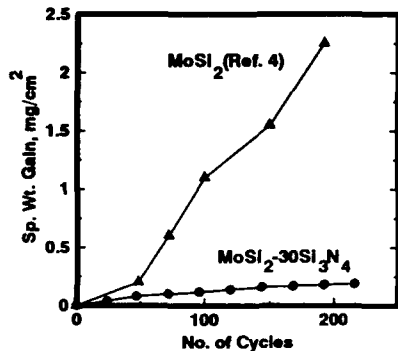
Figure 2: Cyclic oxidation of $MoSi_2$-base alloys at 773 K in dry air.
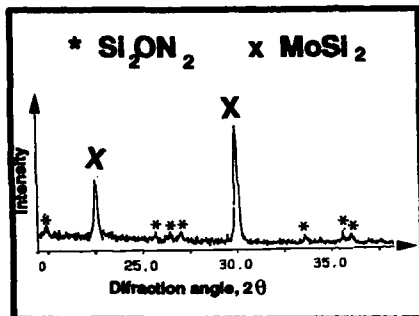
Figure 3: XRD spectrum of $MoSi_2$-30Si_3N_4 after oxidation at 773 K for 200 cycles.

Figure 2 shows a plot of specific weight gain versus number of cycles from cyclic oxidation results at 773 K in dry air. For comparison $MoSi_2$ data [4] is also included. Clearly, the $MoSi_2$-30Si_3N_4 has substantially lower weight gain than the high purity $MoSi_2$, which exhibits the accelerated oxidation behavior. The XRD result (Figure 3) shows complete absence of MoO_3 phase in $MoSi_2$-30Si_3N_4. Instead, it shows predominantly Si_2ON_2 phase which is a protective oxide scale.

The lower weight gain exhibited by $MoSi_2$-30Si_3N_4 can be attributed to Si_3N_4 which probably aids in the formation of Si_2ON_2 thus suppressing the formation of MoO_3. Transmission electron microscopic studies of the oxidized surface are in progress to understand the mechanism of protective oxide formation in this material. It appears that at least 30 vol. % Si_3N_4 is needed to avoid accelerated oxidation or pest. Figure 4 shows an SEM image of the oxidized surface of $MoSi_2$-30Si_3N_4. The oxide surface appeared non uniform, consisting of portions of bare alloy and large areas of a very thin layer of oxides rich in Si with small amounts of Mo. A few small isolated areas consisting of lath-like MoO_3 were also present indicating that the segregated areas were rich in $MoSi_2$ due to inefficient mixing in the attritor. This can be minimized by modifying the attritor arm configuration or by increasing the volume fraction of Si_3N_4 in $MoSi_2$. The cross -sectional microstructure of the oxidized specimen indicated that a very thin uniform and continuous oxide layer is formed without any voids or cracks penetrating the alloy.

To examine the influence of cracks on oxidation behavior, an indentation was introduced with a Vickers microhardness indentor using a 245 N load for about 15 seconds in the center of the polished surface of an oxidation coupon. The resulting indent contained four well defined cracks emanating from the corners. The cracked specimen was oxidized at 773 K for 200 cycles

179

Figure 4 SEM-SE image of oxidized surface of MoSi -30Si N. specimen

Figure 5 SEM-SE image of oxidized surface of indented MoSi.-30Si N. specimen

as described earlier. The specific weight gain vs number of cycles followed exactly the same trend as that of uncracked specimen (Figure 2). After 200 oxidation cycles, unlike MoSi., the MoSi.-30Si N. specimen was still in one piece with no sign of pesting. Crack sizes measured by an optical microscopy before and after oxidation showed no change in dimension. SEM examination of the oxidized specimen (Figure 5) did not detect any pest oxides in the cracked areas.

The effect of stress on pest oxidation was examined using a precracked specimen. An indentation was made in the center of a polished rectangular specimen using a 150 N load for 15 seconds. The indented specimen was precracked under controlled tensile stress using the single edge precracked beam (SEPB) fixture [7]. The precracked specimen was bend tested in air at 773 K under constant compressive load of 15 N (approximately 15 % of fast fracture load) for about 100 hours. The specimen did not break nor was there any pest oxide on the surface or in the cracked regions. All of these observations suggest that there is no accelerated oxidation/pest in MoSi.-30Si N. The pesting in MoSi. is mainly due to the formation of voluminous MoO. in cracks and pores [5]. While it is possible that a fully dense microstructure with no microcracks might delay the pesting, it can only be eliminated by reducing the accelerated oxidation due to formation of MoO. It appears that this can be achieved by the addition of large volume fraction of fine sized Si N. as shown in this investigation.

Other Properties of MoSi.-30Si N.

The addition of Si N. also improves the high temperature oxidation resistance. Figure 6 shows the comparison of the weight gain after isothermal exposure for 24 hours at various temperatures between 1273 K and 1773 K. The MoSi.-30Si N. exhibits a superior oxidation resistance. The XRD of surface oxides on MoSi.-30Si N. indicated *α-crystobalite*, a crystalline form of SiO.

The measured average CTE values obtained on the MoSi.-30Si N. are plotted as a function of temperature and shown in Figure 7. The CTE of MoSi. Si N. and SiC [3] are also included. It is observed from Figure 7 that the addition of Si N. to MoSi. has effectively lowered
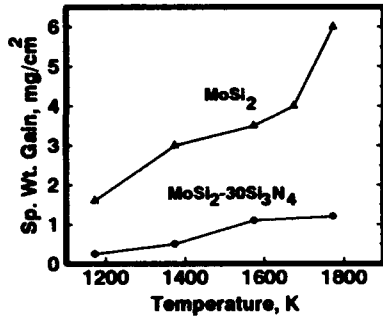
Figure 6: Comparison of 24 hr isothermal oxidation behavior of MoSi₂ alloys.
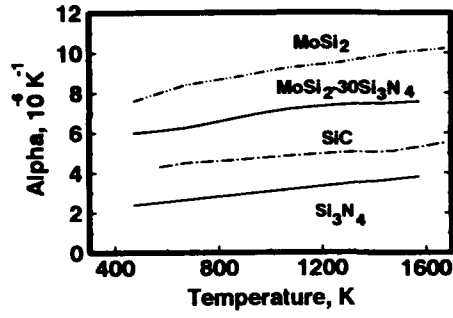
Figure 7: Thermal expansion coefficients of various materials.
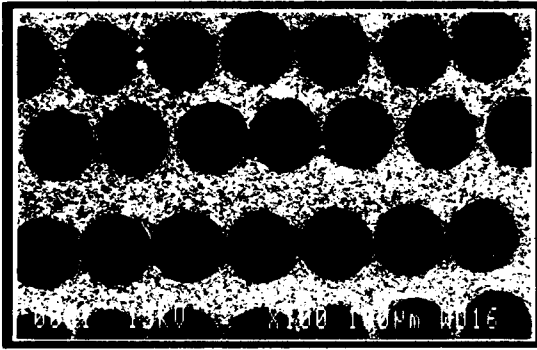
Figure 8: SEM-SE image of as-fabricated 30 vol. % SCS-6/MoSi₂-30Si₃N₄ composite.
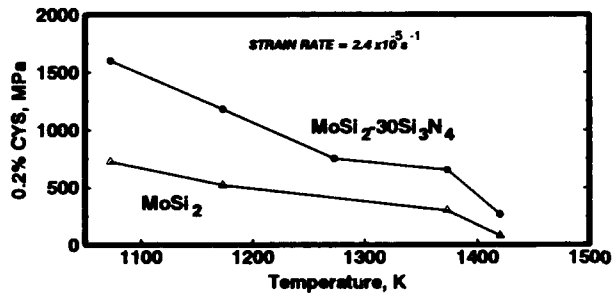
Figure 9: Compressive yield strength versus temperature plot for MoSi₂-base alloys.

181

the CTE thereby reducing the CTE mismatch with the SiC reinforcing phase such that cracking was eliminated in a 30 vol. % SCS-6 reinforced hybrid composite (Figure 8).

Compressive stress-strain curves indicated that between 1073 K and 1273 K, the $MoSi_2$-$30Si_3N_4$ specimens exhibited yielding and about 8-10 % plastic strain before fracture. Above 1373 K, specimens exhibited substantial plasticity. Figure 9 shows a comparison of compression yield strengths of $MoSi_2$-$30Si_3N_4$ with that of binary $MoSi_2$ as a function of temperature. Figure 9 clearly illustrates that $MoSi_2$-$30Si_3N_4$ is much stronger than $MoSi_2$ at temperatures between 1073 and 1473 K.

SUMMARY

A 30 vol. % addition of thermodynamically stable and oxidation resistant Si_3N_4 in particulate form to $MoSi_2$ improved the low temperature accelerated oxidation resistance by forming a Si_2ON_2 protective scale and thereby eliminated the catastrophic 'pest' failure. The Si_3N_4 addition also improved the high temperature oxidation resistance and more importantly, significantly lowered the CTE of the $MoSi_2$ and eliminated cracking in SCS-6 reinforced composite. The high-temperature compressive strength of $MoSi_2$-$30Si_3N_4$ was also higher than that of binary $MoSi_2$.

CONCLUSION

A 30 vol. % addition of fine Si_3N_4 particles to $MoSi_2$ produces a composite with advantages in pest resistance, strength, and CTE compared to binary $MoSi_2$. It is envisioned that a hybrid composite with both Si_3N_4 particulates and continuous SiC fibers will provide the best combination of strength, environmental resistance, and reliability compared to any $MoSi_2$-base materials. This hybrid composite will compete with metal, intermetallic and ceramic composites. Mechanical tests to validate this vision are in progress.

ACKNOWLEDGMENTS

REFERENCES

1. J. J. Petrovic and R. E. Honnell and W. S. Gibbs, US Patent 4,970,179, (1990).
2. D. M. Shah and D. L. Anton, in High Temperature Ordered Intermetallic Alloys IV, edited by L. A. Johnson, D. P. Pope and J. O. Stiegler, (Mater. Res. Soc. Proc. 213, Pittsburgh, PA, (1991) pp. 63-68.
3. M. J. Maloney and R. J. Hecht, Mater. Sci. and Eng., A155, 19 (1992).
4. P. J. Meschter, Metall. Trans., 23A, 1763 (1992).
5. D. A. Berztiss, R. R. Cerachiara, E. A. Gulbransen, F. S. Pettit and G. H. Meier, Mater. Sci. and Eng., A155, 165 (1992).
6. T. C. Chou and T. G. Nieh, Scr. Met., 27, 19 (1992).
7. T. Nose and T. Fujii, J. Amer. Ceram. Soc. 71, 328 (1988).

DUCTILE PHASE TOUGHENING OF MoSi₂:
EFFECT OF REINFORCEMENT MORPHOLOGY

Long-Ching Chen*, Nedhal Bahtishi*, Richard Lederich**, and Wolé Soboyejo*
*The Ohio State University, Department of Materials Science and Engineering,
  Columbus, OH 443210-1179
**McDonnell Douglas Corporation, St. Louis, MO 63166-0516

ABSTRACT

The effects of ductile reinforcement morphology on the mechanical behavior of MoSi$_2$ reinforced with 20 vol.% Nb are presented. While all the composites exhibit improved fracture toughness relative to the monolithic MoSi$_2$, the most significant improvement is obtained in the composite with laminate reinforcement, followed by coarse fiber, fine fiber and particulate reinforcements. Bend strength measurements indicate a ductile-brittle-transition-temperature of ~1250°C, and highlight the attractive properties of laminate reinforced composite. Preliminary studies of room temperature fatigue crack growth in particulate reinforced composites show a stable fatigue crack growth, which is not achieved in monolithic MoSi$_2$. Possible ways of achieving a better combination of mechanical properties are also discussed.

INTRODUCTION

Molybdenum disilicide (MoSi$_2$) has been proposed as a model material for high temperature structural applications due to its high melting point, moderate density and excellent oxidation/corrosion resistance [1-4]. However, the low damage tolerance at room temperature, especially in terms of fracture toughness and fatigue crack growth resistance, has restricted the use of monolithic MoSi$_2$. Recently, there have been a number of attempts to improve the damage of MoSi$_2$ tolerance via composite approaches. For example, brittle phases such as SiC whiskers [5,6], SiC particles [7], and Al$_2$O$_3$ whiskers [8] have been used to strengthen the MoSi$_2$ matrix. Transformation toughening with partially stabilized zirconia (PSZ) particles has also been examined [9-11]. Although the fracture toughness is improved by brittle phase reinforcements, the highest fracture toughness level achieved to date in such composites is ~ 8 MPa√m. Since a fracture toughness level of at least 15 MPa√m is desirable for possible structural applications, other types of reinforcements, e.g. ductile phases, need to be explored.

The increase in toughness of a ductile phase reinforced composite is due largely to the extra strain energy required for plastic deformation of the ductile bridging ligaments. Due to its high ductility, high melting point (2468°C), and similar thermal expansion coefficients to MoSi$_2$, niobium has been considered as one of the most promising ductile reinforcements to toughen MoSi$_2$ [12-15]. Soboyejo et al. have conducted fracture toughness measurements on a MoSi$_2$ composite reinforced with 20 vol.% Nb particles. They obtained a fracture toughness value of ~ 5.7 MPa√m, 24 % higher than that of the monolithic alloy [12]. Microstructural examination and EDS (energy dispersive spectroscopy) analysis revealed the existence of a (Mo,Nb)$_5$Si$_3$ reaction zone at the interface of Nb particles and MoSi$_2$ matrix, after composite fabrication. This reaction zone is so brittle that interfacial decohesion occurs before Nb particles are plastically stretched [13]. Lu et al. [14], and Shaw and Abbaschian [15], have investigated the effects of Nb laminate reinforcement on the fracture behavior of MoSi$_2$. The fracture toughness level could be as high as 14.9 MPa√m, close to the lower limit required for practical structural applications. The effects of reinforcement orientation and size has also been investigated [15].

The current paper presents the results of an ongoing study of the effects of ductile phase reinforcement morphology on fracture toughness. The preliminary data presented in this paper suggest fiber and laminate forms of reinforcements result in the greatest improvements in fracture toughness. However, as suggested by Kajuch et al. [16] and Mendiratta et al. [17] who had shown that the grain growth of Nb and silicon diffusion into Nb laminates had significant effects on the ductility of Nb, the direct comparison of the fracture toughness data must be done very carefully since the material processing conditions are not the same. The effects of reinforcement morphology on other mechanical properties, such as elevated temperature strength and fatigue crack growth are also discussed.

EXPERIMENTAL PROCEDURES

Four types of $MoSi_2$ composites, with different Nb reinforcement morphologies, were fabricated using 100-200 μm diameter powder, 250 μm diameter fiber, 750 μm diameter fiber, and 200 μm thick foil. The $MoSi_2$ powder was procured from Cerac, Milwaukee, WI. The Nb powder was supplied by Nuclear Metals, Concord, MA, and had a 99.8% purity, while the Nb fiber and foil were of commercial grade. The mixing of powders, and the lay-ups of fibers and foils, were done to give a reinforcement volume fraction of 0.2. The mixtures were consolidated by HIPing (hot isostatic pressing), which was carried out at McDonnell Douglas, St. Louis, MO, the HIPing conditions were: 1700°C, 107 MPa argon pressure, and 4 hours for the particulate-reinforced composite; and 1400°C, 107 MPa argon pressure, 2 hours for the other composites. The resulting microstructures are shown in Figure 1. It can be seen that a reaction layer exists in the matrix/reinforcement interface. HIPing at higher temperature, and for longer durations results in a much thicker reaction layer (~75 μm) in the particulate-reinforced composite, when compared to ~15 μm in the other two composites.

Fracture toughness tests were conducted at room temperature under three point bend loading (with an inner span 22.2 mm) using single-edge-notched (SEN) specimens, with rectangular cross sections (3.18 mm thick X 6.35 mm wide). Notches of 2.54 mm deep were introduced by electro-discharge machining (EDM). For the laminate composite, the notches were made perpendicular to the plane of the laminate reinforcements. The fracture toughness tests were carried out under load control in accordance with ASTM-E399 specifications. The SEN samples were loaded monotonically to failure at a loading rate that corresponded to a stress intensity increase rate of 0.92 MPa$\sqrt{m}$/sec. The failure load was obtained from an automated data acquisition system, and used to calculate the fracture toughness. Bend (strength) tests were performed in vacuum at temperatures between 25-1400°C. These tests were done on rectangular bars with dimensions of 3.18 mm x 4.06 mm x 31.8 mm. The bend specimens were machined by EDM and fractured at a strain rate of ~10^{-5} sec^{-1} under four point bend loading. Fatigue tests were conducted on monolithic $MoSi_2$ and the particulate-reinforced composite at room temperature. The test on the particulate-reinforced composite was performed in air on disc-shaped compact tension specimens with a diameter of 25 mm, width of 19 mm, and thickness of 5 mm, while the test on the monolithic $MoSi_2$ was performed on the same geometry as the previously described SEN samples. Cyclic constant amplitude fatigue tests (stress ratio, R= 0.1), were conducted at a cyclic frequency of 25 Hz. In-situ monitoring of crack growth was carried out, with a high resolution (2.5μm) telescope connected to a video monitor. Fractographic analysis was carried out in an SEM (scanning electron microscope).

(a)   (b)

(c)   (d)

(e)   (f)
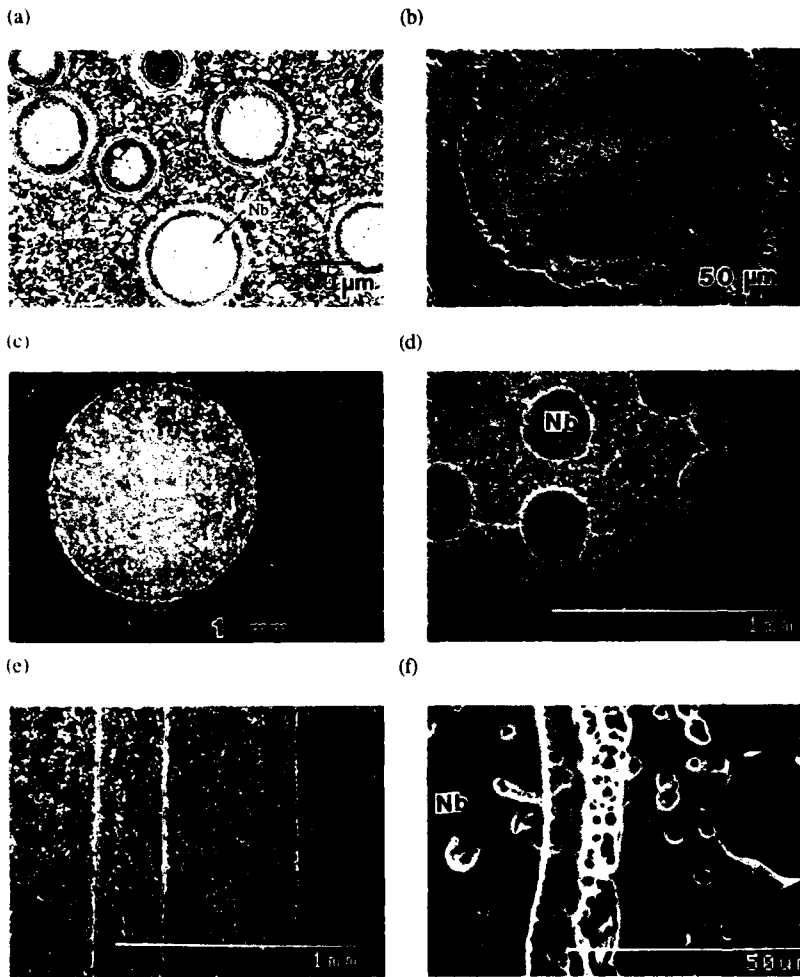
Figure 1. As-HIPed microstructure of $MoSi_2$ composite reinforced with Nb of
different morphologies. (a) particulate reinforcement, 50X; (b) interfacial
reaction zone of (a), 400 X; (c) coarse fiber reinforcement, 50X; (d) fine fiber
reinforcement, 50X; (e) laminate reinforcement, 50X; and (f) interfacial
reaction zone, typical of (c), (d) and (e), 1000X.

RESULTS

The average fracture toughness values obtained from multiple (duplicate or triplicate) tests for each reinforcement morphology are listed in Table I. Reinforcement with Nb improves the fracture toughness of $MoSi_2$. The extent of toughening strongly depends on the morphology, with the highest toughness obtained in the laminate reinforced composite, followed by the coarse fiber-reinforced, then fine fiber reinforced, and finally the particulate reinforced composites.

Table I. Average fracture toughness values of monolithic $MoSi_2$ and its composites.

Specimen Type	K_{IC} (MPa$\sqrt{m}$)
Monolithic $MoSi_2$	3.6 ± 0.6
200 µm Nb particulate	5.7 ± 0.5
250 µm Nb fiber	9.1 ± 0.9
750 µm Nb fiber	11.3 ± 4.1
200 µm Nb laminate	18.0 ± 2.0

The results of the bend strength tests at various temperatures are presented in Table II. The bend strength data obtained for the monolithic $MoSi_2$ increases with increasing temperature, and reaches a maximum at 1250°C. Such a trend reflects the low fracture toughness of the unreinforced alloy at low temperatures. The high flaw-sensitivity of the material, coupled with the presence of high flaw density (porosity), causes the specimens to fail long before the actual ultimate strength is reached. Similar behavior is observed in the fiber and laminate reinforced materials, but to a lesser degree. The DBTT (ductile-brittle-transition-temperature) determined from the bend strength measurements is ~1250°C in all the materials that were examined in this study.

Table II. Four-point bend strengths (in MPa) of monolithic $MoSi_2$ and its composites.

Specimen Type	20°C	1050°C	1100°C	1250°C	1300°C	1350°C	1400°C	1450°C
Monolithic $MoSi_2$	212	-	390	446	427	-	241	-
200 µm Nb particulate	177	224	-	184	-	117	-	72
250 µm Nb fiber	232	-	286	92	-	-	-	-
750 µm Nb fiber	133	-	260	245	-	-	237	-
200 µm Nb laminate	386	-	188	176	-	-	152	-

The results of the fatigue crack growth investigation on the particulate-reinforced composite are shown in Figure 2. Stable crack growth was detected at ΔK as low as 1.7 MPa$\sqrt{m}$. Plotted on a log-log scale, the exponent of ΔK was found to be ~14, indicating that the crack growth rate was strongly dependent on ΔK. Stable fatigue crack growth was not achieved in monolithic $MoSi_2$. This suggests that the damage accumulation in the unreinforced material was insufficient to promote stable crack growth at stress intensities below the fracture toughness, K_c. Therefore, the fatigue crack growth resistance is degraded by the Nb particulate reinforcements.

DISCUSSION

The fracture toughness data presented in this paper clearly demonstrate that the toughness improvement of $MoSi_2$ strongly depends on the morphology of the ductile Nb reinforcements. Fractographic analysis of the particulate reinforced composite showed that the fracture surface was covered with holes and mounds generated by the decohesion of Nb particles. Examination of the crack profiles on a polished surface showed that fracture occurred along the brittle $(Mo,Nb)_5Si_3$ reaction layer. No evidence of plastic stretching or crack bridging phenomena was observed. As a result, only a slight
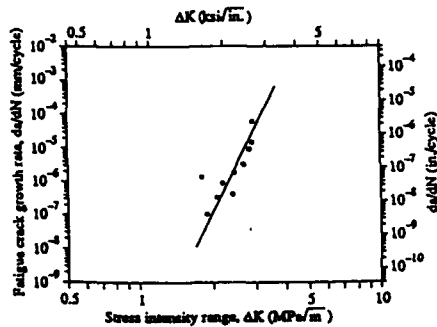
Figure 2. Fatigue crack growth rates of Nb particulate reinforced $MoSi_2$.

improvement in fracture toughness due to crack twisting and tilting was observed in the particulate reinforced composite [12].

The occurrence of interfacial debonding in the fiber reinforced and laminate reinforced composites had some significant effects. Lu et al. [14] have coated Nb laminates with a layer of Y_2O_3 to avoid the growth of the brittle reaction layer during subsequent hot pressing with pre-split $MoSi_2$ plates. They found that the work of rupture obtained from the Y_2O_3-coated Nb foil was similar to that of the uncoated Nb foil, indicating presumably a similar level of fracture toughness improvement. In contrast, a significantly higher work of rupture was obtained from the coated Nb foil when a similar coating technique was applied to Nb reinforced TiAl [18]. Apparently, the mechanical property of the interfacial products is the dominating factor that controls the strain energy to failure of the ductile phase reinforced composites. Generally, however, a higher degree of interfacial debonding of the ductile phase reinforcements reduces the deformation constraint, and allows a better utilization of the ductility of the bridging ligaments. Nevertheless, although the decohesion around the particulate reinforcements results in total decohesion from the matrix (apparently before plastic stretching) [13], the overall toughening is relatively small due to the limited interfacial area available for debonding. Therefore, interfacial debonding is beneficial only when the reinforcements have larger aspect ratios.

The size effect of Nb reinforcement on the fracture toughness of laminated $MoSi_2$ composites has been investigated recently by Shaw and Abbaschian [15]. Working on composites with the same volume fraction, they found that the fracture toughness of the laminates increases with increasing thickness of the Nb foils. The fracture surface appearance of the Nb laminates changed from quasi-cleavage to ductile dimple fracture. In addition, longer decohesion zones, which would offer less deformation constraint, were also observed in the composites with thicker reinforcements [15, 18]. As a result, higher fracture toughness levels would be expected with increasing reinforcement size.

The bend strengths of the fiber and particulate reinforced composites were lower than those of monolithic $MoSi_2$ at room temperature. This may be due to the presence of Kerkendall voids in the reaction layer surrounding the Nb reinforcement. The residual stress due to the thermal expansion mismatch between matrix and reinforcement may also affect the overall composite strength levels. In contrast, the laminate composite is much stronger than monolithic $MoSi_2$ at room temperature. Extensive plastic deformation and good room temperature tensile strength of the Nb layers (400-500 MPa) prevent

premature failure, and contribute to the attractive combination of fracture toughness and bend strength. At elevated temperatures, however, the Nb layers soften and this softening limits the bend strength of the composite.

The degraded fatigue crack growth resistance of the particulate Nb reinforced composite compared with the monolithic $MoSi_2$ can be rationalized by considering the effect of Nb particles on the crack-tip opening displacement (COD) [12]. As COD directly proportional to the crack extension under cyclic loading, the greater COD associated with Nb reinforcement promotes a faster fatigue crack growth rate, since the degree of crack-tip shielding by crack deflection is relatively small [12]. Fatigue crack growth resistance is therefore apparently degraded by Nb-particulate reinforcement. More work is clearly needed in this area.

SUMMARY

The results of the preliminary study of the effects of Nb reinforcement morphology on fracture toughness suggest that laminated configurations result in the greatest degree of toughening. Fiber reinforcement appears to promote intermediate improvements in fracture toughness, and the degree of toughening in fiber reinforced composites increases with fiber diameter. The smallest improvements in fracture toughness are observed in particulate reinforcements. The above results can be rationalized by considering the combined effects of debonding/microcracking phenomena, and the plastic work associated with crack bridging mechanisms.

REFERENCES

1. A.K. Vasudévan and J.J. Petrovic, Mater. Sci. Eng., **A155**, 1 (1992).
2. E. Fitzer and W. Remmele, Proc. 5th Int. Conf. on Composite Materials, ICCM-V, edited by W.C. Harrigan, Jr., J. Strife and A.K. Dhingra (AIME, Warrendale, PA, 1985), p.515.
3. P.J. Meschter and D.S. Schwartz, J. Met., **41**, 52 (1989).
4. S. Maloy, A. H. Heuer, J. Lewandowski, and J. Petrovic, J. Am. Ceram. Soc., **74**, 2704 (1991).
5. J.J. Petrovic and R.E. Honnell, Ceram. Eng. Sci. Proc., **11**, 734 (1990).
6. D.H. Carter, J.J. Petrovic, R.E. Honnell and W.S. Gibbs, Ceram. Eng. Sci. Proc., **10**, 1121, (1989).
7. U. Ramamurty, A.S. Kim, S. Suresh and J.J. Petrovic, J. Am. Ceram. Soc., **76**, 1953 (1993).
8. G.I. Zakharova, S.S. Ordanyan, V.N. Paderno, G.N. Smolina and E.S. Vinogradova, Izvest. Akad. Nauk. SSSR, Neorg. Mater., **20**, 1143 (1984).
9. J.J. Petrovic, R.E. Honnell and T.E. Mitchell, Ceram. Eng. Sci. Proc., **12**, 1633 (1991).
10. J.J. Petrovic and R.E. Honnell, J. Mater. Sci., **25**, 4453 (1990).
11. D. Brooks, L.-C. Chen, R. Lederich and W. Soboyejo, submitted to J. Am. Ceram. Soc. (1994).
12. W.O. Soboyejo, K.T. Venkateswara Rao, C M L. Sastry and R.O. Ritchie, Metall. Trans., **24A**, 585 (1993).
13. K.T. Venkateswara Rao, W.O Soboyejo, and R.O. Ritchie, Metall. Trans., **23A**, 2249 (1992).
14. T.C. Lu, A.G. Evans. R.J. Hecht and R. Mehrabian, Acta Metall. Mater., **39**, 1853 (1991).
15. L. Shaw and R. Abbaschian, Acta Metall. Mater., **42**, 213 (1994).
16. J. Kajuch, J.D. Rigney and J.J. Lewandowski, Mat. Sci. Eng., **A155**, 59 (1992).
17. M.G. Mendiratta, J.J. Lewandowski and D.M. Dimiduk, Metall. Trans., **22A**, 1573 (1991).
18. F. Dève, A.G. Evans, G.R. Odette, R. Mehrabian, M.L. Emiliani and R.J. Hecht, Acta Metall., **38**, 1491 (1990).

Thermal Fatigue of MoSi$_2$ Particulate and Short Fiber Composites

M.T. KUSH, J.W. HOLMES* and R. GIBALA

The University of Michigan, Department of Materials Science and Engineering, Ann Arbor, MI 48109-2136 and *The University of Michigan, Department of Mechanical Engineering and Applied Mechanics, Ann Arbor, MI 48109-2125

ABSTRACT

Induction heating of disk shaped specimens was used to compare and contrast the thermal fatigue behavior of MoSi$_2$ and MoSi$_2$-based composites. Specimens were subjected to 5 s heating and cooling cycles between temperature limits of 700°C and 1200°C. The monolithic material and a MoSi$_2$-10 vol% TiC composite exhibited poor thermal shock resistance and could not be thermally cycled according to this temperature-time profile. A 30 vol% TiC composite exhibited much better thermal shock and thermal fatigue resistance as compared to the monolithic material, but exhibited undesirable oxidation. MoSi$_2$-10 and 30 vol% SiC particulate composites exhibited excellent thermal shock and thermal fatigue resistance compared to that of the monolithic material. A MoSi$_2$-10 vol% SiC whisker composite did not show improved thermal fatigue resistance due to the initial processing defects present in the material. The monolithic material and the 10 vol% TiC composite were also subjected to 30 s heating and cooling cycles between temperature limits of 700°C and 1200°C. Both of these materials exhibited better thermal fatigue resistance at this temperature-time profile, but the 10 vol% TiC composite also exhibited undesirable oxidation. The fatigue results are discussed with reference to the initial microstructure of the specimens and the stress-strain history of the specimens which was obtained by a thermoelastic finite element analysis.

INTRODUCTION

Molybdenum disilicide is an attractive material for high temperature structural applications as well as a matrix material for composites with service temperatures near 1200°C. MoSi$_2$ exhibits excellent high temperature oxidation resistance because of the formation of a protective silica film [1]. Thermal fatigue resistance is a concern for many high temperature applications, but very little is known about the thermal fatigue resistance of MoSi$_2$ based composites. The goal of the present paper is to compare the thermal fatigue resistance of MoSi$_2$ monolithic material to that of MoSi$_2$-based composites. This research is needed to determine the effect of second phases on the thermal fatigue life of MoSi$_2$ for potential applications such as gas turbine airfoils and advanced space vehicles, where thermal gradients will invariably be seen by this material.

Thermal fatigue was obtained by induction heating of disk-shaped specimens [2]. The induction heating technique was employed due to the ease of characterization of the mechanical behavior of this system.

EXPERIMENTAL PROCEDURE

Materials

A monolithic MoSi$_2$ billet was prepared by powder processing. The billet was fabricated from -325 mesh powder obtained from Cerac, Incorporated, Milwaukee, WI. Hot pressing was performed uniaxially in a grafoil-lined graphite die in an argon atmosphere at 1700°C. The hot pressing was conducted for 1 hr at a pressure of 30 MPa. The billet was additionally HIPed at 1700°C for 1 hr at a pressure of 200 MPa.
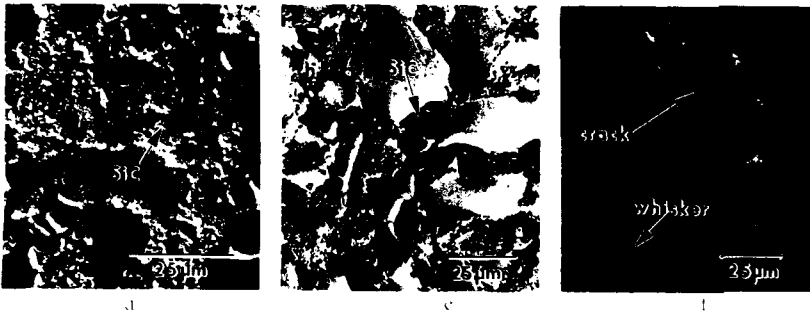
Figure 1. d) MoSi₂-10 vol% SiC, e) MoSi₂-30 vol% SiC, f) MoSi₂-10 vol% SiC_w

Test Apparatus

Thermal gradients were obtained by inductively heating 17.1 mm diameter, 2 mm thick, disk-shaped specimens [6] around their peripheries using a Lepel 2.5 kw (120 kHz) induction generator coupled to a plate concentrator coil. This technique relies upon the skin effect obtained with high frequency induction heating of metals[7], at 120 kHz the skin depth obtained in MoSi₂ is approximately 1 mm. The disks had a 2.85 mm hole centered in the disk to allow them to be spun in the plane of the coil to ensure uniform heating around the periphery. Under rapid heating, the shallow heating depth generates a radial temperature gradient from the specimen periphery to the cooler core.

Temperature History

Test samples were subjected to two different temperature-time profiles (see Figs. 2a and b). Fig. 2a shows a 5 s heating cycle from 700 C to 1200 C, with a 15 s hold at 1200 C, followed by a convection cool for 5 s to 700 C, and a 15 s hold at 700 C. This profile will be referred to in the rest of the paper as the 5 s profile. Fig. 2b shows a 30 s heating from 700 C to 1200 C, with a 15 s hold at 1200 C, followed by a 30 s controlled cool to 700 C, and a 15 s hold at 700 C. This will be referred to as the 30 s profile.
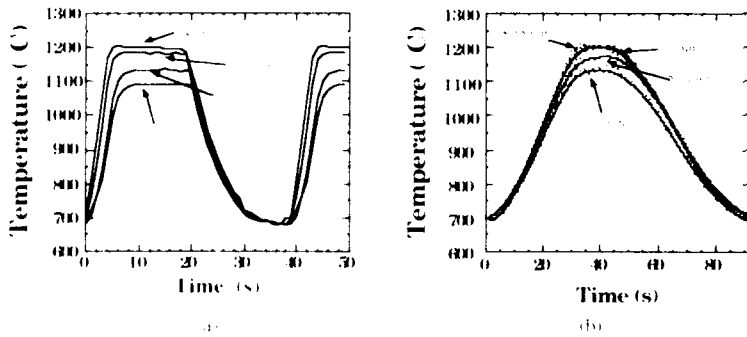
Figure 2. Temperature history of 17.1 mm diameter specimens, at different radial distances from the specimen center used in the thermal fatigue study. (a) 5 s heating and 30 s cooling with 15 s hold at 1200 C (b) 30 s heating and 30 s cooling with 15 s hold at 1200 C

ELASTIC STRESS-STRAIN HISTORY

Finite-Element Modeling (FEM)

The elastic stress-strain history of the test specimens was determined using the finite element program ABAQUS[8]. Only results for the monolithic material are presented at this stage of the research. A 45° octant of the disk specimen was chosen optimum modeling of the stress-strain history of the composite materials, which will be discussed in future publications. The 136 element mesh used was made up of 8-node, bi-quadratic, plane-stress elements, each with nine integration points. Displacements in radial directions were constrained and shear stresses were set to zero to maintain symmetry.

FEM Results

The circumferential stress data from the FEM model is given as a function of radial distance from the specimen center in Fig. 3a for the 5 s profile. At the start of a thermal cycle, the material is nearly at a state of zero stress. After the transient heating period (5 seconds), the inner radius reaches a peak tensile stress of 305 MPa and the outer radius reaches a peak compressive stress of 680 MPa. During the hold at peak temperature (15 seconds), a steady-state stress state is developed where the inner radius is at approximately 177 MPa in tension, while the outer radius is at approximately 170 MPa compression. The subsequent transient cool-down period (10 seconds) develops approximately 15 MPa compression in the inner radius and 130 MPa tension in the outer radius.
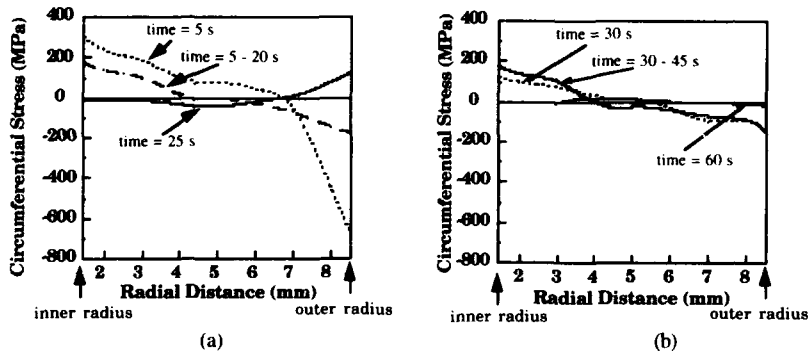
Figure 3. Circumferential stress as a function of radial distance on the sample at various times after initial heat up. a) 5 s profile b) 30 s profile

THERMAL FATIGUE RESULTS

Monolithic MoSi$_2$

When the monolithic material was subjected to the 5 s profile, the material cracked on the initial cycle during the ramp from 700°C to 1200°C. See Fig. 4 for a typical fracture. Detailed SEM analysis shows the fracture to be transgranular. However, the monolithic material could be thermal stress cycled when subjected to the less severe 30 s profile. Specimens could be cycled 5000 times between 700°C and 1200°C without fracture. An adherent SiO$_2$ layer was present on

the material after the fatigue test. There was no evidence of thermal fatigue cracking in the matrix material.
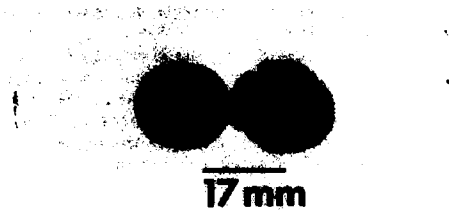
Figure 4. One-cycle fracture of monolithic MoSi$_2$ fatigue specimens.

MoSi$_2$-TiC Composites

The 10 vol% TiC composite material also cracked during the initial heat ramp from 700°C to 1200°C of the 5 s profile. The failure of this material might be related to the amount of SiO$_2$ present in the sample, in that the amount of SiO$_2$ dispersed in the matrix is very similar to the amount of SiO$_2$ in the monolithic material. Future studies on cleaner materials planned for the future should help in understanding the failure of these materials When subjected to the 30 s profile however, the material could be thermal stress cycled for 5000 cycles. A oxide layer was formed during the test, similar to that in Fig. 5 for a 30-vol% TiC composite. The oxide was verified to be TiO$_2$ by microbeam analysis.

The 30 vol% TiC composite material could be subjected to 5000 cycles of the 5 s profile without failure. A TiO$_2$ oxide layer formed during the test. See Fig. 5 for an SEM cross-sectional view of a 30-vol% TiC composite specimen cycled for 5000 cycles. The oxide layer is approximately 75 μm thick and appears to be adherent. The oxide also penetrates into the matrix material to a depth of 200 μm.
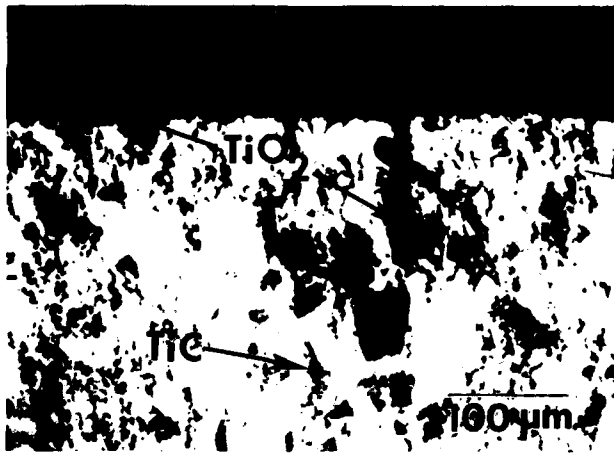
Figure 5. Surface and near-surface oxidation of a MoSi$_2$-30 vol% TiC composite thermally cycled between 700°C and 1200°C.

MoSi$_2$-SiC Composites

Both the 10 vol% SiC particulate and the 30 vol% SiC particulate composites could be subjected to the 5 s profile for 5000 cycles without failure. The SiC composites exhibited excellent thermal fatigue and thermal shock resistance compared to the monolithic material. The material formed an adherent SiO_2 oxide layer during the fatigue test. There was no evidence of cracking in the matrix due to the thermal stress cycling.

The 10 vol% SiC whisker composite cracked during the first 5-10 cycles of the 5 s profile. In spite of this low cycle cracking, the material could be thermal stress cycled through a 5000 cycle fatigue test without failure. A macroscopic crack had developed from the inner radius to the outer radius of the disk on one side, and a partially developed crack 180° from the fully developed crack was noted. The cracking seems to be a result of powder processing induced defects in the material rather than from a thermal fatigue crack mechanism.

SUMMARY

Induction heating of disk-shaped specimens and finite element analysis of the thermal cycling data were used to study the thermal fatigue behavior of $MoSi_2$ and $MoSi_2$-based composites at various heating and cooling rates between 700°C and 1200°C. From these tests, it was found that $MoSi_2$-based composite materials had greatly improved thermal fatigue resistance compared to the monolithic material. Monolithic $MoSi_2$ and a $MoSi_2$-10 vol% TiC composite failed upon initial heating in the first cycle except at the lowest heating rates employed. This could be due to the amount of SiO_2 present in these materials. The $MoSi_2$-30 vol% TiC composite that was subjected to the 5 s profile remained uncracked after 5000 cycles. The material, however, formed an undesirable TiO_2 oxide layer. The SiC particulate composites performed the best of all materials examined. Both the 10 and 30 vol% SiC particulate composites that were subjected to the 5 s profile remained uncracked after a 5000 cycle fatigue test. The SiC whisker composite did not show an improved thermal fatigue resistance, presumably due to the processing induced defects that were present.

ACKNOWLEDGMENTS

REFERENCES

1.   J.B. Berkowitz-Mattuck and R.R.Dils, J. Electrochem. Soc., 112 [6] 583 (1965).
2.   J.W. Holmes, F.A. McClintock, K.S. O'Hara and M.E. Connors, Low Cycle Fatigue, ASTM STP 942, H.D. Solomon et al., eds., ASTM, Philadelphia, PA, 672 (1987).
3.   Y.S. Touloukian, R.K. Kirby, R.E. Taylor and T.Y.R. Lee, Thermophysical Properties of Matter, IFI/Plenum, New York, NY, 13 (1973).
4.   D. Miracle and H. Lipsitt, J. Am Ceram. Soc. 66, 592 (1983).
5.   W.S.Gibbs, J.J.Petrovic and R.E.Honnell, Ceram. Eng. Sci. Proc., 8, 645 (1987).
6.   M.T.Kush, J.W.Holmes and R.Gibala in High Temperature Silicides and Refractory Alloys, edited by B.P.Bewlay, J.J.Petrovic, C.L.Briant, A.K.Vasudevan and H.A.Lipsitt (Mater. Res. Soc. Proc. 322, Pittsburgh, PA, 1994) in press
7.   P.G.Simpson, Induction Heating: Coil and System Design, McGraw-Hill Book Company, Inc., New York, 5 (1960).
8.   ABAQUS Users Manual, Hibbitt, Karlsson and Sorensen, Inc., Providence, R.I., (1982).

WEAR BEHAVIOR OF MoSi₂ AND MoSi₂ MATRIX COMPOSITES

D.E. ALMAN, J.A. HAWK, and A.V. PETTY, Jr.
U.S. Bureau of Mines, Albany Research Center, Albany, OR 97321-2198

ABSTRACT

The U.S. Bureau of Mines is examining the wear behavior of a variety of advanced materials, including the intermetallic compound $MoSi_2$. The high stiffness and hardness of $MoSi_2$ make it attractive for use in applications requiring wear resistance. This research reports on the results of pin abrasion wear tests for a variety of powder processed $MoSi_2$ and $MoSi_2$ matrix composites. The effect of the addition of ductile (Nb) and brittle (SiC) reinforcements, as well as the influence of reinforcement type and orientation geometry, on abrasive wear is discussed. Comparisons of the wear behavior of $MoSi_2$ and $MoSi_2$-based composites with other materials, such as refractory metals, aluminides, and ceramics, are made.

INTRODUCTION

Research at the U.S. Bureau of Mines shows monolithic $MoSi_2$ to be extremely wear resistant in a severe two-body abrasive environment [1]. $MoSi_2$ is attractive as a wear-resistant material because it possesses high hardness (846 kg/mm², Knoop [2]) and high elastic modulus ($\sim$ 400 GPa [3,4]). In addition, $MoSi_2$ is an attractive composite matrix material because of its low density (6.25 mg/mm³ [5]) and excellent resistance to elevated temperature oxidation [6] and hot corrosion [7]. The ambient temperature fracture toughness of $MoSi_2$, however, is poor ($\sim$ 3 MPa$\sqrt{m}$ [8]). Reinforcing $MoSi_2$ with SiC or Nb, for instance, has resulted in significantly improved fracture toughnesses (i.e., an increase to about 8 MPa$\sqrt{m}$ with 20 vol% SiC [8,9] and to about 12 MPa$\sqrt{m}$ with 20 vol% Nb filament [10]). It is also true that the wear rate of many materials can be reduced by as much as a factor of ten by the introduction of a suitable reinforcement phase [11]. Both soft and hard reinforcing phases have been effective in improving the fracture toughness of monolithic $MoSi_2$; consequently, these reinforcements may also enhance the wear resistance of the resulting composite. The $MoSi_2$ and $MoSi_2$-composites of this study are produced by two processing routes: (i) conventional hot-isostatic pressing of pre-alloyed $MoSi_2$ powder, and (ii) initiating an SHS reaction between elemental constituent powders. This latter technique is attractive because it is an economical method of producing reinforced composites *in situ*. In this study, the wear behavior of $MoSi_2$-based composites produced by both techniques is evaluated, along with the effect of Nb reinforcement geometry. Finally, the wear behavior of these composites is compared to the abrasive wear of several aluminides and ceramics.

EXPERIMENTAL PROCEDURES

The $MoSi_2$ and $MoSi_2$-Nb based composites were fabricated using standard powder metallurgical techniques. Commercially available $MoSi_2$ powder was cold isostatically pressed (CIPed), vacuum encapsulated in Ti cans, and consolidated by hot isostatically pressing (HIPing)

at 1350°C and 162 MPa for 3 hours. Niobium fibers or particles (equivalent to 20 vol% or 25 wt%) were incorporated into the $MoSi_2$ powder prior to CIPing, using a hand lay-up infiltration technique for the aligned fibers [12] or standard powder metallurgy mixing of the chopped fibers and particles. The composites were then HIPed as described above. Table I summarizes the geometry and size/orientation parameters of the Nb reinforcements used in this study.

Table I. Reinforcement Parameters Used in $MoSi_2$-20 v% Nb Composites

ID	Composite	Nb Size/Orientation
A	$MoSi_2$	none
B	$MoSi_2$ + Nb fibers	800 μm/random, short
C	$MoSi_2$ + Nb fibers	400 μm/aligned#
D	$MoSi_2$ + Nb fibers	800 μm/aligned#
E	$MoSi_2$ + Nb particles	108 μm/random*

fibers aligned perpendicular to wear surface.
* average size of the Nb particles

To produce a $MoSi_2$-20 vol% SiC composite via an SHS process, elemental powders of Mo and Si were mixed with 8 μm diameter graphite fibers and placed in a graphite die. The powder compact was heated in a vacuum hot press to 1450°C and 20 MPa pressure to initiate the SHS reaction. The compact was then held at this temperature and pressure for one hour to facilitate full density. It was expected that the elemental Si would react with the graphite fibers to produce SiC fibers, in-situ. However, subsequent analysis showed that a partial conversion to SiC occurred, but it was restricted to a thin layer surrounding the graphite fiber [13].

Abrasive wear tests were performed on the Bureau of Mines pin abrasion wear tester. A description of the pin abrasion test and the general operating procedures are given in References 14 and 15. For the wear tests performed in this study, cylindrical pins of the $MoSi_2$, $MoSi_2$-Nb and $MoSi_2$-SiC composites, the refractory alloy Nb, the intermetallic aluminides TiAl and Fe_3Al, and 99.5%-Al_2O_3, and partially stabilized ZrO_2 (PSZ) were abraded on 150 grit garnet, a naturally occurring mineral. The garnet has a Vickers hardness (VHN) of 1336 kg/mm², and the average abrasive particle size for the 150 grit cloth falls in the range of 80 to 100 μm. The results were reported as the density corrected wear rate (mm³/m), W_c, for the materials tested.

The densities listed in Table II were experimentally determined for each material. Note from Table II that neither the $MoSi_2$ nor the $MoSi_2$-Nb composites appear fully dense (about 93 percent dense when compared to the theoretical densities). However, the $MoSi_2$ powder contained 1.8 wt% oxygen (specifications supplied by the vendor), which is common for commercially available $MoSi_2$ powders [16]. Assuming the oxygen reacts with Si to form SiO_2 (ρ = 2.6 mg/mm³), it is estimated that the composites contain 8 vol% SiO_2. The composites are near fully dense when compared to a SiO_2 compensated density for $MoSi_2$ (ρ = 5.96 mg/mm³, making the density of monolithic $MoSi_2$ 97.8% of theoretical). Likewise, the $MoSi_2$-Nb composites are near full density when compensated for the SiO_2 formed during processing. In this case, assuming 8 vol% SiO_2, the composite density with 20 vol% Nb would be 6.42 mg/mm³. This means that the densities of the $MoSi_2$-Nb composites are between 97.4 and 99.5% of theoretical.

Table II. Abrasive Wear Rates of MoSi₂ and MoSi₂-Based Composites

Table II. Abrasive Wear Rates of $MoSi_2$ and $MoSi_2$-Based Composites

Composite/ Alloy	Process Route	Theoretical Density (mg/mm³)	Measured Density (mg/mm³)	Matrix Hardness VHN (kg/mm³)	Wear Rate W_c (mm³/m)
A	HIP	6.25	5.83	813 ± 41	0.11
B	HIP	6.69	6.28	837 ± 51	0.07
C	HIP	"	6.25	847 ± 42	0.04
D	HIP	"	6.39	854 ± 42	0.03
E	HIP	"	6.30	893 ± 31	0.02
MoSi₂+SiC*	SHS	5.64	5.28	---	0.14

* This sample contained a significant amount of free graphite.

RESULTS AND DISCUSSION

The results of the abrasive wear tests for the $MoSi_2$ and $MoSi_2$ composites on 150 grit garnet are listed in Table II along with their measured densities and Vickers hardness (VHN). Table III presents the wear data for the intermetallics and the ceramic materials.

The addition of Nb to $MoSi_2$ as a ductile reinforcing phase results in a significant reduction in the abrasive wear rate for all Nb-containing composites compared to monolithic $MoSi_2$. Notice that Nb wears at a higher rate on garnet than does monolithic $MoSi_2$ (i.e., 2.16 mm³/m versus 0.11 mm³/m). However, reinforcing the $MoSi_2$ with 20 vol% Nb, whether in the form of fibers or particles, dramatically lowers the abrasive wear rates of the composites. Figure 1 shows the wear surfaces of monolithic $MoSi_2$ and the $MoSi_2$-800 μm random Nb fiber composite. Monolithic $MoSi_2$ wears primarily by edge cracking, i.e., micro-fracture of the leading edge of the specimen pin as it contacts the garnet abrasive. Also found in Figure 1(a) are shallow wear grooves in the $MoSi_2$, a sign of micro-cutting. In Figure 1(b), two wear mechanisms are apparent in the composite. In the $MoSi_2$ matrix, both micro-fracture and micro-cutting occur as previously observed for the monolithic $MoSi_2$ (Fig. 1 (a)). However, the primary wear mechanism in the Nb reinforcement is micro-cutting. In this phase, the wear grooves are much more pronounced and deeper in appearance.

This difference in wear groove depth is directly related to the ratio of the hardness of the worn material (H) to the hardness of the abrasive (H_a), i.e., H/H_a [17]. For the monolithic $MoSi_2$, the matrix hardness is 813 kg/mm², leading to a H/H_a ratio of 0.61. In comparison, the H/H_a ratio for Nb is only 0.07. In general, as H/H_a increases, the amount of material removed by abrasion decreases. Consequently, the difference in H/H_a between the $MoSi_2$ and Nb suggests a difference in the abrasive wear rate of approximately one order of magnitude [17]. This is roughly the difference in wear rate observed for these materials.

For the $MoSi_2$-Nb composites, the Nb particle reinforced composite (108 μm particles) possesses the highest abrasive wear resistance. The composite with the aligned Nb fibers (i.e., either the 400 μm or 800 μm fibers aligned perpendicular to the abrasive wear surface) exhibits the next best wear resistance. Of these two composites, the one with the 400 μm diameter fibers wears at a slightly higher rate compared to the one with the 800 μm diameter fibers. The composite with the relatively poorest wear resistance is the one with the short, randomly oriented 800 μm diameter fibers.

Table III. Abrasive Wear Rates for Niobium, Intermetallics, and Ceramics

Alloy/Ceramic	Density (mg/mm³)	Matrix Hardness (kg/mm²)	W_c (mm³/m)
Nb	8.55	92	2.17
Fe₃Al	6.72	235	1.06
TiAl	3.90	255	1.19
99.5 Al₂O₃	3.97	1346	0.04-0.07
PSZ	5.75	1203	0.02
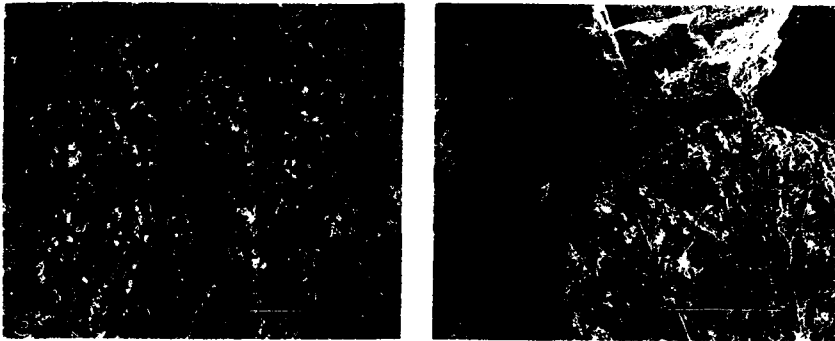
Figure 1   Photomicrographs of abrasive wear in (a) monolithic hot-pressed MoSi₂ and (b) hot-pressed MoSi₂-800 μm random Nb fiber composite.
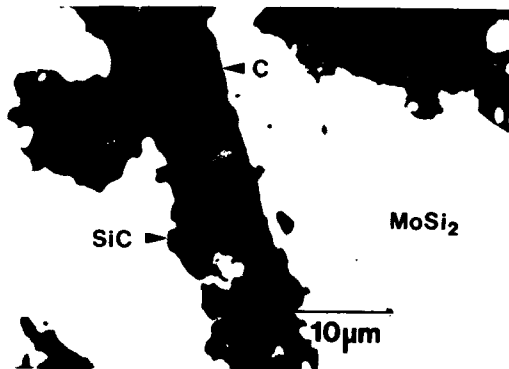
Figure 2   Backscattered electron micrograph showing the partial reaction of the graphite fiber to SiC.

The MoSi$_2$-SiC composite has the highest wear rate of all the MoSi$_2$-based materials tested. The primary reason for the poorer wear resistance is the incomplete reaction of the graphite fibers to SiC during the SHS processing and heat treatment cycle (Figure 2). The composite has a MoSi$_2$ matrix with reinforcing fibers consisting of an outer shell of SiC surrounding a graphite core. Consequently, this reinforcement does not possess the normal high hardness of SiC.

The superior wear behavior of the MoSi$_2$-Nb composites is unexpected since Nb wears at a much higher rate than MoSi$_2$. It was anticipated that the MoSi$_2$-Nb composites would possess a slightly higher wear rate than monolithic MoSi$_2$, because of the incorporation of the larger sized, less wear resistant Nb phase.

In fiber or particulate reinforced composites, wear is dependent on the size and orientation of the reinforcing phase, the bond strength between reinforcement and matrix, and the resistance of the reinforcement to fracture [18]. For example, it is observed that for a TaC fiber reinforced NiCrAl composite, the highest wear rate occurs when fibers are oriented parallel to the wear surface [18]. In such an orientation, it is easier for the fibers to preferentially wear or be separated from the matrix. Therefore, it can be expected that a randomly oriented, short fiber composite would wear at a higher rate than an aligned fiber reinforced composite (i.e., with the fibers oriented perpendicular to the wear surface). It is also observed that aligned fiber composites (i.e., with the long axis of the fibers perpendicular to the wearing surface) wear at a decreased rate compared to composites with fibers oriented parallel to the wearing surface [18]. This same trend in wear behavior is also observed in this study. Only the enhanced wear behavior of the particle strengthened composite is unexplained at this time.

Although the superior wear behavior of the MoSi$_2$-Nb composites was unexpected in magnitude, the increasing wear resistance of these composites does follow the usual trend with increasing composite hardness (Table II). Of the hot-pressed materials, the highest abrasive wear rate belongs to the monolithic MoSi$_2$, which also has the lowest Vickers hardness. Composite E (the Nb particulate reinforce composite) has the lowest wear rate and the highest hardness. This variation in the matrix hardness of the MoSi$_2$ correlates with grain size: composite E has the smallest MoSi$_2$ grain size (5 μm), whereas, composites B, C, and D have a MoSi$_2$ grain size of 10 μm, and the monolithic MoSi$_2$ (material A) has a grain size on the order of 20 μm. The difference in grain size is attributed to variations in the starting MoSi$_2$ powders, as the composites were produced from powders from three different lots of a specific grade powder obtained from a sole vender (composites B, C, and D are from the same lot, while A and E are from different lots). However, the variation in hardness between the high and low values is only 9%, while the variation in wear rate between these two extremes is 82%. This seems to indicate that hardness alone is not responsible for the increased wear rate and that the other factors mentioned above may also be important.

The wear rates of Nb, the intermetallic alloys (Fe$_3$AL and TiAl), and the ceramics (99.5% Al$_2$O$_3$ and PSZ) span the range of wear rates for the MoSi$_2$ and MoSi$_2$-based composites. The wear rate for MoSi$_2$ is approximately a factor of ten less than the wear rates for Nb and the intermetallics. The wear rates for the MoSi$_2$ composites are of equivalent magnitude to those of the ceramics. The mechanisms of material removal for the Nb and the intermetallics is identical to that observed in the Nb reinforcement. Conversely, the mechanisms of material removal for the ceramics are the same as those observed in the MoSi$_2$. This is not surprising since the MoSi$_2$ is brittle and its hardness is nearly the same as that of the garnet abrasive. Consequently, little plastic deformation and cutting occur, and wear must proceed through brittle fracture.

199

SUMMARY AND CONCLUSIONS

Reinforcing $MoSi_2$ with ductile Nb fibers and particles produces a more wear resistant composite, with wear rates equivalent to those of 99.5% Al_2O_3 and PSZ. One hundred and eight micrometer diameter, randomly distributed Nb particles result in a composite with a very low wear rate (0.02 mm^3/m) on garnet. Niobium fibers, with their long axis oriented perpendicular to the wear surface, produce intermediate wearing composites (i.e., wear rates of 0.03-0.04 mm^3/m). The composite with randomly oriented, short fibers possesses the highest wear rate (0.07 mm^3/m) of the Nb containing composites. However, each composite has a wear rate that is lower than that of monolithic $MoSi_2$ (0.11 mm^3/m). The wear behavior of the SHS $MoSi_2$-SiC (with residual graphite) is equivalent to that of the monolithic HIPed $MoSi_2$.

REFERENCES

1. J.A. Hawk and D.E. Alman, Scripta Metall. Mater. (submitted for publication).
2. R.A. Long, "Fabrication and Properties of Hot-Pressed $MoSi_2$," NACA RM-E50F22, 1950.
3. N. Nakamura, S. Matsumoto, and T. Hirano, J. Mater. Sci. 25, 3309 (1990).
4. S.R. Srinivasan and R.B. Schwarz, J. Mater. Res. 7, 1610 (1992).
5. A.K. Vasudevan and J.J. Petrovic, Mater. Sci. Engr. A155, 1 (1992).
6. E. Fitzer, in Plansee Proceedings 2nd Seminar, ed. F. Benesovsky (Ruette/Tyrol, 1956), p.57.
7. J. Schlichting, in Special Ceramics-6, ed. P. Popper (The British Ceramic Research Association, Stoke-on-Trent, 1975), p. 161.
8. D.H. Carter and G.F. Hurley, J. Am. Ceram. Soc. 70, C79 (1987).
9. A.K. Bhattacharya and J.J. Petrovic, J. Am. Ceram. Soc. 74, 2700 (1991).
10. L. Xiao, Y.S. Kim, R. Abbaschian, and R.J. Hecht, Mater. Sci. Engr. A144, 277 (1991).
11. T.W. Clyne and P.J. Withers, An Introduction to Metal Matrix Composites (Cambridge University Press, Cambridge, 1993), p. 294.
12. D.E. Alman, K.G. Shaw, N.S. Stoloff, and K. Rajan, Mater. Sci. Engr. A155, 81 (1992).
13. D.E. Alman and C.P. Dogan, Scripta Metall. Mater., 31 (3) (1994).
14. R. Blickensderfer and G. Laird II, J. Test. Eval. 16, 516 (1988).
15. R. Blickensderfer, J.H. Tylczak and B.W. Madsen, Bureau of Mines Information Circular (IC 9001), 1985.
16. D.A. Hardwick, P.L. Martin and R.J. Moores, Scripta Metall. Mater. 27, 391 (1992).
17. M.A. Moore, in Treatise on Materials Science and Technology, Vol. 13, ed. D. Scott (Academic Press, New York, 1979), p. 242.
18. K.H. Zum Gahr, Microstructures and Wear of Materials (Elsevier Science Publishers B.V., Amsterdam, 1987), p. 36.

NiAl Composites and Advanced Intermetallic Composites

STATUS AND DEVELOPMENT OF NICKEL ALUMINIDE (NiAl) COMPOSITES

R. A. AMATO* AND J.-M. YANG**
*GE Aircraft Engines, Cincinnati, OH
**Department of Materials Science and Engineering, University of California,
Los Angeles, CA 90024-1595

ABSTRACT

NiAl-based composites are a new class of engineering materials being developed for high temperature structural applications in oxidizing and aggressive environments. This paper discusses some of the recent advances in developing continuous fiber-reinforced polycrystalline NiAl-based composites. Several key issues including matrix alloy development, fiber development, fabrication development and mechanical behavior will be addressed.

INTRODUCTION

NiAl-based intermetallics have been recognized as one of the most promising candidate materials for high temperature structural applications [1,2]. They possess several attractive properties including low density (~ 6 g/cm^3) which is approximately 2/3 that of state-of-the-art nickel-base superalloys, high melting point (1638°C) which is approximately 300°C higher than the nickel-base superalloys, high modulus (189 GPa) and excellent oxidation resistance up to 1300°C. Furthermore, polycrystalline NiAl exhibits a brittle-to-ductile transition at temperatures ranging from 300°C to 600°C which is significantly lower than other intermetallic compounds, the exact temperature depending on the stoichiometry, impurity content and grain size. However, to make NiAl a viable material, it is necessary to overcome some of its inherent problems. These include low ductility and fracture toughness at ambient temperatures and inadequate strength and creep resistance at elevated temperatures. Accordingly, significant efforts have centered on enhancing the mechanical properties of NiAl through grain refinement and micro- and macro-alloying as well as incorporating second phase reinforcements [3-5]. Recent studies have indicated that the incorporation of continuous reinforcing fibers appears to be the most promising approach to overcome many of NiAl's inherent deficiencies.

The purpose of this paper is to summarize the recent developments in continuous fiber reinforced polycrystalline NiAl-based composites. Several key issues including alloy development, fiber development, fabrication development and mechanical behavior will be addressed.

MATRIX ALLOY DEVELOPMENT

The primary function of the matrix in a composite is to transfer load to the

fibers and provide environmental protection to the composite system (including the fiber or any fiber coating). Of course the matrix properties define the transverse strength limitations of the composite system and hence, the matrix must have enough strength to withstand secondary loading in off-axis directions. The matrix requirements, therefore, are to have adequate strength to transfer load and provide transverse strength and suitable oxidation resistance to protect the composite system. These properties must be retained with time.

Further if a ductile matrix composite approach is intended, enough strain-to-failure is required to account for the fiber strain-to-failure plus any residual tensile strains that develop in the matrix due to thermal expansion mismatches between the fiber and matrix. For oxide fiber reinforced nickel based composites, this total strain-to-failure requirement can be as high as 2.5% at room temperature.

Oxidation resistance at 1100°C for a variety of NiAl based alloys is plotted as a function of elevated temperature yield strength in Figure 1. The alloys included in this comparison were developed for improved toughness, but have less than 2.5% ductility. While several alloys have increased strength compared to NiAl, only three alloys: Ni-50Al-0.05Zr, Ni-32.5Al-20Fe, and Ni-42Al-8Fe, combined strength
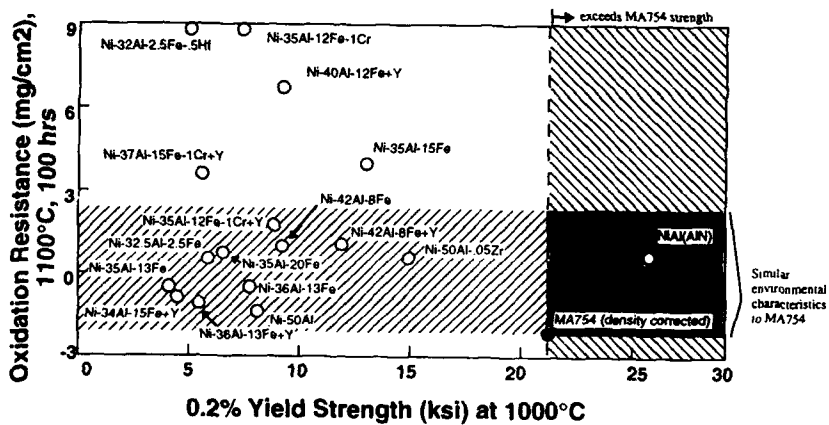
Figure 1   Oxidation resistance at 1100 °C versus elevated temperature yield
strength for a variety of NiAl alloys

with suitable oxidation resistance. It should be pointed out that data for a fourth alloy, NiAl(AlN), has been limited to results from compression testing, and the alloy is expected to have very low toughness and ductility at room temperature. It is therefore considered premature to consider this alloy for a fiber reinforced composite matrix.

For comparison, Figure 1 includes data for a common oxide dispersion strengthened nickel base alloy, MA754. MA754's weight gain after 100 hours at 1100°C is -2.5 mg/cm^2. Its yield strength at 1000°C is approximately 175 MPa. Correcting for comparison to the NiAl based matrices, MA754 has a density corrected strength of 147 MPa (175 MPa x 0.25 mg/cm^3/0.3 mg/cm^3). None of the developmental NiAl alloys exceed the 147 MPa density corrected yield strength capability of MA754.

In summary, no alloys have been developed to date that have the combined strength, ductility, and oxidation resistance equal to that of the oxide dispersion strengthened alloy MA754. Prior to pursuing NiAl matrix composites further, alloys would need to be developed that meet or exceed the capability of MA754 or a similar baseline alloy.

FIBER DEVELOPMENT

Reinforcements for the NiAl based composites have primarily been limited to oxide based systems due to their chemical compatibility and strength. The oxide monofilament, sapphire (Al$_2$O$_3$) as produced by Saphikon Inc. (Milford, NH), has been of particular interest based on its high creep resistance and low reaction potential. Recent investigations have indicated a large time dependent effect on the rupture strength of sapphire fiber (decreasing strength with reduced strain rate). An alternative oxide fiber produced by Saphikon is based on the eutectic composite Y$_3$Al$_5$O$_{12}$ (YAG) and Al$_2$O$_3$. It has indicated a dramatic improvement in rupture strength over sapphire.

The microstructure and fracture morphology of a YAG-Al$_2$O$_3$ eutectic fiber are shown in Figures 2a and b. The fiber has been found to contain either a rod-like or a Chinese script morphology. Figure 2a shows the YAG reinforcement phase (light) in an Al$_2$O$_3$ matrix (dark). The stress rupture life of the YAG-Al$_2$O$_3$ fiber is compared to the sapphire Al$_2$O$_3$ fiber at 1095 °C (2000 °F) in Figure 3. The 100 hour rupture strength of the YAG-Al$_2$O$_3$ fiber was measured to be 910-1145 MPa while the 100 hour rupture strength of the sapphire fiber was measured to be 630 MPa. At a load of 980 MPa, the rupture life of the YAG-Al$_2$O$_3$ fiber is found to be about 4 orders of magnitude higher than the rupture life of the Al$_2$O$_3$ fiber.

The tensile strengths of the YAG-Al$_2$O$_3$ fiber at room temperature and 1100°C are 2.3 and 1.6 GPa, respectively. Sapphire fiber strength is 3.4 and 1.2 GPa at room temperature and 1100°C. Note that for the NiAl based composites room temperature fiber strength has not been considered to be a key requirement.

(a)   (b)
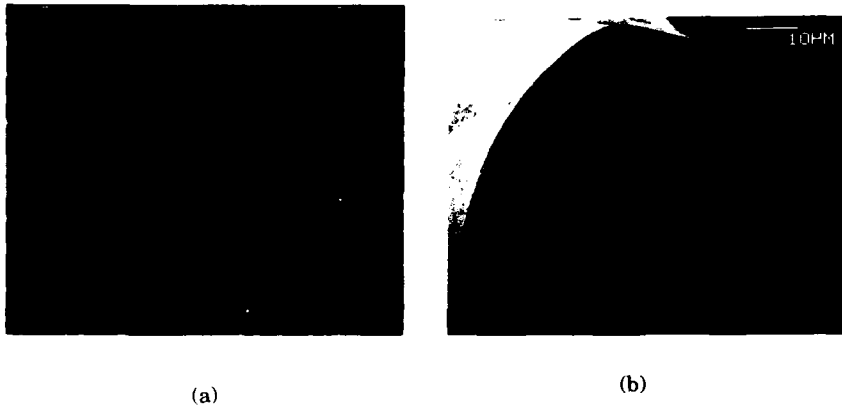
Figure 2   (a) Microstructure and (b) fracture morphology of the YAG-Al$_2$O$_3$
              eutectic fiber

While the YAG-Al$_2$O$_3$ fiber has promising elevated temperature properties,
no NiAl based composites have been fabricated with these new fibers. In other
nickel based matrices, however, the composites incorporating YAG-Al$_2$O$_3$ fibers did
not show significant improvement over composites fabricated with sapphire fibers.
As will be discussed later both the sapphire and the YAG-Al$_2$O$_3$ fibers suffered
degradation after composite processing. Further efforts into protecting the inherent
strength of these fibers during composite fabrication is a critical issue for the success
of NiAl based composites.

FABRICATION DEVELOPMENT

Several approaches are currently used to fabricate NiAl-based composites:
powder cloth, tape casting, powder-coated monofilament or fiber tow and pressure
infiltration casting. However, none of these processes are completely controlled or
reliable process.

Powder Cloth [3]

In this process, polycrystalline NiAl powder is rolled into flexible cloth-like
sheets by combing matrix powder with a fugitive organic binder and an organic

(Goal: 250 ksi, 2000 °F)
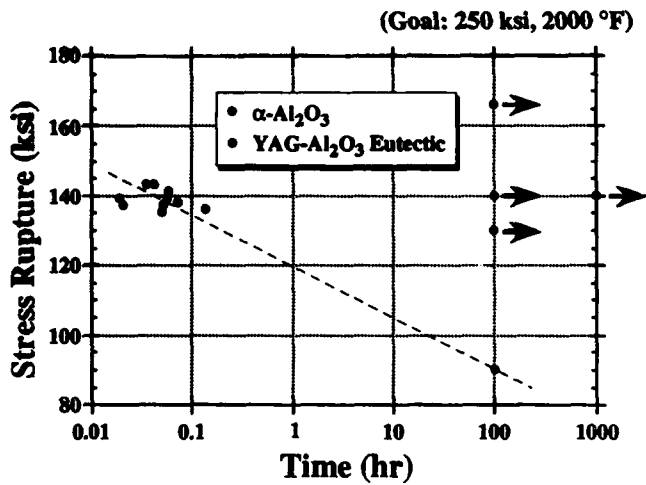
Figure 3   Stress rupture life of YAG-Al$_2$O$_3$ and Al$_2$O$_3$ fibers at 1095 °C.

wetting agent. The reinforcing fiber mats were produced by winding the fibers on a drum and then coated with organic binder to maintain proper fiber spacing. The composite panel was assembled by stacking alternate layers of matrix cloth and fiber mats. This assemblage was heated while under vacuum to an intermediate temperature to remove the binder and consolidated by hot pressing or by HIPing to ensure complete densification of the composite.

Tape Casting [6,7]

In this process, NiAl powder is mixed with organic binder and solvent to form a slurry. The slurry is then casted into a thin sheet using a tape casting process which was developed for fabricating electronic packaging from ceramic powders. The slurry may also be casted directly onto precollimated fiber mats to form a flexible prepreg as shown in Figure 4a. The matrix sheets and fiber mats are stacked and consolidated by hot pressing and/or HIPing. Uniform fiber distribution is easily achieved using tape casting technique to fabricate an Al$_2$O$_3$/Ni-32Al-20Fe composite as shown in Figure 4b.

Powder-Coated Monofilaments or Fiber Tows [8,9]

In this process, a fiber or fiber tow is coated by drawing it through a powder/binder slurry bath or by spraying the slurry directly onto the fiber. After drying, the matrix coated filaments or fiber tows are aligned, stacked and consolidated into a dense composite.
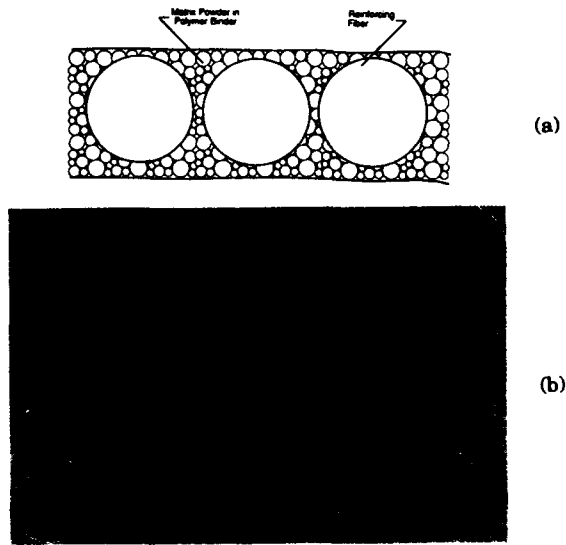
Figure 4   (a) Tape-casted preform, (b) fiber distribution in a tape-casted Al$_2$O$_3$/Ni-32Al-20Fe composite

Pressure Infiltration Casting [10,11]

Pressure infiltration casting utilizes pressurized inert gas to force molten NiAl to infiltrate into a preform of reinforcement material. The liquid metal infiltration route does not require the use of fugitive binders, thus eliminating the contamination problems resulting from incomplete binder burnout. Furthermore, the use of the powder routes also require high pressure to ensure consolidation which tends to cause fiber damage. However, the use of high processing temperatures during pressure casting might severely degrade the fibers and/or result in excessive fiber/matrix interfacial reaction.

MECHANICAL BEHAVIOR

The longitudinal tensile strengths of several unidirectional Al$_2$O$_3$ fiber-reinforced NiAl-based composites as a function of temperature are shown in Figure 5. The calculated tensile strength based upon the rule of mixture (ROM) are also included for compari on. All the composites have a fiber volume fraction of approximately 20 % and were fabricated by the tape casting approach and

consolidated by hot pressing followed by HIPing. It is obvious that the tensile strength is far below that obtained by ROM at both room and elevated temperatures. It is also evident that the tensile strength is sensitive to the matrix alloy composition. All composites exhibited a linear stress-strain response until fracture at room temperature. Examination of the fracture surfaces by scanning electron microscopy revealed a brittle fracture mode without fiber pull out (Figure 6), an indicative of strong interfacial bonding. Fiber pushout test performed on a tape-casted $Al_2O_3/NiAl_{32}Fe_{20}$ composite confirmed the presence of strong interfacial bonding. The interfacial shear strength was found to be 240 MPa [5]. However, at elevated temperatures, the composite exhibited a nonlinear stress-strain repsonse. SEM observation revealed a significant fiber pull out on the fracture surfaces (Figure 6b), indicative of weaker interfacial bonding. The weakening of interfacial bonding due to relaxation of residual compressive clamping stresses would lead to weakening of transverse tensile strength at elevated temperatures.
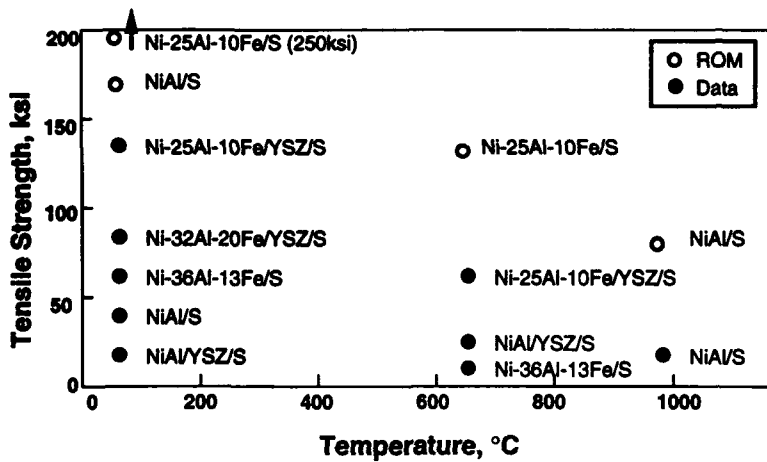
Figure 5   Longitudinal tensile strengths of several $Al_2O_3/NiAl$ composites
as a function of temperature

Etching away the matrix revealed that significant fiber breakage occurred during composite consolidation. Furthermore, the residual strength of the extracted Al_2O_3 fibers embedded in NiAl and $NiAl_{32}Fe_{20}$ was found to have decreased from 3.1 GPa to 1.4 and 2.3 GPa, respectively, as shown in Figure 7. The low composite tensile strength is therefore, attributed to fiber breakage, fiber strength degradation and high residual tensile stresses in the matrix. The residual stresses were generated due to the thermal expansion mismatch of the matrix (16 x 10^{-6}/K) and Al_2O_3 fiber (9 x 10^{-6}/K). However, the strength of the YAG-coated

(a)

(b)

Figure 6   Fracture surfaces of the tape-casted Al₂O₃/NiAl₃Fe₂₀ composite at (a) room temperature and (b) 870° C

Al₂O₃ fiber after thermal exposure to 1205° C (2200° F) for 2 hours was similar to that of the uncoated fiber in the as-received state. Significant strength degradation was also found for YAG-Al₂O₃ eutectic fiber embedded in a nickel-based alloy (HA214). This suggests that appropriate fiber coating is needed to preserve the fiber strength and to manage the residual stresses.

Figure 8 shows the transverse tensile strength of several oxide-coated Al₂O₃ fiber-reinforced NiAl₃Fe₂₀ composites at 980° C (1800° F). Various sol-gel derived oxide coatings including YAG-NiO, ZrO₂, yttrium stabilized ZrO₂ (YSZ) and YAG were used to modify the interfacial bonding. The thickness of the coating layer was approximately 0.5 μm. It is obvious that the transverse tensile strength of the uncoated composite is well below that of the matrix alloy alone. However, the elevated-temperature transverse strength of both ZrO₂ and YAG-coated composites are comparable to that of the monolithic matrix alloy. This clearly indicates that fiber coating is an effective approach to improve the interfacial bonding in Al₂O₃/NiAl₃Fe₂₀ composites.
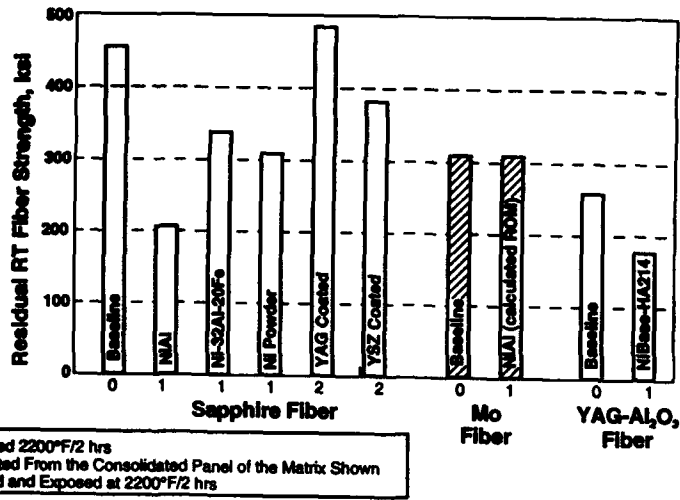
Figure 7   Residual fiber strength of YAG-Al$_2$O$_3$ and Al$_2$O$_3$ fibers after extraction from the matrix and thermal exposure.
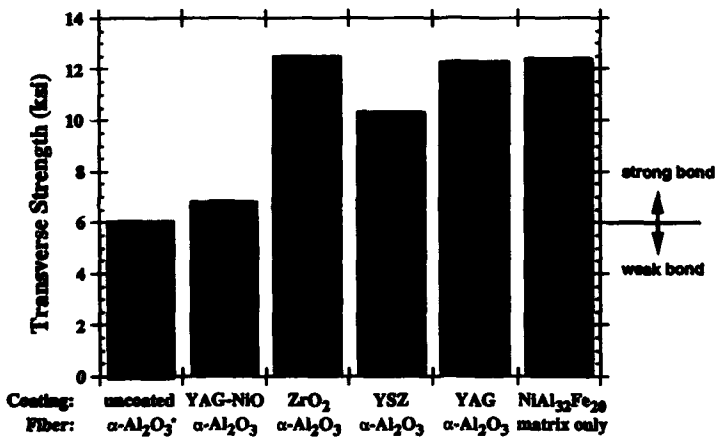
Figure 8   Transverse tensile strengths of several oxide-coated Al$_2$O$_3$/NiAl$_{32}$Fe$_{20}$ composites at 980 °C

SUMMARY

1. The combined strength, ductility and oxidation resistance of the polycrystalline NiAl alloys developed to date are inferior to those of oxide dispersion strengthened nickel-based superalloys.

2. Fiber coating is needed to preserve the fiber strength, to control interfacial properties and to manage residual stress.

3. Tensile properties of NiAl-based composites are well below ROM. Fiber breakage and strength degradation during consolidation need to be resolved.

REFERENCES

1. R. Darolia, JOM, 43 [3], 44 (1991).
2. D. B. Miracle, Acta Metall. Mater., 41[3], 649 (1993).
3. R. R. Bowman, in Intermetallic Matrix Composites II, , edited by D. B. Miracle, D. L. Anton and J. A. Graves (Mater. Res. Sco. Proc. 273, Pittsburgh, PA 1992) pp. 145-156.
4. J. Doychak, JOM, 44 [6], 46 (1992).
5. C. Y. Liu, S. M. Jeng, J.-M. Yang and R. A. Amato, to be published in Mat. Sci. Eng., 1994.
6. J. T. Niemann and J. F. Edd, in Titanium Aluminide Composites, edited by P. R. Smith, S. J. Balsone and T, Nicholas (Air Force Wright Laboratory, WPAFB, OH, 1991) pp. 300-314.
7. J. Sorenson, in Structural Intermetallics, edited by R. Darolia, J. Lewandowski, C. Liu, P. Martin, D. Miracle and M. Nathan (TMS, Warrendale, PA, 1993) pp.717.
8. S. Singerman, R. Boucher, B. Doehnert, R. Tucker and G. Doble, in Titanium Aluminide Composites, edited by P. R. Smith, S. J. Balsone and T, Nicholas (Air Force Wright Laboratory, WPAFB, OH, 1991) pp. 289-299.
9. D. Shah and D. Anton, in Structural Intermetallics, edited by R. Darolia, J. Lewandowski, C. Liu, P. Martin, D. Miracle and M. Nathan (TMS, Warrendale, PA, 1993) pp.755.
10. S. Nourbakhsh and H. Margolin, Mat. Sci. Eng., A144, 133 (1991).
11. A. J. Cook and P. S. Werner, Mat. Sci. Eng., A144, 189 (1991).

MECHANICAL BEHAVIOR OF PRESSURE-CAST Al₂O₃/NiAlFe COMPOSITES

Cyrus Liu*, S. M. Jeng*, J.-M. Yang*, E. Slater**, and A. Cook**
*Department of Materials Science and Engineering, University of California, Los Angeles, CA 90024-1595
**ACC Electronics, Inc., Pittsburgh, PA 15238

ABSTRACT

The microstructure and mechanical behavior of Al₂O₃ fiber-reinforced NiAlFe composites fabricated using the pressure casting technique were investigated. The mechanical response and fracture behavior of these unidirectional composites under tensile and three-point flexural loading were characterized. The results were compared to those measured for Al₂O₃/NiAl-based composites fabricated by powder metallurgy techniques. Preliminary results indicate that pressure casting appears to be a viable processing route for fabricating continuous fiber-reinforced NiAl-based composites.

INTRODUCTION

Nickel aluminide (NiAl) is one of the most attractive high temperature structural materials. NiAl offers a high melting point (1638 °C), a high Young's modulus (189 GPa), low density (~6 g/cm³), and good oxidation resistance to 1300 °C. Despite these advantages, polycrystalline NiAl is very brittle, having a room temperature fracture strain of ≤1% and a brittle-to-ductile transition temperature between 300 and 600 °C, depending on the grain size and alloy composition. Other problems with NiAl include poor fracture toughness at ambient temperatures and insufficient strength and creep resistance at elevated temperatures[1-3]. Continuous single crystal alumina (Al₂O₃) fiber-reinforced NiAl composites have received much attention recently as a more promising approach to improving the mechanical properties of NiAl at both ambient and elevated temperatures[4]. The sapphire fibers exhibit good chemical compatibility with NiAl, making them ideal for use in other intermetallic matrix composite systems[5]. However, these composites were fabricated using conventional powder metallurgy techniques which require the use of a fugitive binder. Incomplete removal of this binder will lead to matrix contamination and degredation of their mechanical properties. Pressure infiltration casting, which utilizes pressurized gas to force molten metal into a preform of reinforcement material[6], on the other hand, does not require the use of fugitive binders, thus eliminating this problem.

The purpose of this study is to examine the microstructure and mechanical properties of pressure-cast alumina fiber-reinforced NiAlFe matrix composites. To gain some insight into the merits of pressure infiltration casting, its behavior will be compared with that of other Al₂O₃/NiAl composites fabricated using powder metallurgy techniques.

EXPERIMENTAL PROCEDURE

The material studied was a unidirectional Al₂O₃ fiber-reinforced NiAlFe matrix composite. The composition of the matrix, a single phase β alloy, consists of 32 atomic percent (at%) Al and

20 at% Fe, with the balance Ni. Single crystal alumina fibers, produced by Saphikon, Inc. (Bedford, NH), with an average diameter of 140 µm and a room temperature tensile strength of 3.15 GPa, were used as reinforcements. Four-ply unidirectional composites were fabricated using the pressure infiltration casting technique[6]. In this processing method, a pressurized inert gas was used to force molten NiAlFe to infiltrate two different unidirectional Al_2O_3 fiber preforms. Although both preforms used alumina cement and AlN particulates at each end to hold the fibers in place, one of the preforms also included AlN particulates packed along the length of the fibers to improve fiber alignment during composite processing.

Specimens for microstructural observation were cut from the pressure-cast composite materials and polished to a 0.05 µm Al_2O_3 finish using standard metallographic techniques. Both optical and scanning electron (SEM) microscopes were used to examine their microstructures. Individual Al_2O_3 fibers from both composites were removed by etching away the matrix and examined under a SEM. Tensile and three-point bend tests were conducted using an Instron servo-mechanical testing machine operated at a crosshead speed of 0.5 mm/min. Tensile specimens measured approximately 76.2×6.35 mm with the fibers parallel to the longitudinal direction; the dimensions of the gauge section were 25.4×6.35×1 mm. The strain-to-failure was measured using a strain gauge connected to a strain gauge indicator. The chevron-notched three-point bend specimens had the dimensions 38.1×6.35×1 mm; their fibers were aligned perpendicular to the loading direction. The ratio of the notch length to the specimen width (a/w) was approximately 1/5 on all of the bend specimens tested. A SEM was used to examine the fracture surfaces of the failed specimens.

RESULTS & DISCUSSION

Microstructure

The microstructure of the pressure-cast composites is shown in Figures 1(a) and (b). The composites were fully dense with the Al_2O_3 fibers randomly distributed within the matrix. The fiber volume fraction ranged from 33-38 %. In both materials, the fiber alignment worsened as the distance from the ends increased, although alignment in the composite with AlN particulates in between the fibers (Figure 1(b)) was much better than in the material without AlN (Figure 1(a)). At the ends, the fiber spacing averaged 129 ± 43 µm in the Al_2O_3/NiAlFe + AlN material and about 117 ± 59 µm in the composite without AlN particulates. In the middle, however, fiber spacing ranged from 83 to 439 µm in the Al_2O_3/NiAlFe composite and from 97 to 306 µm in the material with AlN. SEM examination did not reveal any evidence of chemical reaction between the fiber and matrix in both composites. Figure 2 shows the second phase which was observed at the grain boundaries. Although examination of this second phase using EDX was inconclusive, X-ray diffraction on the composites did indicate the presence of $FeAl_2$. It is believed that the second phase results from segregation which often occurs during solidification. TEM examination of this material may provide additional information about the nature and origin of this second phase. The surface of an Al_2O_3 fiber removed from one of the pressure-cast composites can be seen in Figure 3(a). Although most of the surface remains smooth, there are damaged areas on the fiber surface. From the appearance of the damage, the fiber surface looks like it has been subjected to some type of chemical attack during the fabrication process. This is in marked contrast to the surface of a fiber removed from an Al_2O_3/NiAlFe composite fabricated using tape-casting[7] (Figure 3(b)) which remained quite smooth.
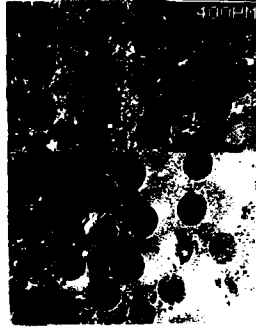
Figure 1. Microstructure of the pressure-cast (a) Al_2O_3/NiAlFe
and (b) Al_2O_3/NiAlFe + AlN particulate composites.

Figure 2. Second phase particles observed at the grain boundaries.
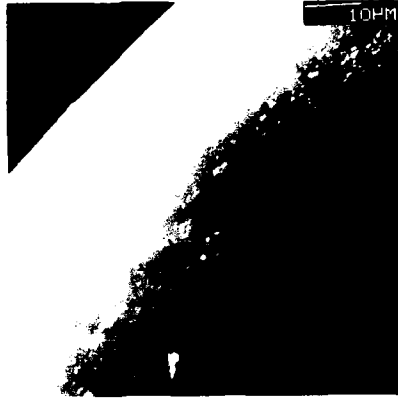
Figure 3. Surfaces of Al_2O_3 fibers removed from (a) pressure-cast
and (b) tape-cast Al_2O_3/NiAlFe composites.

215

Tensile Behavior

Typical tensile stress-strain curves of the pressure-cast Al_2O_3/NiAlFe composites both with and without AlN particulates are shown in Figure 4. Both materials exhibited linear stress-strain behavior until failure. The elastic modulus and ultimate tensile strength of the composites are listed in Table I along with values for monolithic NiAl[8]. Both of the pressure-cast materials had lower tensile strengths but higher elastic moduli than the unreinforced NiAl. This may be due either to the poor fiber alignment in the composites or the degradation in fiber strength caused by the high temperatures used during processing.
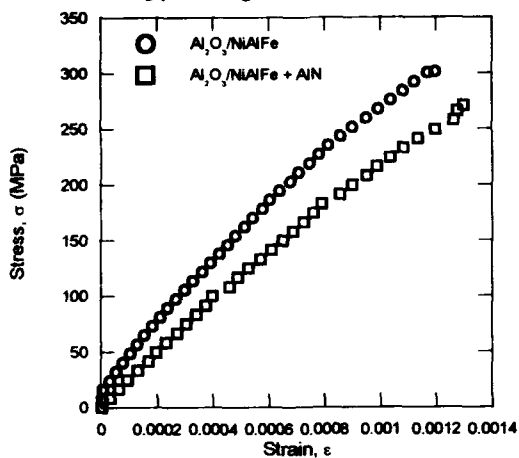
Figure 4: Typical stress-strain curves of pressure-cast Al_2O_3/NiAlFe composites

Table I. Tensile properties of Al_2O_3/NiAlFe composites and monolithic NiAl

	Al_2O_3/NiAlFe*	Al_2O_3/NiAlFe + AlN*	NiAl †
Modulus (GPa)	215	206	133
UTS (MPa)	282	266	185

*Fabricated using pressure infiltration casting; $V_f \sim 33\text{-}38\%$.
†Fabricated using the powder-cloth technique[8].

The tensile fracture surfaces of pressure-cast Al_2O_3/NiAlFe composites are shown in Figures 5(a) and (b). The failure mode in the composite without AlN particulates (see Figure 5(a)) is seen to consist mainly of cleavage in both the matrix and the fibers. The fracture surface looks quite similar to that of powder-spray Al_2O_3/NiAlFe, as shown in Figure 5(c). Failure in the composite with AlN particulates exhibits two different failure modes in the matrix along with cleavage of the Al_2O_3 fibers (see Figure 5(b)). In regions where there is a large concentration of AlN, intergranular fracture dominates. This may be due to the weak interfacial bonding between the matrix grains and the particulate phase which may lead to microcracking. Cleavage, on the other hand, is

216

hand, is still the main failure mode when there are few AlN particulates present. There is little, if any, evidence of fiber pull-out in either material, indicating that the interfacial bonding in these composites is quite strong.

(a)

(b)

(c)
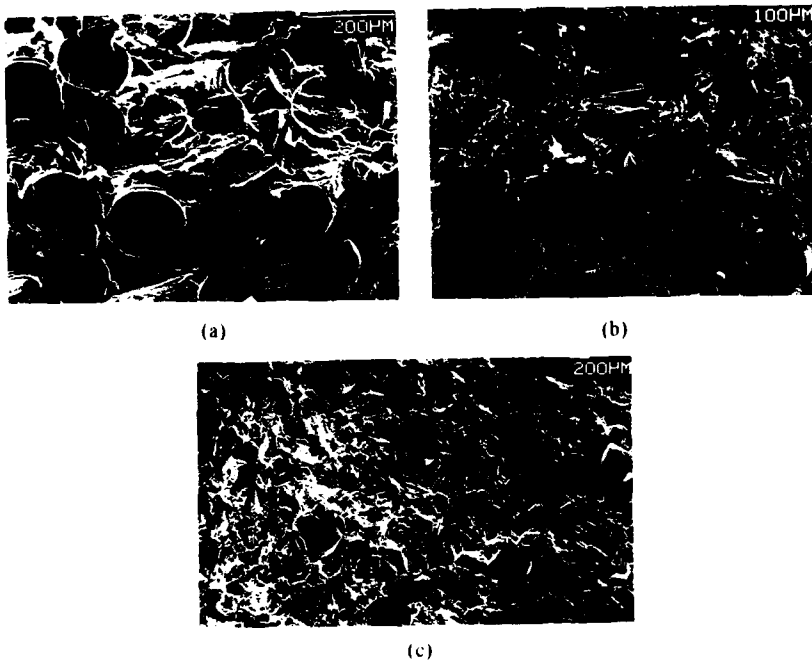
Figure 5. Tensile fracture surfaces of Al_2O_3/NiAlFe composites: (a) pressure-cast without AlN: (b) pressure-cast with AlN particulates: (c) powder-sprayed.

Fracture Behavior

Figure 6 shows the typical crack propagation pattern in a notched Al_2O_3/NiAlFe composite under three-point bending. It is obvious that the composite exhibits mode I catastrophic failure behavior which is similar to a continuous fiber-reinforced ceramic matrix composite with a strong bond. The crack propagation behavior in the composite with AlN is similar to that in the material without AlN though the surfaces are rougher due to the presence of the AlN particulates. The results confirm that the pressure-cast materials have a relatively high interfacial bond strength at room temperature. The fracture surfaces of the two composite materials, shown in Figures 7(a) and (b), are quite similar to the tensile fracture surfaces. The composite without AlN exhibits cleavage of both the matrix and the Al_2O_3 fibers (Figure 7(a)). In the composite with AlN particulates (Figure 7(b)), two different matrix fracture morphologies and cleavage of the Al_2O_3 fibers are again observed. Intergranular fracture occurs in areas of high AlN concentration while cleavage dominates where there is little AlN. The crack behaves similarly in the composite with AlN, although the surfaces are rougher due to the presence of the AlN particulates.

217

Figure 6 Typical crack propagation pattern in a notched Al₂O₃/NiAlFe composite under three-point bending.

(a)

(b)
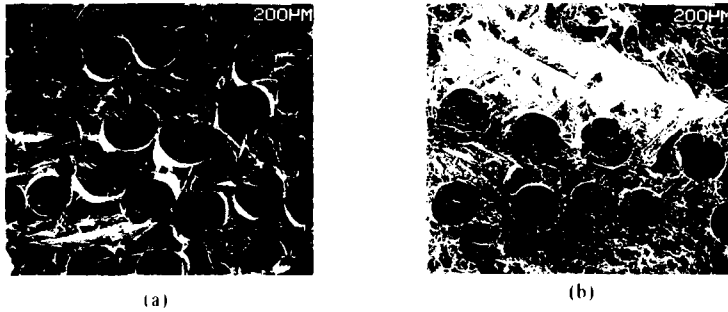
Figure 7 Fracture surfaces of pressure-cast (a) Al₂O₃/NiAlFe and (b) Al₂O₃/NiAlFe · AlN particulate composites

REFERENCES

R Darolia, *JOM*, 43(3), p 44 (1991)

F P George and C T Liu, *J Mater Res*, 5, p 754 (1990)

D B Miracle, *Acta Metall Mater*, 41(3) p 649 (1993)

C Liu, S M Jeng, J -M Yang, and R A Amato, submitted to *Mater Sci Engg*

R E Tressler and D J Barber, *J Am Ceram Soc*, 57, p 13 (1974)

A J Cook and P S Werner, *Mater Sci Engg*, A144, p 189 (1991)

J I Niemann and J F Edd, in Titanium Aluminide Composites - Workshop Proceedings, WL -TR-91-4020 (1991), p 300

R R Bowman, in *Intermetallic Matrix Composites II*, edited by (Mater Res Soc Proc 273, Pittsburgh, PA, 1992), p 145

SYNTHESIS AND MECHANICAL PROPERTIES OF NANO-SCALE NiAl and NiAl/Al₂0₃ COMPOSITES

Timothy R. Smith
Institute for Mechanics and Materials, University of California, San Diego, La Jolla, CA.

ABSTRACT

This work reports on the synthesis, characterization and preliminary mechanical properties of nanocrystalline NiAl/Al$_2$O$_3$ composite materials. Nano-scale crystallites of NiAl were formed by high energy milling of pre-alloyed powder with and without Al$_2$O$_3$ under an Ar atmosphere. Consolidation of the nano-scale powders was done by sinter-forging at < 0.4 T$_m$ in air. Characterization of the powders and consolidated microstructures and hardness data are reported.

INTRODUCTION

Unique mechanical properties are thought obtainable upon refinement of the grain size to nano-scale dimensions [1]. While refinement of grain size is a well known technique for increasing the strength of alloys (i.e., Hall-Petch behavior), nanocrystalline materials have the added advantage of a containing boundaries with such a high concentration of defects that the spacings between them approach inter-atomic distances. This feature may enable new deformation modes (e.g., superplastic behavior) and this may be utilized in forming net-shape components at low temperature.

Mechanical alloying (M/A) by ball milling has been employed by a number of researchers in the synthesis of intermetallic compounds [2], including B2 aluminides FeAl [3] and NiAl [4,5]. Previous attempts at consolidation of M/A NiAl by Whittenberger et al.[4] and Nash et al.[5] have relied on extruding or hot pressing at 1275-1400 K and no attempts were made to retain an ultra-fine grain size in the matrix. The present study utilizes mechanical attrition of pre-alloyed NiAl powder to form a nano-scale substructure of crystallites . The objective of this study is to form fully-dense nano-scale NiAl, with and without Al$_2$O$_3$ additions, by sinter-forging of mechanically attritted powder (T< 0.5 T$_m$) and to obtain a preliminary assessment of the mechanical properties.

EXPERIMENTAL

Approximately 10 ml of powder charges of stoicheometric NiAl (-325 mesh; A.E. Engineers, Bergenfield, NJ) were loaded into a milling vial under Ar in a glove box and processed using a Spex 8000 ball mill (Spex Industries, Edison, NJ). Two milling processes were investigated; Process 1 using a hardened steel vial and two steel balls and Process 2 using an alumina vial and one alumina ball. In one process batch, ≈1.4 wt.% of γ-Al$_2$O$_3$ (d=33 nm; Nanophase Technologies Corp., Darien , Il.) was added to the charge prior to milling. The γ-Al$_2$O$_3$ addition was expected to transfer to the more stable α-phase during milling [6]. Powder charges were milled for up to 50 hours. Process 1 was found to be more efficient, producing a smaller crystallite size in less time than Process 2. It was noted also that there was a strong tendency for the powders in Process 1 to cluster into agglomerations, varying in size up to about 50 μm. These may be the result of collisions between the two balls in the mill and thus may be highly consolidated. Process 2 had the unexpected result that the alumina ball used in milling was broken and partly destroyed. This produced fragments up to 20 μm of α-Al$_2$O$_3$ in the milled powder.

The as-received powder was characterized by optical metallography and the processed powder was characterized by optical metallography, BET, x-ray diffraction, SEM and TEM (Table 1). Particle sizes were calculated from the BET data, giving a equivalent spherical particle diameters in the range 3-4 microns which was confirmed by optical metallography and SEM. The powders were analyzed by x-ray diffraction using a Scintag θ-θ Diffractometer before and after milling, Fig. 1. Considerable broadening of the peaks occurred and is attributable to the presence of sub-micron crystallites and strain in the material. The diffractometer traces for the 50 hr milled powders, Fig.

1(b), also showed narrow peaks corresponding to additions of 45μm Si powder used as an internal standard. Line broadening of the NiAl peaks was analyzed by several methods, shown in Table 1.

Table 1: Powder Characterization

Process	Milling time (hrs)	Particle Size (μm)	Crystallite Size (nm)	Method
1	0	45	-	Metallography
	30	4.4	12.9 11.3-11.9 13.4 10-100	BET, SEM Scherrer Warren-Averbach Hall plot TEM
	50	3.7	12.3	BET Warren-Averbach
2	48	3.4	13.7-18.6	BET Warren-Averbach
1	30		- 12.5	Warren-Averbach

Notes:
1. XRD instrument broadening determined by measurement of 45 μm Si powder (99.99% purity).
2. Scherrer analysis based on crystallite size given by: $l = 0.9\lambda/(\beta\cos\theta)$ where $\lambda = 1.54 \times 10^{-10}$ m.
3. Warren-Averbach analysis based on the broadening of (110) peaks of NiAl.
4. Hall plot analysis based on the intercept of $\beta\cos\theta$ vs $\sin\theta$ plot.
5. BET analysis using Quantasorb Jr. (Quantachrome Corp., Syosset NY). BET calculations based on adsorption of a monolayer of N_2 gas onto perfectly spherical particles of diameter $d_{sp} = 6/(\rho_t A_{sp})$, where ρ_t is the theoretical density and A_{sp} is the specific surface area.

Chemical analysis of the processed powders was done by flame spectroscopy and atomic absorption spectroscopy, Table 2. A small concentration of Fe was noted (0.31 at.%) which represents contamination from the steel vial and balls used in processing. This analysis also showed ≈ 6 at.% oxygen and ≈1 at.% nitrogen.

Table 2: Chemical Analysis in at. % (Process 1, 50 hrs milling)

Ni	Al	Fe	Cr	Co	Mg	Si	C	N	O	Mn
44.28	47.99	0.31	0.01	0.03	0.03	0.04	0.07	0.95	6.28	0.01

Transmission electron microscopy confirmed the presence of crystallites, Fig. 2. Images were obtained from an aperture selecting the first two diffraction rings of Fig. 2(a). The crystallite size distribution appeared to range from approximately 10 to 100 nanometers. This sub-structure has been observed in similar form after mechanical attrition of other intermetallics (e.g. Nb_3Sn [7]).

Powder charges of 0.5 to 1 gram were sinter-forged (hot pressed) in a double acting compaction die of wrought Udimet 718 superalloy using an Instron load frame and attached furnace. The die had a square cross-section of 9.6 mm x 9.6 mm. To assist in separation and lubrication of the die, the rams were coated with colloidal graphite solution and a layer of Nb foil (0.013 mm thick) was inserted between the rams and the powder. Samples were sinter-forged in air with the simultaneous application of heat and pressure. Approximately 1 hour was necessary to equilibrate at the process setpoint, after which the temperature of the die was controlled to within ± 5 K and the pressure was maintained to within 15 MPa. After processing, the die was air-cooled to ≈ 373 K and the specimen was retrieved. All specimens were net-shape and free from cracks.

Results of the sinter-forging operation are shown in Table 3. After retrieval, specimens were polished and weighed. Bulk densities were calculated from the specimen weights in air and during water immersion. Selected specimens were x-rayed to determine the crystallite size after processing, Fig. 1(c) and (d).

Aliminum nickel

silicon

Relative Intensity (%)

2θ (Degrees)
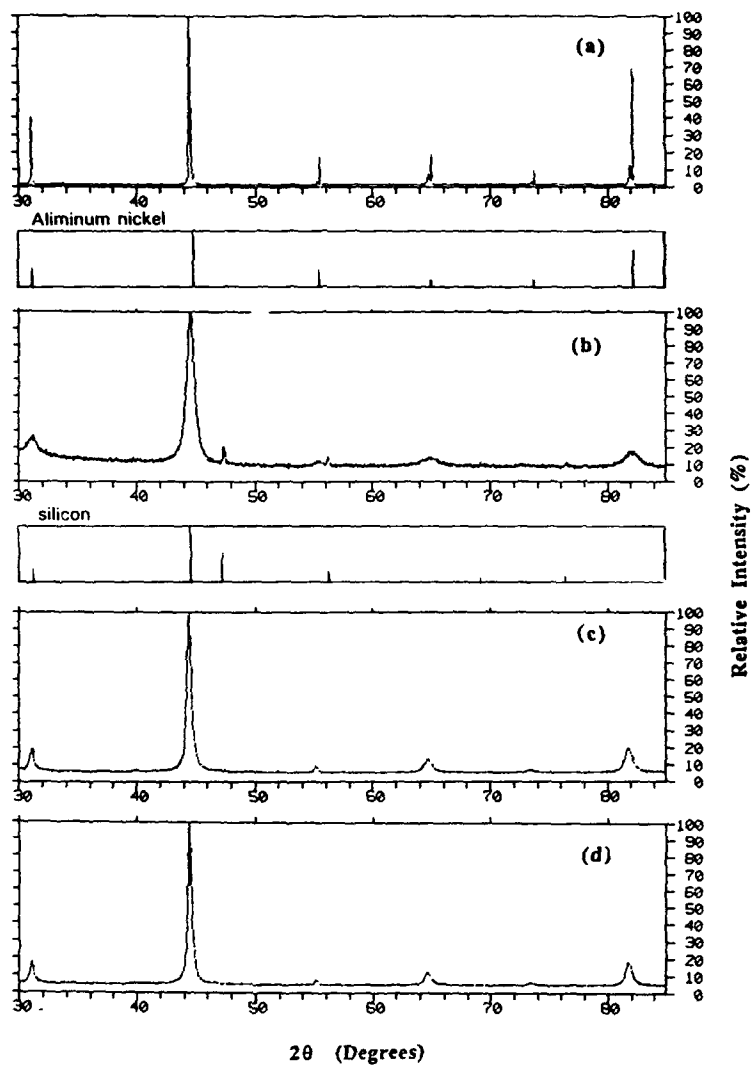
Figure 1   Diffractometer Traces of NiAl Powder and Specimens
(a) NiAl Powder 45 μm
(b) 50 hrs milling, Process 1
(c) Sinter-forged 620 MPa, 698 K, 3 hr
(d) Sinter-forged 500 MPa, 798 K, 1 hr

221
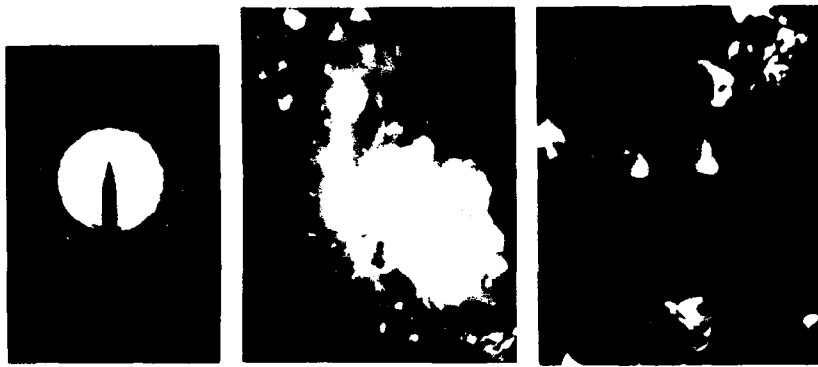
Fig. 2   TEM Results of NiAl Powder after milling 30 hr
(a) Diffraction pattern
(b) Darkfield Image showing larger scale crystallites (25-100 nm)
(c) Darkfield Image showing finer crystallites (10-50 nm)
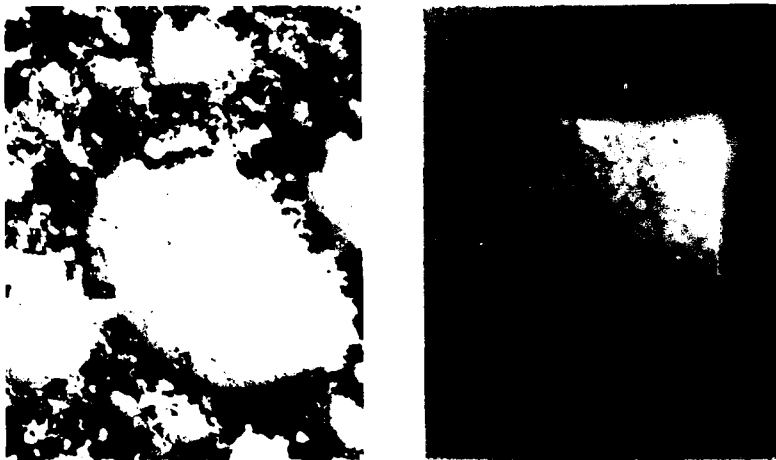
Fig. 3   Optical Micrographs of Sinter-forged Specimens
(a) Sinter-forged   620 MPa, 698 K, 3 hr   85% of theoretical density
     Note "island" morphology of full dense regions
(b) Sinter-forged   740 MPa, 698 K, 1 hr   90% of theoretical density
     Note pyramidal hardness indention and cracking at the periphery of it

Table 3: Sinter-Forging Results

Sample	Process	Relative Bulk Density	Crystallite Size (nm)	Hardness	Hardness (Max)
150	Powder, 50 hrs milling Process 1	–	12.9	–	–
	740 MPa, 613 K, 3 hrs	0.79	–	463 ± 122	678
	620 MPa, 698 K, 3 hrs	0.85	4, 22, 25	466 ± 130	683
	500 MPa, 798 K, 1 hr	0.77	18 , 32	508 ± 67	625
248	Powder, 48 hrs milling Process 2	–	17.3	–	–
	510 MPa, 538 K, 3 hrs	0.71	–	–	–
	520 MPa, 623 K, 3 hrs	0.80	–	272 ± 20	295
	500 MPa, 758 K, 3 hrs 600 MPa, 758 K, 1 hr	0.86	19.5, 48	309 ± 15	367
330	Powder, 30 hrs milling Process 1	–	12.5	–	–
	740 MPa, 698 K, 1 hr	0.90	20, 24	483 ± 48	631

Notes:

1. Relative bulk density based on the density of stoicheometric of NiAl of 5.85 g/cm^3.

2. Vickers Hardness values; 1 kg load, 15 seconds duration. Values are the average of five to fifteen indentations and the ± figure is the standard deviation about the mean.

Figure 3 shows optical micrographs of typical specimens. Fig. 3(a) illustrates that the residual porosity was far from uniform. Large regions (100-200 µm) of apparently fully dense material are evident as "island" structures. These islands are likely related to the clustering of the powder noted earlier. In the dense regions, a fine distributed network of ceramic particles (probably Al_2O_3 and AlN) is seen which are typical of M/A NiAl consolidated microstructures [4]. Hardness of the specimens (Table 3) were determined with a Vickers microhardness tester. The indentations were made in regions of the specimen which were apparently near full density. The indentations showed microcracking at the periphery (e.g., Fig. 3(b)) and this was observed in many, but not all, cases. Notably, cracking was nearly absent at the indentations with the highest hardness values.

Discussion

The sinter-forging results are encouraging for the use of this processing route to form fully dense ultra-fine microstructures in NiAl. The physical processes during sinter-forging are rearrangement of the particles, grain boundary sliding, diffusional creep, creep by dislocation climb and plastic deformation [8]. Full densification cannot be achieved by rearrangement of the particles alone and so its contribution is expected to be modest. Grain boundary sliding and diffusional accomodation may contribute more strongly than for larger-scale powders due to possible enhanced diffusion paths at the nano-scale. Such enhancements would be necessary as the process temperature regime explored is < 0.5 T_m and, accordingly, bulk diffusivities are low [9]. Plastic deformation is expected to play a significant role at elevated temperature as the stresses used are greater than the polycrystalline yield stress for stoicheometric NiAl above 650 K [9].

For the sinter-forged specimens, the lack of densification (79%) at 740 MPa and 613 K for 3 hrs is contrasted with the best result (90%) at 740 MPa and 698 K for 1 hr. This suggests that the onset of plasticity at the higher temperature is responsible for the additional densification. This is consistent with the brittle-to-ductile-transition temperature (≈ 650 K) reported for NiAl, although this temperature is very sensitive to composition [9]. A factor which may be contributing to the densification is enhanced ductility, which enables the void space in the powder compact to be more fully occupied. There is some preliminary evidence to suggest that nanometer-scale dislocation sub-structures increase the ductility of NiAl [10]. The Fe contamination may be beneficial also as Darolia et al [11] have shown that small (< 0.5 wt. %) ternary additions of Fe have a substantial effect in increasing the ductility at room temperature of single crystal NiAl.

The hardness results in Table 3 show some interesting effects. The material from Process 1 consolidated below 698 K showed average values in the range VH 460-480 but with large standard

deviations. This average value compares well with VH 475 reported for M/A NiAl, extruded at 1400 K [5]. Interestingly the "islands" of apparently fully-dense material had VH values consistently in the range 625 to 680. Haubold et al.[12] report HV 540 for 78% dense NiAl (d=10 nm), prepared by compacting of inert gas condensed powder at room temperature. After annealing at 723 K for 5 hrs, the hardness increased to 723 (≈ 80% dense). Nash et al [5] report VH 550-575 for M/A NiAl hot pressed at 58 MPa and 1273-1300 K. For the present work, the x-ray results (Table 3) show the retention of a significant volume fraction of fine (< 20 nm) crystallites in the specimens. It is suggested that a refined microstructure may be incorporated in the "islands" and thus is responsible for the higher hardness. The 90% dense material showed VH values of 483 ± 48 MPa. Although a maximum of 631 was seen, the lower standard deviation for this specimen suggests that some of the fine structure may be lost.

An unexpected result is that consolidated material from Process 2 shows very low hardness values over a range of densities, although similar to stoicheometric NiAl (≈VH 330 [12]). The presence of the coarse alumina particulate does not increase the hardness which may be the result of poorly-formed bonding with the matrix. The low hardness of the NiAl matrix, however, is surprising as a large volume fraction of fine (< 20 nm) crystallites was present after milling but appears to be disappearing during consolidation.

Conclusions

1. Mechanical attrition by ball milling of pre-alloyed NiAl results in a powder 3-4 micron in size with a substructure of crystallites in the range 10-100 nm. Larger agglomerations of particles are seen.
2. Sinter-forging of attrited powder has successfully consolidated net-shape specimens to 90% of the theoretical density of stoicheometric NiAl at $< 0.4 T_m$. Further work to optimize the processing is underway.
3. Vickers hardness values range from 272 to 683. This spans the range from those found for conventional grain-sizes up to close to the values reported for partly-consolidated nanocrystalline (d= 15 nm) NiAl.

Acknowledgments

References

1. H. Gleiter, NanoStructured Materials, 1, 1 (1992).
2. C. C. Koch, NanoStructured Materials, 2, 109 (1993).
3. J. H. Schneibel, P. Grahle and J. Rosler, Mat. Sci. & Eng., A153, 684, (1992).
4. J. D. Whittenberger, E. Arzt and M. J. Luton, J. Mat. Res., 5(2), 271 (1989).
5. P. Nash, S. C. Ur and M. Dollar, in (Proc. 2nd Int. Conf. Struct. Appl. Mech. Alloying, Vancouver, Canada, 1993) pp. 291-296.
6. P. A. Zielinski, R. Schulz, S. Kaliaguine and A. Van Neste, J. Mat. Res., 8(11), 2985 (1993).
7. Y. S. Cho and C.C. Koch, Mat. Sci. & Eng., A141, 139 (1991).
8. K. Hayashi and H. Kihara, in Sintering '87 Vol. 1, edited by S. Somiya, M. Shimada, M. Yoshimura and R. Watanabe, (Elsevier Science Publishers, New York, 1987), pp. 255-260.
9. R. D. Noebe, R. R. Bowman and M. V. Nathal, Int. Mat. Rev., 38, 193 (1993). .
10. T. Cheng, NanoStructured Materials , 1, 19 (1992).
11. R. Darolia, D. Lahrman and R. Field, Scripta Metall. Mater., 26, 1007, (1992).
12. T. Haubold, R. Bohn, R. Birringer and H. Gleiter, Mat. Sci. & Eng., A153, 679 (1992).

FATIGUE AND FRACTURE OF NICKEL ALUMINIDE COMPOSITES

PADU RAMASUNDARAM*, RANDY BOWMAN** AND WOLE SOBOYEJO*
*The Ohio State University, Dept. of Materials Science and Engineering, Columbus, OH 43210
**NASA Lewis Research Center, Cleveland, OH 44135

ABSTRACT

The results of preliminary investigations of the room-temperature fatigue and fracture mechanisms in model NiAl composites are presented. The composite systems studied include: NiAl reinforced with ductile second phase particles (Mo); ductile fibers (Mo); brittle second phase particles (zirconia partially stabilized with yttria) and brittle fibers+particles (Al$_2$O$_3$ + zirconia). Mechanisms of fatigue crack growth in heat treated specimens of the fiber-reinforced composites are also elucidated. The investigations indicate that both ductile and brittle reinforcements can enhance the toughness of NiAl significantly, and the ductile phase particulate reinforcement may even contribute to room-temperature ductility in the composite.

INTRODUCTION

NiAl has become one of the prime candidates for high temperature aerospace applications due to several of its attractive properties. These include: low density; good creep resistance and excellent high-temperature oxidation resistance [1]. Two of the serious obstacles that currently limit its use are low room-temperature toughness and ductility. It has now been firmly established that room-temperature ductility in NiAl is low due to the absence of five independent slip systems which are required for homogeneous plastic deformation/grain-boundary compatibility during extensive plastic deformation [2]. Attempts to improve the room-temperature toughness and ductility of NiAl by promoting alternative slip systems and increasing the grain-boundary strength have met with only limited success [2]. It has been suggested that an inherently low cleavage strength and the inherent difficulty in nucleating dislocations still limits the tensile ductility in NiAl [3]. Thus, "intrinsic" toughening of NiAl has not been very successful to date.

The incorporation of ductile second phase reinforcements into brittle matrices has been tried in other systems and found to enhance fracture toughness by crack bridging, crack blunting and crack deflection mechanisms [4]. Transformation toughening of NiAl by the addition of zirconia partially stabilized with yttria (PSZ) has also been reported in one study [5]. The metastable tetragonal zirconia undergoes a stress-induced transformation to the stable monoclinic form in the crack-wake, resulting in a volume increase (approx. 4%) of the zirconia particles, and consequent shielding of the crack-tip [6].

In this study, five model NiAl composite systems have been chosen for investigation: NiAl reinforced with 20 vol% Mo fibers; NiAl reinforced with 20 vol% ZrO$_2$; NiAl reinforced with 15 vol% ZrO$_2$ + 20 vol% Al$_2$O$_3$ fibers; NiAl reinforced with 20% particulate PSZ, stabilized to varying levels by the addition of 2 , 4 and 6 mol % Y$_2$O$_3$; and NiAl reinforced with 10, 20 and 30 vol % Mo particles. In addition to their desirable properties as reinforcements, Al$_2$O$_3$ and Mo were chosen due to their thermodynamic compatibility with NiAl matrix at higher temperatures [2]. Fracture toughness data are reported for monolithic NiAl and the above composites in the as-processed condition. In addition, fracture toughness data of the fiber reinforced composites heat-treated at 900°C for 2 hours are reported. Preliminary results from fatigue crack growth experiments on heat-treated fiber-reinforced composites are also presented. The results indicate that the PSZ- and the Mo-reinforced composites are the most promising systems for near-term applications. The alumina fiber reinforcement does not enhance the toughness properties of NiAl significantly due to reasons that will be discussed subsequently.

EXPERIMENTAL PROCEDURES

Four-ply NiAl+20 vol% Mo fiber and NiAl+15 vol%+ZrO_2+20 vol% Al_2O_3 composites were prepared by hot-pressing at the NASA, Lewis Research Center, Cleveland, OH [8]. NiAl powder of -325 mesh procured from Homogeneous Metals, Inc., Clayville, NY, was phase-blended with 10, 20 and 30 vol% of -325 mesh Mo powder of 99.9% purity procured from Cerac, Milwaukee, WI. The mixtures were obtained by ball-milling with zirconia media for 24 hours. The powder mixtures were hot isostatically pressed (HIPed) at 1260°C and 138 MPa for 4 hours in stainless steel cans. NiAl+ZrO_2 and NiAl+PSZ(2Y, 4Y and 6Y) blanks were also prepared by the same method. The partially stabilized zirconia powders (average size ~ 0.7 µm) were obtained from Tosoh Corporation, Bound Brook, NJ. Compact tension specimens of dimensions 15mmX15mmX3mm were machined from the blanks by electro-discharge machining (EDM). The specimens were ground and diamond polished down to 1µm surface finish. Fracture toughness tests were performed at room temperature on a servo hydraulic testing machine under load control. All tests were carried out in duplicate.

The fiber-reinforced composites were heat-treated at 900°C for two hours and air-cooled. Temperature was monitored using a K-type thermocouple and temperature control was estimated to be within ± 2K. Fatigue tests were performed using the same machine under load control. A stress ratio, R=0.1 and a frequency of 10 Hz were employed. Fatigue crack growth was monitored using a high resolution (2.5 µm) telescope. However, the measurements of crack length were not made using the telescope, due to the high incidence of multiple cracking. Instead, crack lengths were measured from optical micrographs of the crack-profile that were taken at 500X. The fatigue specimen of the heat-treated Mo-fiber reinforced NiAl was not fatigued to failure. The test was stopped after 700000 cycles, when it was observed that a certain amount of stable crack growth had occurred (~2mm). Fractography was performed on the fracture toughness specimens using secondary electron images from a Hitachi S-510 scanning electron microscope.

The 900°C/2h/NiAl+Mo-fiber fatigue specimen and the fractured zirconia reinforced composites were observed under an optical interference microscope for evidence of plasticity and transformation toughening, respectively, in the crack wake, and near the fracture surface. Deviations in optical fringes from linearity indicate surface features that deviate from planar geometry.

RESULTS AND DISCUSSION

(a) Microstructure

The microstructures of the as-processed Al_2O_3+zirconia specimen is shown in Fig. 1a. The zirconia particles are present mainly at the grain boundaries, presumably as a result of their small size (~0.7 µm) compared with the NiAl grains (~ 60 µm). Extensive grain boundary microcracking occurred in the heat treated coupon of this composite. Fig. 1b shows the microstructure of the as-processed Mo fiber reinforced composite. There were no clear changes in the microstructure of the Mo fiber composite due to heat treatment. In the zirconia reinforced composites, the zirconia is again mainly present at the grain boundaries (Fig. 1c). The Mo reinforcements are present as distinct particles (Fig. 1d).

(b) Fracture Toughness

Table I shows the fracture toughness results of the composites studied and that of the monolithic NiAl material. These values are generally consistent with those reported in the literature [1]. One study [5] does report significantly higher toughness values for the monolithic NiAl at room-temperature (~ 14MPa$\sqrt{m}$), which are very different from typical NiAl toughness values between 4 and 6 MPa$\sqrt{m}$ [1]. It can be seen that toughening due to Al_2O_3+ZrO_2 reinforcement is marginal. This may be due to three reasons: first, the size of the

zirconia particles (~0.7 μm) is so small that they are present mainly at the grain boundaries, thus promoting intergranular fracture and low fracture resistance. Secondly, the unstabilized zirconia used in this composite does not contribute to toughening either, since the zirconia transforms spontaneously to its stable monoclinic phase during processing and subsequent cooling. Thirdly, the inadequate interfacial characteristics between the uncoated alumina fiber and the matrix do not promote debonding and pull-out phenomena required for improved toughness.

The ductile second phase reinforcement (both fiber and particulate) increases the toughness significantly. The PSZ reinforcements also toughen the NiAl matrix significantly in all cases, as shown in Table I. Optical interference microscopy of the fractured specimens did not show conclusive evidence of transformation toughening. However, it is conjectured that this is due to the large size of the transformation zone. Optical interferometry has been used to determine the transformation zone sizes where the zone size is small [7]. The actual transformation zone sizes can be measured by Raman spectroscopy near the fracture surface and away from it. The toughness values of the Mo-particulate reinforced NiAl remained roughly constant irrespective of the volume % of reinforcement. Fig. 2 shows the fracture surface morphologies of the different composites. Fracture in monolithic NiAl is intergranular. With the addition of Mo, there is a transition to cleavage fracture. The fracture surface morphologies of all three Mo reinforced composites were similar. The Mo particulate reinforcement fractured in a ductile manner. It is interesting to note, however, that the Mo fiber failed by intergranular fracture. This may be possible due to the constraint imposed on the fiber by the matrix during plastic deformation. Such constraint may limit the extent of plastic deformation of the fiber and promote brittle intergranular fracture. Considerable debonding of the fibers occurred near the notch. Secondary microcracking was observed in both the matrix and in the ductile reinforcements. Fracture in the alumina composite was also intergranular, due to reasons discussed previously. There was little debonding of the fiber in this composite indicating a strong interface.

(a)

(b)

(c)

(d)
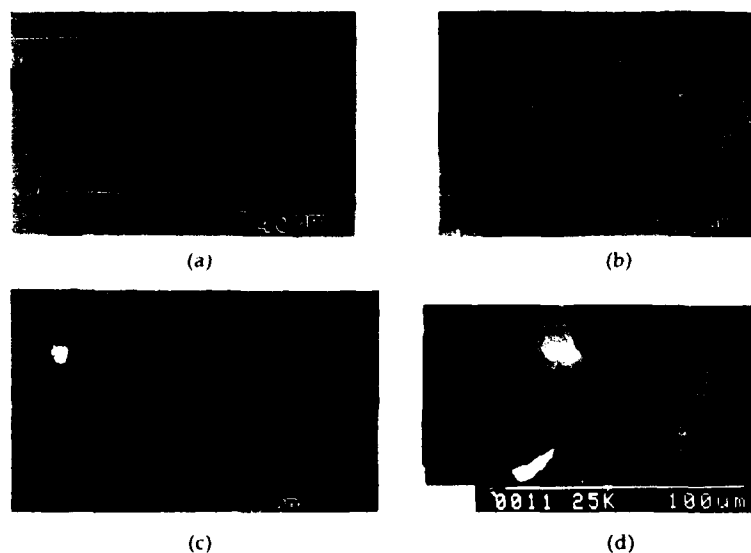
Fig. 1. Microstructures of NiAl composites (a) As-processed NiAl+Al$_2$O$_3$+ZrO$_2$ (b) As-processed NiAl+Mo fiber (c) NiAl+ZrO$_2$ (d) NiAl+Mo particles.

227

TABLE I Fracture toughness values of NiAl and NiAl-composites

Specimen	Fracture Toughness ($MPa\sqrt{m}$)	
	As-Processed	Heat-treated
NiAl	5.3	-
NiAl+20% Mo (fiber)	17.2	15.9
NiAl+15% ZrO_2 + 20% Al_2O_3	6.6	5.4
NiAl+10% Mo	12.8	-
NiAl+20% Mo	14.5	-
NiAl+30% Mo	14.3	-
NiAl+20% ZrO_2	5.0	-
NiAl+20% PSZ(2Y)	13.1	-
NiAl+20% PSZ(4Y)	9.6	-
NiAl+20% PSZ(6Y)	10.2	-

(c) Fatigue Crack Growth

Attempts to grow stable fatigue cracks in the as-processed fiber reinforced composites were not successful. The specimens failed abruptly in all cases at low stress intensity factor ranges, ΔK. Several cracks were found to propagate along grain-boundaries when the heat-treated Al_2O_3+ZrO_2 composite was tested in fatigue. When the test was stopped at an intermediate stage, several of the fibers were found to be broken both in the plane of the notch and away from it. More careful testing is required to elucidate further mechanistic information pertaining to fatigue crack growth in this composite.

A successful fatigue crack growth test was performed on the heat-treated Mo fiber composite. Extensive crack-bridging was found in this composite under cyclic loading (Fig. 3). The crack also tended to branch as it approached the fiber. However, the applied stresses were not sufficient to cause significant yielding or debonding of the fiber during fatigue. Evidence of plastic deformation in the matrix was also found in the optical interference pictures that were taken surrounding the crack (Fig. 4). The deviation from linearity of the fringes around the crack indicates a change in surface geometry surrounding the crack tip. This technique has been used previously to detect transformation zones associated with the transformation from tetragonal-to-monoclinic zirconia phases in $MoSi_2$ composites [7].

SUMMARY

1. Ductile reinforcement, either in particulate or fiber form, yields the most significant toughening effect. The volume percentage of Mo does not seem to affect the toughness value significantly. However, it might affect the room temperature ductility to different extents. Possible ductility enhancement has not been assessed yet.

2. Brittle reinforcement by ZrO_2+Al_2O_3 fibers did not increase the toughness very much. However, this is due to the relatively small size of the zirconia particles, the absence of transformation effects and the inadequate interfacial characteristics of the alumina fibers.

3. Crack bridging appears to be the predominant mechanism of toughening in heat-treated Mo fiber-reinforced composite. Debonding may also play a limited role which is yet to be evaluated.

4. There are clear indications that transformation effects contribute to toughening in all the PSZ reinforced composites. However, the volume of the phases undergoing transformation, and their extent, need to be estimated. Further X-ray inspection and Laser Raman spectroscopy of the fractured specimens are expected to provide this information.

(a)

(b)

(c)

(d)

(e)

(f)
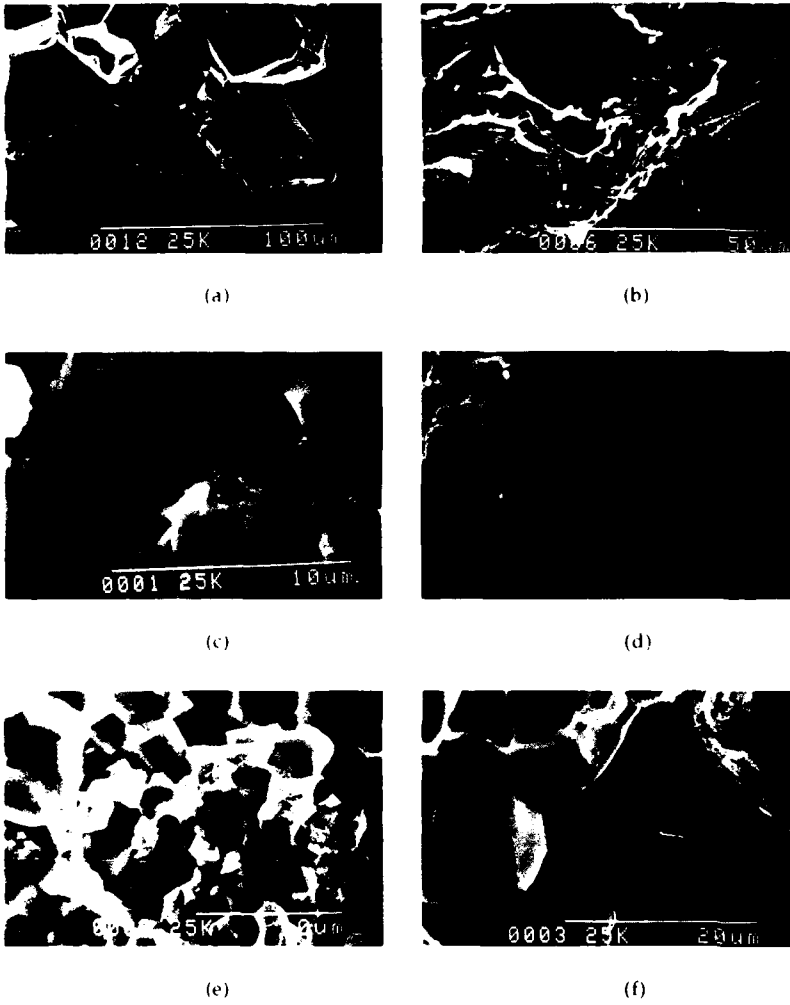
Fig. 2 Fracture surface morphologies. (a) NiAl (b) NiAl+20%Mo (c) NiAl+20%Mo (indicating ductile particle fracture) (d) NiAl+Mo fiber (matrix) (e) NiAl+Mo fiber (fiber) (f)NiAl+15%ZrO_2+Al_2O_3

229

Fig.3 Heat treated NiAl+Mo fiber fatigue specimen Crack bridging
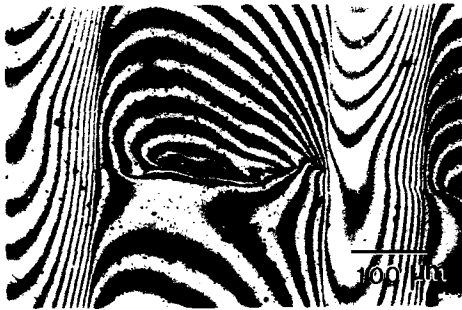
Fig 4 Optical interference micrograph of heat treated NiAl+Mo fatigue specimen showing
evidence of plasticity in surrounding the crack

REFERENCES

1 R D Noebe, R.R Bowman and M V Nathal. International Materials Reviews 38 (4), 193-232
(1993)
2 R D Noebe, A Misra and R Gibala. ISIJ International 31 (10), 1172 (1991).
3 R R Bowman, R D Noebe, S V Raj and I E Locci. Metall Trans A 23A, 1493 (1992)
4 K S Chan. Metall Trans A 21A 2687 (1990)
5 S M Barimov and V Yu Evdokimov. Acta Metall Mater 41 (3), 801-804 (1993)
6 P F Becher, Acta Metal. Mater 34 (10), 1885-1891 (1986).
7 D Brooks, I C Chen,R Lederich and W O Sobovejo, J Am Cer Soc (Submitted)
8 J W Pickens, R D Noebe, G K Watson,P K Brindley and S L Draper, NASA TM 102060,
1989 (Unclassified)

MICROSTRUCTURAL CHARACTERIZATION OF CREEP TESTED CRYOMILLED
NiAl-13vol. % AlN

A. Garg, J. D. Whittenberger, and B. J. M. Aikin*
NASA Lewis Research Center, Cleveland, OH 44135
* Case Western Reserve University, Cleveland, OH 44106

ABSTRACT

Cryomilling of prealloyed NiAl powders, followed by extrusion, has been used to produce a particulate strengthened NiAl-13vol.% AlN material. At 1300 K, the compressive strain rate-flow stress diagram has two distinct deformation regimes, with the transition occurring near 150 MPa. The low and the high stress regimes have power law creep exponents of ~ 6.1 and 14.2, respectively. Microstructural characterization of the as-extruded and tested samples has been performed to develop an understanding of the superior mechanical properties of the material. The microstructure of the as-extruded material was inhomogeneous and consisted of mantle regions containing a mixture of small NiAl grains (diameter ~ 50-150 nm) and fine AlN particles (size ~ 5-50 nm) that surround larger NiAl grains (diameter ~ 0.3-8.0 μm) which were mostly particle free. In the low-stress regime, samples tested to steady state exhibited a structure composed of subgrain boundaries in the particle-free NiAl grains. In addition, some of the subgrains had developed a well defined dislocation network. AlN particles occasionally found within large NiAl grains acted as pinning centers for dislocations. Small NiAl grains and the AlN particles constituting the mantle coarsened during these tests. In the high-stress regime, samples tested to steady state exhibited a high density of dislocations in most of the particle-free NiAl grains. Subgrain boundaries were found occasionally but dislocation networks were rare. The AlN particles had not significantly coarsened due to the shorter times at temperature.

INTRODUCTION

The need to operate gas turbines at higher temperatures has renewed interest in intermetallic compounds with increased high-temperature strength and oxidation resistance. B2 nickel aluminide, NiAl, is an attractive member of this class as it posseses a high melting temperature, low density, high thermal conductivity, and excellent oxidation resistance [1]. However, NiAl also suffers from some disadvantages. It is weak at high temperatures and has low room-temperature ductility and toughness. One recently developed avenue [2] to improve elevated temperature strength involves the use of cryomilling, where NiAl powder is subjected to high energy grinding in liquid nitrogen. During such grinding, the exterior surface of the aluminide powder reacts with the nitrogen to form a thin aluminide layer enriched with AlN particles. Subsequent hot extrusion of cryomilled NiAl powder yields a very inhomogeneous microstructure [2], where thin AlN-rich mantles surround cigar-shaped particle-free NiAl grains. Since unreinforced NiAl has little strength at elevated temperatures, cryomilled NiAl is presumably hardened by inhibiting dislocation motion through the AlN-rich mantles. This paper reports the microstructure, as examined by transmission electron microscopy (TEM), of cryomilled and hot extruded NiAl powder after being tested at 1300 K and strain rates ranging from 10^{-9} to 10^{-3} s^{-1}.

EXPERIMENTAL DETAILS

Prealloyed Ni-50 at. % Al powder was cryomilled for 16 h in a modified attritor. The ground powder was vacuum sealed in mild steel cans which were then hot extruded at 1505 K using a 12:1 reduction ratio. Chemical analysis of both the as-cryomilled powder and the extruded bar indicated that the nitrogen and oxygen content increased on average from ~ 300 at. ppm to 7.18 and 0.96 at. % respectively. Assuming that all the nitrogen and oxygen are in the form of aluminium nitride and alumina respectively, the densified material contains 13.1±3.0 vol.

% AlN and 0.9±0.2 vol. % Al$_2$O$_3$ in a Ni-45.2±2.9 Al (at. %) matrix. Complete details of the processing are given in [3].

Cylindrical samples for compression creep testing were electrodischarge machined parallel to the extrusion direction from the as-extruded bar. The test samples were 5 mm in diameter and 10 mm long. Compression testing was conducted in air at 1300 K under both constant load or constant velocity until a steady state condition was reached. True compressive strains, stresses, and strain rates were calculated from the autographically recorded load-time and contraction-time curves assuming conservation of volume and uniform deformation throughout each specimen.

Foils for TEM were prepared from the as-extruded and crept specimens by ion milling. The samples were sectioned into thin slices perpendicular to the compression axis using a diamond circular saw. Disks of 3 mm diameter were drilled from 5 mm diameter slices, polished to 100 μm thickness and dimpled on both sides to a minimum thickness of 10 μm. The foils were ion-beam thinned to electron transparency using typical ion milling voltage of 6 kV, gun current of 1mA and specimen tilt of 12°. Induced damage due to ion milling was found to be insignificant.

RESULTS

Steady state strain rate ($\dot{\varepsilon}$) - flow stress (σ) data from the 1300 K compression testing are presented in Fig. 1. The results were fitted to the usual power law equation $\dot{\varepsilon} = A\sigma^n$, where A is a constant and n is the stress exponent. As shown in Fig. 1, the data yielded two distinct deformation regimes, with the transition occurring near 150 MPa. Such behavior is typical for NiAl-AlN [4], where at higher strain rates the stress exponent is on the order of 14 while at lower rates of deformation n is about 6.

A bright-field TEM image showing the general microstructure of the as-extruded cryomilled NiAl is shown in Fig. 2(a). The structure consisted of a mixture of NiAl grains, marked A, and mantle regions, marked B, containing fine particles. A selected-area diffraction-pattern of the mantle region (Fig. 2(b)) showed a ring diffraction pattern, which after indexing confirmed that most of the particles were

Fig. 1. True 1300 K compressive flow stress-strain rate behavior for cryomilled NiAl.

AlN. In addition to rings, some diffraction spots (arrowed) belonging to NiAl grains were also visible in the pattern. The dark-field TEM image (Fig. 2(c)) of the area shown in Fig. 2(a) obtained from the first AlN ring clearly displayed the size and distribution of these particles in the mantle region. This region is enriched with fine AlN particles (size ~ 5-50 nm) and contained small NiAl grains (size ~ 50-150 nm). These are marked C' and D respectively, in Fig. 2(c). The cross sectional diameter of large NiAl grains, marked A in Fig. 2(a), was found to vary between 0.3μm-8.0μm and most of these grains were devoid of AlN particles. The AlN-rich mantle regions were found between these large NiAl grains (A) and their distribution was

inhomogeneous in the microstructure. Finally, remnants of partial dynamic recovery after hot
extrusion, as evident by the presence of subgrain boundaries in some of the larger NiAl grains
(Fig. 2(d)), was also observed.
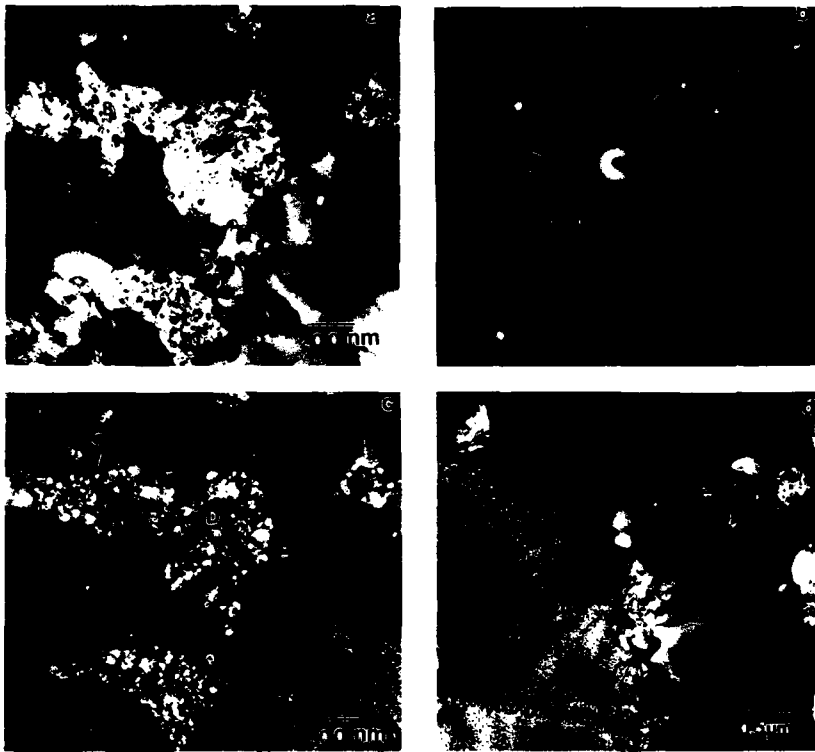
Fig. 2. TEM micrographs showing the general microstructure of cryomilled and extruded NiAl-
13AlN; (a-c) B.F. image, SADP, and the corresponding D.F. image, and (d) B.F. image showing
evidence of recovery in a NiAl grain.

Deformation Structure for Sresses < 150 MPa

　　Comprehensive TEM studies of the cryomilled samples tested to steady state at 50, 100
and 150 MPa were carried out. The general microstructural features of all these samples were
very similar. The particle-free NiAl grains developed subgrain boundaries and dislocation
networks (Fig. 3(a-c)). The subgrain boundaries consisted of either an array of edge dislocations
or two sets of dislocations in screw or mixed orientation. The edge dislocations were generally of
b = <100> type. An example is shown in Fig. 3(a) with arrays of b_1 = [100] and b_2 = [010] edge
dislocations forming two tilt boundaries within a NiAl grain. It is interesting to note that these
boundaries seemed to have originated from dissociation of the b_3 = [110] tilt boundary.
Although the dissociation results in an increased boundary area, it would be energetically
favorable since the motion of b = <110> dislocations is expected to be sluggish due to their
extended core [5]. The test temperature of 1300 K is high enough for sufficient diffusion to
occur and allow b = <100> dislocations comprising the extended b = <110> core to move out of

233

their {110} glide plane. Such a decomposition was postulated by Forbes et. al. [6] to explain networks of b = <100> dislocations observed in [001] oriented NiAl single crystals. The dislocation networks (Fig. 3(b)) within the subgrains were mostly well developed and consisted of dislocations of b = <100> lying along <$\bar{1}$10> direction, which is their low energy line direction. These networks were generally formed in {111} plane, but networks formed in other planes and consisting of dislocations with non <100> Burger's vectors were also found. In a few NiAl grains that contained AlN particles, dislocation pinning at particles was pronounced hence obstructing in the formation of regular networks in these grains (Fig. 3(c)). In the mantle regions, the small NiAl grains had coarsened due to the long term exposture during lower stress, 1300 K testing and were pinned by clusters of AlN particles; however, as can be seen in Fig. 3(d), some small nitrides also existed within the aluminide grains. AlN particles in the mantle had also coarsened but at a much slower rate. Qualitatively, within the mantle region the original 5-50 nm particles had coarsened to 10-80 nm and the NiAl grains had grown from 50-150 nm to 0.3-1.5 μm. Random dislocations and networks were occasionally found in the coarsened NiAl grains of the mantle.
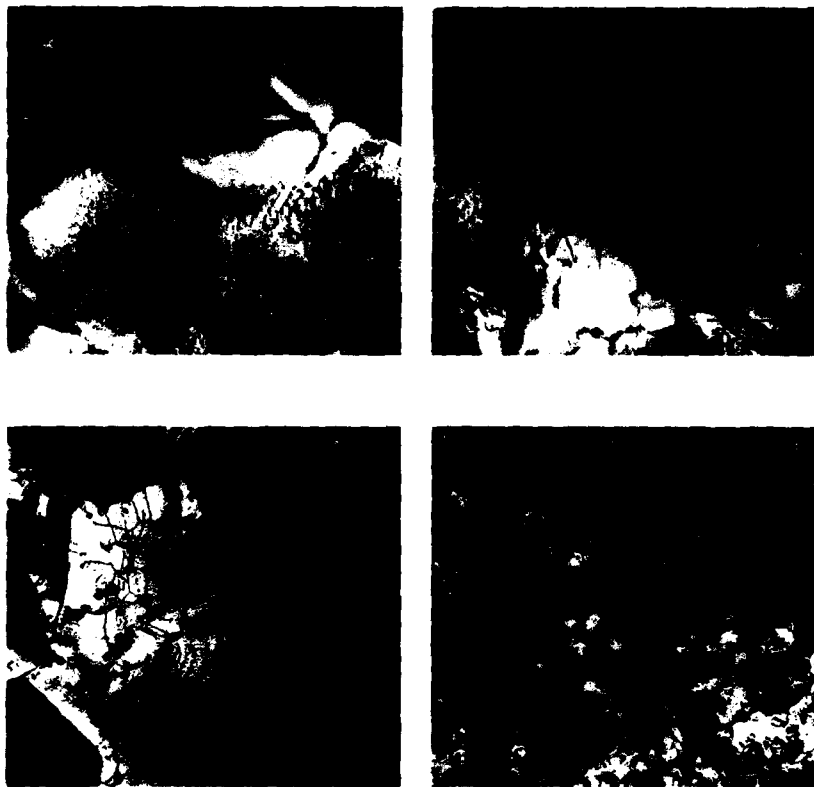
Fig. 3. TEM micrographs of deformed samples for stresses < 150MPa showing (a,b) formation of subgrain boundaries and dislocation networks in NiAl grains, (c) dislocation pinning at AlN particles within a NiAl grain, and (d) coarsening of the mantle region.

Deformation Structure at Sresses > 150MPa

The deformed microstructures were examined for samples tested at steady state flow stress of 184 and 212 MPa (Fig. 4). At the highest stress of 212 MPa ($\dot{\epsilon}$ ~ 2.2 x 10^{-4} s^{-1}) almost all of the large AlN-free NiAl grains contained a high density of dislocations and a few subgrain boundaries. This is illustrated in Fig. 4(a) where the foil has been tilted to bring the dislocations in one grain into strong contrast. Fig. 4(b) is a high magnification TEM micrograph showing the arrangement of dislocations within a dense dislocation region inside a NiAl grain. Figures 4(a,b) demonstrate that high densities of dislocations can exist in NiAl-AlN subjected to high flow stresses. Study of the mantle regions for the 212 MPa stress test did not reveal any growth of the AlN or NiAl grains nor was any residual dislocation activity seen in the mantle. Samples tested at a slightly lower stress of 184 MPa ($\dot{\epsilon}$ ~ 2.2 x 10^{-5} s^{-1}) exhibited subgrain boundaries and a low density of random dislocations in the NiAl grains (Fig. 4(c,d)); dislocations networks were very rare and regions of high dislocation densities were not observed. Again, as was the case for the highest stress test, neither the AlN particles or NiAl grains in the mantle coarsened significantly during deformation, nor were any residual dislocations found in the mantle regions.
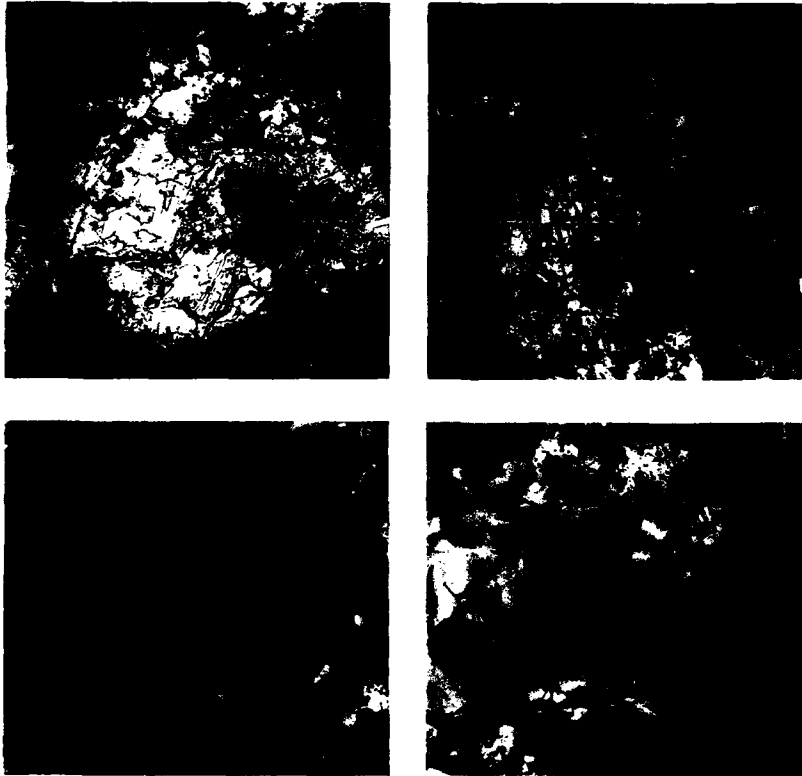
Fig. 4. TEM micrographs of deformed samples showing (a,b) a high density of dislocations in NiAl grains in samples tested at 212 MPa, (c,d) subgrain boundaries and random dislocations in samples tested at 180 MPa.

DISCUSSION

Comparison of the TEM microstructures in Fig. 2-4 illustrate some clear differences in terms of dislocation activity in the NiAl grains and changes in the mantle regions. Subjecting the extruded NiAl-AlN to 1300 K high stress, relatively fast deformation conditions introduced a large number of dislocations in the NiAl grains (Fig. 4(a,b)). With a decreasing strain rate (flow stress), the high density of dislocations in the large NiAl grains disappeared and subboundaries became evident (Fig. 4(c,d)). At stress levels below ~ 150 MPa ($\dot{\epsilon} \leq 2 \times 10^{-6}$ s^{-1}), well developed subgrains and dislocation networks were found in the large NiAl grains (Fig. 3). Both the latter microstructure and the observed stress exponent of ~ 6 for the lower stress regime in NiAl-AlN (Fig. 1) are typical of unreinforced NiAl [7].

Concurrent with variations in the dislocation structure in the NiAl grains, changes have been noted in the AlN enriched mantles. Specifically, long term testing at 1300 K (Fig. 3(d)) encouraged growth of both the NiAl grains and the AlN particles, while short term exposure (fast $\dot{\epsilon}$ / high σ tests) produced little, if any, change from the as-extruded state (Fig. 2). Conventional annealing of NiAl-AlN at 1600 K has been shown to coarsen both NiAl and AlN phases in the mantle [4], thus, it is likely that coarsening in this region is simply the result of Oswald ripening. Somewhat surprisingly, few dislocations have been found in the mantle of the strained samples. Clearly for deformation to occur in cryomilled NiAl, dislocations must pass through the mantle; thus, in spite of the myriad of particles to act as pinning sites, few residual dislocations remain in the mantle regions.

SUMMARY OF RESULTS

TEM studies at 1300 K of compression tested AlN particulate reinforced NiAl with an inhomogeneous grain and mantle structure has shown that significant microstructural changes occur in the particle-free grains. Under high strain rate-high stress conditions regions of high dislocation density were found in the particle-free NiAl grains; however, as the deformation rate and flow stress decrease, subboundaries dominate and regions of high dislocation density disappear. Below ~ 150 MPa, corresponding to a nominal strain rate of 2 x 10^{-6} s^{-1}, only subgrains and dislocation networks were seen in the NiAl grains. While phase coarsening was noted in the AlN-enriched mantles after long term testing, it was probably due to simple Oswald ripening. Regardless of the prior deformation conditions, dislocation activity within the mantle was not very evident.

ACKNOWLEDGEMENTS

REFERENCES

1.   R. D. Noebe, R. R. Bowmen, and M. V. Nathal, Int. Mater. Revs. **38**, 193 (1993).
2.   J. Daniel Whittenberger, Eduart Arzt, and Michael J. Luton, J. Mat. Res. **5**, 271 (1990).
3.   B. J. M. Aikin, J. Daniel Whittenberger, and M. G. Hebsur, in Mechanical Alloying for Structural Applications, edited by J. J. deBarbadillo, F. H. Froes and R. Schwarz (ASM International, Materials Park, OH, 1993), pp. 283-290.
4.   J. Daniel Whittenberger in International Symposium on Structural Intermetallics, edited by R. Darolia, J. J. Lewandowski, C. T. Liu, M. L. Partin, D. B. Miracle, and M. V. Nathal (TMS, Warrendale, PA, 1993), pp. 819-828.
5.   M. J. Mills and D. B. Miracle, Acta Metall. Mater. **41**, 85 (1993).
6.   K. R. Forbes, U. Glatzel, R. Darolia and W. D. Nix in High Temperature Ordered Intermetallic Alloys V, edited by I.Baker, R. Darolia, J. Daniel Whittenberger, and Man H. Yoo (Mater. Res. Soc. Proc. **288**, Pittsburgh, PA, 1993), pp. 45-58.
7.   J. Daniel Whittenberger, J. Mat. Sci. **22**, 394 (1987).

THE ATHERMAL STRENGTHENING OF DISCONTINUOUS REINFORCED NiAl COMPOSITES[*]

L. WANG, K. XU AND R.J. ARSENAULT
Metallurgical Materials Laboratory, Dept. of Materials & Nuclear Engineering,
University of Maryland, College Park, MD 20742-2115

ABSTRACT

An increase in the athermal component of the yield stress at low temperatures is the caused of the high temperature strengthening of discontinuously reinforced NiAl matrix composites. The reinforcements stabilize the microstructure. The strengthening in the temperature range of 300-1273K, is believed to be related to the grain size refinement and effective pinning of grain boundaries. This conclusion was obtained from analysis of data from AlN, TiB_2 and Al_2O_3/NiAl particulate composites.

INTRODUCTION

Recent experimental data indicates that there are at least two different phenomena contributing to the strengthening of NiAl through the addition of discontinuous reinforcements. First, the high-temperature strength of NiAl can be enhanced 2-3 fold by adding a small amount (2-4 wt%) of small particles (~50 nm in size), such as TiB_2, HfC, and HfB_2 [1,2]. The strengthening behavior in these dispersion hardened NiAl materials was found similar to that of the oxide dispersion strengthened (ODS) Ni-based alloys. The grain size was found unstable in compression in the temperature range of 1200-1300 K. It has been observed, in HfC reinforced NiAl, that the larger the grain size, the stronger the composites at high-temperatures [2]. Surprising results were obtained, during the mechanical alloying of NiAl with Y_2O_3 in the liquid nitrogen environment, a process called cryomilling, in order to disperse the Y_2O_3 into the NiAl [3,4]. A considerable amount of AlN (~10 vol%), in addition to the small volume fraction of Y_2O_3, was found in these cryomilled composites. The strengthening rate for AlN reinforcement was found to be considerably higher than other discontinuous reinforcements. Preliminary microstructure investigations revealed that the AlN particles were not uniformly dispersed, but non-homogeneously distributed mainly along grain boundaries.

The second phenomenon is related to the strengthening of NiAl through the addition of discontinuous reinforcements with considerably larger volume fractions (20-30 vol%) of relatively large (~1 μm) particulates, such as TiB_2 particulates. The high-temperature strength of NiAl has increased 2-3 fold and the modulus is enhanced [5-7]. The behavior or the mechanism for this second type of strengthening is still unclear. Although strengthening through the grain size refinement has been observed in monolithic NiAl at high temperatures, it is unlikely that very small grains (< 5μm) would be stable at temperatures above 1200K and introduce significant strengthening [8]. The grain size or the subgrain size of these composites are extremely small (1-3 μm) [9-11], which would generally result in lack of elevated-temperature strength. One important difference, however, between dispersion hardened

---

237

NiAl and the NiAl reinforced with micron-size particulates is that the grain size of the latter, though small, is stable at elevated temperatures (1200-1300 K) [9-11].

Questions concerning the high-temperature strengthening of the NiAl arise from the previous investigations. What is the strengthening mechanism or mechanisms when the reinforcements are not dispersoids? And how important is the matrix grain size in the strengthening of NiAl? This paper is a report of some results of recent investigations of various kinds of discontinuous reinforced NiAl composites intending to cast some insight of the strengthening mechanisms of these composites.

MATERIALS AND EXPERIMENTAL METHODS

Five kinds of composites were used in the current investigations. They are: monolithic NiAl, XD^{TM} processed 0, 10, 27 V% TiB$_2$/NiAl, and cryomilled NiAl composites. The XD^{TM} processed nickel aluminide reinforced with 0,10, and 27 Vol% TiB$_2$ was obtained from Martin Marietta Laboratories. The details of this process can be found elsewhere [5,6]. Subsequent processing included canning in steel plus extrusion at ~1473 K at an extrusion ratio of 8:1. The measured volume fraction of the TiB$_2$ particulates is ~0, 10, and 27 Vol% corresponding to the nominal volume fractions respectively. All other composites were prepared by a four-step, powder processing route involving milling, cold isostatic pressing (CIP), hot isostatic pressing (HIP), and extrusion. Two types of milling were coupled; milling in a rotating ball mill and cryomilling. Cryomilling is a high intensity ball-milling process performed in liquid nitrogen. All materials in this study were cryomilled at Exxon Research and Engineering Laboratory under the direction of M.J. Luton. Nickel aluminide powders (50 at%Ni:50 at%Al), -150 +325 mesh, were purchased from CERAC, Inc. of Milwaukee, WI. The unreinforced NiAl material was produced by ball milling 22 hours, CIP, HIP and extrusion at 1373 K and an extrusion ratio of 36:1. The cryomilled NiAl composite was produced by cryomilling followed by CIP, HIP (4 hours), and extrusion at 1473 K and an extrusion ratio of 9:1. CIP conditions in all cases were 770 MPa for 15 minutes. HIP conditions were: 1473 K, 210 MPa, 2 hours.

The composites were ground into cylindrical samples with height-to-diameter (h/d) ratio of 2 and diameter of 4.7~5 mm for compression tests. The cylindrical axis of the sample is parallel to the extrusion direction. The compression tests were conducted on an Instron universal testing machine equipped with high-temperature vacuum chamber. All the tests were conducted at a constant cross-head speed, and in a vacuum of ~10^{-4} torr. The compressive yield stress and flow stress were measured as a function of temperature from 300 K to 1273 K, and with a strain rate of 10^{-4} sec^{-1}. The yield stress was taken as the stress at 0.002 true plastic strain. Activation volumes, V*, were measured as a function of shear stress, τ, in the temperature range of 300 ~ 1273 K, by using the method of changing the strain rate, which follows

$$V^* = kT\left(\frac{\partial \ln \dot\gamma}{\partial \tau}\right)$$

where $\dot\gamma$ is the shear strain rate and kT are Boltzman's constant and temperature, respectively. One half of the true compressive flow stress (σ) was taken as the shear stress (τ) in the calculation of the activation volume.

RESULTS AND DISCUSSION

All the five composites exhibit steady state flow or slight strain softening after yielding at temperature above ~900 K, and can be compressively deformed up to ~0.1 plastic strain without fracture at room temperature, and displays a considerable strain hardening at the deformation temperatures of 800 K or below, as shown in Fig. 1. As expected, the yield stress of the monolithic NiAl exhibits a typical temperature dependent behavior as common metals and alloys do, as shown in Fig. 2. This behavior can be described as, in both the low temperature (< 500 K) and the high temperature range (>700 K), the yield stress decreases as the temperature increases, indicating that the deformation of these composites is thermally activated in these temperature ranges; and there exists an intermediate temperature range (500-700 K) in which the yield stress is relatively independent of temperature, i. e. an athermal state of the deformation is clearly defined in this temperature range. The temperature dependent behavior of all other composites more or less duplicated this behavior of the monolithic NiAl with an obvious but less profound athermal stage. The athermal stress level of the cryomilled NiAl composite is about three times as high as that of the monolithic NiAl, and apparently higher than that of the XD^{TM} processed 27 Vol% TiB$_2$/NiAl composite. It is evident that the overall strengthening of all the composites, in the whole testing temperature range, were initiated by the increase of the athermal stress, i.e., athermal component of the strength of these composites. The activation volume measurements also supported the above observations. As shown in Fig.3, the activation volume displays a peak value at the corresponding athermal stress level for all the monolithic and XD^{TM} processed TiB$_2$/NiAl composites which indicates the existence of the athermal stress.
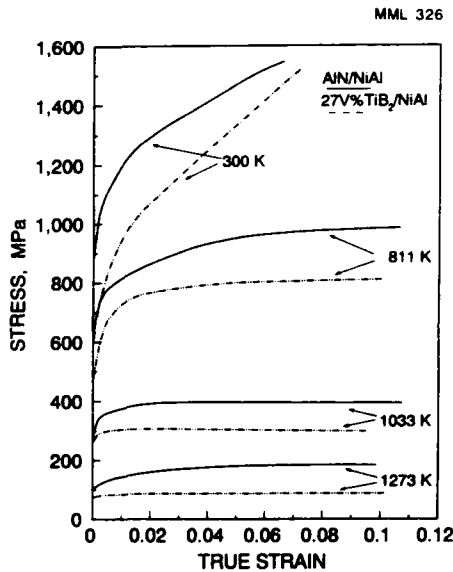
MML 326

Fig.1
Stress-strain curves of the Al/NiAl and the 27 V% TiB$_2$/NiAl composites deformed at different temperatures.
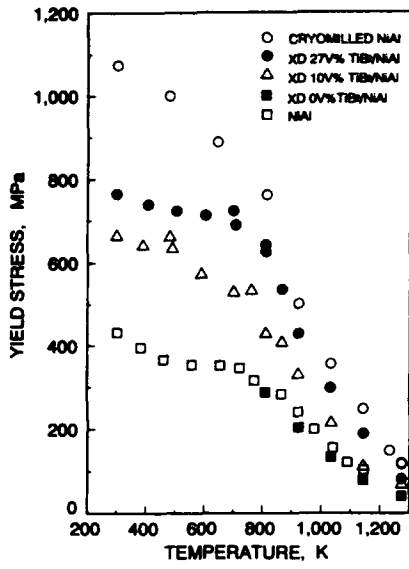
Fig.2
Temperature dependent of yield stresses of monolithic NiAl and the NiAl matrix composites.
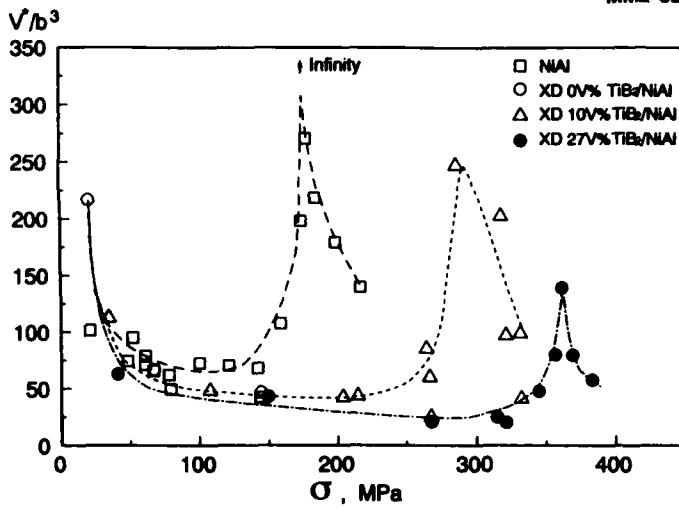
Fig.3 Activation volumes of monolithic NiAl and 0, 10, and 27 V% TiB$_2$/NiAl composites as function of yield shear stress in the temperature range of 300 - 1273 K.

Based on the above observations and the previous TEM observations of primarily screw dislocation [12], it is proposed that the strengthening, resulting from the reinforcements addition, is due to an increase in the athermal component of the yield stress, i.e., the reinforcements produce an increase in strength at low temperatures. This increase in strength is simply translated into an increase in strength at higher temperatures due to the stabilization of the microstructures of the composites which ensures that the mechanism for the increase in the athermal strengthening is stable with respect to testing temperature and time of testing, and the mechanism of thermally activated deformation remains the same. One of the most important reason for the increase of the athermal stress is due to the substantial reduction of the grain or subgrain size. The strengthening through the grain size refinement becomes true only under the condition that the grain boundary sliding must have been effectively stopped. At high temperatures, this condition can be fulfilled with the addition of a considerable amount of thermally stable reinforcements, such as AlN and TiB_2.

If we make the assumption that the reinforcement only produces an increase in the athermal component of the yield stress and the thermal activated process is the motion of jogged screw dislocations, then the following equation can be derived for the time necessary to make a thermally "jump"

$$t_i = K\left(\frac{\sigma_i^2 - \sigma^{*2}}{2\sigma_i\sigma^*}\right)e^{\frac{Q_a}{RT}}$$

where K is a constant, σ_i is the athermal stress, σ^* is the instantaneous effective stress, the apparent activation energy is as follows:

$$Q_a = Q_{SD} - \frac{\partial n}{\partial\left(-\frac{1}{RT}\right)}\ln\frac{\sigma_a}{\sigma_i}$$

where Q_{SD} is activation energy of self diffusion of NiAl, n is the stress exponent which is a function of temperature, σ_a is the applied stress and RT are the gas constant and temperature respectively. If it assumed that athermal stress varies with a periodicity corresponding to the subgrain or grain size, then a computer simulation investigation of the total time required to traverse the grain can be obtained and then the average dislocation velocity. Finally it is possible to obtain a plot of stress vs temperature which can be compared to the experimental data. The comparison was found to be quite good.

CONCLUSIONS

From a consideration of the experimental data, the following conclusions were drawn:

1. Reinforcements causes an increase in the athermal component of the yield stress at low temperatures and this results in the high temperature strengthening due to microstructure stabilization by the reinforcement. The strengthening obtained in the NiAl matrix composites is believed to be related to the grain size refinement, and the effective resistance of the grain boundaries to sliding due to the pinning by reinforcements. The most effective reinforcement should be the one that reduces stress concentrations in the matrix.

2. The yield strength of all the NiAl matrix composites exhibit typical temperature dependent behavior in a temperature range of 300-1273 K, and can be plastically deformed, compressively, at room temperature.

ACKNOWLEDGEMENT

REFERENCES

1. J.D. Whittenberger, R. Ray, C.C. Jha, and S. Draper, Mater. Sci. Eng., **A138**, 83(1991).

2. J.D. Whittenberger, R. Ray, S.C, Jha, and S. Draper, Mater. Sci. Eng., **A151**, 137(1992).

3. J.D. Whittenberger, Eduart Arzt, and M.J. Luton, J. Mater. Res., **5**, 271(1990).

4. J.D. Whittenberger, Eduart Arzt, and M.J. Luton, J. Mater. Res., **5**, 2819(1990).

5. R. K. Viswanadham, S. K. Mannan, and B. Sprissler, Annual Report of Martin Marietta Lab., MML TR 87-66C, 1987.

6. K. Sharvan Kumar, and S. K. Mannan, Progress Report of Martin Marietta Lab., MML TR 87-66C, 1988.

7. J. D. Whittenberger, R. K. Viswanadham, S. K. Mannan, and K. S. Kumar, J. Mater. Sci. **25**, 35(1990).

8. J.D. Whittenberger, J. Mater. Sci., **23**, 235(1988)

9. L. Wang and R.J. Arsenault, Mater. Sci. Eng., **A127**, 91(1990).

10. L. Wang and R. J. Arsenault, in *Intermetallic Matrix Composites*, edited by D. L. Anton, P. L. Martin, D.B. Miracle and P. McMeeking, (MRS Proc. 194, 1990) p.199.

11. L. Wang and R. J. Arsenault, in *High-Temperature Ordered Intermetallic Alloys IV*, MRS Proc. (Eds. L.A. Johnson, D.P. Dope, and J.O. Stiegler), (MRS Proc. **213**, 1991) p. 1063.

12. L. Wang and R. J. Arsenault, Mater. Sci. and Eng., **A127**, 91(1990).

THE INFLUENCE OF MOBILE DISLOCATION DENSITY ON THE FRACTURE TOUGHNESS OF B2-BASED Ni-Fe-Al ALLOYS

A.MISRA , R.D. NOEBE* and R.GIBALA,
Department of Materials Science and Engineering, The University of Michigan, Ann Arbor, MI 48109 -2136;
* NASA Lewis Research Center, Cleveland, OH 44135.

ABSTRACT

The deformation and fracture behaviors of two directionally solidified multi-phase Ni-Fe-Al ordered alloys were investigated. One alloy consisted of continuous $\beta+\gamma$ lamellae with fine γ' precipitates within the γ phase. The NiAl-based β phase of this alloy exhibited <100> slip even when deformed parallel to the [001] growth direction. This material exhibited an initiation fracture toughness of ~ 30 MPa√m and tensile ductility of 10%. The second alloy consisted of aligned but discontinuous γ lamellae within a continuous β phase. Again, the γ phase contained γ' precipitates, but unlike the previous alloy, the β phase also contained a fine dispersion of bcc precipitates due to spinodal decomposition. The β phase of this alloy deformed by <111> slip. This four-phase alloy exhibited a fracture toughness of ~ 21 MPa√m and tensile ductility of 2%. Observations of the plastic zone in both alloys indicated significant plasticity in the β phase due to easy slip transfer from the ductile second phase. The enhanced fracture resistance of these multiphase materials compared to single phase β alloys is attributed in large part to intrinsic toughening of the β phase by an increased mobile dislocation density due to efficient dislocation generation from the β/γ interfaces.

INTRODUCTION

It is well established that the ductility and toughness of refractory metals at low homologous temperatures $(T/T_m < 0.15)$ depends critically on the mobile dislocation density [1]. This is because the flow stress increases rapidly with decreasing temperature at $T/T_m < 0.15$ due to the low mobility of a/2<111> screw dislocations [2]. Thus, dislocation motion and multiplication processes at a crack tip are considerably reduced [3]. Similarly, Noebe and Gibala [4] have shown that the mechanical behavior of the intermetallic compound β-NiAl at low homologous temperatures is controlled by a low dislocation density and in the case of <001> single crystals, a low dislocation mobility. The same authors showed that surface films greatly reduce the flow stress and enhance the compressive ductility of β-NiAl due to an efficient generation of mobile dislocations at the film/substrate interface. <001> NiAl which deforms by "hard" a<111> dislocations in the unconstrained form was seen to deform by mobile <001> dislocations in film-coated compression specimens [5]. Further, directionally solidified multi-phase Ni-30Al and Ni-30Fe-20Al (at.%) alloys with the β phase as the matrix were found to exhibit up to 10% tensile ductility at room temperature, largely due to efficient dislocation generation from interphase interfaces [6]. In the present investigation, the fracture toughness

of two directionally solidified Ni-Fe-Al ordered alloys is evaluated. The role of the mobile dislocation density in controlling the fracture toughness of these multi-phase alloys is strongly indicated by these results.

EXPERIMENTAL PROCEDURES

Directionally solidified (DS) ingots of Ni-Fe-Al were prepared at NASA-Lewis Research Center by a modified Bridgeman technique. From these ingots, cylindrical tension specimens with 3 mm gage diameter and 10 mm gage length were prepared by centerless grinding followed by electropolishing. Four-point bend specimens, 50 mm long, 4 mm thick and 7 mm wide with a 150 μm thick notch which was 3 mm deep, were prepared by wire EDM and the sides were polished to 0.05 μm finish prior to testing. Load controlled cycling in the four-point bend fixture, between stress intensity of 24 MPa√m and 8 MPa√m, was done to introduce fatigue starter cracks. Approximately 3000 cycles were required for the crack to initiate and grow to a length of ~80 μm as seen on the side surface of the specimen. All mechanical tests were performed on an Instron 1137 testing machine. An initial strain rate of 2×10^{-4} s^{-1} was used for tension tests and an initial crosshead speed of 8.5×10^{-4} mm /s for bend tests.

RESULTS

Microstructural Characterization

Two DS ingots, both solidified at 5 mm/h, with nominal compositions (in at.%) Ni-30Fe-20Al and Ni-33Fe-21Al (designated alloy X and alloy Y respectively hereafter) were used in this investigation. The microstructures are shown in Fig. 1. Alloy X has a lamellar/rod microstructure with an [001] β (B2) matrix and a γ (fcc) second phase containing fine γ' (L1$_2$) precipitates. The γ phase is continuous and aligned in the growth direction. Alloy Y has a discontinuous but aligned γ phase which again has fine γ' precipitates. The discontinuous morphology is presumably due to a lower temperature gradient and lower volume fraction of the γ phase. The β matrix of alloy Y contains fine Fe-rich bcc precipitates, as shown in Fig. 2, formed due to the presence of a miscibility gap in the Ni-Al-Fe system [7].
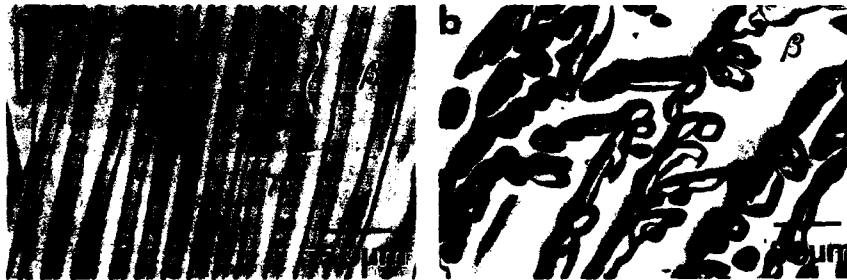
Fig. 1 Optical micrographs showing the longitudinal sections of (a) DS Ni-30Fe-20Al, alloy X, and (b) DS Ni-33Fe-21Al, alloy Y.
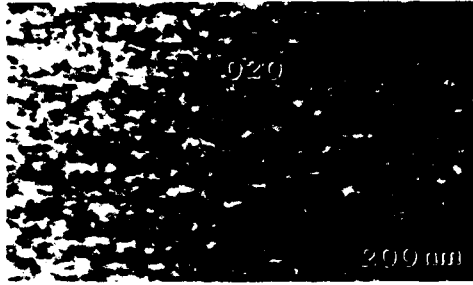
Fig. 2 Bright Field TEM micrograph showing fine Fe-rich bcc precipitates in the β matrix of alloy Y. $\underline{B}$ = [001].

Mechanical Tests Results

The results of the tension and four-point bend tests are shown in Fig. 3. Alloy X exhibits 10% tensile ductility and a 0.2% offset yield stress, σ_{ys}, of 600 MPa, whereas alloy Y has only 2% tensile ductility but a much higher yield stress of 1150 MPa. In contrast, [001] NiAl does not exhibit tensile ductility at room temperature [8]. No tensile data exists for monolithic [001] β-Ni-20Fe-30Al, the nominal composition of the β-matrix phase. However, columnar grain, <001> textured, β-Ni-20Fe-30Al deforms by "hard" a<111> dislocations in compression and has a yield stress comparable to [001] NiAl [9], whereas polycrystalline β-Ni-20Fe-30Al has a much lower yield stress and deforms by <100> slip, similar to binary NiAl [6]. These results indicate that the addition of 20% Fe to NiAl causes no significant change in the room temperature mechanical behavior of the ternary alloy. Therefore, the β/(γ+γ') Ni-Fe-Al alloys show significant enhancement in tensile ductility as compared to single phase β-NiAl or β-Ni-20Fe-30Al alloys.

K_Q values calculated from the load-displacement (l-d) curves shown in Fig. 3(b), using the standard offset methods [10], were 30.4 MPa√m for alloy X and 21.6 MPa√m for alloy Y. For alloy X, a fatigue starter crack was used but the value of the parameter, $2.5(K_Q/\sigma_{ys})^2$, was found to be less than the thickness of the specimen and the crack length. Thus, the measured fracture toughness value is reported as K_Q and not as K_{IC}. Tests done without fatigue starter cracks had yielded K_Q values of 35 MPa√m. For alloy Y, even without a fatigue starter crack the ASTM requirements were satisfied for the same specimen dimensions as used for alloy X, mainly due to the high σ_{ys} value of alloy Y; hence the fracture toughness value is reported as K_{IC}. Thus, the β/(γ+γ') Ni-Fe-Al alloys show a significant enhancement in the initiation fracture toughness as compared to single phase β-NiAl, (K_{IC}= 4-8 MPa√m [8]) or β-Ni-20Fe-30Al, (K_{IC} = 4-6.5 MPa√m [11]).

DISCUSSION

Tensile Ductility

The observations of the gage sections of the deformed tensile specimens reveal slip traces in the brittle matrix phase in both alloys X and Y, as shown in Fig. 4. Note the one-to-one correspondence between the slip traces, indicating slip transfer from the softer γ to the harder β phase. After fracture, a few secondary cracks were

seen but all these were very close to the fracture surface (within 20 μm), such that the contribution of multiple matrix cracking to the plastic strain was <0.5%.
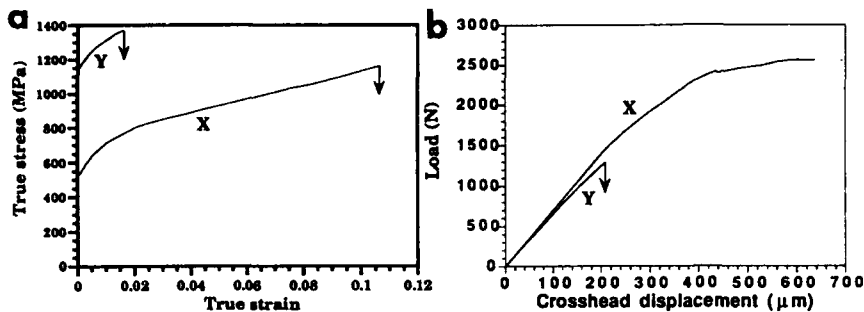
Fig. 3 (a) True stress-true strain curves in tension and (b) load- crosshead displacement curves for four-point bend tests for the alloys X and Y.

TEM analysis [9] indicated that slip transfer from the γ phase nucleates <100>{011} slip in the β phase of alloy X, even though the loading axis is parallel to <001>β. This is mainly because the critical resolved shear stress (CRSS) for <111> slip is 6-7 times the CRSS for <100> slip in β NiAl at room temperature [6, 8]. Resolving the dislocation pile-up stress tensor on all the possible slip systems in the β phase has shown that CRSS for <100> slip will be exceeded before the CRSS for <111> slip [9]. However, in alloy Y <111>{110} slip was seen in the β phase as a result of slip transfer from the γ phase. It is believed that the percentage increase in the CRSS for <100> slip by the fine bcc precipitates is much more than the percentage increase in the CRSS for <111> slip, since the latter is already quite high. Thus, the CRSS<111> / CRSS<100> ratio will decrease resulting in the activation of <111> slip in β, as expected by Schmid's law for <001> NiAl. The operation of "hard" <111> slip in the β phase of alloy Y instead of the higher mobility <100> dislocations seen in alloy X most likely explains the lower ductility and higher strength of alloy Y.
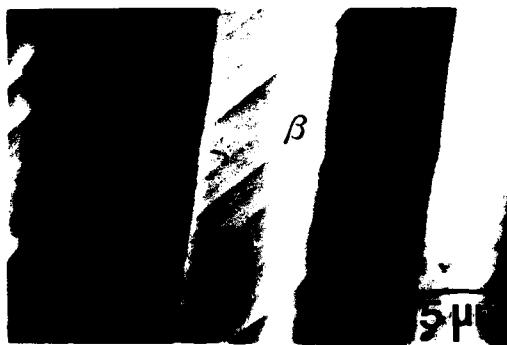
Fig. 4 SEM micrograph showing slip traces on the side surface of a fractured tensile specimen of alloy X. Note the indication of slip transfer from γ to β.

246

Fracture Toughness

In the β/γ+γ composites a high initiation fracture toughness was seen as compared to the initiation toughness of the monolithic matrix material. The l-d curves in Fig.3(b) also indicate stable crack propagation in alloy X. The test was stopped at the point indicated in Fig. 3(b) to examine the crack tip process zone. Fig.5(a) is a SEM micrograph showing the crack tip region in alloy X. Note the evidence of slip in both phases in the plastic zone, similar to that observed in tensile tests. No evidence of crack deflection along the interface or the formation of a significant crack bridging zone for the primary crack was observed. Few secondary cracks in the β phase were seen along the slip traces, indicating plastically induced cleavage. Thus, it appears that the large plastic zone due to the absence of plane strain conditions gives rise to the stable crack propagation in this specimen of alloy X. Alloy Y fractured unstably immediately after the l-d curve had deviated from linearity. The crack path was ~45° to the notch plane indicating that fracture occurs by cleavage on {110} planes in the β phase. Fig.5(b) shows the fracture surface of the notched bend specimen of alloy Y. The β phase has cleaved and the ductile γ phase appears to have necked to a chisel-edge morphology. The same general fracture appearance was seen in alloy X. However, necking of the ductile γ phase to a chisel-edge was less pronounced in alloy Y. The high angle views of the fracture surfaces indicated that the amount of plastic stretching of the γ phase prior to fracture was small, as expected for the case of strong interfaces which show no decohesion [12].

Fig. 5 SEM micrographs showing (a) crack tip plastic zone in alloy X and (b) fracture surface of alloy Y, both from notched bend specimens.

For brittle/ductile laminates where the matrix is assumed to be an elastic medium, any enhancement in the initiation fracture toughness is usually attributed to a crack renucleation mechanism [13], wherein the crack nucleates easily in the brittle phase but is stopped at the ductile layer. Crack propagation, then, occurs by renucleation of the crack in the next brittle layer. Slip in the ductile phase or interface decohesion may offer resistance to crack renucleation in the next brittle layer, thus causing the increase in K_{IC}. Further, decohesion was found to be much more effective in increasing K_{IC} than crack blunting due to slip in the ductile phase [13]. In the present case, the matrix cannot be regarded as an elastic medium. Thus, in addition to the crack blunting by the ductile phase, slip in the brittle phase

247

contributes significantly to the increase of K_{IC}. A small increment in K_{IC} may also be expected due to the misorientation of the cleavage plane with respect to the notch plane [8,14]. Nevertheless, these results suggest that the efficient emission of dislocations in the β phase from the β/γ interfaces leads to an increase in the intrinsic toughness of the β phase, in a manner consistent with the model of Ashby and Embury [3] for dislocation mobility limited materials such as bcc metals at low homologous temperatures. Below a critical dislocation density, ρ_c, crack-tip plasticity may be insignificant for materials with high lattice resistance, and fracture may occur in a brittle manner with low K_{IC}. According to the Ashby-Embury model, ρ_c is directly related to the ratio of the yield stress to the Griffith fracture toughness of the material. Thus, ρ_c is expected to be lower for alloy X (with <100> slip in β) as compared to alloy Y (with <111> slip in β). Therefore, crack-tip plasticity is expected to be more pronounced for alloy X than alloy Y and may explain the higher toughness of the former alloy. Similarly, increasing the mobile dislocation density has been shown to increase the fracture toughness of "soft" orientation NiAl [15]. These results are consistent with Chan's [16] analysis that tensile ductility in brittle intermetallics can be imparted more effectively by intrinsic toughening mechanisms than by extrinsic ones.

SUMMARY

The efficient generation of dislocations from second phase interfaces can significantly enhance the intrinsic fracture toughness and tensile ductility of dislocation density limited intermetallics like β-NiAl. A higher K_{IC} was seen with <100> slip activated in the β phase as compared to the case of "hard" <111> slip.

REFERENCES

1. L.L. Seigle and C.D. Dickinson, in Refractory Metals and Alloys II, ed. by M. Semchyshen and I. Perlmutter (Interscience Publishers, NY, 1962) p. 65.
2. J.W. Christian, Met.Trans. 14A, 1237 (1983).
3. M.F. Ashby and J.D. Embury, Scripta Met. 19, 557 (1985).
4. R.D. Noebe and R. Gibala, Scripta Met. 20, 1635 (1986).
5. J.T.Kim, R.D. Noebe and R. Gibala, in Intermetallic Compounds : Structure and Mechanical Properties, ed. by O.Izumi (Proc. 6th JIM Int. Sym., 1991) p. 591.
6. R.D. Noebe, A. Misra and R. Gibala, ISIJ International 31, 1172 (1991).
7. A. J. Bradley, J. Iron and Steel Inst. 168, 233 (1951).
8. R. Darolia , J. of Metals 43, 44 (1991).
9. A. Misra , Ph.D. thesis, University of Michigan, in progress.
10.ASTM Stand. E 399, Annual Book of ASTM Standards, 03.01, 519 (1984).
11. S.V. Raj, Met.Trans. 23A, 1691 (1992).
12. M.F. Ashby, F.J. Blunt and M.Bannister, Acta Met. 37, 1847 (1989).
13. F.E. Heredia, M.Y. He, G.E. Lucas, A.G. Evans, H.E. Deve and D. Konitzer, Acta Met. 41, 505 (1993) .
14. K.M. Chang, in Intermetallic Matrix Composites, ed. by D.B. Miracle et al., (MRS Sym. Proc. 273, 1992) p. 191.
15.J.M.Brzeski, J.E.Hack, R.Darolia and R.D.Field, Mat.Sci.Eng. 170A, 11 (1993).
16. K.S. Chan, Met. Trans. 25A, 299 (1994).

FRACTURE TOUGHNESS OF TWO Cr₂Hf+Cr INTERMETALLIC COMPOSITES AS A FUNCTION TEMPERATURE

K. S. Ravichandran, D. B. Miracle* and M. G. Mendiratta
UES, Inc., 4401 Dayton-Xenia Road, Dayton, OH 45432-1894
*WL/MLLM, Materials Directorate, Wright Patterson AFB, OH 45433

ABSTRACT

Fracture toughness as a function of temperature was evaluated for two Cr₂Hf+Cr intermetallic composites, each in two different microstructural conditions. The proeutectic microstructures based on Cr-6.5Hf (at%) showed a significant increase in fracture toughness with an increase from room temperature to 600°C. The coarse microstructure obtained by heat treatment at 1500°C showed evidence of ductile behavior of Cr at a lower test temperature (200°C) relative to that of one heat treated at 1250°C (400°C). In the eutectic microstructures based on Cr-13Hf, only a small increase in fracture toughness at 600°C was seen. The results are analyzed in the light of fracture micromechanisms.

INTRODUCTION

Fracture resistance is one of the primary requirements for successful implementation of intermetallics in high temperature structural applications. Fracture toughness of many intermetallics are low, often in the range of 1-5 MPa√m. The approach to increasing the fracture toughness through ductile particles is promising in a number of intermetallic systems, such as TiAl+Nb [1], Nb₅Si₃+Nb [2], MoSi₂+Nb/Ta [3] NiAl+Mo [4]. However, the requirements for high temperature use also include the thermochemical stability of phases or constituents at those temperatures. This has been a major concern in systems which are not in thermodynamic equilibrium, made by powder metallurgical techniques, since considerable reaction could occur at high temperatures causing interface reactions and loss of ductility of the toughening phase.

In-situ intermetallic composites, by virtue of their thermochemical equilibrium of phases show potential for high temperature applications [5]. Recent interest on systems such as Cr₂Hf+Cr [6,7], Cr₂Ta+Cr [6], Cr₂Nb+Cr [5] and Cr₃Si+Cr [8] is primarily based upon the fact that Cr is oxidation resistant up to 1000°C. The kinetics of oxidation of Cr is low relative to other refractory metals [9]. Cr also exhibits little weight gain up to about 1000°C [10].

In this investigation, fracture toughness levels of composites based on the Cr₂Hf+Cr system [11] were evaluated. In earlier works [6, 7], fracture toughness of a composite having a bulk composition of Cr-6.5Hf (at.%) was evaluated. In the present study, two composites having compositions of Cr-6.5Hf (proeutectic) and Cr-13Hf (eutectic), with two different microstructural conditions obtained by heat treatment, were selected for fracture toughness measurement. The objective is to evaluate fracture toughness as a function of temperature under both microstructures. Fractographic analyses were performed to determine fracture modes.

EXPERIMENTAL PROCEDURE

Alloy ingots with nominal compositions of Cr-6.5Hf (at%) and Cr-13Hf were arc melted and cast in copper molds. The ingots were enclosed in Mo cans and extruded at 1500°C with an approximate reduction ratio of 4:1. The extruded bars were decanned by electric discharge machining (EDM), and bars of size, 32mm X 6.35mm X 6.35mm were machined for fracture toughness testing. The bars were heat treated at 1250°C and 1500°C for 100 hrs. under the flow of high purity (>99.5%) gettered argon at a low rate and furnace cooled. Specimens were wrapped in Ta foils during heat treatment. Cr losses due to high vapor pressure at these temperatures were minimal. After heat treatment, specimen surfaces were polished to a 600 grit finish to remove the surface layer. Subsequently, notches of 2.5 mm in depth and about 50 μm in root radius were machined by EDM. Fracture toughness tests were performed at a displacement rate of 8.5×10^{-3} mm/min. in 3 point bending at room temperature and at 200, 400 and 600°C in argon atmosphere. Fracture surfaces were examined in a scanning electron microscope (SEM) to document fracture micromechanisms.

RESULTS AND DISCUSSION

The chemical composition of the alloys are presented in Table I. Microstructures in the as-extruded condition consisted of elongated primary Cr grains and eutectic structure in Cr-6.5Hf and a deformed eutectic lamellar structure in Cr-13Hf. Preliminary observations indicated that the microstructures recrystallized but did not coarsen up to 1300°C when heat treated for 100 hrs. Above 1300°C, microstructural coarsening was noticeable. Figs. 1 & 2 show the microstructures, as seen in longitudinal sections, after heat treatment at 1250°C and 1500°C for Cr-6.5Hf and Cr-13Hf alloy, respectively. Coarsening of the eutectic structure in both the alloys can be seen. Quantitative image analysis indicated that the relative volume fractions of Cr and Cr_2Hf differed only by a few % between the heat treatments in both the alloys.

Table I Chemical composition of alloys (wt.%)

Alloy	Hf	Zr	Cu	Fe	Ti	O	N	C
Cr-6.5Hf	17.1	0.15	0.02	0.08	0.03	0.044	0.005	0.0076
Cr-13Hf	33.1	0.2	0.04	0.07	0.02	0.032	0.005	0.0067

Results of fracture toughness tests are presented as a function of temperature in Figs. 3a&b for the heat treatment and alloy combinations studied. In both fine and coarse microstructural conditions, the proeutectic alloy shows an increase in fracture toughness (Kq) from about 7 MPa√m at room temperature to 15-18 MPa√m at 600°C. Fractographic examination revealed a cleavage fracture mode (Figs. 4a&b) suggesting that both the Cr and Cr_2Hf phases are brittle at room temperature. At 600°C, Cr exhibited ductility and Cr_2Hf failed in a brittle manner. Ductile rupture of the Cr phase surrounded by Cr_2Hf cleavage regions can be seen in Figs. 4c&d. At 200°C, fracture toughness of the coarse microstructure is significantly higher compared to that of the fine microstructure (13 vs. 9 MPa√m). While Cr grains which fractured in a ductile fashion could be rarely seen in the fine microstructure, several Cr grains exhibiting ductile fracture and debonding were seen in the coarse microstructure (Figs. 4e&f).
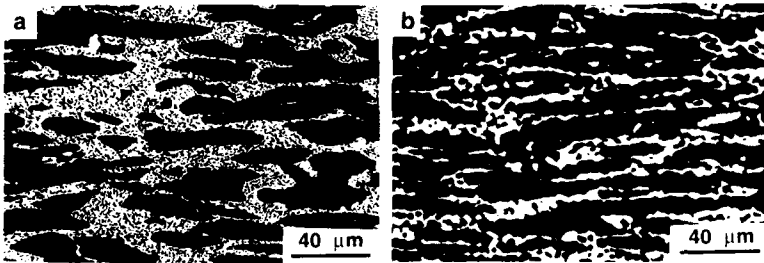
Fig. 1 Microstructures of Cr-5.5Hf alloy after heat treatment at (a) 1250°C and (b) 1500°C for 100 hrs.
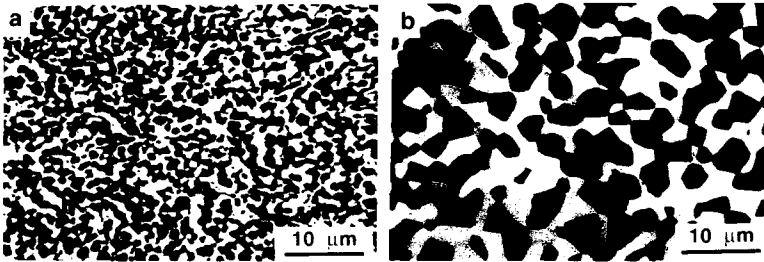
Fig. 2 Microstructures of Cr-13Hf alloy after heat treatment at (a) 1250°C and (b) 1500°C for 100 hrs.
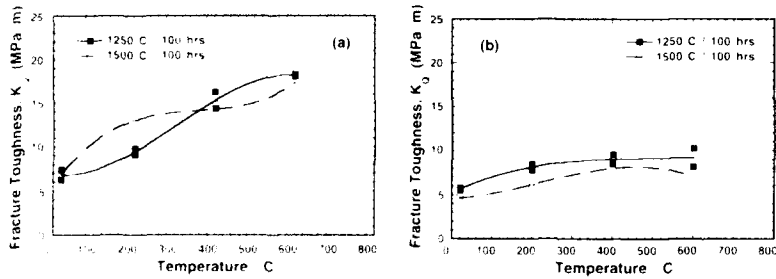
Fig. 3 Fracture toughness as a function of temperature for (a) Cr-5.5Hf and (b) Cr-13Hf alloy.

Fracture toughness levels in both the fine and the coarse eutectic microstructures increase only slightly with an increase in test temperature (Fig. 3c). At all temperatures, the coarse microstructure exhibited lower Kq (by about 1-2 MPa√m) values relative to the fine microstructure. Similar to the proeutectic alloy, the fracture mode was completely brittle in RT tests (Fig. 5a&b) and partially ductile due to the plastic

251
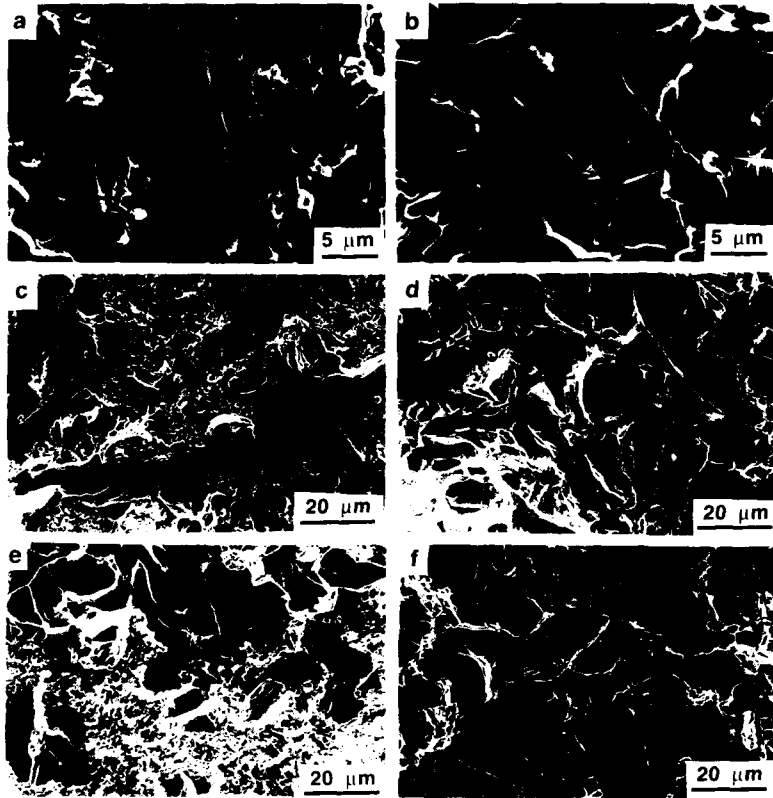
Fig. 4 Fracture modes in Cr-6.5Hf alloy tested at (a) & (b) at room temperature, (c) & (d) at 950° C, and (e) & (f) at 200° C. Heat treatment (a), (c) and (e) at 1250° C, (b), (d) and (f) at 1500° C.

deformation of Cr at 950° C (Figs. 5c&d). There was no discernible difference in fracture mechanism between coarse and fine eutectic microstructures at all temperatures.

In all microstructures, it is evident that the transition from brittle to ductile failure of Cr results in the increase in fracture toughness with temperature. It is well known [12, 13] that the brittle to ductile transition temperature (BDTT) of Cr depend on prior deformation history, interstitial content (O, N and C), presence of elements in solid solution, surface finish etc. In these investigations, the BDTT temperature was
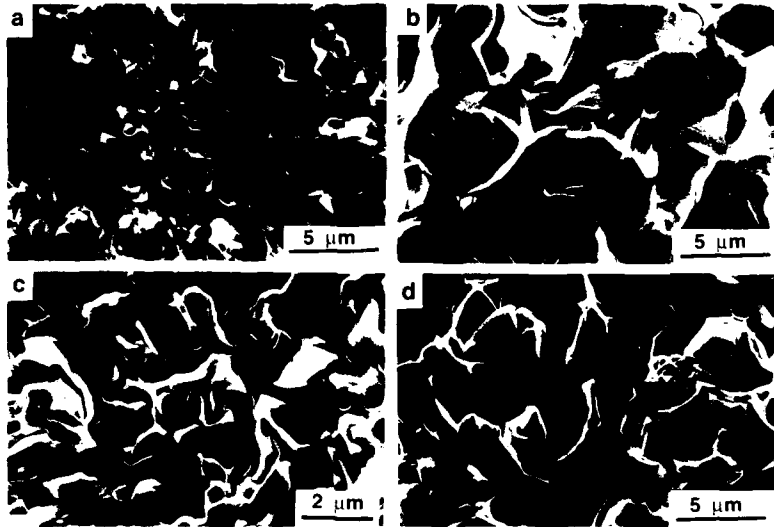
Fig. 5. Fracture modes in Cr-13Ht alloy tested at (a) & (b) at room temperature, (c) & (d) at 600°C. Heat treatment: (a) and (c) at 1250°C, (b) and (d) at 1500°C.

found to vary from -?°C to 500°C depending on the above variables. In particular, interstitial content has been known to have a strong effect on the BDTT. Although the N content in the present alloys are lower than the reported [12, 13] levels required to cause brittleness, O levels are higher, falling in the range of compositions causing brittle behavior in Cr.

A noticeable feature in the microstructures of the proeutectic alloy is that after heat treatment at 1250°C fine particles, much smaller in size compared to Cr₂Ht phase, were seen in the interior of recrystallized primary Cr grains. These are absent after heat treatment at 1500°C. Internal precipitation in Cr, yet unidentified, were seen in both cases under TEM for both heat treatment conditions. Further work is in progress to clarify the factors causing the different Cr behavior (brittle vs. ductile) which resulted in the high Kq values at 600°C for the microstructure heat treated at 1500°C.

The reasons for the decrease in fracture toughness in the eutectic microstructure after coarsening are not clear. The volume fractions of Cr and Cr₂Ht in both heat treatments were nearly the same and the phases are co-continuous. According to models for ductile phase toughening [14, 15], the coarse microstructure with a Cr particle size of about 4 times that in the fine microstructure should result in an increase in toughness at least by a factor of 2. It should be noted that the size of the Cr₂Ht also is larger by the same amount, and could lead to a larger perturbation of crack front in Cr₂Ht. It appears that the reduction in Kq due to increased size of brittle fracture of Cr₂Ht outweighs the increase in toughness due to increased ductile particle size.

SUMMARY

Due to the brittle behavior of Cr, fracture toughness levels at room temperature were only modest (5-7 MPa√m) in both Cr-6.5Hf and Cr-13Hf alloys with proeutectic and eutectic microstructures respectively. However, Cr showed extensive ductility at 600°C and resulted in a significant increase in fracture toughness to 15-18 MPa√m in Cr-6.5Hf. In Cr-13Hf alloy with eutectic microstructure an increase in temperature caused only a small increase (1-2 MPa√m) in fracture toughness, possibly due to the opposite effects of ductile Cr phase and brittle Cr₂Hf phase on crack resistance. It appears that minimization of microstructural continuity of Cr_2Hf, in addition to an increase in the amount and size of ductile particles, could increase fracture toughness.

ACKNOWLEDGMENT

REFERENCES

1. C. K. Elliot, G. R. Odette, G. E. Lucas and J. W. Sheckherd; in High Temperature/High Performance Composites, edited by A. G. Evans, S. G. Fishman and J. R. Strife (Mater. Res. Soc. Proc. 120, Pittsburgh, PA, 1988) pp. 95-100.
2. M. G. Mendiratta, J. J. Lewandowski and D. M. Dimiduk; Metall. Trans. A, 22, 1573 (1991).
3. D. H. Carter and P. L. Martin; in Intermetallic Matrix Composites, edited by D. L. Anton, P. L. Martin, D. B. Miracle and R. McMeeking (Mater. Res. Soc. Proc. 195, Pittsburgh, PA, 1990) pp. 131-137.
4. P. R. Subramanian, M. G. Mendiratta, D. B. Miracle; Metall. Trans. A, In Press.
5. D. M. Shah and D. L. Anton; in Intermetallic Matrix Composites II, edited by D. B. Miracle, D. L. Anton and J. A. Graves (Mater. Res. Soc. Proc. 273, Pittsburgh, PA, 1992) pp. 385-397.
6. S. Mazdiyasni and D. B. Miracle; in Ref. 3, pp. 155-162.
7. K. S. Kumar and D, B. Miracle; J. Intermetallics, In Press.
8. J. W. Newkirk and J. A. Sago; in Ref. 3, pp. 183-189.
9. W. D. Wilkinson; Properties of Refractory Metals, (Gordon and Breach Publishers, NY, 1967) p. 51-55.
10. T. E. Tietz and J. R. Wilson; Behavior and Properties of Refractory Metals, (Stanford University Press, Stanford, 1965), p. 17.
11. Binary Alloy Phase Diagrams Vol. 2, 2nd Edition, edited by T. B. Massalski, H. Okamoto, P. R. Subramanian and L. Kacprzak (Metals Park, OH, 1990) p. 1281.
12. A. H. Sully; in Ductile Chromium and its Alloys, (American Society for Metals, Cleveland, 1957) p. 14-26.
13. G. T. Hahn, A. Gilbert and R. I. Jaffee; in Refractory Metals and Alloys II, edited by M. Semchyshen and I. Perlmutter (Interscience Publishers, NY, 1963), pp. 23-63.
14. M. F. Ashby, F. J. Blunt and M. Bannister; Acta Metall., 37, 1847 (1989).
15. K. S. Ravichandran; Scripta Metall. Mater., 26, 1389 (1992).

PROCESSING AND MECHANICAL PROPERTIES
OF LAMINAR Al$_2$O$_3$-Ni$_3$Al COMPOSITES

J. H. SCHNEIBEL AND K. B. ALEXANDER
Metals and Ceramics Division, Oak Ridge National Laboratory, Oak Ridge, TN 37831

ABSTRACT

Several compositions of the intermetallic alloy Ni$_3$Al were examined with respect to (a) their wetting of Al$_2$O$_3$ and (b) their energy absorption capability in Al$_2$O$_3$/Ni$_3$Al laminates. Wetting is enhanced by small additions of carbon (e.g., 0.1 at. %), and bonding by additions of zirconium (e.g., 1 at. %). Chevron-notched laminate specimens were tested in three-point bending to assess the energy absorption due to the presence of a thin layer of Ni$_3$Al. A nickel aluminide with the composition Ni-22Al-1Zr-0.1C-0.1B was found to have a reasonable combination of wetting, adhesion and energy absorption. Interfacial bonding was found to be weak in all laminates.

INTRODUCTION

Composites based on Al$_2$O$_3$ ceramics and Ni$_3$Al intermetallics offer potentially interesting properties. Al$_2$O$_3$ as well as Ni$_3$Al exhibit excellent oxidation properties. The yield strength of Ni$_3$Al increases with increasing temperature up to approximately 1000 to 1300 K (1). Since boron-doped Ni$_3$Al exhibits ductilities of up to 50% at room temperatures, it may provide acceptable ductile-phase toughening of alumina. Similarly, Ni$_3$Al reinforced with Al$_2$O$_3$ particulates may potentially exhibit a good combination of strength, toughness, and wear resistance.

The microstructures produced by powder processing of Al$_2$O$_3$/Ni$_3$Al composites can be inhomogeneous (2, 3, 4). It is therefore difficult to differentiate between the influence of microstructure and alloying elements, respectively, on the mechanical properties of powder-processed composites. For this reason simpler model geometries, such as thin Ni$_3$Al films sandwiched between Al$_2$O$_3$ platelets, are preferable. Bannister and Ashby (5) have employed such a geometry in their model experiments with glass and lead. Their tensile data as well as their fracture surface observations allowed them to make clear predictions about the degree of constraint during the deformation of the ductile phase. Owing to higher strengths and processing temperatures, such experiments are not as easily carried out with the Al$_2$O$_3$/Ni$_3$Al system. At the beginning of this research it was also not clear, how reproducible the processing of Al$_2$O$_3$/Ni$_3$Al laminates would be, and to what extent the Ni$_3$Al would be constrained during deformation. It was therefore decided to carry out a number of relatively simple screening tests based on laminated Al$_2$O$_3$/Ni$_3$Al chevron-notched bend specimens in order to ascertain (a) reproducibility and (b) the effect of changes in the composition of the Ni$_3$Al intermetallic on the mechanical properties. In addition, wetting experiments were carried out in order to determine to what extent suitable alloying might reduce the wetting angle of liquid Ni$_3$Al on solid Al$_2$O$_3$.

EXPERIMENTAL PROCEDURE

Ni$_3$Al alloy buttons with typical masses of 15 g were arc-cast in argon. A few compositions were prepared in larger quantities. Wetting studies were carried out in vacuum furnaces at pressures between 10^{-3} and 10^{-4} Pa. Pieces of Ni$_3$Al approximately 3x3x6 mm were placed with one of their long faces on ground alumina substrates (Coors Ceramics AD995 or AD998). These assemblies were heated to 1723 K over a period of approximately 2 hours, held for 900 s at this temperature, and subsequently furnace cooled. Wetting angles were determined from measurements of the average contact diameter and the height of the Ni$_3$Al beads, assuming a uniform curvature across their surface. Several direct measurements of the wetting angle in an optical comparator gave similar values (within ±3°).

Al_2O_3/Ni_3Al laminates were processed via hot-pressing of thin plates cut from the alloy buttons, which were sandwiched between two Coors AD995 or AD998 Al_2O_3 discs. The compositions containing 0.4 and 0.5 at. % Zr were already available as rolled sheets. The Al_2O_3 discs had diameters and thicknesses of approximately 40 and 3 mm, respectively. One of the two alumina discs used for each laminate had an approximately 100 μm deep recess approximately 20 mm wide machined into its center in order to achieve a reasonably well controlled Ni_3Al thickness at the processing temperature of 1723 K, at which the Ni_3Al was liquid. Hot-pressing was usually carried out in flowing argon in a $MoSi_2$ furnace at a pressure of 1 MPa for 1 hour. In order to minimize the oxygen partial pressure, a crucible with Ti powder was placed next to the specimens. One laminate was fabricated in vacuum (10^{-4} Pa) with an imposed uniaxial stress of approximately 4 kPa.

Specimens with a width of approximately 5 mm were sliced from the Al_2O_3/Ni_3Al laminates using a slow-speed diamond saw and then chevron-notched in a crack-dividing orientation as shown schematically in Fig. 1. These specimens were tested in three-point bending with a span L$\approx$20 mm at room temperature. Since the Al_2O_3 on the side opposite to the chevron notch tip acts as hinge, this type of test may be regarded as a (severely misaligned) tension test. Referring to Fig. 1 we define a normalized displacement as u_n = u/t = 4 (d/L)x(h/t), where u is the opening displacement at the tip of the chevron, d the crosshead displacement, h the height of the chevron notch, and t the thickness of the Ni_3Al layer. Integration of the load-displacement curves provides an energy absorption. Assuming G_{Ic} (Al_2O_3) = 50 J/m^2 the contribution of the fracture of the Al_2O_3 to the energy absorption is calculated from the known area of the triangular section connecting the two specimen halves in Fig. 1(a) and subtracted from the measured values. This results in the work E absorbed by the Ni_3Al. Following Bannister and Ashby (5), we introduce a normalized energy absorption E_V = $E/(h\ t^2)$. Whereas Bannister and Ashby defined the maximum debond lengths during the preparation of their specimens, this was not done in the present case. A rigorous comparison between different alloys is therefore not possible, since the values of the debonding lengths, which influence the load-displacement curves significantly, are not known. However, following Bannister and Ashby, post-mortem fractography should give at least a qualitative idea about the degree of constraint and whether debonding occurred or not. It should also be possible to check (a) reproducibility of the mechanical property measurements and (b) any substantial effects arising due to differences in alloy composition.
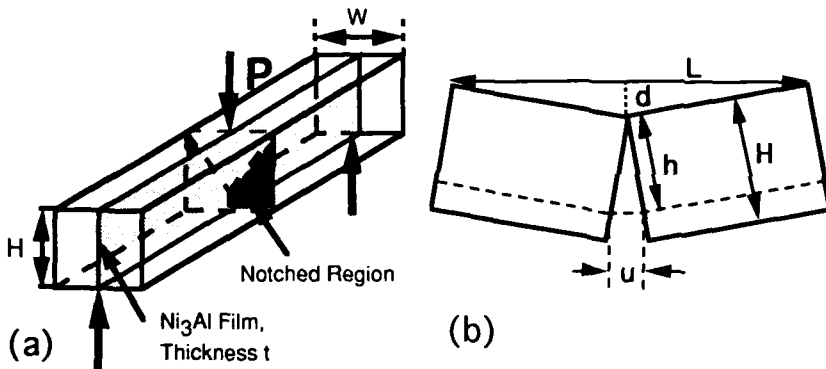
Fig. 1. (a) Schematic view of chevron-notched specimen and (b) side view.

WETTING OF Ni₃Al ON Al₂O₃

The wetting angle measurements are summarized in Table I. Note that compositions are always given in at. %. In agreement with Moorhead (6), carbon additions to Ni₃Al tend to reduce the wetting angle. In a number of cases the Ni₃Al beads fractured off the alumina during cool-down from 1723 K. The fracture in these cases occurred usually along the Ni₃Al/Al₂O₃ interface. In other cases the Ni₃Al beads could only be removed by shearing them off, which resulted always in fracture within the alumina. Zirconium additions generally enhanced the bonding, and bonding was also observed in the absence of wetting (i.e., if the wetting angle exceeded 90°). Chromium additions had no significant influence on wetting and adherence. In contrast to Ni₃Al beads alloyed with Zr, those alloyed with Ti did not adhere. Yttrium additions produced neither wetting nor adherence. Ni-22Al-1Zr-0.1C-0.1B appeared to have a good combination of interfacial strength and wetting behavior. Increasing the carbon content to 1 at. % had a negative effect on the adherence. This does not necessarily mean that the interfacial strength decreased, since fracture could also result from higher internal stresses caused by strengthening of the Ni₃Al by carbon. An experiment with sapphire did not show a significant effect of the substrate purity or crystallography on the wetting angle, although the Ni₃Al bead did not adhere in this case.

Table I. Wetting angles of Ni₃Al alloys on alumina after 900 s at 1723 K in vacuum

Specimen Number	Composition, at.%	Fracture Path if sample disintegrated	Fracture Path when shearing off bead	Wetting Angle (Degrees)
C50-1	Ni-23Al-1C-0.1B	Interface		76
C48-1	Ni-22Al-1Zr-0.1B		Al₂O₃	>90
C48-2	Ni-22Al-1Zr-0.1B		Al₂O₃	>90
C59-1	Ni-22Al-1Zr-0.1C-0.1B		Al₂O₃	76
C59-2	Ni-22Al-1Zr-0.1C-0.1B		Al₂O₃	77
C59-5	Ni-22Al-1Zr-0.1C-0.1B		Al₂O₃	76
C51-1	Ni-22Al-1Zr-1C-0.1B	Interface		78
C51-2	Ni-22Al-1Zr-1C-0.1B		Al₂O₃	77
C51-3	Ni-22Al-1Zr-1C-0.1B*	Interface		83
C51-4	Ni-22Al-1Zr-1C-0.1B		Al₂O₃	76
C60-1	Ni-18Al-5Zr-0.1B	Interface		>90
C49-1	Ni-16Al-8Cr-1Zr-0.1B	mixed		>90
C67	Ni-16Al-8Cr-1Zr-0.1C-0.1B		Al₂O₃	80
C68	Ni-22Al-1Ti-0.1B-0.1C	Interface		80
C69	Ni1-8Al-5Ti-0.1B-0.1C	Interface		79
C70	Ni-22Al-1Y-0.1B-0.1C	Interface		>90

*sapphire substrate

FRACTURE OF LAMINAR Al₂O₃-Ni₃Al COMPOSITES

Figures 2 to 4 show typical load-displacement curves and micrographs of the fracture specimens for some of the laminates listed in Table II. Each of the load-displacement curves exhibits an initial load peak which is thought to be due to the fracture of the Al₂O₃ in the triangular ligament in the center of the chevron-notched specimens. The part of the curve following this peak is due to the deformation, pull-out and fracture of the thin (typically 100 μm) Ni₃Al film sandwiched between the Al₂O₃. Figure 2 shows (after the Al₂O₃ peak) a nearly constant load which is interrupted by occasional load drops. The SEM micrograph of the fracture surface indicates necking and debonding. Figure 3 pertains to a material containing more Zr (1 at. %) as well as 0.1 at. % C. The load plateau following the Al₂O₃ peak is distinctly higher as compared to the previous example. At a displacement of about 300 μm the load drops significantly. At this point the Ni₃Al

257

film probably starts tearing apart. The fracture surface looks similar to that in the previous example. Vacuum-processed material with the same composition (see Table II) showed similar mechanical behavior. However, its fracture surface showed some porosity as well as a cleavage-like appearance. Figure 4 is for a material containing 1 at. % C. The load drop occurs now at a displacement of only 100 μm. Presumably, the substantial porosity shown in Fig. 4 (b) is
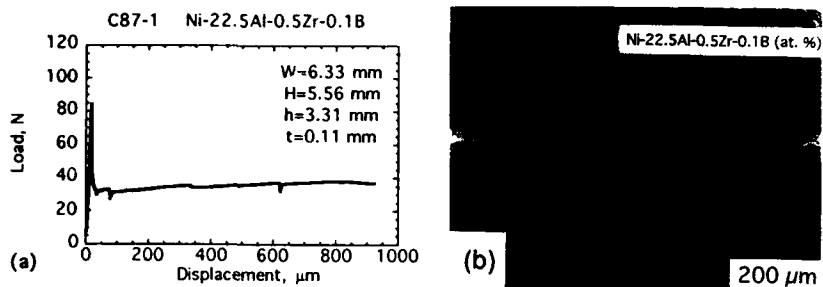
Fig. 2. (a) Load vs. displacement plot for 3-pt. bend test and (b) corresponding SEM micrograph of fracture surface.
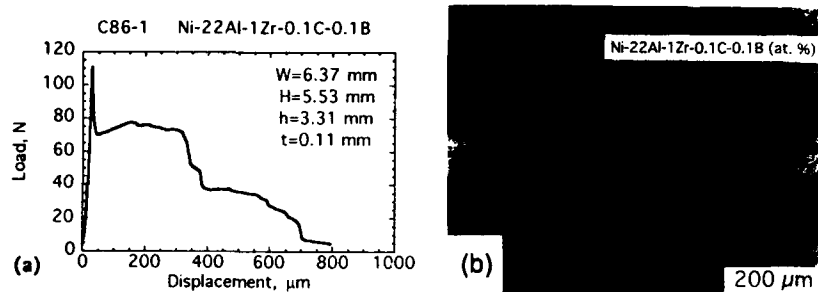
Fig. 3. (a) Load vs. displacement plot for 3-pt. bend test and (b) SEM micrograph of fracture surface.
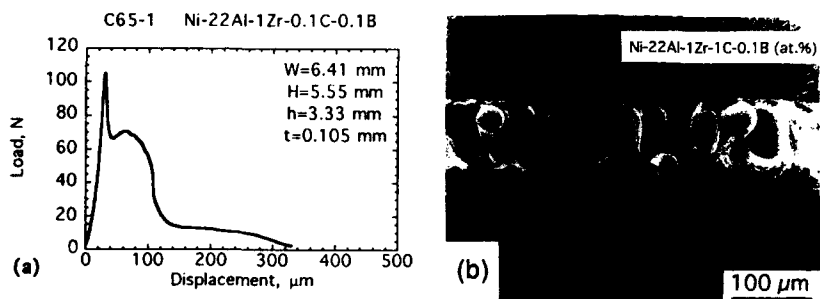
Fig. 4. (a) Load vs. displacement plot for 3-pt. bend test and (b) SEM micrograph of fracture surface.

responsible for this behavior. This porosity might be caused by CO_2 evolution due to a reaction of the dissolved carbon with residual oxygen in the argon cover gas, or with residual oxides such as ZrO_2.

None of the fractographs in Figs. 2 through 4 shows evidence for constrained fracture of the Ni_3Al. In particular, the gaps between the Ni_3Al and the Al_2O_3 indicate weak interfacial bonding. The plateaus followed by load drops in Figs. 3 and 4 are consistent with debonding followed by fracture of the Ni_3Al layer, whereas Fig. 2 (a) suggests frictional pull-out as a major mechanism. In the case of strong interfacial bonding and constrained fracture, which was not found in any of our composites, fracture would presumably have occurred after much smaller displacements.

The normalized values of the absorbed energies for the different alloys examined are summarized in Table II. Several observations can be made. The Ni-22.5Al-0.5Zr-0.1B alloy was associated with relatively small energy absorptions. This is rationalized by the low Zr concentration, which does not strengthen the alloy very much (7) and does not enhance interfacial bonding sufficiently. Consequently, when the Zr concentration is increased to 1 at. %, significantly higher normalized

Table II. Compositions and thicknesses of the Ni_3Al films in Al_2O_3/Ni_3Al laminates. The normalized energies E_v absorbed by the Ni_3Al films after different normalized displacements are also shown. Samples which exhibited anomalous fracture behavior (such as non-representative fracture surfaces as compared to specimens cut from the same disc, or anomalously low strengths) have been excluded from the calculation of the average energy values (see values in brackets)

Specimen Number	Composition, at. %	Film Thickness, t, μm	E_v (GJ/m³) u/t=1	E_v (GJ/m³) u/t=2	E_v (GJ/m³) u/t=4
C52-1	Ni-22.5Al-0.5Zr-0.1B	88	(0.091)		
C52-2	"	80	0.139	0.272	
C87-1	"	110	0.126	0.268	0.564
C87-2	"	100	0.16	0.333	0.689
C87-3	"	70	0.18	0.403	0.866
	Average E_v		0.151±0.024	0.319±0.063	0.706±0.152
C56-1	Ni-22Al-1Zr-0.1B	48	0.443	0.928	1.695
C56-2	"	60	0.288	0.619	
C56-3	"	65	(0.200)	(0.331)	(0.506)
	Average E_v		0.366±0.110	0.773±0.219	
C66-1	Ni-22Al-1Zr-0.1C-0.1B	80	0.287	0.495	0.619
C66-2	"	70	0.263	0.496	0.665
C86-1	"	110	0.288	0.602	0.898
C86-2	"	80	0.319	0.674	1.134
C86-3	"	70	0.422	0.774	1.127
C124-1	" Processed in Vac	130	0.276	0.597	0.825
C124-2	" Processed in Vac	105	0.321	0.703	1.233
C124-3	" Processed in Vac	120	(0.069)	(0.117)	(0.181)
	Average E_v		0.311±0.053	0.620±0.104	0.929±0.242
C65-1	Ni-22Al-1Zr-1C-0.1B	105	0.184	0.227	
C65-2	"	130	0.085	0.131	
C85-2	"	110	0.158	0.226	0.345
C85-3	"	80	0.438	0.803	
	Average E_v		0.216±0.154	0.347±0.308	
C88-1	Ni-16.7Al-8Cr-0.4Zr-0.1B	88	0.246	0.444	0.725
C88-2	"	110	0.205	0.399	0.617
C88-3	"	100	0.193	0.302	0.366
	Average E_v		0.215±0.028	0.382±0.073	0.569±0.184
C84-1	Ni-16Al-8Cr-1Zr-0.1C-0.1B	65	0.406	0.860	1.134
C84-2	"	53	0.217	0.374	0.627
	Average E_v		0.314±0.134	0.617±0.344	0.881±0.358

energies were observed. An addition of 0.1 at. % carbon, which enhances the wetting, did not improve the energy absorption significantly, but it seemed to result in somewhat better reproducibility of the mechanical data. Increasing the carbon level to 1 at. % reduced the energy absorption. The detrimental effect of high levels of carbon is due to significantly increased porosity. Chromium additions did not cause significant improvements. The Ni_3Al/Al_2O_3 interfaces tended to be weak in all cases, as evidenced by delamination during the fracture experiments.

SUMMARY AND CONCLUSIONS

The wetting behavior of Ni_3Al intermetallics on alumina and the properties of Al_2O_3/Ni_3Al laminates have been examined. Carbon additions reduced the wetting angles to values of about 76°. Increasing the carbon level from 0.1 to 1 at. % did not reduce the wetting angles any further and resulted in a preference for interfacial fracture. Zr additions enhanced bonding, whereas Ti additions did not.

Laminates consisting of typ. 100 μm thick Ni_3Al films sandwiched between Al_2O_3 discs were fabricated. Chevron-notched specimens cut from the laminates were tested in three-point bending. The load-displacement curves showed usually a sharp initial peak, which is attributed to fracture of the alumina. Following this peak, the loads may be fairly constant, with occasional dips, indicating friction effects. In most cases, distinct load drops suggesting fracture of the Ni_3Al film were eventually observed. The energy absorption due to the Ni_3Al tended to increase as its Zr-content increased. For high carbon contents (1 at. %) significant porosity, which resulted in reduced energy absorption, has been observed. The composition Ni-22Al-1Zr-0.1C-0.1B offered reasonably high energy absorptions. However, bonding tended to be weak in all laminates investigated and neither fracture surfaces nor load-displacement curves showed evidence for constrained fracture of the Ni_3Al layer. This suggests that composites based on the Al_2O_3/Ni_3Al system may have to be topologically interpenetrating in order to eliminate the need for a strong Al_2O_3/Ni_3Al interface.

ACKNOWLEDGMENTS

REFERENCES

1. C. T. Liu, J. O. Stiegler, and F. H. Froes in *Metals Handbook* , Vol. 2, 10th edition, ASM International, 1990, pp. 913-942.
2. C. G. McKamey and E. H. Lee, in *Intermetallic Matrix Composites* , Proceedings of Materials Research Society Symposium, 1990, vol. 194, pp. 163-168.
3. G. L. Povirk, J. A. Horton, C. G. McKamey, T. N. Tiegs, and S. R. Nutt, J. Mat. Sci. **23**, 3945 (1988).
4. K. B. Alexander, H. T. Lin, J. H. Schneibel, and P. F. Becher, to be published in Proceedings of Symposium on *Processing and Fabrication of Advanced Materials* , TMS Fall Meeting, Pittsburgh, 1993.
5. M. Bannister and M. F. Ashby, Acta Metall. Mater. **39**, 2575 (1991).
6. A. J. Moorhead, United States Patent **4,596,354** (1986).
7. S. Miura, Y. Mishima, and T. Suzuki, Z. Metallkde. **80**, 48 (1989).

CREEP BEHAVIOR AND MICROSTRUCTURES OF
Nb-26Ti-48Al ALLOY AND COMPOSITE

C.R. Feng and D.J. Michel
Materials Science and Technology Division
Naval Research Laboratory, Washington, DC 20375-5343.

ABSTRACT

The creep behavior of Nb-26Ti-48Al alloy and its composite were investigated. After creep testing, precipitates were observed in the composite and mobile dislocations were found to be pinned by these precipitates. The combined effects of the reinforcements and the pinned dislocations were responsible for a reduced creep rate of the composite. The possible creep mechanisms were discussed based on the stress exponent and the activation energy of creep.

INTRODUCTION

The need for high temperature, structurally efficient alloys for use in advanced turbine applications has lead to renewed interest in oxidation-resistant, refractory-based intermetallic alloys. The addition of ceramic reinforcements via the XD™ process [1] provides the opportunity to tailor the microstructure of the alloy to improve the mechanical behavior. The influence of these particles, which will affect the response of the alloy by affecting grain size, deformation mode, transformations, and microstructural characteristics, is an important part of the development of new, high performance refractory based intermetallic alloys. The purpose of this study is to investigate the creep behavior of Nb-26Ti-48Al alloy and its composite.

MATERIALS AND EXPERIMENTAL PROCEDURES

The materials used in this investigation were extruded Nb-26Ti-48Al alloy (alloy) and XD™ processed and extruded Nb-26Ti-48Al reinforced with 10vol%(Nb,Ti)B whisker (composite). After extrusion, both materials were thermally treated at 1400°C (β-phase field) for 30 minutes, cooled at 25°/hour to 900°C (γ + σ phases field), then cooled at 200°/hour to room temperature.

The creep tests were conducted in the air in the temperature range of 760° - 928°C (1400° - 1700°F) using a constant load lever arm creep frame. The displacement as a function of time was measured using a LVDT. After the steady state creep rate (minimum creep rate) was reached, the stress was incrementally increased; each incremental stress step was 34.5MPa (5ksi). The creep tests were terminated when either the creep rate reached 10^{-5}/sec or the specimen ruptured. The unbroken specimens were cooled under load to room temperature.

The microstructures prior to and after the creep test were examined by TEM. All foils were examined in a JEM 200CX TEM operated at 200kV [2].

RESULTS AND DISCUSSION

Both materials were found to exhibit an $\gamma + \sigma$ two-phase microstructure [2]. The average sizes of γ grains and σ grains in the alloy and the composite were 100μm and 30μm and 40μm and 20μm, respectively. The volume fraction of σ grains was 20% in both materials, and 1/2[110] and [101] dislocations, {111} twins and stacking faults were observed in γ grains. After creep testing, increased dislocation and twin densities were noted in both materials, Fig. 1a. However, two different types of precipitates, TiB_2 plates and Ti_3AlC needles, were observed in the γ grains in the composite, with dislocations pinned by these precipitates, Fig. 1b.

Creep rates as a function of stress at various temperatures are presented in Figs. 2 and 3. Because of the longer period of exposure to the elevated temperatures and the smaller grain size (more grain boundaries), the composite specimens were severely oxidized and the assumption of a constant volume during the creep tests was not applicable. Although the exact values of the true stress were indeterminate, the lower limit and the upper limit of the true stresses can be determined. Both sets of data are presented in Fig. 4. The data presented in Figs. 2 and 3 indicate that, despite the larger grain size (100μm vs. 40μm), at same stress level, the creep rates of the alloy were at least one order of magnitude higher than those of the composite. The lower creep rates of the composite were due to the combination effects of the (Nb,Ti)B whisker reinforcements and the slow movement of the pinned dislocations in the γ grains. It was noted that as the stress increased, n also increased. For stresses less than 80MPa, n=2, for stresses between 80MPa and 200MPa, n=5, and for stresses greater than 200MPa, n=7. Since all curves were continuous rather than with discrete inflections, the division into different regimes was somewhat arbitrary. Similar creep behavior has been also reported in other TiAl alloys and composites [3].

The Arrhenius plot giving the activation energy, Q_C, at various stresses is shown in Figs. 4 and 5. For both materials, at higher temperatures (> 760°C), Q_C = 374kJ/mol at all stresses. This value was consistent with the activation energy of Ti self-diffusion in TiAl, Q_L, 291kJ/mol, [4]. The higher value observed in this study may be due to the higher Nb content. However, at 760°C and at higher stresses (>70MPa), Q_C increased to 521kJ/mol for the alloy and to 591kJ/mol for the composite.

In the following discussion, only n and Q_C will be used as the guidance for the creep mechanism evaluation. When n=2 and $Q_C \approx Q_L$, the transition from n=1 to n=5 may reflect the creep mechanism change from bulk, diffusion-controlled, Newtonian viscous flow to

climb-controlled dislocation glide. When n=5 and $Q_c \approx Q_L$, the creep mechanism was presumed to be lattice diffusion-controlled dislocation climb. The same suggestions have been made for many TiAl alloys and composites [3]. The mechanism responsible for the higher Q_c observed at the lower temperature (<760°C) was not clear. However, a previous report has indicated that the ductile-brittle transition temperature (DBTT) of Ti-54Al alloy was 700°C [5]; this is very close to the temperature boundary which separates the high and the low Q_c in the present study. The same report [5] also suggested that, at temperatures below DBTT, the dislocations were pinned by obstacles and that this phenomenon may contribute to a high Q_c. With n≈7 and $Q_c \approx Q_L$, the creep process could be the recrystallization [6] or the dynamic recovery [7 and 8]. In addition, Jin et al [9] report that mechanical twinning was one of the creep mechanisms in TiAl.

Because all curves presented in Figs. 2 and 3 are continuous rather than with discrete inflection points, the relationship between the creep rate and the stress can also be expressed as a *sinh* function [10]:

$$\dot{\varepsilon} = A \; sinh(B\sigma) \; exp(-Q_c/RT) \qquad (1)$$

where A and B are material constants. The stress dependence of creep rates in the form of *sinh* function suggests that there was an overlap of several mechanisms operating in parallel at each stress level. However, because $Q_c \approx Q_L$, these mechanisms were considered to be lattice diffusion related.

SUMMARY

The creep behavior and the microstructures of Nb-26Ti-48Al alloy and (Nb,Ti)B whiskers reinforced composite were investigated. The observations are summarized as follows:

1) Increased dislocation density and twin density were observed in the γ grains in both materials;
2) TiB_2 type precipitate plates and Ti_3AlC type precipitate needles were observed in the composite, but not in the alloy and dislocations were pinned by these precipitates;
3) As stress increased, the value of stress exponent increased from 2 to 7;
4) Reinforcements and pinned dislocations contributed to the reduced creep rate observed for the composite; and
5) Although no unique creep mechanism was found through-out the tested stress range, the activation energy suggests that the creep mechanisms were lattice diffusion related.

ACKNOWLEDGMENT

REFERENCES

1. A.R.C. Westwood, Metall. Trans. A, **19A**, 749 (1988).

2. C.R. Feng and D.J. Michel, Mat. Sci. Eng., **A152**, 202 (1992).

3. C.R. Feng and K. Sadananda, Mat. Sci. Eng., **A170**, 199 (1993).

4. S. Kroll, H. Mehrer, N. Stolwijk, C. Herzig, R. Rosenkranz and G. Frommeyer, Z. Metallkd. **83**, 591 (1992).

5. H.A. Lipsitt, D. Shechtman and R.E. Schafrik, Metall. Trans., **6A**, 1991 (1975).

6. W.O. Soboyejo and R.J. Lederich, at TMS Inter. Sym. on Structural Intermetallics, Champion, PA, 1993.

7. S.L. Kampe, presented at the TMS Sym. on Creep and Fatigue of Metal Matrix Composites, New Orleans, 1991 (unpublished).

8. C.R. Feng, H.H. Smith and D.J. Michel, 1993 (unpublished).

9. Z. Jin, and T.R. Bieler, Scripta Metall. Mater., **27** 1301 (1992).

10. F. Garofalo, Trans. AIME, **227**, 351 (1963).

Figure 1 TEM micrographs of the microstructures after creep testing at 760°C: a) the alloy, and b) the composite.
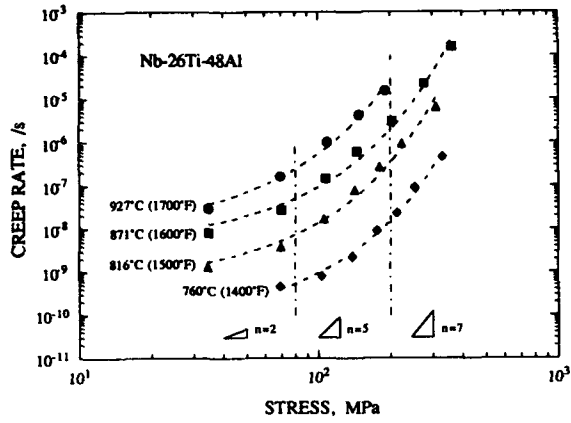
Figure 2   Creep rate as a function of stress at various
temperatures for the alloy.
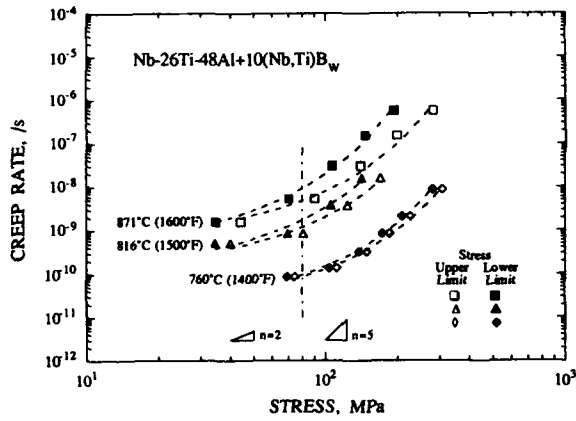
Figure 3   Creep rate as a function of stress at various
temperatures for the composite.
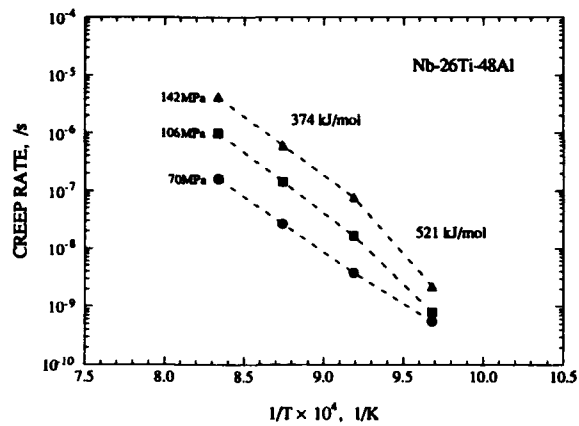
Figure 4   Activation energy of creep for the alloy.
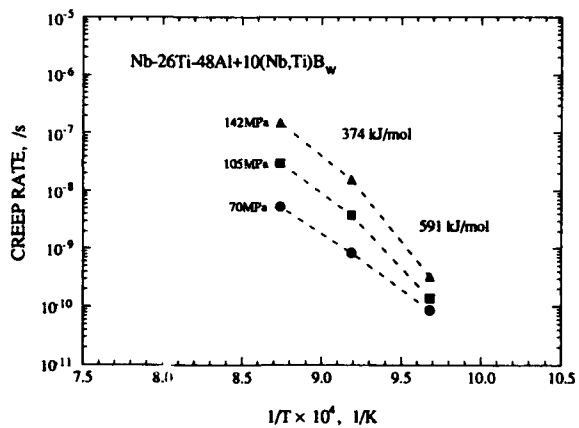
Figure 5   Activation energy of creep for the composite.

Thermal Misfit and Thermal Fatigue Induced Damage in Brittle Composites

N. Sridhar[+], J. M. Rickman[*] and D. J. Srolovitz[+,Δ]

[+]Department of Materials Science and Engineering, The University of Michigan, Ann Arbor, MI 48109, U.S.A.,[*]Department of Materials Science and Engineering, Lehigh University, Bethlehem, PA 18015, U.S.A., [Δ]Department of Materials and Interfaces, Weizmann Institute of Science, Rehovot 76100, Israel

ABSTRACT

We examine the conditions under which differences in thermal expansion between a particle and the matrix leads to crack growth within the matrix. Using linear elastic fracture mechanics, we obtain closed-form, analytical results for the case of a penny shaped crack present in the matrix interacting with a spherical inclusion which is misfitting with respect to the matrix. A simple and direct relationship is established between the strain energy release rate, the crack size, the crack orientation with respect to the inclusion, the crack/inclusion separation, the degree of thermal expansion mismatch and the elastic properties of the medium. We also analyze the size to which these cracks can grow and find that for a given misfit strain and material properties, crack growth is inhibited beyond a certain critical crack size. Finally, the preferred orientation of these cracks as a function of misfit strain is predicted. The implication of these results for thermal cycling are analyzed.

1. INTRODUCTION

The phenomenon of microcracking in particulate reinforced composites, induced by a mismatch in thermal expansion between the matrix and particles, has received a great deal of attention, both experimentally [1-4] and theoretically [5-7]. The presence of such microcracks can modify, for example, such physical properties as the thermal diffusivity, dielectric constant, elastic moduli, toughness and the overall fracture strength of the composite [8]. In cases where the thermal expansion of particle and matrix differ, microcracking has been traced to the localized residual stresses within the matrix and particles induced by a changed in temperature. These thermal expansion mismatch induced stresses can provide the stresses required to nucleate cracks and the stress intensity factors needed to propagate normally sub-critical cracks within the matrix.

Several continuum theories of microcracking induced by thermal misfit mismatch have been put forward [1,2,5-7]. Davidge and Green [1] considered the microcracking process in terms of a Griffith energy balance, where the residual elastic strain energy provided the energy required to form the fracture surface. Lange [5] developed generalized conditions for the propagation of an interface defect in a residual stress field, also based on an energetic analysis. An alternative approach is to determine the stress intensity factor for a given crack and loading geometry and compare it with a material dependent critical stress intensity factor. This approach has been successfully adopted to model cracking within an inclusion as well as radial cracks emanating from a misfitting inclusion [6,7]. Several experiments [1-4] have shown that the stress field associated with a misfitting particle can also activate an already existing crack within the matrix. Therefore, in this paper, we examine the conditions under which pre-existing cracks or crack-like defects can grow under the loading associated with (hydrostatically) misfitting spherical particles in an elastic matrix.

267

2. MATHEMATICAL FORMULATION AND METHOD OF SOLUTION
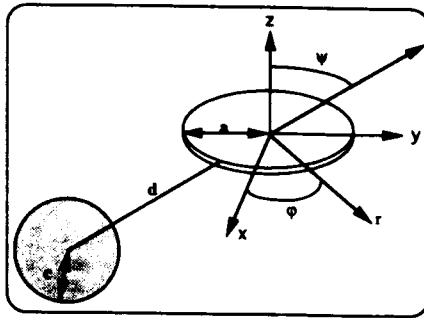
Figure 1. Schematic of crack-inclusion configuration and notation employed.

We explicitly consider the case of a single misfitting spherical inclusion and a nearby isolated penny-shaped crack in an otherwise homogeneous, isotropic, linear elastic body as shown in Fig. 1. The relevant length scales are the inclusion radius c, the crack size a and the crack/inclusion separation d. Since the inclusion is spherically symmetric, the relative orientation of the crack with respect to the inclusion can be characterized by a single parameter ψ, the angle between the crack face normal and the line containing the centers of the crack and the inclusion. The coordinate system on the crack face has been defined such that $\varphi = 3\pi / 2$ is the crack edge closest to the inclusion and $\varphi = \pi / 2$ is the crack edge farthest from the inclusion.

In order to make the analyses tractable, it is necessary to make several simplifications. Firstly, we consider the the elastic mismatch between the matrix and the inclusion to be negligible in comparison to the thermal expansion mismatch and hence the medium is treated to be elastically homogeneous. Secondly, we only consider a single isolated defect, namely an infinitesimally thick penny -shaped crack because it is generally conjectured that macroscopic fracture of the material will initiate at and propagate from a "dominant crack" within the matrix. Thirdly, the matrix is considered to be perfectly brittle and, hence, the "dissipation" zone associated with the crack tip is negligible in size as compared to the characteristic crack size. This assumption validates our use of linear elastic fracture mechanics analysis. Finally, based on the assertion of Lange [9] we also assume that the single crack-inclusion interaction effectively models a system containing a dilute concentration (< 0.1) of inclusions.

The superposition principle of linear elasticity theory now allows us to construct and analyze the system in two successive steps. In the first step, an isolated, misfitting spherical inclusion is introduced into a brittle, isotropic matrix and the associated stress fields are calculated by using the Eshelby procedure [10]. The misfit is denoted by an uniform volume dilatation, $E_{\alpha\beta}^T = \frac{\varepsilon^T}{3}\delta_{\alpha,\beta}$, where $\delta_{\alpha,\beta}$ is the usual Kronecker delta, $\varepsilon^T = 3\Delta\alpha\,\Delta T = 3(\alpha_i - \alpha_m)\Delta T$, ΔT is the temperature change and α_i and α_m are the thermal expansion coefficients of the inclusion and the matrix, respectively. The displacement fields, u, in both the matrix and the inclusion must satisfy the equilibrium equation for an isotropic linear elastic body and the matrix displacement fields [10] are found to be

$$\mathbf{u} = \frac{(1+\nu)\,\sigma\,c^3}{2\,E}\,\frac{\hat{\mathbf{e}}_R}{R^2}$$

, (1)

where we employ spherical coordinates (R, θ, φ), $\sigma = 2Ee^T/[9(1-\nu)]$, E is Young's modulus, n is the Poisson ratio, and $\hat{\mathbf{e}}_R$ is the unit vector in the radial direction.

268

In the second step, a penny-shaped crack is introduced into the matrix. The requirements of mechanical equilibrium necessitate the application of tractions to the crack face in order to guarantee that it is traction-free (i.e., the applied tractions must be equal and opposite to those on the crack face due to the misfit stress associated with the inclusion). If the crack face normal is defined along the Z direction we note that due to the axisymmetry of the unperturbed stress fields, no corrective solution corresponding to $\sigma_{\varphi z}$ has to be added on to the crack face. Hence the only corrective stresses to be applied to the crack face are those corresponding to the unperturbed stresses σ_{zz} and σ_{rz}. Using the superposition principle, this problem can further be decomposed into two sub-problems, the first corresponding to the normal stress σ_{zz} acting on the crack face and the second corresponding to the shear stress σ_{rz} acting on the crack face. These sub-problems can further be reduced into mixed boundary value problems by formulating the stresses in terms of derivatives of a displacement potential function. The techniques of potential theory [11,12] can then be applied to evaluate the stress fields in the medium. This method is described in detail in ref.[13]. Once the stress fields are evaluated, other physical quantities of interest such as the crack opening displacement, stress intensity factors and the strain energy release rate can be computed.

3. RESULTS AND DISCUSSION

We first consider the special case of $\psi = 0$. In this orientation, the crack plane is perpendicular to the line joining the centers of the crack and the inclusion. We shall refer to this crack configuration as the circumferential crack. The analysis is greatly simplified for this particular crack orientation because the normal and the shear tractions generated by the corrective solution are axisymmetric. The total stress intensity factors at the crack tip, for the crack in the $\psi = 0$ configuration is found to be [13],

$$K_I = \frac{-2 \sigma c^3 d \sqrt{a}}{\pi (d^2 + a^2)^2} \qquad K_{II} = \frac{2 \sigma c^3 a \sqrt{a}}{\pi (d^2 + a^2)^2} \qquad K_{III} = 0 \tag{2}$$

where $\sigma = 2 E \varepsilon^T / [9(1-v)]$ and $\varepsilon^T = 3(\alpha_i - \alpha_m)\Delta T$ and $\alpha_i(\alpha_m)$ is the coefficient of thermal expansion for the inclusion (matrix). Several comments on the physics underlying Eq. (2) are in order. First, the mode I stress intensity factor, K_I, should be positive since mode I crack propagation can only occur under a tensile, as opposed to a compressive, stress. This is true when the misfit strain, ε^T, is negative. Thus, for a particulate reinforced composite containing inclusions that have, for example, a higher coefficient of thermal expansion than the surrounding matrix ($\alpha_i > \alpha_m$), the circumferential crack (the $\psi = 0$ crack) can exhibit mode I growth only under thermal cooling and not under thermal heating. Second, by contrast, the circumferential crack can have mode II growth both under thermal heating and thermal cooling because reversing the direction of the shear stresses acting on the crack face merely changes the sense of the relative sliding motion of the crack faces.

The calculated stress intensity factors can now be utilised to compute the crack energy release rate. Further, the crack energy release rate can be re-expressed in terms of dimensionless variables by scaling with the radius of the inclusion, c. For $\varepsilon^T < 0$, G can be normalized as

$$\overline{G} = \frac{\pi^2 E G}{4 \sigma^2 c (1-v^2)} = \frac{\overline{a}}{(\overline{a}^2 + \overline{d}^2)^3} \tag{3}$$

269

where $\bar{a} = a/c$ and $\bar{d} = d/c$. Crack growth can proceed as long as $G > G_c$, where G is the energy release rate associated with crack growth for the given loading and G_c is the critical strain energy release rate, which is a material dependent property. We can likewise define the crack growth condition as $\bar{G} > \bar{G}_c$, where $\bar{G}_c$ is the normalized critical strain energy release rate, which is normalized in the same fashion as $\bar{G}$. Figure 2 shows the variation of $\bar{G}$ with $\bar{a}$ for different $\bar{d}$. The strain energy release rate, $\bar{G}$, is observed to decrease for increasing $\bar{d}$ at fixed $\bar{a}$. This is obviously due to the fact that the magnitude of the stress field exerted by the inclusion decays with distance (as $1/R^3$), where R is the distance from the inclusion. More importantly, for fixed $\bar{d}$, $\bar{G}$ initially increases as with crack size $\bar{a}$ (see Fig. 2). This increase is not monotonic, however, and $\bar{G}$ exhibits a maximum and then decreases at large $\bar{a}$. This variation in $\bar{G}$ can be rationalized as follows. In the small $\bar{a}$ regime, the strain energy release rate $G \propto \sigma^2 a$ is proportional to the crack size, the stress being approximately uniform, as a result of which $\bar{G}$ increases approximately linearly with crack size $\bar{a}$. In the large $\bar{a}$ regime, the edge of the crack is moving away from the inclusion and hence the stress it "feels" from the inclusion decays. Since the magnitude of the stress field from the inclusion decays as $\sigma \propto 1/r^3$, G which scales as $G \propto \sigma^2 a$ decays with crack size as $G \propto 1/a^5$ for large a. Therefore, the strain energy release rate on growing the crack is controlled by an interplay between two competing factors, an increasing crack size and a decreasing stress field.
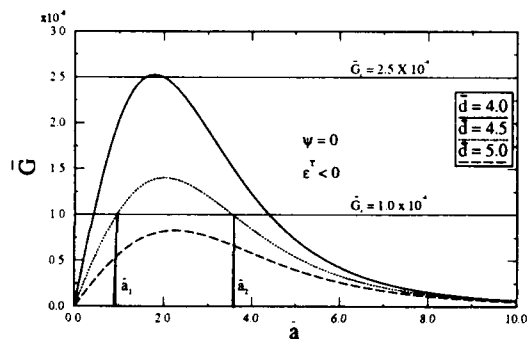
Figure 2. The dimensionless strain energy release rate $\bar{G}$ in the $\psi = 0$ configuration as a function of the defect size $\bar{a}$ for different crack-inclusion separations $\bar{d}$. Also shown are lines for the normalized critical strain energy release rate $\bar{G}_c$, which is a material toughness parameter that also depends on the misfit stress and particle size in its scaled form.

Crack propagation can occur for any crack size $\bar{a}$ such that $\bar{G} > \bar{G}_c$. The horizontal lines in Fig. 2 represent different values of $\bar{G}_c$. Once $\bar{G}$ reaches a particular $\bar{G}_c$ at some lower critical crack length, $\bar{a}_1$, crack growth is initiated. Since $\bar{G}$ monotonically decays with crack size $\bar{a}$ for large $\bar{a}$, crack growth must stop when $\bar{a} > \bar{a}_2$ where $\bar{a}_2$ is an upper critical crack length. Therefore, crack growth is only possible over a finite range of crack sizes $\bar{a}_1 < \bar{a} < \bar{a}_2$. If a pre-existing crack within the matrix is either smaller than $\bar{a}_1$ or larger than $\bar{a}_2$, no crack growth will occur. Since no cracks can grow beyond $\bar{a}_2$, unstable or catastrophic crack growth can never occur in the medium due to the thermal misfit effect alone. However, as a result of the misfit strain, large matrix cracks can be formed which, under subsequent external loading, can in fact lead to component failure.

We next consider the more general case of $\psi \neq 0$ where the crack has an arbitrary orientation relative to the inclusion. Since the prescribed normal and shear tractions on the crack

face are non-axisymmetric, it is necessary to solve the more general mixed boundary value problem. In order to extract the essential physics, an asymptotic expansion (in a/d) of the boundary conditions can be performed and the resulting stress intensity factors can then be expressed as expansions in powers of a/d. If the crack/particle separation is much larger than the crack size, this approximation works well. The details of this procedure and the expressions for the stress intensity factors are described in ref.[13]. For ease of further analysis, the stress intensity factors can be re-expressed in terms of dimensionless variables, using the radius of the inclusion, c, as the characteristic length scale.

Figure 3 shows the normalized mode I stress intensity factor, $\overline{K}_I$, as a function of orientation angle ψ. Since the inclusion is spherically symmetric, it is necessary to only consider the interval $0 \le \psi \le \pi/2$. $\overline{K}_I$ is not axisymmetric, in general, and so the variation in $\overline{K}_I$ as a function of ψ is shown at two positions along the crack tip; the site closest to the inclusion ($\varphi = 3\pi/2$) and the site farthest from the inclusion ($\varphi = \pi/2$). Figure 3 also shows a comparison between the results obtained from the expansion technique (Eq. 23) and the results that are obtained with the numerical integration technique [14]. The agreement between these two approaches is excellent, thereby validating the asymptotic expansions employed in the potential method. Figure 3 also shows that there is a critical ψ beyond which $\overline{K}_I < 0$. This, in turn, implies that, beyond a critical ψ, there can be no mode I crack propagation for $\varepsilon^T < 0$. In particular, a circumferential ($\psi = 0$) crack can exhibit mode I crack growth whereas a radial crack ($\psi = \pi/2$) will not grow. The calculated stress intensity factors can now be used to determine the crack energy release rate with the proviso that for regimes where $\overline{K}_I$ is negative, $\overline{K}_I$ is set to zero. Since the $\varepsilon^T < 0$ and $\varepsilon^T > 0$ cases have $\overline{K}_I = 0$ in complementary ψ regimes, distinctly different behaviors in $\overline{G}$ as a function of ψ should be expected under thermal cycling.
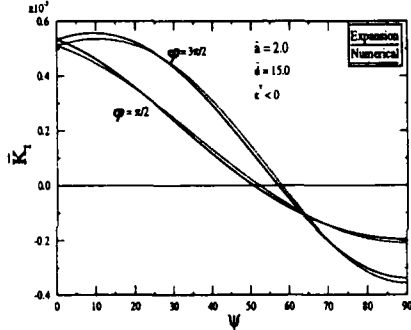
Figure 3. The variation of the normalized mode I stress intensity factor $\overline{K}_I$ as a function of the orientation angle ψ.
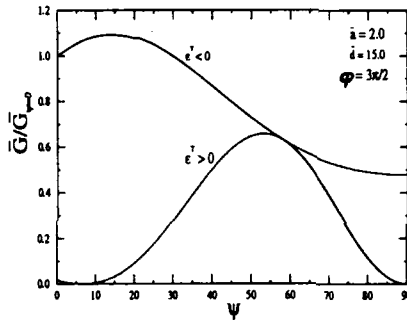
Figure 4. The variation in the dimensionless strain energy release rate $\overline{G}$ at the crack edge ($\varphi = 3\pi/2$) as a function of the orientation ψ.

Figure 4 shows $\overline{G}(\psi, \varphi = 3\pi/2)$ (normalized by $\overline{G}(\psi = 0, \varphi = 3\pi/2)$), as a function of ψ both under negative $\varepsilon^T < 0$ and positive $\varepsilon^T > 0$ misfit. Considering, for example, the matrix reinforced with inclusions such that $\alpha_i > \alpha_m$, Fig. 4 shows that the orientational dependence of the normalized strain energy release rates are considerably different under thermal heating and thermal cooling conditions. On cooling, for example, one observes that the circumferential crack

271

can grow whereas a radial crack cannot. This is because, on cooling, there are both tensile and shear stresses driving the crack face in the $\psi = 0$ orientation whereas there are compressive stresses acting on the crack face in the $\psi = \pi / 2$ orientation. Since crack growth cannot occur under a compressive field, the radial crack cannot grow under thermal cooling. On heating, we observe a qualitatively different behavior. The radial crack can show mode I growth due to tensile stresses acting on the crack face, whereas a circumferential crack can only exhibit mode II growth due to the shear stresses; where, again, the compressive stresses do not contribute to mode I crack growth. This orientational dependence of the cracking process suggests that an orthogonal set of cracks should be formed in the microstructure due to thermal cycling, the radial cracks being formed during thermal heating and the circumferential cracks formed during thermal cooling.

4. CONCLUSIONS

The incidence of matrix cracking in brittle matrix composites induced by a thermal expansion mismatch between the reinforcing particles and the matrix has been examined based on a continuum elastic fracture mechanics formulation. For cases where matrix cracking has to be avoided, the present analysis could be used to analytically predict the critical inclusion size. Although, this provides a lower bound estimate on the inclusion size, use of this critical particle size provides a conservative estimate of the maximum particle size which can be employed to avoid matrix cracking. The predicted maximum size to which a crack can grow can be used as a measure of the degree of damage (maximum crack size) that can result from particles as a result of thermal cycling. Finally as described above, the orientation of the cracks depends on the sign of the misfit strain. It is predicted that cycling the temperature can produce an orthogonal array of cracks around individual particles.

REFERENCES

[1]   R. W. Davidge and T. J. Green, *J. Mater. Sci.* **3**, 629 (1968).
[2]   A. G. Evans, *J. Mater. Sci.* **9**, 1145 (1974).
[3]   N. Claussen, J. Steeb, and R. F. Pabst, *Bull. Am. Ceram. Soc.* **56**, 559 (1977).
[4]   W.-H. Gu, K. T. Faber and R. W. Steinbrech, *Acta metall.* **40**, 3121(1992).
[5]   F. F. Lange, in *Fracture Mechanics of Ceramics*, Vol. 2, p.599, Edited by R.C. Bradt, D.P.H. Hasselman and F.F. Lange (Plenum, New York, 1976).
[6]   D. J. Green, *J. Amer. Ceram. Soc.* **64**, 138 (1981).
[7]   D. J. Green, in *Fracture Mechanics of Ceramics*, Vol. 5, p.457, Edited by R.C. Bradt, A.G. Evans, D.P.H. Hasselman and F.F. Lange (Plenum, New York, 1983).
[8]   J. P. Singh, D. P. H. Hasselman, W. M. Su, J. A. Rubin and R. Palicka, *J. Mat. Sci.* **16**, 141 (1981).
[9]   F. F. Lange, in *Fracture Mechanics of Ceramics*, Vol. 4, p.799, Edited by R.C. Bradt, D.P.H. Hasselman and F.F. Lange (Plenum, New York, 1978).
[10]   J. D. Eshelby, *Prog. Sol. Mech.* **2**, 89 (1961).
[11]   I. N. Sneddon and M. Lowengrub, *Crack Problems in the Classical Theory of Elasticity* (Wiley, New York, 1969).
[12]   J. R. Barber, *Elasticity.* (Kluwer Academic Publishers, Boston, 1992).
[13]   N.Sridhar, J.M.Rickman and D.J.Srolovitz, Submitted to *Acta metall.*
[14]   J. T. Guidera and R. W. Lardner, *J. Elasticity* **5**, 59 (1975).

PROCESSING MAP AND FLOW LOCALIZATION OF A TiAl/TiB₂ XD® COMPOSITE*

D. ZHAO, P.K. CHAUDHURY, M. THIRUKKONDA, AND J.J. VALENCIA
Concurrent Technologies Corporation, 1450 Scalp Avenue, Johnstown, PA 15904, U.S.A.

ABSTRACT

Isothermal compression tests were conducted on a particulate reinforced Ti-44Al-3V+7.5v/o TiB₂ composite produced by the XD® process over wide ranges of temperatures and strain rates, 1050 to 1300 C and 0.001 to 1.0 s⁻¹, respectively. Flow localization parameter analysis was performed to analyze the flow behavior of the composite under various processing conditions, and the results were compared to those by dynamic material modeling. Microstructural characterization was also conducted to correlate the flow behavior with post-deformation microstructures. With combined information on flow behavior and microstructures, the processing condition for relatively stable flow and uniform microstructure was determined to be 1300 C and 0.01 to 0.1 s⁻¹.

INTRODUCTION

Titanium aluminide alloys have potential applications in the aerospace industry due to their high specific strength and stiffness at high temperatures. It has been shown that the incorporation of an inert second phase, such as TiB₂ particulates with these alloys can result in fine grains and improve their creep properties at high temperatures compared to the monolithic alloys [1, 2]. The grain refining effect of the TiB₂ particles can also improve the hot workability of as-cast titanium aluminide based alloys [3]. In order for titanium aluminide composites to be accepted for practical applications, they should be easily processed by conventional metalworking operations, such as rolling, extrusion, and forging. Additionally, the forming process needs to be designed with processing parameters that maximize the formability of the composite material, while minimizing defects.

In a previous study [4], dynamic material modeling (DMM) was performed on a particulate reinforced Ti-44Al-3V+7.5v/o TiB₂ composite. DMM [5-6] considers the workpiece to be a power dissipater, and process efficiency is represented by efficiency of the power dissipation calculated from the flow data. An empirical description of flow stress $\sigma = A \dot{\epsilon}^m$ was adopted, where A is a constant, $\dot{\epsilon}$ is strain rate, and m is the strain rate sensitivity. The efficiency, η, is represented by

$$\eta = \frac{2m}{1+m} \tag{1}$$

Since the strain rate sensitivity is not constant over the temperature and strain rate regime, it is possible to generate an efficiency map in strain rate and temperature space. The stability criteria were developed by applying the principles of continuum mechanics and thermodynamics

$$1 > m > 0; \qquad \frac{d\eta}{d\log\dot{\epsilon}} < 0 \tag{2}$$

$$s > 0; \qquad \frac{ds}{d\log\dot{\epsilon}} < 0 \tag{3}$$

where s is defined as:

® XD is a registered trademark of Martin Marietta, Baltimore, MD.

$$s = \frac{d \log \sigma}{T \, d(1/T)} \Big|_{\varepsilon, \dot{\varepsilon}} \qquad (4)$$

where T is the absolute temperature. These criteria are applied to the processing map to identify stable and unstable regimes,

Another study examined Ti-48Al-2Mn-2V+8.5w/oTiB$_2$ and Ti-52Al-2Nb+8.5w/oTiB$_2$ composites [7] using flow localization parameter [8]. This parameter characterizes the extent of flow localization. Flow stress is assumed to be a function of strain, strain rate, and temperature independently for simplicity. A normalized strain hardening rate at a constant strain rate is defined as:

$$\gamma' = \frac{1}{\sigma} \frac{d \sigma}{d \varepsilon} \Big|_{\dot{\varepsilon}} \qquad (5)$$

Since compressive stress and strain are both negative, the strain hardening rate γ' would be negative for strain hardening and positive for strain softening flow curves. The flow localization parameter is defined as:

$$\alpha = \frac{\gamma' - 1}{m} \qquad (6)$$

It is clear from Equation (6) that the flow localization parameter, α, is greater for strain softening than for strain hardening.

The two analyses have different merits and limitations when applied to intermetallic composites. In the present work, flow localization parameter analysis was performed on the Ti-44Al-3V+7.5v/o TiB$_2$ composite, and the results were compared to those by DMM [4]. Microstructural characterization of the deformed specimens was performed to verify the predictions of the two methods.

EXPERIMENTAL PROCEDURE

The material used in this work was a Ti-44Al-3V(a/o)+7.5v/o TiB$_2$ XD® composite. The as-cast material was HIP'ed to reduce porosity and to homogenize the ingot microstructure. Figure 1 shows an optical micrograph of the as-HIP'ed composite. The microstructure consists of an $\alpha_2+\gamma$ lamellar matrix, a uniform distribution of TiB$_2$ particulates, and dispersed pockets of γ at the $\alpha_2+\gamma$ lamellar grain boundaries. The lamellar colony size is approximately 30 μm, and the size of TiB$_2$ particulates is in the range of 1 to 15 μm.
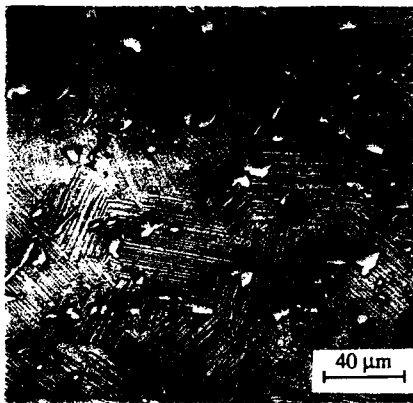
Figure 1. Optical micrograph of as-HIP'ed Ti-44Al-3V+7.5v/o TiB$_2$ XD® composite.

Compression tests were conducted at temperatures 1050, 1100, 1150, 1200, 1250 and 1300 C, and strain rates 0.001, 0.003, 0.01, 0.03, 0.1, 0.3, and 1 s^{-1}. The temperature was selected so that the flow behavior in $\alpha_2+\gamma+\beta$, $\alpha_2+\alpha+\beta$ and $\alpha+\beta$ phase fields can be studied according to recent Ti-Al-V ternary and pseudobinary phase diagrams [9-10]. Cylindrical specimens with 0.5 inch diameter and 0.625 inch height were used. Tests were performed in vacuum on an MTS testing machine. Boron nitride was used as lubricant between the compression platens and the specimens. Prior to compression, the specimens were held for 10 minutes at the test temperature. Immediately after the test, the specimens were quenched with forced helium gas to retain the deformed microstructure. Microstructural analysis of the deformed specimens was performed using both optical and scanning electron microscopy (SEM) on the longitudinal section of the specimens.

274

RESULTS AND DISCUSSION

Flow Behavior and Microstructure
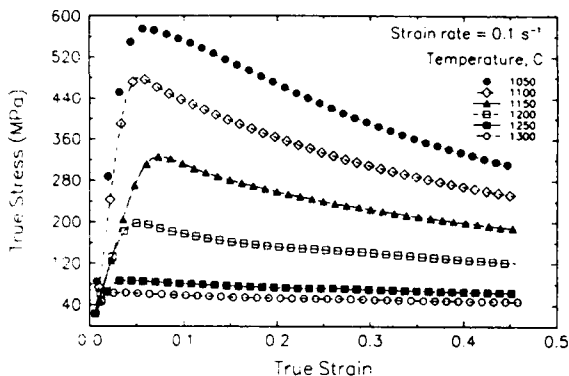
Figure 2. Flow curves as a function of temperature at 0.1 s^{-1}.
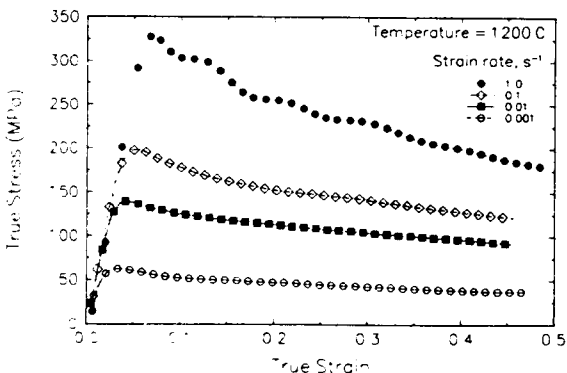
Figure 3. Flow curves as a function of strain rate at 1200 C.

Figures 2 and 3 show the typical flow curves as a function of temperature and strain rate respectively. The level of flow stress increased with decreasing temperature and increasing strain rate. According to recent high temperature X-ray and DSC studies [10, 11], β phase is present at temperatures above 1000 C because of the presence of V as a β stabilizer. As temperature is increased, the percentage of β phase increases, and the matrix becomes more ductile. Flow softening is the general feature of all the stress-strain curves. At strain rate of 1 s^{-1}, multiple peaks were observed on the flow curves at all test temperatures.

Three types of deformed microstructures were observed. The first one was observed at relatively low temperatures (1050 to 1200 C), where the α$_2$+γ lamellar structure was heavily deformed (Figure 4, 1050 C and 0.001 s^{-1}). The individual colonies deformed as a unit (like a grain) with the lamellae inside such that the lamellae would tend to become perpendicular to compression axis. The flow softening observed in the flow curves at these conditions are mainly due to the localized shear active for this kind of deformation behavior. However, in some colonies, the lamellae parallel to the compression direction were buckled due to constraints from surrounding colonies that deform unfavorably to oppose their realignment. This effect was more evident at high strain rates (Figure 5, 1050 C and 1 s^{-1}). Another contribution to flow softening was the formation of very fine β grains at colony boundaries. The amount of the β grains increased with increasing temperature and decreasing strain rate. As the strain rate increased, along with substantial reduction in the amount of β-phase at the colony boundaries, void nucleation at particle/matrix interfaces was observed (Figure 5) because of more difficult deformation accommodation. Although a transformation from α$_2$+γ+β to α$_2$+α+β is expected as temperature is increased to approximately 1100 C [11], the reaction did not seem to occur. There are two possible reasons for this: (a) reactions are sluggish in this system, and (b) boron (TiB$_2$) and oxygen raise the transformation temperature [12, 13].

275

Figure 4. Optical micrograph of the specimen deformed at 1050 C and 0.001 s^{-1}, longitudinal section (compression axis: vertical).
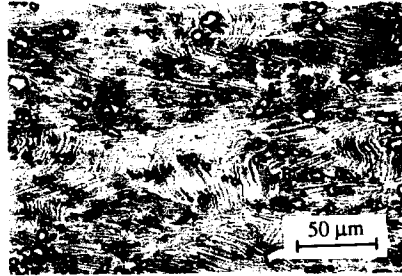
Figure 5. Optical micrograph of the specimen deformed at 1050 C and 1 s^{-1}, longitudinal section (compression axis: vertical).

Figure 6. Optical micrograph of the specimen deformed at 1250 C and 0.01 s^{-1}, longitudinal section.
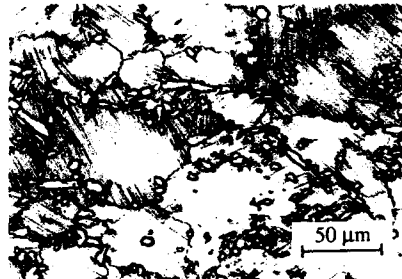
Figure 7. Optical micrograph of the specimen deformed at 1300C and 0.01 s^{-1}, longitudinal section.
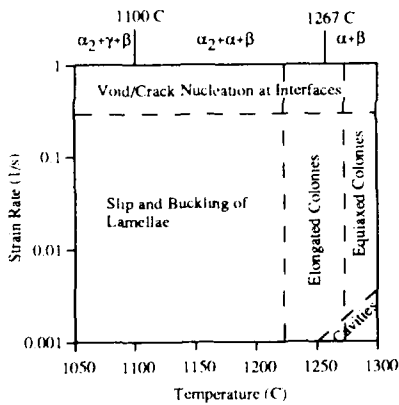
Figure 8. Microstructure map for Ti-44Al-3V-7.5v/o TiB$_2$.

The second type of microstructure was observed at 1250 C, Figure 6 (1250 C and 0.01 s^{-1}). At this temperature, the deformation took place definitely in the $\alpha_2+\alpha+\beta$ phase field. The material was more ductile than at lower temperatures, and the colonies were heavily deformed and elongated. However, the lamellae are straight, indicating that the transformation of α into $\alpha_2+\gamma$ occurred after deformation.

The third type of microstructure resulted from tests at 1300 C and all strain rates (Figure 7, 1300 C and 0.01 s^{-1}). At this temperature, the deformation took place in $\alpha+\beta$ phase field [10,11] and the microstructure consisted of equiaxed grains that transformed upon cooling to $\alpha_2+\gamma$ lamellar colonies. The equiaxed nature of grains indicates complete recrystallization. The size of the colonies slightly decreased with increasing strain rate. Some retained β–phase was visible at the colony boundaries. At both

276

Figure 9. DMM processing map for Ti-44Al-3V-7.5v/oTiB$_2$ [4].

Figure 10. Flow localization parameter map for Ti-44Al-3V-7.5v/o TiB$_2$.

the highest and the lowest strain rates, 1 and 0.001 s^{-1}, a number of voids were observed at particle/matrix interfaces. Void nucleation at the lowest strain rate appeared to be caused by the relatively easy flow of matrix and therefore increased incompatibility at particle/matrix interfaces.

The multiple peaks on flow curves at the strain rate of 1 s^{-1} resemble those from multiple dynamic recrystallization. However, this behavior was observed at all temperatures while no evidence of dynamic recrystallization was observed at low temperatures. This behavior could not be attributed to dynamic recrystallization and its origin is not clear from the microstructures. Void/crack nucleation at the particle/matrix interfaces was more severe at this strain rate and all temperatures, and may be responsible for the multiple peaks on flow curves. The occurrence of repeated peaks and void nucleation were also identified, but not correlated by other investigators [7].

Finally, the microstructural observations are summarized in a microstructure map as shown in Figure 8. It shows occurrence of flow localization at low temperatures, recrystallization at high temperatures, void/crack nucleation at high strain rates, and cavitation at the highest temperature and lowest strain rate. Approximate equilibrium phase fields [10,11] are also indicated on this map to show the influence of different phase fields on the deformation process and the resulting microstructure.

Dynamic Material Modeling

The DMM map developed in a previous study [4] is shown in Figure 9. The contours represent efficiency of power dissipation, and is highest at the lowest strain rate and 1200 C. The DMM predicted that there were two unstable regions: the first one covered all temperatures and the strain rates 0.1 s^{-1} and above, and the second one occurred at high temperatures and low strain rates. The first unstable region was caused by high strain rate that promotes void nucleation at particle/matrix interface and buckling of lamellar structures. This region corresponds to the void nucleation zone of the microstructural map, but extend to much lower strain rate. There are also some voids observed in the specimen tested at 1300 C and 0.001 s^{-1}. However, the zone in the microstructural map was smaller than that on the processing map.

Flow Localization

A map with contours of flow localization parameters was developed as shown in Figure 10. This map showed that flow localization is most severe at the lowest temperature and highest strain

277

rate, reaching an α value of 20. This is understandable because of the high stress level and deformation rate experienced by the specimens tested in this regime. Buckling of lamellar structures is also most severe in these specimens. The corner of the lowest temperature and lowest strain rate also showed relatively high α values, approximately 10. This may be associated with the formation of fine β-grains at colony boundaries, at which localized flow is enhanced. The lowest value of flow localization parameter resulted from the high temperature and low strain rate regime, where recrystallized microstructure was observed. It has been observed that α values of 3.5 and below generally indicate a uniform flow for CP Ti grade 2 [14]. For this composite material, α values of 2.5 and less correspond to the temperatures 1250 to 1300 C and the strain rates of 0.001 to 0.1 s^{-1}.

SUMMARY

Flow behavior and deformed microstructures of a Ti-44Al-3V(a/o)+7.5v/o TiB$_2$ XD® composite were studied over wide ranges of temperatures and strain rate. The flow behavior was analyzed by flow localization parameter and compared to that by DMM. The material basically exhibited flow softening caused by a number of mechanisms. Shearing and buckling of lamellar structure were observed at low and intermediate temperatures, and the extent increased with increasing strain rate. Void/crack nucleation was observed at high strain rate 1 s^{-1}, and cavitation occurred at the highest temperature 1300 C and the lowest strain rate 0.001 s^{-1}. Flow localization parameter characterized the flow instability caused by shearing and buckling of lamellar structure as well as the void/crack nucleation at high strain rate, while DMM processing map predicted the flow instability caused by void/crack nucleation. Combined with the information on deformed microstructures, a processing condition at the temperature of 1300 C and the strain rates of 0.01 to 0.1 s^{-1} is recommended for stable flow as well as a microstructure with uniform equiaxed lamellar colonies.

Both DMM and flow localization parameter analysis need to be verified by microstructural characterization. DMM tends to overpredict unstable regimes for this alloy. Flow localization parameter analysis can not predict cavitation at high temperatures and low strain rates which does not cause significant flow softening.

REFERENCES

1. S.L. Kampe, J.D. Bryant, and L. Cristodoulou, Metall. Trans A, **22A**, 447 (1991).
2. S.L. Kampe, and L. Cristodoulou, presented at TMS Fall Meeting, Cincinnati, OH, 1991 (unpublished).
3. L. Rothenflue, A. Szaruga, and H.A. Lipsitt, ibid, (unpublished).
4. K.G. Anand, D. Zhao, J.J. Valencia, and S.J. Wolff, in Application of Mechanics and Material Models to Design and Processing III, edited by E. S. Russell (TMS, Warrendale, PA, 1992) pp. 57-71.
5. Y.V.R.K. Prasad, et al., "Modeling of Dynamic Material Behavior in Hot Deformation: Forging of Ti-6242", Metall. Trans. A, **15A**, 1883 (1984).
6. H.L. Gegel, J.C. Malas, S.M. Doraivelu, and V.A. Shede, in Metals Handbook, Vol. 14, (ASM International, Metals Park, OH, 1988), pp. 417-438.
7. J.D. Bryant, M.L. Adams, A.R.H. Barrett, J.A. Clarke, G.B. Gaskin, L. Christodoulou, and J. Brupbacher, NASP Contractor Report 1095, Martin Marietta Laboratories, 1990.
8. S.L. Semiatin and J.J. Jonas, Formability and Workability of Metals (ASM International, Metals Park, OH, 1984) p. 43.
9. P.K. Chaudhury and H.J. Rack, Scripta Metall. et Mat., **26**, 691 (1992).
10. P.K. Chaudhury (unpublished research).
11. P.K. Chaudhury, M. Long and H.J. Rack, Mater. Sci. Eng., **A152**, 37 (1992).
12. C.R. Feng, D.J. Michel and C.R. Crowe, Scripta Metall. et Mat., **24**, 1297 (1990).
13. S.C. Huang and P.A. Siemers, Metall. Trans. A, **20A**, 1899 (1989).
14. M. Thirukkonda, P.K. Chaudhury, D. Zhao, and J.J. Valencia, Harold Margolin Symp. on Micro./Prop. Rela. of Ti Alloys, TMS Spring Meeting, San Francisco, CA, 1994.

Microstructure and Deformation of Ti-22Al-23Nb Orthorhombic-Based Monolithic and Composite Titanium Aluminides

FRANÇOIS-CHARLES DARY*, SHIELA R. WOODARD AND TRESA M. POLLOCK
Materials Science and Engineering Dept., Carnegie Mellon University, Pittsburgh, PA 15213
* Current address: Materials Dept., University of California, Santa Barbara, CA 93106

ABSTRACT:

A new class of intermetallic matrix composites (IMC's) based on orthorhombic titanium aluminides offer attractive properties for high-temperature structural components at temperatures up to 760°C. Results from an ongoing study on the microstructural stability and mechanical properties of the orthorhombic-based alloy Ti-22Al-23Nb (at%), in both monolithic and composite forms, are discussed. Oxygen acquired during processing or as a result of high-temperature exposure in air or vacuum has a pronounced influence on the microstructure of the monolithic and composite materials. Two-phase lath microstructures of ordered beta (β_o) + orthorhombic (O) phases produced by processing low oxygen material above the beta transus are morphologically stable at 760°C. Conversely, in higher-oxygen three-phase microstructures containing O+β_o+ α_2(Ti$_3$Al), lath coarsening and additional precipitation of α_2 in oxygen-enriched sheet surface regions is observed. At 760°C/69MPa the two-phase lath microstructure has a higher creep resistance and lower tensile strength compared to the three-phase α_2-containing microstructures of the higher oxygen material.

INTRODUCTION:

Titanium aluminide alloys containing the Ti$_2$AlNb orthorhombic (O) phase [1] exhibit high specific yield strengths and room temperature fracture toughnesses, as well as good creep resistance [2,3]. It has recently been demonstrated that the orthorhombic-based alloy Ti-22Al-23Nb can be processed to sheet and foil by conventional rolling practices [4], and for this reason it is an excellent matrix candidate for foil/fiber/foil processed composites. The crystallographic rolling texture, matrix/fiber reaction zone growth kinetics, thermal fatigue and oxidation kinetics of Ti-22Al-23Nb have been investigated [4-6]. It has also been shown that the beta transus as well as the equilibrium phases, i.e., the amount of α_2, O, and β_o, present in this alloy are a strong function of interstitial oxygen content [4].

To obtain an understanding of the high-temperature behavior of Ti-22Al-23Nb composites, initial microstructural and mechanical evaluations have been conducted on low oxygen (740 wppm) Ti-22Al-23Nb monolithic sheet material, a higher oxygen (1940 wppm) unreinforced Ti-22Al-23Nb "neat" bonded foil composite and a Ti-22Al-23Nb composite (4240 wppm oxygen) unidirectionally reinforced with Sigma 1140+ fibers.

EXPERIMENTAL PROCEDURE:

The monolithic sheet was fabricated from a low oxygen ingot (740 wppm) that was HIP'ed, hot rolled, creep flattened and ground to a final thickness of 1 mm. The 420μm thick "neat" composite consisted of five layers of rolled 87μm foil which had been consolidated without fibers via the composite consolidation cycle. The composite consisted of 5 layers of the aforementioned foil consolidated with 4 layers of unidirectional Sigma 1140+ fibers.

To examine the microstructural stability and oxygen sensitivity of the alloy, monolithic, "neat" and composite materials were subjected to long-term air and dynamic (10^{-7} torr) vacuum exposures at 760°C. Flat sheet specimens were utilized for both creep and tensile experiments. Room-temperature tensile tests were conducted at a constant crosshead speed of 0.5mm/sec, i.e., at an initial strain rate of 8.33x10^{-4} sec^{-1}. Tensile experiments were conducted on samples from the "neat" composite, both transverse and longitudinal to the rolling direction, and on the monolithic sheet. Creep experiments were performed on the monolithic sheet material in a dynamic (10^{-7} torr) vacuum chamber at 760°C.

RESULTS AND DISCUSSION:

Microstructural evaluation:
I. Monolithic sheet:

Of the three forms of the alloy studied, the monolithic sheet represents the lowest-oxygen material, with only 740 wppm oxygen. A low magnification micrograph of the as-received microstructure is shown in Figure 1(a). It is composed of lath-like ordered O phase primarily arranged in packets of aligned precipitates lying in a continuous β_o (ordered B2) matrix. In this low oxygen material no α_2 phase was detected by either X-ray Diffraction (XRD) or Transmission Electron Microscopy (TEM) observations. Examination of the microstructure in the transverse and both longitudinal planes did not reveal significant anisotropy.

(a)   (b)

Figure 1 - (a) Microstructure of the as-received monolithic sheet; (b) Surface region of monolithic sheet following air exposure of 760^0C/100hrs.

Compared to the as-received monolithic microstructure, SEM examinations of the vacuum- and air-exposed samples (760^0C/100hrs) did not reveal any noticeable microstructural changes, aside from an oxide layer, about 2-3 μm thick at the surface of the air-exposed sample, Figure 1(b). The Vickers microhardness results shown in Figure 2 confirmed this observation, $i.e.$, the microhardness was essentially constant in all three samples. Through-thickness Auger Electron Spectroscopy (AES) analyses of the as-received, vacuum- and air-exposed specimens revealed that the air exposure resulted in an ~175μm-deep oxygen enriched layer on each side of the sheet beneath the oxide layer. In addition, the vacuum exposure also resulted in the formation of a thin oxide layer, although no significant oxygen enrichment below the oxide layer was observed. The bulk oxygen chemical analyses shown in Figure 2 are in agreement with the AES results. Note that although a significant increase in the average oxygen content was observed after the air exposure, there was no increase in microhardness, apparently due to a non-uniform distribution of oxygen through the thickness of the sheet.

II. "Neat" panel:

With 1940 wppm oxygen, the "neat" material represents an intermediate level of oxygen, between the monolithic and IMC material. The higher oxygen content, acquired from processing, results in a three-phase microstructure characterized by equiaxed primary α_2 grains in a continuous β_o phase, Figure 3(a). The O phase is present in acicular form in the β_o phase and as a thin film encircling the α_2 grains. The volume fraction of the O phase increased during "neat" consolidation through additional precipitation of laths in the β_o phase and growth of the film encircling the α_2 grains. During sheet consolidation an α_2-depleted zone, ~5μm in depth, developed on the surface of the foils. This processing-induced zone was retained on the surface of the "neat" composite, but was not visible along the foil/foil bonding regions in the matrix interior, Figure 3(a). Finally, it should be emphasized that a strong microstructural anisotropy was observed. Thus, by contrast with the view transverse to the rolling direction, shown in

Figure 3(a), the microstructure in the longitudinal plane exhibited elongated α_2 precipitates, aligned in the rolling direction.
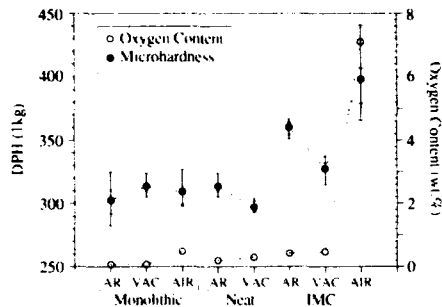
Figure 2 - Oxygen content and microhardness for the monolithic,"neat" and IMC materials in as-received (AR), vacuum-exposed (VAC) and air-exposed (AIR) conditions.

The oxygen sensitivity of the "neat" material was studied in a series of long-term heat treatments at 760°C. Dynamic vacuum exposures produced additional small α_2 precipitates in the oxygen-rich surface regions of the sheet, along the O/β_o interfaces. This "environmentally-induced" α_2 formed both on the O film encircling the primary α_2 and along the thin O laths in the β_o matrix, as indicated by arrows in Figure 3(b). After a 300hr vacuum exposure these small α_2 precipitates were observed greater than 50µm below the sheet surface. Shorter exposures reduced the depth of the "environmental" α_2; after 100hrs at 760°C these precipitates were only observed within 10µm of the surface.

(a)   (b)

Figure 3 - (a) Microstructure of the as-received "neat" panel; (b) Surface region of a "neat" panel following vacuum exposure of 760°C/300 hrs.

It should be noted that both the aforementioned "neat" samples treated at 760°C were polished prior to the exposure to remove the consolidation-induced surface layer. A similar specimen, with the surface layer removed, was wrapped in Ta and subjected to a vacuum exposure of 760°C for 100hrs. In this sample no significant "environmental" α_2 was observed near the surface. Finally, if the processing-induced layer was not removed prior to exposure, no environmental α_2 was observed, within the limit of the SEM resolution. Although the composite processing-induced surface layer was apparently less permeable to oxygen, the reason for this is unclear; further characterization is currently in progress.

Unlike the low oxygen monolithic material, the microstructure of the "neat" material was observed to be thermally unstable in its as-received condition. This was reflected in the exposure induced drop in microhardness (Figure 2). SEM observations indicated that the O phase coarsened with increasing exposure times at 760°C, both in the film surrounding the α_2 and the lenticular phase in the β_o, Figures 3(b).

III. Composite panel:

The Sigma 1140+/Ti-22Al-23Nb IMC exhibited a three-phase matrix microstructure almost identical to that described for the "neat" material, Figures 4(a) and (b). The higher oxygen content of the composite panel (4240wppm), compared to the "neat" material, may be due in part to the presence of the SiC fibers. A reaction zone ~0.6μm in extent formed between the matrix and fiber coating during consolidation. The higher microhardness observed with the as-received IMC (Figure 2), compared to that of the as-received "neat" panel, arises in part from an overall refinement of the microstructure in the former, *i.e.*, smaller α_2 precipitates and significantly thinner O laths. The IMC matrix microstructure was also thermally unstable at 760°C, exhibiting a more pronounced microhardness drop (Figure 2), compared to the "neat" material.

With the fibers exposed to the environment during a 760°C/100hrs air treatment, a dramatic increase in the oxygen content was observed and this was associated with a sharp increase of the microhardness (Figure 2). An oxide layer, similar to that observed on the monolithic sheet (Figure 1b), was observed at the panel surface and at the fiber/matrix interface. In addition, the environmentally-stabilized α_2 precipitates, present in the vacuum-exposed "neat" panel, were observed beneath the oxide layer.

(a)   (b)
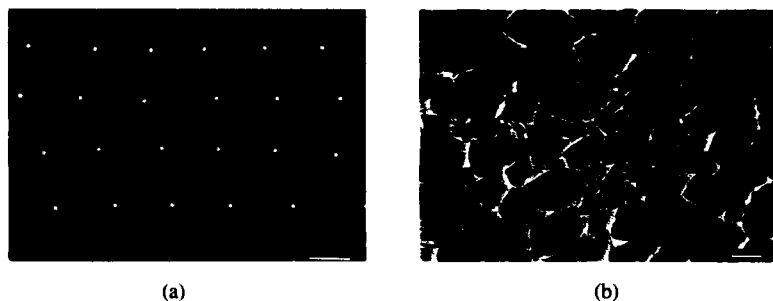
Figure 4 - Microstructure of as-received composite panel (a); as-received composite matrix (b).

Tensile Results:

Room-temperature tensile engineering stress-strain curves are shown in Figure 5. The as-received monolithic (MONO/AR) material exhibited a significant tensile ductility. On the surface of the fractured sheet specimen, O/β_o surface offsets and shear bands were observed. As shown in Figure 5, the monolithic material subjected to a 760°C/100hr vacuum exposure (MONO/VAC) exhibited a much higher strain at failure than did the as-received monolithic sample (MONO/AR). In contrast to the as-received material, the entire gauge section of the fractured (MONO/VAC) sample was covered with a high density of surface cracks, oriented perpendicular to the loading axis. To understand the origin of the surface cracking, a sample was subjected to a vacuum exposure of 760°C/100hrs and subsequently polished prior to room-temperature tensile testing (MONO/VAC-P). Tensile deformation of this exposed + polished sample produced a tensile response and a specimen surface similar to those of the (MONO/AR) specimen, with few surface cracks at grain boundaries. The surface cracks in the (MONO/VAC) sample were apparently initiated by the brittle surface oxide layer and may have contributed to the overall elongation of the sample. Note that the lower strength of the (MONO/VAC) sample is due to the use of a sample with a slightly different microstructure. Additional work, not presented herein, has

shown that, aside from the strength, the change in microstructure does not affect the surface cracking behavior or the overall elongation of the material in tension. The three phase microstructure of the as-received "neat" panel resulted in significantly higher strength and elongation, compared to the monolithic sheet. However, the texture in the sheet was apparent, as the transverse sample (NEAT/AR-TRANS) exhibited markedly higher flow stresses and lower failure strain than that of the longitudinal specimen (NEAT/AR-LONG).
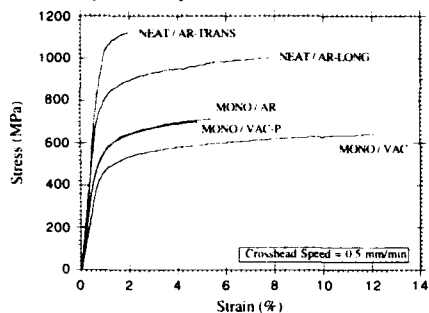
Figure 5 - Tensile stress-strain curves for as-received and vacuum-exposed monolithic and composite materials.

Creep Results:

Figure 6 shows the primary creep curve of the as-received monolithic sample tested at 760°C/69MPa in vacuum. For comparison, two primary creep curves [7] obtained at 760°C/69MPa for Ti-22Al-23Nb containing a high volume fraction α_2 and an ($\alpha_2+\beta/\beta_o$) Ti-24Al-11Nb alloy are also provided. Note that in contrast with the present work, the previous creep experiments were conducted in a laboratory air environment. The present monolithic sample clearly exhibits the highest creep resistance. This may be due to the absence of α_2 and the high volume fraction of the orthorhombic phase, which in the bulk form has a higher creep resistance, compared to α_2 [3]. The Ti-24Al-11Nb and Ti-22Al-23Nb samples of Smith, *et al.* ruptured at ~8.5% strain after ~58hrs and ~4.5% strain after ~144hrs, respectively, while the present monolithic sample exhibited only 2.58% strain after 688hrs. A series of stress increments were imposed after 688hrs at 69MPa and the resultant changes in creep rate are summarized in Table I. The observed creep rates in the stress increment experiment correspond to a creep stress exponent of n=3.7. Note that failure occurred at 500MPa stress after a cumulative time of 884 hrs.
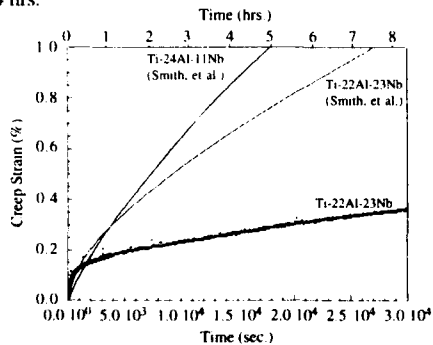
Figure 6 - The 760°C/69MPa primary creep response of the monolithic two-phase Ti-22Al-23Nb material (present study), a three-phase Ti-22Al-23Nb and an ($\alpha_2 + \beta/\beta_o$) alloy [7].

Table I - Results of stress increment creep experiment on low-oxygen monolithic Ti-22Al-23Nb.

Stress (MPa)	Creep Rate (s^{-1})	Strain at Jump (%)	Time at Jump (hrs)
69	$0.50 \ 10^{-8}$	2.58	688
100	$1.82 \ 10^{-8}$	3.13	761
110	$2.40 \ 10^{-8}$	3.74	831
130	$5.26 \ 10^{-8}$	4.72	881

SUMMARY:

A study of the deformation and the thermal and environmental stability of monolithic, "neat" and composite Ti-22Al-23Nb produced the following observations:

- Oxygen acquired either during processing or as a result of high temperature exposures stabilizes the α_2 phase. Oxygen diffusion during high temperature air and vacuum exposures resulted in enhanced α_2 precipitation in the near-surface regions of the "neat" and composite materials, consistent with the earlier observation that the α_2 content of Ti-22Al-23Nb is sensitive to the bulk interstitial oxygen content.

- Monolithic ($O+\beta_o$) material subjected to vacuum exposures at 760°C developed a thin surface oxide layer which subsequently produced a dense array of surface cracks on samples subjected to room temperature tensile deformation.

- The coarse ($O+\beta_o$) microstructure of the monolithic material demonstrated good thermal stability and creep resistance at 760°C, but possessed a low room-temperature tensile strength.

- In the higher strength ($\alpha_2+O+\beta_o$) "neat" and composite microstructures, coarsening of the orthorhombic laths was observed at 760°C. The texture in the "neat" panel resulted in significant anisotropy of tensile strength and elongation.

ACKNOWLEDGMENTS:

REFERENCES:

1. D. Banerjee, A.K. Gogia, T.K. Nandi and V.A. Joshi, Acta Metall. **36**, (1988), pp. 871-882.
2. R.G. Rowe, in Microstructure/Property Relationships in Titanium Aluminides and Alloys, Y.K. Kim and R.R. Boyer, eds., TMS, Warrendale, PA, (1991), pp. 387-398.
3. T.K. Nandy, R.S. Mishra and D. Banerjee, Scripta Metall. Mater. **28**, (1993), 569-574.
4. C.G. Rhodes, J.A. Graves, P.R. Smith and M.R. James, in Structural Intermetallics, R. Darolia et al., eds., TMS, Warrendale, PA, (1993), pp. 45-52.
5. J.A. Graves, P.R. Smith and C.G. Rhodes in Intermetallic Matrix Composites II, Mat. Res. Soc. Symp. Proc. Vol. 273, D.B. Miracle et al., eds., MRS, Pittsburgh, PA, (1992), pp 31-42.
6. J.A. Graves, P.R. Smith and C.G. Rhodes in Intermetallic Matrix Composites II, Mat. Res. Soc. Symp. Proc. Vol. 273, D.B. Miracle et al., eds., MRS, Pittsburgh, PA, (1992), pp 43-52.
7. P.R. Smith, M. Khobaib and J.A. Graves, Scripta Metall. Mater. **29**, (1993), pp 1313-1318.

Processing and Properties of Nb5Si3/Nb Laminates

John Short, Jan Kajuch, and John J. Lewandowski
Case Western Reserve University

Abstract

Mechanical alloying(MA) and Reactive Sintering(RS) techniques were successfully used to produce Nb5Si3. Model laminates of mechanically alloyed Nb5Si3 and commercially pure niobium were prepared via vacuum hot pressing. Tensile properties for the as-received, vacuum heat treated and niobium with a solid solution of silicon were obtained at 298K and 77K. 298K bend tests were conducted in an *in situ* deformation stage in a SEM. 77K bend tests were also conducted. Toughness values are correlated to the ligament properties and effect of constraint.

Introduction

The Nb5Si3-Nb system has been chosen as a model system to evaluate ductile phase toughening due to its thermodynamic stability at temperatures up to 1500°C.[1-3] Much of the previous research has focused on formation of the Nb5Si3/Nb composites through arc-casting techniques. *In-situ* powder processing methods[4,5] as well as environmental stability[6] have also been evaluated.

Ductile phase toughening has been quantified by Mataga.[7] The factors relating to the increase in toughness due to bridging by the ductile particles is given by:

$$\Delta G_c = V_f \sigma_o a_o \chi$$

Where σ_y is the yield strength of the unconstrained ligament, V_f is the volume fraction of the ductile constituent, a_o is the half thickness of the ligament in the crack plane, and χ is the work of rupture term related to the constraint of the ligament. X is calculated by the equation:

$$\int_0^{u^*/a_o} \sigma / \sigma_o d(u / a_o)$$

This is simply the area under the normalized stress(σ/σ_y)-normalized displacement(u/a_o), where u is the crack opening displacement.

Experimental Procedures

The processing of the monolithic silicide is given elsewhere.[5,8] Monolithic silicide was electrodischarge machined(EDM) and laminated with commercially pure, 250μm thick, Nb foils(average grain size 10μm) from Aldrich Chemical Company. Figure 1 represents the diffusion bonding process and bend sample preparation. Bonding was accomplished in a vacuum hot press at 10MPa and 1473K for 5 hrs. The laminates were subsequently electrodischarge machined into 4 x 8 x 45mm bars for 3 point bend tests and subsequent metallographic analyses. An EDM notch of approximately 125μm root radius was placed about 250μm from the silicide-niobium interface. A wire saw was utilized to extend the notch to within 125μm from the interface with a 50μm root radius.

Tensile tests of the as-received niobium(AR-Nb), vacuum heat treated niobium(VHT-Nb), and niobium with a solid solution of silicon(Nb(ss)) were conducted on an Instron Model 1125 at 298K and 77K. VHT-Nb was obtained by heat treating niobium foil in a vacuum hot press at

285

1473K for 5 hours to simulate diffusion bonding conditions. Nb(ss) was placed between two monolithic silicide wafers and heat treated at 1473K for 5 hours, but no pressure was applied other than the weight of the graphite rams. The foils were subsequently removed and tested. Postfailure analyses of the fracture surfaces were conducted on a JEOL 840A SEM.

Metallographic analyses and mechanical testing were accomplished in a SEM equipped with an Oxford Instruments deformation stage. The bend bars were tested in 3 point bending at a loading rate of 1μm/s and continuous video monitoring enabled accurate calculation of fracture initiation and observation of fracture behavior. Liquid nitrogen test were performed on an Instron Model 1125. Postfailure analyses included scanning electron microscope examination of the fracture surfaces and quantification of the fracture modes present.

Results and Discussion

Table 1: Impurity Analyses presents the results of the grain size and impurity analyses of the monolithic silicide and the Nb foil under various processing conditions. Commercially pure AR-Nb exhibited a partially wrought, fine grained structure. Upon heat treatment in a vacuum hot press significant increases in the carbon and oxygen levels was noted. In the Nb(ss), impurity levels indicated a solid solution of silicon had been achieved as well as a significant increase in the oxygen level due to equilibration with the monolithic silicide.

Figures 2a and 2b represent the results of the unconstrained tensile behavior of the 298K and 77K tests respectively. At 298K, the vacuum heat treatment(i.e. VHT) results in a loss of the beneficial dislocation substructure due to recrystallization resulting in lower strengths and increased elongation, although nearly identical reduction in area to the other two samples tested. The solid solution of silicon in Nb produced increased strength in comparison to both the AR-Nb and VHT-Nb. Ductile rupture with reductions in area greater than 75% were present in all samples. At 77K, the increase in the flow stress caused an increase in the strengths and reductions in elongation for all samples. The Nb(ss) exhibited the greatest elongation with the VHT-Nb and AR-Nb showing similar elongation. 100% cleavage fracture was present in the large grained(i.e. 210μm) Nb(ss) and VHT-Nb. However, the fine grained(i.e. 10μm) AR-Nb exhibited 100% ductile rupture with reductions in area approaching 100%.

Figure 3 shows the load-load point displacement trace for the diffusion bonded samples. The shaded area indicates the fracture energy of the monolithic silicide. As noted by the trace, the energy to fracture the laminate is much greater than the monolithic silicide. The laminate also exhibits a non-linear region near fracture due to the deformation of the ligament and microcracking of the silicide as seen in Figure 4.

The fracture surface as seen in Figure 5, shows mixed mode fracture with a magnification of a microcrack and the ductile rupture of the Nb ligament. At 77K, 100% cleavage fracture of the Nb ligament with no microcracking of the silicide was present.

Table 2:Toughness Comparison summarizes the bond condition, Nb ligament properties, test temperature, toughness(using peak load) and the failure mode(s) present. The significant point from this table is that the peak load toughness decreased about 25% with the change of the fracture mode from mixed mode to 100% cleavage. This may be rationalized using energy concepts and the realization that the toughness of Nb is still in excess of $25MPa\sqrt{m}$[9]. A greater amount of energy is absorbed by the Nb(ss) ligament as compared to the AR-Nb ligament with a radical difference in fracture mode at 77K as noted in the unconstrained tensile behavior(i.e. Figure 2b). With no microcracking, the constraint imposes a hydrostatic component felt by the ligament that localizes the stress at the crack tip. Thus the load will increase until the fracture stress has been reached at the crack tip. Further discussion of the effects of the interface and constraint is found elsewhere.[9]

286
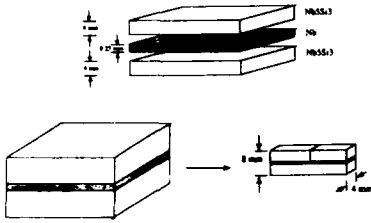
Figure 1, Diffusion Bonding and 3 Point Bend Samples
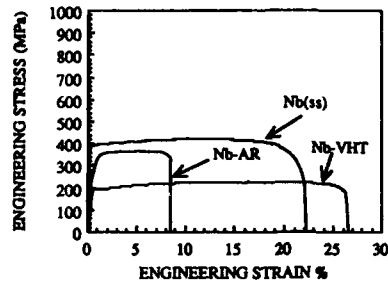
Figure 2a, 298K Nb Tensile Properties
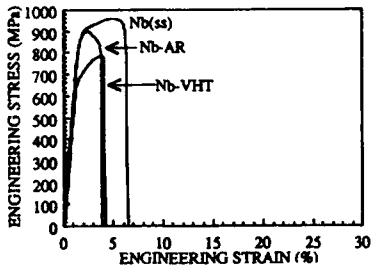
Figure 2b, 77K Nb Tensile Propeties
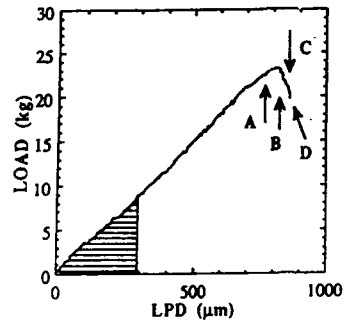
Figure 3, Load-Load Point Displacement Trace for Diffusion Bonded Laminates.

Figure 4, Deformation and Microcracking of Nb5Si3/Nb Laminate

287
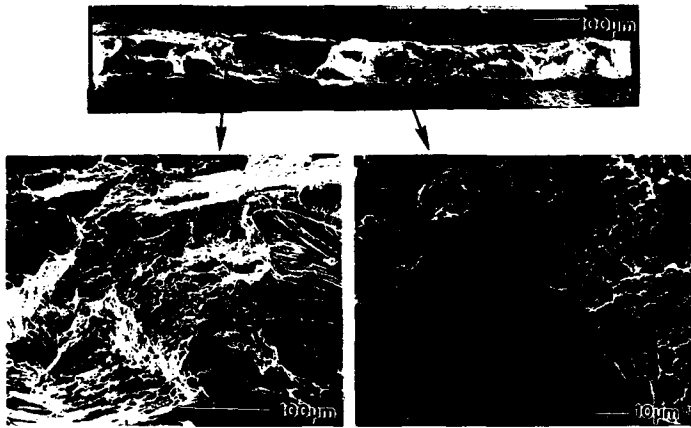
Figure 5. Fracture Surface of Nb5Si3/Nb Laminate. Magnification of Microcrack(Right) and Ductile Rupture(Left)

MATERIAL & CONDITION	GRAIN SIZE (µm)	C (ppm)	O_2 (ppm)	N_2 (ppm)	H_2 (ppm)	Si (ppm)
AR	10	< 10	< 125	< 50	< 5	<100
VHT	210	420	490	120	NA	90
Nb(ss)	210	210	1300	190	NA	1050
Nb$_5$Si$_3$	5	980	1260	NA	NA	16.9wt%

Table 1. Impurity Analyses

Bond Type	Nb Condition	Test Temp (K)	Avg. K_q (MPa√m)	Failure Mode(s)
Diffusion	Nb(ss)	298	8.6	Ductile +
			7.1 - 11.4	Cleavage
Diffusion	Nb(ss)	77	6.2	Cleavage

Table 2. Toughness Comparison

288

Conclusions

Conclusions reached in this work are as follows:

(1) Monolithic Nb5Si3 and Nb5Si3 laminates were successfully produced.

(2) Diffusion bonding of the silicide to the 250μm Nb foil resulted in a large recrystallized grain structure with a solid solution of silicon. This significantly increases the tensile properties, elongation, and energy to fracture.

(3) The toughness of the laminate(8.6MPa√m) is five times the monolithic silicide(1-2 MPa√m).

(4) Microcracking of the silicide relieved the constraint on the Nb ligament and resulted in the mixed mode fracture of the Nb ligament.

(5) The slight decrease in the toughness at 77K with 100% cleavage fracture indicates that cleavage fracture is not necessarily detrimental if enough energy can be absorbed by the ductile ligament. Thus the ligaments for ductile phase toughening must be tough. Ductility plays a key role in the work of rupture or in the region past the peak load of the load-load point displacement trace.

References

1. J.J. Lewandowski, D. Dimiduk, W. Kerr, and M. G. Mendiratta, *MRS Symp. Proc.*, **129**, (1988), 103.
2. M.G. Mendiratta and D.M. Dimiduk, *Scripta Met.et Mat.*, **25**, (1991), 237.
3. M.G. Mendiratta, J.J. Lewandowski, and D.M. Dimiduk, *Met. Trans. A*, **22A**, (1991), 1573.
4. R.M. Nekkanti and D.M. Dimiduk, *MRS Symp. Proc.*, **194**, (1990), 175.
5. Jan Kajuch, Ph.D. Thesis, Case Western Reserve University, (1993).
6. J.D. Rigney, P.M. Singh, and J.J. Lewandowski, *JOM*, (August 1992), 36.
7. P.A. Mataga, *Acta Metall.*, **37**, no. 12, (1989), 3349.
8. J. Kajuch, J.D. Rigney and J.J. Lewandowski, *Mat. Sci. and Eng.*, **A155**, (1992), 59.
9. J.D. Rigney and J.J. Lewandowski, unpublished research.
10. J. Kajuch, J. Short, and J.J. Lewandowski, submitted to *Acta Met.* for pub., (1994).

PART V

Intermetallic Materials
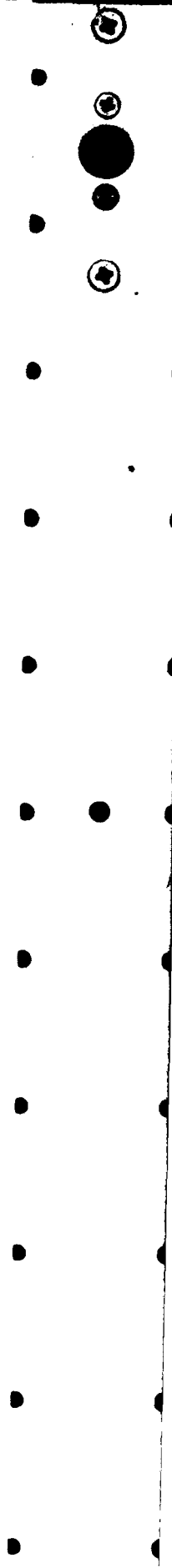
ATOMISTIC SIMULATION OF DISLOCATION MOTION AS DETERMINED BY CORE STRUCTURE

Kevin Ternes, Diana Farkas, and Zhao-Yang Xie
Department of Materials Science and Engineering
Virginia Polytechnic Institute and State University, Blacksburg VA 24061

ABSTRACT

Two different interatomic potentials of the embedded atom type were used to study the relationships between dislocation core structure and mobility. Core structures were computed for a variety of dislocations in $B2$ NiAl. Several non-planar cores were studied as they reacted to applied stress and moved. The results show that in some cases, the dislocation core transforms to a planar structure before the dislocation glides, whereas in some other cases the core retains the non-planar structure at stresses sufficient to sustain glide. The effects of stoichiometry deviations on the core structure and motion were also studied.

INTRODUCTION

Dislocation core structures have been simulated atomistically for many years now [1]. In general, it has been the accepted view that planar core structures move at relatively low applied stresses whereas non-planar cores move at relatively higher stresses. It has also been generally believed that non-planar cores require a transformation to a planar structure before the onset of dislocation motion and the subsequent plastic deformation. Finally, it is important to point out that the values of the Peierls stresses obtained from atomistic simulations are usually an overestimate of the actual stress required for dislocation motion due to the effects of the boundary conditions used in the calculations and the uncertainties in the interatomic potential used. The purpose of the present work is to address the question of a relationship between core structure and dislocation motion in intermetallic alloys. For this purpose, we used two different interatomic potentials for the Ni-Al system and computed a variety of dislocations in the $B2$ NiAl phase. We also studied the sensitivity of the results to the different interatomic potentials used.

NiAl, among other structural intermetallics, is of interest due to its low density and high temperature strength. Current research interests are directed to find ways of preserving these characteristics while overcoming its shortcoming of low-temperature brittleness in polycrystal form. NiAl and its ternary-alloyed derivatives in general have suffered from brittleness in polycrystal, but it has been found that the accurate stoichiometric alloy of NiAl shows several percent ductility [2].

In our previous work [3], we have analyzed the core structures of [100] dislocations in NiAl and found that the cores are in general non-planar. In the present work, we use a standard static simulation technique to compute the stresses necessary to initiate dislocation motion and study the possible transformations that the cores undergo under the applied stress. We are particularly interested in the form in which non-planar cores move under stress.

INTERATOMIC POTENTIALS AND THE CALCULATION OF PEIERLS STRESSES

One of the main questions in the atomistic simulation of dislocation cores is the sensitivity of the calculated structures to the details of the interatomic potential used. In several cases in our previous work it was found that the basic core structure obtained using different interatomic potentials is very similar. This is even true when results of current many body calculations

Table I: Parameters for $B2$ NiAl given by the potentials. Cohesive Energies are given in eV/atom, distances in $10^{-1}nm$ and fault energies in mJ/m^2.

Property	Experimental	Present Work	Calculated [9]	Calculated [10]
a (0.1nm)	2.88	2.88	2.87	2.88
E_{coh} (eV)	4.50	4.49	4.38	4.43
$c_{11}(eV/A^2)$	1.24	1.16	1.74	1.18
$c_{12}(eV/A^2)$	0.85	0.77	1.15	0.79
$c_{44}(eV/A^2)$	0.72	0.77	1.11	0.81
APB(110)	—	286	340	425
APB(100)	—	340	410	460
$\gamma_{US}[110](110)$	—	1200	1160	1200 [11]
$\gamma_{US}[100](110)$	—	970	916	900 [11]

are compared with earlier results obtained using model pair potentials. One example of this is the calculation of the [111] screw dislocation in pure Fe using EAM potentials [5] which gives essentially the same core structure calculated by Vítek and co-authors in 1974 [6]. Another example is the simulation of core structures in $L1_2$ Ni$_3$Al [7] which agrees with the results of Yamaguchi et al. in 1981 [8] using model pair potentials for the $L1_2$ structure. Peierls stresses, however, are expected to be possibly more sensitive to the details of the potential and for this reason, in the present work, we used two different EAM descriptions of the Ni-Al system.

The first EAM description used in the present work is that of Voter and Chen [9] developed based on the $L1_2$ Ni$_3$Al phase. Although these potentials have proven quite useful in the modeling of Ni-Al, interatomic potentials cannot be expected to model an intermetallic phase for which they are not specifically developed. The potentials of Voter, do not predict the $B2$ phase to actually be a stable structure at stoichiometry. The $L1_0$ is predicted as having a slightly lower energy. The predicted elastic constants are 40 % higher than those experimentally observed. The second EAM description used is a new potential developed in the present work based on NiAl which predicts the correct phase stability and elastic constants for the NiAl $B2$ phase. The potentials developed by Voter for Al-Al and for Ni-Ni interactions are retained. Only the cross interactions (Ni-Al) are changed. The $B2$ phase was obtained as stable, with an energy difference of 0.03 eV, with the $L1_0$ phase. Table I shows the values predicted for the various properties of $B2$ NiAl and those predicted by both potentials. Parthasarathy, Rao and Dimiduk have published results for dislocation core structure and mobility simulations [11] using a potential developed by Rao et al. [10]. Their data are also included for comparison purposes in Table I. We also compared the values that the different potentials give for γ_{US}, the unstable stacking fault energies (the maxima of the γ surface). These values are given in Table I for the (110) . Note that the results for the various potentials differ by a maximum of 10%.

Peierls stresses are also expected to be very sensitive to the effects of the boundary conditions used in the simulations. In the present work, we used a cylindrical array with a 24 nm diameter for the inner block of the simulation containing the atoms that are free to relax in the energy minimization process. This relatively large array size was necessary to insure that no size effects were present in the results for Peierls stresses. It is interesting to note that significantly smaller sizes were appropriate for *some* but not all of the dislocations simulated.

CORE BEHAVIOR

The pure edge dislocations with a (100) slip plane have a core extended along two perpendicular planes and tend to hold their original configuration as they glide. See Figure 1. This

Figure 1: (001) edge dislocation in stoichiometric NiAl, simulated using (a) Ni₃Al-based potential, (b) new NiAl potential. Circles represent Al atoms and triangles represent Ni atoms. These views are approximately 3nm square.

1 (a)

2 (a)

1 (b)

2 (b)
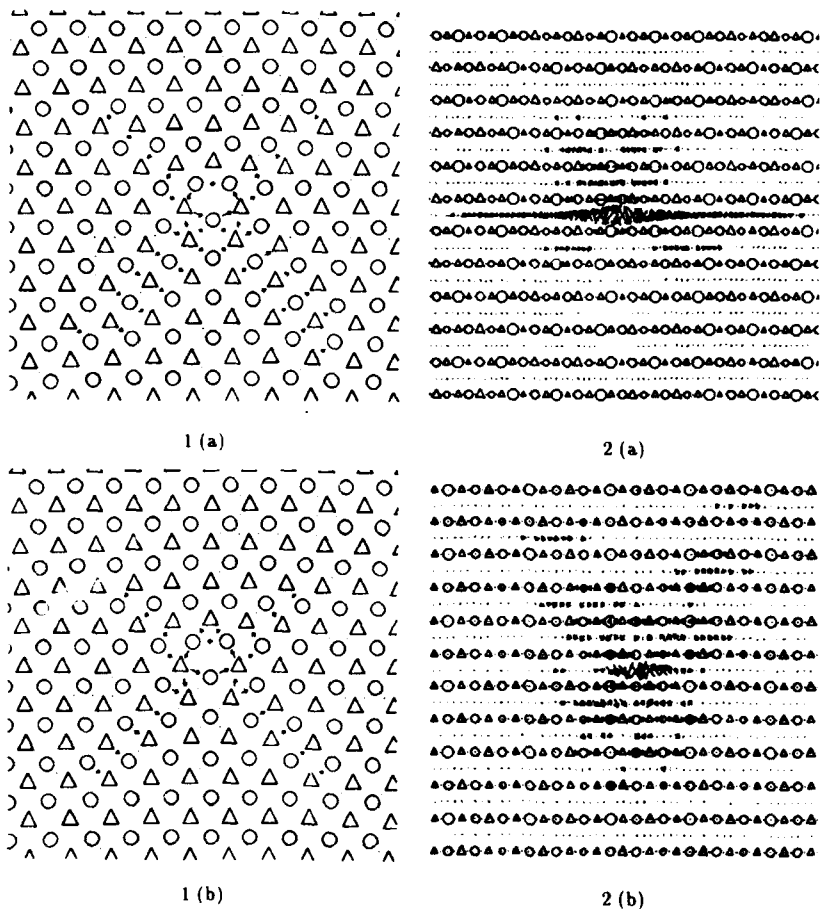
Figure 2: Multilayer faults in (a) ($\bar{1}2\bar{2}$) (01$\bar{1}$) and (b) (211) (011). The views are of a 5nm square.

Table II: Simulated Peierls Stresses for Stoichiometric $B2$ NiAl

geometry				σ_p (MPa)			structure
b	x	y	z	Ni$_3$Al-based	new NiAl-based	Rao[10]	
[100]	[100]	[001]	[0$\bar{1}$0]	2890	2680	2580	cross †
-[100]	[$\bar{2}$10]	[001]	[120]	320	360		multi
[001]	[100]	[010]	[001]	>52*	>100*	>270*	cross †
[100]	[100]	[01$\bar{1}$]	[011]	450	401	320	multi
[100]	[$\bar{4}$11]	[01$\bar{1}$]	[$\bar{1}$22]	850	750		multi
[100]	[$\bar{2}$11]	[01$\bar{1}$]	[111]	1680	1650	1290	cross †
[100]	[$\bar{1}$11]	[01$\bar{1}$]	[211]	460	200		multi
[100]	[0$\bar{1}\bar{1}$]	[01$\bar{1}$]	[100]	260/47	390/70	220/-	cross † /planar

* The dislocation for this geometry was observed to actually move on (110).

† "cross" indicates faults not parallel to the slip plane.

represents an example of a "cross" non-planar core that is best described by faults that are not parallel to the slip plane.

Figures 1(a) and (b) illustrate the results of both potentials applied to the same dislocation. There are two possible cores for this dislocations (Ni-rich and Al-rich). Figures 1(a) and (b) show the Al-rich core. These figures are also very similar to Fig. 6 of Parthasarathy et al. [11].

All the cores generated via the new NiAl potential tend to be qualitatively similar in both appearance and behavior to the cores generated using the Voter potential. The cores for the mixed dislocations mostly exhibited a structure which can be described as a multilayer fault. These multilayer cores maintain their basic structure as they glide. Only very slight transformations were observed where the cores become more extended along the direction of slip and less extended onto planes parallel to the central one. Examples of this type of core are shown in Figure 2.

In addition to the multilayer cores, the pure screw dislocation showed two possible structures, which were obtained in the simulation when different elastic centers were chosen at the start of the minimization process. These two configurations are actually equivalent under no applied load since the pure screw dislocation has no uniquely defined slip plane. When stress is applied, the two configurations are not equivalent and they move at different applied stresses. In this case a transformation of one core structure into the other was observed before the dislocation could move. This is shown in Figures 3(a) and (b). No other dislocations have been found to present two different structures that can be studied by different initial choices of the elastic center. The values of the Peierls barriers obtained in the present work for non-planar cores in [100] [0$\bar{1}\bar{1}$] agree with those obtained by Parthasarathy, et al (Table II) [11].

It is very difficult to rank slip systems or compare with experimental CRSS stresses on the basis of simulated Peierls stress data. However, in Table II, the calculated Peierls stresses for the experimentally observed [100] (01$\bar{1}$) slip are generally lower than those for [100] (001).

RELATIONSHIP OF CORE SHAPE AND PEIERLS STRESS

Peierls stresses for a number of geometries using both potentials are also shown in Table II. The Peierls barriers computed by Parthasarathy et al are also included for comparison. Generally, the more planar a core initially is, the easier it moves under a stress applied parallel to the planes. Also, the fewer parallel planes that the core is spread over, the easier it is to move. The highest Peierls stresses result for cores with components lying on planes not parallel to the applied stress. However, these cores do not seem to transform before moving.

A simple generalization of the Peierls-Nabarro model would indicate that the more constricted

Figure 3: (100) pure screw dislocation in NiAl with differing initial elastic centers, no stress applied. The views are of a 3nm square.

3 (a)

4
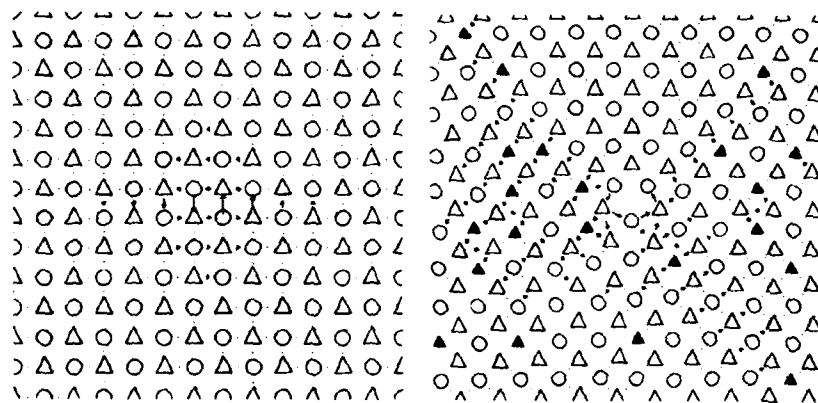
3 (b)

5

Figure 4: (100) pure screw dislocation in NiAl, 70MPa applied stress.

Figure 5: (001) edge dislocation simulated using Ni_3Al-based potential in Ni-42Al.

cores would be the ones with relatively higher Peierls stresses. Our simulations indicate that this is not necessarily the case for non-planar cores. The largest Peierls stresses are obtained for the cores that consist of a mixture of faults in different crystallographic planes. The multi-layer cores that can be viewed as consisting of faults all parallel to the slip plane are the ones with relatively lower Peierls stresses.

STOICHIOMETRY EFFECTS ON CORE STRUCTURE AND MOBILITY

We investigated the effects of deviations in composition on the observed behavior of the dislocation cores. Off stoichiometric runs were made for Ni-48Al and Ni-42Al using both Voter and Chen's Ni_3Al-based and the new NiAl potentials. As an example, see Fig 5. For this purpose, random number generating routines were used to distribute the extra element in the alloy. The shapes of the cores were found to be more irregular as to follow the random distribution of the extra element added. The core was slightly more irregular and the Peierls stress was found to remain basically the same at 2700MPa in edge Ni-42Al dislocations relative to their stoichiometric counterparts.

CONCLUSIONS

The Peierls barriers computed using different potentials for the same dislocation usually vary within 20% of one another. The actual values of the Peierls stress may be sensitive to boundary conditions up to array block sizes of about 24nm diameter. Cross non-planar cores are more difficult to move than multi-layered or planar cores. Wider non-planar cores do not appear to be easier to move than narrower ones. Off-stoichiometric alloys present wider, more irregular cores and higher Peierls stresses. Non-planar cores do not need to transform to a planar configuration before they can move. It is possible that the non-planar cores actually move by constriction to narrower cores. This possibility seems to be supported by a video study of the motion of the ⟨100⟩ edge dislocation.

REFERENCES

1. V. Vítek, Philisophical Magazine **58**, 193 (1988).
2. R. W. Cahn, The Materials Research Society Bulletin , 18 (1991).
3. R. Pasianot, D. Farkas, and E. Savino, J. Phys. III **1**, 997 (1991).
4. Z.-Y. Xie, C. Vailhe, and D. Farkas, Materials Science and Engineering A **170**, 59 (1993).
5. D. Farkas and P. Rodriguez, Scripta Metallurgica et Materialia **30**, 921 (1994).
6. V. Vítek, R. C. Perrin, and D. K. Bowen, Phil. Mag **21**, 1049 (1970).
7. D. Farkas and E. Savino, Scripta Metallurgica et Materialia **22**, 557 (1988).
8. M. Yamaguchi, V. Paidar, D. Pope, and V. Vítek, Philisophical Magazine .
9. A. F. Voter and S. P. Chen, MRS Symposia Proceedings **82**, 175 (1987).
10. S. Rao, C. Woodward, and T. A. Parthasarathy, Material Research Soc. Symposia Proceedings . **213**, 125 (1991).
11. T. A. Parthasarathy, S. I. Rao, and D. Dimiduk, Phil. Mag. A **67**, 643 (1993).

TRANSFORMATION TOUGHENING SIMULATED AT DIFFERENT LENGTH SCALES

P. C. Clapp, Y. Zhao and J. A. Rifkin
Center for Materials Simulation, Institute of Materials Science, University of Connecticut, Storrs, CT 06269-3136, USA

ABSTRACT

The microscopic mechanism of "transformation toughening" is thought to be the stress reduction at a crack tip resulting from a displacive phase transformation induced by the stress field of a crack under external loading. Whether transformation toughening or "transformation embrittlement" is the result depends on many different characteristics of the displacive transformation, as well as the geometry of the stress field of the crack. Since both crack and displacive transformation dynamics are sufficiently rapid to be suitably simulated in a molecular dynamics scheme we have explored this approach with the ordered intermetallic NiAl, employing Embedded Atom Method (EAM) potentials. These potentials, in turn, have allowed the construction of a Ginzburg-Landau strain free energy functional (with all the material dependent parameters determined from molecular dynamics simulations) which may then be used to carry out Monte-Carlo simulations of the crack-transformation zone interaction on a substantially larger spatial scale. The simulations reported here show the complex microstructure involving self-accommodating martensite variants which result from the stress induced martensitic transformation near a crack tip in NiAl, and also measure the resulting reduction of stress intensity factor due to the transformation. It is concluded that current continuum mechanics models of transformation toughening need to be substantially revised if they are to adequately model the size, shape and microstructure of the transformation zone and produce accurate predictions of transformation toughening.

INTRODUCTION

Martensitic transformations are first order displacive phase transformations, often involving a marked volume change and shape change of the crystal. Martensite transformations can be stress-induced. Under appropriate stresses, the parent phase will transform to martensite at temperatures higher than the stress-free transformation temperature, M_s. The irreversible deformation occurring during a martensitic transformation is called "transformation plasticity" and, when induced by the stress field near a crack tip, may provide an important mechanism for resisting the crack's advance and thereby improving the fracture toughness of materials. This will be especially so if other modes of plasticity are very limited, as in the case of many intermetallics or ceramics[1].

Both crack propagation and martensitic transformation are sufficiently rapid processes to be simulated at the atomic scale using molecular dynamics. Although our Center has carried out a number of simulations of this type for both fracture[2,3,4,5,6] and martensitic transformations[7,8,9] it was realized that a simulation of transformation toughening[10,11] would involve a crack tip and a surrounding transformation zone that would be at a much larger length scale than the interatomic distance, so that some method of simulation which bridged the length scales from the atomic to

the macroscopic would have to be utilized. This paper reports one possible approach to achieving this goal. The intermetallic alloy NiAl has been used to illustrate the method.

A number of workers have used non-linear elastic continuum descriptions with a Ginzburg-Landau strain free energy functional to model martensitic transformations. The calculation is carried out utilizing a variational minimization procedure with assigned boundary conditions. Exact solutions exist for the one-dimensional martensitic nucleation[12,13,14] and growth[15] problems, as well as a two dimensional twinning problem[16], but the two or three-dimensional martensite problem has not as yet been solved. However by using a finite-element grid representation of a non-linear 3D elastic continuum, this variational calculation can be performe ' approximately by using Monte Carlo techniques in conjunction with an appropriate Ginzburg-Landau strain energy potential. In the case treated here, the Metropolis Monte Carlo method[17] was employed to simulate the stress induced martensitic transformation around a crack tip of a NiAl alloy in Mode I loading, whose parent phase is a B2 structure. The martensite phase is a $L1_0$ structure, which can be related to the B2 structure by a tetragonal distortion. A Ginzburg-Landau strain energy potential was constructed from the Voter-Chen Embedded Atom Method (EAM) interatomic potentials[18] for this alloy system. The simulation generated a near tip strain field "solution" showing a mixed microstructure of parent and martensite phases. The simulation also provided very rich information on the size and shape of the transformation zone, as well as the spatial distribution of the martensite variants. Further calculations of the near-tip stress intensity factor before and after the transformation showed striking evidence of a toughening effect.

METHODOLOGY

The Metropolis Monte Carlo method

This method can be used to minimize the energy of a system with a large number of degrees of freedom. The upper half of a sample of an NiAl alloy containing a crack was represented by a 3D array of cells shown schematically in Figure 1. Sixty cells were used in the direction of crack propagation (x), thirty in the direction normal to the crack plane (y), and two in the crack width direction (z). The cell size may be chosen appropriate to the scale of the phenomena and microstructure of interest, as long as it is at least an order of magnitude larger than the atomic spacing (in order to preserve some semblance of a continuum approximation). In most of the cases studied it was chosen as ten NiAl unit cell lengths, or 287.12 Å.
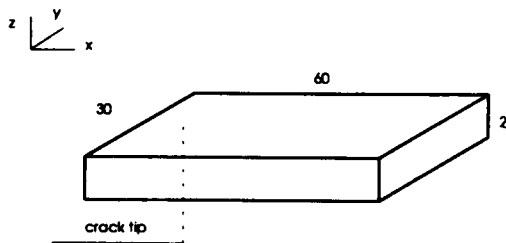
Figure 1 - Dimensions of the 3D grid used for simulating half of the cracked NiAl solid

300

The crack was placed on the zx plane at the bottom of the grid and the crack tip at node 25 (counting from the left edge). Assuming that the upper and lower halves of the sample would behave symmetrically, the y displacements of the nodes on the crack plane beyond the crack tip (nodes 25+) were not allowed to change from their initial zero values, although their x and z displacements were permitted.

To keep computational times manageable, only three layers of nodes (two cells) were used in the z direction. It was decided not to impose periodic boundary conditions in this direction, thus the simulations were carried out under plane stress conditions. The load was imposed so that the lattice was deformed according to a near crack tip deformation field given by isotropic continuum elasticity theory. The displacements of the top, left and right outer surfaces of the grid were then kept at these values during the rest of the simulation.

The Monte-Carlo method employed in this study consisted of the following steps:

I. Set up the initial grid configuration using the displacements calculated from isotropic continuum elasticity theory, given an assumed external load.
II. Apply a Monte Carlo "annealing" procedure, i. e. :
    a) Generate random lattice displacements for all the nodes allowed to move (within prechosen limits of some fraction of the cell spacing).
    b) From the Ginzburg-Landau strain free energy function, calculate the change in total grid strain free energy, ΔE, caused by the displacements.
    c) If ΔE is less than zero, the move is accepted and the grid adopts the new configuration. If ΔE is greater than zero, the old configuration remains.
III. Repeat steps II.a to II.c until E appears to have reached a practical minimum, or up to a target number of steps (typically 10^6-10^7).

A Ginzburg-Landau strain free energy function for NiAl

Since our intent was to model a system capable of undergoing a martensitic phase transformation, this energy function must have two minima, one for the parent phase and one for the martensite phase. A polynomial expansion was used for the strain free energy. In order to represent a bi-stable minimum with respect to a single strain variable, the energy expansion must be carried out to at least fourth order terms in that variable. In the case of a three dimensional body center cubic (BCC) to body center tetragonal (BCT) transformation, the minimum number of terms necessary to adequately represent the corresponding strain free energy is:

$$f(\eta) = \frac{1}{2}C_{11}(\eta_1{}^2 + \eta_2{}^2 + \eta_3{}^2) + C_{12}(\eta_1\eta_2 + \eta_2\eta_3 + \eta_3\eta_1) + \frac{1}{2}C_{44}(\eta_4{}^2 + \eta_5{}^2 + \eta_6{}^2)$$

$$+ \frac{1}{6}C_{111}(\eta_1{}^3 + \eta_2{}^3 + \eta_3{}^3)$$

$$+ \frac{1}{2}C_{112}(\eta_1^2\eta_2 + \eta_1{}^2\eta_3 + \eta_2^2\eta_3 + \eta_2^2\eta_1 + \eta_3^2\eta_1 + \eta_3^2\eta_2)$$

$$+ C_{123}\eta_1\eta_2\eta_3$$

$$+ \frac{1}{2}C_{144}(\eta_1\eta_4^2 + \eta_2\eta_5^2 + \eta_3\eta_6^2)$$

$$+ \frac{1}{2}C_{166}(\eta_1(\eta_5^2 + \eta_6^2) + \eta_2(\eta_4^2 + \eta_6^2) + \eta_3(\eta_4^2 + \eta_5^2))$$

$$+ C_{456}\eta_4\eta_5\eta_6$$

301

$$+\frac{1}{24}C_{1111}(\eta_1{}^4 + \eta_2{}^4 + \eta_3{}^4)$$

$$+\frac{1}{6}C_{1112}(\eta_1^3\eta_2 + \eta_1^3\eta_3 + \eta_2^3\eta_3 + \eta_2^3\eta_1 + \eta_3^3\eta_1 + \eta_3^3\eta_2)$$

$$+\frac{1}{4}C_{1122}(\eta_1^2\eta_2^2 + \eta_2^2\eta_3^2 + \eta_3^2\eta_1^2)$$

$$+\frac{1}{2}C_{1123}(\eta_1{}^2\eta_2\eta_3 + \eta_2{}^2\eta_3\eta_1 + \eta_3{}^2\eta_1\eta_2) \qquad\qquad (1)$$

$$+\frac{1}{24}C_{4444}(\eta_4{}^4 + \eta_5{}^4 + \eta_6{}^4)$$

$$+ K\,(\nabla\eta)^2$$

where η_i ($i=1,6$) are the Lagrangian strain components in Voigt notation, and C_{ij}, C_{ijk}, and C_{ijkl} are the 2nd, 3rd, and 4th order elastic constants in the same notation. K is the strain gradient coefficient which controls the energy of any regions of rapidly changing strain (such as the interfaces between phases). The $K\,(\nabla\eta)^2$ term also provides the basis for determining the scale in our simulations (since without it the simulations are scale invariant) and we have used terms of the form: $K\,\{(\partial\eta_1/\partial x)^2 + (\partial\eta_2/\partial x)^2 + (\partial\eta_3/\partial x)^2\}$ to show the effect on dimensions of the martensite microstructure, but here we consider the simplest case of $K = 0$, which is the limit when the interfacial energies are negligible in comparison to the volume dependent strain and chemical energies. Simulation examples when $K \neq 0$ will be reported elsewhere[19].

The strain and the elastic constants are referred to the same coordinate system as that of the grid. The state of $\eta_i = 0$ represents the stress free parent phase, which also satisfies,

$$\left.\frac{\partial f}{\partial \eta_i}\right|_{\eta_i=0} = 0$$ To simulate the transformation, C_{ij}, C_{ijk}, and C_{ijkl} need to be determined so that there exists a lower energy minimum at a non-zero finite strain state for the martensite phase.

The simulated NiAl alloy

Ideally one would use experimental data to determine all of the elastic constants in Eq. (1), but in practice the third and fourth order constants in particular are very difficult to obtain by measurement. An alternative, and much quicker approach to obtaining approximately correct values for these numbers is to use a molecular statics calculational method in conjunction with Embedded Atom Method[20] interatomic potentials. The set we have used were developed by Voter and Chen[6] based on experimental data from four phases of the Ni-Al alloy system: Ni, Ni$_3$Al, NiAl and Al. They have the advantage that in the NiAl phase region they predict that a tetragonal L1$_0$ martensite phase will have a somewhat lower energy at 0 K than the parent B2 phase, and furthermore that as the Ni content increases, the energy of L1$_0$ decreases relative to B2. Both these facts agree with experiment, except that the composition at which the two phases are equal in energy appears to be closer to 60 atom %Ni, rather than the less than 50 atom %Ni predicted

302

with the Voter-Chen potentials. Since it was convenient to study a hypothetical martensite transformation in a perfectly ordered stoichiometric B2 NiAl that was closely related to that observed at nearby compositions without involving a myriad of questions about the precise effect of compositional disorder on the transformation, we chose not to modify the potentials to make them "more accurate".

By imposing a series of chosen strain fields on a large periodic atomic array ($\cong$ 10,000 atoms) of B2 NiAl the variation of the lattice energy with a designated deformation pattern can be calculated by computer and fit (in a least squares fashion) to the continuum expression for the strain free energy, Eq. (1). If a strain gradient term is to be included in the Ginzburg-Landau strain free energy function, its coefficient can be determined by applying periodically varying strain fields to the array.

It is especially important to fit the energy surface near the second martensitic minimum as well, i. e. near the strain values: $\eta_1 = 0.20$, $\eta_2 = \eta_3 = -0.07$, $\eta_4 = \eta_5 = \eta_6 = 0$. Special attention was paid to fitting the energy contours of Figure 2. The martensite minimum energy state (as predicted by the Voter-Chen EAM potentials) has an energy of -80 Kelvin/atom relative to the B2 austenite state, involves a volume expansion of 4.65% and is a global minimum. Experimental estimates of the volume expansion in Ni rich NiAl transforming alloys range from 2-5%.
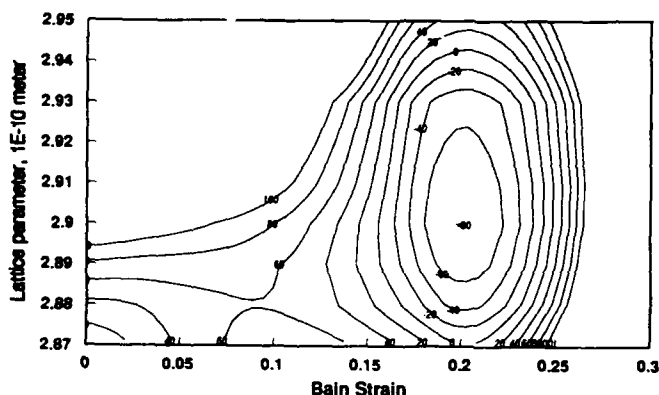
Figure 2 - Plot of strain energy vs. lattice parameter and Bain strain determined from EAM potentials in a molecular statics calculation. The Bain strain is measured by the value of η_1, given the constraints: $(1+\eta_1)(1+\eta_2)(1+\eta_3)=1$; $\eta_2=\eta_3$, and $\eta_4=\eta_5=\eta_6=0$.

SIMULATIONS OF STRESS INDUCED MARTENSITIC TRANSFORMATION NEAR A CRACK TIP

Monte Carlo simulations of the martensitic transformation near a crack tip were performed with the 3-D block shown in Figure 1. The load was imposed so that the lattice was deformed according to a near crack tip deformation field given by isotropic continuum elasticity theory using a suitable average of the NiAl second order elastic constants and a stress intensity factor of 10.0 MPa-m$^{1/2}$. The displacements on the top, left and right surfaces of the grid were then fixed

303

during the simulation as the interior nodes were allowed to relax. If we used imposed stress levels substantially less than this number, no stress induced martensite would appear, at least within a span of 10^7 Monte-Carlo steps/node. However, we made no systematic attempt to determine the minimum stress intensity factor required to induce the transformation.

Two simulation cases are illustrated here. Case 1 was a continuous 10 million step run which showed a significant amount of martensite appearing near the crack tip. Case 2 was carried out in two stages to evaluate the effect of the transformation on the near crack stress field. The first stage consisted of a harmonic relaxation stage for 3 million steps, where the anharmonic third and fourth order terms in expression (1) were set to zero to simulate an ideal linear elastic non-transforming solid. The third and fourth order coefficients were then "switched on" after 3 million steps to provide the possibility of a martensitic transformation, and the relaxation continued for another 7 million steps in the second stage. This provided a direct comparison of the stress intensity factors near the crack tip before and after the transformation.

The plot of energy vs. step in Case 1 is given in Figure 3, which shows a steady decrease of the system energy caused by both the elastic and plastic (i. e. transformation) relaxations. Although the martensite phase has an energy of -80 K/atom (and the B2 austenite phase an energy of 0 K/atom), the total energy of the grid approaches a steady-state value of ~ +120 K/atom. This is because the transformation zone is confined to a small area near the crack tip, strains will arise in both the austenite and martensite, and the transition regions between the two phases will have an even higher energy than either.
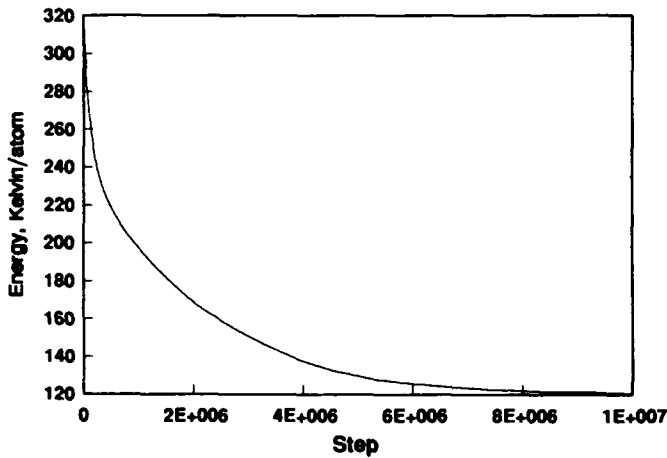
Figure 3 - Energy vs. step showing both elastic and plastic (transformation) relaxation, Case 1

To show the transformation sequence, strain plots at several different times of the second (middle) layer in the z direction of the 3-D block are given in Figure 4. Strains at each of the nodes are calculated from the differential displacements of nearest neighbor nodes. The strains are divided into 8 levels, each being represented by one symbol. The correspondence between symbols and the strain levels are given in the legend to the left of each plot. Three strain plots of
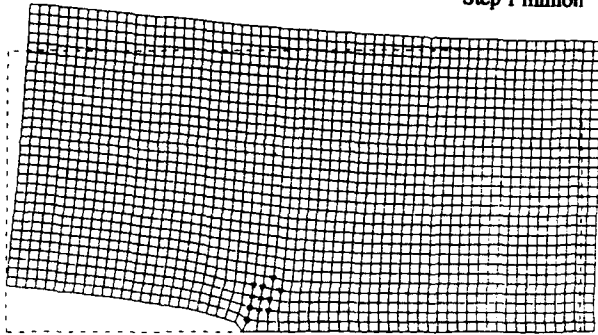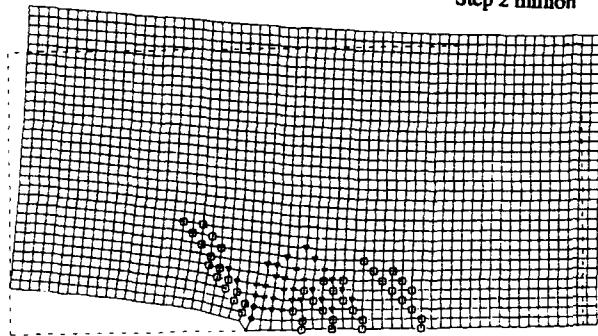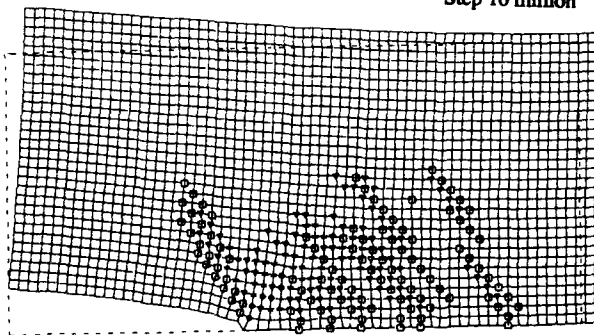
Figure 4. Strain profiles around the crack tip, η_2. Case 1.

characteristic strain of $\eta_1 = 0.20$, $\eta_2 = \eta_3 = -0.07$ (variant I). The cubic symmetry of the austenite implies another two crystallographically equivalent martensite variants at $\eta_2 = 0.20$, $\eta_1 = \eta_3 = -0.07$ (variant II), and $\eta_3 = 0.20$, $\eta_2 = \eta_1 = -0.07$ (variant III). The occurence of these martensite variants in the simulations can be easily identified by these strain values, as a nodal strain in the vicinity of either 0.20 or -0.07 indicates a martensitic transformation occurred at this node. To highlight the transformation zone near the crack tip, only the lowest level and the two highest levels of the strain are plotted in Figure 4.

Figure 5 illustrates the energy vs. step curve of Case 2. The first 3 million steps were purely linear elastic relaxation, and the grid approached a steady-state energy of ~ 220 K/atom. No martensite was expected under these conditions, nor was any observed. The jump of energy at 3 million steps corresponded to the material property changes produced by switching on the third and fourth order elastic constants, which included the capability of a martensitic transformation. The subsequent decrease of energy due to the onset and development of the martensitic transformation was then observed. The strain profile of η_2 at 10 million steps is plotted in Figure 6, and reveals the same features of variant mixing as that of Figure 4. However, Case 2 does not exactly reproduce Case 1, reflecting the random nature of the Monte Carlo simulation and the fact that a number of transformation morphologies are all close to having the lowest energy. This was borne out by the fact that even for the same case, separate simulations (involving different random number sequences) would produce slightly different but qualitatively quite similar final state morphologies.

Stress Induced Martensitic Transformation Near the Crack Tip

Figures 4 and 6 reveal a very interesting transformation pattern near the crack tip. It is apparent that there are two major transformation zones around the crack tip. One is in front of the crack with most of the martensite plates concentrated in a sector from 0° to 45° away from the crack advance direction. The other is behind the tip and extends along a direction 120° away from the crack direction. The transformation zone ahead of the crack is much bigger than that behind, which might be expected. In both regions, two types of variants were observed, but the relative volume fractions were different. The predominance of variant I is seen in the transformation zone behind the tip. Variant II is more predominant in the near front of the tip where the highest tensile stress, σ_{22}, exists. Further away from the tip, there was a well balanced mixing of variants I and II, with slightly more of variant I. No trace of variant III was observed in the simulations, probably due to the fact that there were only three nodes in the z direction, making relaxation along the z direction easy. This changing mixture of variants is presumably caused by the strongly varying initial stress distribution around the crack tip, and the tendency of martensite to form self-accommodating clusters of variants to minimize the net transformation strain.

Effect of Martensitic Transformation on the Stress Intensity Factor

By comparing the before and after transformation states in Case 2, the change of the stress intensity factor caused by the martensite could be approximately evaluated. For ideally elastic materials, the stress intensity factor K_I is considered to be a valid measure of the stress concentration near a crack tip. For plastic materials where large scale yield can occur, the
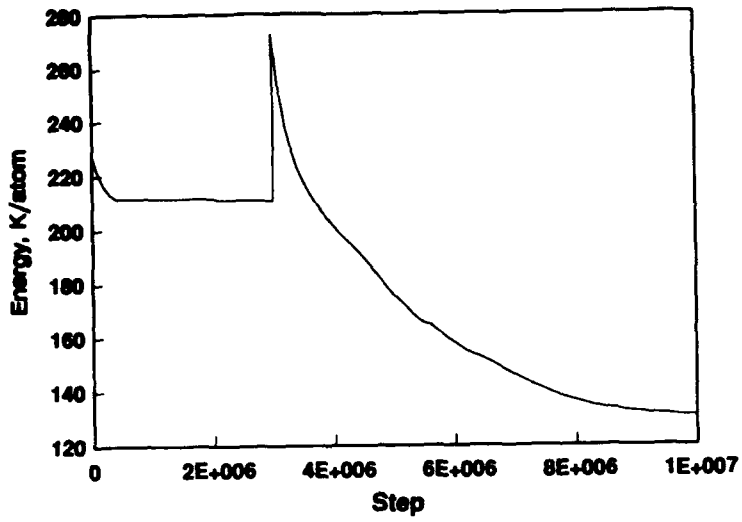
Figure 5   Energy vs. step, case C2.
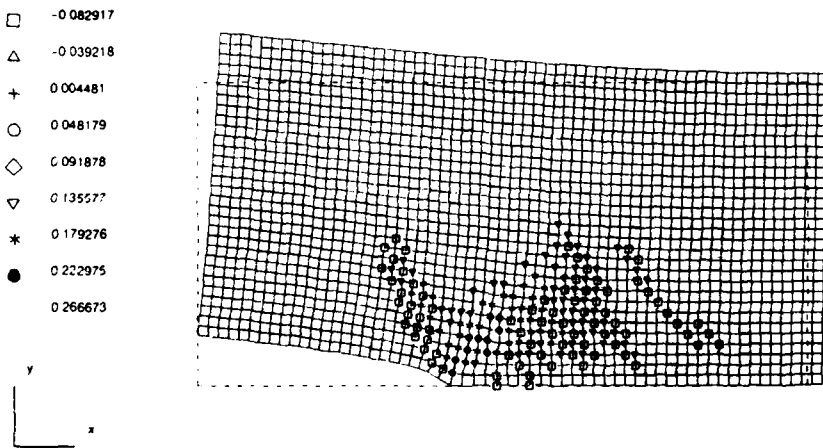
Figure 6.   Strain profile around the crack tip, η_2. Case 2.

307

evaluate a J-integral (generalized to a discrete lattice) over a grid of nodes with displacements containing random small fluctuations led to a large accumulation of errors. However, by using the definition of K_I as the limit of the nodal stress intensity factor, K_N, as the crack tip is approached, we obtained much more reproducible and sensible results. This technique has been previously used in finite element calculations by others[21].

The nodal stress intensity factor, K_N, is calculated by the following formula:

$$K_N = \frac{\sqrt{2\pi x}}{f_{yy}(\theta)} \sigma_{yy}$$ (2)

where

$$f_{yy} = \cos\frac{\theta}{2}\left(1 + \sin\frac{\theta}{2}\sin\frac{3\theta}{2}\right)$$ (3)

as given by the continuum elasticity solution. The formula for the stress σ_{yy} was calculated analytically as the derivative of the strain energy density function, f, with respect to strain η_2. This in turn was evaluated at each nodal point based on the local strains, which themselves are calculated from finite differences of the nodal displacement field. Calculations were done along two orthogonal lines approaching the tip as shown in Figure 7. The comparison of K_N before and after the transformation is provided in Figure 8.
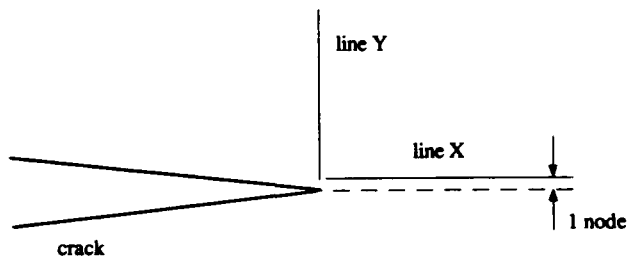
Figure 7   Lines X and Y along which the K_N calculations were performed.

Calculation at step 0 gave a K_N of ~10 Pa√m. The linear elastic relaxation of 3 million steps reduced it to ~7 Pa√m, exhibiting the differences between an isotropic continuum with averaged NiAl elastic constants, and the discrete grid interacting according to a solid with cubic symmetry and three independent second order elastic constants. As may be seen from Figure 8, when the higher order elastic constants were "switched on" at 3 million steps, providing the grid with the possibility of transforming, the subsequent transformation caused a significant reduction of the nodal stress intensity factor.

Along line Y, K_N experienced an order of magnitude decrease. A few nodes near the crack tip even had negative values of K_N, indicating complete stress shielding by the transformation zone. Along line X, there was a more pronounced fluctuation in K_N from node to
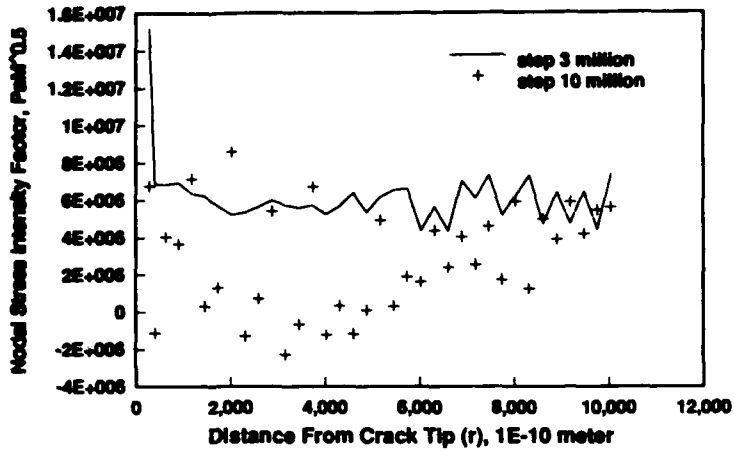
a. Line X
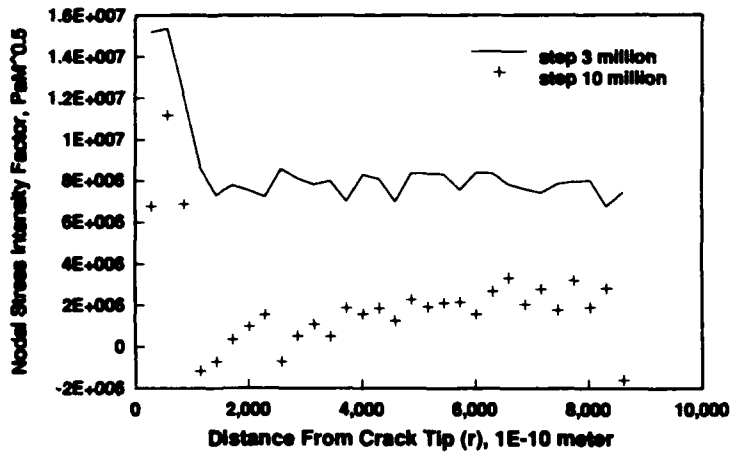
b. Line Y

Figure 8.   Node stress intensity factor as a function of distance from the crack tip.

substantially lower with some becoming negative. Although the average acting on the crack should be determined statistically throughout the whole region, Figure 8 shows that a K_N reduction was obtained at most of the nodes, enabling one to conclude that a significant degree of transformation toughening is evident.

CONCLUSION

In this paper, a new method (as far as we are aware) has been demonstrated for linking atomistic simulations to indefinitely larger scale simulations via a Ginzburg-Landau strain free energy function generated from semi-empirical atomic interactions. This function was constructed via molecular statics simulations in which the atomic array interacted via NiAl Embedded Atom Method potentials. This function was then used to determine the behavior of a finite element grid representing the solid at any chosen scale as calculated by a Monte-Carlo annealing simulation. The example illustrated here involved the stress induced martensitic transformation near a crack tip in NiAl, showing details of the complex patterns of transformation that may be expected in such a situation, including the occurence of self-accommodating martensite variants. Calculation of nodal stress intensity factors before and after the transformation provided a quantitative measure of the degree of transformation toughening to be expected.

The size, shape and microstructure of the transformation zone are of crucial importance to the understanding and analysis of transformation toughening.[22] Our results show that the situation is far more complex than that envisioned by the current continuum mechanics models of transformation toughening, which typically assume an isotropic medium, generally use some simple critical stress criterion (isostatic stress or maximum principal stress) for the nucleation of the martensite, and make no allowance for the simultaneous existence in close proximity of different martensite variants. We believe that with the techniques demonstrated here it will be possible to produce a much more complete analysis of this complicated phenomenon.

ACKNOWLEDGMENT

REFERENCES

[1] Green, D. J., Hannink, R. H. J., and Swain, M. V. (1989), Transformation Toughening of Ceramics, CRC Press, Inc, Florida.

[2] D. Kim - Ph. D. Thesis, Univ. of Connecticut (1993)

[3] C. Becquart - Ph. D. Thesis, Univ. of Connecticut (1993)

[4] D. Kim, P. C. Clapp and J. A. Rifkin - MRS Symposia Proceedings, 288, 507-12(1993)

[5] C. S. Becquart, P. C. Clapp and J. A. Rifkin - MRS Symposia Proceedings, 288, 519-24(1993)

[6] C. S. Becquart, D. Kim, J. A. Rifkin and P. C. Clapp - Mat. Sci. and Eng. 2, 1-8 (1994)

[7] P. C. Clapp, Y. Shao and J. A. Rifkin MRS Symposia Proceedings, 246, 1-10 (1992)

[8] Y. Shao - Ph. D. Thesis, Univ. of Connecticut (1993)

9 S. Chen, P. C. Clapp and J. A. Rifkin, MRS Symposia Proceedings 238, 65-72 (1992)

10 P. C. Clapp, C. S. Becquart, D. Kim, Y. Shao and J. A. Rifkin,
     J. Mater. Sci. Technol., 9, 355-9 (1993)

11 Y. Zhao - Ph. D. Thesis, Univ. of Connecticut (1993)

12 G. Guenin and P. C. Clapp, Proc. of the International Conference on Martensitic
     Transformations (ICOMAT), Japan Institute of Metals, pp. 171-179 (1986)

13 P. C. Clapp, Physica D 66, 26-34 (1993)

14 W. Cao, J. A. Krumhansl, and R. J. Gooding, Phys. Rev. B, 41, p. 319, (1990).

15 S. K. Chan, J. Chem. Phys. 67, 5755-5762 (1977)

16 G. R. Barsch and J. A. Krumhansl, Phys. Rev. Let., 53, p. 1690, (1984)

17 N. Metropolis, A. W. Rosenbluth, M. N. Rosenbluth, A. H. Teller, E. Teller,
     J. Chem. Phys., 21, p. 1087, (1953)

18 A. F. Voter and S. P. Chen, Mat. Res. Soc. Proc., p. 3997, (1986).

19 Y. Zhao, P. C. Clapp and J. A. Rifkin - to be published, see also ref. (11)

20 M. S. Daw and M. I. Baskes, Phys. Rev. B29, p. 6443, (1984)

21 S. A. Meguid, "Engineering Fracture Mechanics", Elsevier Applied Science, London (1989)

22 A. G. Evans and R. M. Cannon, Acta Metall., 34, p. 761, (1986)

Author Index

Subject Index